Vol. 45 No. 3 (2024)

ARCHIVES OF THERMODYNAMICS

ISSN: 1231-0956
ISSN: 2083-6023 (Online)

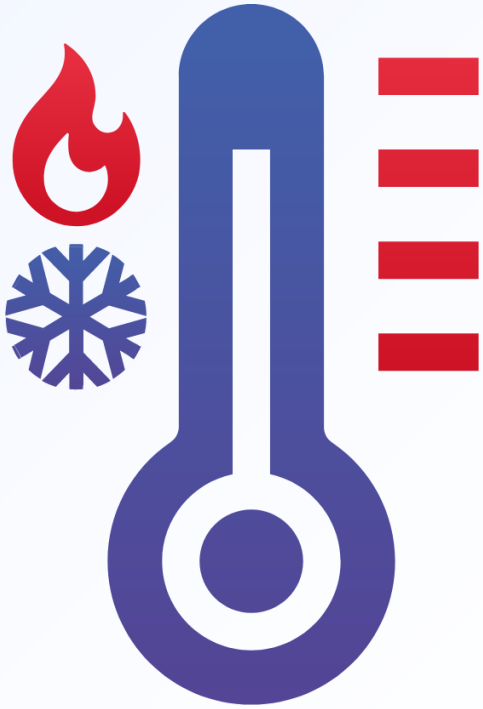

Co-published by

Institute of Fluid Flow Machinery
Polish Academy of Sciences

Committee on Thermodynamics and Combustion
Polish Academy of Sciences

WYDAWNICTWO IMP PAN

Aims and Scope

The aim of the quarterly journal Archives of Thermodynamics (AoT) is to disseminate knowledge between scientists and engineers worldwide and to provide a forum for original research conducted in the field of thermodynamics, heat transfer, fluid flow, combustion and energy conversion in various aspects of thermal sciences, mechanical and power engineering. Besides original research papers, review articles are also welcome.

The journal scope of interest encompasses in particular, but is not limited to:

- Classical and extended non-equilibrium thermodynamics
- Thermodynamic analysis including exergy
- Thermodynamics of heating and cooling
- Thermodynamics of nuclear power generation
- Thermodynamics in defence engineering
- Advances in thermodynamics
- Experimental, theoretical and numerical heat transfer
- Thermal and energy system analysis
- Renewable energy sources including solar energy
- Secondary fuels and fuel conversion
- Heat and momentum transfer in multiphase flows
- Nanofluids
- Energy transition
- Advanced energy carriers
- Energy storage and efficiency
- Energy in buildings
- Hydrogen energy
- Combustion and emissions
- Turbomachinery
- Thermal and energy system analysis
- Integrated energy systems
- Distributed energy generation
- Thermal incineration of wastes
- Waste heat recovery.

Vol. 45 No. 3 (2024)

ARCHIVES OF THERMODYNAMICS

ISSN: 1231-0956
ISSN: 2083-6023 (Online)

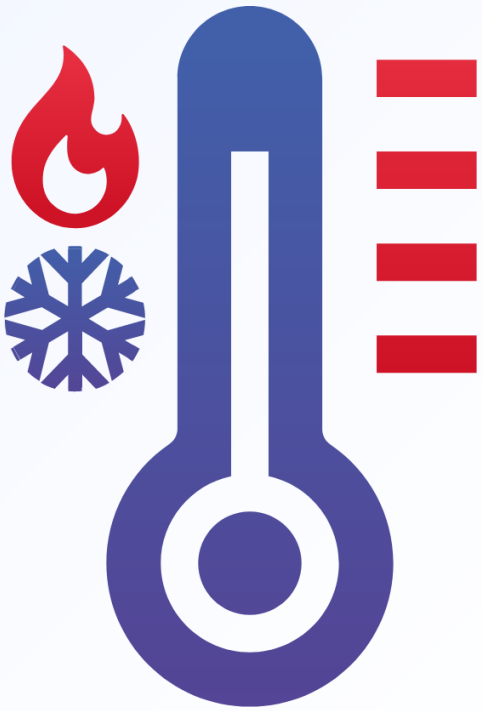

Co-published by

Institute of Fluid Flow Machinery
Polish Academy of Sciences

Committee on Thermodynamics and Combustion
Polish Academy of Sciences

WYDAWNICTWO IMP PAN

Editorial Office
IMP PAN Publishers
Institute of Fluid Flow Machinery, Fiszera 14, 80-231 Gdańsk, Poland,
Phone: (+48) 58-341-12-71 int. 230, e-mail: redakcja(at)imp.gda(.)pl
https://www.imp.gda.pl/archives-of-thermodynamics/
Journals PAS – Electronic Library Polish Academy of Sciences
https://journals.pan.pl/ather

Subscription outside Poland
From 2024, Archives of Thermodynamics appear only in electronic version as an open access journal. However, printed archive volumes or issues are still available. The price of a full volume outside Poland is **120 EUR**. The price of a single issue is **30 EUR**. Archived volumes or issues are available on request. Orders should be sent directly to IMP PAN Publishers:
Institute of Fluid-Flow Machinery,
Fiszera 14, 80-231 Gdansk, Poland,
e-mail: redakcja(at)imp.gda.pl or jfrk(at)imp.gda(.)pl or jrybka(at)imp.gda(.)pl.
Payments should be transferred to the bank account of IMP PAN:
IBAN 28 1130 1121 0006 5498 9520 0011 at Bank Gospodarstwa Krajowego; Code SWIFT: GOSKPLPW.

Prenumerata w Polsce
Od 2024, czasopismo ukazuje się tylko w formie elektronicznej otwartej. Osiągalne są jednak wydania papierowe archiwalne. Cena pojedynczego numeru wynosi **50 PLN**. Cena rocznika **200 PLN**. Zamówienia z określeniem numeru (rocznika), nazwiskiem i adresem odbiorcy należy kierować bezpośrednio do Wydawcy:
Instytut Maszyn Przepływowych PAN
ul. Fiszera 14, 80-231 Gdańsk,
e-mail: redakcja(at)imp.gda(.)pl lub jfrk(at)imp.gda(.)pl lub jrybka(at)imp.gda(.)pl.
Wpłaty prosimy kierować na konto Instytutu Maszyn Przepływowych PAN:
nr 28 1130 1121 0006 5498 9520 0011 w Banku Gospodarstwa Krajowego.

Articles in Archives of Thermodynamics are abstracted and indexed within:
Applied Mechanics Reviews • Arianta • Baidu Scholar • BazTech • Cabell's Directory • Celdes • Chemical Abstracts Service (CAS) – CAplus • CNKI Scholar (China National Knowledge Infrastucture) • CNPIEC • EBSCO (relevant databases) • EBSCO Discovery Service • Elsevier – SCOPUS • ESCI (Emerging Sources Citation Index) • Genamics JournalSeek • Google Scholar • Inspec • Index Copernicus • J-Gate • Journal TOCs • Naviga (Softweco) • Paperbase • Pirabase • POL-index • Polymer Library •Primo Central (ExLibris) • ProQuest (relevant databases) • ReadCube • Referativnyi Zhurnal (VINITI) • SCImago (SJR) • Summon (Serials Solutions/ProQuest) • TDOne (TDNet) • TEMA Technik und Management • Ulrich's Periodicals Directory/ulrichsweb • WorldCat (OCLC)

ISSN 1231-0956
ISSN 2083-6023 (Online)

Publication funding of this journal is provided by resources of the Polish Academy of Sciences and the Institute of Fluid Flow Machinery

Contents

Selected papers from the 25th Jubilee Congress of Thermodynamicists, 11–14 September, Gdańsk, Poland

Other papers

Contents (*cont'd*)

Co-published by
Institute of Fluid-Flow Machinery
Polish Academy of Sciences
Committee on Thermodynamics and Combustion
Polish Academy of Sciences

http://www.imp.gda.pl/archives-of-thermodynamics/

Issues on numerical modelling of transport processes in granular reactive media – an approach with thermal relaxation

Sylwia Polesek-Karczewska[a*], Dariusz Kardaś[a]

[a]Institute of Fluid-Flow Machinery, Polish Academy of Sciences, Fiszera 14, Gdańsk PL 80-231, Poland
*Corresponding author email: sylwia.polesek-karczewska@imp.gda.pl

Received: 14.02.2024; revised: 24.06.2024; accepted: 25.06.2024

Abstract

The steadily growing interest in applying granular media in various novel and advanced technologies, particularly in the energy sector, entails the need to gain in-depth knowledge of their thermal and flow behaviour and develop simulation predictive tools for systems' design and optimisation. The focus of the present study is on the numerical modelling of the thermal decomposition of solid fuel grains in a packed bed while considering a non-classical description of heat transfer in such a medium. The work aims to assess the influence of the relaxation time and thermo-physical properties of the medium on the nature of the solution and highlight the factors that are the source of local non-equilibrium affecting thermal wave speed propagation. The analysis of the predicted temperature distribution was carried out based on the developed transient one-dimensional thermal and flow model, taking into account the moisture evaporation and the devolatilization of fuel particles. Obtained simulation results showed a significant increase in the temperature gradients with increased relaxation times for the case of wet granular bed. They also demonstrated the variable dynamics of thermal wave propagation due to the change in the packed bed structure with the process progress. For a relaxation time of 100 s, a several-fold increase in the temperature signal propagation speed during the fuel bed thermal decomposition was predicted.

Keywords: Reactive media; Granular material; Non-Fourier model; Relaxation time; Hyperbolic equations

Vol. 45(2024), No. 3, 5–12; doi: 10.24425/ather.2024.150450

Cite this manuscript as: Polesek-Karczewska, S., & Kardaś, D. Issues on numerical modelling of transport processes in granular reactive media – an approach with thermal relaxation. *Archives of Thermodynamics*, 45(3), 5–12.

1. Introduction

Granular materials have wide and growing applications in modern technologies, especially in the field of energy systems and devices. As filling porous materials, owing to their structure, they could offer far higher Nusselt numbers, and thereby increased heat transfer rates in the case of laminar flow, compared to non-filled flow spaces [1,2].

Recent advances involve the use of porous materials to enhance heat transfer in energy storage systems, such as shell-and-tube thermal energy storage (TES) units with composites in the form of multiple PCMs with alumina nanoparticles, or cascaded aluminium foam [3], or porous SiC/paraffin composite PCMs [4]. In thermochemical energy storage systems, porous materials are the constituents of composite thermochemical materials [5]. Fluid-saturated porous cavities are also the subject of extensive studies in terms of convection heat transfer in various cooling

Nomenclature

a – thermal diffusivity, m^2/s
$\boldsymbol{A}$, $\boldsymbol{B}$ – matrices of coefficients
c – specific heat, J/(kg K)
$\boldsymbol{c}$ – vector of source terms
h – enthalpy, J/kg
p – pressure, Pa
$\boldsymbol{q}$ – heat flux, W/m^2
R – particle diameter, m
t – time, s
T – temperature, K
V – velocity, m/s
$w^{(1)}$, $w^{(2)}$ – variables
x – space coordinate, m
$\boldsymbol{y}$ – vector of unknowns

Greek symbols

ρ – density, kg/m^3
λ – thermal conductivity, W/(m K)
σ – Stefan-Boltzmann constant, 5.67×10^{-8} $W/(m^2 K^4)$
ξ – wave propagation speed, s
θ – relaxation time, s

Subscripts and Superscripts

c – conduction
g – gas
r – radiation
s – solid
sg – solid to gas
w – water
wg – water to gas
0 – initial

Abbreviations and Acronyms

PCM – phase change materials
TES – thermal energy storage

applications in the area of electronics, solar and nuclear energy systems, or heat exchangers [6]. In addition, granular packed beds serve as the adsorption media in refrigeration devices [7]. Furthermore, axially graded porous materials have gained an interest in the context of cooling systems, where not only the required temperature but also its uniformity in the medium is of concern [8]. Following the efforts towards sustainable development through energy saving, pollution reduction, and the use of available alternative biogenic fuels, the common have become porous burners [9], which due to enhanced heat transfer ensures more efficient and stable combustion, and thus enables the combustion of low-grade fuels with low pollutant emission levels. Along with this, porous materials have also been considered in the context of direct-contact heat exchangers for flue gas heat recovery [10]. Therefore, modelling heat transfer in such media becomes one of the key aspects in predicting the performance of energy-efficient systems. This also refers to various technologies of thermal conversion of solid fuels. The description of transient heat transport in granular media such as reactive packed beds is a difficult issue due to all heat transport mechanisms being involved and the variability of the particle structure during the material physicochemical transformations that accompany its thermal conversion. During the process, the particles change shape, can swell, shrink, and fragment, but above all their porosity changes. These changes in structure significantly affect the dynamics of gas flow through the bed and its diffusion in the particles themselves, and thus the efficiency of phase transitions and chemical reactions. This may cause large local temperature differences between the solid and gas phases, reaching in the case of high-temperature processes even several hundred degrees [11]. Numerical analyses indicate that even for particles of relatively small size, with a diameter of a few millimetres, the predicted heating times of the particles when taking into account the intra-particle convection of water vapour and released pyrolysis gases are longer compared to the case with no convection accounted for [12]. Due to non-uniform porosity distribution in packed beds of fuel particles, this effect can lead to local thermodynamic non-equilibrium.

The classical equilibrium description of transport phenomena in thermal-flow devices, based on Fick's, Newton's and Fourier's laws of gradient type, brings the issues to parabolic equations [13,14]. Their solutions demonstrate an instantaneous change in parameters at any point in the medium (e.g. temperature, pressure) in response to a change in parameters at another point in the medium. This nature of change is due to the assumed infinite speed of signal propagation, which is a non-physical effect. Closer to reality is the non-equilibrium approach, which introduces the hyperbolic-type equations for mass, momentum and heat fluxes. These take into account the relaxation times of the fluxes and thus satisfy the assumption of a non-zero propagation speed of disturbances [15].

Among the works regarding the non-classical, i.e. non-Fourier, description of heat transfer, theoretical analyses dominate. Following the need to account for the complex geometry, different boundary conditions and the variability of thermo-physical parameters, research has largely focused on numerical studies with the use of different solution methods [16]. It shall be noted that the limited number of experimental data in this area [17] significantly hinders the verification of the non-Fourier model predictions, leaving the question of the validity of its applicability to inhomogeneous materials still unresolved.

The literature review indicates that few works are dedicated to the analysis of the application of a non Fourier-type heat conduction model in the mathematical description of thermochemical processes. These include the works on combustion, both experimental [18] and theoretical [19], which point to the non-Fourier model as a more adequate description of heat transfer. This paper thus focuses on the numerical modelling of transport phenomena in a thermally processed reactive granular packed bed. The objective is to demonstrate the effect of variable structure-

related medium properties on the speed of a heat propagation wave. Based on the variant simulation results of a packed bed of solid particles undergoing thermal decomposition, the meaning of a relaxation time in the approach considered is discussed.

2. Modelling heat transfer in granular media

The classical heat conduction model, based on Fourier's law, is considered to sufficiently reproduce the characteristics of the heat transfer process in most engineering issues, also involving granular media when processes are slowly varying and heat pulses are small. However, due to the wave-like nature of the heat transfer [20], also in homogeneous materials, in processes of high dynamics and large thermal pulses, the predictions of the classical heat conduction model deviate significantly from the experimental data. Then, the problem description requires the use of an alternative model, proposed by Cattaneo and Vernotte, defining the heat flux as follows:

$$\boldsymbol{q} + \theta\frac{\partial \boldsymbol{q}}{\partial t} = -\lambda\nabla T, \qquad (1)$$

where λ represents the thermal conductivity of a material, t is the time. Parameter θ is the relaxation time, which is a key factor in the description that determines the delay of heat flux with respect to the temperature gradient. It is a function of the thermodynamic parameters of the medium and, thereby, is a variable quantity. The higher the temperature, the shorter the relaxation time. It is therefore recognised that a non-classical approach to heat transfer (Eq. (1)) should be used when the relaxation time is of an order of characteristic process time. proposed procedure is correct for the class of problems).

Experimental studies regarding granular media indicate much longer relaxation times compared to those reported for gases and solids and are of the order of a few to several seconds [19,21]. The reason behind this is a significant difference in heat transfer patterns through gas and solid phases. In engineering practice (e.g. pyrolysis reactors, gasifiers) the packed bed structure is complex, wherein the fuel particles are of irregular shape sizes with dimensions ranging from millimetres and centimetres. Nevertheless, just to highlight and visualize the possible occurrence of significant local temperature gradients in a two-component (solid/gas) reactive system, an example of non-homogeneous medium of a simplified geometry, heated on one side, may be considered, as illustrated in Fig. 1. The figure shows the temperature (Fig. 1a) and gas (air) flow velocity fields (Fig. 1b) in a chequerboard-type geometry (sized 6 cm × 4 cm) that represent a small section of the granular bed. It is composed of square solid elements (grey fields in Fig. 1b) and voids (closed cavities), each sized 1 cm × 1 cm. Though very simplified, such a case may mimic the densely packed granular (solid/air) bed of fuel particles with high flow resistance, to show the general thermal and flow patterns in such a system. The discussed computational case is two-dimensional and transient. Each element of the domain consisted of 100 cells (10×10). The thermo-physical properties of coal and air were adopted for the solid and voids, respectively. The initial temperature of the domain was set to

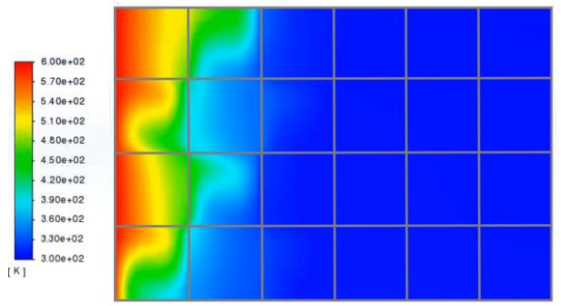

(a)

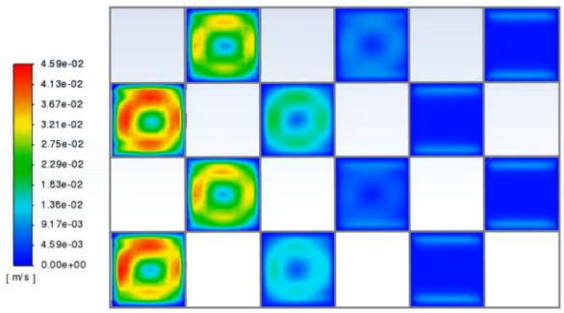

(b)

Fig. 1. Temperature field (a) and gas velocity distribution (b) in heated granular bed – 2D simulation in a simplified chequerboard-type geometry, t = 60 s.

300 K and the stepwise increase of temperature to 600 K at the left boundary of the domain was assumed.

The simulation results displayed in Fig. 1a, showing the parameters' distribution after the 60 seconds of bed heating, clearly indicate the uneven temperature distribution in the packed bed cross-section transverse to the thermal wave propagation, which is due to the difference in thermal behaviour between the phases. As can be observed from the figure, the temperature differences in the granular bed cross-section may exceed 100 K. For the case considered, when comparing temperatures of the upper and bottom sub-layers, these differences may be estimated at ~150 K, 120 K and 70 K, at the cross-lines representing x = 0.5 cm, x = 1 cm, and x = 1.5 cm, respectively. Obviously, the thermal front propagates faster through the solid owing to larger material thermal conductivity as compared to gas medium, leading to more uniform heat transfer through the solid. By contrast, in the cavities, the convective flows are generated as a result of the temperature gradient-induced variations in gas density, as demonstrated in Fig. 1b. In consequence, thermal convection in cavities slows down heat transfer by conduction through the medium. The issue of energy transfer in the granular medium becomes far more complex for a reactive case, when additional intense mass exchange phenomena related to devolatilization, evaporation and chemical reactions, affecting the fluid flow dynamics come into play. Relaxation time as the resultant of these coupled effects depends on the particle diameter, bed porosity and heating rate.

2.1. Thermal wave propagation

The analysis of thermal wave propagation may be reduced to the solution of the energy balance problem while taking into account the equation for the heat flux of relaxation type (Eq. (1)).

In a one-dimensional case, assuming there is no macroscopic gas movement (i.e., for a porous bed with closed pores), the problem reduces to a system of equations:

$$\begin{cases} \rho c \frac{\partial T}{\partial t} + \frac{\partial q}{\partial x} = 0 \\ \theta \frac{\partial q}{\partial t} + \lambda \frac{\partial T}{\partial x} = -q \end{cases}, \tag{2}$$

where ρ and c denote material density and specific heat, respectively. This system of equations for a given vector of unknowns

$$\boldsymbol{y} = \begin{bmatrix} T \\ q \end{bmatrix} \tag{3}$$

may be represented in matrix form [19]

$$\boldsymbol{A}\frac{\partial \boldsymbol{y}}{\partial t} + \boldsymbol{B}\frac{\partial \boldsymbol{y}}{\partial x} = \boldsymbol{c}, \tag{4}$$

where

$$\boldsymbol{A} = \begin{bmatrix} \rho c & 0 \\ 0 & \theta \end{bmatrix}, \boldsymbol{B} = \begin{bmatrix} 0 & 1 \\ \lambda & 0 \end{bmatrix}, \boldsymbol{c} = \begin{bmatrix} 0 \\ -q \end{bmatrix}.$$

Considering the source-free conditions, the analysis of the problem given by Eqs. (3) and (4), and using the method of characteristics, one may arrive at the solution given as

$$\begin{cases} \frac{dw^{(1)}}{dt} = 0 \quad \text{if} \quad \frac{dx}{dt} = \xi \\ \frac{dw^{(2)}}{dt} = 0 \quad \text{if} \quad \frac{dx}{dt} = -\xi \end{cases}, \tag{5}$$

where the variables $w^{(1)}$ and $w^{(2)}$ are defined as

$$\delta w^{(1)} = \delta T + \sqrt{\frac{\theta}{\rho c \lambda}}\delta q, \tag{6}$$

$$\delta w^{(2)} = \delta T - \sqrt{\frac{\theta}{\rho c \lambda}}\delta q. \tag{7}$$

Parameter ξ in Eq. (5) represents the temperature signal propagation speed, which is dependent on the thermo-physical properties of a medium and the relaxation time, and is expressed as:

$$\xi = \sqrt{\frac{\lambda}{\rho c \theta}}. \tag{8}$$

One should note that in the case of non-homogeneous media, parameter λ is an effective quantity ($\lambda = \lambda_{ef}$) that accounts for all mechanisms of heat transfer. The signal propagation speed is therefore influenced by the structure of the packed bed, such as the packing density, additionally affecting the fluid flow characteristics. It is thus related to the thermochemical process type. For instance, measurements regarding large-scale coal carbonisation report the temperature front to propagate through the packed coal layer with the speed of the order of 10^{-6} m/s during the main process stage, which further increases up to the order of 10^{-4} m/s at the end stage owing to largely increased post-devolatilization bed porosity [22,23]. Experimental studies on the combustion of biomass reveal that the propagation speed of the burning front through such beds may vary between ~1×10^{-4} m/s and 5×10^{-4} m/s, depending on the single particle combustion characteristics and bed density [24].

2.2. Integrated model of transport phenomena in a reactive granular bed

The one-dimensional numerical model, developed to simulate the thermal decomposition process of a packed bed of fuel particles was utilised to study the impact of relaxation time and physical parameters of the bed on the predicted dynamics of heat propagation. This model was previously used for simulating the real-scale coal coking process ([22]) and showed good agreement between the predictions and experimental data in terms of the total duration time of fuel decomposition. However, a discrepancy was observed in the temperature profile representing the moisture evaporation stage, which was considered to be due mostly to the simplified model of drying implemented. Having regard to the multiparameter impacts, the focus in the present work is on the effect of the key properties of a packed bed, such as moisture content and porosity, on the thermal wave propagation speed.

The process to be considered involves the packed bed drying and devolatilization stages. The proposed model is composed of balance equations, including mass balance for (i) solid and (ii) moisture released from the fuel, (iii) mass transport for gas mixture, (iv) momentum balance equation for gas mixture, (v) energy balance equation with convection term for packed bed, given as, respectively [22]:

$$\frac{\partial(\varepsilon_s \rho_s)}{\partial t} = -\dot{W}_{sg}, \tag{9}$$

$$\frac{\partial(\varepsilon_w \rho_w)}{\partial t} = -\dot{W}_{wg}, \tag{10}$$

$$\frac{\partial(\varepsilon_g \rho_g v_g)}{\partial x} = \dot{W}_{sg} + \dot{W}_{wg}, \tag{11}$$

$$\frac{\partial(\varepsilon_g \rho_g v_g v_g)}{\partial x} = -\frac{\partial(\varepsilon_g p)}{\partial x} - \frac{\varepsilon_g \mu v_g}{K}, \tag{12}$$

$$\frac{\partial(\rho c T)}{\partial t} + \frac{\partial(\varepsilon_g \rho_g v_g T)}{\partial x} = -\frac{\partial q}{\partial x} - \dot{W}_{sg} h_{sg} - \dot{W}_{wg} h_{wg}. \tag{13}$$

wherein the heat flux is described by the relaxation-type equation

$$q + \theta\frac{\partial q}{\partial t} = -\lambda_{ef}\frac{\partial T}{\partial x}. \tag{14}$$

Parameter ε in Eqs. (9) – (13) represents the volume fraction of the component (phase), and subscripts s, w, g refer to solid, water, and gas, respectively. Source term $\dot{W}_{sg}$ stands for the mass release rate due to thermal decomposition (devolatilization) and is described through Arrhenius law, whereas $\dot{W}_{wg}$ denotes the evaporation rate that is defined using a simplified approach [25], and p is the pressure. Quantities μ and K stand for fluid viscosity

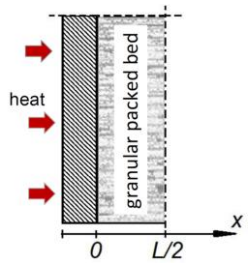

Fig. 2. A schematic representation of the considered one-dimensional problem of transport processes in reactive granular packed bed; L – total width of the bed layer.

and packed bed permeability. The bed is assumed to be isotropic, wherein the properties are averaged in the control volume. Thermo-physical properties of the packed fuel bed, i.e. density (ρ), specific heat (c) and thermal conductivity (λ_{ef}) are the effective properties resulting from the fractions of solid, gas, and moisture. In addition, as regards the thermal conductivity, both, conduction (λ_c) and radiation through the bed voids (λ_r), were taken into account [22]. For the purpose of the analysis, the data of air were adopted for the gas mixture. The properties of gas and solid are summarised in Table 1.

The case of a layer (L) of granular packed bed heated on both sides is considered. Assuming the process to be symmetric, the simulations were performed for the half-width of the considered packed bed, i.e. the calculation domain was $0 \le x \le L/2$ (Fig. 2). The initial conditions were as follows:

$$T(x,0) = T_0, \tag{15}$$

$$p(x,0) = p_0, \tag{16}$$

$$v_g(x,0) = 0, \tag{17}$$

$$\varepsilon_s(x,0) = \varepsilon_{s,0}, \tag{18}$$

$$\varepsilon_w(x,0) = \varepsilon_{w,0}. \tag{19}$$

The assumed boundary conditions include the values for temperature, evolved gas velocity and pressure, respectively:

$$T(0,t) = f(t), \quad \left.\frac{\partial T}{\partial x}\right|_{(L/2,t)} = 0, \tag{20}$$

$$v_g(0,t) = 0, \quad \left.\frac{\partial v_g}{\partial x}\right|_{(L/2,t)} = 0, \tag{21}$$

$$p(L/2,t) = p_0. \tag{22}$$

Function $f(t)$ in boundary conditions (Eq. (20)) represent the time-varying temperature at $x = 0$, adopted from measurements [22,23].

The problem was solved partly implicitly. The mass and momentum equations were solved using explicit schemes, while an unconditionally stable implicit Crank-Nicolson algorithm was used to solve the energy equation. Further details of the model, including the numerical schemes used, can be found in the previous work [22].

Table 1. Thermo-physical properties adopted for simulation.

Parameter	Value	Ref.
$\varepsilon_{s,0}$	0.55	
ρ_s [kg/m³]	$\rho_s = \rho_s(T)$	[26]
c_s [J/(kg K)]	$c_s = c_s(T)$	[27]
ρ_g [kg/m³] c_g [J/(kg K)] μ_g [Pa s] λ_g [W/(m K)]	(air, approximation of tabulated data) $\rho_g = \rho_g(T)$ $c_s = c_s(T)$ $\mu_g = \mu_g(T)$ $\lambda_g = \lambda_g(T)$	[22]
K [m²]	5.0×10^{-11}	
λ_{ef} [W/(m K)]	$\lambda_{ef} = \lambda_{ef}(T) = \lambda_c(T) + \lambda_r(T)$, $\lambda_c(T) = 0.0031\exp(0.063T) + +\varepsilon_w\rho_w$, $\lambda_r(T) = 4\sigma ReT^3$	[22], [26], [28]
ρ_w [kg/m³]	1000.0	
c_w [J/(kg K)]	4200.0	
h_{wg} [J/kg]	2200.0×10^3	
h_{sg} [J/kg]	200.0×10^3	[29]

3. Results and discussion

The variant simulations were performed to demonstrate the effect of packed bed properties, such as initial moisture content and porosity on the nature of solution and thermal front propagation speed, depending on the assumed relaxation time. Following previous studies [22], the relaxation time of 900 s was adopted as the maximum value considered. Furthermore, it shall be noted that simulation results regarding thermal behaviour of a spherical porous fuel particle undergoing decomposition in a hot gas stream indicate its heating times to be of the order of tens of seconds [12]. The mentioned study revealed that the outflow of released moisture and gas from the grain interior greatly contributes to slowing down the dynamics of its heating and decomposition. The characteristic process times for less porous particles are longer due to higher flow resistance. For instance, in the case of a 3 mm wet coal particle with a uniform thermal boundary condition at its surface and the intraparticle gas convection accounted for, the predicted heating time is around 60 s, whereas in the case of the same size wet biomass particle (far more porous) it is more than twice as short (~26 s). One may expect these times to be larger when considering the three-dimensional nature of transport processes and associated non-uniform particle surface heating in a granular packed bed.

In Fig. 3 the time-varying temperature evolution in reactive moist granular bed (ε_w=0.08, Fig. 3a) is compared with that for dry granular bed (Fig. 3b). In both bed cases, two significantly

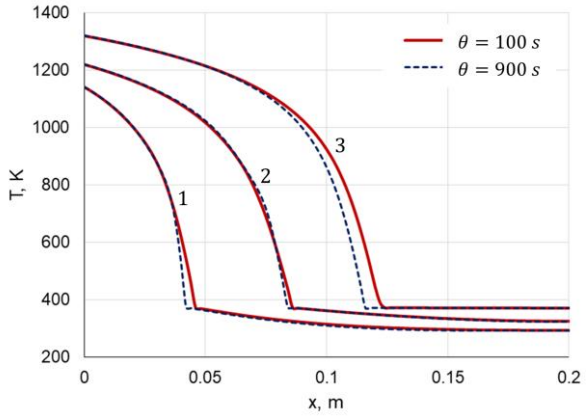

(a)

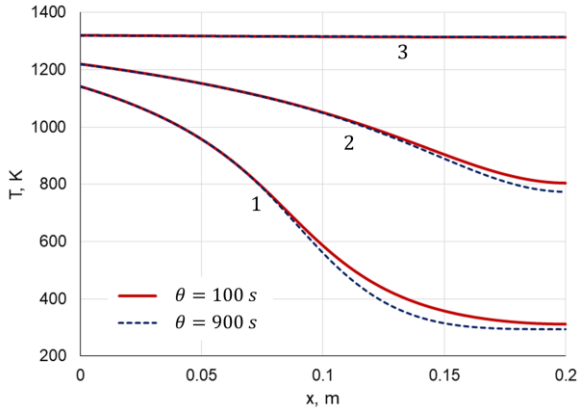

(b)

Fig. 3 An effect of moisture content on the propagation speed of thermal front in reactive granular bed (half of the medium) with initial porosity of ε_g = 0.45, for different relaxation times, θ = 100 s (solid line) and θ = 900 s (dashed line): a) ε_w=0.08, b) ε_w=0 (dry fuel); 1 – t = 1.8 h, 2– t =5.4 h, 3 – t =14.4 h

different relaxation times are taken into account, i.e. θ = 100 s and θ = 900 s. The simulation results show similar trends for both packed beds as regards the effect of relaxation time. Namely, for lower relaxation time the thermal front propagates through the granular medium faster than for the larger one. As expected, however, a considerable difference is observed in heating dynamics between wet and dry medium. In the case of a moist bed, there is a delay pronounced in the temperature increase above 373 K that is due to the thermal energy consumption for moisture evaporation. Unlike for the dry bed case, the results demonstrate a thermal front clearly separating the heated medium part from the cooler one. In other words, for the wet medium, the temperature gradients (dT/dx) are larger. As a consequence, the difference between temperatures predicted for different relaxation times may reach hundreds of degrees. This may be seen in the case of simulated temperature curves for the process duration time of 14.4 hours (curves marked with 3, Fig. 3a), wherein the difference between predictions obtained for considered relaxation times at the distance of approx. x = 0.12 m from the heated boundary (x = 0) exceeds 200 degrees. For the dry

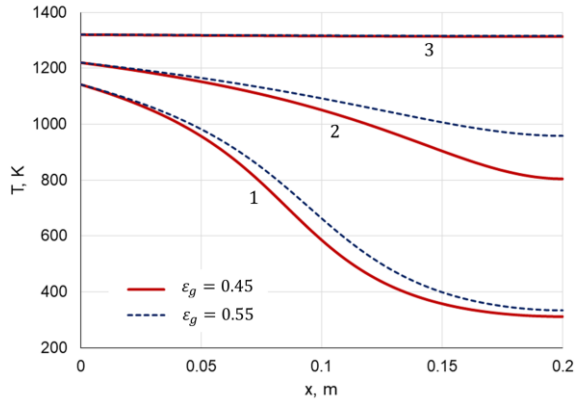

Fig. 4. An effect of initial porosity, ε_g = 0.45 (solid line) and ε_g = 0.55 (dashed line), on the propagation speed of thermal front in reactive granular packed bed, ε_w=0, θ = 100 s; 1 – t = 1.8 h, 2– t =5.4 h, 3 – t =14.4 h.

bed case, characterized by a less sharp thermal front, these differences are far below 100 degrees, as displayed in Fig. 3b.

The model predictions indicated a quite significant impact of porosity (gas volume fraction) on the heat front propagation speed. The time–varying temperature distribution in dry packed granular bed (ε_w = 0) for different porosities, 0.45 and 0.55, and relaxation time of 100 s, are depicted in Fig. 4. As can be seen, heat propagates faster in the less dense packed bed, i.e. of larger porosity, owing to an increased contribution of radiation through the inter-particle voids. Furthermore, the differences in the temperature evolutions between granular beds differing in porosities increase with time, which clearly reveals the influence of variable structure-related bed properties. Nevertheless, these differences are smaller than those observed for temperature distributions, when water phase transition (moisture evaporation) comes into play, as shown in Fig. 3a (curves no. 3). The global effect of variable bed properties on the thermal wave propagation speed can be demonstrated by the analysis of a change in thermal diffusivity term ($a = \lambda/(\rho\, c)$) during the process. Figure 5 presents the variation of thermal diffusivity in time along the

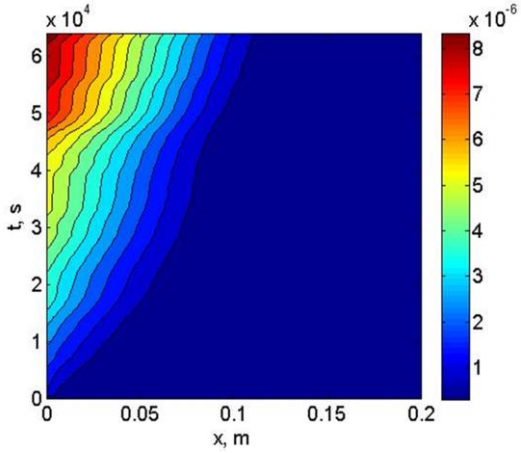

Fig. 5. The predicted change of thermal diffusivity ($a = \lambda/(\rho\, c)$) in wet granular bed undergoing thermal decomposition, ε_g=0.45, ε_w=0.08, θ = 100 s.

packed bed layer of initial moisture content of 8%vol. and porosity of 0.45 during its thermal decomposition. As can be seen from the figure, the *a* value is below 1×10^{-6} m^2/s in the cool unreacted part of a packed bed. As the process of decomposition proceeds, the thermal diffusivity increases by several times with the temperature rise and related change in the bed structure, reaching the value of over 8×10^{-6} m^2/s at the end stage of the process. This corresponds with a nearly fivefold increase in the temperature signal propagation speed, i.e. from ~ 0.7×10^{-5} to ~ 2.7×10^{-5} m/s, respectively.

4. Conclusions

In the paper, the non-classical approach was used to describe heat transfer in the reactive granular bed. Based on the predictions of the developed thermal and flow model that involves the relaxation-type (non-Fourier) heat conduction equation, the impact of the bed properties, including moisture content and porosity, on the thermal wave propagation speed through the medium was discussed. The simulation results served to indicate the role of a non-classical approach in the modelling of transport processes in reactive media of non-homogeneous inner structure. The obtained numerical results showed the dominant impact of moisture on slowing down heat propagation in the packed bed, leading to an increase in local temperature gradients.

The relaxation time accounted for in the developed one-dimensional model is a parameter that involves the coupled effects contributing to the change in energy flow direction in the interparticle voids, and thereby, to the delay in heat conduction in the medium. In this sense, the estimated value of relaxation time is affected by a degree of mathematical model simplification and, in particular, whether it accounts for the microscale effects of mass transfer. As regards the thermal processing of fuel particles, the precise determination of this characteristic time would require the detailed analysis of particle heating and devolatilization under a temperature gradient field. This would involve the use of mesoscale models enabling to map the interphase surface, as well as their experimental verification.

References

[1] Targui, N., & Kahalerras, H. (2008). Analysis of fluid flow and heat transfer in a double pipe heat exchanger with porous structures. *Energy Conversion and Management*, 49, 3217–3229. doi:10.1016/j.enconman.2008.02.010

[2] Wang, B., Hong, Y., Hou, X., Xu, Z., Pengfei Wang, P., Fang, X., & Ruan, X. (2015). Numerical configuration design and investigation of heat transfer enhancement in pipes filled with gradient porous materials. *Energy Conversion and Management*, 105, 206–215. doi: 10.1016/j.enconman.2015.07.064

[3] Mahdi, J.M., Mohammed, H.I., Hashim E.M., Talebizadehsardari, P., & Nsofor, E.C. (2020). Solidification enhancement with multiple PCMs, cascaded metal foam and nanoparticles in the shell-and-tube energy storage system. *Applied Energy*, 257, 113993. doi: 10.1016/j.apenergy.2019. 113993

[4] Song, Y., Xu, Q., Liu, X., Xuan Y., & Ding,Y. (2022). High-performance thermal energy storage and thermal management via starch-derived porous ceramics-based phase change devices. *International Journal of Heat and Mass Transfer*, 197, 123337. doi: 10.1016/j.ijheatmasstransfer.2022.123337

[5] Deka, P., & Szlęk, A. (2022). Thermal energy storage in buildings: Opportunities and challenges. *Archives of Thermodynamics*, 43(4) 21–61. doi: 10.24425/ather.2022.144405

[6] Messaoud, H., Adel, S., & Ouerdia, O. (2023). Mixed convection heat transfer of a nanofluid in a square ventilated cavity separated horizontally by a porous layer and discrete heat source. *Archives of Thermodynamics*, 44(2) 87–114. doi: 10.24425/ather.2023. 146560

[7] Janusz, Sz., Szudarek, M., Rudniak L., & Borcuch, M. (2023). Mixed convection heat transfer of a nanofluid in a square ventilated cavity separated horizontally by a porous layer and discrete heat source. *Archives of Thermodynamics*, 44(2), 177–194. doi: 10.24425/ather.2023.146564

[8] Bai, X., Zheng, Z., Liu, C., & Nakayama, A. (2022). Achievement of wall temperature uniformity by axially graded porous materials. *International Journal of Heat and Mass Transfer*, 197, 123335. doi: 10.1016/j.ijheatmasstransfer.2022. 123335

[9] Fierro, M., Mayne, G., & Toledo, M.. (2023). Second stage porous media burner for syngas enrichment. *International Journal of Hydrogen Energy*, 48(51), 19450–19458. doi: 10.1016/j.ijhydene. 2023.02.023

[10] Wei, H., Huang, S., & Zhang, X.. (2022). Experimental and simulation study on heat and mass transfer characteristics in direct-contact total heat exchanger for flue gas heat recovery. *Applied Thermal Engineering*, 200, 117657. doi: 10.1016/ j.applthermaleng.2021.117657

[11] Kardaś, D., Kluska, J., & Kazimierski, P. (2018). The course and effects of syngas production from beechwood and RDF in updraft reactor in the light of experimental tests and numerical calculations. *Thermal Science and Engineering Progress*, 8, 136–144. doi: 10.1016/j.tsep.2018.08.020

[12] Wardach-Święcicka, I., & Kardaś, D. (2021). Modelling thermal behaviour of a single solid particle pyrolysing in a hot gas flow. *Energy*, 221, 119802. doi: 10.1016/j.energy.2021.119802

[13] Bilicki, Z. (2001). Extended thermodynamics of irreversible processes and thermodynamics of internal parameters. In: *Modern trends in thermodynamics*, 49–80, IFFM PASc. Publishers, Gdańsk (in Polish).

[14] Jou, D., Casas-Vazquez, J., & Lebon, G. (2010). *Extended irreversible thermodynamics*, Springer.

[15] Mikielewicz, J. (1995). *Modelling of thermal and flow processes* (Series: Maszyny Przepływowe, vol. 17). Ossolineum, Wrocław (in Polish).

[16] Rahideh, H., Malekzadeh, P., & Golbahar Haghighi, M.R. (2011). Non-Fourier heat conduction analysis with temperature-dependent thermal conductivity. *ISRN Mechanical Engineering*, 321605. doi: 10.5402/2011/321605

[17] Vadasz, P., & Carsky, M. (2012). Thermal resonance in hyperbolic heat conduction in porous media due to periodic Ohm's heating. *Transport in Porous Media*, 95, 507–534. doi: 10.1007/s11242-012-0059-0

[18] Chao, C.Y.H., Wang, J.H., & Kong, W. (2004). Effects of fuel properties on the combustion behaviour of different types of porous beds soaked with combustible liquid. *International Journal of Heat and Mass Transfer*, 47, 5201–5210. doi: 10.1016/j.ijheatmasstransfer.2004.07.004

[19] Antaki, P.J. (1998). Importance of nonfourier heat conduction in solid-phase reactions. *Combustion and Flame*, 112, 329–341. doi: 10.1016/S0010-2180(97)00131-4

[20] Tzou, D.Y. (1997). *Macro- to microscale heat transfer*. Series in Chemical and Mechanical Engineering, Taylor& Francis.

[21] Roetzel, W., Putra, N., & Das, S.K. (2003). Experiment and analysis for non-fourier conduction in materials with a non-homogeneous inner structure. *International Journal of Thermal Science*, 42, 541–552. doi: 10.1016/S1290-0729(03)00020-6

[22] Polesek-Karczewska, S., Kardaś, D., Wardach-Święcicka, I., Grucelski, A., & Stelmach, S. (2013). Transient one-dimensional model of coal carbonization in stagnant packed bed. *Archives of Thermodynamics*, 34(2) 39–51. doi: 10.2478/aoter-2013-0009

[23] Nomura, S., & Arima, T. (2000). Coke shrinkage and coking pressure during carbonization in a coke oven. *Fuel*, 79(13), 1603–1610. doi: 10.1016/S0016-2361(00)00018-1

[24] Polesek-Karczewska, S., Turzyński, T., Kardaś, D., & Heda, Ł. (2018). Front velocity in the combustion of blends of poultry litter with straw. *Fuel Processing Technology*, 176, 307–315. doi: 10.1016/j.fuproc.2018.03.040

[25] Kardaś, D., Kluska, J., & Polesek-Karczewska, S. (2014). *Introduction to problems of biomass gasification*. IFFM PASc. Publishers, Gdańsk, 2014. (in Polish).

[26] Stelmach, S., Kardaś, D., & Polesek-Karczewska, S. (2011). Experimental verification of the non-Fourier model of heat transfer within coke oven charge. *Karbo*, 3, 156–165. (in Polish).

[27] Merrick, D. (1983). Mathematical models of the thermal decomposition of coal: Specific heats and heats of reaction. *Fuel*, 62, 540–546. doi: 10.1016/0016-2361(83)90223-5

[28] Siegel, R., & Howell, J. (1992). *Thermal radiation heat transfer*. Taylor Francis, London.

[29] Ściążko, M. (2010). *Models of coal classification in a thermodynamic and kinetic approaches*. AGH University Press, (Rozprawy. Monografie, No. 210), Kraków (in Polish).

Co-published by
Institute of Fluid-Flow Machinery
Polish Academy of Sciences
Committee on Thermodynamics and Combustion
Polish Academy of Sciences

http://www.imp.gda.pl/archives-of-thermodynamics/

Understanding of RANS-modelled impinging jet heat transfer trough turbulence kinetic energy, momentum and energy budgets

Sebastian Gurgul[a], Elzbieta Fornalik-Wajs[a*]

[a]AGH University of Krakow, Al. Mickiewicza 30, Krakow 30-059, Poland
*Corresponding author email: elzbieta.fornalik@agh.edu.pl

Received: 09-05-2024; revised: 20-06-2024; accepted: 21-06-2024

Abstract

Impinging jets are one of the most effective techniques of heat transfer intensification, therefore they are continuously applied in various engineering areas. On the other hand, a numerical modelling of complex phenomena contributing to an overall heat transfer effect (and the Nusselt number value) is still not sufficient and suffers from lack of generalization. The extensive studies have been conducted to unify approach to the impinging jet modelling and construct the model (in Ansys Fluent software), which allows mirroring of the results. Presented work discusses differences in representation of impinging jet between various turbulence models based on the turbulence kinetic energy, momentum and energy budgets. It allows deep understanding of influence of geometrical and flow parameters on fluid mechanics phenomena interaction and final effect. The most significant results are connected with linking of Nusselt number distribution with analyzed budgets' terms. Each term contributes to the distribution and cannot be omitted. Drawn conclusions explain the origin of reported in literature differences and includes suggestions, how to evaluate the Nusselt number distribution results coming from various turbulence models. At this stage of research to have a complete image of relation between the particular quantities budgets and heat transfer effect it is suggested to consider also the turbulence kinetic energy dissipation budget, which will fil opened by this research gap.

Keywords: Round impinging jet; Turbulence kinetic energy budget; Momentum budget; Energy budget; Nusselt number

Vol. 45(2024), No. 3, 13–30; doi: 10.24425/ather.2024.150451

Cite this manuscript as: Gurgul, S., & Fornalik-Wajs, E. (2024). Understanding of RANS-modelled impinging jet heat transfer trough turbulence kinetic energy, momentum and energy budgets. *Archives of Thermodynamic*s, 45(3), 13–30.

1. Introduction

Turbulent round jet impingement has been studied for a long time. However, due to its complexity and high heat transfer performance, this phenomenon still attracts the attention of researchers and is a subject of both numerical and experimental studies [1]. The description of this process is influenced by various factors such as the Reynolds number, the Prandtl number, the nozzle-to-impingement-plate distance ratio (H/D), the nozzle shape, the inlet velocity profile, and many others [1–4], whose make it challenging to compare the results from different studies [5]. Numerical analysis of jet impingement can be carried out using direct numerical simulation (DNS), large eddy simulation (LES), or Reynolds averaged Navier-Stokes (RANS) approach. The first two methods provide insight into the physics of the process but are computationally expensive compared to

Nomenclature

C_P – specific heat capacity, J/(kg K)
D – inlet diameter, m
f – elliptic relaxation function
H – nozzle-to-impingement-plate-distance, computational domain height, m
H/D – nozzle-to-impingement-plate-distance to inlet diameter ratio
k – turbulence kinetic energy, m^2/s^2
Nu – Nusselt number
P – average pressure, Pa
Pr – Prandtl number
$\dot{q}$ – wall heat flux, W/m^2
Re – Reynolds number
S – strain rate tensor, 1/s
T – average temperature, K
T_{in} – reference inlet temperature, K
T_w – local wall temperature, K
$\overline{u_i u_j}$ – Reynolds stress term, m^2/s^2
U – average radial velocity, m/s
$|U|$ – average inlet velocity, m/s
U_i, U_j – average velocity components, m/s
$\overline{v^2}$ – velocity fluctuation
V – average axial velocity, m/s
x – radial coordinate, m
x_i, x_j – Cartesian coordinates, m
x/D – radial coordinate to inlet diameter ratio
y – axial coordinate, m
$y+$ – dimensionless distance from the wall

Greek symbols

α – heat transfer coefficient, W/(m^{2}K)
α_k – inverse effective Prandtl number
β^* – model constant
γ – intermittency
ε – turbulence dissipation rate, m^2/s^3
λ – thermal conductivity, W/(m K)
μ – dynamic viscosity, Pa s
μ_{eff} – effective viscosity, Pa s
μ_t – turbulent viscosity, Pa s
$\overline{u_j\theta}$ – turbulent heat flux, Km/s
ρ – density, kg/m^3
σ_k, σ_t – turbulent Prandtl number
ω – specific turbulent dissipation rate, 1/s
Ω – magnitude of the vorticity rate, 1/s

Subscripts and Superscripts

E – energy equation
k – turbulence kinetic energy equation
M – momentum equation

Abbreviations and Acronyms

CONV – convection term
DIFF – diffusion term
DISS – dissipation term
DNS – direct numerical simulation
LES – large eddy simulation
PRESS – pressure term
PROD – production term
RANS – Reynolds averaged Navier-Stokes
RNG – renormalisation group
RS – Reynolds stress term
SST – shear stress transport
TDIFF – turbulent diffusion term
TKE – turbulence kinetic energy
UDF – user-defined function

the last one [1]. The third method is more suitable from an engineering perspective, where turbulent flow is more common, and it is a valuable tool for analyzing and predicting heat transfer performance [1]. Despite many research efforts in this field, there are still discrepancies in predicting the local Nusselt number distribution numerically, especially in the position of its secondary maximum [6,7].

According to Kořínek et al. [8], the resolution of near-wall mesh significantly affected the heat transfer of the round jet impingement when using scale-resolving-simulation methods. They found that mesh refinement in the longitudinal direction is more crucial than in the perpendicular direction. Furthermore, they observed that grid refinement was particularly beneficial for LES and DES (detached eddy simulation) calculations when dealing with cases of low nozzle-to-plate distance. The paper by Domino and Wenzel [9] described the results of DNS calculations for a series of non-isothermal turbulent impinging jet configurations. The simulations showed an increase in radial mixing as the jet temperature increased. Regions of large negative production of turbulence kinetic energy were noted to be a function of the difference between the axial and radial normal stresses, with crucial inflection points occurring where their magnitudes changed. A large recirculation structure was evident in all simulations, highlighting a faster mixing of nest-like structures at the higher nozzle-to-impingement-plate-distance ratio. Magagnato et al. [4] conducted DNS calculations to examine the impact of the Prandtl number on the heat transfer of a circular impinging jet. In this study, the temperature field was considered as a passive scalar. The study confirmed that the Prandtl number affects the value of the Nusselt number at a fixed Reynolds number. The distribution of the Nusselt number along the plate exhibited similar features at different Prandtl numbers and showed a characteristic secondary maximum for both analyzed Reynolds numbers (5 300 and 10 000) at Pr = 0.025 and Pr = 0.01. Huang et al. [10] developed a turbulence model for jet impingement heat transfer based on the k–ω SST (shear stress transport) turbulence model, which considered the effects of the cross-diffusion term and the Kato-Launder model. The modified model agreed well with the cases studied and overcame the false sec-

ondary Nusselt number maximum (not observed in the experimental studies) at a high nozzle-plate spacing for slot jets, which the standard k–ω SST turbulence model predicted. The study indicated that the pressure gradient played an essential role in turbulent slot impinging jet, and the effect of the cross-diffusion term should be taken into account in the boundary layer. Developed shear stress transport (SST) model was used by Zhang et al. [11] to simulate turbulent round jet impingement heat transfer. The model included an additional switching function for cross-diffusion correction, which provided accurate results in terms of heat transfer by capturing the closest first maximum, local minimum, and secondary maximum compared to other models, except for problems at low nozzle-plate spacing. The inner maximum at the stagnation point was linked to the radial pressure gradient, Therefore reinforcing sensitivity to pressure in a turbulence model can help to improve the prediction of heat transfer characteristics. The paper by Huang et al. [12] discussed a modification of the k–ω SST model for swirling impinging jets, specifically the SST model with curvature correction (SSTCC) and the modified SST model using the cross-diffusion term (SSTCD). They noticed that the SSTCC model might falsely enhance the effect of swirl/streamline curvature compared to the experimental results. However, the effect of curvature correction could be ignored downstream, leading to a similar performance of the SSTCC and SST models. The authors concluded that the SSTCD model significantly improves the SST model to predict heat transfer in the flows demonstrated in the paper. Menzler et al. [6] evaluated the Ansys GEKO turbulence model for its ability to determine the local and integral Nusselt number of an impinging jet. The GEKO (generalized k-ω) turbulence model has some parameters that can be adjusted. The authors achieved an accuracy of about 10% in the prediction of the local Nusselt number, while adjusting those parameters, but the limits of the recommended parameters were exceeded. The study by Chitsazan et al. [2] presented the results of numerical simulations of a single impinging round jet using different numerical parameters. The researchers compared the results of different implementations of the k–ω SST model, identifying the low Reynolds number damping modification (correction of turbulent viscosity) as essential to predict the secondary maximum. The study was concluded that good results could be achieved with a coarse grid if the boundary region is resolved adequately. Moreover, polyhedral grids lead to good quality results with lower memory requirements, cell numbers, and shorter run times than other cell shapes. The quality of results obtained for various shapes of the elements was similar to that of polyhedral grids. Huang et al. [13] investigated the effects of roughness on heat transfer and flow structures for round jet impingement using the shear stress transport model with the transition model. The study showed that roughness enhanced heat transfer by 2.53% to 6.08% compared to a smooth surface, but this enhancement is nonmonotonic due to changes in the secondary maximum of heat transfer. Increasing roughness height enhanced turbulent intensity and led to an early occurrence of the secondary heat transfer maximum, which is crucial for heat transfer augmentation. Kaewbumrung and Plengsa-Ard [14] examined a single air jet impingement at a constant temperature, employing different RANS turbulence models ($\overline{v^2} - f$ and four Reynolds stress turbulence models) to compare with published measurement data. The focus was on the secondary maximum of the Nusselt number, which was clearly generated using the ratio of H/D = 2. The $\overline{v^2} - f$ model was found to have better numerical precision in analysis of the local Nusselt number and velocity profiles. The first maximum of the Nusselt number location was observed at 0.5 diameter from stagnation point (x/D) due to the change in the radial flow velocity, while a secondary maximum was observed at a radial distance of approximately x/D = 2.05. The study by Siddique et al. [15] aimed to predict the flow pattern and determine the local value of the Nusselt number for varying heat flux input boundary conditions. The research based on the SST + Gamma-Theta turbulence model, successfully captured the turbulence phenomenon of intermittency, flow separation, local velocity gradient, and transition. The findings suggested that the Nusselt number is the least affected by the nozzle-target spacing in the stagnation region because the velocity gradient development was dominated by an impinging jet momentum. However, the development of the velocity gradient on the target surface dominated after the stagnation region. Finally, the dependency of the nozzle-target spacing caused a more significant impact under constant heat flux boundary conditions as a result of the further development of a thermal boundary layer. The experimental study by Kumar et al. [16] referred to the heat transfer characteristics of a free-surface single-phase circular liquid jet impinging on a smooth, flat surface under varying nozzle diameter, nozzle-to-plate spacing, and Reynolds number. The results revealed that the local Nusselt number reached maximum in the stagnation region and decreased downstream. The Nusselt number was found to be a function of the Reynolds number, the Prandtl number, system length, and the Weber number. Comparison of a free surface and a submerged jet exhibited that the heat transfer rate was higher in the case of a submerged jet. Some recent review publications have collected research in various areas of the jet impingement, such as the influence of target surface shape and geometry configuration [1,17], excited jets [17], nanofluids [17–19], single jet impingement [1,19], jet arrays [1,19], swirling jet impingement [19] and synthetic jets [19].

The literature overview reveals a focus on improving heat transfer prediction through the modification or development of existing turbulence models. Additionally, there has been an increase in the number of publications that present DNS analysis, which can provide valuable insight into jet impingement flow and heat transfer physics. Other investigations aimed to enhance heat transfer using various working fluids or target surfaces. In addition to numerous numerical investigations, new experimental studies emerged. According to Barbosa et al. [1], the behavior of geometric and flow parameters in the jet impingement is well understood, but their interactions are complex. Recent studies on the numerical simulation of jet impingement have mainly concentrated on a single jets. The choice of turbulence model plays a crucial role, and based on various studies, the k–ω SST turbulence model has been identified as a reliable and efficient option for accurate modeling of jet impingement while minimizing computing time.

Despite extensive numerical research, it remains challenging to find studies in the literature that attempt to identify, describe, and explain the sources of differences in the heat transfer behavior of various turbulence models. Before modification and development of turbulence models, it is crucial to conduct an analysis that provides a deeper understanding of the physics behind commonly used turbulence models. Such an analysis can be based on turbulence kinetic energy (TKE), momentum, and energy budgets, and it gives valuable insights into the characteristics of these models.

The literature contains several publications that focus on the transport equations and analysis of TKE, which can be broadly classified into two groups. The first group includes studies that rely on DNS and experimental methods, while the second group comprises budgets obtained through RANS calculations. In a DNS study by Domino and Wenzel [9], the TKE values were calculated on the surfaces parallel to the impinged one at three different inlet temperature values. The authors observed that the TKE values increased with increasing inlet temperature, with the maximum value found at $x/D \approx 0.5$. Negative TKE production was noted near the impinged surface at values of $x/D < 6$. The study also showed that the sign of TKE production changed when the axial component of the Reynolds stress surpassed the radial one. An experimental study by Alekseenko et al. [3] was related to a budget of axial momentum and TKE on lines parallel to the impinged surface for conventional and swirling jets. For the momentum budget, the study showed that the viscous term was negligible compared to other terms, and convection was characterized by an almost constant positive value near the jet axis. For the TKE budget, the viscous term, the same as for momentum, was negligible. Maximum magnitudes of dissipation, diffusion of pressure and shear stress production were observed near $x/D \approx 0.5$, corresponding to the region of the mixing layer. The convection term and turbulent diffusion possessed opposite signs, and the production term had local maxima in the mixing regions for all analyzed cases. In two publications by Ries et al. [20,21], DNS numerical analysis and PIV (particle image velocimetry) experimental study were presented. They studied jet impingement on inclined surfaces at 0°, 45° and 90°. The production of TKE was negative in the vicinity of the wall in the stagnation region, and was balanced by pressure-related diffusion rather than viscous dissipation. Molecular and pressure-related diffusion dominated, while dissipation was relatively small. In an experimental study conducted by Nishino et al. [22], the TKE budget was presented. The study exhibited that the negative TKE production occurred near the wall and was compensated by pressure diffusion.

The analysis of TKE, the budget of TKE, and the momentum calculated on the basis of the RANS results can be found in four publications by Kura et al. In the first paper [23], the authors presented the TKE values in two parallel lines: one at the impinged wall and another outside the boundary layer. They noted that only the values inside the boundary layer are meaningful. The TKE values were then compared with the distribution of the local Nusselt number, where inflection points were observed at nearly the exact locations of the Nusselt number maxima. In the second paper [24], the TKE budget obtained by $\zeta - f$ turbulence model was presented to show the difference between various impinged surfaces such as flat, convex, and concave. Additionally, a comparison between momentum budgets by $\zeta - f$ and $\overline{v^2} - f$ turbulence models was presented. In the case of the TKE budget, the authors concluded that the overall trend is the same for all types of surfaces, but the only differences refer to the maximal values and their positions. The momentum budget was prepared on two lines perpendicular to the impinged surface, the first being located at the stagnation zone that begins to decay, and the further where the second Nusselt maximum occurs. The $\overline{v^2} - f$ turbulence model was characterized by a significantly higher momentum diffusion near the wall than the $\zeta - f$ turbulence model. The third investigation [25] compared TKE production and dissipation between different types of target surfaces. The general conclusion was that the tendency was similar, but the highest TKE production was observed in the stagnation zone for the convex case. The last investigation [26] presented a comparison between the TKE budget for two different inlet conditions. Regarding the budget, the authors showed that diffusion and dissipation dominated production and convection ones. The convective term possessed a negative value near the stagnation point and changed its sign near the location of the Nusselt number secondary maxima occurrence. The link between the values and trends of TKE and Nusselt number were pointed out.

Numerical investigations such as the DNS and experimental studies are priceless for understanding the physics of jet impingement, but they are expensive and time-consuming. On the other hand, analysis of the TKE and transport equations based on the RANS calculations may only partially explain this phenomenon, because they are just the models. However, such an analysis can still help to identify why various turbulence models lead to a different tendency of the results in simulating jet impingement and to modify and further develop the RANS turbulence models. Unfortunately, finding a comparative and complex analysis of various turbulence models in the literature that describes and explains the sources of discrepancies in heat transfer results is challenging. There are very few comprehensive analyses, which enable configuration of the numerical model. Therefore, the authors decided to present their research, which fills the gap and meets the need of the readers.

The previous research [27] considered the heat transfer of classic jet impingement. In the numerical studies, 80 different cases were investigated, which included five different turbulence models (k–ε RNG Kato-Launder, k–ω SST Kato-Launder, intermittency transition, transition SST, and $\overline{v^2} - f$), four geometrical configurations described by the dimensionless ratio of H/D (where H is the computational domain height, D is the inlet diameter) such as H/D = 1, 2, 4 and 6, and 4 hydrodynamic parameters defined by the Reynolds number (Re = 10 000, 20 000, 23 000 and 30 000),

$$\mathrm{Re} = \frac{\rho |U| D}{\mu}, \tag{1}$$

where: ρ is the fluid density; $|U|$ is the average inlet velocity, D is the inlet diameter, and μ is the fluid dynamic viscosity.

The study produced valuable findings, including the 80 distributions of local Nusselt number along the heated wall. The local Nusselt number was defined as follows:

$$\mathrm{Nu} = \frac{\alpha D}{\lambda}, \tag{2}$$

$$\alpha = \frac{\dot{q}}{T_w - T_{in}}, \tag{3}$$

where: α is the heat transfer coefficient, D is the inlet diameter, λ is the fluid thermal conductivity, $\dot{q}$ is the wall heat flux, T_w is the local wall temperature, and T_{in} is the reference inlet temperature.

Based on the previous analysis [27], the authors could compare various turbulence models and investigate their features under various geometrical and hydrodynamical conditions and presented systematic analyses with precise definitions of numerical model settings and comparisons with numerous experimental and numerical studies. As a result of the research, three turbulence models, which are the k–ε RNG Kato-Launder, k–ω SST Kato-Launder, and the Intermittency transition model, have been selected. This paper is an extension of previous studies towards the TKE values. Analyses were conducted for the three above-mentioned turbulence models and two geometrical configurations with presentation of the TKE, momentum, and energy budgets. The results are compared with the local Nusselt number distribution. They lead to explanation of differences between turbulence models prediction of heat transfer and formulation of the guidelines for selection of turbulence model suitable for particular research problem. An additional benefit of presented studies is a transparent and easy-to-be reproduced numerical model. It is worth to mention that listing of own function used to calculate diffusion term of momentum and energy equations is included.

2. Mathematical model, geometry, and boundary conditions

Figure 1 shows the geometry and boundary conditions of the 2D axisymmetric model. The justification of the 2D axisymmetric model was based on the numerical analysis of 3D and 2D geometries presented in [27]. In this model, air at a constant temperature of 293 K and a fully developed profile enters the computational domain through the inlet channel. After forming a jet, the air impinged on the bottom wall (heated with a constant heat flux of 1000 W/m^2), then creates a wall jet along the heated surface and escapes the computational domain via the right surface. The air used in the analysis was considered as Newtonian, incompressible fluid with constant thermophysical properties (ρ = 1.225 kg/m^3, C_P = 1006.43 J/(kg K), λ = 0.0242 W/(m K), μ = 1.7894×10^{-5} Pa s). The steady-state analysis involved three transport equations, mass, momentum, and energy [28]:

$$\frac{\partial U_j}{\partial x_j} = 0, \tag{4}$$

$$\rho \frac{\partial (U_i U_j)}{\partial x_j} = -\frac{\partial P}{\partial x_i} + \frac{\partial}{\partial x_j}\left[\mu\left(\frac{\partial U_i}{\partial x_j} + \frac{\partial U_j}{\partial x_i}\right) - \rho\overline{u_i u_j}\right], \tag{5}$$

$$\rho \frac{\partial (U_j T)}{\partial x_j} = \frac{\partial}{\partial x_j}\left(\frac{\lambda}{C_P}\frac{\partial T}{\partial x_j} - \rho\overline{u_j \theta}\right), \tag{6}$$

where: U_i, U_j are the average velocity components, x_i, x_j are the Cartesian coordinates, ρ is the density, P is the average pressure, μ is the dynamic viscosity, $\overline{u_i u_j}$ is the Reynolds stress term, calculated by the Boussinesq hypothesis, T is the average temperature, λ is the thermal conductivity, C_P is specific heat capacity, $\overline{u_j \theta}$ is the turbulent heat flux.

Additionally, RANS equations such as turbulence kinetic energy k, turbulent dissipation rate ε, specific turbulent dissipation rate ω and intermittency γ were incorporated for turbulence modeling [28]. To ensure accuracy, a block-structured mesh was prepared for each geometrical configuration, and y+ was kept equal to or below 1. The y+ value is a dimensionless parameter that represents the distance from the first grid cell to the surface wall. The total cell number for the first geometrical configuration (H/D = 2) was equal to 63 100, and for the second (H/D = 6) it was 68 600 cells. Both meshes have passed the grid independence test. The discretization of the second geometrical case is presented in Fig. 2.

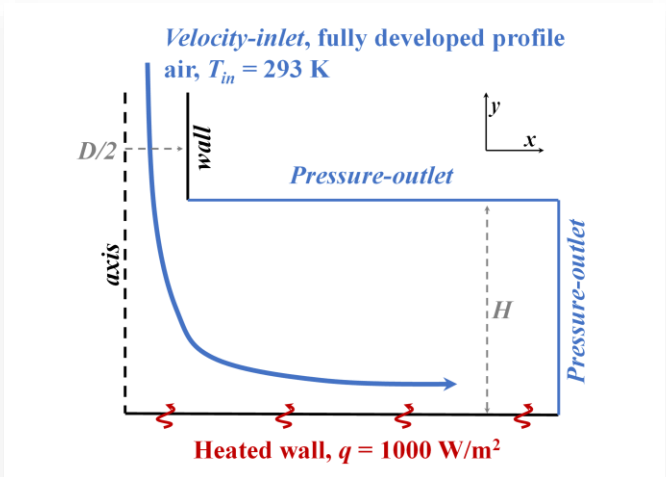

Fig. 1. Geometry and boundary conditions. Inlet diameter D = 0.02 m.

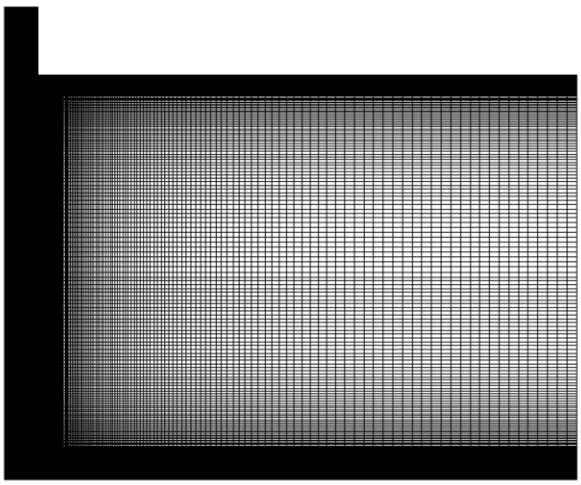

Fig. 2. Mesh for H/D = 6, D = 0.02 m, $y^+ < 1$, and total cell number = 68 600.

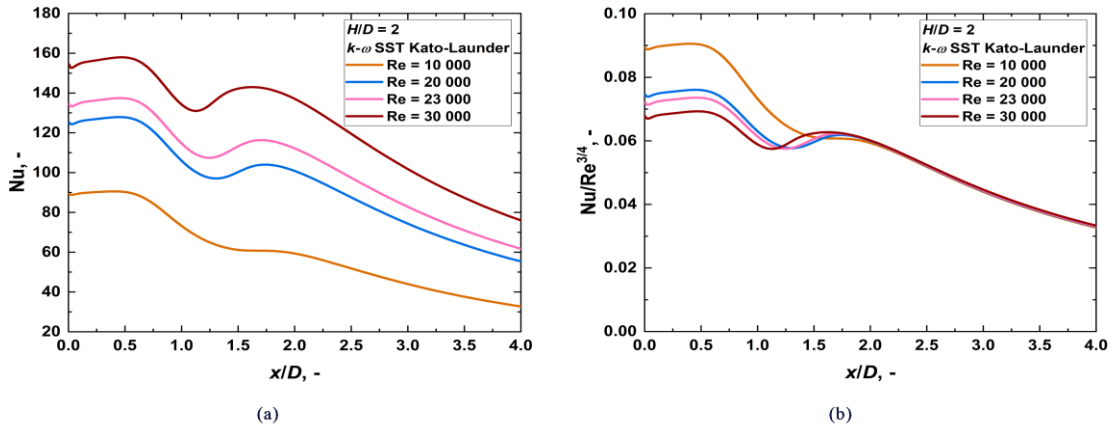

Fig. 3. (a) Local Nusselt number distribution. (b) Normalized local Nusselt number distribution. k–ω SST Kato-Launder turbulence model, H/D = 2.

The numerical calculations were performed in Ansys Fluent 18.1, where the pressure-based solver with SIMPLE (Semi-Implicit Method for Pressure Linked Equations) algorithm was used. The second-order numerical scheme was chosen for the pressure, momentum, turbulence, and energy equations. The insight of the mesh and detailed description of the numerical procedure can be found in the previous publication [27]. The model validation presented in this publication included a comparison of 16 turbulence models with 11 different experimental analyses. All source data are stored in the open repository [29].

Figure 3 presents the local Nusselt number distribution along the heated wall for different Reynolds number values and one geometrical configuration (H/D = 2). The purpose of this figure is to demonstrate that for the same geometrical configuration, the Nusselt number distribution does not vary significantly with different Reynolds numbers, which is particularly evident for normalized Nusselt number which is defined as Nu/Re^m. In the literature, the scaling factor for the Nusselt number is typically set to be $Nu/Re^{2/3}$ [1,11,30], but the exponent m can vary between 0.55 and 0.87 for a single jet impingement [1]. At values of x/D greater than 2.0, no differences in the Nusselt number distribution are observed at various Reynolds numbers which is especially very clear when the scaling factor is equal to $Nu/Re^{3/4}$ (Fig. 3(b)). However, near the stagnation point (x/D < 2.0), some discrepancies are visible, primarily due to variations in the inlet profile, which significantly affects the local Nusselt number distribution in that region. Furthermore, comparing the local Nusselt number distribution for geometrical configuration (H/D = 2 and 6) at the same Reynolds number in Fig. 4 reveals different trends, especially at various H/D. Two particular trends of the Nusselt number distribution can be distinguished depending on the H/D parameter [2,4,7,10,11,31,32]. At H/D < 6.0 (confirmed in [27]), there is a characteristic secondary maximum in the Nusselt number distribution. In contrast, at higher values of H/D, the second Nusselt number maximum does not occur (some turbulence models may exhibit an artificial/false secondary Nusselt number maximum, which is not observed in experimental studies [10,27]). Therefore, in this publication, the authors will compare the results of two H/D values at a constant Reynolds number of 23 000. Based on the literature and previous studies the authors have selected three turbulence models which are most appropriate for modeling the jet impingement phenomenon. These models will also be used for the comparison of results.

In the presented study, the analysis is focused on the Reynolds number equal to 23 000, two different configurations (H/D = 2 and 6), and three previously selected turbulence models (k–ε RNG Kato-Launder, k–ω SST Kato-Launder, intermittency transition). The primary objective of this analysis is to demonstrate the differences between turbulence models concerning low (H/D = 2) and high (H/D = 6) geometrical configurations and to provide valuable insights into the turbulence modeling of round jet impingement.

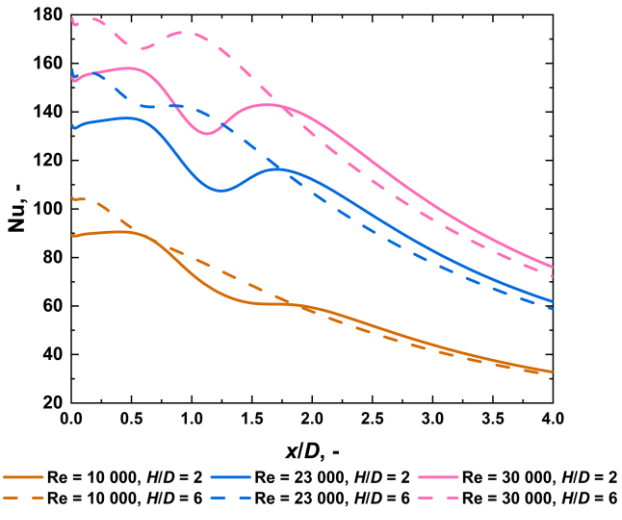

Fig. 4. Comparison of local Nusselt number distribution at heated wall, between different values of H/D and Reynolds number. k–ω SST Kato-Launder turbulence model.

3. The budgets

To conduct a comparative study, the authors utilize the values of k (turbulence kinetic energy, TKE) and budget of TKE, axial

Table 1. The turbulence kinetic energy equation terms [28].

Term	*k–ε* RNG Kato-Launder	*k–ω* SST Kato-Launder	Intermittency transition
Convection	$\rho\left(U\frac{\partial k}{\partial x}+V\frac{\partial k}{\partial y}\right)$		
Production	$\min(\mu_t S\Omega, 10\rho\varepsilon)$	$\min(\mu_t S\Omega, 10\rho\beta^* k\omega)$	$\gamma\min(\mu_t S\Omega, 10\rho\beta^* k\omega)$
Dissipation	$\rho\varepsilon$	$\rho\beta^* k\omega$	$\min(\max(\gamma, 0.1), 1.0)\rho\beta^* k\omega$
Diffusion	$\frac{\partial}{\partial x}\left(\alpha_k\mu_{eff}\frac{\partial k}{\partial x}\right)+\frac{\partial}{\partial y}\left(\alpha_k\mu_{eff}\frac{\partial k}{\partial y}\right)$	$\frac{\partial}{\partial x}\left(\left(\mu+\frac{\mu_t}{\sigma_k}\right)\frac{\partial k}{\partial x}\right)+\frac{\partial}{\partial y}\left(\left(\mu+\frac{\mu_t}{\sigma_k}\right)\frac{\partial k}{\partial y}\right)$	$\frac{\partial}{\partial x}\left(\left(\mu+\frac{\mu_t}{\sigma_k}\right)\frac{\partial k}{\partial x}\right)+\frac{\partial}{\partial y}\left(\left(\mu+\frac{\mu_t}{\sigma_k}\right)\frac{\partial k}{\partial y}\right)$

where: ρ is the density, g/m^3; k is the turbulence kinetic energy, m^2/s^2; U is the average radial velocity, m/s; V is the average axial velocity, m/s; x is the radial coordinate, m; y is the axial coordinate, m; μ is the dynamic viscosity, Pa·s; μ_t is the turbulent viscosity, Pa·s; $S=\begin{bmatrix}\frac{\partial U}{\partial x} & \frac{1}{2}\left(\frac{\partial U}{\partial y}+\frac{\partial V}{\partial x}\right)\\ \frac{1}{2}\left(\frac{\partial V}{\partial x}+\frac{\partial U}{\partial y}\right) & \frac{\partial V}{\partial y}\end{bmatrix}$ is the strain rate tensor, 1/s; $\Omega=\begin{bmatrix}0 & \frac{1}{2}\left(\frac{\partial U}{\partial y}-\frac{\partial V}{\partial x}\right)\\ \frac{1}{2}\left(\frac{\partial V}{\partial x}-\frac{\partial U}{\partial y}\right) & 0\end{bmatrix}$ is the magnitude of the vorticity rate, 1/s; ε is the turbulence dissipation rate, m^2/s^3; β^* is a model constant; ω is the specific turbulent dissipation rate, 1/s; γ is the intermittency, -; σ_k is the turbulent Prandtl number, -; μ_{eff} is the effective viscosity, Pa·s; α_k is the inverse effective Prandtl number, -.

and radial momentum, and energy. The analysis thoroughly compares the terms of the budget equations, which are defined below. The generic form of the turbulence kinetic energy equation *k*, which consists of four terms, is presented as follows:

$$\mathrm{CONV}_k = \mathrm{PROD}_k - \mathrm{DISS}_k + \mathrm{DIFF}_k, \tag{7}$$

where: CONV – convection term, PROD – production term, DISS – dissipation term, DIFF – diffusion term. The subscript *k* means turbulence kinetic energy.

The choice of the turbulence model influences the *k* transport equation. In the post-processing stage, the convection, production, and dissipation terms can be directly calculated, while the diffusion term is determined as a closure term. Table 1 presents details of each term in Eq. (7) for analyzed turbulence models.

The generic form of the axial and radial momentum equations, which consists of four terms, is presented as follows:

$$\mathrm{CONV}_{M,i} = \mathrm{PRESS}_{M,i} + \mathrm{DIFF}_{M,i} + \mathrm{RS}_{M,i}, \tag{8}$$

where: CONV – convection term, PRESS – pressure term, DIFF – diffusion term, RS – Reynolds stress term. The subscript *M* means the momentum equation, and *i* indicates the axial (*y*) or radial (*x*) coordinate.

The axial and radial momentum equations are the same for all turbulence models. During the post-processing stage, the convection and pressure terms can be calculated quickly and directly. On the other hand, the diffusion term is obtained using a 'User-Defined Function' (UDF), a script that uses the Gauss-Ostrogradsky Theorem (see the Appendix). Lastly, the Reynolds stress term is determined as a closure term. The details of each term in the momentum budget can be found in Table 2.

The last one is the energy transport equation; it consists of three terms and is presented below in a generic form:

$$\mathrm{CONV}_E = \mathrm{DIFF}_E + \mathrm{TDIFF}_E, \tag{9}$$

where: CONV – convection term, DIFF – diffusion term, TDIFF – turbulent diffusion term. The subscript *E* means the energy equation.

The energy equation is the same for all turbulence models. The convection term is calculated directly in the post-process, but similarly to the momentum equation, the diffusion term is obtained by the UDF (see the Appendix). The turbulent diffusion term is determined as the closure term. Each term of the energy equation is presented in Table 3.

It is commonly seen in literature that budgets are typically prepared on a single line that is either parallel or normal to the heated wall [3,20–22,24–26,32]. The location at which the budget is calculated plays a crucial role. When the budget is calculated near the wall, the dissipation and diffusion terms in the TKE equation tend to dominate over the other terms, making it

Table 2. The momentum equation terms [28].

Term	*k–ε* RNG Kato-Launder, *k–ω* SST Kato-Launder, Intermittency transition	
	Axial	Radial
Convection	$\rho\left(U\frac{\partial V}{\partial x}+V\frac{\partial V}{\partial y}\right)$	$\rho\left(U\frac{\partial U}{\partial x}+V\frac{\partial U}{\partial y}\right)$
Pressure	$-\frac{\partial P}{\partial y}$	$-\frac{\partial P}{\partial x}$
Diffusion	$\frac{\partial}{\partial x}\left(\mu\frac{\partial V}{\partial x}\right)+\frac{\partial}{\partial y}\left(\mu\frac{\partial V}{\partial y}\right)$	$\frac{\partial}{\partial x}\left(\mu\frac{\partial U}{\partial x}\right)+\frac{\partial}{\partial y}\left(\mu\frac{\partial U}{\partial y}\right)$
Reynolds stress	$\frac{\partial}{\partial x}\left(\mu_t\left(\frac{\partial U}{\partial y}+\frac{\partial V}{\partial x}\right)\right)+\frac{\partial}{\partial y}\left(\mu_t 2\frac{\partial V}{\partial y}-\frac{2}{3}k\right)$	$\frac{\partial}{\partial x}\left(\mu_t 2\frac{\partial U}{\partial x}-\frac{2}{3}k\right)+\frac{\partial}{\partial y}\left(\mu_t\left(\frac{\partial U}{\partial y}+\frac{\partial V}{\partial x}\right)\right)$

where: ρ is the density, kg/m^3; U is the average radial velocity, m/s; V is the average axial velocity, m/s; x is the radial coordinate, m; y is the axial coordinate, m; μ is the dynamic viscosity, Pa·s; μ_t is the turbulent viscosity, Pa·s; P is the average static pressure, Pa.

Table 3. The turbulence kinetic energy equation terms [28].

Term	k–ε RNG Kato-Launder, k–ω SST Kato-Launder, Intermittency transition
Convection	$\rho\left(U\frac{\partial T}{\partial x}+V\frac{\partial T}{\partial y}\right)$
Diffusion	$\frac{\partial}{\partial x}\left(\frac{\lambda}{C_P}\frac{\partial T}{\partial x}\right)+\frac{\partial}{\partial y}\left(\frac{\lambda}{C_P}\frac{\partial T}{\partial y}\right)$
Turbulent diffusion (turbulent heat flux)	$\frac{\partial}{\partial x}\left(\frac{\mu_t}{\sigma_t}\frac{\partial T}{\partial x}\right)+\frac{\partial}{\partial y}\left(\frac{\mu_t}{\sigma_t}\frac{\partial T}{\partial y}\right)$

where: ρ is the density, kg/m^3; U is the average radial velocity, m/s; V is the average axial velocity, m/s; x is the radial coordinate, m; y is the axial coordinate, m; μ is the dynamic viscosity, Pa·s; μ_t is the turbulent viscosity, Pa·s; T – average static temperature, K; λ is the thermal conductivity, W/(m·K); C_P is specific heat capacity, J/(kg·K); σ_t is the turbulent Prandtl number, -.

challenging to observe the tendency of the convection and production terms, which are more significant away from the wall. The results of other studies [3,20–22,26] support this statement. In this paper, the authors analyze the budgets along vertical lines perpendicular to the heated wall to eliminate local value disturbances and observe the tendency of all equations terms. Each vertical line originates at the wall and extends 3 mm away. The endpoint of each line is selected to capture the region of maximum TKE values, located between 2 mm (0.1D) and 3 mm (0.15D) away from the heated wall, for both H/D = 2 and 6, and Re = 23 000. The results represent the integral value along the distance mentioned. Figure 5 shows the contour plot of the TKE values with the placement of its maximum, and velocity magnitude for k–ω SST Kato-Launder turbulence model. At H/D = 2 (Fig. 5(a)), the maximum occurs between x/D = 1.25 and 2, and approximately 0.1D from the wall. The literature results show similar region where the TKE maximum is located [9,14,23, 26,30]. At H/D = 6 (Fig. 5(c)) the maximum is located closer to the axis, between x/D = 0.9 and 1.4, and approximately the same distance from the heated wall (0.1D). Comparison between the TKE values (Figs. 5(a) and (c)) and velocity magnitude (Figs. 5(c) and (d)) for the same value of H/D suggests that the position of the maximal value of TKE is placed in the region of the strong interaction of the wall jet with the jet stream.

4. Results

4.1. Turbulence kinetic energy

Figure 6 compares the local turbulence kinetic energy (TKE) values on the line parallel to the heated wall between two geometrical configurations (H/D = 2 and 6) for three turbulence models. Analysis of the local k values for both geometrical configurations and all turbulence models shows that there is a maximum in their distribution, and further (x/D > 2.5) the values gradually decrease. Furthermore, it can be observed that the TKE values are relatively low in the stagnation region (x/D < 0.5), this statement is supported by the DNS results [20]. The high turbulence kinetic energy values at the stagnation point cause overprediction in the Nusselt number value. However, this problem can be resolved by incorporating the Kato-Launder limiter, which restricts the production of TKE at the stagnation point [10,27,33]. The results shown in Figs. 5 and 6 indicate a shift of relatively high values of k toward the stagnation point in the case of H/D = 6, which is consistent with the location of the highest values of the Nusselt number around the centerline, as suggested in [7]. On the other hand, at H/D = 2, the first Nusselt number maximum moved from the stagnation point and occurs at about x/D = 0.5. The relation between the local Nusselt number distribution of presented turbulence models is consistent with the relation between their TKE local values. If at the same radial position (x/D), the local TKE values obtained with the k–ε RNG Kato-Launder turbulence model are lower than values of TKE obtained with the intermittency transition turbulence model, and the same tendency is observed between their local Nusselt number values. The same pattern is observed across the entire range of x/D values for both geometrical configurations (except the near stagnation region at x/D < 0.5 and H/D = 6). It has been observed that the maximal values of the TKE are consistent with the second maximum of the Nusselt number distribution. It appears that other researchers have observed the occurrence of high values of TKE or turbulence intensity near the second Nusselt number maximum, as mentioned in [1,13,23,26, 32,34]. Interestingly, for a case of H/D = 2, the maximum value of k is observed ahead of the second maximum of the Nusselt number distribution and at H/D = 6, the maximum value of k is observed after the second maximum of the Nusselt number (for the k–ω SST Kato-Launder and Intermittency turbulence models). On the other hand, the k–ε RNG Kato-Launder turbulence model gives a results in which maximum in TKE values exists, but there is no second maximum in the Nusselt number (which is more consistent with experimental studies [35– 40]). Increasing the H/D value causes a shift of the TKE maximal values towards the stagnation point for all analyzed turbulence models. Additionally, the TKE values obtained with k–ω SST Kato-Launder and k–ε RNG Kato-Launder turbulence models decrease with an increase in the H/D parameter. However, the results obtained with the intermittency transition model exhibit a different tendency with an increase in the H/D parameter, leading to a rise in maximal value of TKE. The maximal values of TKE at H/D = 2 occur between x/D = 1.25 and x/D = 2.0, while for H/D = 6, they occur between x/D = 1.0 and x/D = 1.5. The analysis of the lowest H/D value confirms similarities in the local TKE distribution between all analyzed turbulence models. In the case of H/D = 6, the local TKE value distribution obtained with the k–ε RNG Kato-Launder turbulence model differs from the other two models of a constant offset.

4.2. Turbulence kinetic energy budget

In Fig. 7, a budget of turbulence kinetic energy, Eq. (7), is presented, and a few observations can be formulated. The TKE production and dissipation terms exhibit maximum positive and negative values in the case of k–ε RNG Kato-Launder and intermittency transition turbulence models, while the diffusion and dissipation terms dominate in the case of k–ω SST Kato-Launder turbulence model. These findings are consistent with an experimental study [3], which also reported maximum magnitudes of the production and dissipation terms. However, their maximal values in the experimental study are located near the x/D = 0.5,

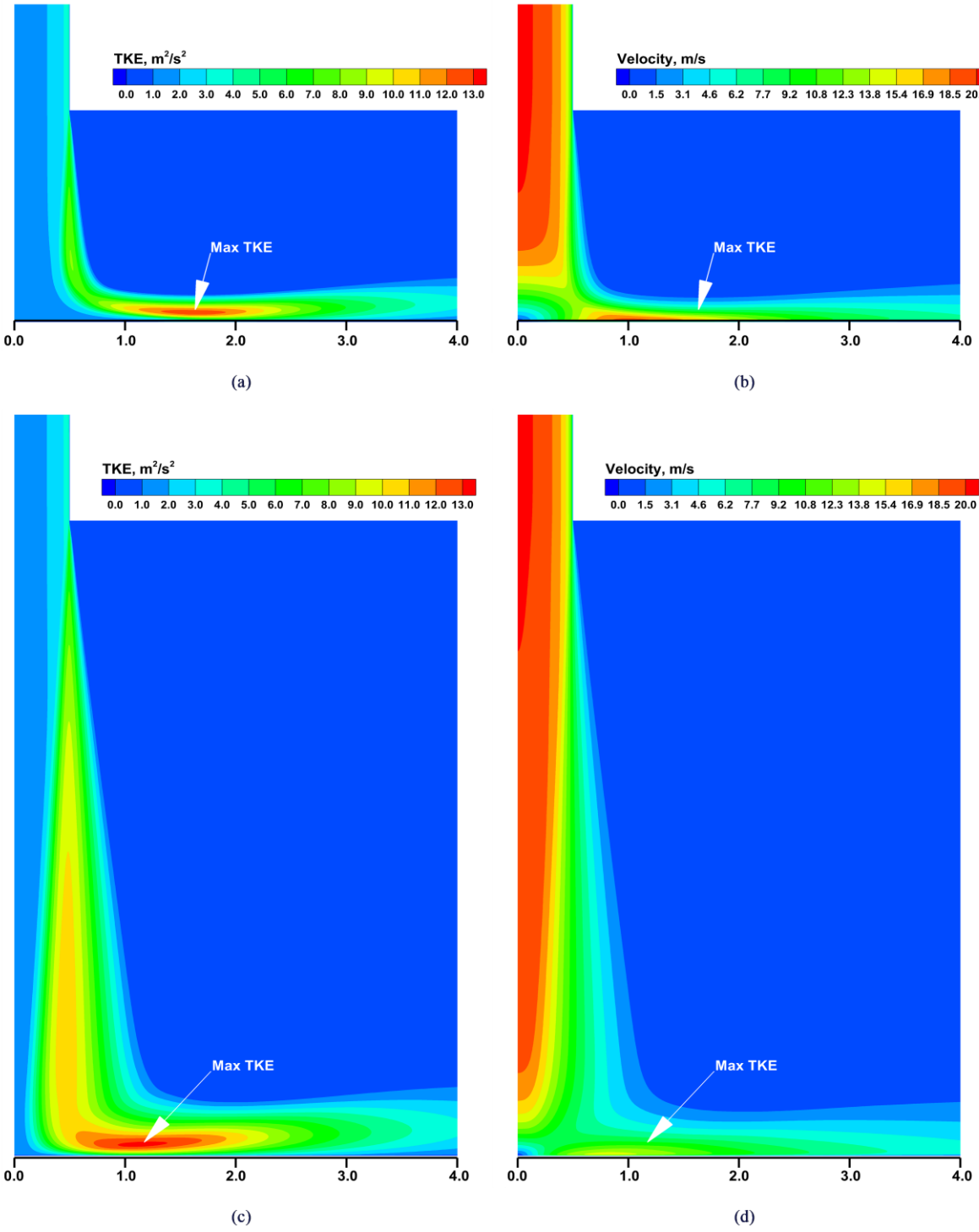

Fig. 5. Local values of TKE, with a position of its maximum, and local values of velocity magnitude. k–ω SST Kato-Launder turbulence model, Re = 23 000, D = 0.02 m. (a) TKE, H/D = 2. (b) Velocity magnitude, H/D = 2. (c) TKE, H/D = 6. (d) Velocity magnitude, H/D = 6.

which is closer to the stagnation point than the position of production and dissipation terms maximal values obtained by the presented numerical analysis. In the case of H/D = 2, the maxima and minima of all terms in the TKE equation are located between x/D = 1.0 and x/D = 2.0. A shifting towards the stagnation point can be seen for the second geometrical configuration (H/D = 6). The maxima and minima values are smaller than those of the H/D = 2 case. Another interesting observation is that the convection term changes sign, what was also reported in [3]. Other terms, such as production and diffusion, are always positive, while dissipation is negative. The research conducted through experimental and numerical (DNS) studies [9,20,22,41] has revealed that the production of turbulence kinetic energy is negative in the stagnation region, which is opposite to the values

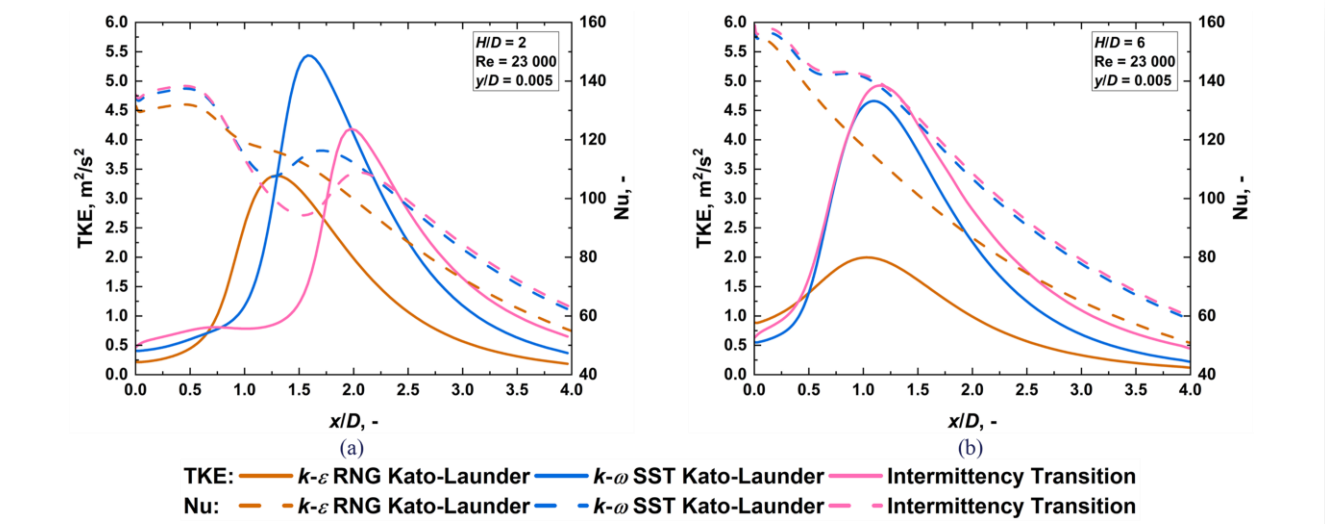

Fig. 6. Comparison of local values of TKE on a parallel to the heated wall line, between two geometrical configurations H/D values and Re = 23 000, for various turbulence models (a) H/D = 2; (b) H/D = 6. Re = 23 000.

predicted by RANS turbulence models. According to the results of the RANS, the production of turbulence kinetic energy is always positive, indicating the energy transfer from the mean flow to the eddies. As mentioned in [9], this challenges the RANS and LES models. The relatively low TKE production values in the stagnation region are due to the Kato-Launder limiter [10]. The production term of TKE (Fig. 7) and local values of TKE (Fig. 6) exhibit a similar tendency, location of their maxima correspond to each other. The maximum values of the production term correspond to the second maximum value of the local Nusselt number. When the H/D parameter is equal to 2, all turbulence models exhibit similar behavior in terms of the TKE production. The analysis of the convection term reveals a positive value near the stagnation point, and its sign change near the location of the first and second local Nusselt number maxima. In addition, the convection term's lowest value corresponds with the local Nusselt number minimum, while its maximal value occurs behind the secondary Nusselt number maximum. Moreover, the k–ε RNG Kato-Launder turbulence model results show a different behavior in the second geometrical configuration (H/D = 6), as presented in Fig. 7(f). The convection term in this configuration has its local minima and maxima, but it is always positive. This observation is particularly interesting as the k–ε RNG Kato-Launder turbulence model does not show a false secondary Nusselt number maximum in this geometrical configuration. Hence, it suggests a connection between the Nusselt number distribution and the convection term of the turbulence kinetic energy budged. The shape of the dissipation term mirrors the production term, what has been noticed in [9]. The diffusion maximum and dissipation minimum are observed near the Nusselt number second maximum. Compared to the other two models, the k–ε RNG Kato-Launder turbulence model exhibits flatter and lower absolute values for these two terms. All terms of the turbulence kinetic energy equation exhibit higher absolute values for H/D = 2 than for H/D = 6. The tendency of all terms is quite similar for the k–ω SST Kato-Launder and intermittency transition turbulence models across both geometrical configurations (Fig. 7(a)–(d)). The k–ε RNG Kato-Launder turbulence model results show differences in trend between H/D = 2 and H/D = 6 cases. In the first geometrical configuration, the shape is similar to the other two turbulence models, but in the second case the shape does not exhibit second maximum and all terms except dissipation are positive.

4.3. Momentum budget

The momentum equation budget, Eq. (8), is considered separately for the axial and radial coordinates. Figures 8 and 9 show the radial and axial components of the momentum budget, respectively. The characteristic of all terms in the momentum equation is similar for all analyzed turbulence models and both geometrical configurations. In the case of the radial (x) component, the convection and pressure terms are the dominant ones, while the Reynolds stress term takes the lowest values. Comparing the H/D = 6 case with the H/D = 2 shows that features of all terms' are similar, but the values are significantly lower in the case of H/D = 6. The analysis of the axial momentum component budget reveals some similarities to that of the radial component. The convection and pressure terms are also dominant, whereas the Reynolds stress term is larger than the same term in the case of the radial momentum equation. The diffusion term is almost negligible, which aligns with the findings presented in [22]. There is a significant difference in the characteristics of axial (y) momentum equation terms between H/D = 2 and H/D = 6, especially visible in the stagnation region x/D < 1.0. Almost whole turbulence kinetic energy is concentrated in this region. With an increase in the x/D parameter, especially in the range x/D > 2.0, all terms tend to approach 0. On the basis of the analysis of all cases, the convection and pressure terms exhibit a mirror-like shape. In the case of the radial (x) momentum, the pressure term is always positive, the diffusion and Reynolds stress terms are always negative, and the convection term changes sign. On the other hand, the pressure term is always negative for the axial (y) momentum equation, while the convection and Reynolds stress terms are positive. The almost negligible diffusion term changes sign near x/D = 2.5. The large absolute values of the convection

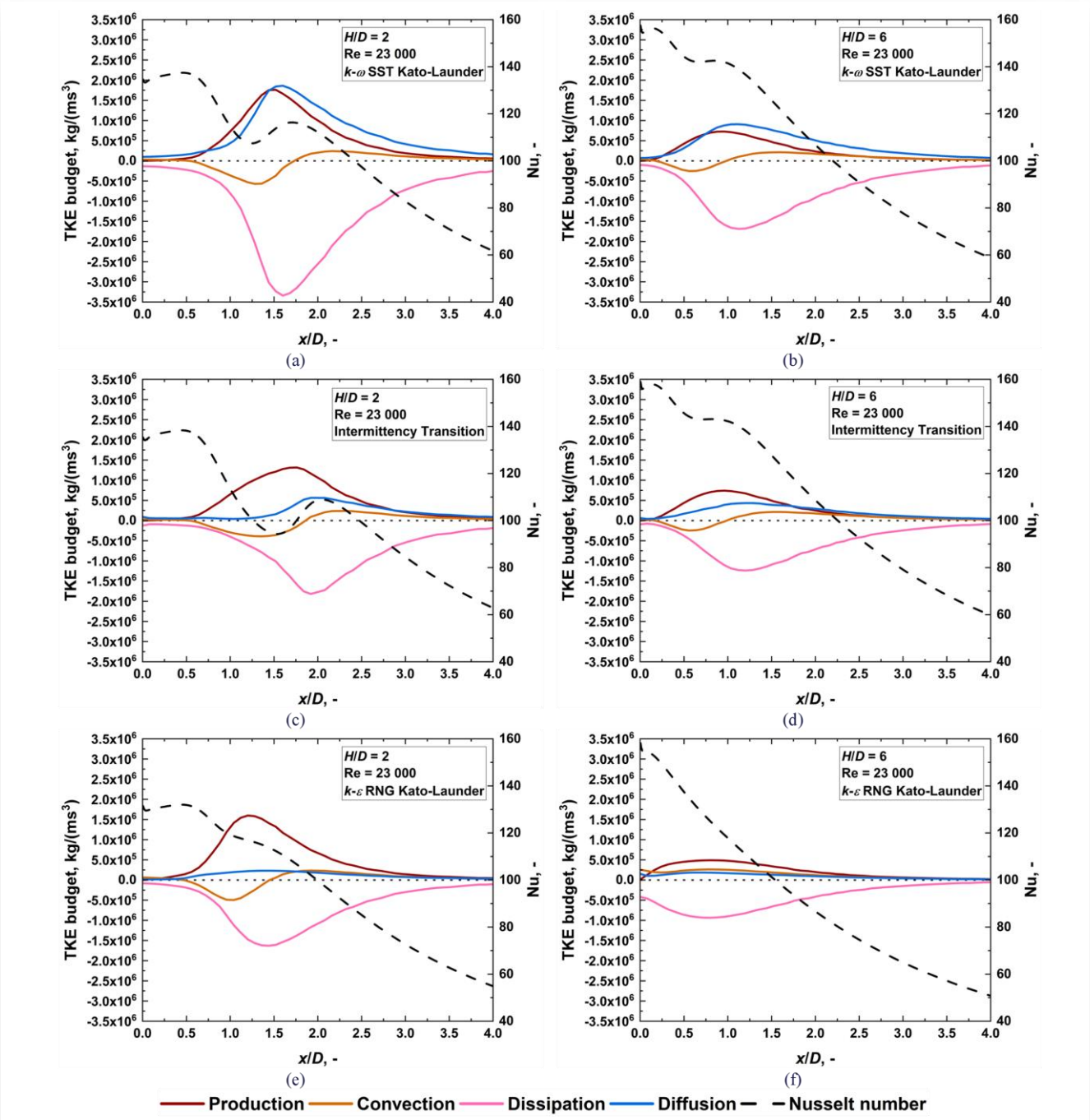

Fig. 7. Comparison of TKE budget, between two geometrical configurations (H/D values 2 and 6) and for various turbulence models. (a) k–ω SST Kato-Launder, H/D = 2; (b) k–ω SST Kato-Launder, H/D = 6; (c) intermittency transition, H/D = 2; (d) intermittency transition, H/D = 6; (e) k–ε RNG Kato-Launder, H/D = 2; (f) k–ε RNG Kato-Launder, H/D = 6; Re = 23 000.

and pressure terms in both components of the momentum equation clearly mark the limit of the stagnation region at $x/D \approx 1.0$. The minimum and maximum values of the pressure and convection terms correspond to the first maximum value of the local Nusselt number. A link between radial (x) pressure gradient and the first Nusselt number maximum has been mentioned in [11]. The maximum and minimum values of the pressure and convection terms are closer to the stagnation point at H/D = 6 ($x/D \approx 0.25$) than at H/D = 2 ($x/D \approx 0.5$). This is also reflected in the shift of the first maximum of the local Nusselt number towards the jet axis. In contrast to the budget of TKE, it is hard to see any relation between the sign change in the convection term of the radial momentum component and the local Nusselt number distribution in this case. For example, at H/D = 2, the sign change occurs before the local minimum in the Nusselt number and behind the second Nusselt number maximum at H/D = 6. The convection and pressure terms of the axial momentum equation component show values that are almost constant near the axis. A similar observation on the constant value of the convection term can be found in [3]. The Reynolds stress term in the axial momentum component equation takes higher values for the k–ε RNG Kato-Launder turbulence model at the stagnation point than the other two models in the case of H/D = 6.

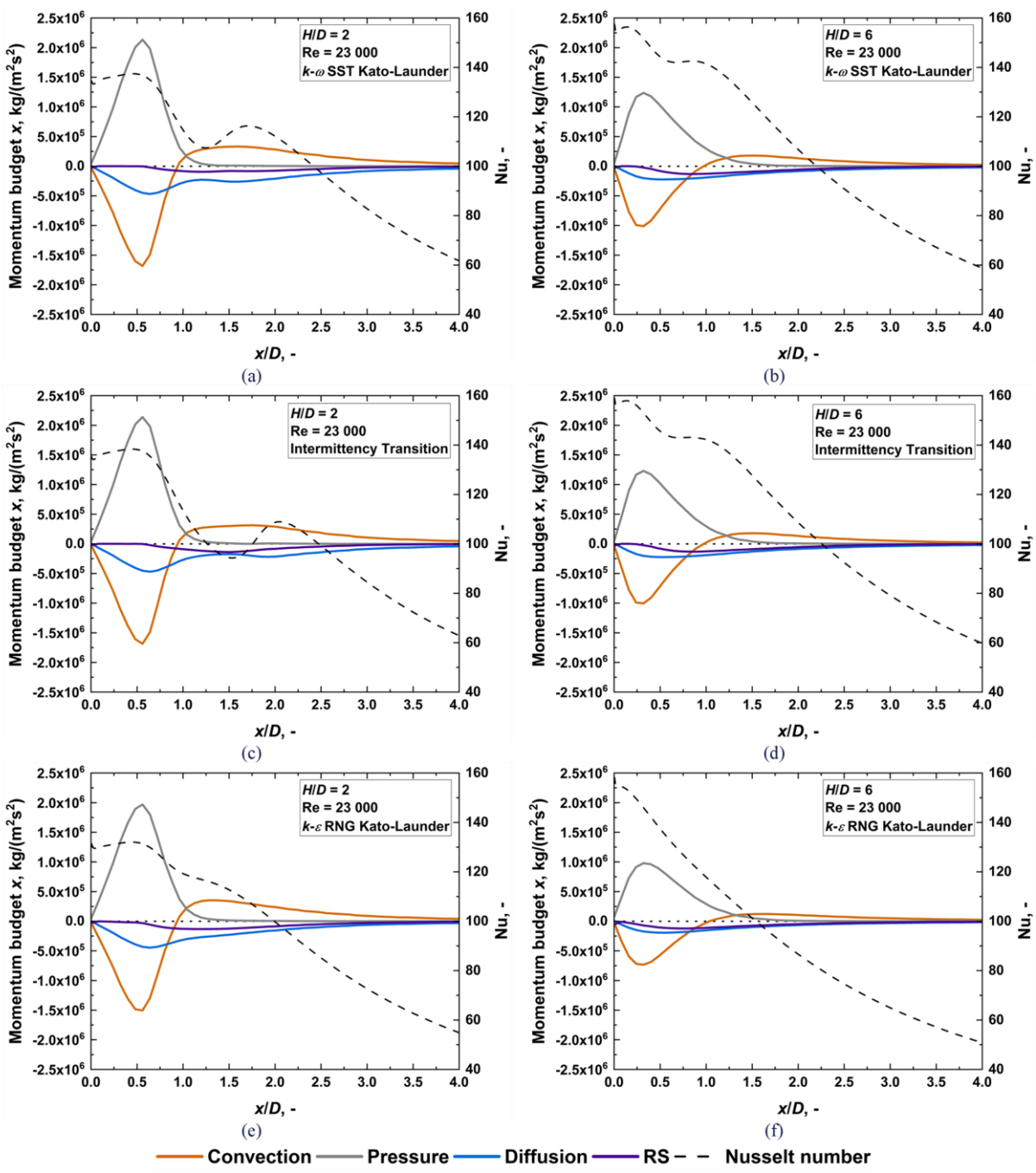

Fig. 8. Comparison of radial momentum budget, between two geometrical configurations (H/D values 2 and 6) and for various turbulence models. (a) k–ω SST Kato-Launder, H/D = 2; (b) k–ω SST Kato-Launder, H/D = 6; (c) itermittency transition, H/D = 2, (d) intermittency transition, H/D = 6; (e) k–ε RNG Kato-Launder, H/D = 2; (f) k–ε RNG Kato-Launder, H/D = 6; Re = 23 000.

4.4. Energy budget

The last budget is related to the energy equation, Eq. (9), and presented in Fig. 10. It was observed that the shapes of all terms remain similar, regardless of the turbulence model used and the geometrical configurations. However, there was one exception to this observation, which is presented in Fig. 10(f). The diffusion term is always positive for all cases, and the convection and turbulent diffusion terms are always negative. The crossing point between convection and turbulent diffusion terms is very characteristic. This point occurs prior to the second Nusselt number maximum. In Fig. 10(f), which presents the results of the k–ε RNG Kato-Launder turbulence model at H/D = 6, the crossing point is located far from the stagnation point at x/D > 3.0, and the curves tend to converge. The observation is particularly interesting because, for this geometrical configuration and this specific turbulence model, the second Nusselt number maximum does not exist. This raises the possibility of a potential correlation between these two terms and the distribution of the

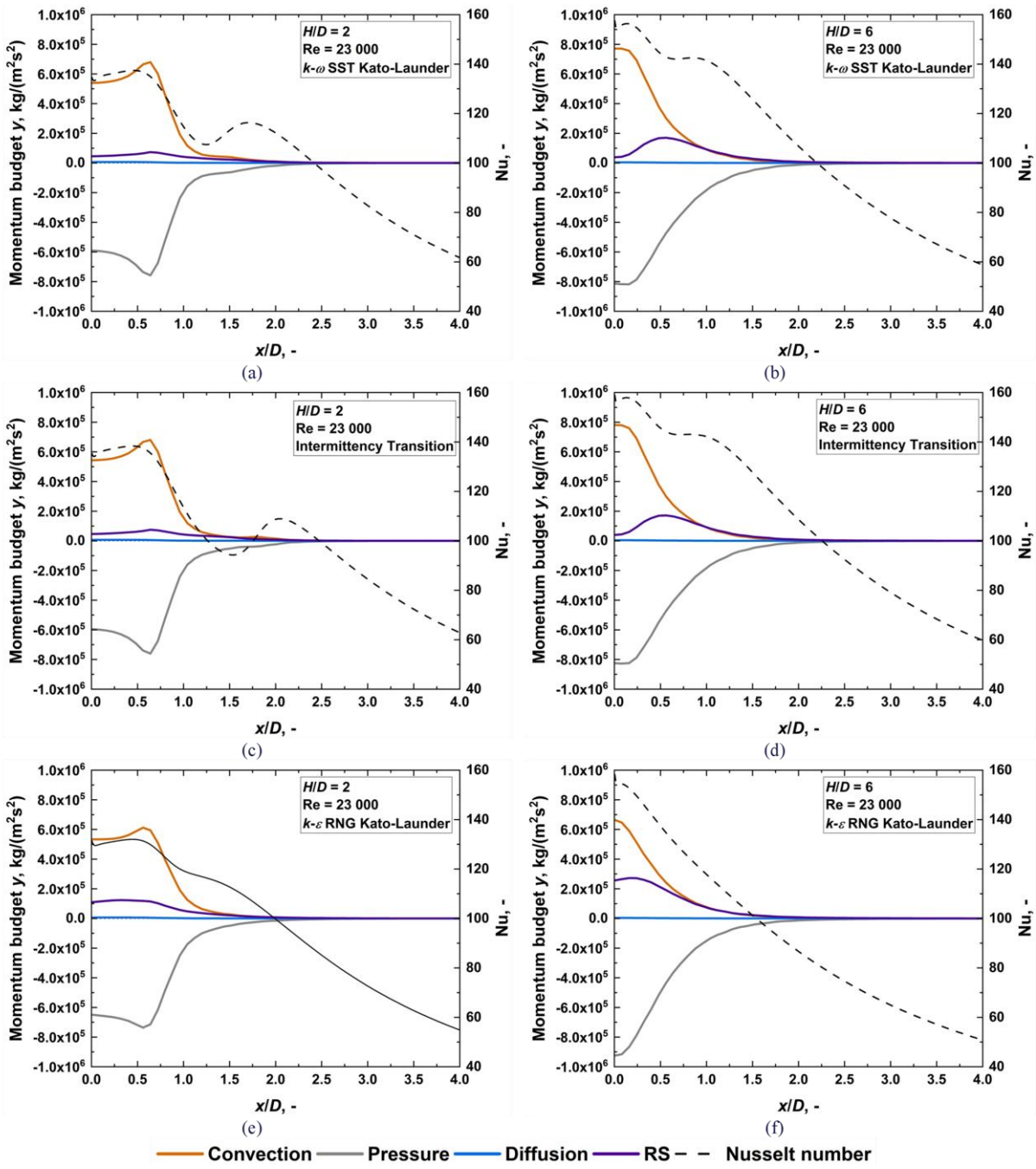

Fig. 9. Comparison of axial momentum budget, between two geometrical configurations (H/D values 2 and 6) and for various turbulence models. (a) k–ω SST Kato-Launder, H/D = 2; (b) k–ω SST Kato-Launder, H/D = 6; (c) intermittency transition, H/D = 2; (d) intermittency transition, H/D = 6; (e) k–ε RNG Kato-Launder, H/D = 2; (f) k–ε RNG Kato-Launder, H/D = 6; Re = 23 000.

local Nusselt number. The convection and diffusion terms dominate in the stagnation region, while the turbulent diffusion term is close to 0. As the value of x/D increases, the role of turbulent diffusion becomes more significant, while the impact of the convection term decreases. This tendency is clear, especially outside the stagnation region $x/D > 1.0$. In the k–ω SST Kato-Launder and intermittency transition turbulence models, the diffusion term shows local minima and maxima, which correspond to the distribution of the local Nusselt number, but in the k–ε RNG Kato-Launder turbulence model the diffusion term does not exhibit the extrema. The tendency of all terms is similar for the k–ω SST Kato-Launder and intermittency transition turbulence models but differs for the k–ε RNG Kato-Launder turbulence model. The absolute values of all terms are lower at H/D = 6 compared to H/D = 2. It has been observed that the k–ω SST Kato-Launder and intermittency transition turbulence models exhibit local minima and maxima in the convection and turbulent diffusion terms at H/D = 2. This corresponds to the second Nusselt number maximum. However, at H/D = 6, the maxima and minima are small or non-existent. All terms have almost constant values near the axis at $x/D < 0.5$.

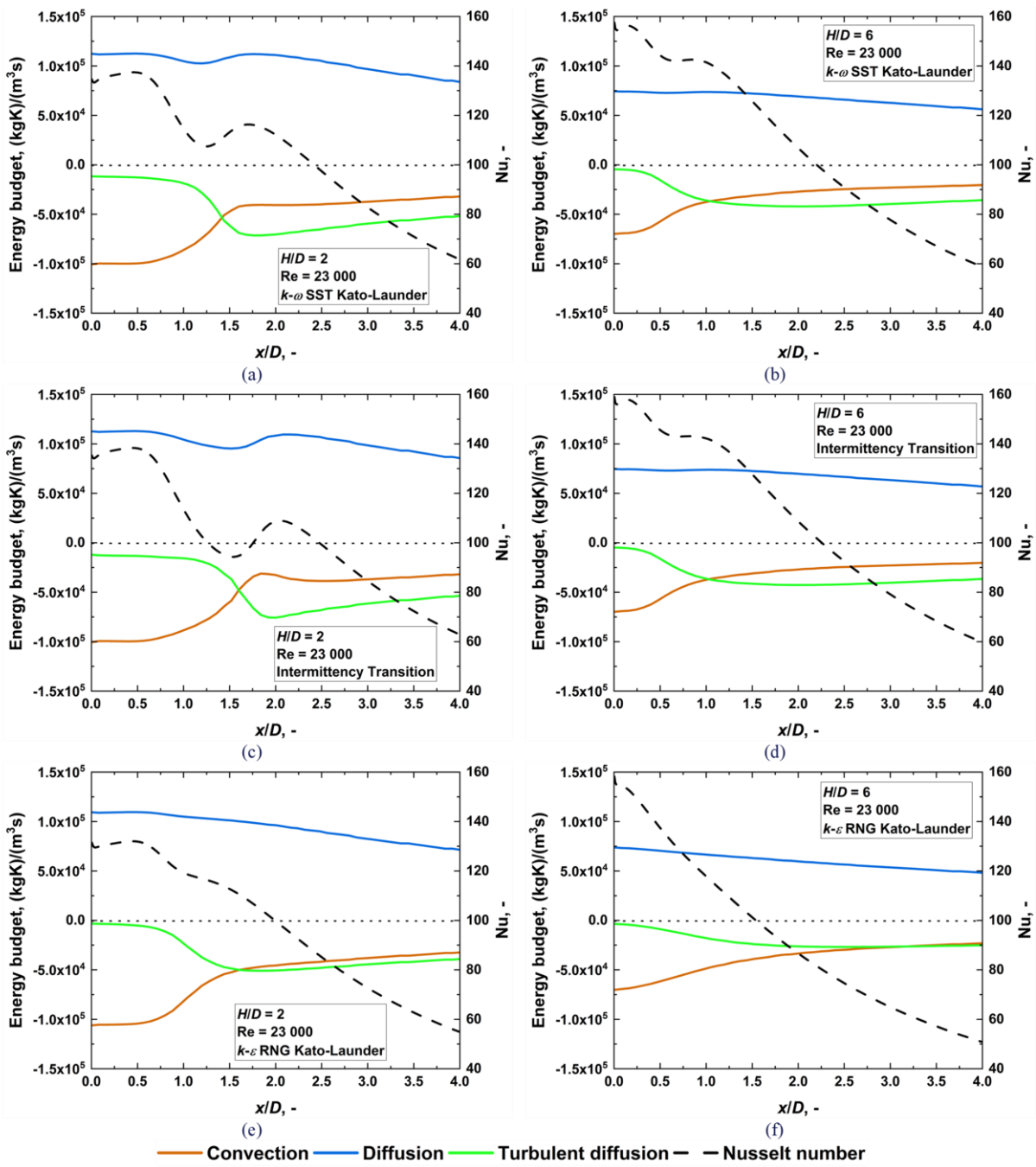

Fig. 10. Comparison of energy budget, between two geometrical configurations (H/D values 2 and 6) and for various turbulence models. (a) k–ω SST Kato-Launder, H/D = 2; (b) k–ω SST Kato-Launder, H/D = 6; (c) Intermittency transition, H/D = 2; (d) intermittency transition, H/D = 6; (e) k–ε RNG Kato-Launder, H/D = 2; (f) k–ε RNG Kato-Launder, H/D = 6. Re = 23 000.

5. Summary

The publication presented a budget of the turbulence kinetic energy, momentum, and energy equations together with the local values of TKE in the case of turbulent round jet impingement. The comparative analysis was prepared for one Reynolds number (Re = 23 000), three selected turbulence models, and two geometrical configurations (H/D = 2 and 6). This analysis might help identify the essential transport phenomena in the RANS numerical modeling of turbulent heat transport. The study also includes comparison of the results of transport equation budgets with the local Nusselt number values, which might provide insights into the relation between transport equation terms and the local Nusselt number distribution. This study can be used for further analysis and considerations, and in the future, it can be enriched with more formal analysis such as the curve sketching technique. This method would allow for a more precise determination of minima and maxima, inflection points for budgets, and the local Nusselt number. Some general conclusions from this study are presented below:

TKE and TKE budget

- Maximal values of TKE are consistent with the location of the second Nusselt number maximum, at H/D = 2 occurring between x/D = 1.25 and 2.0, while at H/D = 6, it is between x/D = 1.0 and 1.5.
- In the TKE budget, production and dissipation terms dominate in the k–ε RNG Kato-Launder and intermittency transition turbulence models. In contrast, the diffusion and dissipation terms dominate in the k–ω SST Kato-Launder turbulence model.
- The maxima and minima of all terms in the TKE budgets can be found between x/D = 1.0 and 2.0 at lower geometrical configuration (H/D = 2). An increase in the H/D value shifts those maxima and minima towards the stagnation point.
- The maximal values of the production term in the TKE budget correspond to the maximal values of the local Nusselt number distribution.

Momentum budget

- The behavior of all terms in the momentum equation is similar for all analyzed turbulence models for both geometrical configurations.
- The convection and pressure terms in the radial and axial momentum equations dominate. The diffusion term in the axial momentum equation is almost negligible.
- The large absolute values of the convection and pressure terms in the equations of both momentum components identify the stagnation region's limit at $x/D \approx 1.0$.
- The minimum and maximum values of the pressure and convection terms in the momentum budgets correspond to the first Nusselt number maximum.

Energy budget

- In the energy equation budget, the convection and diffusion terms dominate in the stagnation region.
- The crossing point between the convection and turbulent diffusion terms in the energy equation budget coincides with the second Nusselt number maximum for the k–ω SST Kato-Launder and intermittency transition turbulence models. This crossing point does not occur for the k–ε RNG Kato-Launder turbulence model at the H/D = 6 case, which corresponds to a lack of secondary Nusselt number maximum.

General

- The trend of the transport equation budget for the k–ε RNG Kato-Launder turbulence model at the H/D = 6 case differs from the other two presented turbulence models.
- The convection term is the only term in TKE and radial momentum budget that changes its sign across the x/D parameter.
- The analysis of all transport equation budgets shows that in the H/D = 6 case, the values of all terms are lower than in the H/D = 2 case, maybe with one exception for the axial momentum budget, where they are higher at the stagnation point.

Guideline

- None of the presented budgets alone describes the Nusselt number distribution. Each equation contributes to it, so only together they properly describe the physics of this phenomenon. Moreover, none of the equation terms can be neglected (even if they are relatively small compared to other terms), and each of them influences the heat transfer.
- In the boundary layer, molecular diffusion transports the heat from the wall, and then in the outer layer the convection mechanism plays a significant role in the heat transfer mechanism. Those two terms are the most important ones in the energy equation, which creates the general shape of the Nusselt number distribution and its high values. Moreover, the convection term is responsible for the first Nusselt number maximum. However, convection and molecular diffusion terms alone cannot describe the second Nusselt number maximum, for which the turbulent diffusion term is responsible. Because of that, the energy equation budget might seem to be the most important one to analyze, but both terms responsible for Nusselt number maxima – convection (first one) and turbulent diffusion (second one) are described by other transport equations – momentum and TKE equations, respectively. Therefore, the focus should be on the momentum (axial and radial) and the turbulence kinetic energy budgets.
- Jet's movement toward the wall is represented by the convective term in the momentum budget, then it impinged on the wall, which causes the increase in the pressure due to slowing down of the fluid. The high pressure in the stagnation region forced radial movement of the fluid, so it can be said that the pressure term of the momentum budget contributes to the development of the flow. Both phenomena (convection term in axial momentum budget supported by the pressure term in radial momentum budget) determined the existence of the first Nusselt number maximum.
- The second Nusselt number maximum represents the development of a turbulent boundary layer in a wall jet and its interaction with the jet stream. Proper modeling of turbulence (like TKE equation terms) is crucial to adequately describe the Nusselt number distribution in a whole range, which is why various turbulence models describe the Nusselt number distribution differently.
- Both the k–ω SST Kato-Launder and the intermittency transition turbulence models tend to generate a secondary Nusselt number maximum. For low values of H/D (H/D = 2), it is the real (observed in the experimental studies), but for high values of H/D (H/D = 6) is the fake one (not observed in the experimental studies). On the other hand, the k–ε RNG Kato-Launder turbulence model does not tend to generate a secondary Nusselt

number maximum, and it is a better option for higher H/D values.

- The selection of the best turbulence model that describes the heat transfer of the impingement jet in a range of various Reynolds numbers and values of H/D cannot be made on the presented study. It only supports the recommendations of the previous analysis. The source of the difference is probably in the dissipation and diffusion terms of the TKE equation. Further research should also include the ε/ω transport equations budgets.

Acknowledgements

This research was supported by the Ministry of Education and Science.

Appendix

In general, the diffusion term of any variable in finite volume method can be calculated by the equation:

$$\frac{\partial}{\partial x}\left(\Gamma\frac{\partial\phi}{\partial x}\right)+\frac{\partial}{\partial y}\left(\Gamma\frac{\partial\phi}{\partial y}\right)=\frac{1}{V_c}\sum_f \Gamma_f \frac{\phi_c-\phi_{nc}}{d_{nc}}A_f\overrightarrow{n_f}, \qquad (10)$$

where: ϕ is the variable (e.g.: temperature, velocity, etc.); Γ is the diffusion coefficient; V_c is the cell volume; A_f is the face area; $\overrightarrow{n_f}$ is the face unit normal vector; d_{nc} is the distance between the cell centroids; ϕ_c is the variable value at the cell center; ϕ_{nc} is the variable value at the neighbor cell center; subscript f indicates cell face.

Figure 11 shows a graphical representation of all variables in that equation:

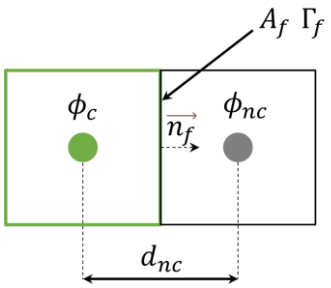

Fig. 11. Graphical representation of all variables in Eq. (10).

The implementation of Eq. (10) for 2D axisymmetric model, using built-in UDF functions, such as connectivity macros [42], for the energy equation, the diffusion term is presented below. The code must be compiled first and then used in the Ansys Fluent model.

```
#include "udf.h"
#include "sg.h"

DEFINE_ON_DEMAND(on_demand_energy_diffusion_term){
Domain *d;
Thread *t;
cell_t c;
d = Get_Domain(1);
real xc[ND_ND];  /* cell centroid */
real xf[ND_ND]; /* face centroid */

thread_loop_c(t,d){

/* loop through all cells in the model */
begin_c_loop(c,t){

/* face variables */
face_t f;
Thread *tf;
int n;
C_CENTROID(xc,c,t);     /* get cell centroid data */
real phi_f = 0;         /* values at the face center */
real diff = 0;          /* diffusion term */
/* cell, face connectivity macros defined in [42] */
real A[2];
real ds;
real es[2];
real A_by_es;
real dr0[2];
real dr1[2];

/* loop through all faces in the cell */
c_face_loop(c, t, n){

    f = C_FACE(c,t,n);
    tf = C_FACE_THREAD(c,t,n);
    F_CENTROID(xf,f,tf); /* get face centroid data */
```

```
    if (BOUNDARY_FACE_THREAD_P(tf)){ /* if face is the boundary face */

        BOUNDARY_FACE_GEOMETRY(f,tf,A,ds,es,A_by_es,dr0);
        phi_f = 0.0242/1006.43; /* thermal conductivity/Cp */

        phi_f = phi_f*(C_T(F_C0(f,tf),THREAD_T0(tf))-F_T(F_C0(f,tf),THREAD_T0(tf)))*A_by_es/ds;
    }
    else{   /* if face is an interior face */

        INTERIOR_FACE_GEOMETRY(f,tf,A,ds,es,A_by_es,dr0,dr1);
        phi_f = 0.0242/1006.43; /* thermal conductivity/Cp */

        phi_f = phi_f*(C_T(F_C0(f,tf),THREAD_T0(tf))-C_T(F_C1(f,tf),THREAD_T1(tf)))
        *A_by_es/ds;
    }

    if (THREAD_TYPE(tf) == THREAD_F_AXIS){ /* if axis */
        diff  -= 0;
    }
    else{

        /* phi_f * face normal */
        phi_f = phi_f * (xf[0] - xc[0])/sqrt((xf[0] - xc[0])*(xf[0] - xc[0])+(xf[1] - xc[1])*(xf[1] - xc[1]))
        + phi_f * (xf[1] - xc[1])/sqrt((xf[0] - xc[0])*(xf[0] - xc[0])+(xf[1] - xc[1])*(xf[1] - xc[1]));

        diff += -phi_f/xf[1]; /* scale face value by face center radius and sum */
    }
}

/* The diffusion term for a cell (for 2D axisymmetric case, volume must be scaled by radius) */
C_UDMI(c,t,0) = xc[1] * diff / C_VOLUME(c,t);

}
end_c_loop(c,t)
}
}
```

References

[1] Barbosa, F.V., Teixeira, S.F.C.F., & Teixeira, J.C.F. (2023). Convection from multiple air jet impingement – A review. *Applied Thermal Engineering*, 218, 119307. doi: 10.1016/j.applthermaleng.2022.119307

[2] Chitsazan, A., Klepp, G.,& Glasmacher, B. (2021). Numerical prediction of the second peak in the Nusselt number distribution from an impinging round jet. *International Journal of Heat and Technology*, 39(4), 1243–1252. doi: 10.18280/ijht.390422

[3] Alekseenko, S.V., Bilsky, A.V., Dulin, V.M., & Markovich, D.M. (2007). Experimental study of an impinging jet with different swirl rates. *International Journal of Heat and Fluid Flow*, 28(6), 1340–1359. doi: 10.1016/j.ijheatfluidflow.2007.05.011

[4] Magagnato, F., Secchi, F., Forooghi, P., Straub, S., & Frohnapfel, B. (2021). DNS of turbulent heat transfer in impinging jets at different Reynolds and Prandtl numbers. *World Congress in Computational Mechanics and ECCOMAS Congress*, 300, 1–12. doi: 10.23967/wccm-eccomas.2020.299

[5] van Hout, R., Rinsky, V., & Grobman, Y.G. (2018). Experimental study of a round jet impinging on a flat surface: Flow field and vortex characteristics in the wall jet. *International Journal of Heat and Fluid Flow*, 70, 41–58. doi: 10.1016/j.ijheatfluidflow.2018.01.010

[6] Menzler, J. E., Klusmann, M., Wulfmeier, M., Büschgens, D., & Pfeifer, H. (2023). Simulation of gas jet impingement cooling in continuous heat treatment lines with the ANSYS GEKO turbulence model. *HTM - Journal of Heat Treatment and Materials*, 78(2), 91–104. doi: 10.1515/htm-2022-1042

[7] Ahmed, Z.U., Al-Abdeli, Y. M., & Guzzomi, F.G. (2017). Flow field and thermal behaviour in swirling and non-swirling turbulent impinging jets. *International Journal of Thermal Sciences*, 114, 241–256. doi: 10.1016/j.ijthermalsci.2016.12.013

[8] Korinek, T., Frana, K., Hujer, J., & Škarohlíd, J. (2022). Influence of local grid refinement on prediction of impinging jet heat transfer using Scale-Resolving-Simulation methods. *Case Studies in Thermal Engineering*, 36, 102159. doi: 10.1016/j.csite.2022.102159

[9] Domino, S.P., & Wenzel, E.A. (2023). A direct numerical simulation study for confined non-isothermal jet impingement at moderate nozzle-to-plate distances: Capturing jet-to-ambient density effects. *International Journal of Heat and Mass Transfer*, 211, 124168. doi: 10.1016/j.ijheatmasstransfer.2023.124168

[10] Huang, H., Sun, T., Zhang, G., Li, D., & Wei, H. (2019). Evaluation of a developed SST k–ω turbulence model for the prediction of turbulent slot jet impingement heat transfer. *International Journal of Heat and Mass Transfer*, 139, 700–712. doi: 10.1016/j.ijheatmasstransfer.2019.05.058

[11] Zhang, G., Huang, H., Sun, T., Li, N., Zhou, B., & Sun, Z. (2019). Analysis of the performance of a new developed shear stress transport model in a turbulent impinging jet flow. *Physics of Fluids*, 31(11), 115110. doi: 10.1063/1.5118675

[12] Huang, H., Sun, T., Li, N., & Zhang, G. (2022). Sensitization of the modified SST model to the swirling and curvature for turbulent

impinging jet heat transfer. *International Journal of Heat and Mass Transfer*, 182, 121980. doi: 10.1016/j.ijheatmasstransfer.2021.121980

[13] Huang, H., Sun, T., Zhang, G., Liu, M., & Zhou, B. (2021). The effects of rough surfaces on heat transfer and flow structures for turbulent round jet impingement. *International Journal of Thermal Sciences*, 166, 106982. doi: 10.1016/j.ijthermalsci.2021.106982

[14] Kaewbumrung, M., & Plengsa-Ard, C. (2023). Numerical simulation of jet impingement relaminarization using nonlinear eddy viscosity turbulence models. *Engineering Applications of Computational Fluid Mechanics*, 17(1), 2162132. doi: 10.1080/19942060.2022.2162132

[15] Siddique, M.U., Syed, A., Khan, S.A., & Meyer, J.P. (2022). On numerical investigation of heat transfer augmentation of flat target surface under impingement of steady air jet for varying heat flux boundary condition. *Journal of Thermal Analysis and Calorimetry*, 147(6), 4325–4337. doi: 10.1007/s10973-021-10785-4

[16] Kumar, A., Yogi, K., & Prabhu, S.V. (2023). Experimental and analytical study on local heat transfer distribution between smooth flat plate and free surface impinging jet from a circular straight pipe nozzle. *International Journal of Heat and Mass Transfer*, 207, 124004. doi: 10.1016/j.ijheatmasstransfer.2023.124004

[17] Hussain, L., Khan, M.M., Masud, M., Ahmed, F., Rehman, Z., Amanowicz, Ł., & Rajski, K. (2021). Heat transfer augmentation through different jet impingement techniques: A state-of-the-art review. *Energies*, 14(20), 6458. doi: 10.3390/en14206458

[18] Wai, O.J., Gunnasegaran, P., & Hasini, H. (2022). A Review on Experimental and Numerical Investigations of Jet Impingement Cooling Performance with Nanofluids. *Micromachines*, 13(12), 2059. doi: 10.3390/mi13122059

[19] Plant, R.D., Friedman, J., & Saghir, M.Z. (2023). A review of jet impingement cooling. *International Journal of Thermofluids*, 17, 100312. doi: 10.1016/j.ijft.2023.100312

[20] Ries, F., Li, Y., Rißmann, M., Klingenberg, D., Nishad, K., Bohm, B., Dreizler, A., Janicka, J., & Sadiki, A. (2018). Database of near-wall turbulent flow properties of a jet impinging on a solid surface under different inclination angles. *Fluids*, 3(1), 1–22. doi: 10.3390/fluids3010005

[21] Ries, F., Li, Y., Klingenberg, D., Nishad, K., Janicka, J., & Sadiki, A. (2018). Near-wall thermal processes in an inclined impinging jet: analysis of heat transport and entropy generation mechanisms. *Energies*, 11(6), 1354. doi: 10.3390/en11061354

[22] Nishino, K., Samada, M., Kasuya, K., & Torii, K. (1996). Turbulence statistics in the stagnation region of an axisymmetric impinging jet flow. *International Journal of Heat and Fluid Flow*, 17(3), 193–201. doi: 10.1016/0142-727X(96)00040-9

[23] Kura, T., Fornalik-Wajs, E., Wajs, J., & Kenjeres, S. (2019). Heat transfer intensification by jet impingement – numerical analysis using RANS approach. *E3S Web of Conferences*, 108, 01025. doi: 10.1051/e3sconf/201910801025

[24] Kura, T., Fornalik-Wajs, E., Wajs, J., & Kenjeres, S. (2018). Local Nusselt number evaluation in the case of jet impingement. *Journal of Physics: Conference Series*, 1101(1), 012018. doi: 10.1088/1742-6596/1101/1/012018

[25] Kura, T., Fornalik-Wajs, E., Wajs, J., & Kenjeres, S. (2018). Turbulence models impact on the flow and thermal analyses of jet impingement. *MATEC Web of Conferences*, 240, 01016. doi: 10.1051/matecconf/201824001016

[26] Kura, T., Wajs, J., Fornalik-Wajs, E., Kenjeres, S., & Gurgul, S. (2020). Thermal and Hydrodynamic Phenomena in the Stagnation Zone—Impact of the Inlet Turbulence Characteristics on the Numerical Analyses. *Energies*, 14(1), 105. doi: 10.3390/en14010105

[27] Gurgul, S., & Fornalik-Wajs, E. (2023). On the Measure of the Heat Transfer Performance of RANS Turbulence Models in Single Round Jet Impingement. *Energies*, 16(21), 7236. doi: 10.3390/en16217236

[28] *Ansys Fluent, Release 18.1: Theory Guide*. ANSYS Inc., 2018.

[29] Gurgul, S., & Fornalik-Wajs, E. (2023). Turbulent single round jet impingement – numerical data collection, V1, *AGH University of Krakow*. doi: 10.58032/AGH/2SRV8O

[30] Uddin, N., Neumann, S.O., & Weigand, B. (2013). LES simulations of an impinging jet: On the origin of the second peak in the Nusselt number distribution. *International Journal of Heat and Mass Transfer*, 57(1), 356–368. doi: 10.1016/j.ijheatmasstransfer.2012.10.052

[31] Hadžiabdić, M., & Hanjalić, K. (2008). Vortical structures and heat transfer in a round impinging jet. *Journal of Fluid Mechanics*, 596, 221–260. doi: 10.1017/S002211200700955X

[32] Hattori, H., & Nagano, Y. (2004). Direct numerical simulation of turbulent heat transfer in plane impinging jet. *International Journal of Heat and Fluid Flow*, 25(5), 749–758. doi: 10.1016/j.ijheatfluidflow.2004.05.004

[33] Wienand, J., Riedelsheimer, A., & Weigand, B. (2017). Numerical study of a turbulent impinging jet for different jet-to-plate distances using two-equation turbulence models. *European Journal of Mechanics - B/Fluids*, 61, 210–217. doi: 10.1016/j.euromechflu.2016.09.008

[34] Zuckerman, N., & Lior, N. (2005). Impingement Heat Transfer: Correlations and Numerical Modeling. *Journal of Heat Transfer*, 127(5), 544–552. doi: 10.1115/1.1861921

[35] Katti, V., & Prabhu, S.V. (2008). Experimental study and theoretical analysis of local heat transfer distribution between smooth flat surface and impinging air jet from a circular straight pipe nozzle. *International Journal of Heat and Mass Transfer*, 51(17–18), 4480–4495. doi: 10.1016/j.ijheatmasstransfer.2007.12.024

[36] Gao, N., Sun, H., & Ewing, D. (2003). Heat transfer to impinging round jets with triangular tabs. *International Journal of Heat and Mass Transfer*, 46(14), 2557–2569. doi: 10.1016/S0017-9310(03)00034-6

[37] Baughn, J.W., Hechanova, A.E., & Yan, X. (1991). An experimental study of entrainment effects on the heat transfer from a flat surface to a heated circular impinging jet. *Journal of Heat Transfer*, 113(4), 1023–1025. doi: 10.1115/1.2911197

[38] Baughn, J. W., & Shimizu, S. (1989). Heat transfer Measurements from a surface with uniform heat flux and an impinging jet. *Journal of Heat Transfer*, 111(4), 1096–1098. doi: 10.1115/1.3250776

[39] Lytle, D., & Webb, B. (1994). Air jet impingement heat transfer at low nozzle-plate spacings. *International Journal of Heat and Mass Transfer*, 37(12), 1687–1697. doi: 10.1016/0017-9310(94)90059-0

[40] Lee, D.H., Song, J., & Jo, M.C. (2004). The effects of nozzle diameter on impinging jet heat transfer and fluid flow. *Journal of Heat Transfer*, 126(4), 554–557. doi: 10.1115/1.1777583

[41] Tummers, M.J., Jacobse, J., & Voorbrood, S.G.J. (2011). Turbulent flow in the near field of a round impinging jet. *International Journal of Heat and Mass Transfer*, 54(23–24), 4939–4948. doi: 10.1016/j.ijheatmasstransfer.2011.07.007

[42] *Ansys Fluent, Release 18.1: ANSYS Fluent UDF Manual*. ANSYS Inc., 2018.

Co-published by
Institute of Fluid-Flow Machinery
Polish Academy of Sciences
Committee on Thermodynamics and Combustion
Polish Academy of Sciences

http://www.imp.gda.pl/archives-of-thermodynamics/

ARCHIVES OF THERMODYNAMICS

Mathematical model of a three-stage vacuum ejector system

Robert Matysko[a*]

[a]Institute of Fluid-Flow Machinery, Polish Academy of Sciences, Fiszera 14, Gdańsk 80-231, Poland
*Corresponding author email: matyskor@imp.gda.pl

Received: 20.09.2023; revised: 12.01.2024; accepted: 12.06.2024

Abstract

This paper presents a mathematical model of a vapour vacuum system, which is a crucial component of steam power plants of critical importance for energy efficiency. This system consists of three stages, with each stage containing a steam ejector and a gas phase separator in the form of an interstage heat exchanger. The primary purpose of this system is to remove inert gases and maintain the appropriate level of vacuum in the power plant condenser. The presented mathematical model can be used to analyse the operation of the vacuum system in a steady state. Preliminary pressure calculations in various components of the vacuum system show the influence of additional measurement orifice resistance on the vacuum drop in the condenser, which can reduce the efficiency of the entire energy system. It is worth noting that the presented model can be used as a tool for analysing elements of the vacuum system in energy systems.

Keywords: Ejector; Vacuum; Steam power plant; Inert gases

Vol. 45(2024), No. 3, 31–38; doi: 10.24425/ather.2024.150876

Cite this manuscript as: Matysko, R. (2024). Mathematical model of a three-stage vacuum ejector system. *Archives of Thermodynamics*, 45(3), 31–38.

1. Introduction

Steam-based vacuum systems, employed within steam power plant cycles, hold tremendous significance in improving their energy efficiency. They are usually structured as a three-stage assembly, comprising a steam jet (steam ejector) and a mixing heat exchanger. Figure 1 presents a schematic diagram illustrating such a vacuum system.

The arrangement depicted above draws a vapour-air mixture from the condenser space in order to eliminate inert gases and maintain a vacuum during its operation. In such a system, the ejector draws vapours from the condenser space and compresses them into a mixing chamber to separate air from steam. The configuration of three such interconnected elements allows for a high vacuum to be achieved in the condenser, thereby improving heat exchange parameters and the overall efficiency of the energy system by enhancing the thermal cycle efficiency. In the literature [1–3] there exist vacuum system models based on thermodynamics and gas dynamics. In reference [2], thermodynamic functions are employed to calculate the enthalpy and entropy of superheated and saturated steam. The paper provides a detailed discussion of a single-stage vacuum cycle model, and then, for a larger number of stages, repeats the calculation sequence using this model. An important observation in this work is the statement that multi-zone heat exchangers can only be considered in the lowest stage of the condenser, which, in a cascading condensate flow configuration, means that sequentially cooled condensates achieve subcooling only in the final stage.

Nomenclature

A – heat exchange surface area, m^2
d_{eo} – diameter of the outlet nozzle of the supply nozzle, m
d_m – diameter of the mixing chamber (cylindrical section), m
h_p – enthalpy of saturated steam, $h_p = f(p_{vs}, x)$, J/(kg·K)
h_s – enthalpy of condensate, $h_s = f(p_{vs}, x)$, J/(kg·K)
$h_{\mathrm{H_2O}}^{in}$ – enthalpy of the cooling water at the inlet of the heat exchanger, J/(kg·K)
$h_{\mathrm{H_2O}}^{out}$ – enthalpy of the cooling water at the outlet of the heat exchanger, J/(kg·K)
k – polytropic exponent for superheated steam
l_m – length of the mixing chamber, m
$\dot{m}_e$ – mass flow rate of the feed stream to the ejector, kg/s
$\dot{m}_n^{in}$ – mass flow rate of water vapour at the inlet of the mixing heat exchanger (excluding the feed steam to the ejector), kg/s
$\dot{m}_n^{out}$ – mass flow rate of water vapour at the outlet of the mixing heat exchanger, kg/s
$\dot{m}_p$ – mass flow rate of inert gas, kg/s
$\dot{m}_s$ – mass flow rate of condensate stream, kg/s
$\dot{m}_{s,op}$ – mass flow rate at the ejector suction, kg/s
$\dot{m}_{t,op}$ – mass flow rate at the ejector outlet, kg/s
$\dot{m}_w$ – mass flow rate of the cooling water, kg/s
P_{at} – atmospheric pressure, Pa
P_s – suction pressure in the ejector, Pa
P_t – discharge pressure of the ejector, Pa
P_{ws} – steam pressure in the heat exchanger, Pa
$q_{\mathrm{H_2O}}$ – heat flow carried by the exiting cooling water, W
t_s – saturation temperature, $t_s = f(p_{vs})$, °C
$t_{w,in}$ – inlet water temperature to the heat exchanger, °C
$t_{w,out}$ – temperature of the cooling water, °C
$t_{w,out}$ – outlet water temperature from the heat exchanger, °C

Greek symbols

ΔP_{dpp} – measured difference of pressure at orifice system, Pa
Δt_{log} – logarithmic temperature difference, °C
η_d – efficiency of the ejector diffuser
π_t – ejector compression ratio
$\chi_m = \frac{\dot{m}_{s,op}}{\dot{m}_e}$ – ejection ratio

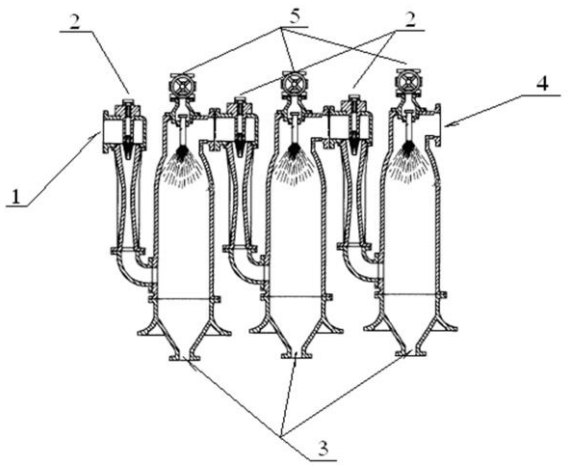

Fig. 1. Three-stage vacuum system: 1– inlet of steam-air mixture from the steam power plant condenser, 2 – inlets of driving steam into the ejectors, 3 – outlets of condensate from the mixing heat exchangers, 4 – vapour outlet, 5 – supply of cooling water to the heat exchangers.

The paper also utilizes an analogy to the flow through an orifice for modeling the flow of inert gas through microporosities. However, this analogy is debatable because the flow occurs through microporosities (long channels with small diameter), where the influence of viscosity on channel permeability plays a significant role. The idealized model of gas flow through an orifice assumed by the authors (short channel with a large diameter) does not correspond to the physics of flow through microchannels (porosities in the condenser). Consequently, it may be inferred that an erroneous assumption was made in this case. In the case of such flow, a more physically accurate model describing channel permeability with viscosity taken into account should be used. A proposed model for viscous flow through microporosities without heat exchange could be the Fanno model, and if heat exchange also occurs in such a microchannel, the Rayleigh model could be applied. In papers [1,3], highly simplified models are presented, allowing only for the determination of pressure values in the prevailing heat exchangers, while neglecting heat exchange processes. Unfortunately, due to the complex phase separation process in intercooler condensers, the models discussed above do not delve into the physics of the heat exchange phenomenon in intercooler condensers. Publication [4] focuses on the analysis and assessment of the performance of steam power plants, including vacuum systems. The author introduces advanced methods for evaluating energy efficiency and optimizing thermal processes. Book [5] provides extensive information on the design and applications of steam turbines, including vacuum systems. It also discusses re-rating techniques that can help improve the efficiency of existing installations. The functioning of the condenser in the presence of inert gases has been discussed in prior studies [6,7] emphasizing the critical role played by vacuum maintenance systems utilised in steam power plant setups.

The topic related to the impact of the operation of vacuum systems remains relevant. Research is being conducted using new computational methods, such as in the work [8], where a model of a steam power plant's vacuum system was presented, and attempts were made to extrapolate and approximate operational parameters using a neural network. In the work [9], calculations of the vacuum system were presented using ejector characteristics obtained from a CFD model. There are also numerous other works related to vacuum systems themselves or focused on improving the performance of energy condensers due to the presence of inert gases. However, these are not the subject of this analysis.

The application of steam ejector systems in power plants is not limited to providing vacuum in condensers. In the following studies, other uses of steam ejector systems in steam power plants are presented. Two-phase ejector systems can also be employed as safety systems for nuclear reactors [10]. Additionally, a 660MW supercritical coal-fired power plant, combined with a steam ejector, is suggested to raise the feedwater temperature,

ensuring NO_x reduction capability during low load operation [11].

The presented model allows for the prediction of the parameters of a power condenser system (pressure and saturation temperature) based on equations that describe the processes occurring in the inert gas extraction system.

2. Model of the air removal system for the power plant condenser

A model of the air removal system, as presented here, can be employed in the comparative analysis of component performance within the energy system. Through a differential analysis of theoretical calculations against measurement data, one can gather information to identify the causes of deteriorating performance in energy systems. This holds significant operational and economic importance due to the cost associated with replacing worn-out components (potential shutdown of the entire power block) and reducing fuel consumption to compensate for additional heat losses resulting from inefficient condenser operation. Given that the power block operates for extended periods in a steady-state condition, with transient states occurring only during start-up or shutdown, the focus of this study is on the analysis of the steady-state condenser air removal system. Figure 2 illustrates an example of such a system along with a description of the variables used in the presented theoretical model.

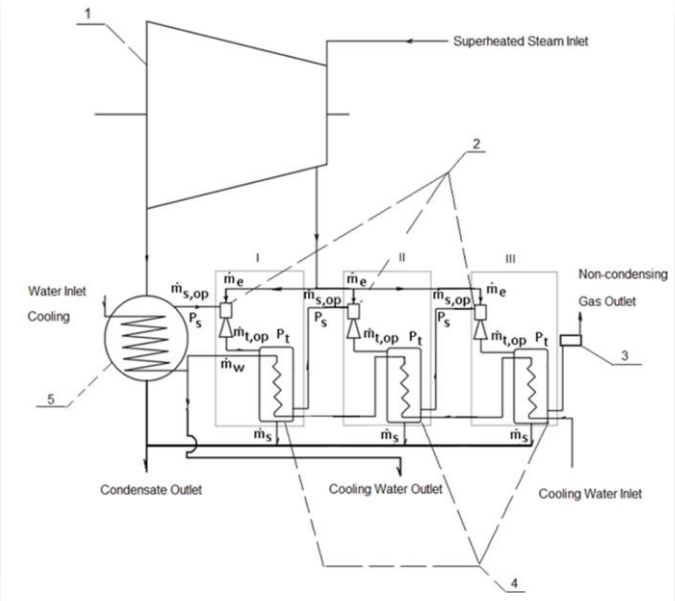

Fig. 2. Steam vacuum system employed in steam power plant systems: 1 – steam turbine, 2 – ejectors, 3 – measurement orifice, 4 – interstage heat exchangers, 5 – steam power plant condenser, I – first stage, II – second stage, III – third stage.

In the model, it was assumed that the initial state of variables for calculations is set as for the system operating under nominal working conditions. Known boundary conditions at the outlet of the final heat exchanger and the supply parameters of individual ejectors were used in the calculations.

To calculate the changes in system parameters during venting, a model consisting of fundamental equations was established.

The equations were applied as follows:

- equations (1) and (2), were utilized to determine variables governing heat exchangers at I, II, III stage parameters,
- equations (3) and (4) were employed to determine variables defining the functioning of the ejectors at I, II, III stage.

The equations were formulated separately for each stage, taking into account boundary values characterizing the limits of each stage.

Input data required for the calculations of the heat exchanger (Fig. 3) includes the following parameters: $\dot{m}_n^{out}$, $\dot{m}_p$, $\dot{m}_e$ and $P_{w,s}$. The calculations for this heat exchanger are intended to determine two specific data points: $\dot{m}_n^{in}$ and $\dot{m}_{op}$. These values are essential for assessing and understanding the performance of the heat exchanger. Additionally, there are parameters and variables that are derived from closure equations, with one of them being $\dot{m}_s$. These derived values play a crucial role in the overall analysis of the heat exchanger's behaviour and characteristics. In summary, this information provides a framework for conducting calculations and analysis related to the specified heat exchanger, with a focus on input data, sought data, and derived parameters and variables.

Mass balance of the steam-gas mixture at the inlet to the heat exchanger (see Fig. 3) is expressed by:

$$\dot{m}_n^{in} + \dot{m}_p + \dot{m}_e = \dot{m}_s + \dot{m}_n^{out} + \dot{m}_p, \tag{1}$$

$$\dot{m}_{op} = \dot{m}_n^{in} + \dot{m}_p + \dot{m}_e, \tag{2}$$

where $\dot{m}_{op}$ is the total mass flow rate of the steam-gas mixture at the inlet to the heat exchanger.

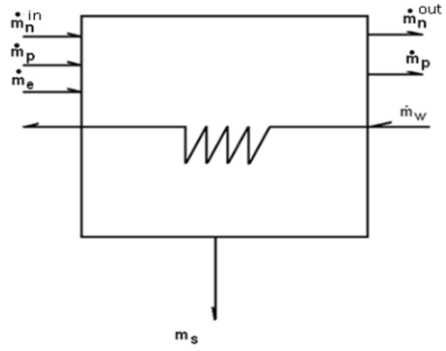

Fig. 3. Schematic diagram of the modeled heat exchanger.

Ejectors, as illustrated in Fig. 4, involve the following key details:

- Input data essential for performing calculations for the ejector consists of the following parameters: P_t (specifically equal to P_{ws}), $\dot{m}_p$, $\dot{m}_e$, and $\dot{m}_{op}$. These parameters are fundamental for conducting accurate assessments and analyses.
- The calculations for the ejector aim to determine two specific pieces of data: P_s, and $\dot{m}_n^{in}$. These values are sought to gain a comprehensive understanding of the ejector's operational characteristics.

– Furthermore, within the context of closure equations, there are parameters and variables that result from these equations. One such variable is π_t. These derived variables play a significant role in the overall analysis of the ejector's performance.

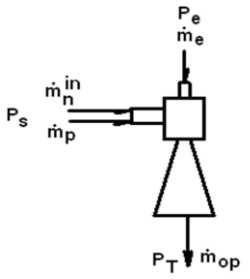

Fig. 4. Schematic diagram of the vacuum ejector.

In summary, this information provides a structured framework for conducting calculations and assessments related to the ejector, highlighting input data, sought data, and variables that result from closure equations to comprehensively evaluate the ejector's functionality.

The required parameters are determined from the system of equations:

$$P_s = \frac{P_t}{\pi_t}, \tag{3}$$

$$\dot{m}_{op} - \dot{m}_e = \dot{m}_p + \dot{m}_n^{in}. \tag{4}$$

The labels used in Fig. 4 and the symbols in Eqs. (3) and (4) represent the following, respectively (see also Nomenclature): P_s – suction pressure in the ejector, P_t – discharge pressure of the ejector, P_e – supply pressure in the ejector, π_t – ejector compression ratio.

The remaining stages of the vacuum system and their basic components are described by similar equations as in the previously described systems. It is evident that the condenser pressure is $P_{sk} = P_s$, at the first stage of ejector system, and the mass flow rate of vapour sucked from the condenser is $\dot{m}_{sk,op} = \dot{m}_{s,op}$.

The system of equations provided earlier has been augmented with additional closure equations that describe the flow characteristics of the ejector and heat exchanger. This comprehensive description includes equations that characterize the behaviour of the analysed components of the vacuum system.

2.1. Supplementary equations for the ejector

In Fig. 5, the symbols adopted in the ejector calculation are presented. The figure also presents proprietary software for determining the parameters of the designed steam ejector. The software was developed based on the mathematical description of the steam ejector as presented in [3] with all the necessary symbols provided to determine the ejector's parameters.

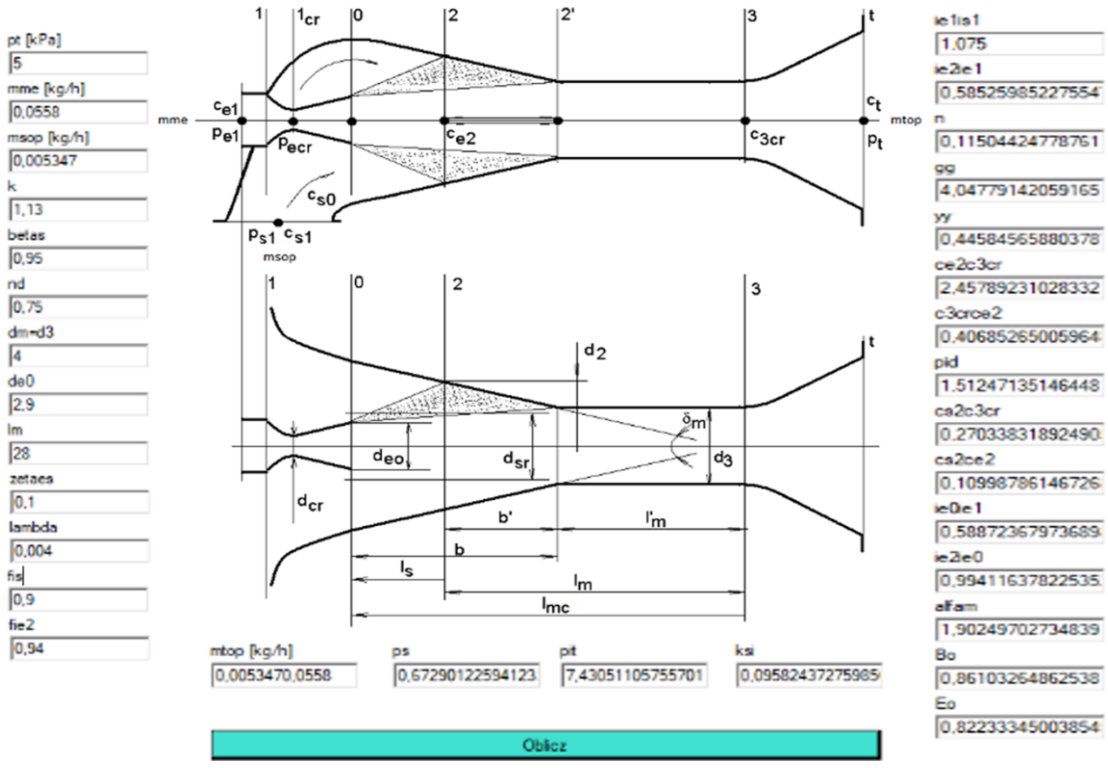

Fig. 5. Sample calculations of the steam ejector subsystem.

The general equations utilized are:

$$P_s = \frac{P_t}{\pi_t}, \tag{5}$$

$$\dot{m}_{s,op} = \dot{m}_{t,op} - \dot{m}_e, \tag{6}$$

where: $\dot{m}_{s,op}$ – mass flow rate at the ejector suction, $\dot{m}_{t,op}$ – mass flow rate at the ejector outlet.

The parameter π_t is determined based on the equation:

$$\pi_t = \frac{\beta_s \pi_d}{\left[1 - k\frac{Bo - \chi_m E_o}{1+\chi_m}\right]}, \tag{7}$$

where each parameter is determined from the following relationships:

$$\pi_d = \left(1 + \eta_d \frac{k-1}{2}\right)^{\frac{k}{k-1}}, \tag{8}$$

$$\beta_s = \frac{p_2}{p_{s1}} \approx \left(\frac{i_{s2}}{i_{s1}}\right)^{\frac{k}{k-1}}. \tag{9}$$

For an ejector with a conical-cylindrical geometry of the mixing chamber, additional auxiliary equations are:

$$B_o = \left[1 - \frac{\zeta_{es}}{2}\frac{l_m}{d_m}\frac{\left(1-\frac{c_{s2}}{c_{e2}}\right)^2}{\left(1+\frac{c_{3,cr}}{c_{e2}}\right)}\sqrt[4]{\frac{\alpha_m}{2{,}25}}\right]\frac{c_{e2}}{c_{3cr}} - \left(1 + \lambda\frac{l_m}{d_m}\right), \tag{10}$$

$$E_o = 1 + \frac{\lambda}{2}\frac{l_m}{d_m}\left(2 + \frac{1}{1{,}5 - \frac{1}{\sqrt{\alpha_m}}}\right) - \left(2 + \frac{\frac{\lambda l_m}{2 d_m}}{1{,}5 - \frac{1}{\sqrt{\alpha_m}}}\right)\frac{c_{s2}}{c_{3cr}}, \tag{11}$$

where (see also Nomenclature): ζ_{es} – hydraulic resistance coefficient ($\zeta_{es}/2 \approx 0.05$), λ – coefficient of friction of the fluid against the chamber wall ($\lambda = 0.004$), c – fluid velocity for a given ejector geometry (Fig. 5),

$$\alpha_m = \left(\frac{d_m}{d_{eo}}\right)^2, \tag{12}$$

$$\frac{c_{e2}}{c_{3cr}} = \phi_{e2}\sqrt{\frac{k+1}{k-1}}\sqrt{\frac{i_{e1}}{i_{s1}}\left(1 - \frac{i_{e2}}{i_{e1}}\right)\left(\frac{1+\chi_m}{\frac{i_{e1}}{i_{s1}}+\chi_m}\right)}, \tag{13}$$

$$\frac{c_{s2}}{c_{3cr}} = \phi_s\sqrt{\frac{k+1}{k-1}}\sqrt{\left(1 - \frac{i_{s2}}{i_{s1}}\right)\left(\frac{1+\chi_m}{\frac{i_{e1}}{i_{s1}}+\chi_m}\right)}, \tag{14}$$

$$n = \frac{k-1}{k}, \tag{15}$$

$$\frac{c_{s2}}{c_{e2}} = \frac{c_{s2}}{c_{3cr}}\frac{c_{3cr}}{c_{e2}}. \tag{16}$$

In the initial stage of calculations, preliminary values for the compression ratio as a function of the ejection ratio should be assumed (β_s), as well as the geometry of the ejector and parameters resulting from gas transformations, i.e., the enthalpy ratios (pressure) during expansion in the suction chamber and the driving nozzle:

$$k, \quad \frac{i_{e2}}{i_{e0}} = \frac{i_{s2}}{i_{e1}} \approx \left(\frac{p_{s2}}{p_{s1}}\right)^n, \quad \frac{i_{eo}}{i_{e1}} \approx \left(\frac{p_{s1}}{p_{e1}}\right)^n, \quad \phi_{e2}, \quad \phi_s.$$

where: i – fluid enthalpy for a given ejector geometry (Fig. 5), ϕ_s – coefficient for velocity determining the influence of fluid friction against the suction chamber wall, ϕ_{e2} – coefficient for velocity determining the influence of fluid friction against the nozzle wall, k – isentropic exponent.

2.2. Additional equations for heat exchange in the condensate separator

The equations describing the heat transfer from condensing steam to cooling water, assuming that the heat fluxes are equal, are presented, i.e. ($q_{\mathrm{H_2O}} = q_k = q_s$)

$$q_{\mathrm{H_2O}} = \dot{m}_w\left(h^{in}_{\mathrm{H_2O}} - h^{out}_{\mathrm{H_2O}}\right), \tag{17}$$

$$q_k = kA\Delta t_{log}, \tag{18}$$

$$q_s = \dot{m}_s\left(h_p - h_s\right). \tag{19}$$

From the above equations, variables resulting from additional closure equations were determined, describing parameters such as: $t_{w,out}$ – the temperature of the cooling water heated by the condensing steam stream at the outlet of the heat exchanger (where $t_{w,out} = f\left(h^{out}_{\mathrm{H_2O}}\right)$), $h^{out}_{\mathrm{H_2O}}$ – enthalpy of the cooling water at the outlet of the heat exchanger, $\dot{m}_w$ – mass flow rate of the cooling water, $h^{in}_{\mathrm{H_2O}}$ – enthalpy of the cooling water at the inlet of the heat exchanger, $q_{\mathrm{H_2O}}$ – heat flow carried by the exiting cooling water, $\dot{m}_s$ – mass flow rate of condensate at the outlet of the heat exchanger, t_s – saturation temperature ($t_s = f(p_{vs})$), $t_{w,in}$ – inlet water temperature to the heat exchanger, Δt_{log} – logarithmic temperature difference, and:

$$h^{out}_{\mathrm{H_2O}} = \frac{q_{\mathrm{H_2O}} - \dot{m}_w h^{in}_{\mathrm{H_2O}}}{\dot{m}_w}, \tag{20}$$

$$\dot{m}_s = \frac{kA\Delta t_{log}}{\left(h_p - h_s\right)}, \tag{21}$$

$$\Delta t_{log} = \frac{\left(t_s - t_{w,in}\right) - \left(t_s - t_{w,out}\right)}{ln\left(\frac{\left(t_s - t_{w,in}\right)}{\left(t_s - t_{w,out}\right)}\right)}. \tag{22}$$

3. Methodology and calculation results

The computational algorithm for a steam power plant vacuum system is presented in Fig. 6. The diagram illustrates the sequence of initializing individual calculation steps along with boundary conditions for the specific heat exchangers and ejectors. Table 1 presents the constants used in the calculations, which allow for the reproduction of the calculations presented in this paper. The key system in the vacuum system of a steam power plant is the ejector system, for which the constants used in the calculations are presented in Fig. 5. The mass flow rate from the feed stream to the ejector determines the suction and delivery flows and pressure to the heat exchangers according to the algorithm shown in Fig. 6.

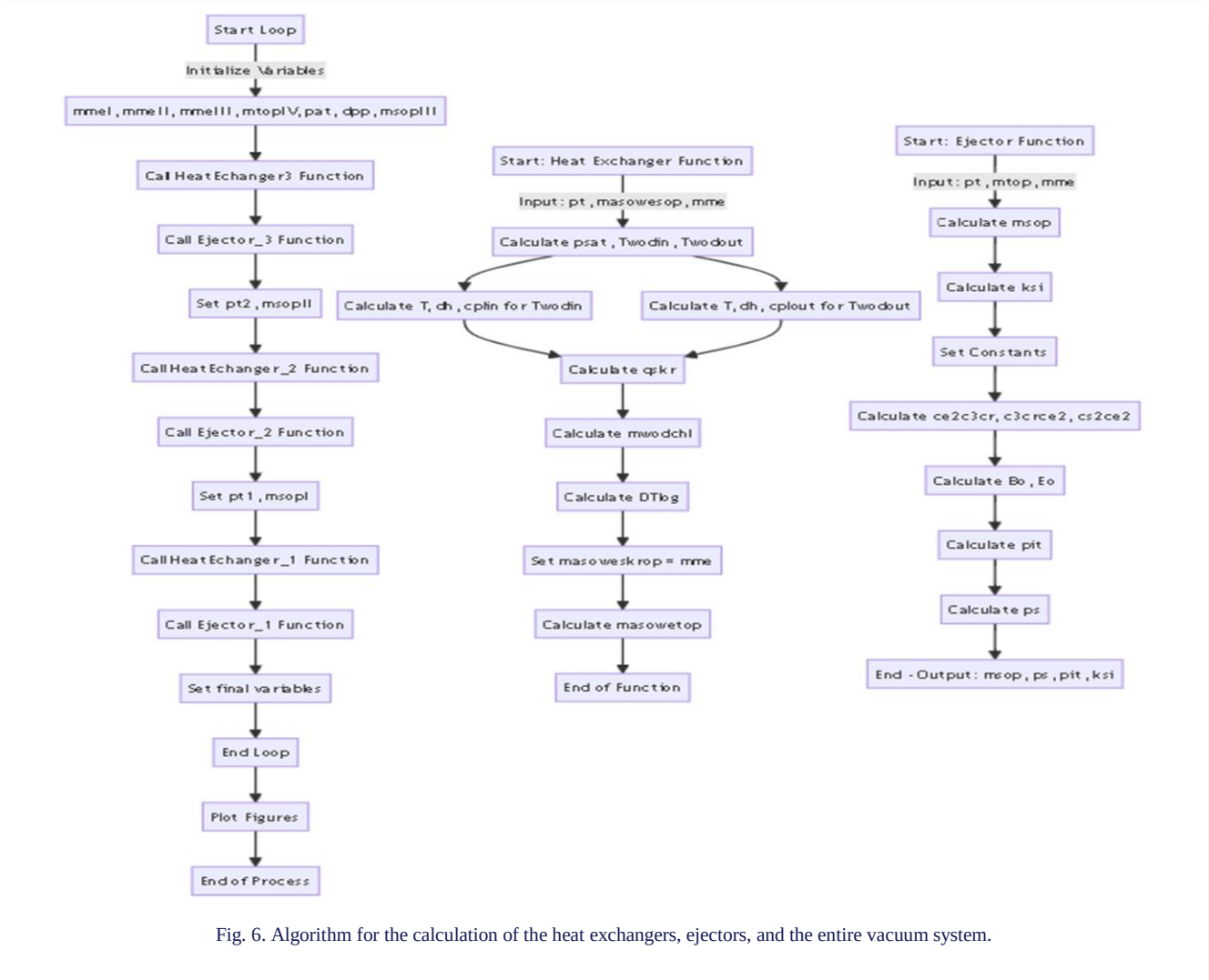

Fig. 6. Algorithm for the calculation of the heat exchangers, ejectors, and the entire vacuum system.

Table 1. Assumed input parameters for calculations.

Mass flow rate of the feed stream to the ejector.	$\dot{m}_e = loop\,\{0.8:0.2:24\}$ kg/h
Atmospheric pressure.	$P_{at} = 101.325$ kPa
Measured difference of pressure at orifice system.	$\Delta P_{dpp} = 10$ kPa
Assumed nominal inlet temperature of the cooling water.	$t_{w,in} = 20$ °C
Assumed nominal outlet temperature of the cooling water.	$t_{w,out} = 25$ °C
Flow rate of inert gases measured in orifice system.	$\dot{m}_{t,op3} = 1$ kg/h

The preliminary calculation results for the pressure in the condenser and individual heat exchangers (condensate separators) are presented. The calculation results show the influence of an additional element, namely the measurement cross, on the pressure in the condenser. It is evident that the vacuum is deteriorated due to the additional resistance posed by the measurement cross, contributing to the overall efficiency reduction of the thermal circuit. This suggests that additional measurement elements placed at the outlet of the vacuum system should have low flow resistance. Please note that the model used has not been verified with the actual vacuum system of the power generation system. Figure 7 shows the calculation results of the pressure in the individual elements of the vacuum system. Figure 8 presents the characteristic of the jet considered in the vacuum system calculations. The characteristic describes the behaviour of three jets installed in the vacuum system.

In Figs. 9, 10, and 11, characteristics describing the operation and thermodynamic parameters of heat exchangers associated with the ejector system of each vacuum stage are presented. It is evident that the influence of the ejection ratio on the saturation pressure in the individual heat exchangers is a nonlinear function dependent on mass flow rates. The logarithmic temperature difference is also related to the mass flow rates of condensate extracted from the inter-stage heat exchangers. It can be observed that for a constant difference in cooling water temperature, the logarithmic difference depends on the saturation temperature value, which is linked through the thermodynamic properties of water vapour with the saturation pressure.

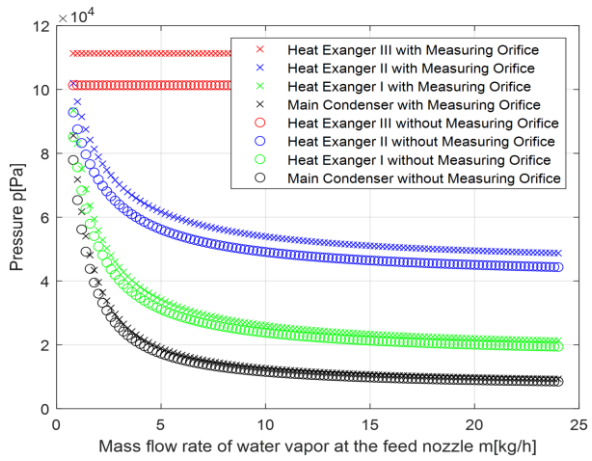

Fig. 7. Calculation of pressure values in the heat exchanger system of the steam venting and condensation in the power plant condenser.

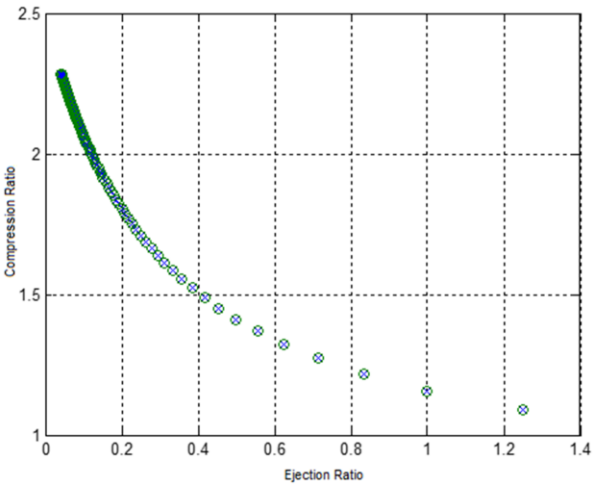

Fig. 8. Characteristic of jets obtained from calculations in the vacuum system of the power generation system.

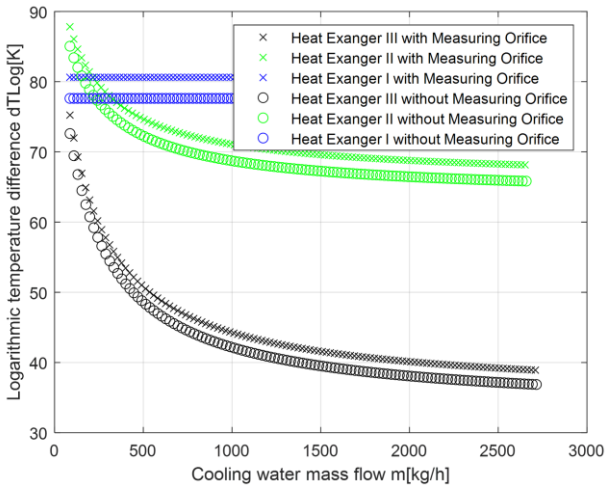

Fig. 9. Logarithmic temperature difference as a function of the mass flow rate of cooling water.

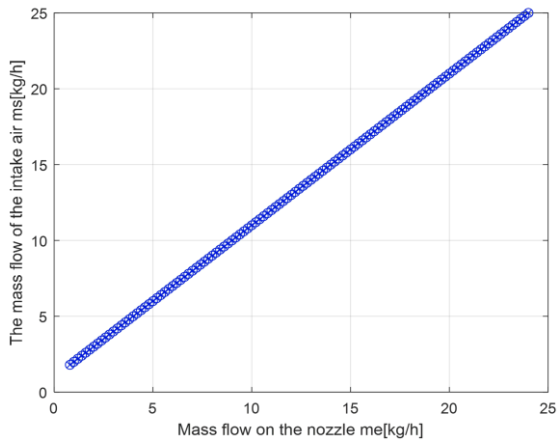

Fig. 10. Mass flow rate of inert gases as a function of the mass flow rate of steam supplied to the ejector nozzle.

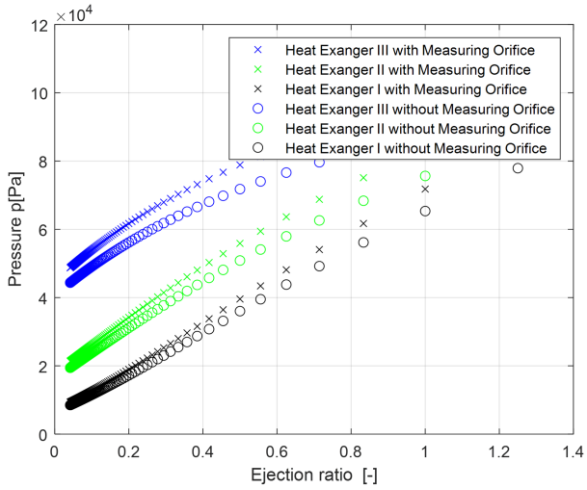

Fig. 11. Pressure in heat exchanger systems as a function of the ejection ratio.

4. Conclusions

In the paper, a vacuum cycle model has been presented, which was developed for the purpose of diagnosing elements of the vacuum system in the energy system.

The results of preliminary pressure calculations in various elements of the vacuum system revealed the influence of additional measurement probe resistance on the vacuum drop in the condenser, which may reduce the overall system efficiency. The presented results draw attention to the magnitude of the vacuum drop in the condenser resulting from the installation of the measuring system at the outlet of the vacuum system chimney. The results also allow for the determination of the pressure value in the water separators at different stages of the vacuum system. However, it is worth noting that the presented model serves as a diagnostic tool that can be used to analyse elements of the vacuum system in energy systems. Nevertheless, this model still requires verification with real data and further research.

The paper provides a significant contribution to understanding and improving vacuum systems in steam power plants, which may contribute to increasing the energy efficiency of such systems in the future.

References

[1] Paliwoda, A. (1971). *Jet Refrigeration Devices*. WNT, Warsaw (in Polish).

[2] Shakor, A., & Szafran, R. (1996). Digital Model of the Turbo-Unit Vacuum System. *Energetyka*, 8 (in Polish).

[3] Goliński, J.A., & Troskolański, A.T. (1979). *Ejectors: Theory and Design*. WNT, Warsaw (in Polish).

[4] de Souza, G.F.M. (2012). *Thermal Power Plant Performance Analysis*. Springer.

[5] Bloch, H.P., & Singh, M.P. (2009). *Steam Turbines: Design, Applications, and Rerating* (2nd ed.). New York.

[6] Drożyński, Z. (2018). Steam condensation analysis in a power plant condenser. *Archives of Thermodynamics*, 39(4), 3–32. doi: 10.1515/aoter-2018-0027

[7] Laskowski, R., Smyk, A., Ruciński, A., & Szymczyk, J. (2021). Determining steam condensation pressure in a power plant condenser in off-design conditions. *Archives of Thermodynamics*, 42(3), 45–62. doi: 10.24425/ather.2020.138109

[8] Strušnik, D., Marčič, M., Golob, M., Hribernik, A., Živić, M., & Avsec, J. (2016). Energy efficiency analysis of steam ejector and electric vacuum pump for a turbine condenser air extraction system based on supervised machine learning modelling. *Applied Energy*, 173, 386–405. doi: 10.1016/j.apenergy.2016.04.047

[9] Jahangiri, A., Aliabadi, M.A.F., Pourranjbar, D., Mottahedi, H. R., Gharebaei, H., & Ghamati, E. (2023). A comprehensive investigation of non-condensable gas and condenser temperature effects on power plant ejector performance by considering condensation flow regime. *Thermal Science and Engineering Progress*, 45, 102–128. doi: 10.1016/j.tsep.2023.102128

[10] Yuto, T., Shuichiro, M., Takashi, H., & Michitsugu, M. (2015). Application of steam injector to improved safety of light water reactors. *Progress in Nuclear Energy*, 78, 80–100. doi: 10.1016/j.pnucene.2014.07.045

[11] Weixiong, C., Guozhu, Z., Bingxin, L., Ming, L., & Jiping, L. (2017). Simulation study on 660MW coal-fired power plant coupled with a steam ejector to ensure NOx reduction ability. *Applied Thermal Engineering*, 111, 550–561. doi: 10.1016/j.applthermaleng.2016.09.104

Co-published by
Institute of Fluid-Flow Machinery
Polish Academy of Sciences
Committee on Thermodynamics and Combustion
Polish Academy of Sciences

http://www.imp.gda.pl/archives-of-thermodynamics/

CFD analysis of the effect of bed geometry on H_2O adsorption and desorption efficiency

Szymon Janusz[a,b*], Marcin Borcuch[b], Piotr Cyklis[a]

[a]Cracow University of Technology, Jana Pawla II 37, 31-864 Kraków, Poland
[b]M.A.S. Sp z o.o., Research and Development Department, Składowa 34, 27-200 Starachowice, Poland
*Corresponding author email: szymon.janusz@doktorant.pk.edu.pl

Received: 29.01.2024; revised: 22.05.2024; accepted: 12.06.2024

Abstract

The article presents a comprehensive computational fluid dynamics analysis of the adsorption and desorption cycles in adsorption refrigeration systems, focusing on the impact of the adsorbent bed geometry. The entire adsorption/desorption cycle has been modeled, allowing for the observation of events during the transitional period between processes and how these influence their progression. This approach is a novelty in the field. The developed numerical model was verified against experimental data available in the literature, demonstrating excellent convergence with the experiment, with a deviation not exceeding 2%. The study illustrates how the geometrical parameters such as height and length of the bed affect the efficiency of the adsorption and desorption processes, emphasizing the importance of bed geometry in the adsorption of heat and mass exchangers in energy and adsorbate transfer. The research findings provide valuable insights for designing more efficient cooling devices using adsorption technology, highlighting the role of bed geometry in optimizing these systems. Modeling the entire adsorption/desorption cycle is a novelty and allows for the observation of what happens during the transitional period between processes and how this influences their progression.

Keywords: Heat transfer; Adsorption; Computational fluid dynamics; Mass transfer; Refrigeration devices

Vol. 45(2024), No. 3, 39–47; doi: 10.24425/ather.2024.151214

Cite this manuscript as: Janusz, S., Borcuch, M., & Cyklis P. (2024). CFD analysis of the effect of bed geometry on H_2O adsorption and desorption efficiency. *Archives of Thermodynamics*, 45(3), 39−47.

1. Introduction

The ongoing pursuit of energy-efficient and environmentally sustainable cooling technologies has catalyzed the development of several alternatives to conventional vapour compression systems. A notable breakthrough in this domain is adsorption cooling technology, which harnesses the principles of adsorption and desorption of a refrigerant onto an adsorbent material. This approach has garnered significant attention for its ability to effectively utilize waste heat and significantly reduce greenhouse gas emissions, marking a substantial leap in eco-conscious cooling solutions. Due to their innovative operating mechanism, adsorption cooling systems present a promising prospect, yet they are continuously subject to enhancements and development. These systems are characterized by a relatively modest Coefficient of Performance (COP) and considerable size, factors which currently limit their competitiveness in the broader market. The challenge in optimizing these devices lies in the complexity and cost associated with adjusting various interdependent parameters, which intricately affect the device's performance. In this

Nomenclature

a_{sv} – interfacial area density, m^{-1}
D_p – diameter of the bed particles, m
h_{sv} – heat transfer coefficient in porous bed, $W/(m^2K)$
k – thermal conductivity of the medium W/(m K)
$\dot{m}$ – mass flow rate
Nu – Nusselt number
P – pressure, Pa
T – temperature, K

Greek symbols

ε – porosity of the medium
τ – time, s

Subscripts and Superscripts

a – average
A – absolute
f – fluid
s – surface
t – total
v – vapour

Abbreviations and Acronyms

CFD – computational fluid dynamics
COP – coefficient of performance
PISO – pressure implicit with splitting of operators
UDF – user defined function

context, Computational Fluid Dynamics (CFD) emerges as an invaluable tool for advancing our understanding and enhancing the efficiency of these systems.

In paper [1], numerical simulations of a real-scale adsorption chiller, including a sorption chamber with a bed, condenser, and evaporator, were conducted. The results were verified against experimental setups, showing high consistency with deviations not exceeding 2%. This demonstrates the legitimacy of the usage of numerical models for optimizing adsorption chillers. In the study [2], the authors present a methodology for conducting numerical simulations of adsorption and desorption processes in adsorbent beds, utilizing CFD techniques. The research focuses on analyzing the impact of various factors, such as the cooling water temperature and cycle duration, on the performance of adsorption chillers. In another work, researchers employed CFD simulations to examine the influence of silica gel grain size on the efficiency of the adsorption process, thereby identifying optimal grain dimensions for maximal operational effectiveness [3]. Similarly, investigations into the spatial distribution of porosity gradients have illuminated their critical role in enhancing the cooling performance of adsorption-based systems. Employing CFD simulations, researchers have validated the significance of directional porosity distribution in improving cooling efficiency [4]. Analysis of various adsorbent-adsorbate combinations has revealed superior performance in coated beds versus densely packed ones [5]. The impact of the temperature of the cooling and heating medium on the sorbent bed was described in the paper [6]. Despite these advancements, there remains a need to fully comprehend the impact of adsorbent bed geometry on the performance of adsorption chillers, particularly in light of novel adsorbent materials and innovative bed configurations that have emerged in recent years. In the study [7], the authors designed and constructed a fin of the heat exchanger, increasing the efficiency of the adsorption process. The improvement was not significant due to the limitations of 3D printing; however, this remains an interesting direction for future research. In the paper [8] the authors proposed using a modified plate heat exchanger in adsorption devices. Both experimental and numerical results showed a 310% increase in differential water absorption after 300 seconds from the start of adsorption compared to standard adsorbers with aluminium fins.

One of the most critical components in adsorption chillers is the adsorbent bed. The design and structural geometry of the bed significantly influences heat and mass transfer processes, thus directly impacts the overall efficiency of the adsorption chiller. Extensive research has been undertaken to explore the effect of bed geometry on the efficiency of the adsorption process. Studies have shown, that a thin, flatbed geometry outperforms a cylindrical configuration in analyzed conditions [9]. Additionally, research findings suggest that a compact bed layout with a high surface-to-volume ratio can enhance chiller efficiency [5]. In the study [10], the authors conducted research on optimizing the adsorbent bed. It focuses on optimal geometric parameters and the impact of metal additives. Numerical simulations were used, analyzing the adsorbent bed with metals and silica gel/water pair. The study reveals that adding aluminium particles significantly enhances cooling performance, showing a 300% efficiency increase with the addition of aluminium particles. In a different study [11], adsorbent beds with vacuum tubes and fins were experimentally tested. It was found that beds with more fins shortened the cooling time but lengthened the preheating and desorption times. The system's optimal performance was achieved with four fins, and additional fin enhancement did not further improve the efficiency of the adsorption cooling system. This suggests that each bed geometry has an optimal number of fins, and more fins do not always equate to better performance. In the paper [12], the impact of fin thickness and height, as well as plate type, on the efficiency of an adsorbent bed were investigated. The study revealed that decreasing fin thickness could enhance water adsorption by up to 8%, and reducing fin height from 30mm to 20mm could increase adsorption by up to 17%. Additionally, the type of plate used was found to be significant, with a copper plate improving water adsorption by up to 9% compared to an aluminium plate. Using CFD simulations, the importance of the Z-direction in porosity distribution and its significant impact on cooling efficiency have been validated [13]. Furthermore, investigations into different adsorbent-adsorbate pairings have demonstrated improved performance in coated beds compared to packed beds [14].

Despite these research advancements, a comprehensive understanding of how the geometry of the adsorbent bed influences the performance of adsorption chillers remains crucial. The efficiency of adsorption in cooling systems is a complex measure of how effectively the system utilizes the adsorption-desorption cycle to generate a cooling effect. This process is more complicated than a simple relationship between the amount of water

vapour adsorbed by the adsorbent and the efficiency of cooling. Key aspects, such as adsorption capacity and rate, are significant but represent only a part of the equation. In thermodynamic terms, the timing of the cycle involving adsorption and desorption is fundamental. A cycle that is too short may not provide sufficient regeneration of the adsorbent, while a cycle that is too long can decrease overall operational efficiency. Therefore, not only the intensity of vapour adsorption is important, but also the optimization of the cycle time based on specific conditions and system requirements. Furthermore, the geometry and size of the device are crucial. The time required to switch between the adsorption and desorption phases and the stabilization of the process can impact efficiency to the extent that lengthening the cycle becomes more advantageous. In this context, optimizing the adsorbent bed and heat exchanger geometries is particularly important. Efficient and controlled heat transfer is essential for maximizing the cycle's efficiency. This research aims to demonstrate specific correlations between the geometry of the adsorbent bed and the adsorption process, ultimately influencing the efficiency of adsorption-based cooling devices.

2. Methods

The sample analyzed is a representative part of a plate heat exchanger used in adsorption refrigeration devices. The model consists of a wall simulating the heat exchanging surface, where a convective boundary condition is established with a heat transfer coefficient of 600 W/(m²K), consistent with the experimental setup described in the literature [15], and a temperature of 303 K, corresponding to the cooling water temperature for the adsorbent bed. On this wall, a layer of silica gel, serving as an adsorbent in a water vapour atmosphere (adsorbate), is applied. The silica gel sample is enclosed in an aluminium frame, which restricts vapour flow in one direction, and an adiabatic boundary condition is applied to it. This inflow is modelled as a pressure boundary condition with a P_A = 2000 Pa and an incoming water vapour temperature T_v = 290.15 K. The operating pressure within the model is set to 0 Pa, and the model features only a vapour inlet with no outlet. The study involved simulating the adsorption process in beds of various dimensions, where the base dimensions are set as 100×80×6 mm (Fig. 1).

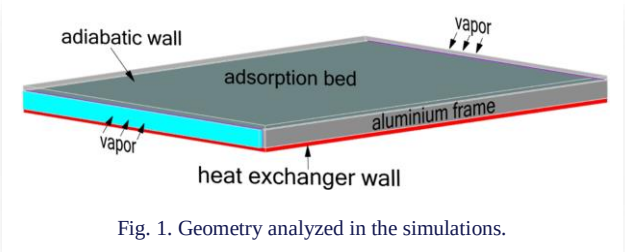

Fig. 1. Geometry analyzed in the simulations.

The model was discretized using the SWEEP method. Prepared geometry enabled the creation of a well-organized structural mesh across the entire model. In order to perform grid convergence tests, three grids differing by a factor of 1.5 in their characteristic dimension were generated. Each grid was characterized by a minimum orthogonal quality equal to 1. Detailed information about the prepared grids is gathered in Table 1. Differences in the values of adsorbed vapour and average temperature in the adsorption bed between the results obtained for the individual grids result from the applied global grid size. Considering the very small differences in values between the fine and medium grids, it was decided to use the medium density grid (Fig. 2) for further work, as a compromise between computational cost and solution accuracy.

Table 1. Parameters of meshes used in the grid convergence study.

Mesh	Characteristic dimension of mesh elements [mm]	Total number of mesh elements	Orthogonal quality	Average bed temperature [K]	Uptake [kg/kg]
Coarse	0.7	125350	1	315.255	0.1209
Medium	0.5	207360	1	314.925	0.1212
Fine	0.3	613452	1	314.903	0.1212

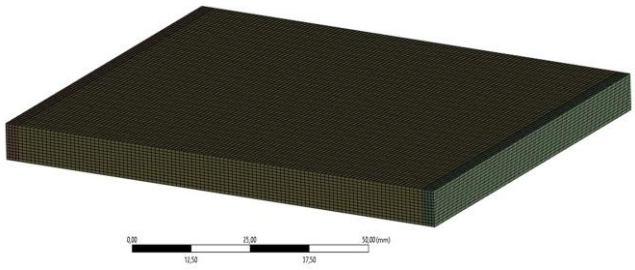

Fig. 2. Numerical mesh generated.

In this study, a CFD modelling approach for the adsorption process as described in paper [2] was adopted. The calculations were performed using Ansys Fluent software. For the modeling of the porous volume, the equilibrium model was replaced with a non-equilibrium model, which is defined by two parameters: Interfacial Area Density and Heat Transfer Coefficient in ANSYS Fluent software.

Interfacial Area Density a_{sv} is a parameter used in multiphase flow simulations within porous media. It measures the area of the interface between different phases (e.g. liquid and solid) per unit volume of the porous material. This parameter is crucial for predicting phenomena such as mass and heat transfer accurately

$$a_{sv} = \frac{6(1-\varepsilon_t)}{D_p}. \quad (1)$$

Heat transfer coefficient h_{sf} in a porous medium is a parameter that quantifies the efficiency of heat transfer between the fluid and the solid structure within the porous material

$$\frac{1}{h_{sf}} = \frac{D_p}{k_f \mathrm{Nu}} + \frac{D_p}{10k_f}. \quad (2)$$

The simulation was conducted under transient conditions. It was assumed that the flow of water vapour is laminar. The Green-Gauss node based gradient computation scheme, along with the QUICK momentum discretization scheme, were employed. A pressure-based solver utilizing the PISO scheme was used.

The model was verified against an experiment available in the literature [15]. The experiment was conducted on a specially constructed experimental setup that simulated the operation of an adsorption refrigeration device. The sorption capacity of a silica gel sample was analyzed under various temperatures of the cooling/heating medium. The maximum deviation between the numerical simulation and experimental data did not exceed 2% (Fig. 3), indicating very good convergence of the developed numerical model.

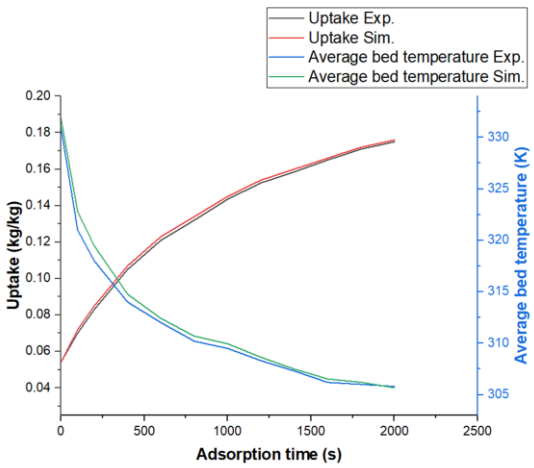

Fig. 3. Comparison of experimental and numerical results: average bed temperature and the amount of adsorbed water vapour in the bed.

For further simulations, initial conditions were set: T = 303.15 K, P = 2000 Pa, and H_2O uptake 0 g/g. Each cycle consisted of two stages: adsorption, where the sorption bed was cooled, and regeneration (desorption), where the bed was heated. As the adsorption process ends and desorption begins, the function of the heat exchanger plate switches from cooling to heating. Consequently, expressions for the cyclic change of the boundary condition from 303.15 K to 353.15 K were introduced. During desorption, as vapour is released from the bed, the boundary condition changes from a pressure inlet to a pressure outlet. For this purpose, a UDF (user defined function) was prepared and implemented to monitor the P in the adsorption bed. This function calculates and returns the P_a in a specified area, allowing observation of P changes over time. Moreover, it defines pressure boundary conditions that trigger the change in boundary conditions. Iterative calculations, consisting of 3000 time steps (5 full cycles of 600 seconds each) were performed. Each step lasted one second and could include up to 500 iterations until a reduction of normalized residuals by four orders of magnitude was achieved. However, it's important to note that sudden changes in temperature and pressure may lead to discrepancies in simulation results. Therefore, during transitions from adsorption to desorption and vice versa, a reduction in the time step of the simulation from 1 s to 0.005 s for the next 5 seconds was applied. As a result, convergence was achieved at the level of $4x10^{-5}$ for all residuals. Additionally, the vapour velocity at the inlet, temperature in the adsorption bed, and the amount of water vapour adsorbed by the bed were monitored.

Within the scope of this study, the adsorption process was simulated for beds of various dimensions. The base dimensions of the bed were 100×80×6 mm. The first step involved examining the effect of increasing the bed height to 6 mm and 9 mm (Fig. 4a). Subsequently, an analysis was conducted on changing the bed length to 50 mm and 150 mm (Fig. 4b).

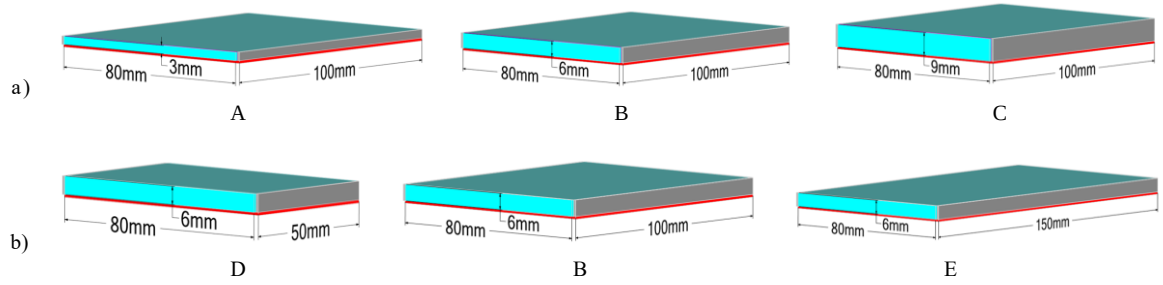

Compilation of silica gel mass depending on the geometry of the bed.

Geometry	A	B	C	D	E
Mass of silica gel [kg]	0.01776	0.03552	0.05328	0.00888	0.02664

Fig. 4. Dimensions of the simulated samples: a) various heights of the adsorbent bed, b) various lengths of the adsorbent bed.

3. Results

Due to significant differences in saturation values between various stages of the simulation, different scales were applied to better illustrate the processes occurring within the bed (Figs. 5a, 5b). Graphical distribution of the amount of vapour adsorbed by the sorption bed (Figs. 5a, 6a,7a) at τ = 300 s, corresponding to the end of the adsorption process in the first cycle, and at 600 s, corresponding to the end of the desorption process in the first cycle. Similarly, the amount of vapour adsorbed after 2700 s (Figs. 5b, 6b, 7b) – marking the end of the adsorption process in the last cycle, and at 3000 s - marking the end of desorption in the last analyzed cycle. The graphical distributions (Figs. 5, 6, 7) indicate that for all analyzed geometries, both adsorption and desorption processes occur most efficiently near the wall

heated/cooled by the heat exchanger and at the water vapour inlet surface, highlighting the significance of *T* on the adsorption/desorption processes. It is observed that the saturation of the bed with water vapour increases with each process cycle, suggesting that adsorption and desorption do not occur uniformly. The ratio of the amount of adsorbed vapour to the size of the bed is highest for the bed with the smallest height and lowest for the tallest bed, confirming the importance of the distance from the centre of the bed to the heat exchange surface.

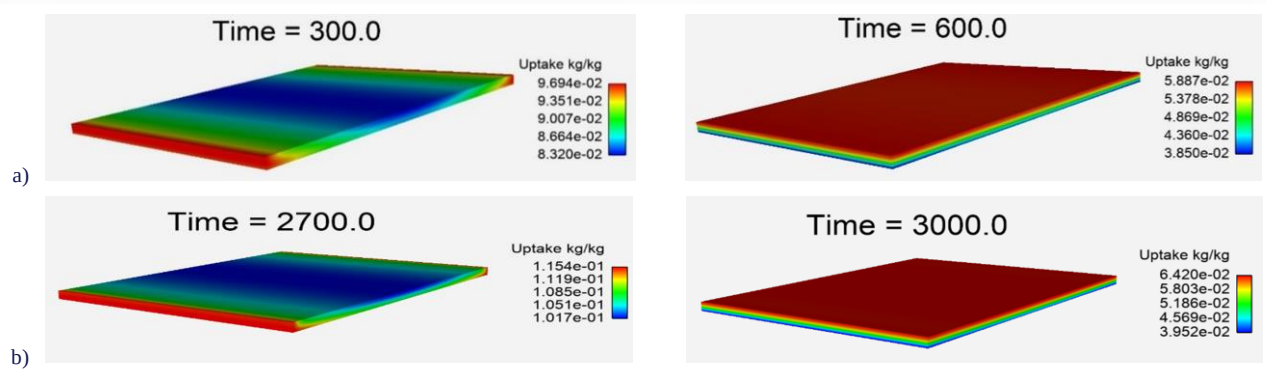

Fig. 5. Distribution of the amount of vapour adsorbed by the sorption bed with dimensions of 100×80×3 mm (A) after adsorption and desorption process: a) in the first cycle of the process b) in the last cycle of the process.

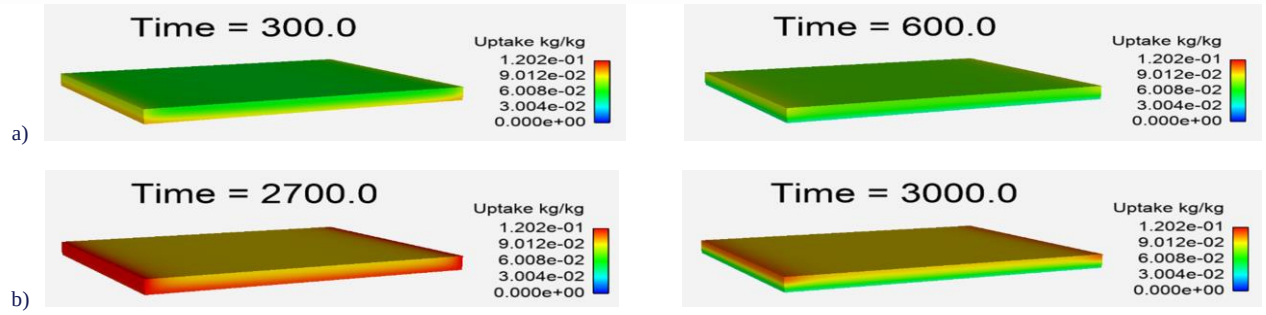

Fig. 6. Distribution of the amount of vapour adsorbed by the sorption bed with dimensions of 100×80×3 mm (B) after adsorption and desorption process a) in the first cycle of the process b) in the last cycle of the process.

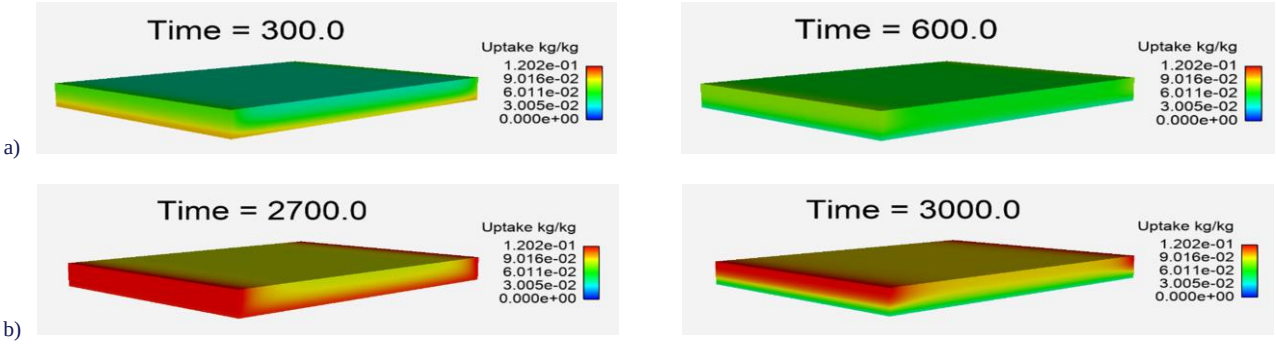

Fig. 7. Distribution of the amount of vapour adsorbed by the sorption bed with dimensions of 100×80×3 mm (C) after adsorption and desorption process a) in the first cycle of the process b) in the last cycle of the process.

The amount of vapour adsorbed was analyzed for beds of varying heights (Fig. 8). The stabilization of the process in successive cycles was quickest for the bed with the lowest height and slowest for the bed with the greatest height. For beds B and C heights, similar saturation values after the desorption process were observed in the initial cycles, which increased with subsequent cycles. According to the analysis of graphical distributions, the most vapour relative to the amount of adsorbent material in each cycle was adsorbed by bed A, stabilizing at 0.132 kg/kg. The least amount of vapour was adsorbed in bed C, stabilizing at 0.111 g/g which represents a difference of approximately 20%. In the adsorption bed A, vapour desorbed to a level of 0.041 kg/kg, whereas in the bed C, it desorbed to 0.074 kg/kg, constituting a difference of about 45%. The dynamics of the process varied depending on the height of the bed. Adsorption was most intense for the bed A and least intense for the bed C. This can be attributed to the fact that cooling of the bed during the adsorption process significantly influences its progression, and

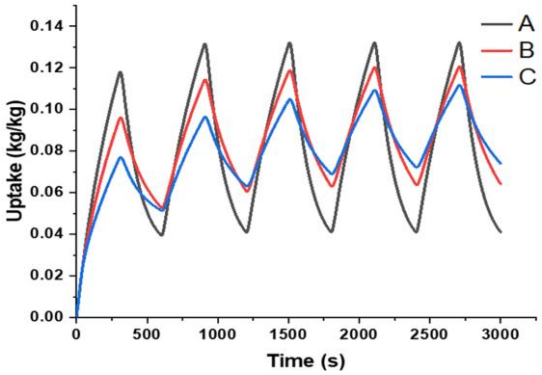

Fig. 8. Comparison of the amount of water vapour adsorbed for different bed heights.

heat exchange within the bed itself is inefficient.

A comparison of T_a in sorption beds with different geometries during the processes of adsorption and desorption was examined (Fig. 9).

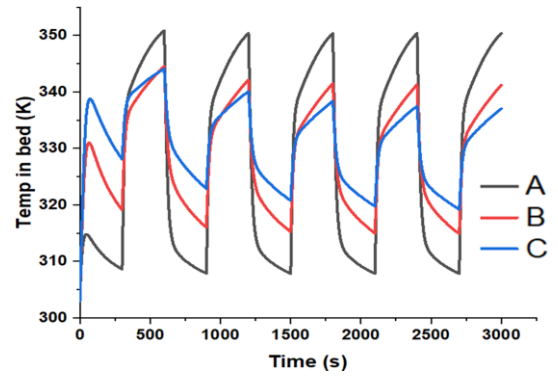

Fig. 9. Comparison of the T_a in sorption beds for different bed heights.

The bed A reaches an T_a at the end of each cycle stage that is closest to the T occurring in the heat exchanger, 308 K after adsorption and 350 K after desorption. This facilitates the most efficient adsorption/desorption process and has a direct impact on greater control over the process. In the case of the bed C, the T_a in the bed deviates more significantly from the T of the cooling/heating medium, recording 320 K at the end of the adsorption process and 337 K after desorption, which affects the amount of vapour adsorbed.

The mass flow of water vapour adsorbed by the sorption bed is illustrated (Fig. 10). Negative values indicate that vapour is being released and evaporates from the sorption bed. During the first cycle, where the saturation of each bed with water vapour was 0 kg/kg, the most intense $\dot{m}_v$ occurred in the bed C, reaching 1.13×10^{-2} g/s, which directly depended on the volume of the sorbent. In subsequent cycles, as conditions stabilize, the differences in $\dot{m}_v$ decrease, in the last cycle for beds B and C, they are very similar, with the initial adsorption rate being approximately 3.02×10^{-3} g/s.

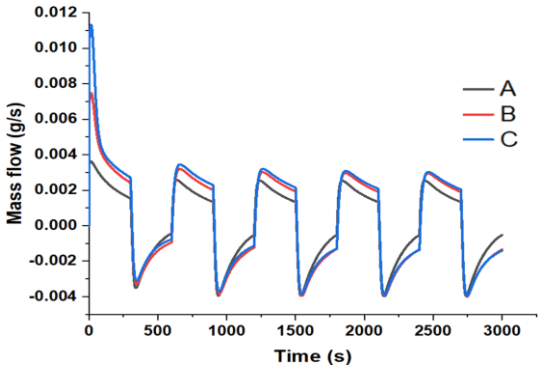

Fig. 10. Results of solar collector field simulation – hourly heating output.

Subsequently, an analysis was conducted to assess the impact of bed length on the adsorption process. An aluminium frame restricted the steam inlet and directed the steam along the length of the bed. Beds with dimensions of 50×80×6 mm (D), 100×80×6 mm (B), and 150×80× 6 mm (E) were analyzed (Fig. 5b).

Similarly to Figs. 5–7, Figs. 11–13 illustrate the graphical distribution of the amount of vapour adsorbed by the sorption bed at times corresponding to the end of the adsorption process in the first and last cycles, as well as at times corresponding to the end of the desorption process in the first and last cycles. The graphical distributions indicate similar dependencies as observed in the earlier analysis. The most efficient adsorption and desorption processes occur near the wall heated/cooled by the heat exchanger and at the surface where water vapour enters.

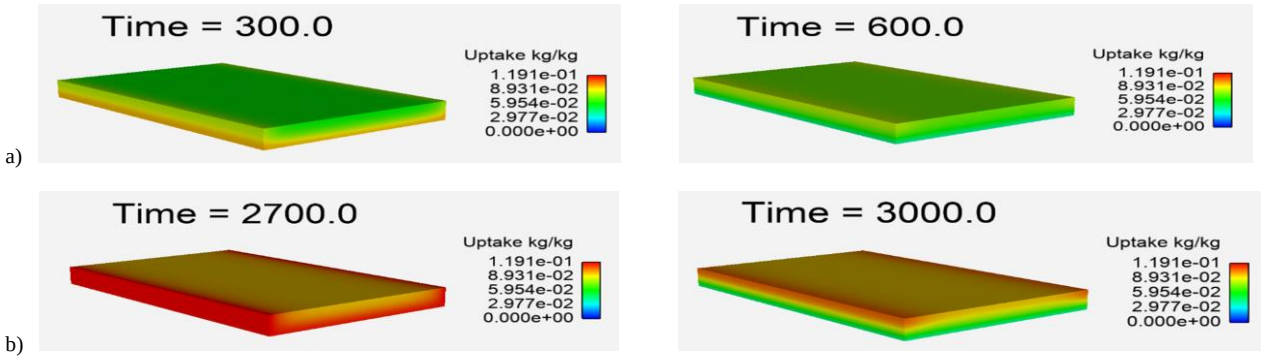

Fig. 11. Distribution of the amount of vapour adsorbed by the sorption bed with dimensions of 50×80×6 mm (D) after adsorption and desorption process a) in the first cycle of the process, b) in the last cycle of the process.

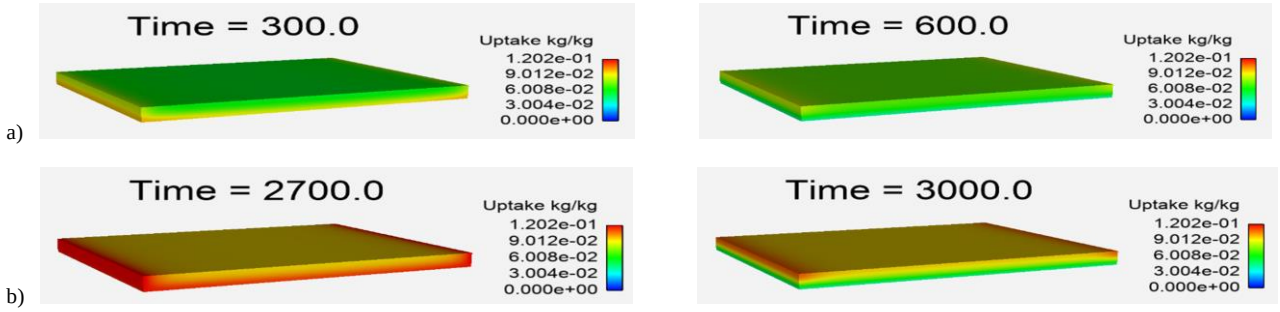

Fig. 12. Distribution of the amount of vapour adsorbed by the sorption bed with dimensions of 100×80×6 mm (B) after adsorption and desorption process a) in the first cycle of the process, b) in the last cycle of the process.

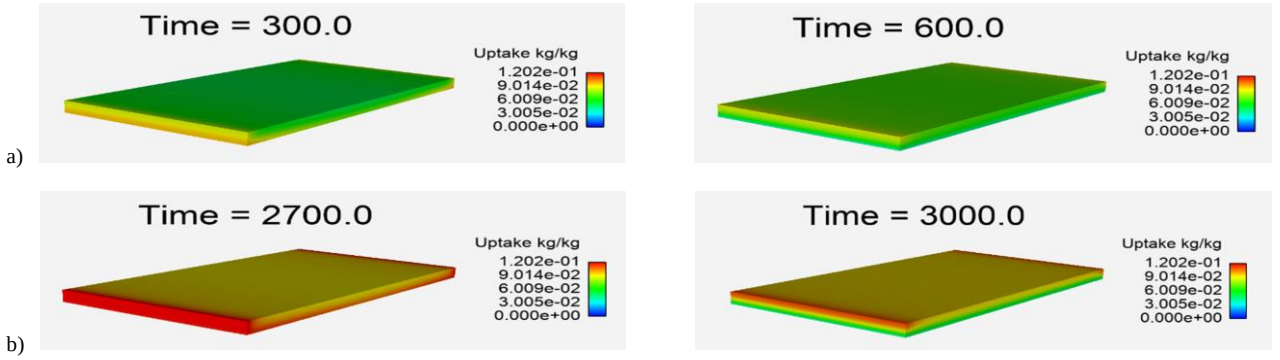

Fig. 13. Distribution of the amount of vapour adsorbed by the sorption bed with dimensions of 150×80×6 mm (E) after adsorption and desorption process a) in the first cycle of the process b) in the last cycle of the process.

The amount of vapour adsorbed for beds of varying lengths was analyzed (Fig. 14). The saturation value for the shortest bed D in the fifth cycle at the end of adsorption was 0.123 kg/kg, while for the longest bed E it was 0.117 kg/kg. In the case of desorption at the end of the process, the saturation for a bed D was 0.0645 kg/kg, and for E it was 0.0641 kg/kg. The length of the bed was more significant for the adsorption process than for desorption. It is observed that the impact of bed length on the process is less significant compared to the previously discussed bed height. It is noteworthy that as the duration of a single cycle increases, the differences in saturation also increase. This is attributed to the fact that the more saturated the bed is, the greater the resistance it poses to the flow of adsorbed vapour. Such a connection can be beneficial in selecting the optimal cycle time for a heat exchanger of a specific size.

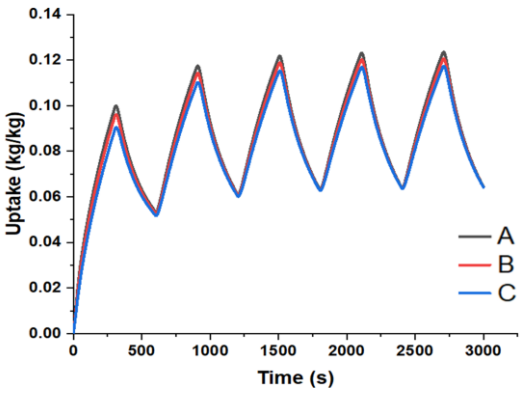

Fig. 14. Comparison of the amount of water vapour adsorbed for different lengths of the bed.

Similarly to the case of vapour adsorbed by the bed, the T_a within the sorption bed shows little variation for different lengths of the adsorption bed (Fig. 15). T_a stabilizes by the second cycle, reaching 314 K at the end of adsorption and 341 K at the end of desorption. These similar T_a in the sorption bed may explain the comparable dynamics of the adsorption and desorption processes discussed earlier.

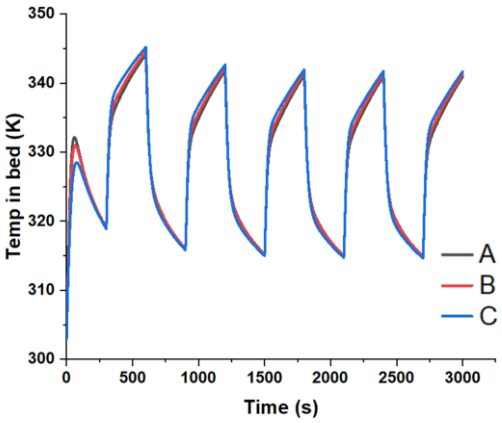

Fig. 15. Comparison of the average temperature in sorption beds for different lengths of the bed.

The mass flow of water vapour adsorbed by the bed for different lengths of the bed is illustrated (Fig. 16). Similar to the analysis of the height of the sorption bed, during the first cycle, where the saturation of each bed with water vapour was 0 kg/kg, the most intense $\dot{m}_v$ occurred. The $\dot{m}_v$ stabilizes by the second

cycle for each of the analyzed cases. For the bed E, $\dot{m}_v$ is highest, registering 4.094×10^{-3} g/s at the beginning of the adsorption stage and -5.554×10^{-3} g/s at the end of desorption. The lowest $\dot{m}_v$ was in the bed D, with values of 1.559×10^{-3} g/s at the beginning of adsorption and -2.112×10^{-3} g/s at the beginning of desorption. In the case of varying bed lengths, a clear difference in $\dot{m}_v$ between the beds is observed for all cases. It can be concluded that increasing the length of the bed has a direct impact on enhancing the suction force of water vapour.

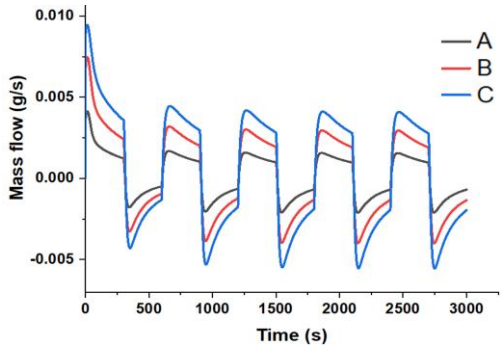

Fig. 16. Comparison of the mass flow of water vapour at the inlet to sorption beds for different lengths of the bed.

The saturation of water vapour in the adsorbent bed during the last, fifth cycle of simulation post-adsorption and desorption processes for all analyzed bed geometries was compiled (Fig. 17). Additionally, the mass of water vapour adsorbed by these beds is presented. The highest saturation, indicating the greatest sorption capacity, was exhibited by bed A, characterized by the shortest distance from the heat source to the centre of the bed, measuring 3 mm. Despite having a sorbent material volume three times smaller than bed C, bed A adsorbed only 20% less vapour. This underscores the significant impact of this parameter on the adsorption process and thus the efficiency of the device. For the analyzed cycle length (300 s), the saturation differences in samples varying in length (B, D, E) are minimal, whereas the differences in the amount of adsorbed vapour are substantial, reaching about 70%. In the analyzed case, designing a longer and thinner bed in the adsorption device would be much more advantageous.

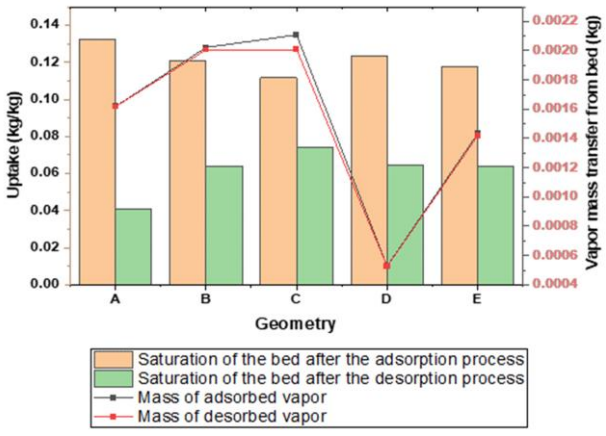

Fig. 17. Summary of water vapor saturation and adsorbed vapor mass for various geometries of the adsorbent bed.

4. Conclusions

The paper presents a method for CFD modelling of the entire adsorption and desorption cycles which enhances understanding of the relationship between these processes and the impact of various factors such as the cycle duration, the temperature of the cooling/heating medium, operating pressure, and the geometry of the sorbent bed on their dynamics. Until now, literature has only modelled either adsorption or desorption processes individually, not the full cycles. This approach allows for the observation of what happens during the transitional period between processes and how this affects their course, which is a novel aspect.

The obtained results demonstrate a significant impact of the adsorbent bed's geometry on the adsorption and desorption processes, emphasizing the crucial role of the distance from the bed centre to the cooling or heating source in the efficiency of these processes. The difference in the amount of vapour adsorbed relative to the amount of sorbent material in beds of different analyzed heights during the adsorption process was 20% higher for the 3 mm bed (A) compared to the 9 mm bed (C). During desorption, the difference in desorbed vapour relative to the amount of sorbent was even greater among these cases of geometry and exceeded 40%. The results indicate that heat exchange significantly influences the progression and control of the adsorption and desorption processes. The length of the bed, affecting the water vapour path to the bed's centre, also impacts these processes, particularly in longer cycles. This discovery highlights the increased resistance caused by water vapour saturation in the sorption bed, which becomes more significant in a more saturated bed, a condition more common in longer cycle durations. These results offer valuable insights for designers of cooling devices based on adsorption technology. Appropriately tailored geometry of the heat exchanger with the sorbent bed can achieve the same effects despite a smaller amount of sorbent, which translates into a smaller device size and cost.

Acknowledgements

The research was conducted within the framework of the "Industrial Doctorate" program by the Ministry of Education and Science (MEiN) titled "Optimization of adsorption and desorption processes in a cooling device using 3D simulations", carried out at the Cracow University of Technology and the company M.A.S. Ltd., under contract number DWD/6/0534/2022.

References

[1] Sztekler, K., Siwek, T., Kalawa, W., Lis, L., Mika L., Radomska E., & Nowak, W. (2021). CFD Analysis of Elements of an Adsorption Chiller with Desalination Function. *Energies*, 14(22), 7804. doi: 10.3390/en14227804

[2] Janusz, S., Szudarek, M., Rudniak, L., & Borcuch, M. (2023). Analysis of heat and mass transfer in an adsorption bed using CFD methods. *Archives of Thermodynamics*, 44(2), 177−194. doi: 10.24425/ather.2023.146564

[3] Manila, M., Mitra, S., & Dutta, P. (2020). Studies on dynamics of two-stage air cooled water/silica gel adsorption system. *Applied Thermal Engineering*, 178, 115552. doi: 10.1016/j.applthermaleng.2020.115552

[4] Li, M., Zhao, Y., Long, R., Liu, Z., & Liu, W. (2022). Computational fluid dynamic study on the adsorption-based desalination and cooling system. *Applied Thermal Engineering*, 508, 115048. doi: 10.1016/j.desal.2021.115048

[5] Gado, M., Ookawara, S., & Hassan, H. (2023). Utilization of triply periodic minimal surfaces for performance enhancement of adsorption cooling systems: Computational fluid dynamics analysis. *Energy Conversion and Management*, 277, 116657. doi: 10.1016/j.enconman.2023.116657

[6] Wang, D., Wu, J., Xia, Z., Zhai, H., Wang, R., & Dou, W. (2005). Study of a novel silica gel–water adsorption chiller. Part II. Experimental study. *International Journal of Refrigeration*, 28(7), 1084−1091. doi: 10.1016/j.ijrefrig.2005.03.002

[7] Petrovic, F., & Mario, K. (2023) Numerical and experimental performance investigation of a heat exchanger designed using topologically optimized fins. *Applied Thermal Engineering*, 218, 119232. doi: 10.1016/j.applthermaleng.2022.119232

[8] Mikhaeil, M., Gaderer, M., & Dawoud B. (2022) Experimental Investigation of the Adsorption and Desorption Kinetics on an Open-Structured Asymmetric Plate Heat Exchanger; Matching Between Small-Scale and Full-Scale Results. *Frontiers in Energy Research*, 10, 818486. doi: 10.3389/fenrg.2022.818486

[9] Critoph, R., & Metcalf, J. (2004). Specific cooling power intensification limits in ammonia–carbon adsorption refrigeration systems. *Applied Thermal Engineering*, 24(5), 661−678. doi: 10.1016/j.applthermaleng.2003.11.004

[10] Gamze, I., Hasan, D., Moghtada, M., & Bidyut, S. (2019). A new adsorbent bed design: Optimization of geometric parameters and metal additive for the performance improvement. *Applied Thermal Engineering*, 162, 114270. doi: 10.1016/j.applthermal-eng.2019.114270

[11] Zepeng, W., Yuan, Z., Du, C., Liu, Y., & Wang, J. (2022). Performance of solar adsorption cooling system with internal finned vacuum tube bed. *Case Studies in Thermal Engineering*, 34, 102063. doi: 10.1016/j.csite.2022.102063

[12] Bakhshandeh, M., Zarei, T.Z., & Khorshidi, J. (2022). CFD study on Beds of an Adsorption desalination system in order to improve bed performance. *Chemical Process Design*, 1(2), 60−74. doi: 10.22111/CPD.2023.44116.1015

[13] Boruta, P., Bujok, T., Mika, Ł., & Sztekler, K. (2022). Adsorbents, Working Pairs and Coated Beds for in Adsorption Chillers − State of the Art. *Energies*, 14(15), 4707. doi: 10.3390/ en14154707

[14] Li, M., Zhao, Y., & Long, R. (2021). Gradient porosity distribution of adsorbent bed for efficient adsorption cooling. *International Journal of Refrigeration*, 128, 153−162. doi: 10.1016/j.ijrefrig.2021.03.013

[15] Mohammed, H., Mesalhy, O., Elsayed, M., & Chow, L. (2019). Assesment of numerical models in the evaluation of adsorption cooling system performance. *International Journal of Refrigeration*, 99(1), 166–175. doi: 10.1016/j.ijrefrig.2018. 12.017

Co-published by
Institute of Fluid-Flow Machinery
Polish Academy of Sciences
Committee on Thermodynamics and Combustion
Polish Academy of Sciences

http://www.imp.gda.pl/archives-of-thermodynamics/

Modelling of heat transfer during flow condensation of natural refrigerants under conditions of increased saturation pressure

Stanisław Głuch[a], Dariusz Mikielewicz[a]

[a]Gdańsk University of Technology, Faculty of Mechanical Engineering and Ship Technology, Narutowicza 11/12, 80-233 Gdańsk, Poland
*stanislaw.gluch@pg.edu.pl

Received: 31.12.2023; revised: 13.05.2024; accepted: 12.06.2024

Abstract

The paper presents a modified in-house model for calculating heat transfer coefficients during flow condensation, which can be applied to a variety of working fluids, but natural refrigerants in particular, at full range thermodynamic parameters with a particular focus on increased saturation pressure. The modified model is based on a strong physical basis, namely the hypothesis of analogy between the heat transfer coefficient and pressure drop in two-phase flow. The model verification is based on a consolidated database that consists of 1286 data points for 7 natural refrigerants and covers the reduced pressure range (the ratio of critical pressure and saturation pressure) from 0.1 to 0.8 for different mass velocities and diameters. The new version of the in-house model, developed earlier by Mikielewicz, was compared with 4 other mathematical models widely recommended for engineering calculations and obtained the best consistency results. The value of the mean absolute percentage error was 28.13% for the modified model, the best result among the scrutinised methods.

Keywords: Condensation, Heat transfer coefficient; Reduced pressure; Saturation pressure; Saturation temperature

Vol. 45(2024), No. 3, 49–56; 10.24425/ather.2024.151215

Cite this manuscript as: Głuch, S., & Mikielewicz, D. (2024). Modelling of heat transfer during flow condensation of natural refrigerants under conditions of increased saturation pressure. *Archives of Thermodynamics*, 45(3), 49–56.

1. Heat transfer during flow condensation in trending application

There is a gap in knowledge about condensation at elevated saturation temperatures and corresponding high reduced pressures. The condensation process in high-temperature heat pumps occurs usually at temperatures higher than 80°C. Most of the existing experimental data has been collected for temperatures below 40°C, which is related to HVAC (heating, ventilation, air conditioning) applications of refrigerants. For temperatures higher than 120°C, most low boiling fluids operate at parameters close to the thermodynamic critical point, where there are significant changes in density and viscosity of the liquid and vapour phases, which has a significant impact on interfacial phenomena. Over the past century, there have been many papers that have dealt with the modelling of the heat transfer coefficient during condensation. Most of the literature models are created for specific experimental parameters and are not intended to be applied to a wide range of refrigerants. In recent years, research on high-temperature heat pumps where saturation temperatures and saturation pressures are much higher than in classical applications have become important [1]. The use of new environmentally neutral refrigerants is also principal. For this reason,

Nomenclature

c_p – specific heat capacity, J/(kg K)
Con – confinement number
d – inner diameter od tube, m
g – gravitational acceleration, m/s^2
G – total mass flux, kg/(m^{2}s)
h_{lv} – latent heat of evaporation, J/kg
Jg – dimensionless vapour velocity, $Jg = \frac{xG}{\sqrt{gd\rho_v(\rho_l-\rho_v)}}$
Nu – Nusselt number
P – pressure, N/m^2
Pr – reduced pressure, $Pr = P_{sat}/P_{crit}$
Pra – Prandtl number
Re – Reynolds number
T – temperature, °C
v – specific volume, m^3/kg
x – vapour quality
Xtt – Martinelli's correlating parameter, $Xtt = \left[\frac{\mu_l}{\mu_v}\right]^{0.1}\left[\frac{1-x}{x}\right]^{0.9}\left[\frac{\rho_v}{\rho_l}\right]^{0.5}$

Greek symbols

α – heat transfer coefficient, W/(m^{2}K)
μ – dynamic viscosity, Pa s
ρ – density, kg/m^3
λ – thermal conductivity, W/(m K)
σ – surface tension, N/m

Subscripts and Superscripts

crit – critical
l – liquid
LO – liquid only
sat – saturation
tf – two phase
v – vapour
VO – vapour only

Abbreviations and Acronyms

MAPE – mean absolute percentage error
RMS – two phase multiplier due to Muller-Steinhagen and Heck

natural refrigerants such as isobutane or propane are gaining popularity in heat pump applications and others. Condensation heat transfer coefficient prediction is also important for the potential application of advanced thermodynamic cycles [2]. Some novel cycles require modelling of such complex phenomena as condensation inside spray ejector [3].

2. Methods of calculating the heat transfer coefficient during condensation

In [4] model for the calculation of heat transfer coefficient during condensation within channels has been published, hereinafter named an in-house model. The method was based on a correlation originally developed for flow boiling. The basis for the analysis involved predicting heat transfer coefficients in flow condensations and assessing them against correlations developed for annular flow structures. In this context, flow boiling and flow condensation were treated as symmetrical phenomena. The comparisons yielded satisfactory results. Additionally, the study examined nonadiabatic effects in the heat transfer coefficient model, incorporating the blowing parameter into the modelling process. The modifications were found to have significant effects on condensation for small qualities, affirming that nonadiabatic effects are less critical for higher qualities. Similarly, in the case of flow boiling, the most substantial changes to the heat transfer coefficient occurred for smaller qualities. Later in [5] a method for calculation of heat transfer coefficient during flow boiling was proposed to take into account the reduced pressure effect. In this paper, a modified Muller-Steinhagen and Heck two-phase multiplier was introduced to consider the effects of increased reduced pressures. Promising results have been obtained, however there was still room left for further modifications. In [6] authors presented the newest version of two phase pressure drop model based on the Müller-Steinhagen and Heck method.

The outcomes of modelling focused on heat transfer and pressure drop during the condensation of R134a and R404A refrigerants in minichannels have been presented in [7]. Internal diameters ranged from 0.31 mm to 3.30 mm. The study specifically examines the local heat transfer coefficient and pressure drop in individual minichannels, with a comparative analysis against methods proposed by other researchers. Drawing from the measured data, the authors introduced their own correlation for calculating the local heat transfer coefficient.

The study [8] introduces a novel and straightforward model for determining the local heat transfer coefficient during flow condensation within plain pipes. The proposed model accounts for two distinct regimes distinguished by the value of mass flux. For both regions, a new correlation is presented, resembling the single-phase heat transfer coefficient model. Corresponding Reynolds and Prandtl numbers are based on the sum of superficial liquid and vapour versions. These models emphasize the significant role of the superficial vapour Reynolds number in governing the heat transfer coefficient. The model demonstrates predictive capability for estimating the heat transfer coefficient across a range of channels including microchannels and conventional channels, encompassing various refrigerants.

Shah [9] presented a straightforward dimensionless correlation designed for predicting heat-transfer coefficients in the context of film condensation inside pipes. The dataset encompasses various fluids such as water, R-11, R-12, R-22, R-113, methanol, ethanol, benzene, toluene, and trichloroethylene undergoing condensation in pipes of horizontal, vertical, and inclined orientations with diameters ranging from 7 mm to 40 mm. Additionally, a dataset for condensation within an annulus has been analysed. The parameter range covered includes reduced pressures spanning from 0.002 to 0.44, saturation temperatures ranging from 21°C to 31°C and vapour velocities from 3 m/s to 300 m/s, and vapour qualities from 0% to 100%. A new version [10] of correlation extended for a wider range of parameters was published in 2009. The presented method has been shown to be in

Table 1. Formulas of analysed methods.

Model	Formula	Purpose
Mikielewicz [4,5]	$\frac{\alpha_{TPB}}{\alpha_{LO}} = \sqrt{R_{MS}^{n}}$ $R_{MS} = \left[1 + 2\left(\frac{1}{f_1} - 1\right) x\mathrm{Con}^{m}\right](1-x)^{\frac{1}{3}} + x^{3}\frac{1}{f_{1z}}$ Turbulent flow: $f_1 = \frac{\left(\frac{\rho_l}{\rho_v}\right)}{\left(\frac{\mu_l}{\mu_v}\right)^{0.25}}$, $f_{1z} = \frac{\left(\frac{\mu_v}{\mu_l}\right)}{\left(\frac{\lambda_l}{\lambda_v}\right)^{1.5}}\left(\frac{c_{pl}}{c_{pv}}\right)$ Laminar flow: $f_1 = \frac{\frac{\rho_l}{\rho_v}}{\frac{\mu_l}{\mu_v}}$, $f_{1z} = \left(\frac{\lambda_v}{\lambda_l}\right)$	General correlation for condensation inside conventional and mini/ microtubes
Bohdal [7]	$\mathrm{Nu} = 25.084\mathrm{Re}_l^{0.258}\mathrm{Pra}_l^{-0.495}Pr^{-0.288}\left(\frac{x}{1-x}\right)^{0.266}$	Condensation in mini/ microchannels
Dorao and Fernandiono [8]	$\mathrm{Nu}J = 0.023\mathrm{Re}_{tf}^{0.8}\mathrm{Pra}_{tf}^{0.3}$ $\mathrm{Nu}JJ = 41.5d^{0.6}\mathrm{Re}_{tf}^{0.4}\mathrm{Pra}_{tf}^{0.3}$ $\mathrm{Nu} = \sqrt[9]{(\mathrm{Nu}J^9 + \mathrm{Nu}JJ^9)}$	General correlation for condensation in tubes
Shah 1979 [9]	$\alpha = 0.023\mathrm{Pra}_l^{0.4}\mathrm{Re}_l^{0.8}\frac{(1-x)^{0.8} + [3.8x^{0.76}(1-x)^{0.04}]}{Pr^{0.38}}\frac{\lambda_l}{d}$ $\mathrm{Re}_l > 3000$	Correlation for condensation in tubes for annular flow
Shah 2009 [10]	$\alpha = hi$ for $Jg \geq JgC$ $\alpha = hi + h_{\mathrm{Nu}}$ for $Jg < JgC$ $hi = 0.023\mathrm{Re}_l^{0.8}\mathrm{Pra}_l^{0.4}\left(\frac{\mu_l}{14\mu_v}\right)^{n2}(1-x)^{0.8} + \frac{3.8x^{0.76}(1-x)^{0.04}}{Pr^{0.38}}\frac{\lambda_l}{d}$ $n2 = 0.0058 + 0.557Pr$ $h_{\mathrm{Nu}} = 1.32\mathrm{Re}_l^{-\frac{1}{3}}\left[\frac{\rho_l(\rho_l-\rho_v)gk_l^3}{\mu_l^2}\right]^{1/3}$ $Z = \left(\frac{1}{x-1}\right)^{0.8}Pr^{0.4}$ $JgC = 0.98(Z+0.263)^{-0.62}$ $Jg = \frac{xG}{\sqrt{gD\rho v(\rho_l-\rho_v)}}$	General correlation for condensation in plain tubes
Shah 2019 [11]	$\alpha = hi$ for $Jg \geq JgC,\ Frl > 0.012$ and $Wef \geq 100$ $\alpha = hi + h_{\mathrm{Nu}}$ for $Jg < JgC,\ Frl > 0.012$ for other regimes $h = hII + h_{\mathrm{Nu}}$ $hi = 0.023\mathrm{Re}_l^{0.8}\mathrm{Pra}_l^{0.4}\left(\frac{\mu_l}{14\mu v}\right)^{n2}(1-x)^{0.8} + \frac{3.8x^{0.76}(1-x)^{0.04}}{Pr^{0.38}}\frac{\lambda_l}{d}$ $n2 = 0.0058 + 0.557Pr$ $hII = 0.023\mathrm{Re}_l^{0.8}\mathrm{Pra}_l^{0.4}(1 + 1.128x^{0.8170}\frac{\rho_l}{\rho_v}^{0.3685}\frac{\mu_l}{\mu_v}^{0.2363}\frac{1-\mu_v}{\mu_l}^{2.144}\mathrm{Pra}_l^{-0.1}\frac{\lambda_l}{d}$ $h_{\mathrm{Nu}} = 1.32\mathrm{Re}_l^{-\frac{1}{3}}\left[\frac{\rho_l(\rho_l-\rho_v)gk_l^3}{\mu_l^2}\right]^{1/3}$ $Z = \left(\frac{1}{x-1}\right)^{0.8}Pr^{0.4}$ $JgCC = 0.95(1.254 + 2.27Z^{1.249})^{-1}$ $JgC = 0.98(Z+0.263)^{-0.62}$ $Jg = \frac{xG}{\sqrt{gD\rho v(\rho_l-\rho_v)}}$	General correlation for condensation in conventional and mini/micro tubes
Cavallini 2006 [12]	$J_G = \frac{xG}{\sqrt{gD\rho v(\rho_l-\rho_v)}}$ $J_G^T = \sqrt[-3]{\left(\frac{7.5}{4.3Xtt^{1.111}}\right)^{-3} + CT^{-3}}$ For hydrocarbons: CT = 1.6 ; for other refrigerants: CT = 2.6 Modified Dittus-Boelter correlation: $\alpha_{LO} = 0.023\mathrm{Re}_l^{0.8}\mathrm{Pra}_l^{0.4}\frac{\lambda_l}{d}$ ΔT-independent flow regime ($J_G > J_G^T$) $\alpha_A = \alpha_{LO}\left[1 + 1.128x^{0.817}\left(\frac{\rho_l}{\rho_v}\right)^{0.3685}\left(\frac{\mu_l}{\mu_v}\right)^{0.2363}\left(1-\frac{\mu_v}{\mu_l}\right)^{2.144}\mathrm{Pra}_l^{-0.1}\right]$ ΔT - dependent flow regime ($J_G < J_G^T$) $\alpha_{strat} = 0.725\left\{1 + 0.741\left[\frac{1-x}{x}\right]^{0.3321}\right\}^{-1}\left[\frac{\lambda_l^3\rho_l(\rho_l-\rho_v)gh_{lv}}{\mu_l D\Delta T}\right]^{0.25} + (1-x^{0.087})\alpha_{LO}$ $\alpha_D = \left[\alpha_A\left(\frac{J_G^T}{J_G}\right)^{0.8} - \alpha_{strat}\right]\left(\frac{J_G}{J_G^T}\right) + \alpha_{strat}$	General correlation for condensation in channels with D > 3 mm

good agreement with data ranging from highly turbulent flows to laminar flow conditions. The ability to predict heat transfer in mini- and microchannels was introduced in [11]. Improved versions of correlation are much more complex in comparison to the original form.

Cavallini et al. [12] introduced a novel method for determining the condensation heat transfer coefficient of refrigerants within horizontal plain tubes with inner diameters exceeding 3 mm (D > 3 mm). The proposed method was intentionally designed for simplicity, facilitating its immediate application in heat exchanger modelling and design for both traditional and emerging fluids in the HVAC industry. Notably, the method prioritizes accuracy and has been tested across an experimental database from various researchers, ensuring reliability with reduced experimental uncertainties. To maintain simplicity, the method employs two equations, each catering to temperature difference independent and dependent fluid flows. Parameters influencing condensation heat transfer are incorporated into the equations. The accuracy of the method was validated through a comprehensive comparison with data from HCFCs (hydrochlorofluorocarbons), HFCs (hydrofluorocarbons), HCs (hydrocarbons), carbon dioxide, ammonia, and water. Application of the temperature-dependent part of correlation is often complicated because wall temperature is usually not known. Nearly no data source provides precise information on the experimental value of the wall temperature. For design purposes, wall temperature has to be calculated iteratively. Equations for analysed methods are presented in Table 1.

2.1. Modification of in-house model

Mikielewicz and Mikielewicz [4] developed earlier a semi-empirical method for modelling heat transfer during boiling and condensation in minichannels. It is based on the hypothesis the total energy dissipation in the two-phase flow with boiling is a sum of two contributions, namely the dissipation of energy from the shearing flow and dissipation due to bubble generation. In case of condensation in the flow, the dissipation due to bubble generation is not present. The main equation includes the term modelling the resistance in two-phase flow and the term modelling the flow resistance associated with the nucleation process during boiling. The modified main equation presents only the term corresponding to the flow resistance because this paper focus on the modelling of heat transfer during condensation:

$$\frac{\alpha_{TPB}}{\alpha_{LO}} = \sqrt{R_{MS}^{n}\mathrm{Con}^{0.34}}, \tag{1}$$

where n = 0.76 for $\mathrm{Re_l}$ > 2300 and n = 2 for $\mathrm{Re_l}$ < 2300.

The flow resistance term is modelled using the modified Muller-Steinhagen and Heck correlation [5]: presented in Eq. (2),

$$R_{MS} = \left[1 + 2\left(\frac{1}{f_1} - 1\right)x\mathrm{Con}^{m}\right](1-x)^{1/3} + x^{3}\frac{1}{f_{1z}}, \tag{2}$$

where for turbulent flow

$$f_1 = \frac{\left(\frac{\rho_l}{\rho_v}\right)}{\left(\frac{\mu_l}{\mu_v}\right)^{0.25}}, \quad f_{1z} = \frac{\left(\frac{\mu_v}{\mu_l}\right)}{\left(\frac{\lambda_l}{\lambda_v}\right)^{1.5}}\left(\frac{c_{pl}}{c_{pv}}\right) \tag{3}$$

and for laminar flow

$$f_1 = \frac{\frac{\rho_l}{\rho_v}}{\frac{\mu_l}{\mu_v}}, \quad f_{1z} = \left(\frac{\lambda_v}{\lambda_l}\right). \tag{4}$$

Parameter α_{LO} is the heat transfer coefficient for the single-phase liquid flow and α_{TPB} represents the heat transfer coefficient during condensation in Eq. (1). Authors recommend standard Dittus-Boelter correlation for prediction of forced internal convection for single liquid phase heat transfer coefficient. The modification introduced in the present work is based on the introduction of the confinement number (Con), which is variation of Bond number, into the two-phase flow multiplier RMS. The flow resistance part was multiplied by the confinement number raised to the power of 0.34. The Con number,

$$\mathrm{Con} = \frac{\sqrt[2]{\frac{\sigma}{g(\rho_l - \rho_v)}}}{D}, \tag{5}$$

describes changes in the nature of the flow at high values of reduced pressure. It includes gas and liquid phase densities, surface tension, diameter and gravitational acceleration. This modification allows to take into account the change in physical properties that affect the heat transfer process at high values of reduced pressure. Surface tension alongside density has an immense effect on two phase flow structures which has been shown in experimental research [13]. For reduced pressure 0.2 where surface tension and difference in phase specific densities are high annular flow was observed at quality as low as 7%. For a reduced pressure 0.8 in the vicinity of the critical point annular flow occurred at around 50% quality. Surface tension and difference in phase densities decrease significantly for high values of reduced pressure.

2.2. Consolidated database

The modelling was based on a consolidated database that consists of 1286 measurement points published in 7 research papers. It includes data for 7 different natural refrigerants, different diameters, mass velocities and reduced pressures. The database includes values of reduced pressures ranging from 0.1 to as high as 0.809. Internal tube diameters vary from 0.76 mm to 9.43 mm. Mass velocity ranges from 75 kg/m^{2}s to 1000 kg/m^{2}s. Variation of quality is from 0% to 100%. Consolidated database is presented in Table 2.

2.3. Results

The consolidated database was compared with 7 methods for predicting the heat transfer coefficient during condensation due to Bohdal et al. [7], Dorao and Fernandiono [8], Shah [9–11] and Cavallini et al [12]. The calculation code was written in Engineering Equation Solver EES.

The mean absolute percentage error is given by the equation

$$\mathrm{MAPE} = \frac{1}{N}\sum\frac{A-F}{A} \times 100\%, \tag{6}$$

where: N – number of points, A – real value, F – forecast value.

Results of calculations are presented in Table 3. The best result was the modified Mikielewicz correlation for which the

Table 2. Consolidated database.

	Authors	Diameter [mm]	Fluid	Mass velocity [kg/(m²·s)]	Reduced pressure	Number of measurement points
1	Macdonald et al. [14,15]	0.76–1.45	R290	150–450	0.254–0.809	260
2	Zhuang et al. [16]	4	Ethane	101–255	0.22–0.522	230
3	Zhuang et al. [17]	4	Methane	99–254	0.43–0.76	286
4	Milkie et al. [18]	7.75	n-Pentane	150–600	0.04–0.17	163
5	Moreira et al. [19]	9.43	Propylene, R290, R600a	50–250	0.12–0.32	110
6	Del Col et al. [20]	1	Propylene	80–1000	0.35	109
7	Longo [21]	4	Propylene, R290	75–400	0.15–0.88	125

mean absolute percentage error (MAPE) was 28.13%. The second best model was the Cavallini [12] correlation. The third best correlation was the original Mikielewicz correlation which achieved MAPE = 38.97%. The fourth best method was the model due to Shah [11] which resulted in MAPE = 40.04%. Doaro and Fernandiono achieved a slightly worse result of 40.78%. The other correlations returned worse results due to their empirical nature – they were created for completely different conditions and specified refrigerants. The results of the calculations are shown in Table 3 and the histogram of discrepancies is in Fig. 1. Figure 2 presents histogram with modelling results. Figure 3 shows the results of modelling with the modified Mikielewicz correlation for all considered data sources separately.

Table 3. Results of calculations for eight modelling methods.

Model	Mean relative absolute error	Number of points within ±30%	Percentage of points within ±30%
Mikielewicz modified	28.13%	892	69.36%
Mikielewicz [4]	38.97%	662	51.48%
Bohdal [7]	163.46%	223	17.34%
Dorao and Fernandiono [8]	40.78%	724	56.30%
Shah 1979 [9]	93.17%	273	21.23%
Shah 2009 [10]	45.55%	727	56.53%
Shah 2019 [11]	40.04%	727	56.53%
Cavallini 2006 [12]	38.38%	772	60.03%

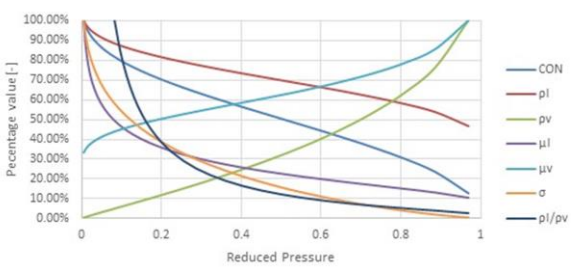

Fig. 1. Properties change in function of reduced pressure for R290.

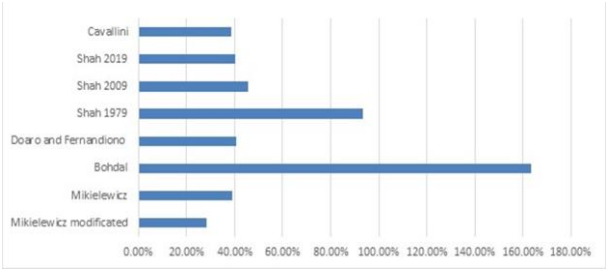

Fig. 2. Comparison of MAPE for calculated methods.

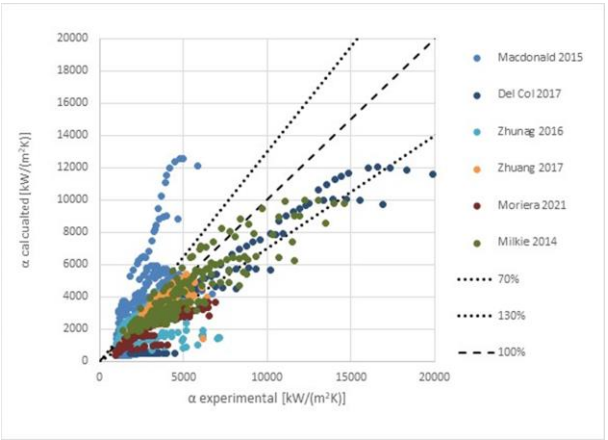

Fig. 3. Results of modeling with modified Mikielewicz correlation.

Results of modelling for data above reduced pressure 0.5 is presented in Table 4. Table 5 presents results for data below reduced pressure 0.5. The new modification slightly lowered values of error for low pressure experiments to 26.29% from 30.89%. Both values are close to the typical measurement error for two phase flow heat transfer measurement which is usually between 20% and 30%. The main improvement lies in data points with high pressure. In this region, new correlation has an error 31.63% whereas the old version has 54.33% and the best other correlations have values of MAPE around 50%. The main goal of the research was to correct modelling results for high values of saturation pressure, but new modification managed to increase accuracy in the whole spectrum of reduced pressure.

Table 4. Results of calculations for eight modelling methods for data points with reduced pressure higher than 50%.

Model	Mean relative absolute error	Number of points within ±30%	Percentage of points within ±30%
Mikielewicz modified	31.63%	319	72.01%
Mikielewicz [4]	54.33%	167	37.70%
Bohdal [7]	176.58%	47	10.61%
Dorao and Fernandiono [8]	57.58%	242	54.63%
Shah 1979 [9]	167.00%	19	4.29%
Shah 2009 [10]	49.67%	272	61.40%
Shah 2019 [11]	52.32%	272	61.40%
Cavallini 2006 [12]	51.61%	278	62.75%

Table 5. Results of calculations for eight modelling methods for data points with reduced pressure lower than 50%

Model	Mean relative absolute error	Number of points within ±30%	Percentage of points within ±30%
Mikielewicz modified	26.29%	573	67.97%
Mikielewicz [4]	30.89%	495	58.72%
Bohdal [7]	156.57%	176	20.88%
Dorao and Fernandiono [8]	31.95%	482	57.18%
Shah 1979 [9]	54.38%	254	30.13%
Shah 2009 [10]	43.39%	455	53.97%
Shah 2019 [11]	33.58%	455	53.97%
Cavallini 2006 [12]	31.43%	494	58.60%

Although changes below a reduced pressure of 0.5 are not spectacular, corrections for high saturation pressure are significant. The new version also managed to fit the most points inside the 30% error area for both regions.

Graphical comparison of correlations for all analysed data sources are shown in Figs. 4–10. Figure 4 presents graph for Macdonald et al. [14,15] data. Figure 5 presents graph for Zhuang et al. [16] data. Figure 6 presents graph for Zhuang et al. [17] data. Figure 7 presents graph for Del Col et al. [18] data. Figure 8 presents graph for Moreira et al. [19] data. Figure 9 presents graph for Milkie [20] data. Figure 10 presents graph for Longo et al. [21] data. Distributions present data for R290, ethane, methane, propylene and R600a. The modified Mikielewicz method performed the best of all analysed methods for all data sources.

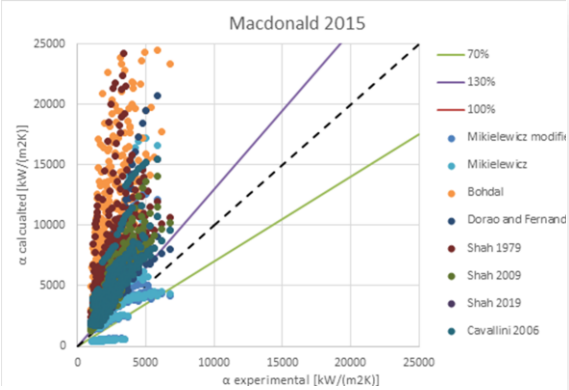

Fig. 4. Comparison of correlations for R290 [14,15].

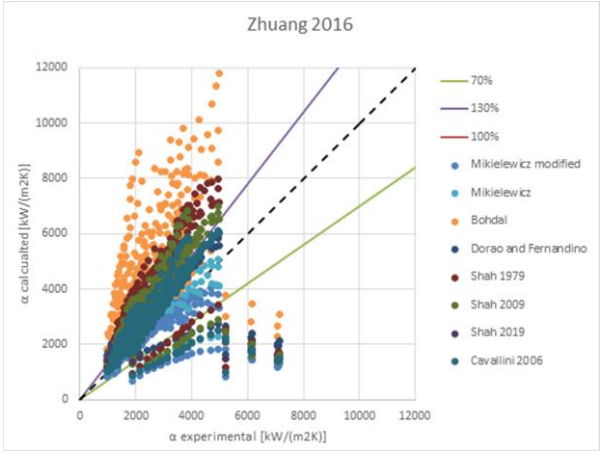

Fig. 5. Comparison of correlations for ethane [16].

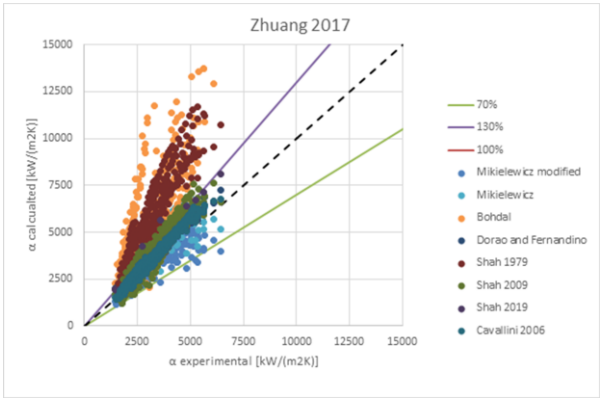

Fig. 6. Comparison of correlations for methane [17].

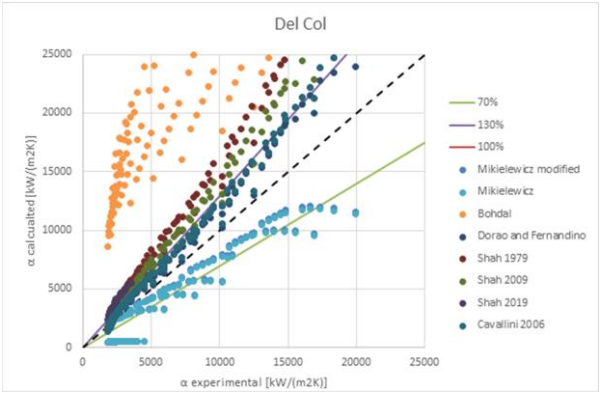

Fig. 7. Comparison of correlations for propylene [20].

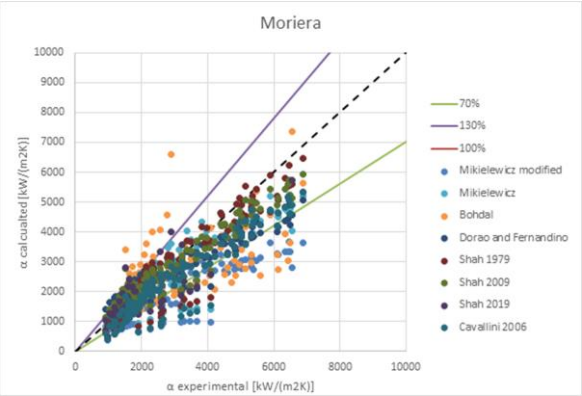

Fig. 8. Comparison of correlations for propylene, R290, R600a [19].

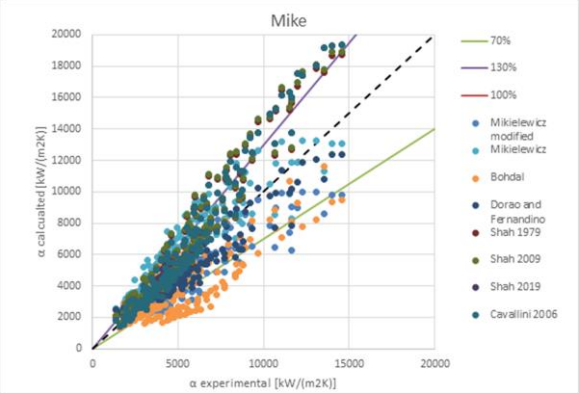

Fig. 9. Comparison of correlations for R290 [18].

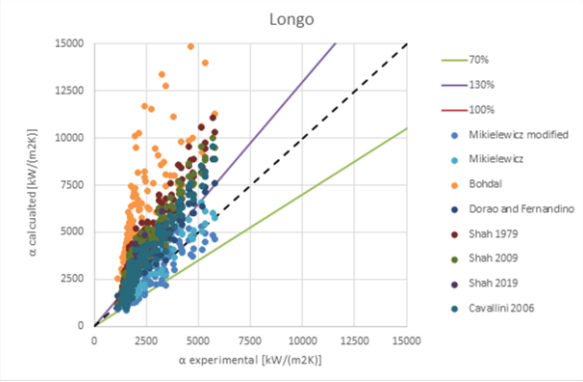

Fig. 10. Comparison of correlations for R290 and propylene [21].

3. Conclusions

A modified in-house method for the prediction of heat transfer coefficients during condensation of natural refrigerants with special emphasis on high values of reduced pressure has been proposed. A developed model has been formulated with the aim of achieving high accuracy while maintaining a straightforward structure. The modification is based on the fact that the two-phase flow multiplier used in the in-house model is modified with the adjusted value of the confinement number. Significant improvements have been obtained especially in the high range of reduced pressure values.

The modelling was based on an accumulated database of experimental measurement data, which consists of 1286 measurement points for 7 natural refrigerants. The database includes values of reduced pressures ranging from 0.1 to as high as 0.809. Channel internal diameters range from 0.76 mm to 9.43 mm. Mass velocity range from 75 kg/(m^{2}s) to 1000 kg/(m^{2}s). A full range of distribution of quality from 0% to 100% is considered. The new method was compared with 7 models from the literature and obtained the smallest value of mean absolute percentage error (MAPE) 28.13% while 69.36% had an error value lower than 30%. The second best method achieved 38.38% MAPE and 60.03% points below 30%error value. For data above 50% of reduced pressure model achieved 31.64% MAPE while second best method in this region achieved 49.67%. The other methods surpassed 50% MAPE. The outcomes reveal a highly satisfactory agreement with experimental data.

Acknowledgements

This research was funded in whole or in part by National Science Centre, Poland 2021/41/N/ST8/04421. For the purpose of Open Access, the author has applied a CC-BY public copyright licence to any Author Accepted Manuscript (AAM) version arising from this submission.

References

[1] Pysz, M., Głuch, S., & Mikielewicz, D. (2023). Experimental study of flow boiling pressure drop and heat transfer of R1233zd(E) at moderate and high saturation temperatures. *International Journal of Heat and Mass Transfer*, 204, 123855. doi: 10.1016/j.ijheatmasstransfer. 2023.123855

[2] Szewczuk-Krypa, N., Drosińska-Komor, M., Głuch, J., & Breńkacz, L. (2018). Comparison analysis of selected nuclear power plants supplied with helium from high-temperature gas-cooled reactor. *Polish Maritime Research*, 25(S1), 204–210. doi: 10.2478/pomr-2018-0043

[3] Głuch, S.J., Ziółkowski, P., Witanowski, Ł., & Badur, J. (2021). Design and computational fluid dynamics analysis of the last stage of innovative gas-steam turbine. *Archives of Thermodynamics*, 42(3), 255–258. doi: 10.24425/ ather.2021.138119

[4] Mikielewicz, D., & Mikielewicz, J. (2011). A common method for calculation of flow boiling and flow condensation heat transfer coefficients in minichannels with account of nonadiabatic effects. *Heat Transfer Engineering*, 32(13-14), 1173–1181. doi: 10.1080/01457632.2011. 562728

[5] Jakubowska, B., & Mikielewicz, D. (2019). An improved method for flow boiling heat transfer with account of the reduced pressure effect. *Thermal Science*, 23(4), S1261–S1272. doi: 10.2298/TSCI19S4261J

[6] Mikielewicz, D., & Mikielewicz, J. (2022). An improved Müller-Steinhagen and Heck model for two phase pressure drop modelling at high reduced pressures. *Journal of Power Technologies*, 102(3), 81–87. https://papers.itc.pw.edu.pl/index.php/JPT/article/view/1783

[7] Bohdal, T., Charun, H., & Sikora, M. (2011). Comparative investigations of the condensation of R134a and R404A refrigerants in pipe minichannels. *International Journal of Heat and Mass Transfer*, 54(9-10), 1963–1974. doi: 10.1016/j.ijheatmasstransfer.2011.01.005

[8] Dorao, C.A., & Fernandino, M. (2018). Simple and general correlation for heat transfer during flow condensation inside plain pipes. *International Journal of Heat and Mass Transfer*, 122, 290–305. doi: 10.1016/j.ijheatmasstransfer.2018.01.097

[9] Shah, M.M. (1979). A general correlation for heat transfer during film condensation inside pipes. *International Journal of Heat and Mass Transfer*, 22(4), 547–556. doi: 10.1016/0017-9310(79)90058-9

[10] Shah, M.M. (2009). An improved and extended general correlation for heat transfer during condensation in plain tubes. *HVAC and R Research*, 15(5), 889–913. doi: 10.1080/10789669.2009. 10390871

[11] Shah, M.M. (2019). Improved correlation for heat transfer during condensation in conventional and mini/micro channels. *International Journal of Refrigeration*, 98, 222–237. doi: 10.1016/ j.ijrefrig.2018.07.037

[12] Cavallini, A., Col, D.D, Doretti, L., Matkovic, M., Rossetto, L., Zilio, C., & Censi, G. (2006). Condensation in horizontal smooth tubes: A new heat transfer model for heat exchanger design. *Heat Transfer Engineering*, 27(8), 31–38. doi: 10.1080/ 01457630600793970

[13] Głuch, S., Pysz, M., & Mikielewicz, D. (2023). Flow maps and flow patterns of R1233zd(E) in a circular minichannel at low, medium and high values of saturation pressure. *36th International Conference on Efficiency, Cost, Optimization, Simulation and Environmental Impact of Energy Systems, ECOS 2023*, 402–413. 25-30 June, Las Palmas De Gran Canaria, Spain. doi: 10.52202/069564-0037

[14] Macdonald, M., & Garimella, S. (2016). Hydrocarbon condensation in horizontal smooth tubes: Part I – Measurements. *International Journal of Heat and Mass Transfer*, 93, 75–85. doi: 10.1016/j.ijheatmasstransfer.2015.09. 018

[15] Macdonald, M., & Garimella, S. (2016). Hydrocarbon condensation in horizontal smooth tubes: Part II - Heat transfer coefficient and pressure drop modeling. *International Journal of Heat and Mass Transfer*, 93, 1248–1261. doi: 10.1016/j.ijheatmasstransfer.2015.09.019

[16] Zhuang, X.R., Gong, M.Q., Zou, X., Chen, G.F., & Wu, J.F. (2016). Experimental investigation on flow condensation heat transfer and pressure drop of R170 in a horizontal tube. *International Journal of Refrigeration*, 66, 105–120. doi: 10.1016/j.ijrefrig.2016.02.010

[17] Zhuang, X.R., Chen, G.F., Zou, X., Song, Q.L., & Gong, M.Q. (2017). Experimental investigation on flow condensation of methane in a horizontal smooth tube. *International Journal of Refrigeration*, 78, 193–214. doi: 10.1016/j.ijrefrig.2017.03.021

[18] Col, D.D., Azzolin, M., Bortolin, S., & Berto, A. (2017). Experimental results and design procedures for minichannel condensers and evaporators using propylene. *International Journal of Refrigeration*, 83, 23–38. doi: 10.1016/ j.ijrefrig.2017.07.012

[19] Moreira, T.A., Ayub, Z H., & Ribatski, G. (2021). Convective condensation of R600a, R290, R1270 and their zeotropic binary mixtures in horizontal tubes. *International Journal of Refrigeration*, 130, 27–43. doi: 10.1016/j.ijrefrig.2021.06.031

[20] Milkie, J.A. (2014). *Condensation of hydrocarbons and zeotropic hydrocarbon/refrigerant mixtures in horizontal tubes*. PhD thesis, Georgia Institute of Technology. http://hdl.handle.net/1853/51825

[21] Longo, G.A., Mancin, S., Righetti, G., & Zilio, C. (2017). Saturated vapour condensation of HFC404A inside a 4 mm ID horizontal smooth tube: Comparison with the long-term low GWP substitutes HC290 (Propane) and HC1270 (Propylene). *International Journal of Heat and Mass Transfer*, 108, 2088–2099. doi: 10.1016/j.ijheatmasstransfer.2016. 12.087

Co-published by
Institute of Fluid-Flow Machinery
Polish Academy of Sciences
Committee on Thermodynamics and Combustion
Polish Academy of Sciences

http://www.imp.gda.pl/archives-of-thermodynamics/

Research of the physical properties of bio-based building materials with phase change material

Mateusz Wendołowicz[a*], Natalia Mikos-Nuszkiewicz[a], Łukasz Cieślikiewicz[a], Maris Sinka[b], Diana Bajare[b], Piotr Łapka[a]

[a]Warsaw University of Technology, Faculty of Power and Aeronautical Engineering, Institute of Heat Engineering, Nowowiejska 21/25, 00-665 Warsaw, Poland
[b]Riga Technical University, Faculty of Civil Engineering, Institute of Materials and Structures, Kalku 1, LV-1658 Riga, Latvia
*Corresponding author email: mateusz.wendolowicz.dokt@pw.edu.pl

Received: 11.02.2024; revised: 01.07.2024; accepted: 02.07.2024

Abstract

This article presents the results of experimental measurements of the physical properties of new environmentally friendly bio-based composite building materials containing hemp shives bonded with a magnesium binder. Some of the tested materials contained an admixture of phase change material (PCM) of variable proportions in the binder to increase the heat capacity of building elements (walls), which can positively affect room temperature regulation. Densities and porosities are key parameters describing building materials, directly affecting mechanical, acoustic, and, most importantly, hygrothermal properties, including thermal conductivity, water vapor permeability, water absorptivity, and sorption curves. The experiment was carried out for ten different samples of bio-based building composites, differing in the bulk density obtained during the manufacturing process and in the PCM proportion. As part of the experiment, true density tests were conducted on a helium pycnometer. Then, the geometric densities of the tested materials (which may differ from the bulk density obtained during production) were measured using the Archimedes method, making it possible to obtain the total, closed, and open porosity values. Tests were also carried out for selected traditional building materials, such as red brick and autoclaved aerated concrete, to compare the results obtained.

Keywords: Bio-based building materials; Bio-based composites; Magnesium binder; Hemp shives; Phase change material (PCM); Helium pycnometer; Porosity measurement

Vol. 45(2024), No. 3, 57–66; doi: 10.24425/ather.2024.151216

Cite this manuscript as: Wendołowicz, M., Mikos-Nuszkiewicz, N., Cieślikiewicz, Ł., Sinka, M., Bajare, D., & Łapka, P. Research of the physical properties of bio-based building materials with phase change material. *Archives of Thermodynamics*, 45(3), 57–66.

1. Introduction

The growing interest in sustainability across all industries is prompting, among others, a search for innovative building materials in which environmentally friendly plant wastes can partially replace standard building materials. A major advantage of such solutions is concrete utilization reduction in the production of building materials, which contributes to decreasing carbon dioxide emissions into the atmosphere while ensuring the use of plant waste such as hemp shives [1,2]. Moreover, bio-based building composites are easier to recycle and often have an additional advantage as they have better thermal conductivity than traditional building materials, making buildings more energy efficient.

Nomenclature

m_{dry} – mass of a dry sample, kg
m_{sat} – mass of a saturated sample containing isopropyl alcohol, kg
$m_{sat,air}$ – mass of a saturated sample containing isopropyl alcohol, measured in isopropyl air, kg
$m_{sat,iso}$ – mass of a saturated sample containing isopropyl alcohol, measured in isopropyl alcohol, kg
V_g – geometric volume, m^3
V_p – open pore volume, m^3
V_t – total volume, m^3

Greek symbols

ϵ_c – closed porosity
ϵ_o – open porosity
ϵ_t – total porosity
ρ_g – geometric density, kg/m^3
ρ_l – liquid density, kg/m^3
ρ_t – true density, kg/m^3

Subscripts and Superscripts

Air – measurement performed in air
Iso – measurement performed in isopropyl alcohol

Abbreviations and Acronyms

PCM – phase change material

Moreover, this solution can still be improved by adding phase change materials (PCMs) to the binder, e.g., in the form of microcapsules, which are designed to increase the thermal capacity of building elements (e.g., walls) through phase change transformation [3–5]. In this way, energy losses to the environment can be reduced during cold weather, while heat gains can be decreased during hot periods [5], and, as a result, energy consumption needed for space heating and cooling can be lowered [6]. Hemp-based building materials have very good thermal insulation properties (i.e., their thermal conductivity is typically in the range of 0.08–0.2 W/(m K) [7]), good acoustic performance, and very good moisture accumulation and buffering behavior. However, traditional hemp concrete based on a lime binder is very fragile and has very weak mechanical properties, i.e. its compressive strength is typically below 0.5–0.6 MPa [7]. It cannot be used in places directly exposed to water, i.e. the hemp concrete wall must be protected from direct rainfall with plaster and by protruding roof eaves and from groundwater by horizontal waterproofing and a raised foundation. However, hemp concrete is characterized by low microbiological corrosion because hemp shives consist of only the woody inner part of the hemp stalk and contain no nutrient elements. It is mainly used as a wall filling material, for thermal insulation, and to regulate the indoor microclimate, but it cannot be considered a load-bearing material. Therefore, many modifications of this material were proposed in the literature [8] in order to improve its mechanical performance and increase its application range. One of the possible ways is to use alternative binders that have better mechanical properties than those based on lime ones [9]. For example, the use of magnesium binders, as in the case of the material analyzed in this paper, can increase the strength up to 3.8 MPa [9].

The prospects for using PCMs in the building sector, including application in bio-based composite building materials, are widely reported in the literature. These materials are studied on both the numerical simulation and experimental levels. For example, Sawadogo et al. [10] conducted experiments in which different properties of hemp concrete with PCM (i.e. capric acid), such as melting and solidification temperatures and enthalpies, thermal conductivity, and general thermal performance, were investigated. A similar experiment was conducted by Meng et al. [11] where, by using simulations and an experiment, they compared the parameters inside an ordinary room and a room additionally insulated with a PCM layer and presented possible efficiency gains with the use of this material.

Hemp concrete as a bio-based composite material does not have clearly and easily defined thermal and moisture parameters [12]. It is influenced by many factors, from the type of binder and its admixtures [8,13], the amount of binder used, the degree of grinding of the plants [7,14], and the harvesting period of the hemp seed [15]. The plurality of solutions available, whether in terms of available binders, PCMs, or the form of PCM added to the building material itself, makes it necessary to pay great attention to the development of available experimental databases that could be used for mathematical modeling of hygro-thermal performances [16,17] or comparison of bio-based building materials.

Key physical parameters describing the structure of building materials include density and porosity. Their values directly affect mechanical [18], acoustic [19], and hygro-thermal properties [20,21], including thermal conductivity [22,23], water vapor permeability [8], and moisture sorption [24,25]. It is supposed that some of these properties depend more specifically on the pore size or the type of pores in the structure of the materials [26,27], hence it is important not only to know the total porosity but also the open and closed porosity or the pore size distribution in the structure. Glé et al. [24] point out that open and closed porosity values have an especially important role in determining the acoustic properties of materials. Wei et al. [28] conclude that the lower open porosity results in lower water absorption and weaker evaporation performance.

Methodology for measuring the porosity of building materials containing bio-additives, like hemp shives, is a matter of concern due to the occurrence of pores in biocomposite materials ranging in size from a few nanometers to even millimeters [29]. Brewer et al. [29] used helium pycnometry combined with powder micro-granular pycnometry to calculate the densities and porosities of biochar. Jiang et al. [30] identify radiation-based (e.g. microscopy) and porosimetry-based (such as water immersion porosimetry) methods as the main experimental techniques while suggesting the use of several of them to be able to achieve a comprehensive research result. Glé et al. [24] extensively describe aspects of density and porosity measurements of hemp shives themselves and suggest pycnometry (powder, helium, air, nitrogen, or mercury-based) as the optimal method for measuring the properties of ground biocomposites. They also suggested

X-ray computed tomography as one option, but due to its time-consuming nature, it should be rather used for local structure studies. Delanoy et al. [31] studied the porosities of two different hemp concretes (with a lime-based binder and a natural cement) using an air porosimeter. Wei et al. [28] studied the properties of bio-based composite building materials created from corn residue and magnesium cement using the Archimedes method and acetone-based pycnometry. Ferroukhi et al. [32] used pycnometry to find densities and porosities of hemp concrete based on a lime binder containing PCM. However, experimental data on the physical properties of bio-based building composites studied in this paper, i.e. hemp concrete created with magnesium binder, is difficult to find in the literature, and additionally, such results for materials containing PCM are also notably lacking.

This article presents the results of an experimental study in which the values of geometric and true density, as well as total, open, and closed porosity, were measured for 10 samples of bio-based building composites made of hemp shives and magnesium binder. Three of them contained microencapsulated PCM in different proportions, seven were bio-based composite samples with a different bulk density, and additionally, two conventional building materials were studied for comparison purposes. A helium pycnometer was used to determine total porosity and true density, while the Archimedes method based on measurements in isopropyl alcohol was used to determine open porosity.

2. Description of the method and materials investigated

2.1. Investigated materials

Bio-based composite materials with different bulk densities obtained during the manufacturing of the biocomposite samples by the research team from the Riga Technical University were tested [9]. All samples were made by mixing hemp shives, magnesium binder (MgO), magnesium chloride ($MgCl_2$) water solution, and water needed for the initial preparation of materials. To 3 samples, microencapsulated PCM was added in the form of concentrated water dispersion. Different mass shares of constituents were used to obtain tested composites, as presented in Table 1.

In the applied hemp shives (Natūralus Pluoštas, Lithuania), almost 74% of all plant pieces were characterized by lengths ranging from 1 to 30 mm, with the longest pieces reaching up to 40 mm. The base bulk density of the hemp components was in the range of 80–110 kg/m^3, while compacted bulk density was 115 kg/m^3. Magnesia named RKMH-F (produced by RHI AG, Austria) and calcined at the temperature of 750°C was used to prepare the composite. Its composition consists of 74% MgO with an admixture of CaO, SiO_2, Fe_2O_3, and Al_2O_3 in a range of 1–4%. Magnesium chloride (Chemische Fabrik Kalk, Germany) in the form of flakes was applied and, before adding to the mixture, was initially diluted in water in a 1:1 by-mass proportion. Additionally, some water was used to initially moisturize dry hemp particles, which strongly absorb water [33].

PCM-containing samples were produced by adding concentrated water dispersion of microcapsules MikroCapsPCM25-S50 (MikroCaps d.o.o., Slovenia) with the paraffin wax enclosed in a polyurethane shell. The average size of the microcapsules varied from 1 to 15 μm, and the PCM content inside the dry capsule was 82–86%, while in the dispersion, it was 41-45% wt. Paraffin used was characterized by latent heat in the range of 140–175 kJ/kg and melting/solidification temperature of 23–27°C.

The PCM-free materials were designated D200, D300, D400, D500 and D600 (as listed in Table 1) referring to their approximate bulk densities. The densities of these samples varied due to the use of variable amounts of MgO and $MgCl_2$ solution relative to the other components (see Table 1). Also, the sample Ind400 was analyzed, which was specified for its different industrial methods of manufacture. Samples containing PCMs were named PCM0, PCM5, PCM10 and PCM20. Moreover, autoclaved aerated concrete and red brick, available in the Polish market, were used as comparative conventional building materials.

The compositions of all tested bio-based composite samples were calculated with reference to the mass proportion of hemp shives (see Table 1). The numbers in the names of samples with PCM, i.e. 0, 5, 10 and 20, refer to the mass ratio of the PCM-water dispersion to the mass of MgO used for composite preparation. In fact, sample PCM0 does not contain PCM, but is the

Table 1. Ingredients contents for preparing bio-based composite samples referring to 1 unit of hemp shives (mass proportions).

Sample name	Hemp shives	MgO	$MgCl_2$ solution 1:1 with water	Water to initially moisten the hemp	PCM water dispersion (41-45% wt. of PCM)	PCM mass fraction (%)
D200	1.00	0.50	0.32	1.30	-	-
D300	1.00	1.00	0.63	0.70	-	-
D400	1.00	1.93	1.22	0.50	-	-
D500	1.00	2.44	1.53	0.50	-	-
D600	1.00	3.00	1.89	0.50	-	-
Ind400	1.00	1.85	1.17	1.00	-	-
PCM0	1.00	2.00	1.26	1.00	0.00	0.0
PCM5	1.00	2.00	1.26	1.00	0.10	1.2
PCM10	1.00	2.00	1.26	1.00	0.20	2.3
PCM20	1.00	2.00	1.26	1.00	0.40	4.5

reference sample for other materials in this batch, the production of which required a different composition of ingredients than the samples named "D", as shown in Table 1. Sample PCM0 has a composition most similar to D400, but during production, a bit more binder and twice as much water to pre-wet the hemp shives were used. Taking into account the mass shares of the individual components, the mass shares of PCM in the samples were 0.0, 1.2, 2.3 and 4.5% for samples PCM0, PCM5, PCM10 and PCM20, respectively.

2.2. Total porosity investigation using a helium pycnometer

Four small fragments were extracted from different parts of a larger block of tested materials to measure the true density and total porosity of developed bio-based building composites, from which 13 finely ground samples were prepared for measuring on a helium pycnometer. The materials were ground to fine dust using a laboratory grinder, with liquid nitrogen applied to increase the brittleness of the bio-based fibers and facilitate the grinding of these samples. All samples were then dried in a laboratory drier at 60°C for at least 5 days. Weight measurements showed that this period was sufficient to consider the ground samples dried. After drying, density measurements were started using a helium pycnometer AccuPyc 1345.

The ground material (as shown in Fig. 1) was poured into a cleaned, dry-air rinsed and weighed 3.5 cm^3 steel vessel and then weighed. A laboratory scale with an accuracy of 0.001 g was used to weigh the samples. To increase the accuracy of the measurement, an effort was made to place as much powdered material as possible in the vessel, additionally kneading it (the device required a certain minimum mass of material to be placed inside the steel vessel). The sample was then placed inside the device and sealed tightly. Figure 1 also shows a filter, which is essential for conducting experiments on bulk substances. The measurement began with 10 cycles of purging the prepared sample with helium to remove air and any residual moisture and ensure homogeneous conditions inside, followed by 30 measurement cycles. Each cycle consisted of filling the vessel with a certain volume of helium until an overpressure of about 1.35 bar at 25°C was reached. When pressure stability was reached, an automatic valve to a vessel of known volume was opened, and the system was again waiting for equilibrium to be reached. Knowing the thermodynamic parameters, the device calculated the volume of the material, and using the known mass of the sample, its true density (ρ_t) could be determined. Based on the information about the true density and geometric density, the total porosity of the test samples was determined.

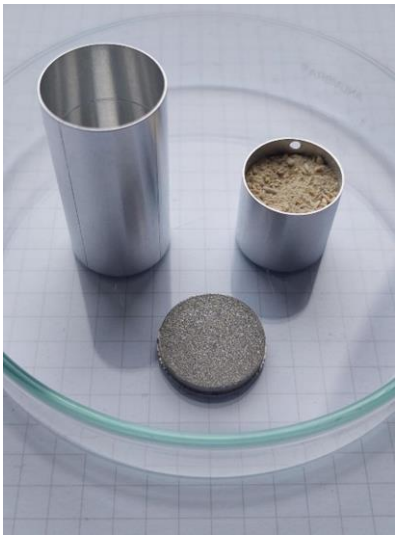

Fig. 1. Exemplary sample prepared for testing in helium pycnometer.

2.3. Open porosity investigation

The bio-based composite samples in the shape of cubes with sides of about 50 mm (some of which are shown in Fig. 2), 3 of each type that came from the same production batch as the samples investigated on the pycnometer, were tested. For conventional materials, 4 cuboidal samples were prepared from autoclaved aerated concrete and brick with volumes similar to the bio-based composite samples (i.e. in the range of 105–180 cm^3). Samples were cut out of the large blocks using an angle grinder, and then they were smoothed and aligned with sandpaper to obtain parallel walls. After the samples were prepared, they were placed in a laboratory drier and dried at about 60°C to remove moisture from them. Over the following days, the weights of the samples were recorded until they reached a constant mass of m_{dry} in three consecutive measurements. Then, the dimensions of the samples were measured to the nearest 0.01 mm, three times in each of the three dimensions, to be able to estimate their geometric volumes (V_g) and then calculate their geometric densities (ρ_g).

After drying, the samples were weighed, and then saturated with isopropyl alcohol. To do this, they were placed inside a sealed vessel filled with isopropyl alcohol to the point that the samples were completely submerged, and then a vacuum pump was used to create a vacuum (at –0.85 bar gauge pressure) to remove air from the pores. The samples were in the vessel until it was determined that no more air bubbles were coming out. Higher-density materials required several hours to remove air, while porous materials required at least 2–3 hours. After saturation, the samples were removed from the vessel and immediately placed in a dish with isopropyl alcohol located on a scale, where their apparent masses ($m_{sat,iso}$) were measured (the operation is shown in Fig. 3). During the measurements, care was taken that the sample placed in the glass beaker did not come into contact with the walls and the wires that held the dish. Measuring the mass in isopropyl alcohol took from 2 to as long as 5 hours. Samples with higher density needed much more time to stabilize. After the tests, the density of isopropyl alcohol (ρ_l) was determined using Archimedes' law and a standard of known volume. This one may have varied depending on the room conditions or as a result of the dissolution of substances contained in the bio-based building composite samples.

Fig. 2. Archimedes test samples (from the left: D300, D500, PCM20, red brick, and autoclaved aerated concrete).

After measuring the apparent mass, the samples were removed from the vessel, slightly wiped from the outside to remove the lingering liquid layer from the surface, and then weighed to obtain the mass of the sample saturated with isopropyl alcohol ($m_{sat,air}$). The open porosity was calculated based on mass measurements, and with known total porosity, the closed porosity value can be obtained. This was done using the following steps.

Geometric density is defined as the ratio of a dry sample's mass (m_{dry}) to its geometric volume (V_g):

$$\rho_g = \frac{m_{dry}}{V_g}. \tag{1}$$

The volume of open pores is calculated from the following equation:

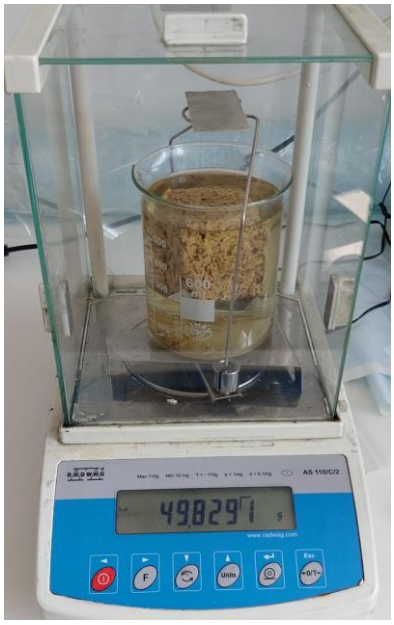

Fig. 3. A sample during measurement of apparent mass in isopropanol.

$$V_p = \frac{m_{sat,air} - m_{dry}}{\rho_l}, \tag{2}$$

where: ρ_l is isopropyl alcohol density, and $m_{sat,air}$ is the mass of the sample saturated with isopropyl alcohol measured in air.

The total volume, which is the volume of the solid, including the pores inside its structure, is defined as the difference in the saturated weight of the sample measured in air ($m_{sat,air}$) and in isopropyl alcohol ($m_{sat,iso}$):

$$V_t = \frac{m_{sat,air} - m_{sat,iso}}{\rho_l}. \tag{3}$$

Open porosity is defined as the ratio of open pore volume (V_p) to total volume (V_t):

$$\epsilon_o = \frac{V_p}{V_t}, \tag{4}$$

while total porosity is determined from the formula:

$$\epsilon_t = \left(1 - \frac{\rho_g}{\rho_t}\right) \cdot 100\%, \tag{5}$$

where ρ_t is a true density, which is the density of a solid phase.

Closed porosity is calculated as the difference between total porosity and open porosity:

$$\epsilon_c = \epsilon_t - \epsilon_o. \tag{6}$$

3. Results

From the results shown in Fig. 4 it can be deduced that the geometric density results of samples that do not contain PCM are very close to the assumed bulk density values included in the sample names. The largest difference occurs for D200 samples containing the lowest amount of binder. The largest standard deviation values were also achieved for these samples. This may be due to the brittleness of the samples since the small amount of binder used in their production made them extremely fragile, and they may have lost some material. As a result, their mass might be smaller and their geometric dimensions irregular, resulting in difficulties in measuring accurately. It is worth noting

that the geometric density value of Ind400 samples is slightly higher than that of D400. For the comparative materials, it can be seen that red brick is much denser, which means it is also more massive, while autoclaved aerated concrete places its density between D500 and D600 samples.

Samples containing PCM achieve similar geometric densities for each composite type (see Fig. 5). As the content of the PCM increases, no clear trend in the density variation is noticed. Moreover, the standard deviations for the samples with PCM are low, and all results obtained were similar for every sample type. Most interestingly, even though the basic PCM0 samples were manufactured with ingredients fractions very similar to the samples labeled D400, it can be seen from a comparison of Figs. 4 and 5 that the values of their geometric densities are much closer to those of D500. This is due to the higher amount of water used during the preparation of the PCM0 mixture than for D400, which resulted in a more liquid mixture consistency and greater susceptibility to compaction.

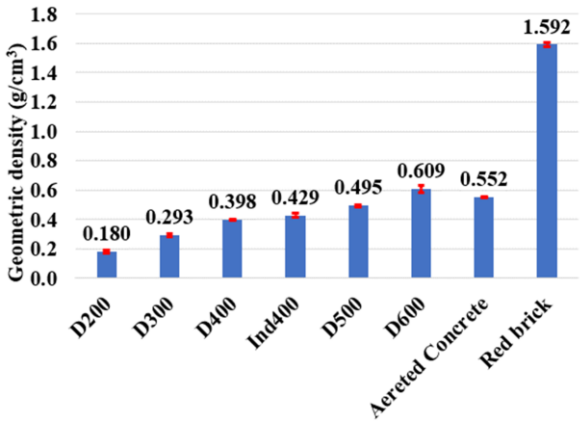

Fig. 4. Mean geometric density of the tested samples without PCM (minimal and maximal expanded uncertainty: 0.004 and 0.044 g/cm^3, respectively).

The results in Fig. 6 show the relationship between true density and bulk density (bio-based composite samples are ordered according to the rise in geometric density). An increase in true density with an increase in bulk density can be observed due to a higher amount of binder in denser samples and, thus, a lower proportion of hemp shives – the trend is clear. Moreover, the values of the true density of pure hemp shives and magnesium binder are also presented for comparison. Since magnesium binder is denser than plant fibers, samples with higher bulk density have more of it. Samples labeled D200 and D300 differ significantly in their true density from the observed trend for others, and a significant spread of results for D200 should be pointed out. These results show that achieving an even distribution of the binder in the low-density samples in the manufacturing process is difficult, and samples could be highly macroscopically non-homogenous. In contrast to the results of the geometric density test, the differences between D400, D500, D600 and Ind400 samples are relatively small. In this case, the density of the D400 samples is higher than the value for Ind400. However, it is worth noting that autoclaved aerated concrete has a higher

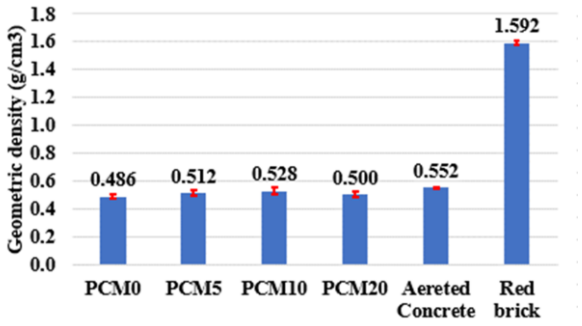

Fig. 5. Mean geometric density of the tested samples containing PCM (minimal and maximal expanded uncertainty: 0.004 and 0.055 g/cm^3, respectively).

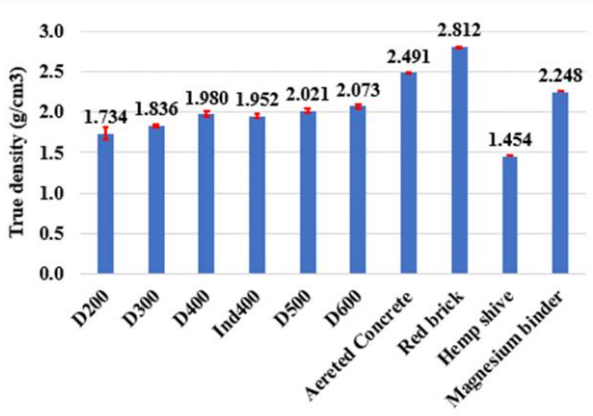

Fig. 6. Mean true density of the tested samples without PCM (minimal and maximal expanded uncertainty: 0.019 and 0.0149 g/cm^3, respectively).

true density than all bio-based composite samples, unlike its geometric density.

Samples containing PCM have almost the same true densities. However, comparing Figs. 6 and 7, it can be seen that they have values slightly smaller than those of the D400 and Ind400 samples and much lower than those of D500.

True density values (sometimes called solid density) for hemp concrete made of lime-metakaolin binder found in the literature range from 1.655 to 2.155 g/cm^3 [34]. These values should be considered only as a certain point of reference due to the different compositions of the materials tested and the use of different binders. Nevertheless, they allow for the conclusion that the results obtained in this work are realistic. Interesting results of density studies were presented by Ferroukhi et al. [32], who show that as the proportion of PCM in the bio-based composite structure increased (i.e., PCM amount was 0, 5, 10, and 15% of the mass of lime binder), the values of true density and geometric density significantly decreased. For samples investigated in this work, Figs. 5 and 7 show only small changes in density values with a change in the PCM proportion. Figure 5 shows an increase in density with an increase in PCM for samples PCM0, PCM5 and PCM10, but sample PCM 20 disrupts this trend, while in Fig. 7, true density decreases with the rise in the PCM amount, similarly as in [32]. Slightly different trends

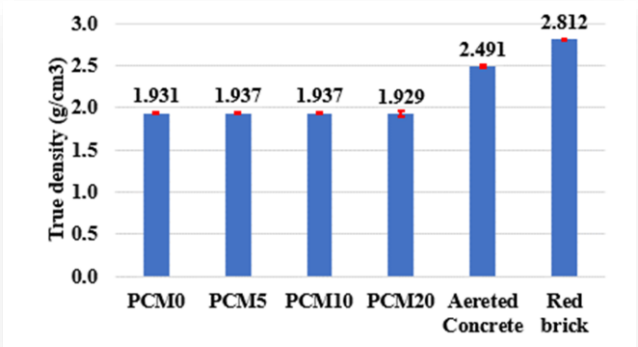

Fig. 7. Mean true density of the tested samples containing PCM (minimal and maximal expanded uncertainty: 0.019 and 0.057 g/cm^3, respectively).

in [32] can be due to much higher shares of PCM in the tested composites than in this work, i.e. 3.3, 6.6 and 9.2% wt. vs. 1.2, 2.3 and 4.5%, respectively, that can better reflect general composites behaviour.

The total porosity values of the bio-based composites shown in Fig. 8 vary from nearly 90% for the D200 samples to 70% for the D600 samples. These differences are naturally due to the varying mass content of hemp shives, which are much more porous than the magnesium binder, i.e., the lower the sample density, the higher the mass share of hemp shives, and the higher the porosity. Moreover, less binder resulted in more macropores in the composite. The porosity value of autoclaved aerated concrete does not differ from biocomposites and is very close to Ind400, while red brick is much less porous through its very compact structure.

The results in Fig. 9 show that the total porosity of the samples with PCM is similar to each other and close to that of the D500 samples but slightly lower than that of autoclaved aerated concrete. No correlation between the PCM content in the composite and its porosity value was observed.

The open porosity results in Fig. 10 show that this porosity decreases with the bulk density of the samples. Again, the values for D200 and D300 are significantly different (i.e., higher) than for the other composites. A similar level of open porosity as for

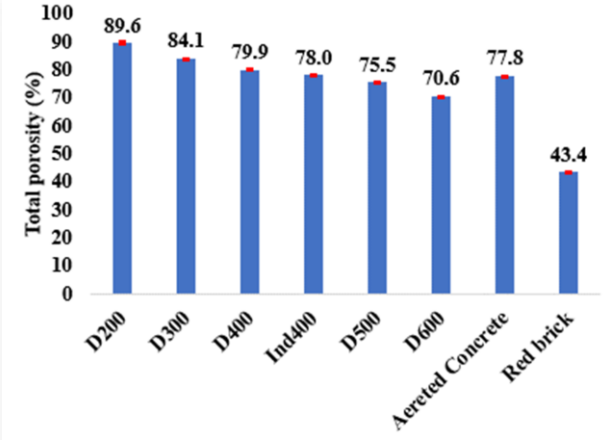

Fig. 8. Mean total porosity of the tested samples without PCM (minimal and maximal expanded uncertainty: 0.61 and 3.04 pp, respectively).

D200 and D300 achieves the autoclaved aerated concrete. Moreover, the Ind400 open porosity value clearly exceeds that of D400. Among all the samples tested, the values of open porosity significantly exceed those of closed porosity, which is largely related to the structure of the hemp shives that are highly porous with closed pores.

The lowest open and closed porosity has red brick. Its closed porosity value is only 3.2%, while the open one is 40.2%. The autoclaved aerated concrete has a slightly higher open porosity of 3.6%. This shows well the structure of autoclaved aerated concrete, which is blown during production, and many small cracks are formed in it. The closed porosity values of bio-based composites range from 10.3% to 16.5% and seem chaotic – no relationship between bulk density and closed porosity is visible.

For PCM samples, the open porosity fluctuates around 63%, which is comparable to D400 samples and much less than autoclaved aerated concrete (see Fig. 11). This time, however, an interesting relationship was obtained for the closed porosity results – as the proportion of PCM increases, the value of closed porosity decreases from 11.5% for PCM0 to 10.0% for PCM20.

Literature values for the total porosity of lime-metakaolin-based hemp concrete reach values in the range of 72–79% [34].

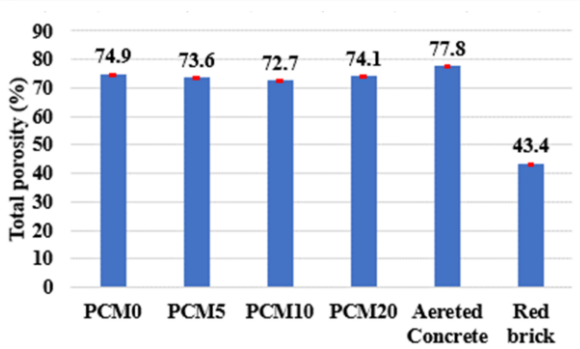

Fig. 9. Mean total porosity of the tested samples containing PCM (minimal and maximal expanded uncertainty: 0.61 and 3.51 pp, respectively).

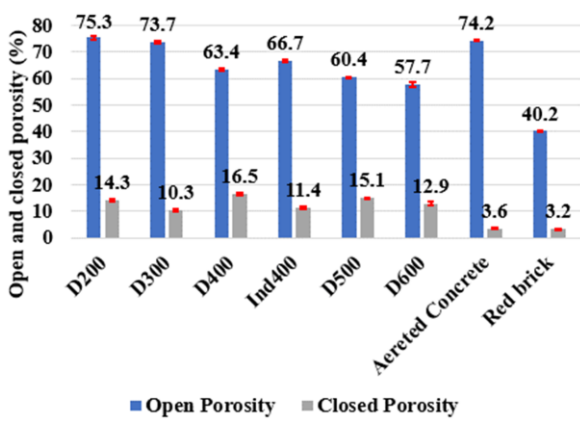

Fig. 10. Mean closed and open porosity of the tested samples without PCM (minimal and maximal expanded uncertainty: 0.74 and 1.74 pp for open porosity, and 1.54 and 4.09 pp for closed porosity, respectively).

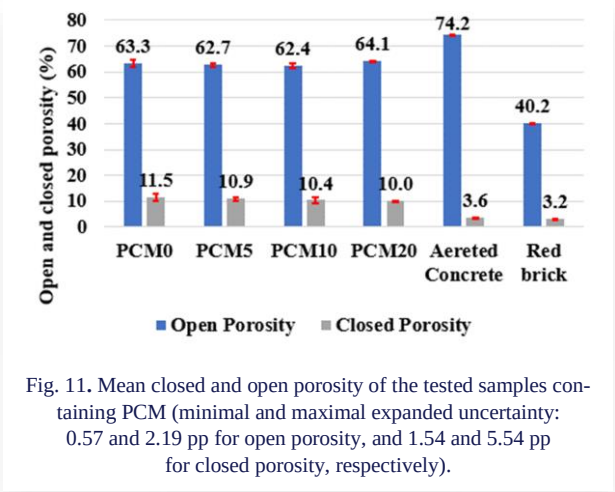

Fig. 11. Mean closed and open porosity of the tested samples containing PCM (minimal and maximal expanded uncertainty: 0.57 and 2.19 pp for open porosity, and 1.54 and 5.54 pp for closed porosity, respectively).

In this study, total porosities of 89.6% and 84.3% were achieved for specimens D200 and D300, respectively, with a much lower density than those tested in the literature, while other composites' results are in line with the data presented in [34]. An interesting aspect is the studies of open porosity presented in the literature, where results ranged from 50% for the vacuum saturation method [35] to 76% for the air porosimetry [36]. The porosity results achieved by Ferroukhi et al. [32] for PCM materials were in the range from 74.9% for a reference sample to 73.1% for a sample named HC15PCM. The values shown in Fig. 9 are very close to these, although one should consider the different compositions of the biocomposite samples and different constituents used in [31] and this study.

All combined standard uncertainties presented in Figs. 4–11 take into account both measurement uncertainties due to inaccuracies of the instruments (mainly related to weight measurements on balances, but also geometrical measurements, volume with a pycnometer or isopropyl alcohol density) and standard deviations of the results obtained from multiple samples. In the case of the uncertainty calculation for total porosity, where each of the 13 samples had a different uncertainty in volume measurement, the measurement with the largest relative uncertainty was selected, and this error was assumed for the whole material. Finally, an expanded uncertainty was calculated by applying a coverage factor $k = 2$, for which the confidence coefficient is better than 95%.

4. Conclusions

In the conducted experiments, the values of the basic parameters of bio-based composite building materials, such as densities (i.e. true and geometric) and porosities (total, open, and closed), were measured. The results obtained can find application as input data in numerical models simulating the hygro-thermal behavior of wall elements or help in assessing the utility of considered building materials. The basic properties of the biocomposites were also compared with autoclaved aerated concrete, some of whose properties were quite similar to bio-based materials, and with the much denser and less porous red brick.

The applied measurement techniques achieved results that can be considered realistic when compared to similar experiments described in the literature. For densities, total porosity, and open porosity measurements, results with satisfactory measurement uncertainties were obtained, while it should be highlighted that a significant part of these uncertainties may be due to the heterogeneous structure of the biocomposite building materials. However, it should be emphasized that the calculated values of the closed porosity of the tested materials, due to the large relative uncertainties (i.e. reaching even close to 100%), can only be considered indicative. To achieve more reliable closed porosity measurement results, a different measurement method should be developed, which is dependent on a lower number of intermediate measurements.

Most of the parameters studied show a clear relationship between the bulk density of the samples (which is controlled by the amount of binder added to their production) and the individual parameters. As the bulk density decreases, the true and geometric densities decrease also while the porosity increases. The situation is completely different in the case of samples containing PCM – a correlation between the mass share of microcapsules with PCM and the studied parameter was found only for the closed porosity. This may indicate a lack of regularity during manufacturing or a small effect of the microencapsulated PCM on the studied parameters. In terms of properties, the samples with PCM reach values between those obtained for D400 and D500.

Acknowledgements

This work was supported by the NCBiR (Poland) under M-ERA.NET 2 grant No. M-ERA.NET2/2019/4/2020 “Manufacturing technology of building products made of ecological high-performance fibre composites with encapsulated PCM for the NZEB application, HEMP4NZEB”.

References

[1] Jami, T., Karade, S.R., & Singh, L.P. (2019). A review of the properties of hemp concrete for green building applications. *Journal of Cleaner Production*, 239, 117852. doi: 10.1016/J.JCLEPRO.2019.117852

[2] Ahmed, A.T.M.F., Islam, M.Z., Mahmud, M.S., Sarker, M.E., & Islam, M.R. (2022). Hemp as a potential raw material toward a sustainable world: A review. *Heliyon*, 8(1), e08753. doi: 10.1016/J.HELIYON.2022.E08753

[3] Wu, D., Rahim, M., El Ganaoui, M., Bennacer, R., Djedjig, R., & Liu, B. (2022). Dynamic hygrothermal behavior and energy performance analysis of a novel multilayer building envelope based on PCM and hemp concrete. *Construction and Building Materials*, 341, 127739. doi: 10.1016/J.CONBUILDMAT.2022.127739

[4] Rathore, P.K.S., & Shukla, S.K. (2021). Enhanced thermophysical properties of organic PCM through shape stabilization for thermal energy storage in buildings: A state of the art review. *Energy and Buildings*, 236, 110799. doi: 10.1016/J.ENBUILD.2021.110799

[5] Lamrani, B., Johannes, K., & Kuznik, F. (2021). Phase change materials integrated into building walls: An updated review. *Renewable and Sustainable Energy Reviews*, 140, 110751. doi: 10.1016/J.RSER.2021.110751

[6] Bennai, F., Ferroukhi, M.Y., Benmahiddine, F., Belarbi, R., & Nouviaire, A. (2022). Assessment of hygrothermal performance of hemp concrete compared to conventional building materials at overall building scale. *Construction and Building Materials*, 316, 126007. doi: 10.1016/J.CONBUILDMAT.2021.126007

[7] Brzyski, P., Gładecki, M., Rumińska, M., Pietrak, K., Kubiś, M., & Łapka, P. (2020). Influence of Hemp Shives Size on Hygro-Thermal and Mechanical Properties of a Hemp-Lime Composite. *Materials*, 13(23), 5383. doi: 10.3390/MA13235383

[8] Łapka, P., Brzyski, P., Pietrak, K., Cieślikiewicz, Ł., & Suchorab, Z. (2023). Hygro-thermal characterization of the hemp concrete modified with the gum Arabic admixture. *Construction and Building Materials*, 368, 130392. doi: 10.1016/J.CONBUILDMAT.2023.130392

[9] Zorica, J., Sinka, M., Sahmenko, G., Vitola, L., Korjakins, A., & Bajare, D. (2022). Hemp Biocomposite Boards Using Improved Magnesium Oxychloride Cement. *Energies*, 15(19), 7320. doi: 10.3390/EN15197320/S1

[10] Sawadogo, M., Benmahiddine, F., Hamami, A.E.A., Belarbi, R., Godin, A., & Duquesne, M. (2022). Investigation of a novel bio-based phase change material hemp concrete for passive energy storage in buildings. *Applied Thermal Engineering*, 212, 118620. doi: 10.1016/J.APPLTHERMALENG.2022.118620

[11] Meng, E., Yu, H., & Zhou, B. (2017). Study of the thermal behavior of the composite phase change material (PCM) room in summer and winter. *Applied Thermal Engineering*, 126, 212–225. doi: 10.1016/J.APPLTHERMALENG.2017.07.110

[12] Ghosn, S., Cherkawi, N., & Hamad, B. (2020). Studies on Hemp and Recycled Aggregate Concrete. *International Journal of Concrete Structures and Materials*, 14(1), 1–17. doi: 10.1186/S40069-020-00429-6

[13] Brzyski, P. (2021). The Influence of Gum Arabic Admixture on the Mechanical Properties of Lime-Metakaolin Paste Used as Binder in Hemp Concrete. *Materials*, 14(22), 6775. doi: 10.3390/MA14226775

[14] Williams, J., Lawrence, M., & Walker, P. (2018). The influence of constituents on the properties of the bio-aggregate composite hemp-lime. *Construction and Building Materials*, 159, 9–17. doi: 10.1016/J.CONBUILDMAT.2017.10.109

[15] Li, Y., Pickering, K.L., & Farrell, R. L. (2009). Analysis of green hemp fibre reinforced composites using bag retting and white rot fungal treatments. *Industrial Crops and Products*, 29(2–3), 420–426. doi: 10.1016/J.INDCROP.2008.08.005

[16] Dietrich, F., Łapka, P., Cieślikiewicz, Ł., Furmański, P., Sinka, M., Vitola, L., & Bajare, D. (2021). Micro-scale modeling-based approach for calculation of thermal conductivity of bio-based building composite. *AIP Conference Proceedings*, 2429, 020023. doi: 10.1063/5.0071466

[17] Łapka, P., Dietrich, F., Furmanski, P., Cieslikiewicz, L., Sinka, M., & Bajare, D. (2023). Method for Prediction of Thermal Conductivity of Bio-Based Building Composites Enhanced With Microencapsulated PCM. *AIP Conference Proceedings*, 2801, 030020. doi: 10.1063/5.0146677

[18] Madsen, B., Thygesen, A., & Lilholt, H. (2009). Plant fibre composites – porosity and stiffness. *Composites Science and Technology*, 69(7–8), 1057–1069. doi: 10.1016/J.COMPSCITECH.2009.01.016

[19] Degrave-Lemeurs, M., Glé, P., & Hellouin de Menibus, A. (2018). Acoustical properties of hemp concretes for buildings thermal insulation: Application to clay and lime binders. *Construction and Building Materials*, 160, 462–474. doi: 10.1016/J.CONBUILDMAT.2017.11.064

[20] Chikhi, M. (2020). Effective thermal conductivity of porous biomaterials: Numerical investigation. *Journal of Building Engineering*, 32, 101763. doi: 10.1016/J.JOBE.2020.101763

[21] Li, Z.J., Huang, Z.W., Dai, H.L., Yao, Y., & Li, Y.S. (2024). Hygrothermal coupled modeling and behavior analysis of natural fiber-reinforced tubular composites. *Construction and Building Materials*, 411, 134384. doi: 10.1016/J.CONBUILDMAT.2023.134384

[22] Chikhi, M., Agoudjil, B., Boudenne, A., & Gherabli, A. (2013). Experimental investigation of new biocomposite with low cost for thermal insulation. *Energy and Buildings*, 66, 267–273. doi: 10.1016/J.ENBUILD.2013.07.019

[23] Frantz, N., Dutra, L.F., Nguyen, D.M., Almeida, G., & Perré, P. (2024). Effects of phase ratios, density and particle shapes on directional thermal conductivity of vegetable concrete: A predictive model. *Construction and Building Materials*, 410, 134238. doi: 10.1016/J.CONBUILDMAT.2023.134238

[24] Glé, P., Lecompte, T., Hellouin de Ménibus, A., Lenormand, H., Arufe, S., Chateau, C., Fierro, V., & Celzard, A. (2021). Densities of hemp shiv for building: From multiscale characterisation to application. *Industrial Crops and Products*, 164, 113390. doi: 10.1016/J.INDCROP.2021.113390

[25] Collet, F., Bart, M., Serres, L., & Miriel, J. (2008). Porous structure and water vapour sorption of hemp-based materials. *Construction and Building Materials*, 22(6), 1271–1280. doi: 10.1016/J.CONBUILDMAT.2007.01.018

[26] Abbas, M.S., Gourdon, E., Glé, P., McGregor, F., Ferroukhi, M. Y., & Fabbri, A. (2021). Relationship between hygrothermal and acoustical behavior of hemp and sunflower composites. *Building and Environment*, 188, 107462. doi: 10.1016/J.BUILDENV.2020.107462

[27] Lawrence, M., & Jiang, Y. (2017). Porosity, pore size distribution, micro-structure. *RILEM State-of-the-Art Reports*, 23, 39–71. doi: 10.1007/978-94-024-1031-0_2

[28] Wei, Y., Song, C., Chen, B., & Ahmad, M.R. (2019). Experimental investigation on two new corn stalk biocomposites based on magnesium phosphate cement and ordinary Portland cement. *Construction and Building Materials*, 224, 700–710. doi: 10.1016/J.CONBUILDMAT.2019.07.100

[29] Brewer, C.E., Chuang, V.J., Masiello, C.A., Gonnermann, H., Gao, X., Dugan, B., Driver, L.E., Panzacchi, P., Zygourakis, K., & Davies, C.A. (2014). New approaches to measuring biochar density and porosity. *Biomass and Bioenergy*, 66, 176–185. doi: 10.1016/J.BIOMBIOE.2014.03.059

[30] Jiang, Y., Ansell, M.P., Jia, X., Hussain, A., & Lawrence, M. (2017). Physical characterisation of hemp shiv: cell wall structure and porosity. *Academic Journal of Civil Engineering*, 35(2), 22–28. doi: 10.26168/ICBBM2017.1

[31] Delannoy, G., Marceau, S., Glé, P., Gourlay, E., Guéguen-Minerbe, M., Diafi, D., Nour, I., Amziane, S., & Farcas, F. (2019). Influence of binder on the multiscale properties of hemp concretes. *European Journal of Environmental and Civil Engineering*, 23(5), 609–625. doi: 10.1080/19648189.2018.1457571

[32] Ferroukhi, M. Y., Mesticou, Z., & Si Larbi, A. (2023). Impact of microencapsulated phase change material on a bio-based building composite, hygrothermal and mechanical behavior. *Construction and Building Materials*, 409, 133925. doi: 10.1016/J.CONBUILDMAT.2023.133925

[33] Sahmenko, G., Sinka, M., Paurins, U., & Bajare, D. (2023). Production Technology of Ecological High Performance Fibre Composite Construction Materials. *Journal of Physics: Conference Series*, 2423, 012005. doi: 10.1088/1742-6596/2423/1/012005

[34] Seng, B., Magniont, C., & Lorente, S. (2019). Characterization of a precast hemp concrete. Part I: Physical and thermal properties. *Journal of Building Engineering*, 24, 100540. doi: 10.1016/J.JOBE.2018.07.016

[35] Rahim, M., Douzane, O., Tran Le, A. D., Promis, G., & Langlet, T. (2016). Characterization and comparison of hygric properties of rape straw concrete and hemp concrete. *Construction and Building Materials*, 102, 679–687. doi: 10.1016/J.CONBUILDMAT.2015.11.021

[36] Gourlay, E., Glé, P., Marceau, S., Foy, C., & Moscardelli, S. (2017). Effect of water content on the acoustical and thermal properties of hemp concretes. *Construction and Building Materials*, 139, 513–523. doi: 10.1016/J.CONBUILDMAT.2016.11.018

Co-published by
Institute of Fluid-Flow Machinery
Polish Academy of Sciences
Committee on Thermodynamics and Combustion
Polish Academy of Sciences

http://www.imp.gda.pl/archives-of-thermodynamics/

Phase change material selection for energy storage units using a simple and effective decision-making method

Ravipudi Venkata Rao[a*]

[a]Sardar Vallabhbhai National Institute of Technology, Ichchanath, Surat-395007, India
*Corresponding author email: rvr@med.svnit.ac.in

Received: 12.05.2024; revised: 17.06.2024; accepted: 21.06.2024

Abstract

This study provides a simple and effective decision-making method to choose the best phase-change material for different energy storage applications. Three case studies are provided to demonstrate the proposed decision-making method. The first case study addresses the problem of best phase-change material selection for a domestic water heating latent heat storage system by considering 15 different phase-change materials and 8 selection attributes; the second case study addresses the problem of selecting the best phase-change material for a triple tube heat exchanger unit by considering 12 different phase-change materials and 5 selection attributes; the third case study addresses the problem of best phase-change material selection for latent heat thermal energy storage within the walls of Trombe to enhance performance considering 11 phase-change materials and 4 selection attributes. The results of the proposed decision-making method are compared with those of other well-known multi-attribute decision-making methods. The proposed method is shown to be simple to implement, providing a logical way for allocating weights to the selection attributes and adaptable to phase-change material selection problems in different energy storage contexts.

Keywords: Energy storage; Phase-change material selection; Selection attributes; Decision-making method.

Vol. 45(2024), No. 3, 67–79; doi: 10.24425/ather.2024.151217

Cite this manuscript as: Rao, R.V. (2024). Phase change material selection for energy storage units using a simple and effective decision-making method. *Archives of Thermodynamics*. 45 (3), 67−79.

1. Introduction

A new area of research that connects energy generation and consumption is thermal energy storage. Phase change materials with high energy storage density and isothermal working qualities are particularly significant in latent heat storage units. The effective and efficient heat storage of the thermal energy storage system depends on the use of phase change material (PCM). Finding a compromise between competing PCM selection attributes is usually necessary when choosing the best PCM to meet specific requirements. Thermal properties (e.g., latent heat of transition, thermal conductivity, specific heat, thermal stability, etc.); physical properties (e.g., density, volume change, vapour pressure); chemical properties (e.g., recycle, toxicity, flammability); kinetic properties (e.g., supercooling, phase separation); economic performance (e.g., cost); and certain managerial considerations are among the important requirements that must be met. All these requirements are considered as the PCM selection attribu-

Nomenclature

Cp – specific heat, kJ/(kg K)
K – thermal conductivity, W/(m K)
LH – latent heat of fusion, kJ/kg
t – time, min
T – temperature, °C

Greek symbols

ρ – density, kg/m^3

Subscripts and Superscripts

i – attribute
j – alternative
l – liquid
s – solid

Abbreviations and Acronyms

AHP – analytic hierarchy process
BWM – best-worst method
CoCoSo – combined compromise solution
COPRAS– complex proportional assessment
CRITIC – criteria importance through intercriteria correlation
EDAS – evaluation based on distance from average solution
EXPROM2– extension of PROMETHEE
MADM – multi-attribute decision-making
MEREC – method based on the removal effect of criteria
MOORA – multi-objective optimization of ratio analysis
MULTIMOORA – multi-objective optimization of ratio analysis plus the full multiplicative form
PCM – phase change material
PROMETHEE – preference ranking organization method for enrichment evaluations
TOPSIS – technique for order preference by similarity to ideal solution
VIKOR – višekriterijumsko kompromisno rangiranje
WASPAS– weighted aggregated sum product assessment
WPM – weighted product method

tes. As a number of PCM materials are available in the market, selecting the right PCM for a particular application becomes difficult and challenging. No single PCM can possess all the required properties and characteristics and hence selection of a best PCM for a given energy storage application is considered as a multi-attribute decision-making (MADM) problem.

Any MADM method for PCM selection involves the (i). PCM alternatives, (ii). PCM selection attributes, (iii). weights of importance assigned to the PCM selection attributes, and (iv). performance data of the PCM alternatives corresponding to the selection attributes. The chosen MADM method process the given data keeping in view of these four components and suggests the best PCM for the given energy storage application for optimal storage performance. The person making the decision (known as decision-maker) considers the importance of each selection attribute for the particular application based on his/her expertise and professional judgment.

Over the past ten years, researchers used several MADM methods to establish reliable methodologies for selecting the best PCMs for certain applications [1–16]. It is observed from the literature review on PCM selection that the researchers used different MADM methods. Even a particular MADM method like TOPSIS (technique for order preference by similarity to ideal solution) was used by the researchers for different applications. Two or more MADM methods were also used for a given application by many researchers in their works. Some of the widely used MADM methods for PCM selection were: technique for order preference by similarity to ideal solution (TOPSIS) [1–3,5,7–12,15,16], višekriterijumsko kompromisno rangiranje (VIKOR) [2,11,16], multi-objective optimization of ratio analysis (MOORA) [6,7], multi-objective optimization of ratio analysis plus the full multiplicative form (MULTIMOORA) [6], complex proportional assessment (COPRAS) and weighted aggregated sum product assessment (WASPAS) [11], preference ranking organization method for enrichment evaluations (PROMETHEE) [2], extension of PROMETHEE (EXPROM2) [16], evaluation based on distance from average solution (EDAS) [7], combined compromise solution (CoCoSo) [6], weighted product method (WPM) [14], etc. For obtaining the weights of importance of the PCM selection attributes, the methods like analytic hierarchy process (AHP) and fuzzy AHP [2], entropy method [3], best-worst method (BWM) [6], criteria importance through intercriteria correlation (CRITIC) [7], method based on the removal effect of criteria (MEREC) [11], range analysis [15], compromise weights approach [16], etc. were used by the researchers and those weights were utilized in the MADM methods for processing the data. Fuzzy scales were also used for converting the qualitative attributes into quantitative ones [2,16]. However, the fuzzy logic uses different membership functions and defuzzification methods and application of these functions and approaches may produce different results [17]. It is also observed that TOPSIS method is the widely used method by the researchers for PCM selection.

An important observation is that the researchers [1−16] used the properties and characteristics of the phase change materials such as latent heat of fusion, thermal conductivity for solid state (and liquid state), specific heat for solid state (and liquid state), density for solid state (and liquid state), cost, maintenance and operational costs, technological complexities, compatibility, flammability, risk levels, etc. for selection of a best PCM from amongst the available PCMs. Using the available data related to the properties and characteristics a large number of PCMs, the researchers used MADM methods and conducted simulation studies to choose a best PCM for the given application. After choosing a particular PCM, the researchers had then suggested that particular PCM for use in the given application. However, *real experimentation* was not conducted by the researchers [1−16] on the alternative PCMs to decide the selection of right PCM. It was because of the difficulty of experimenting on a large number of PCMs which is a costly and time-consuming activity.

Only limited number of research works are available on the real experimentation conducted on the PCMs for the purpose of selecting a best PCM out of the available ones. However, the number of PCMs experimented in such works is very less, because of the difficulty of experimenting on a large number of

PCMs. Oró et al. [18] studied a thermal energy storage system using PCM for low temperature applications such as commercial freezers. A set of PCM formulations based on ammonium chloride-water binary system were tested and analyzed to provide information useful for the selection of PCM with regard to their melting range, latent heat, stability under cycling, and cost. Yu et al. [19] conducted testing of GH-33 and GH-37 PCMs in boards mounted on internal surfaces of the main sun-facing walls of buildings for heating and curing of construction elements made of precast concrete. The theoretical and experimental study results suggested that the use of 50 mm thick board made of GH-37 composite PCM on the internal surface of the main sun-facing wall of the curing building provided the best thermal performance. Prieto et al. [20] tested thermal energy storage systems containing PCMs such as LiOH-LiBr and LiOH-KOH for direct steam generation concentrating solar power plants. After a deep characterization process, the LiOH-KOH was selected. Thus, it can be understood that the selection of best PCM for a given application was carried out by most of the researchers using MADM methods and simulations only.

Even though the above-mentioned MADM methods are useful for selection of right PCM for a given application, they also have drawbacks. For example, the TOPSIS approach necessitates extensive computations that become more difficult as the number of alternatives and attributes increases. The ranks of alternatives provided by the TOPSIS method can vary depending on the different normalization techniques applied to standardize the data. In the case of VIKOR method, there is additional processing needed. The method could lead to different outcomes for the same attribute weights in different ranking lists depending upon the weight allotted to "the majority of attributes". The other MADM techniques have drawbacks of their own and require a significant amount of processing [21,22].

The weights of the PCM selection attributes decided by the decision-maker are called the subjective weights. The AHP method [2] generates a large number of comparison matrices by comparing attributes and alternatives on a scale from 1 to 9. The issue of contradictory judgements occasionally comes up. Furthermore, the way the weights are determined (arithmetic mean, geometric mean, etc.) can affect the choice results. The BWM strategy [6] outperforms the AHP method in terms of judgment consistency, but it also requires a significant amount of computational work due to the increase in pairwise comparisons between the worst, best, and other criteria.

The weights of the PCM selection attributes can also be determined using objective approaches by utilizing methods like the entropy method [3], CRITIC [7], MEREC [11], etc. These weights are called the objective weights since the decision-maker has no control over how they are determined. It should be highlighted, nevertheless, that the decision-maker has no role in the objective weights, which are determined by the given numerical values of the attributes. These objective weights may be (most probably) entirely different from the decision-maker's opined subjective weights. The opinions of the decision-makers who actually deal with the practical values of the attributes in a given decision-making situation are therefore not taken into consideration, which makes the evaluation and ranking of the alternatives using such objective attribute weights potentially meaningless. Recently, a few studies have begun using composite weights in PCM selection, which combine the objective and subjective weights [16]. These compromise weights might not be utilized at all in actual decision-making scenarios and simply remain as an academic exercise.

The research questions (RQs) related to selection of a right alternative PCM using MADM methods are:

1. RQ1: Is there a simple and effective MADM method to weigh the PCM selection attributes logically and evaluate the performance of alternative PCMs used in different energy storage units?
2. RQ2: Can such chosen MADM method handle both qualitative and quantitative PCM selection attributes?
3. RQ3: If such simple and effective MADM method exists, will it be easy to comprehend and practical to use for selection of best PCM for different energy storage applications?
4. RQ4: Will the objective weights obtained from the performance data of the PCM selection attributes really meaningful?
5. RQ5: Is it feasible to have an appropriate MADM method that is both reliable and resistant to changes in the PCM selection attributes' weights? Can such kind of MADM method regarded as best?

The main objective of this research paper is to answer to the above-mentioned RQs. Hence, an attempt is made in this paper to develop an improved MADM method based on simple ranking procedure. The proposed decision-making method addresses the above research questions. The proposed method is a simple, systematic, logical, and effective MADM method to process the performance data of the alternative PCMs corresponding to different PCM selection attributes (both quantitative and qualitative), to logically decide the weights of importance of the PCM selection attributes, and to rank the alternative PCMs based on their total performance. The proposed method is applied for PCM selection in three different thermal energy storage applications.

The proposed decision-making methodology, named as, BHARAT-II, is explained in detail in the next section.

2. Proposed decision-making methodology for PCM selection

The following is a description of the steps of the proposed methodology for PCM selection.

Step 1: Determine the PCM selection attributes A_i (i = 1, 2,..., m), and the alternative PCMs B_j (for j = 1, 2,..., n). The PCM selection attributes are both non-beneficial (i.e., lower values are desired) and beneficial (i.e., higher values are desired).

Step 2: Decide the order of importance of the PCM selection attributes to obtain the weights w_i (for i = 1, 2,..., m). The order of importance is in terms of 1, 2, 3, 4, and so on, based on how significant they are in relation to each other. An average rank will be given if two or more attributes are thought to be equally important.

For example, let there are four PCM selection attributes − W, X, Y, and Z − and the ranks of 1, 2, 3, and 4 are assigned to

them. Matrix A1 shows the rank relations:

$$\text{A1} = \begin{array}{c} \\ W \\ X \\ Y \\ Z \end{array} \begin{array}{c} \begin{array}{cccc} W & X & Y & Z \end{array} \\ \begin{bmatrix} 1 & 2 & 3 & 4 \\ 1/2 & 1 & 3/2 & 4/2 \\ 1/3 & 2/3 & 1 & 4/3 \\ 1/4 & 2/4 & 3/4 & 1 \end{bmatrix} \end{array}.$$

It may be noted that in matrix A1, the diagonal elements are 1 (i.e., $r_{WW} = 1$, $r_{XX} = 1$, $r_{YY} = 1$, and $r_{ZZ} = 1$) and the elements below the diagonal are the reciprocals of the rank relations of the selection attributes given above the diagonal (i.e. $r_{XW} = 1/r_{WX}$, $r_{YW} = 1/r_{WY}$, $r_{ZW} = 1/r_{WZ}$, $r_{YX} = 1/r_{XY}$, $r_{ZX} = 1/r_{XZ}$, $r_{ZY} = 1/r_{YZ}$).

The arithmetic means of each row of the A1 matrix are calculated and these are 2.5 (i.e., 10/4), 1.25 (i.e., 5/4), 0.833333 (i.e., 3.33333/4) and 0.625 (i.e., 2.5/4), respectively. The grand summation of these row sums is equal to 5.208333 (i.e., 2.5 + 1.25 + 0.83333 + 0.625). Now dividing each row sum with the grand sum of 5.208333 gives the A2 matrix, which corresponds to the weights of the four selection attributes considered:

$$\text{A2} = \begin{bmatrix} 0.48 \\ 0.24 \\ 0.16 \\ 0.12 \end{bmatrix}.$$

Similar to the AHP and BWM approaches, if the consistency check is performed to check for consistency of rank relations provided in matrix A1, the matrix A3 is computed as A1*A2:

$$\text{A3} = \text{A1*A2} = \begin{bmatrix} 1.92 \\ 0.96 \\ 0.64 \\ 0.48 \end{bmatrix}.$$

Now A4 matrix is computed as A3/A2:

$$\text{A4} = \text{A3/A2} = \begin{bmatrix} 1.92/0.48 \\ 0.96/0.24 \\ 0.64/0.16 \\ 0.48/0.12 \end{bmatrix} = \begin{bmatrix} 4 \\ 4 \\ 4 \\ 4 \end{bmatrix}.$$

Now the maximum eigen value (λ_{max}) is computed:

$$\lambda_{max} = \text{average of A4} = (4+4+4+4)/4 = 4.$$

Consistency index (CI) = $(\lambda_{max} - m)/(m-1) = (4-4)/(4-1) = 0$; the no. of attributes = size of A1 matrix = 4.

The CI value of 0 indicates that the rank relations provided in A1 matrix are *absolutely consistent* and there is no error present in the judgements of rank relations. As a result, weights of 0.48, 0.24, 0.16, and 0.12 can be assigned to the attributes W, X, Y, and Z respectively. *By expanding this method to any number of attributes and giving each one a rank, the attributes' weights may be found*. It may be stated here that techniques such as AHP and BWM *seldom* provide absolute consistency in the assessments of relative importance. Thus, the proposed method is more dependable.

Step 3: For every alternative PCM, obtain the performance data corresponding to the PCM selection attributes. The performances may be in qualitative or quantitative terms. Transform the qualitative attribute data (expressed in descriptive language) into quantitative data by applying a straightforward scale and avoiding the use of fuzzy logic. Rao [21−23] proved that there is no need of using fuzzy scales and simple ordinary scales will serve the same purpose. Simple ordinary scales can simply replace the fuzzy scales provided by different researchers to deal with linguistic or qualitative attributes using different membership functions. Table 1, for example, shows the transformation of a qualitative or linguistic attribute into a quantitative attribute on 11-point scale.

Table 1. Transformation of a qualitative attribute into a quantitative attribute using a 11-point scale.

Linguistic expression	Fuzzy scale value for a beneficial attribute [23]	Fuzzy scale value for a non-beneficial attribute [23]	Simple scale value for a beneficial attribute	Simple scale value for a non-beneficial attribute
Exceptionally low	0.0455	0.9545	0.0	1.0
Extremely low	0.1364	0.8636	0.1	0.9
Very low	0.2273	0.7727	0.2	0.8
Low	0.3182	0.6818	0.3	0.7
Below average	0.4091	0.5909	0.4	0.6
Average	0.5	0.5	0.5	0.5
Above average	0.5909	0.4091	0.6	0.4
High	0.6818	0.3182	0.7	0.3
Very high	0.7727	0.2273	0.8	0.2
Extremely high	0.8636	0.1364	0.9	0.1
Exceptionally high	0.9545	0.0455	1.0	0

Step 4: Normalize the data for a PCM selection attribute by comparing it to the attribute's "best" value for various alternative PCMs. To obtain the normalized data, repeat this normalization process for each attribute. When referring to a beneficial attribute, the term "best" denotes the highest value that is available, and when referring to a non-beneficial attribute, the lowest value that is available. Normalization is required for the performance measurements of alternative PCMs. For a beneficial attribute, the normalized value $(x_{ji})_{norm}$ is $x_{ji}/x_{i.best}$; and for a non-beneficial attribute, it is $x_{i.best}/x_{ji}$. The i-th attribute's best value is represented by $x_{i.best}$. The standing positions of the alternative PCMs in relation to the "best" values of the attributes are clearly displayed by this kind of normalization of the data with reference to the "best" values.

Step 5: Total score of an alternative PCM is $\sum w_i*(x_{ji})_{norm}$ and it is the result of multiplying the selection attributes' weights with the corresponding normalized data of the attributes for the alternatives.

Step 6: Arrange the alternative PCMs in decreasing order, based on their total scores. The alternative PCM that receives the highest total score is considered best for the particular PCM selection problem investigated.

The flowchart of the proposed decision-making method is shown in Fig. 1.

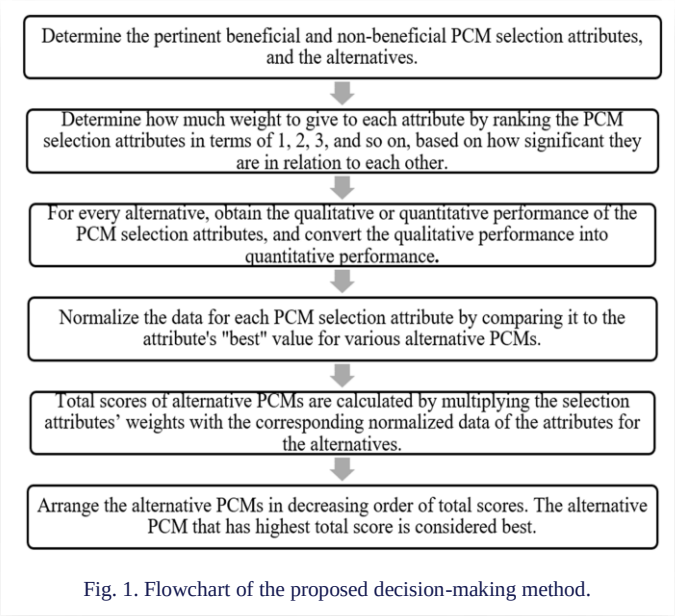

Fig. 1. Flowchart of the proposed decision-making method.

3. Applications of proposed decision-making method to the case studies of phase change material selection for energy storage

3.1. Case study 1: PCM selection for a domestic water heating system using LH storage unit

Gadhave et al. [16] conducted a case study to decide the right PCM for a domestic water heating system containing a PCM-based LH storage system, a storage tank with water, and additional accessories such as a circulation pump, flowmeter, valve, etc. The decision-making problem considered 15 alternative PCMs, designated from M1 to M15, analyzed under 5 selection attributes. Figure 2 shows the goal, selection attributes, and the alternative PCMs for case study 1.

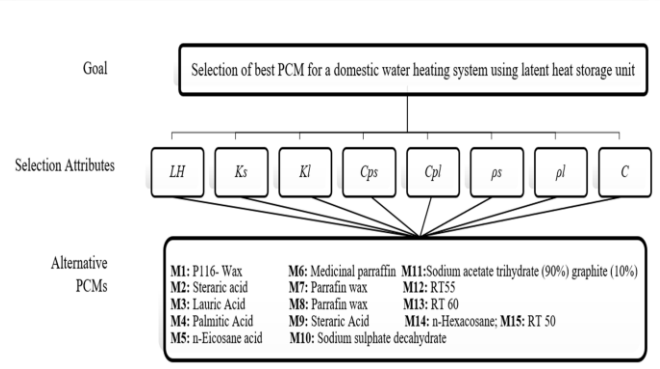

Fig. 2. Goal, selection attributes, and the alternative PCMs of case study 1.

Now to select a best PCM out of 15 PCMs, the steps of the proposed decision-making method are carried out as described below.

Step 1: Table 2 shows the PCM selection attributes and the alternative PCMs considered by Gadhave et al. [16]. The selection attributes are the material properties: latent heat of fusion (*LH*), thermal conductivity for solid state (*Ks*), thermal conductivity for liquid state (*Kl*), specific heat for solid state (*Cps*), specific heat for liquid state (*Cpl*), density for solid state (ρs), density for liquid state (ρl), and cost (*C*). The attributes *LH*, *Ks*, *Kl*, *Cps*, *Cpl*, and ρs, and ρl are beneficial and *C* is non-beneficial. The cost (*C*) is expressed linguistically and the corresponding quantitative values on a simple ordinary scale are assigned using Table 1 and shown in parentheses.

Table 2. Data of the 8 attributes and 15 alternative PCMs of case study 1.

PCM	*LH* kJ/kg	*Ks* W/(m K)	*Kl* W/(m K)	*Cps* kJ/(kg K)	*Cpl* kJ/(kg K)	ρs kg/m³	ρl kg/m³	*C*
P116-Wax (M1)	209	0.14	0.277	2.89	**2.89**	786	786	H (0.3)
Stearic acid (M2)	211.6	1.6	0.3	1.76	2.27	940	940	VH (0.2)
Lauric acid (M3)	178	1.6	0.147	1.6	2.27	870	870	A (0.5)
Palmitic acid (M4)	201	0.29	0.21	2	2.37	942	862	A (0.5)
n-Eicosane (M5)	248	0.426	0.146	1.926	2.4	910	769	L (0.7)
Medicinal paraffin (M6)	146	0.3	2.1	2.25	2.2	830	830	L (0.7)
Paraffin wax (M7)	210	0.24	0.15	**2.9**	2.1	860	780	L (0.7)
Paraffin wax (M8)	190	0.24	0.22	2	2.15	910	790	L (0.7)
Stearic acid (M9)	169	0.29	0.29	1.59	1.59	965	847	A (0.5)
Sodium sulphate decahydrate (M10)	180	0.15	0.3	2	2	**1460**	**1458**	H (0.3)
Sodium acetate trihydrate (90%)+graphite (10%) (M11)	190	**2.5**	**2.5**	2.5	2.5	1350	1350	H (0.3)
RT55 (M12)	172	0.2	0.2	2	2	880	770	L (0.7)
RT60 (M13)	167.6	0.2	0.2	2	2	880	770	**VL (0.8)**
n-Hexacosane (M14)	**256**	0.21	0.21	2	2	778.3	770	A (0.5)
RT50 (M15)	160	0.2	0.2	2	2	880	760	L (0.7)

VH: Very High; H: High; A: Average; L: Low; VL: Very Low

Step 2: To determine the weights of the 8 PCM selection attributes, ranks are assigned. The rank 1 is assigned to LH as it is considered much more important for the given application. In this case study, the attributes ρs and ρl are considered equally significant. Hence, an average rank of 2.5 (i.e., (2+3)/2) is allocated. Comparably, *Ks* and *Kl* have an average rank of 4.5 (i.e., (4+5)/2); *Cps* and *Cpl* have an average rank of 6.5 (i.e., (6+7)/2); and *C* has a rank of 8. The attributes have been assigned the same ranks as those shown in Table 3. The rank relationships and weights of the 8 attributes are shown in Table 3.

Table 3. Rank relationships of the 8 attributes in case study 1.

Attributes	Attributes									
	LH	*Ks*	*Kl*	*Cps*	*Cpl*	*ρs*	*ρl*	*C*	Means of rows	Weights of attributes
LH	1	4.5	4.5	6.5	6.5	2.5	2.5	8	36	0.37353
Ks	1/4.5	1	1	6.5/4.5	6.5/4.5	2.5/4.5	2.5/4.5	8/4.5	8	0.083
Kl	1/4.5	1	1	6.5/4.5	6.5/4.5	2.5/4.5	2.5/4.5	8/4.5	8	0.083
Cps	1/6.5	4.5/6.5	4.5/6.5	1	1	2.5/6.5	2.5/6.5	8/6.5	5.53843	0.05746
Cpl	1/6.5	4.5/6.5	4.5/6.5	1	1	2.5/6.5	2.5/6.5	8/6.5	5.53843	0.05746
ρs	1/2.5	4.5/2.5	4.5/2.5	6.5/2.5	6.5/2.5	1	1	8/2.5	14.4	0.14941
ρl	1/2.5	4.5/2.5	4.5/2.5	6.5/2.5	6.5/2.5	1	1	8/2.5	14.4	0.14941
C	1/8	4.5/8	4.5/8	6.5/8	6.5/8	2.5/8	2.5/8	1	4.5	0.04669
								Total =	96.3768	1.000

The CR value for the rank relations matrix containing 8 PCM selection attributes is 0. Thus, there exists absolute consistency in the judgments of rank relations. The last column of Table 3 gives the weights of the 8 PCM selection attributes.

Step 3: The linguistic expressions of the attribute *C* are transformed to quantitative values using Table 1 without the need of using fuzzy logic. These values are shown in Table 2 in parentheses. The values are assigned to non-beneficial *C* based on Table 1. After assigning like this, the assigned values for C can be considered beneficial for the sake of normalization.

Step 4: The data is normalized based on the "best" PCM for each attribute. The best values of the attributes are shown in bold inside Table 2. Table 4 shows the normalized values. For example, the normalized value of 0.816406 for *LH* corresponding to M1 is obtained by (209/256); the value of 0.056 for *Ks* corresponding to M1 is obtained by (0.14/2.5).

Table 4. Normalized values for case study 1.

PCM	Normalized values							
	LH	*Ks*	*Kl*	*Cps*	*Cpl*	*ρs*	*ρl*	*C*
M1	0.816406	0.056	0.1108	0.996552	1	0.538356	0.539095	0.375
M2	0.826563	0.64	0.12	0.606897	0.785467	0.643836	0.644719	0.25
M3	0.695313	0.64	0.0588	0.551724	0.785467	0.59589	0.596708	0.625
M4	0.785156	0.116	0.084	0.689655	0.820069	0.645205	0.591221	0.625
M5	0.96875	0.1704	0.0584	0.664138	0.83045	0.623288	0.527435	0.875
M6	0.570313	0.12	0.84	0.775862	0.761246	0.568493	0.569273	0.875
M7	0.820313	0.096	0.06	1	0.726644	0.589041	0.534979	0.875
M8	0.742188	0.096	0.088	0.689655	0.743945	0.623288	0.541838	0.875
M9	0.660156	0.116	0.116	0.548276	0.550173	0.660959	0.580933	0.625
M10	0.703125	0.06	0.12	0.689655	0.692042	1	1	0.375
M11	0.742188	1	1	0.862069	0.865052	0.924658	0.925926	0.375
M12	0.671875	0.08	0.08	0.689655	0.692042	0.60274	0.528121	0.875
M13	0.654688	0.08	0.08	0.689655	0.692042	0.60274	0.528121	1
M14	1	0.084	0.084	0.689655	0.692042	0.533082	0.528121	0.625
M15	0.625	0.08	0.08	0.689655	0.692042	0.60274	0.521262	0.875

Step 5: Total scores of alternative PCMs are calculated by multiplying the selection attributes' weights with the corresponding normalized data of the attributes for the alternatives. For example, the total score of PCM designated as M1 is computed as:

Total score (M1) = 0.37353*0.816406 + 0.083 + 0.056 + 0.083*0.1108 + 0.05746*0.996552 + 0.05746*1 + 0.14941*0.538356 + 0.14941*0.539095 + 0.04669*0.375 = 0.612029.

The total scores of the PCMs are given in Table 5.

Table 5. Total scores of 15 PCMs of case study 1.

PCM No.	PCM	Total score	PCM No.	PCM	Total score
M1	P116-Wax	0.612029	**M9**	Stearic acid	0.543704
M2	Stearic acid	0.65604	**M10**	Sodium sulphate decahydrate	0.673313
M3	Lauric acid	0.601936	**M11**	Sodium acetate trihydrate (90%) + graphite (10%)	**0.836491**
M4	Palmitic acid	0.610559			
M5	n-Eicosane	0.679525	**M12**	RT55	0.553467
M6	Medicinal paraffin	0.591894	**M13**	RT60	0.552883
M7	Paraffin wax	0.627383	**M14**	n-Hexacosane	0.654616
M8	Paraffin wax	0.589825	**M15**	RT50	0.534933

Step 6: The alternative PCMs are arranged in decreasing order of their total scores. The PCMs are ranked from highest to lowest total scores as follows: M11-M5-M10-M2-M14-M7-M1-M4-M3-M6-M8-M12-M13-M9-M15.

With the highest total score, the PCM identified as M11 can be considered as the best choice for the given application of domestic water heating system. Gadhave et al. [16] used entropy and AHP methods for obtaining the weights of the attributes and finally combined those weights to get the compromised weights of 0.4208, 0.0853, 0.0805, 0.0353, 0.0354, 0.1624, 0.1616, and 0.0187 for *LH*, *Ks*, *Kl*, *Cps*, *Cpl*, *ρs*, *ρl*, and *C*, respectively. The compromise weights were then used by Gadhave et al. [16] in TOPSIS, VIKOR, and EXPROM2 methods to calculate the scores and then ranked the PCMs. The PCMs were ranked from highest to lowest total scores as follows:

- TOPSIS [16]: M11-M2-M14-M5-M10-M6-M3-M7-M1-M4-M8-M9-M12-M13-M15,
- VIKOR [16]: M11-M5-M14-M2-M1-M7-M10-M4-M8-M3-M12-M9-M13-M15-M6,
- EXPROM2 [16]: M11-M2-M5-M10-M14-M7-M1-M4-M3-M8-M9-M6-M12-M13-M15.

These methods also suggested M11 as the best choice. However, it may be noted that the compromise weights were obtained by combining the objective weights obtained by entropy method and the subjective weights obtained by AHP method. In fact, the objective weights obtained and the subjective weights obtained by Gadhave et al. [16] were completely different. The objective and subjective weights were then combined to form the compromise weights. The compromise weights might not be utilized at all in actual decision-making scenarios and it simply remains as an academic exercise. However, for fair comparison, if the compromise weights used by Gadhave et al. [16] in TOPSIS, VIKOR, and EXPROM2 methods are used in the proposed decision-making method, then the PCMs can be arranged in the following order.

- Proposed method (using the compromise weights): M11-M10-M5-M2-M14-M7-M4-M1-M3-M8-M6-M9-M12-M13-M15.

Using the same compromise weights as those used in VIKOR, TOPSIS, and EXPROM2, the proposed decision-making method also suggested M11 as the best choice. The last choice is M15. It may be noted once again that the proposed decision-making method is involved in simple normalization procedure and the calculation of total scores of PCMs compared to the computationally intensive TOPSIS, VIKOR, and EXPROM2 methods. The ranks assignment procedure and the subsequent determinations of the weights of the PCM selection attributes by the decision maker are more logical compared to the compromise or combined weights used by Gadhave et al. [16]. The proposed method makes it easy to convert qualitative attributes into quantitative, does not require the use of fuzzy scale as that used by Gadhave et al. [16].

3.2. Case study 2: PCM selection for a triple tube heat exchanger unit

Yang et al. [15] presented the results of simulation conducted to investigate the impact of PCMs' thermophysical characteristics on a triple tube heat exchanger (TTHX) unit's heat storage ratio. The weights assigned to the attributes were obtained using range analysis at various time scales. Lastly, the ranking and selection process was carried out using the TOPSIS method. Figure 3 shows the goal, selection attributes, and the alternative PCMs for case study 2.

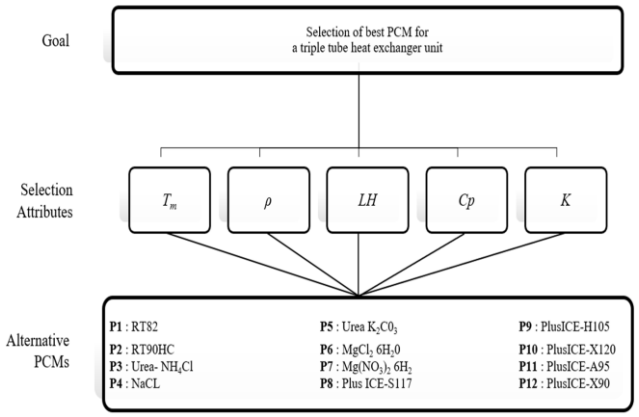

Fig. 3. Goal, selection attributes, and the alternative PCMs of case study 2.

The findings showed that the heat storage rate was significantly influenced by the thermophysical characteristics. The PCM PlusICE-S117 was found to be the ideal PCM when the melting time was 20 minutes, since the PCM density and thermal conductivity attributes were given greater weights. But when the melting time was 150 or 250 min, the most important attributes to take into account were the PCM density and melting enthalpy, and the alternative urea-NaCl was considered as the best one.

The decision-making problem considered 12 alternative PCMs, designated from P1 to P12, analyzed under 5 selection attributes. Now to select a best PCM out of the 15 PCMs, the steps of the proposed decision-making method are carried out as described below.

Step 1: Table 6 shows the PCM selection attributes and the alternative PCMs considered by Yang et al. [15]. The selection attributes are the material properties: melting temperature (T_m), density (ρ), latent heat of fusion (*LH*), specific heat (*Cp*), and thermal conductivity (*K*).

Table 6. Data of the 5 attributes and 12 alternative PCMs of case study 2.

PCM No.	PCM	T_m °C	P kg/m³	*LH* kJ/kg	*Cp* kJ/(kgK)	*K* W/(mK)
P1	RT82	82	770	170	2000	0.2
P2	RT90HC	90	850	170	2000	0.2
P3	Urea-NH_4Cl	102	1348	214	2090	0.58
P4	Urea-NaCl	112	1372	**230**	2020	0.6
P5	Urea-K_2CO_3	102	1415	206	2020	0.58
P6	$MgCl_2{\cdot}6H_2O$	116	1450	167	**2610**	0.57
P7	$Mg(NO_3)_2{\cdot}6H_2$	90	1550	163	2480	0.49
P8	PlusICE-S117	117	1450	160	**2610**	**0.7**
P9	PlusICE-H105	105	**1700**	125	1500	0.5
P10	PlusICE-X120	**120**	1245	180	1500	0.36
P11	PlusICE-A95	95	900	205	2200	0.22
P12	PlusICE-X90	90	1200	135	1510	0.36

Yang et al. [15] ignored the thickness of the tube walls and assumed the thermophysical properties of the PCM as equal in the liquid and solid phases. All these 5 selection attributes are beneficial.

Step 2: For sub-case 1 of Yang et al. [15], when the heat storage rate was considered for the first 20 minutes, density ρ was considered much more important followed by thermal conductivity K. Hence, rank 1 is given to ρ, rank 2 is given to K, rank 3 is given to LH, rank 4 is given to T_m, and rank 5 is given to Cp. Table 7 displays the rankings assigned to the 5 attributes along with the weights derived (similar to the procedure explained in section 2).

Table 7. Rank relationships of the 5 attributes of case study 2 and the corresponding weights (sub-case 1 of considering heat storage rate when the melting process continues up to 20 minutes).

Attributes	T_m	ρ	LH	Cp	K	Means of rows	Weights of attributes
T_m	1	1/4	3/4	5/4	2/4	3.75/5=0.75	0.75/6.85=0.109489
ρ	4	1	3	5	2	15/5=3	3/6.85=0.437956
L	4/3	1/3	1	5/3	2/3	(15/3)/5=1	1/6.85=0.145985
Cp	4/5	1/5	3/5	1	2/5	(15/5)/5=0.60	0.6/6.85=0.087591
K	2	1/2	3/2	5/2	1	7.5/5=1.5	1.5/6.85=0.218978
Total =						6.85	1.000000

It may be noted that the CR value for the rank relations matrix containing 5 PCM selection attributes is 0. Thus, there exists absolute consistency in the judgments of rank relations. The last column of Table 7 gives the weights of the 5 PCM selection attributes.

Step 3: The values shown in Table 6 are already quantitative in nature and there is no need of transformation. All 5 attributes are of beneficial type.

Step 4: The data shown in Table 6 is normalized based on the "best" PCM for each attribute. The best values of the attributes are shown in bold in Table 6. The normalized values are shown in Table 8. For example, the normalized value of 0.683333 for T_m corresponding to P1 is obtained by (82/120). Similarly, the other data is normalized and given in Table 8.

Table 8. Normalized values for sub-case 1 of case study 2.

PCM	T_m	ρ	L	Cp	K
P1	0.683333	0.452941	0.73913	0.766284	0.285714
P2	0.75	0.5	0.73913	0.766284	0.285714
P3	0.85	0.792941	0.930435	0.800766	0.828571
P4	0.933333	0.807059	1	0.773946	0.857143
P5	0.85	0.832353	0.895652	0.773946	0.828571
P6	0.966667	0.852941	0.726087	1	0.814286
P7	0.75	0.911765	0.708696	0.950192	0.7
P8	0.975	0.852941	0.695652	1	1
P9	0.875	1	0.543478	0.574713	0.714286
P10	1	0.732353	0.782609	0.574713	0.514286
P11	0.791667	0.529412	0.891304	0.842912	0.314286
P12	0.75	0.705882	0.586957	0.578544	0.514286

Step 5: Total scores of alternative PCMs are calculated by multiplying the selection attributes' weights with the corresponding normalized data of the attributes for the alternatives. For example, the total score of PCM designated as P1 is computed as:

Total score (P1) = 0.109489*0.683333 + 0.437956*0.452941 + 0.145985*0.73913 + 0.087591*0.766284 + 0.218978*0.285714 = 0510773.

The total scores of the PCMs are given in Table 9.

Table 9. Total scores of 15 PCMs of sub-case 1 of case study 2.

PCM No.	PCM	Total Score
P1	RT82	0.510773
P2	RT90HC	0.538682
P3	Urea-NH_4Cl	0.827748
P4	Urea-NaCl	0.857118
P5	Urea-K_2CO_3	0.837582
P6	$MgCl_2{\cdot}6H_2O$	0.85129
P7	$Mg(NO_3)_2{\cdot}6H_2$	0.821402
P8	PlusICE-S117	0.888427
P9	PlusICE-H105	0.819852
P10	PlusICE-X120	0.707434
P11	PlusICE-A95	0.591309
P12	PlusICE-X90	0.640242

Step 6: The alternative PCMs are arranged in decreasing order of their total scores. The PCMs are ranked from highest to lowest total scores as follows:

P8-P4-P6-P5-P3-P7-P9-P10-P12-P11-P2-P1.

With the highest total score, the PCM identified as P8 (i.e. PlusICE-S117) can be considered as the best choice for the given application of PCM selection for a triple tube heat exchanger unit (for the sub-case-1 of case study-2).

For sub-case 2 of Yang et al. [15], when the heat storage rate was considered for the first 150 minutes, density ρ was considered much more important followed by latent heat L. Hence, rank 1 is given to ρ, rank 2 is given to LH, rank 3 is given to T_m, rank 4 is given to K, and rank 5 is given to Cp. Table 10 displays the rankings assigned to the 5 attributes along with the weights derived.

Table 10. Rank relationships of the 5 attributes of sub-case 2 of case study 2 and the corresponding weights (considering heat storage rate when the melting process continues up to 150 minutes).

Attributes	T_m	ρ	L	Cp	K	Means of rows	Weights of attributes
T_m	1	1/3	2/3	5/3	4/3	5/5=1	1/6.85=0.145985
ρ	3	1	2	5	4	15/5=3	3/6.85=0.437956
L	3/2	1/2	1	5/2	2	7.5/5=1.5	1.5/6.85=0.218978
Cp	3/5	1/5	2/5	1	4/5	3/5=0.6	0.6/6.85=0.087591
K	3/4	1/4	2/4	5/4	1	3.75/5=0.75	0.75/6.85=0.109489
Total=						6.85	1.000000

For sub-case 3 of Yang et al. [15], when the heat storage rate was considered for the first 250 minutes, density ρ was considered much more important followed by latent heat LH, K, T_m, and Cp. Hence, rank 1 is given to ρ, rank 2 is given to LH, rank 3 is given to K, rank 4 is given to T_m, and rank 5 is given to Cp. Table 11 displays the rankings assigned to the 5 attributes along with the weights derived (similar to the procedure explained in section 2).

Table 11. Rank relationships of the 5 attributes of sub-case 3 of case study 2 and the corresponding weights (considering heat storage rate when the melting process continues up to 250 minutes).

Attributes	T_m	ρ	L	Cp	K	Means of rows	Weights of attributes
T_m	1	1/4	2/4	5/4	3/4	3.75/5=0.75	0.75/6.85=0.109489
ρ	4	1	2	5	3	15/5=3	3/6.85=0.437956
L	2	1/2	1	5/2	3/2	7.5/5=1.5	1.5/6.85=0.218978
Cp	4/5	1/5	2/5	1	3/5	3/5=0.6	0.6/6.85=0.087591
K	4/3	1/3	2/3	5/3	1	5/5=1	1/6.85=0.145985
Total=						6.85	1.000000

Table 12 shows the total scores of 12 PCMs corresponding to melting process timings. The alternative PCMs can be arranged in the descending order of the total scores for all the three sub-cases of case study 2

- proposed method (for $t_{melting}$=250 minutes): P4-P8-P6-P5-P3-P7-P9-P10-P12-P11-P2-P1.
- proposed method (for $t_{melting}$=150 minutes): P4-P8-P6-P5-P3-P7-P9-P10-P12-P11-P2-P1.
- proposed method (for $t_{melting}$=20 minutes): P8-P4-P6-P5-P3-P7-P9-P10-P12-P11-P2-P1.

Table 12. Total scores of 12 PCMs corresponding to melting process continued up to 20 minutes (sub-case 1), 150 minutes (sub-case 2) and 250 minutes (sub-case 3).

PCM No.	PCM	Total score ($t_{melting}$=20 min)	Total score ($t_{melting}$=150 min)	Total score ($t_{melting}$=250 min)
P1	RT82	0.510773	0.558381	0.543869
P2	RT90HC	0.538682	0.588723	0.571778
P3	Urea-NH_4Cl	0.827748	0.835966	0.835183
P4	Urea-NaCl	0.857118	0.870326	0.867546
P5	Urea-K_2CO_3	0.837582	0.84326	0.842478
P6	$MgCl_2{\cdot}6H_2O$	0.85129	0.850414	0.844853
P7	$Mg(NO_3)_2{\cdot}6H_2$	0.821402	0.823862	0.822037
P8	PlusICE-S117	0.888427	0.8653	0.866212
P9	PlusICE-H105	0.819852	0.81325	0.807384
P10	PlusICE-X120	0.707434	0.744747	0.72702
P11	PlusICE-A95	0.591309	0.65085	0.633427
P12	PlusICE-X90	0.640242	0.654149	0.645547

The alternative PCM P4 is considered as the best PCM if the melting time of 150 minutes as well for up to 250 minutes. However, the alternative PCM P8 is found as the best alternative PCM for melting time of 20 minutes.

It may be mentioned here that Yang et al. [15] used different weights of the attributes for the three sub-cases of case study 2 and used these weights in TOPSIS method to evaluate the alternative PCMs.

The weights used by Yang et al. [15] for sub-case 1 were: 0.092, 0.404, 0.214, 0.036 and 0.254 for T_m, ρ, LH, Cp and K, respectively.

The weights used by Yang et al. [15] for sub-case 2 were: 0.112, 0.405, 0.320, 0.056 and 0.107 for T_m, ρ, LH, Cp, and K, respectively. The weights used by Yang et al. [15] for sub-case 3 were: 0.094, 0.408, 0.340, 0.053 and 0.105 for T_m, ρ, L, Cp and K, respectively. The ranking of PCMs for different melting times were as given below:

- TOPSIS [15] (for $t_{melting}$=250 minutes): P4-P5-P3-P7-P6-P8-P9-P10-P11-P12-P2-P1.
- TOPSIS [15] (for $t_{melting}$=150 minutes): P4-P5-P3-P7-P6-P8-P9-P10-P12-P11-P2-P1.
- TOPSIS [15] (for $t_{melting}$=20 minutes): P8-P4-P5-P6-P3-P9-P7-P10-P12-P11-P2-P1.

For fair comparison, the same three sub-cases with the same weights of attributes, as considered by Yang et al. [15], are attempted using the proposed decision-making method and the following rankings are obtained

- proposed method (for $t_{melting}$=250 minutes) for the same weights used in TOPSIS [15]: P4-P5-P3-P8-P6-P7-P9-P10-P11-P12-P2-P1.
- proposed method (for $t_{melting}$=150 minutes) for the same weights used in TOPSIS [15]: P4-P5-P3-P8-P6-P7-P9-P10-P11-P12-P2-P1.
- proposed method (for $t_{melting}$=20 minutes) for the same weights used in TOPSIS [15]: P4-P8-P5-P3-P6-P9-P7-P10-P12-P11-P2-P1.

It is clear that using the same weights as those used in TOPSIS [15], the proposed decision-making method also suggested P4 as the first choice and P5 as the second choice for the sub-cases of $t_{melting}$=250 minutes and $t_{melting}$=150 minutes. It may be noted that the TOPSIS method used by Yang et al. [15] involves too lengthy calculations for normalization, calculating the objective weights using range analysis method, and then using those objective weights in the remaining computationally intensive steps. However, the procedure suggested by the proposed method is straightforward and simple to comprehend, in contrast to the TOPSIS method. As seen in this case study, the proposed method allows the use of weights of attributes calculated by other methods or as decided by the decision-maker based on intuition or experience.

3.3. Case study 3: PCM selection for an optimal Trombe wall performance

Thermal energy storage in buildings considerably lowers the energy demand of the building by releasing its stored energy when the need arises. Buildings use Trombe walls to store and distribute thermal energy, which controls the ambient temperature in each space. PCMs have been investigated extensively for latent heat thermal energy storage within the walls of Trombe to enhance performance. Oulah [5] investigated 11 alternative PCMs for selection of a suitable PCM for optimal Trombe wall performance using TOPSIS method. The heat of fusion, thermal conductivity, density, and cost were the four attributes taken into account. Except the cost attribute, the remaining attributes are of beneficial type.

Figure 4 shows the schematic of the PCM selection problem and Table 13 shows the data of the 4 attributes and 11 alternative PCMs. The best values of the attributes are shown in bold in Table 13.

Following the steps of the proposed decision-making method, the data given in Table 13 is normalized and is shown in Table 14. Table 15 displays the rankings assigned to the 4 attributes along with the weights derived.

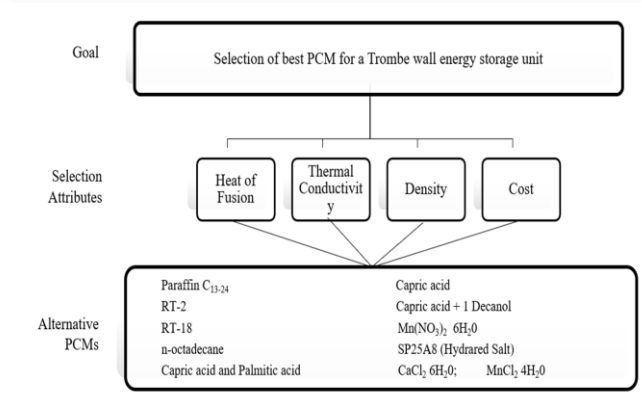

Fig. 4. Goal, selection attributes, and the alternative PCMs of case study 3.

Table 13. Data of the attributes for case study 3.

PCM	Heat of fusion kJ/kg	Thermal conductivity W/(m K)	Density kg/m³	Cost $/kg
Paraffin C13-24 (P1)	**189**	0.21	760	2
RT-27 (P2)	179	0.2	800	3.6
RT-18 (P3)	134	0.2	756	3.6
n-Octadecane (P4)	179	0.2	750	5
Capric acid and palmitic acid (P5)	177	**2.2**	784	1.78
Capric acid (P6)	142.7	0.2	815	**1.5**
Capric acid + 1 decanol (P7)	126.9	0.2	817	1.6
$Mn(NO_3)_2•6H_2O$ (P8)	125.9	0.6	1700	2
SP25A8 Hydrated salt (P9)	180	0.6	1380	1.8
$CaCl_2•6H_2O$ (P10)	187	0.53	**1710**	1.8
$MnCl_2•4H_2O$ (P11)	175	1	1490	2

Table 14. Normalized data of the attributes for case study 3.

PCM	Heat of fusion kJ/kg	Thermal conductivity W/(m K)	Density kg/m³	Cost $/kg
Paraffin C13-24 (P1)	1	0.095455	0.444444	0.75
RT-27 (P2)	0.94709	0.090909	0.467836	0.416667
RT-18 (P3)	0.708995	0.090909	0.442105	0.416667
n-Octadecane (P4)	0.94709	0.090909	0.438596	0.3
Capric acid and palmitic acid (P5)	0.936508	1	0.45848	0.842697
Capric acid (P6)	0.755026	0.090909	0.476608	1
Capric acid + 1 decanol (P7)	0.671429	0.090909	0.477778	0.9375
$Mn(NO_3)_2•6H_2O$ (P8)	0.666138	0.272727	0.994152	0.75
SP25A8 Hydrated salt (P9)	0.952381	0.272727	0.807018	0.833333
$CaCl_2•6H_2O$ (P10)	0.989418	0.240909	1	0.833333
$MnCl_2•4H_2O$ (P11)	0.925926	0.454545	0.871345	0.75

It may be noted that the CR value for the rank relations matrix containing 4 PCM selection attributes is 0. Thus, there exists absolute consistency in the judgments of rank relations. The last column of Table 15 gives the weights of the 4 PCM selection attributes.

Now using the normalized data of the attributes given in Table 14 and the weights of the attributes given in the last column of Table 15, the total scores of the 11 alternative PCMs are calculated and are given in Table 16.

Table 15. Rank relationships of the 4 attributes of case study 3 and the corresponding weights.

Attributes	Heat of fusion kJ/kg	Thermal conductivity W/(mK)	Density kg/m³	Cost $/kg	Means of rows	Weights of attributes
Heat of fusion	1	1/4	3/4	2/4	2.5/4=0.625	0.625/5.20833 = 0.12
Thermal conductivity	4	1	3	2	10/4=2.5	2.5/5.20833 = 0.48
Density	4/3	1/3	1	2/3	(10/3)/4 = 0.83333	0.83333/5.20833 = 0.16
Cost	2	1/2	3/2	1	5/4=1.25	1.25/5.20833 = 0.24
Total=					5.20833	1.00000

Table 16. Total scores of 11 PCMs of case study 3.

PCM	Total Scores of PCMs
Paraffin C13-24 (P1)	0.416929
RT-27 (P2)	0.332141
RT-18 (P3)	0.299453
n-Octadecane (P4)	0.299463
Capric acid and palmitic acid (P5)	0.867985
Capric acid (P6)	0.450497
Capric acid + 1 decanol (P7)	0.425652
$Mn(NO_3)_2•6H_2O$ (P8)	0.54991
SP25A8 Hydrated salt (P9)	0.574318
$CaCl_2•6H_2O$ (P10)	0.594367
$MnCl_2•4H_2O$ (P11)	0.648708

The PCMs are now arranged in the descending order of the total scores:

P5-P11-P10-P9-P8-P6-P7-P1-P2-P4-P3.

From the total scores of 11 PCMs, it can be understood that PCM designated as P5 (i.e., Capric acid and palmitic acid) is the first choice and PCM designated as P11 (i.e. $MnCl_2•4H_2O$) is the second choice for the Trombe wall.

It may be noted that Oulah et al. [5] used the objective weights of the attributes obtained by the entropy method (the weights were: 0.020109, 0.7127, 0.1124 and 0.1549 for the heat of fusion, thermal conductivity, density, and cost respectively). In fact, the objective weights are not much meaningful as they do not take into account the decision-maker's preferences. Using the objective weights, Oulah et al. [5] obtained the following rankings using the TOPSIS method:

- TOPSIS [5]: P5-P11-P8-P9-P10-P6-P7-P1-P2-P3-P4.

It can be seen that the entropy method suggests a bigger weightage of 0.7127 for thermal conductivity. Obviously, the alternative PCM which is the best with reference to the thermal conductivity emerges as the first choice (in this case, the PCM designated as P5) and the ranking of other PCMs will also be affected by such a higher weightage assigned to thermal conductivity. That was why Rao [21] opined that attributes weights should be decided by the decision-maker only as he/she is going to face the advantage or disadvantage of his/her decision. How-

ever, for fair comparison, if the same objective weights are used in the proposed method, the alternative PCMs can be arranged as shown below

- proposed method (using the objective weights of Oulah et al. [5]): P5-P11-P8-P9-P10-P6-P7-P1-P2-P3-P4.

The ranking is exactly same as that given by Oulah et al. [5] due to the reasons explained above.

4. Discussion

The research questions (RQs) related to selection of a right alternative PCM are reproduced below and discussion is made:

1. RQ1: *Is there a simple and effective MADM method to weigh the PCM selection attributes logically and evaluate the performance of alternative PCMs used in different energy storage units*?
   Yes, it is possible to develop such a simple and effective MADM method for PCM selection as proved in three different case studies of energy storage units.
2. RQ2: *Can such chosen MADM method handle both qualitative and quantitative PCM selection attributes*?
   Yes, the proposed decision-making method can handle both qualitative and quantitative attributes. This has been clearly demonstrated in the first case study. The suggested method can transform the qualitative (i.e. linguistically expressed) attributes into quantitative ones with the aid of simple linear scales.
3. RQ3: *If such simple and effective MADM method exists, will it be easy to comprehend and practical to use for selection of best PCM for different energy storage applications*?
   Yes, it is already shown in case studies 1, 2, and 3 that the proposed method can easily deal with information at hand. Even to deal with the qualitative information of the attributes, simple ordinary linear scales can be used instead of fuzzy logic-based scales. The proposed method is easy to comprehend and practical to use for selection of right alternative PCM for different energy storage applications.
4. RQ4: *Will the objective weights obtained from the performance data of the PCM selection attributes really meaningful*?
   No, not meaningful. The objective weights may be (most probably) entirely different from the decision-maker's opined subjective weights. The opinions of the decision-makers who actually deal with the practical values of the attributes in a given decision-making situation are therefore not taken into consideration, which makes the evaluation and ranking of the alternatives using such objective attribute weights potentially meaningless. Recently, a few studies have begun using composite weights in PCM selection, which combine the objective and subjective weights [3,7,16]. These compromise weights might not be utilized at all in actual decision-making scenarios and simply remain as an academic exercise.
5. RQ5: *Is it feasible to have an appropriate MADM method that is both reliable and resistant to changes in the PCM selection attributes' weights? Can such kind of MADM method regarded as best*?
   There is no doubt that an MADM method must be reliable. However, an MADM method need not be resistant to changes in the attributes' weights. How is it justified that the MADM method suggests the same ranking of alternatives even if the attributes' weights changed? It is unjustified and meaningless. It can be seen from the three subcases of case study. When the ranks and the weights importance of the PCM selection attributes are changed, the rankings are changed. Weights of importance are changed means the priorities of the decision-maker are changed. Then how an MADM method should remain insensitive? Rao [21] opined that the researchers may suggest that a particular MADM method indicates a particular alternative as the first choice within certain percentage of variation in each attribute's weight. One need not look upon at an MADM method which is resistant to any changes in the attributes' weights of importance.

The five research questions (RQs) answered above will make the readers more informed about the assignment of weights to the attributes and the application of the proposed MADM method for right PCM selection for a given application.

The three case studies have amply demonstrated the potential of the proposed method as a multi-attribute decision-making method. It is important to observe that the ranking remains the same even if the fuzzy scales given in Table 1—rather than the simple linear scales—are used to translate the linguistic expressions used by the decision-maker. This is quite helpful when making decisions in real-world situations.

5. Conclusions

Thermal energy storage is an emerging field of study that links the production and consumption of energy. Particularly important in latent heat storage units are phase change materials with high energy storage density and isothermal working characteristics. Selecting the right PCM is crucial to the effective and efficient heat storage of the thermal energy storage system. Selecting the right PCM to satisfy certain requirements typically necessitates finding a compromise between opposing attributes. A large number of researchers select PCMs according to cost, availability, and experience. However, PCMs in the present work are chosen using a variety of attributes. The research work reported in this paper tackled the PCM selection problem by using a simple and effective decision-making method, named as BHARAT-II.

Three case studies of PCM selection are presented to illustrate the potential of the proposed methodology. The first case study addressed the issue of choosing the best PCM selection for a domestic water heating latent heat storage system by considering 15 different PCMs and 8 selection attributes; the second case study addressed the problem of selecting the best PCM for a triple tube heat exchanger unit by considering 12 different PCMs and 5 selection attributes with three sub-cases; the third case study addressed the problem of best PCM selection for latent heat thermal energy storage within the walls of Trombe to

enhance performance considering 11 PCMs and 4 selection attributes.

It may be noted that in the case of widely used AHP method for determining the weights of importance of the selection attributes, the decision-maker must indicate the relative relevance of each attribute compared to all other attributes. However, a novel feature of the proposed method is that, it simply ranks all of the attributes (1 to n) according to their priority as per the understanding of the decision-maker. A relative importance matrix is then created using these ranks to further establish the weights. Even though the idea seems to be simple, it has the advantage of ensuring consistency while prioritizing one attribute over another. The consistency index is always 0 (i.e. fully consistent). In AHP or BWM, this is not feasible, particularly for the decision-making problems containing a large number of attributes. Furthermore, the proposed method clearly explained that the objective weights obtained from the performance data of the PCM selection attributes are *not* really meaningful, and the composite weights which combine the objective and subjective weights remain as an academic exercise and actually not used in the real decision-making scenarios.

The second novel feature of the proposed method is that it can include any number of alternative PCMs and any number of quantitative and qualitative PCM selection attributes simultaneously and aids in calculating the total score values that assess the alternative PCMs for the selection problem under consideration. The third novel feature of the proposed method is that it does not require the use of fuzzy scales to transform qualitative attributes into quantitative attributes. Using the simple linear scales that the method suggests, decision-makers may find it simpler to assign numerical values to the qualitative attributes. This fact is explained in the first case study presented. The proposed method tackles the PCM selection problem holistically, and is easy for decision-makers to put into practice.

The proposed methodology offers a general procedure that may be used to address a range of selection problems that emerge in the disciplines of energy and thermal engineering that involve ambiguity, multiple attributes, and alternatives.

Acknowledgements

The research was supported by the Science and Engineering Research Board (SERB) of the Department of Science and Technology (DST), Government of India, under the Mathematical Research Impact Centric Scheme (MATRICS) with the project number MTR/2023/000071.

References

[1] Rastogi, M., Chauhan, A., Vaish, R., & Kishan, A. (2015). Selection and performance assessment of phase change materials for heating, ventilation and air-conditioning applications. *Energy Conversion and Management*, 89**,** 260–269. doi: 10.1016/j.enconman.2014.09.077

[2] Loganathan, A., & Mani, I. (2018). A fuzzy based hybrid multi criteria decision making methodology for phase change material selection in electronics cooling system. *Ain Shams Engineering Journal*, 9, 2943–2950. doi: 10.1016/j.asej.2017.11.005

[3] Yang, K., Zhu, N., Chang, C., Wang, D., Yang, S., & Ma, S. (2018). A methodological concept for phase change material selection based on multi-criteria decision making (MCDM): a case study. *Energy*, 165, 1085−1096. doi: 10.1016/j.energy.2018.10.022

[4] Amer, A.E., Rahmani, K., & Lebedev, V.A. (2020). Using the analytic hierarchy process (AHP) method for selection of phase change materials for solar energy storage applications. *Journal of Physics: Conference Series*, 1614, 12022. doi: 10.1088/1742-6596/1614/1/012022

[5] Oluah, C., Akinlabi, E.T., & Njoku, H.O. (2020). Selection of phase change material for improved performance of Trombe wall systems using the entropy weight and TOPSIS methodology. *Energy and Buildings*, 217, 109967. doi: 10.1016/j.enbuild.2020.109967

[6] Maghsoodi, A.I., Soudian, S., Martínez, L., Herrera-Viedma, E., & Zavadskas, E.K. (2020). A phase change material selection using the interval-valued target-based BWM-CoCoMULTIMOORA approach: A case-study on interior building applications. *Applied Soft Computing*, 95, 106508. doi: 10.1016/j.asoc.2020.106508

[7] Anilkumar, B.C., Maniyeri, R., & Anish, S. (2021). Optimum selection of phase change material for solar box cooker integrated with thermal energy storage unit using multicriteria decision-making technique. *Journal of Energy Storage*, 40, 102807. doi: 10.1016/j.est.2021.102807

[8] Das, D., Sharma, R.K., Saikia, P., & Rakshit, D. (2021). An integrated entropy-based multiattribute decision-making model for phase change material selection and passive thermal management. *Decision Analytics Journal*, 1, 100011. doi: 10.1016/j.dajour.2021.100011

[9] Kumar, A., Kothari, R., Sahu, S.K., & Kundalwal, S.I. (2021). Selection of phase-change material for thermal management of electronic devices using multi-attribute decision making technique. *International Journal of Energy Research*, 45, 2023–2042. doi: 10.1002/er.5896

[10] Mukhamet, T., Kobeyev, S., Nadeem, A., & Memon, S.A. (2021). Ranking PCMs for building façade applications using multi-criteria decision-making tools combined with energy simulations. *Energy*, 215, 119102. doi: 10.1016/j.energy.2020.119102

[11] Nicolalde, J.F., Cabrera, M., Martínez-Gomez, J., Salazar, R.B., & Reyes, E. (2022). Selection of a phase change material for energy storage by multi-criteria decision method regarding the thermal comfort in a vehicle. *Journal of Energy Storage*, 51, 104437. doi: 10.1016/j.est.2022.104437

[12] Pradeep, N., & Reddy, K.S. (2022). Development of an effective algorithm for selection of PCM based filler material for thermocline thermal energy storage system. *Solar Energy*, 236, 666–686. doi: 10.1016/j.solener.2022.02.044

[13] Akgün, H., Yapıcı, E., Özkan, A., Günkaya, Z., & Banar, M. (2023). A combined multi-criteria decision-making approach for the selection of carbon-based nanomaterials in phase change materials. *Journal of Energy Storage*, 60, 106619. doi: 10.1016/j.est.2023.106619

[14] Awan, B., Ma, Z., Lin, W., Pandey, A.K., & Tyagi, V.V. (2023). A characteristic-oriented strategy for ranking and near-optimal selection of phase change materials for thermal energy storage in building applications. *Journal of Energy Storage*, 57, 106301. doi: 10.1016/j.est.2023.106619

[15] Yang, K., Liu, B., Du, N., Liu, J., He, Y., Li, Y., Li, Y., & Zhao, Q. (2023). Effects of thermophysical properties on optimal selection of phase change material for a triple tube heat exchanger unit

at different time scales. *Journal of Energy Storage*, 61, 106822. doi: 10.1016/j.est.2023.106822

[16] Gadhave, P., Prabhune, C., & Pathan, F. (2023). Selection of phase change material for domestic water heating using multi criteria decision approach. *Australian Journal of Mechanical Engineering*, 21, 295–315. doi: 10.1080/14484846.2020.1842297

[17] Saaty, T.L. (2007). On the invalidity of fuzzifying numerical judgments in the analytic hierarchy process. *Mathematical and Computational Modelling*, 46, 962−975. doi: 10.1016/j.mcm.2007.03.022

[18] Oró, E., Barreneche, C., Farid, M.M., & Cabeza, L.F. (2013). Experimental study on the selection of phase change materials for low temperature applications. *Renewable Energy*, 57, 130−136. doi: 10.1016/j.renene.2013.01.043

[19] Yu, N., Chen, C., Mahkamov, K., Makhkamova, I., Li, Q., & Ma, J. (2021). Selection and testing of phase change materials in the physical models of buildings for heating and curing of construction elements made of precast concrete. *Solar Energy*, 226, 309−318. doi: 10.1016/j.solener.2021.08.036

[20] Prieto, C., Cabeza, L.F., Pavon-Moreno, M.C., & Palomo, E. (2024). Thermal energy storage for direct steam generation concentrating solar power plants: Concept and materials selection. *Journal of Energy Storage*, 83, 110618. doi: 10.1016/j.est.2024.110618

[21] Rao, R.V. (2024). BHARAT: A simple and effective multi-criteria decision-making method that does not need fuzzy logic, Part-1: multi-attribute decision-making applications in the industrial environment. *International Journal of Industrial Engineering Computations*, 15, 13−40. doi: 10.5267/j.ijiec.2023.12.003

[22] Rao, R.V. (2024). BHARAT: A simple and effective multi-criteria decision-making method that does not need fuzzy logic, Part-2: role in multi- and many-objective optimization problems. *International Journal of Industrial Engineering Computations*, 15, 1−12. doi :10.5267/j.ijiec.2023.12.004

[23] Rao, R.V. (2013). *Decision Making in the Manufacturing Environment Using Graph Theory and Fuzzy Multiple Attribute Decision-making Methods*. Volume 2**.** Springer-Verlag, London. doi: 10.1007/978-1-4471-4375-8

Co-published by
Institute of Fluid-Flow Machinery
Polish Academy of Sciences
Committee on Thermodynamics and Combustion
Polish Academy of Sciences

http://www.imp.gda.pl/archives-of-thermodynamics/

Heat flow analysis and description of the cooperation of the heat exchange station with heat exchange substations located in apartments

Dawid Taler[a], Tomasz Sobota[a], Jan Taler[b*], Agata Kania[c], Robert Wiśniewski[c]

[a] Department of Thermal Processes, Air Protection and Waste Utilization, Cracow University of Technology, ul. Warszawska 24, Cracow 31-155, Poland
[b] Department of Energy, Cracow University of Technology, al. Jana Pawla I 37, Cracow 31-864, Poland
[c] MPEC S.A. in Cracow, Al. Pokoju 81, 31-564 Cracow, Poland
*Corresponding author email: jan.taler@pk.edu.pl

Received: 16.05.2024; revised: 20.06.2024; accepted: 04.07.2024

Abstract

This paper presents an analysis of the heat flow in a plate heat exchanger located at a building heat exchange station. The plate heat exchanger is the main source of heat for the building system based on microsubstations in the building apartments. The co-operation of the heat exchange station with the substations in the apartments is also described. Such microstations are intended for both domestic hot water preparation and apartment heating. The method of calculating the product of the heat transfer coefficient k and the heat exchange surface area A is presented. In order to verify the correctness of the measured values of the temperatures of hot and cold water at the heat exchange station inlet and outlet, they were compared to the values calculated using the ε-NTU method. Good agreement was found between the results of the calculations and the measurements. Recommendations were made for the temperature of return water to the heating station. The cost of operating the district heating network could be reduced by increasing the surface area of central heating radiators in apartments, so that the temperature of return water to the heating station could be lowered.

Keywords: Monitoring of the heat station; Plate heat exchanger; Heat exchanger efficiency; Building central heating; Residential micro heating station

Vol. 45(2024), No. 3, 81–88; doi: 10.24425/ather.2024.151218

Cite this manuscript as: Taler, D., Sobota, T., Taler, J., Kania, A., & Wiśniewski, R. (2024). Heat flow analysis and description of the co-operation of the heat exchange station with heat exchange substations located in apartments. *Archives of Thermodynamics*, 45(3), 81–88.

1. Introduction

Siegenthaler's comprehensive book [1] presents both individual and central heating systems. Design solutions for building heating systems and issues of heating power control in the entire district heating network as well as in individual buildings are described. Also presented is the principle of the operation of microstations installed in apartments. Such microstations are intended for both domestic hot water (DHW) preparation and apartment heating. With a microstation installed in the apartment, only one heat substation is used instead of the two substations previously required – one to heat the building and the other to supply the apartment with domestic hot water.

A comprehensive analysis of central heating systems, concerning mainly operating and control issues, is presented in [2]. Attention is drawn to the frequent occurrence of excessively high temperatures of return water from apartments and the entire building, which are only 3–5°C lower than the district heating

Nomenclature

A – heat transfer surface area of the exchanger, m^2
$\dot{C}$ – heat capacity rate, W/K
$\bar{c}$ – water mean specific heat, J/(kg K)
k – heat transfer coefficient, W/(m^{2}K)
$\dot{m}$ – water mass flow rate, kg/s
NTU – number of heat transfer units
$\dot{Q}$ – heat flux, W
$\dot{Q}_m$ – mean heat flux, W
T – temperature, °C
$\dot{V}$ – water volume flow rate, m^3/s

Greek symbols

ΔT_m – logarithmic mean temperature difference, °C
ε – heat exchanger efficiency
ρ – density, kg/m^3

Subscripts and Superscripts

max – maximum
min – minimum
np – medium with low parameters (water in the building system)
pnp – water return from the building system to the station exchanger
pwp – water return from the station exchanger to the heat distribution network
znp – outlet of water supplying the building system from the heat exchange station exchanger
zwp – inlet of water from the heat distribution network to the heat exchange station exchanger
wp – medium with high parameters (network water)

Abbreviations and Acronyms

DHW – domestic hot water
SCADA – supervisory control and data acquisition

system water temperature at the heat exchange station supply. It should be added that if a heat exchange station supplies a residential building equipped with microstations in each unit, which is the case analysed in this paper, the temperature of the building return water is only about 2°C lower than that of the water in the district heating system. In such a situation, it is necessary to select optimal values of both the network water temperature and flow rate to ensure a proper supply of heat and hot water to the building, while maintaining low costs of network water generation and low consumption of energy needed for pumping water in the district heating network.

Issues related to the operation and control of district heating networks are the subject of numerous publications in scientific journals. This is partly due to the increasing use of renewable energy sources in central district heating systems and the application of new solutions in the supply of buildings with heat and hot water.

Ensuring a stable room temperature and adequate operating efficiency by means of predictive control for a district heating station is the subject of [3]. In China, the control of a heating station is mostly realized through weather compensation control. This leads to substantial variations in room temperature and to high consumption of energy needed for water pumping in the heating network.

A literature review of the integration of renewable energy sources with low-temperature district heating systems was conducted by Sarbu et al. [4]. A low-temperature district heating system makes it possible to provide large amounts of heat. This is, however, due to the low temperature in decentralized heat pumps (HPs) that are needed to raise the temperature of the medium before it enters buildings.

Heat exchange substations located in individual apartments, also called micro heat exchange stations or logotherms, provide an individual heat supply for heating and hot water preparation. They are used in multi-family housing where the building has one main source generating heat in a boiler room or in a heat exchanger plant. The heating medium from the main source of the building heat supply is transported by the heating system to individual apartments equipped with heat exchange substations (logotherms). Such a thermal energy management system will just as well find application in commercial premises, as it enables individual regulation of the heating medium, making it possible to set individual preferences for thermal comfort. A heating system in a residential or commercial building based on one main heat source and logotherms in individual units makes it possible to produce domestic hot water efficiently and supply the heating medium. The main source of heat for the building can be a gas boiler room, an oil boiler room or a heat exchange station. In the case of a boiler room, heat is produced directly on site, whereas in the case of a heat exchange station, thermal energy is produced at a combined heat and power plant or at a heating plant, and then distributed to the heat exchange station, where it feeds the building internal heating system through a heat exchanger.

The advantage of boiler plants is their operation with modulated power, which makes it possible to adjust the power of the device to the consumers' current heat demand. When logotherms show less demand for heat from the main source, boiler rooms with modulated power lower the operating parameters.

If the heat exchange station is the main heat source, there is a need to take into account the relevant operating parameters of the district heating network. When logotherms co-operate with a heat exchange station, it is necessary to pay attention to the operating parameters of the heat exchange station on the primary side, i.e. on the side of the working medium with high temperature, and on the secondary side, i.e. on the side of the heating system of the building. Thermal energy has to be supplied to the customer in the amount and with parameters strictly defined, and at the same time care has to be taken to ensure appropriate parameters of the district heating network on the primary side so that they should match the performance characteristic of the sources of energy. The parameters of the district heating network are strictly defined by the heat distribution company. The distribution company is obliged to maintain the parameters of the heat distribution network at both the heat consumer's and the heat producer's end.

This paper presents an analysis of the heat flow in a plate heat exchanger located at a heat exchange station. The heat exchanger is the main source of heat for the building system based on substations in the building apartments. The co-operation of

the heat exchange station with the substations in the apartments will also be described.

2. Heat source: the heat exchange station co-operating with the district heating system

Heat exchange stations are sets of devices connecting the heat distribution network to the internal system of a building. They are a part of the heating system affected both by the network and the internal system of the facility.

The station is the place where the heat exchange occurs between the heat distribution network and the consumer. The thermal energy in the heat exchange station is transported through the heating medium. The heat exchange station transforms the high values of temperature and pressure of the heating medium flowing in the network, the so-called high parameter medium, into lower values in the consumers' systems.

The set of devices making up the heat exchange station regulates the heating medium on the side of both high and low parameters.

The main elements of the station are a heat exchanger, a circulation (feed) pump, valves, filters and a heat meter. The composition of the station elements depends on technological aspects, the requirements of the consumer's system and of the distribution network.

Heat exchange stations can be divided based on many criteria. One of them is the number of buildings connected to them. Individual heat exchange stations supply just one facility with thermal energy, whereas group stations supply a few. Heat exchange stations can also be divided depending on the method of the heat distribution network connection to the consumer's system. In this division, direct and indirect heat exchange stations are distinguished. In direct stations, the same medium flows in the network and in the consumer's system. In indirect systems, there are two separate circuits, and the heat exchange is realized through a heat exchanger. Apart from these classification methods, there are also other divisions of heat exchange stations.

Despite their different functions and kinds, the main task of heat exchange stations is to supply thermal energy from the heat distribution network to the consumer.

The parameters of the heat distribution network result from the operating parameters of the receivers. The main parameters are temperature and pressure. Quantitative, qualitative and quantitative-qualitative regulation of the network is used. Qualitative regulation consists in changing the supply and the return temperature. Quantitative regulation consists of changing the heating medium mass flow rate in the pipeline. The supply temperature in the summer period is constant and is about 70°C, whereas in the heating season it is 135°C. It should be remembered that in the heating season the temperature of the heating medium in the network varies depending on the temperature of the ambient air. The heat distribution network must have an appropriate amount of thermal energy to satisfy the current demand of the consumers. The consumers' demand depends mainly on atmospheric conditions, i.e. the ambient temperature. The water circulates in the heat distribution network thanks to the work of circulation pumps. The pumps are located both in the source of heat generation and in special facilities referred to as intermediate pumping stations.

3. Structure and operating principle of a heat exchange microstation

Heat exchange microstations (logotherms), shown in Fig. 1, are made in various configurations. They can be one- and two-function devices. Some deliver heat only for room heating, others can heat domestic water only. Two-function logotherms are able to provide heat for both central heating and domestic hot water preparation. The advantages of microstations are their small size and compact structure [5–10].

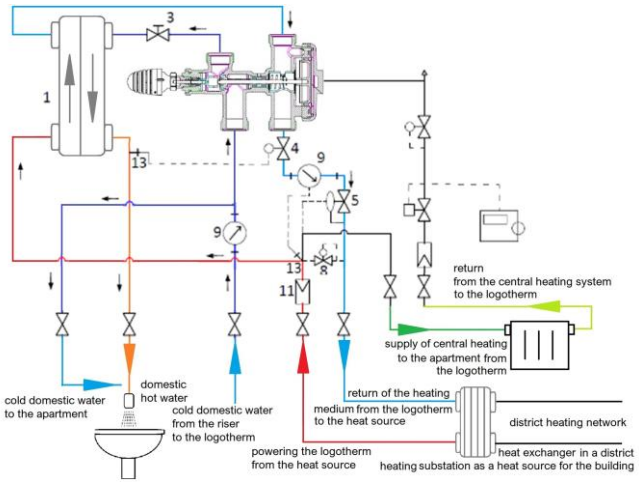

Fig. 1. Diagram of a logotherm fed from a heat exchanger in a district heating substation [11].

The logotherm basic elements are [11] a mounting plate/housing, a console with connections including shut-off valves, piping, a heat exchanger (for domestic hot water systems), a filter, a vent, various types of control valves: a mixing valve, a return limiter, a differential pressure regulator, a thermostatic valve.

The simplest models of microstations do not even need an electronic regulator. The principle of their operation is based, among other things, on specially designed hydraulic regulators, and thermostatic and differential pressure valves.

In their models of microstations, the Herz company used a hydrodynamic regulator, which is the most important element of the heat exchange substation located in an apartment. It is responsible for ensuring the correct temperature of domestic hot water [12]. The basis of the hydrodynamic regulator operation is the pressure difference upstream and downstream of the regulator, caused by the flow of domestic hot water collected by the consumer. Figure 2 shows a simplified diagram of domestic hot water generation in heat exchange substations located in individual apartments based on a self-actuated dynamic regulation unit.

A self-actuated dynamic regulation unit is composed of a primary and a secondary part. One element of the structure of the self-actuated dynamic regulation unit is a movable drive element connected centrally to a stem. The stem moving in the regulator opens and closes the supply of the heating medium on the pri-

mary side of the heat exchanger. The cold water flowing through the primary part of the regulation unit has to be heated in the plate heat exchanger. The cold water is heated by the heating medium flowing through the regulator's secondary part. Flowing through the regulator's primary part, the cold water causes a pressure drop due to hydraulic resistance. The resulting difference in pressure causes the opening of the secondary part, which allows the heating medium to flow. A rise in the flow of cold water involves an increase in the flow of the heating medium. The self-actuated dynamic regulation unit is equipped with a DHW priority valve.

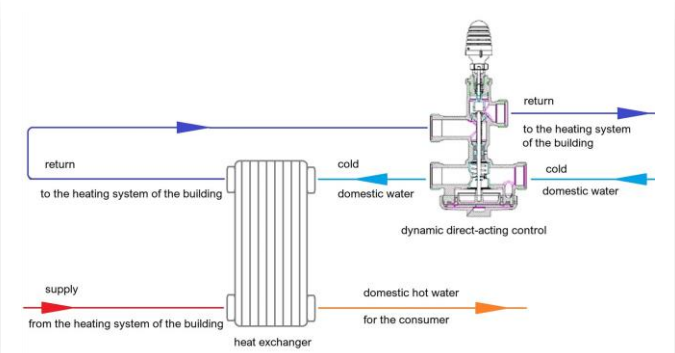

Fig. 2. Simplified diagram of hot water generation in exchanger stations [12].

In their models of microstations, the Flamco company (formerly Meibes) [11] uses three-way PM-Regler valves (Fig. 3). The PM-Regler valve is a hydraulic switching and control valve that controls the process of the switching of the heating medium flow. When domestic hot water is drawn, it directs the heating medium to the heat exchanger to heat cold water. When the domestic hot water intake ends, the PM-Regler valve directs the heating medium to the central heating circuit. Like the Herz self-actuated dynamic regulation unit, the PM-Regler valve has the domestic hot water priority.

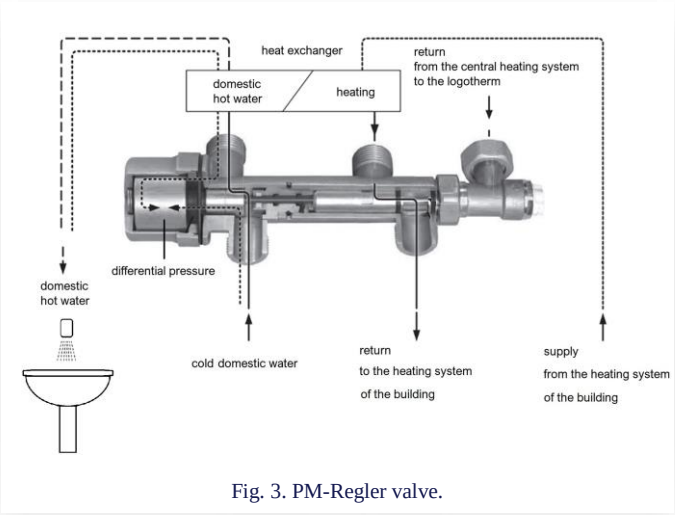

Fig. 3. PM-Regler valve.

Additional equipment of logotherms includes an electric actuator, a water meter, a heat meter, an electronic regulator, a room temperature-setting device, circuit pumps, circulation pumps, etc.

Domestic hot water preparation by the logotherm consists of the rapid heating of cold water in the exchanger, being a part of the logotherm assembly. The heat exchange microstation starts operating only if there is a demand for hot water or central heating. In the standby mode, the heating medium flows through a bypass, referred to as the thermal bridge, the temperature of which is kept at the working temperature level using a return temperature limiter. Owing to that, the heating medium is always available if a need arises to switch on the logotherm. This enables the heating medium minimal circulation which is to ensure an appropriate temperature of the medium at the logotherm inlet.

4. Internal heating system based on heat exchange microstations located in individual apartments

The internal heating systems commonly utilized by thermal energy consumers are pump systems where a circulation pump is used to force the heating medium flow. The circulation pump overcomes hydraulic resistances in the system piping.

Most often, a two-pipe arrangement of the system is used. In the building's internal system feeding logotherms, there are three pipes (Fig. 4). One of them supplies the heat exchange substation with domestic cold water, and another supplies the substation with heat feeding the heating medium. The third pipe carries heating water away from the logotherm.

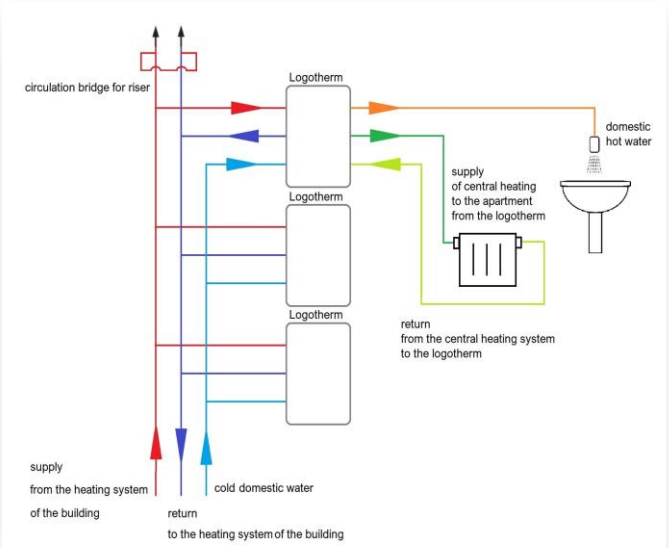

Fig. 4. Diagram of the clip installed at the end of the heating riser.

The pipes in the internal heating system are run both vertically and horizontally. In a system co-operating with logotherms, a circulation bridge, called a clip, should be installed at the end of each riser (Fig. 5). The circulation bridge makes it possible to regulate the temperature of the heating water feeding the microstation and of the water returning from the system to the heat source.

The task of the circulation bridge is to maintain the minimal temperature in the pipe feeding the logotherm. On the market, there are clips with adjustable temperature settings in the range

from 45°C to 65°C and clips with a single pre-setting. In the latter case, if a need arises to regulate the operation of the internal system distributing heat in the building, the clip has to be replaced with a clip with adjustable settings or a clip with a different temperature pre-setting that activates the valve located on the circulation bridge. The operating principle of the valve mounted on risers is to observe the feed water temperature: if the temperature in the riser drops to values below the setting, the valve opens, forcing the heating medium flow from the feed riser to the return riser. In the same way the feed riser is filled with hot water with a temperature higher than the value of the circulation bridge setting.

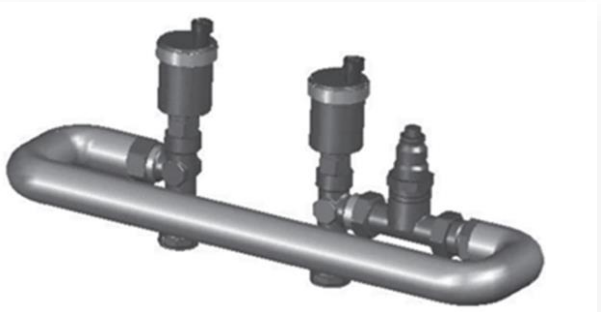

Fig. 5. Circulation bridge installed on the riser [11].

The clips mounted within logotherms operate based on the same principle as the circulation bridges mounted on the internal system risers. This enables the flow of the heating medium close to the logotherm, thus shortening the time of waiting for the heat needed to supply the substation. If the heating medium cools down in the branch feeding the substation, the valve opens, forcing the heating medium flow to the branch returning to the source of supply.

Apart from circulation bridges, the internal network distributing heat in the building can also be regulated using temperature limiters (Fig. 6) intended for the control of the temperature of the return from the apartment's individual central heating system to the heating medium return. This valve regulates the flow by limiting the water flow through the apartment's central heating system, which results in increased cooling of the heating medium and a reduction in the return temperature. Temperature can be regulated in the range from 25°C to 60°C.

Fig. 6. Heating water return temperature limiter of residential central heating system.

The minimum and the maximum temperature of the heating medium in the primary circuit should total 60°C and 80°C, respectively.

5. Description of the heat exchange station and the logotherm system under analysis

The analysis of the operation of the heat exchange station with a system feeding logotherms was performed using the heat exchange system feeding the internal system based on logotherms. Figure 7 presents a schematic diagram of the heat exchange station from which the data for the analysis were obtained.

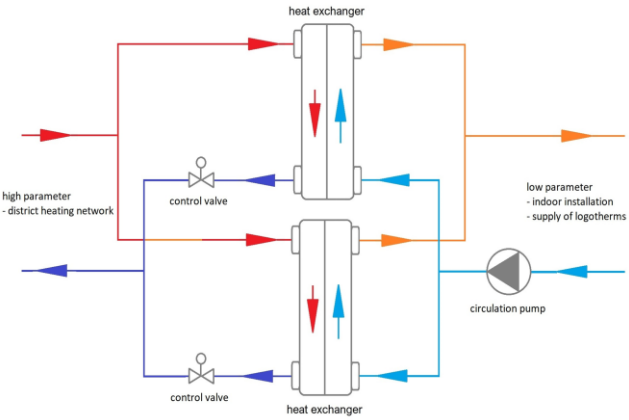

Fig. 7. Schematic diagram of the thermal node from which the data was obtained.

The station is made of two heat exchangers supplied simultaneously and connected in parallel. In both exchangers, the mediums flow in a counter-current configuration. The heat exchange station, both on the exchanger's primary and secondary side, was equipped with heat meters with the ability to transmit data through a communication card and a controller to a supervisory control and data acquisition (SCADA) system, and the data were then recorded. The data transmitted from the station are represented in the on-line mode on the system visualization, in the SCADA system, on purpose-made synoptic schemes showing the heat exchange station operation.

6. Heat flow analysis

The heat flow in a plate heat exchanger was analyzed using the ε-NTU method and the measuring data for which the values of the heat flow rate transferred from the network water to the water heating the building are almost equal.

The exchanger analysis by means of the ε-NTU method makes use of thermal equations transformed into a dimensionless form. The method will be used to assess the impact of changes in the exchanger operating parameters on outlet temperatures of the mediums flowing through the exchanger on the side of the high and the low parameters. The following formula was used to calculate the efficiency of the countercurrent plate heat exchanger:

$$\varepsilon = \frac{1-\exp\left[-NTU\left(1-\frac{\dot{C}_{min}}{\dot{C}_{max}}\right)\right]}{1-\frac{\dot{C}_{min}}{\dot{C}_{max}}\exp\left[-NTU\left(1-\frac{\dot{C}_{min}}{\dot{C}_{max}}\right)\right]}, \quad (1)$$

where the number of heat transfer units (NTU) is expressed as:

$$NTU = \frac{kA}{\dot{C}_{min}}. \quad (2)$$

In order to calculate the number of the heat transfer units, it is necessary to determine the product of the heat transfer coefficient k and the exchanger heat exchange surface area A, using the relation defining the mean heat flux transferred in the exchanger:

$$\dot{Q}_m = kA\Delta T_m. \quad (3)$$

After relevant transformations, product kA can be established using the following equation:

$$kA = \frac{\dot{Q}_m}{\Delta T_m}. \quad (4)$$

In order to determine product kA, it is necessary to establish the mean transferred heat flux $\dot{Q}_m$ and the logarithmic mean temperature difference ΔT_m. Adopting the denotation of the inlet and outlet temperatures of the cold and hot medium presented in Fig. 8, the logarithmic mean temperature difference is calculated using the following formula:

$$\Delta T_m = \frac{(T_{zwp}-T_{znp})-(T_{pwp}-T_{pnp})}{ln\left(\frac{T_{zwp}-T_{znp}}{T_{pwp}-T_{pnp}}\right)}. \quad (5)$$

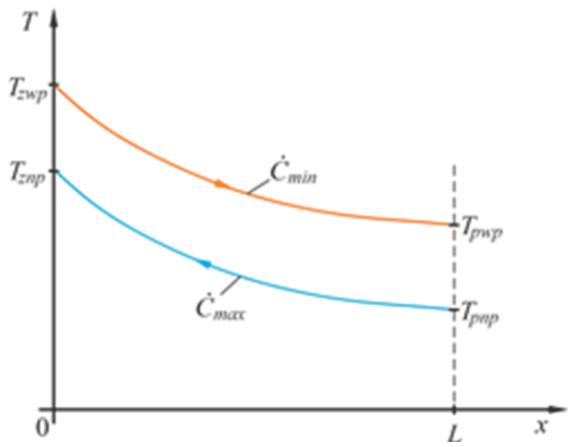

Fig. 8. Changes in the temperature of hot and cold water in a counter-current thermal station.

Heat flow rate $\dot{Q}_m$ in formula (4) was calculated as the arithmetic mean of heat flux $\dot{Q}_{wp}$ given off by hot water and heat flux $\dot{Q}_{np}$ absorbed by cold water. The following formula was used to calculate the heat flow rate transferred from the water with a higher temperature (water from the heat distribution network):

$$\dot{Q}_{wp} = \dot{m}_{wp}\bar{c}_{wp}\left(T_{zwp} - T_{pwp}\right), \quad (6)$$

where the water mean specific heat $\bar{c}_{wp}$ and the water mass flow rate $\dot{m}_{wp}$ are defined by the following relations:

$$\bar{c}_{wp} = \frac{c_{wp}(T_{zwp})+c_{wp}(T_{pwp})}{2}, \quad (7)$$

$$\dot{m}_{wp} = \dot{V}_{wp} \cdot \rho\left(T_{pwp}\right). \quad (8)$$

The heat flow rate absorbed by the building internal system is given by equation given below:

$$\dot{Q}_{np} = \dot{m}_{np}\bar{c}_{np}\left(T_{znp} - T_{pnp}\right), \quad (9)$$

where $\bar{c}_{np}$ and $\dot{m}_{np}$ are calculated as:

$$\bar{c}_{np} = \frac{c_{np}(T_{znp})+c_{np}(T_{pnp})}{2}, \quad (10)$$

$$\dot{m}_{np} = \dot{V}_{np} \cdot \rho\left(T_{pnp}\right). \quad (11)$$

The mean heat flow rate is determined as the arithmetic mean of the given off heat flow rate $\dot{Q}_{wp}$ and the absorbed heat flow rate $\dot{Q}_{np}$:

$$\dot{Q}_m = \frac{\dot{Q}_{wp}+\dot{Q}_{np}}{2}. \quad (12)$$

Knowing the average heat flow rate value from Eq. (4), product kA is calculated, and then the number of heat transfer units (NTU) is established. In order to calculate the exchanger efficiency, it is necessary to know the maximum and the minimum heat capacity rates $\dot{C}_{max}$ and $\dot{C}_{min}$, defined as follows:

$$\dot{C}_{max} = \dot{m}_{np}\bar{c}_{np}, \quad (13)$$

$$\dot{C}_{min} = \dot{m}_{wp}\bar{c}_{wp}. \quad (14)$$

Calculating the heat exchanger efficiency from Eq. (1), it is possible to determine the cold water temperature T_{znp} and the hot water temperature T_{pwp}, taking account of the definition of the exchanger thermal efficiency:

$$\varepsilon = \frac{\dot{C}_{max}(T_{znp}-T_{pnp})}{\dot{C}_{min}(T_{zwp}-T_{pnp})}. \quad (15)$$

Transforming Eq. (15), the following is obtained:

$$T_{znp} = T_{pnp} + \varepsilon\frac{\dot{C}_{min}}{\dot{C}_{max}}\left(T_{zwp} - T_{pnp}\right). \quad (16)$$

After Eq. (16) is used to calculate the temperature of the water feeding the internal system T_{znp}, the exchanger heat balance equation:

$$\dot{C}_{max}\left(T_{znp} - T_{pnp}\right) = \dot{C}_{min}\left(T_{zwp} - T_{pwp}\right), \quad (17)$$

can be used to determine the temperature of the network water leaving the heat exchanger T_{pwp}:

$$T_{pwp} = T_{zwp} - \frac{\dot{C}_{max}}{\dot{C}_{min}}\left(T_{znp} - T_{pnp}\right). \quad (18)$$

The following measuring data of the heat exchange station feeding the logotherm were adopted for the thermal calculations:

- T_{zwp} = 71.1°C – temperature of the heat distribution network water feeding the exchanger of the heat exchange station,
- T_{pwp} = 43.3°C – temperature of the network water leaving the exchanger of the heat exchange station,
- $\dot{V}_{wp}$ = 1.835 m^3/h – network water volume flow rate,

- T_{pwp} = 61.4°C – temperature of the medium heated in the exchanger of the heat exchange station,
- T_{pwp} = 39.8°C – temperature of the medium returning to the exchanger of the heat exchange station,
- $\dot{V}_{np}$ = 2.403 m^3/h – volume flow rate in the building system.

Considering that:

$$\bar{c}_{wp} = c_{wp}\left(\frac{T_{zwp}+T_{pwp}}{2}\right) = c_{wp}(57.2℃) = 4181.82\ \frac{\mathrm{J}}{\mathrm{kg{\cdot}K}},$$

$$\dot{m}_{wp} = \dot{V}_{wp}\cdot\rho\left(T_{pwp}\right) = 1.835\,\frac{\mathrm{m^3}}{\mathrm{h}}\cdot\frac{1}{3600\ \mathrm{s}}\cdot 990.90\ \frac{\mathrm{kg}}{\mathrm{m^3}} = 0.505\ \frac{\mathrm{kg}}{\mathrm{s}},$$

the heat flow given off by hot water $\dot{Q}_{wp}$ totals:

$$\dot{Q}_{wp} = \dot{m}_{wp}\bar{c}_{wp}\left(T_{zwp}-T_{pwp}\right) = 58.81\ \mathrm{kW}.$$

The heat flow rate absorbed by cold water $\dot{Q}_{np}$ was determined in the similar manner:

$$\bar{c}_{np} = c_{np}\left(\frac{T_{znp}+T_{pnp}}{2}\right) = c_{np}(50.6℃) = 4179.88\ \frac{\mathrm{J}}{\mathrm{kg{\cdot}K}},$$

$$\dot{m}_{np} = \dot{V}_{np}\cdot\rho\left(T_{pnp}\right) = 2.403\,\frac{\mathrm{m^3}}{\mathrm{h}}\cdot\frac{1}{3600\ \mathrm{s}}\cdot 992.26\ \frac{\mathrm{kg}}{\mathrm{m^3}} = 0.662\ \frac{\mathrm{kg}}{\mathrm{s}},$$

$$\dot{Q}_{np} = \dot{m}_{np}\bar{c}_{np}\left(T_{znp}-T_{pnp}\right) = 59.66\ \mathrm{kW}.$$

The mean heat flow rate transferred in the exchanger is:

$$\dot{Q}_m = \frac{\dot{Q}_{wp}+\dot{Q}_{np}}{2} = \frac{58810\ \mathrm{W}+59660\ \mathrm{W}}{2} = 59235.0\ \mathrm{W}.$$

After the logarithmic mean temperature difference ΔT_m is established:

$$\Delta T_m = \frac{(T_{zwp}-T_{znp})-(T_{pwp}-T_{pnp})}{ln\left(\frac{T_{zwp}-T_{znp}}{T_{pwp}-T_{pnp}}\right)} = \frac{(71.1℃-61.35℃)-(43.25℃-39.8℃)}{ln\left(\frac{71.1℃-61.35℃}{43.25℃-39.8℃}\right)} = 6.1℃,$$

product *kA* is calculated:

$$kA = \frac{\dot{Q}_m}{\Delta T_m} = \frac{59235.0\ \mathrm{W}}{6.1\ \mathrm{K}} = 9710.7\ \frac{\mathrm{W}}{\mathrm{K}}.$$

Considering that:

$$\dot{C}_{max} = \dot{m}_{np}\bar{c}_{pn} = \dot{m}_{np}\bar{c}_{pn} = 0.662\ \frac{\mathrm{kg}}{\mathrm{s}}\cdot 4179.88\ \frac{\mathrm{J}}{\mathrm{kg{\cdot}K}} = 2767.08\ \frac{\mathrm{W}}{\mathrm{K}},$$

$$\dot{C}_{min} = \dot{m}_{wp}\bar{c}_{pw} = \dot{m}_{wp}\bar{c}_{pw} = 0.505\ \frac{\mathrm{kg}}{\mathrm{s}}\cdot 4181.83\ \frac{\mathrm{J}}{\mathrm{kg{\cdot}K}} = 2111.82\ \frac{\mathrm{W}}{\mathrm{K}},$$

$$\frac{\dot{C}_{min}}{\dot{C}_{max}} = \frac{2111.82\ \frac{\mathrm{W}}{\mathrm{K}}}{2767.08\ \frac{\mathrm{W}}{\mathrm{K}}} = 0.763.$$

The value of the number of the heat transfer units NTU is determined:

$$NTU = \frac{kA}{\dot{C}_{min}} = \frac{9768.06\ \frac{\mathrm{W}}{\mathrm{K}}}{2111.61\ \frac{\mathrm{W}}{\mathrm{K}}} = 4.63.$$

The efficiency of the heat exchange station totals:

$$\varepsilon = \frac{1-\exp\left[-NTU\left(1-\frac{\dot{C}_{min}}{\dot{C}_{max}}\right)\right]}{1-\frac{\dot{C}_{min}}{\dot{C}_{max}}\exp\left[-NTU\left(1-\frac{\dot{C}_{min}}{\dot{C}_{max}}\right)\right]} = \frac{1-\exp[-4.63(1-0.763)]}{1-0.763\exp[-4.63(1-0.763)]} = \frac{0.666}{0.745} = 0.894.$$

Knowing the exchanger efficiency, temperatures T_{znp} and T_{pwp} are found:

$$T_{znp} = T_{pnp} + \varepsilon\frac{\dot{C}_{min}}{\dot{C}_{max}}\left(T_{zwp}-T_{pnp}\right) = 39.8℃ + 0.894\cdot 0.763\cdot(71.1℃-39.8℃) = 61.1℃,$$

$$T_{pwp} = T_{zwp} - \frac{\dot{C}_{max}}{\dot{C}_{min}}\left(T_{znp}-T_{pnp}\right) = 71.1℃ - 1.311(61.4℃-39.8℃) = 42.8℃.$$

The calculated temperature of the medium feeding the logotherm of 61.1°C is very close to the value of measured temperature T_{znp} = 61.4°C. The calculated temperature of the network water in the heat exchange station is 42.8°C, whereas the value of the measured temperature T_{pwp} totals 43.25°C. The difference between the measured and the calculated temperature of the network water leaving the heat exchange station is $\Delta T_{pwp} = (43.3℃-42.8℃) = 0.5℃$. This small temperature difference is an effect of the inaccuracy of the measurement of the volume flow rates of the two mediums and their inlet and outlet temperatures.

7. Conclusions

The paper presents an analysis of the heat flow in a heat exchange station being the main heat source for the heating system of a multi-family building using individual microstations (logotherms) located in each residential unit to supply heat and produce domestic hot water for individual apartments. The method of calculating the product of the heat transfer coefficient k and the heat exchange surface area A is presented. In order to verify the correctness of the measured values of the temperatures of hot and cold water at the heat exchange station inlet and outlet, they were compared to the values calculated using the ε-NTU method. Good agreement was found between the results of the calculations and the measurements.

The heating medium temperature in the district heating system in the summer period is a constant value totalling 70°C. The heating medium temperature can be a bit lower in the case of buildings located far away from the heat source. The minimum temperature of the water feeding the logotherm from this source totals about 60°C, which means that the temperature of the heating medium flowing in the district heating network is only a little higher than the required temperature of the water feeding the heating microstations. The value of the minimum temperature of the medium feeding the logotherms depends on the required maximum temperature of domestic hot water of 55°C.

In the summer period, the demand for heat of systems based on logotherms is low due to the low power needed to heat water for the purposes of domestic hot water preparation. Beyond the heating season, the drop in the system water temperature is slight. The temperature of the medium circulating in the consumer's system to feed the logotherms is maintained at the required level by regulating the mass flow rate of the water flowing through the heat exchange station.

In order for the heat exchange station co-operating with the internal system feeding the logotherms in individual apartments to maintain appropriate operating parameters, both on the side of the high-temperature medium and the low-temperature medium, an adequate well-adjusted network distributing the heating medium to the microstations (logotherms) should be ensured. Otherwise, too high temperatures of the heating medium returning to the district heating system may occur. In apartments heated using micro heat exchange stations (logotherms), it is also possible to install central heating radiators with a larger heat exchange surface area. This will make it possible to lower the water temperature at the return from the central heating system to the heat exchange station. Owing to that, the mass flow rate of hot water in the municipal network can be reduced, which will translate into a lower temperature of the water from the heat exchange station and a reduction in the power needed to pump hot water in the network.

References

[1] Siegenthaler, J. (2022). *Modern Hydronic Heating: For Residential and Light Commercial Buildings* (4th ed.). Cengage Learning, Boston. ISBN 9781337904919.

[2] Wiltshire, R. (2015*). Advanced District Heating and Cooling (DHC) Systems*, Woodhead Publishing, Cambridge. ISBN 9781782423744.

[3] Li, Z., Liu, J., Jia, L., & Wang, Y. (2023). Improving room temperature stability and operation efficiency using a model predictive control method for a district heating station. *Energy and Buildings*, 287, 112990. doi: 10.1016/j.enbuild.2023.112990

[4] Sarbu, I.; Mirza, M., & Muntean, D. (2022). Integration of Renewable Energy Sources into Low-Temperature District Heating Systems: A Review. *Energies*, 15(18), 6523. doi: 10.3390/en15186523

[5] Zaborowska, E. (2023). *Design principles for hydronic district heating substations*. Wydawnictwo Politechniki Gdańskiej, Gdańsk. ISBN 978-83-7348-575-4.

[6] Górski, J., Baran, J., Gniewek–Grzybczyk, B., Maludziński, B., Wojciechowski, J., Wojtas, K., Grela, J., & Krupa, J. (2008). *Thermal power generation: A handbook*. TARBONUS, Kraków – Tarnobrzeg. ISBN: 978-83-7394-219-6 (in Polish).

[7] Koczyk, H. (2009). *Practical heating. Design, installation, energy certification, operation* (2nd ed.). SYSTHERM D. Gazińska s.j., Poznań. ISBN 978-83-61265-12-2 (in Polish).

[8] Kołodziejczyk, L. (1984) *Thermal management in heating*. Wydawnictwo Arkady, Warszawa. ISBN: 83-213-3172-6.

[9] Ojczyk, G. (2011). Hot water 'at a glance'. *Instalator*, 2(1) (in Polish).

[10] Ojczyk, G. (2011). Residential heat exchange stations. Dynamic heating, *Instalator*, 8(8) (in Polish).

[11] *LogoThermic G2 – Installation and operating instructions*. https://flamco.aalberts-hfc.com/pl/docfinder/istrukcje/meibes/t+m [accessed 19 Apr. 2024].

[12] *Herz DeLuxe residential station Krakow*. https://katalog.herz.com.pl/pl/stacje-mieszkaniowe/78-stacja-mieszkaniowa.html (in Polish) [accessed 19 Apr. 2024].

Co-published by
Institute of Fluid-Flow Machinery
Polish Academy of Sciences
Committee on Thermodynamics and Combustion
Polish Academy of Sciences

http://www.imp.gda.pl/archives-of-thermodynamics/

Effects of Joule heating due to magnetohydrodynamic slip flow in an inclined channel

Jagadeeshwar Pashikanti[a*], Santhosh Thota[a], Susmitha Priyadharshini[a]

[a]Indian Institute of Information Technology Tiruchirappalli, Trichy - Madurai Highway, Sethurapatti, Tamil Nadu 620012, India
*Corresponding author email: jagadeeshwarp@iiitt.ac.in

Received: 25.07.2023; revised: 12.01.2024; accepted: 05.05.2024

Abstract

Graphene oxide nanoparticles with higher thermal conductivity aid in enhancing the flow and heat transport in magnetohydrodynamic devices such as magnetohydrodynamic pumps. Modelling such devices with promising applications inherently necessitates entropy studies to ensure efficient models. This investigation theoretically studies the entropy generation in magnetohydrodynamic flow of graphene oxide in an inclined channel. Buongiorno nanofluid model is used including the impacts of nanoparticle attributes, namely thermophoretic and Brownian diffusion along with viscous dissipation effects. The spectral quasi-linearization method with Chebyshev's polynomials is adapted to solve the differential equations under slip conditions. On studying the effects of implanted parameters, it is concluded that the conductive heat transfer enhancement by the Hartmann number is remarked. The Bejan number is found to be greater than 0.9 and hence, heat transfer primarily causes the entropy generation. A good agreement is found between the results for special cases and the results from the literature. Furthermore, investigations conclude that entropy is contributed primarily by heat transfer.

Keywords: Graphene nanofluids; Entropy generation; Buongiorno model

Vol. 45(2024), No. 3, 89–98; doi: 10.24425/ather.2024.151219

Cite this manuscript as: Pashikanti, J., Thota, S., & Priyadharshini, S. (2024). Effects of Joule heating due to magnetohydrodynamic slip flow in an inclined channel. *Archives of Thermodynamics*, 45(3), 89–98.

1. Introduction

Nanofluids are preferred to other conventional viscous and microfluids for their effective heat transfer properties. Additionally, they keep the flow channels from obstruction, deposition and erosion. Literature suggests that thermophoresis and Brownian motion affect the sole significant slip mechanisms in nanofluid flows [1]. The performance of nanofluids varies according to the volume fraction, choice of geometry, base fluids and hybridized nanoparticles, and the needs in demand [2–4]. However, the results from computational studies conclude that graphene oxide (GO) aids in maximizing heat transfer rates because of its excellent thermal conductivity [5–8]. Some of the applications of graphene-based nanofluids include their use in lithium-ion batteries, biosensors, supercapacitors, medical suspensions, etc.

Some classical numerical studies on the fluid flow in inclined channels include the study of fully developed laminar flow in the channel of two parallel plates with an inclination angle. The opposing flow was studied under uniform flux conditions with actual flow characteristics [9]. Choi and Eastman [10] studied the impacts of natural convective flow with a heat source between two parallel plates. The results show a strong dependence of the Nusselt number on the inclination angle for values

Nomenclature

B_0 – magnetic field strength
Be – Bejan number, Be = N_{Sh}/N_S
C – concentration, -
C_p – specific heat capacity, J/(kg·K)
C_f – skin friction
D_B – Brownian diffusivity
Ec – Eckert number, Ec = $U_0^2/(\kappa_{bf}C_{pbf}(T_2-T_1))$
g – gravity, m/s^2
Gr – Grashof number
h – domain height, m
Ha – Hartmann number
J – Joule heating parameter
M_m – parameter of combined mass and heat transfer, $M_m = RD_BC_0/\kappa_{bf}$
N_b – Brownian motion parameter
N_r – Buoyancy ratio
N_s – nondimensional entropy generation number
Nu – Nusselt number
p – pressure, Pa
Pr – Prandtl number, Pr = $\mu C_{pbf}/\kappa_{bf}$
Re – Reynolds number
R_{SC} – suction/injection parameter
S – slip parameter
S_G – entropy generation rate
Sh – Sherwood number
S_u – velocity slip length/factor, m
T – temperature, K
u – velocity, m/s
v_0 – suction/injection velocity
x, y – Cartesian coordinates, m

Greek symbols

α – inclination angle, rad
β – thermal expansion coefficient, 1/K
κ – thermal conductivity, W/(m K)
μ – dynamic viscosity, Pa s
ρ – density, kg/m^3
σ – electrical conductivity
τ – heat capacity ratio
Ω_T – temperature parameter, $\Omega_T = T_2/T_1$

Subscripts and Superscripts

a – upper plate
b – lower plate
bf – base fluid
nf – nanofluid
sp – solid particle
S_G – irreversibilities caused by combined heat and mass transfer
S_h – irreversibilities caused by heat transfer and fluid friction

Abbreviations and Acronyms

GO – graphene oxide
MHD – magnetohydrodynamics
ODE – ordinary differential equation
PHP – pulsating heat pipe
SLM – successive linearization method

higher than π/4. Talabi and Nwabuko [11] numerically analysed the convective heat transfer flow in an inclined channel comprising a parabolic and a horizontal wall under isothermal and constant heat flux conditions. Solutions using the staggered differencing (SD) technique suggest that Grashof and Prandtl numbers improve the Nusselt number for both isothermal and heat flux cases.

Literature suggests that GO and hybrid graphene nanoparticles suspended in ethylene glycol (EG) and water (H_2O) are the common graphene-based nanofluids in theoretical and experimental studies [12]. Analytical investigations on GO nanofluid flow in moving plates suggest a significant improvement in heat transfer with improved nanoparticle volume fractions [13]. Gul et al. [14] conducted a comparative analysis of GO flow dispersed in water and ethylene glycol (W-EG) in an upright channel with interpretations that the ethylene glycol (EG) based nanofluid has a higher thermal efficiency than water. Shahzad et al. [15] analysed the experimental and theoretical impacts of kerosene-based GO nanofluid flow on a parabolic trough surface accumulator (PTSC). A 15% enhancement in heat transfer rate of the nanofluid in comparison to kerosene is documented. Nazari et al. [16] experimented to study the impacts of varying concentrations of W-GO nanofluids on pulsating heat pipe (PHP). From the results, it is interpreted that the nanoparticles positively impacted the heat transfer of water in lower concentrations. The impacts were negative for a high concentration of 1.5 grams per litre. Dehghan et al. [17] analysed the effects of forced convective flow of GO nanofluids in an inclined backwards-facing step (BFS). Simulations of the microchannel of double BFS show a 12.3% enhancement in heat transfer coefficient compared to that of water. Pashikanti et al. [18] conducted an entropy generation analysis on the flow of graphene oxide nanofluid in an inclined channel in the presence of a magnetic field. They concluded that the flow velocity enhancement by the Hartmann number is remarked.

Graphene-based nanofluids yield amplified industrial significance when hybridised with other metal or semi-conductor nanoparticles and polymers. For instance, they are used in adsorbent materials, lubricant additives, humidity sensors, photocatalysis and heat transfer applications. Javanmard et al. [19] investigated the magnetohydrodynamic (MHD) flow of W-GO nanofluids in a horizontal channel due to forced convection. Numerical results are interpreted to enhance the convection at the walls with nanoparticle volume fraction.

Hafeez et al. [20] numerically analysed the Jeffery-Hamel flow of copper and GO nanoparticles in convergent and divergent channels. The magnetic parameter is seen to lower the skin friction drag in the magnetohydrodynamic flow. Raza et al. [21] investigated the impacts of the convective flow of Casson fluid dispersed with GO and molybdenum disulphide (MoS_2) nanoparticles. A fractional derivative model is developed, and the results show that the Atangana-Baleanu (AB) model is stable compared to the Caputo-Fabrizio (CF) model, and the velocity profiles decrease with the fractional parameters. Computational fluid flow investigations on hybrid graphene nanofluids, such as the study of the impacts of shape factors due to the flow of kerosene-based GO and MoS_2 nanofluids in an inclined porous channel, reveal the enhancement of heat transfer with lamina-

shaped nanoparticles [22].

Combining the magnetohydrodynamic studies with nanofluidics is essential for their applications in industries and biomedicine, such as molten pumps contributing to coolants in nuclear reactors, drug delivery, etc. Similarly, studying the impacts of viscous dissipation on fluid flow helps with a better understanding of the energy loss due to the interactions of liquid particles, thereby aiding the utilisation of the fluids as better lubricants. Akram et al. [23] studied the flow of Oldroyd 4-constant nanofluids in a non-uniform inclined channel with magnetic field and cross-diffusion effects. From the results obtained, chemical reaction and Brownian motion are interpreted to reduce mass transfer. Nazeer [24] analysed Eyring-Powell fluid flow suspended with gold and silver particles, including magnetic field effects. The results document a lesser skin friction drag for gold particles than for silver particles. Yasin et al. [25] analysed the impacts of an inclined magnetic field on the flow of blood-based nanofluid hybridised with silver and copper nanoparticles in a symmetric channel. Studying the effects of Joule heating, viscous dissipation, heat sink/source and thermal radiation, the conclusions reveal that the magnetic effects positively affect velocity while reducing the temperature, and the homogeneous reactions are found to improve blood circulation.

Computational fluid flow studies under convective conditions, such as the analysis of entropy in an inclined channel due to micropolar fluid flow under convective and slip conditions by Srinivasacharya and Hima Bindu reveal that the Reynolds number and coupling number keep the entropy in check [26]. The interesting works on steady Maxwell fluid past an exponentially stretching/shrinking sheet with various effects along multiple slip conditions show that the values of the skin friction, Nusselt number and Sherwood number decline due to enhancement in the time relaxation parameter; temperature and concentration distribution decline due to thermal and concentration stratification parameters and incline due to the relaxation parameter, and the mass transfer rate augments due to the thermophoretic parameter [27–29]. Further studies on micropolar fluids over exponentially stretching cylinders under slip conditions with microorganisms reveal that skin friction declines. At the same time, the Nusselt number inclines with stretching and micropolar parameters; velocity, thermal energy, and microorganism numbers enhances by the slip parameter, while temperature increases with the time relaxation parameter. A transient two-dimensional radiative Oldroyd-B nanofluid flow is examined by e.g. Khan, Nadeem and Ahmad et al. [30–34] on an exponentially stretching porous surface with microorganisms to improve the stability of the nanofluid. The results reveal that the higher values of the relaxation parameter correspond to the maximum heat and mass transfer rate.

The contribution of graphene-based nanoparticles to renewable energy and thermal conductivity enhancement reassures economically large-scale applications as coolants and in power storage and capacity. Hence, computationally investigating graphene-based nanofluids flow in several geometries is significant for qualitative references. The novelty of this paper is that it aims to bridge the gap of computationally studying the impacts of Joule heating due to the flow of GO nanoparticles dispersed in water in an inclined channel, which is an unexplored problem. The flow is modelled, and the equations are numerically solved to graph the results.

2. Mathematical formulation

The flow geometry comprises two parallel plates aligned with an angle of inclination α (in radians). Water with dispersed GO nanoparticles flows steadily in the channel. The representative flow picture is shown in Fig. 1.

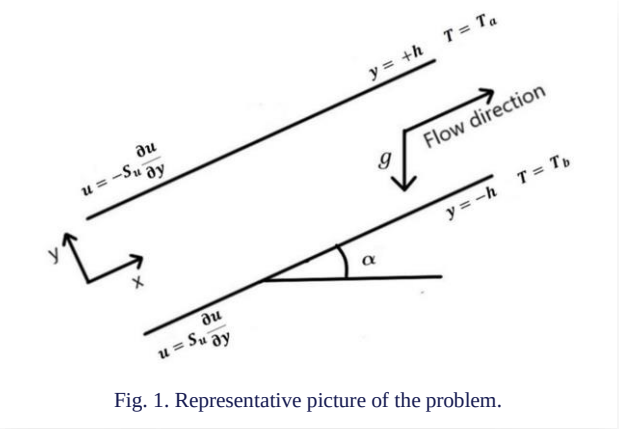

Fig. 1. Representative picture of the problem.

We consider the body forces due to gravity and the characteristic effects such as Brownian motion and thermophoresis, which are the only significant slip mechanisms in nanofluid flows. Irrespective of the flow, Brownian motion is the random motion of nanoparticles in the fluid, and thermophoresis is the movement of the nanoparticles from hotter to colder regions. Thus, the problem is modelled, taking into account the aforementioned effects and adapting the Buongiorno nanofluid model [1] as follows:

$$\frac{\partial u}{\partial x} = 0, \tag{1}$$

$$\rho_{nf} v_0 \frac{\partial u}{\partial y} + \frac{\partial p}{\partial x} = \mu_{nf} \frac{\partial^2 u}{\partial y^2} + \Big((\rho\beta)_{nf}(T - T_a)(1 - C_a) + -\big(\rho_{sp} - \rho_{bf}\big)(C - C_a)\Big) g\sin\alpha - \sigma_{nf} B_0^2 u, \tag{2}$$

$$\frac{\kappa_{nf}}{(\rho c_p)_{nf}}\left(\frac{\partial^2 T}{\partial y^2}\right) + \tau D_B \frac{\partial C}{\partial y} + \tau \frac{DT}{T_a}\left(\frac{\partial T}{\partial y}\right)^2 + \frac{\sigma_{nf}}{(\rho_{cp})_{nf}} B_0^2 u^2 = 0 \tag{3}$$

$$D_B \frac{\partial^2 C}{\partial y^2} + \frac{DT}{T_a}\frac{\partial^2 T}{\partial y^2} = 0, \tag{4}$$

and the slip boundary conditions are

– at $y = -h$: $\quad u = S_u \frac{\partial u}{\partial y}, \quad T = T_a, \quad C = C_a,$ (5a)

– at $y = h$: $\quad u = -S_u \frac{\partial u}{\partial y}, \; T = T_b, \quad C = C_b.$ (5b)

The notations T_a, T_b, C_a and C_b represent fluid temperatures (in Kelvin) and concentrations at the upper and lower plates, respectively and S_u is the velocity slip length/factor (in meter) which reflects the amount of liquid slip at a given surface. The

slip length is the distance beyond the solid–liquid interface where the liquid velocity linearly extrapolates to zero.

Table 1 presents the values of thermophysical properties [35,36], and their definitions are as follows:

$$\mu_{nf} = \frac{\mu_{bf}}{(1-\Phi)^{2.5}}, \tag{6a}$$

$$\rho_{nf} = (1-\Phi)\rho_{bf} + \Phi\rho_{sp}, \tag{6b}$$

$$\left(\rho C_p\right)_{nf} = (1-\Phi)\left(\rho C_p\right)_{bf} + \Phi\left(\rho C_p\right)_{sp}, \tag{6c}$$

$$(\rho\beta)_{nf} = (1-\Phi)(\rho\beta)_{bf} + \Phi(\rho\beta)_{sp}, \tag{6d}$$

$$\frac{\kappa_{nf}}{\kappa_{bf}} = \frac{\kappa_{sp}+2\kappa_{bf}+2\Phi(\kappa_{bf}-\kappa_{sp})}{\kappa_{sp}+2\kappa_{bf}-\Phi(\kappa_{bf}-\kappa_{sp})}, \tag{6e}$$

$$\alpha_{nf} = \frac{\kappa_{nf}}{\left(\rho C_p\right)_{nf}}. \tag{6f}$$

The subscripts *nf*, *sp* and *bf* indicate nanofluid, solid particle and base fluid. In contrast, the quantities κ, C_p, β, μ and ρ, respectively, denote thermal conductivity, specific heat capacity, thermal expansion coefficient, dynamic viscosity and density.

Table 1. Thermophysical properties [37–40].

Property and units	Water	GO
ρ, kg/m³	997.1	1800
C_p, J/(kg K)	4179	717
κ, W/(m K)	0.613	5000
β, 10^{-5}/K	21	28.4
σ, S/m	0.005	10^7

The following similarity variables are used to transform the modelled equations Eqs. (1)–(5):

$$\eta = \frac{y}{h}, \quad u = U_0 f(\eta), \quad \theta = \frac{T-T_a}{T_b-T_a}, \quad \varphi = \frac{C-C_a}{C_b-C_a}. \tag{7}$$

The transformed ODEs are given as:

$$f'' - A_1 R_{SC} f' + \frac{\mathrm{Gr}}{\mathrm{Re}} A_2 (A_3\theta - N_r\phi)\sin\alpha - A_2 P_1 - A_4 \mathrm{Ha} f = 0, \tag{8}$$

$$\theta'' + A_5(N_b\theta'' + N_t\phi'^2) + A_6 J f^2 = 0, \tag{9}$$

$$\phi'' + \frac{N_t}{N_b}\theta'' = 0, \tag{10}$$

such that

– at $\eta = -1$: $f - S f' = 0, \quad \theta = 0, \quad \phi = 0,$ (11a)

– at $\eta = 1$: $f + S f' = 0, \quad \theta = 1, \quad \phi = 1\,.$ (11b)

The constant coefficients (A_i, I = 1 to 6) and the dimensionless parameters used namely the suction/injection parameter R_{SC}, the buoyancy ratio N_r, heat capacity ratio τ, thermophoresis parameter N_t, Brownian motion parameter N_b, Grashof number Gr, Reynolds number Re, Hartmann number Ha, Joule heating parameter J and slip parameter S are defined as:

$$A_1 = 1 - \Phi + \Phi\frac{\rho_{sp}}{\rho_{bf}}, \qquad A_2 = (1-\Phi)^{2.5},$$

$$A_3 = 1 - \Phi + \frac{\Phi(\rho\beta)_{sp}}{(\rho\beta)_{bf}}, \qquad A_4 = \frac{\sigma_{nf}}{\sigma_{bf}}(1-\Phi)^{2.5},$$

$$A_5 = 1 - \Phi + \frac{\Phi\left(\rho C_p\right)_{sp}}{\left(\rho C_p\right)_{bf}}, \qquad A_6 = \frac{\sigma_{nf}}{\sigma_{bf}}\frac{\kappa_{bf}}{\kappa_{nf}},$$

$$\mathrm{Pr} = \frac{\mu_{bf} C_{pbf}}{K_{bf}}, \qquad \mathrm{Ha} = \frac{\sigma_{bf} B_0^2 h^2}{\mu_{bf}}, \qquad J = \frac{\sigma_{bf} B_0^2 U_0^2 h^2}{\kappa_{bf}(T_b - T_a)},$$

$$R_{sc} = \frac{\rho_{bf}}{\mu_{bf}}\nu_0 h, \qquad \mathrm{Gr} = \frac{g\beta_{bf}(1-C_a)(T_b-T_a)h^3\rho_{bf}^2}{\mu_{bf}^2},$$

$$N_r = \frac{(\rho_{sp}-\rho_{bf})(C_b-C_a)}{(\rho\beta)_{bf}(T_b-T_a)(1-C_a)}, \qquad N_t = \frac{\tau D_T (T_b-T_a)}{\alpha_{bf} T_a}, \qquad S = \frac{S_u}{d},$$

$$P_1 = \frac{h^2}{\nu_0\mu_{bf}}\frac{\partial p}{\partial x}, \qquad \mathrm{Re} = \frac{\rho_{bf} U_0 h}{\mu_{bf}}, \qquad N_b = \frac{\tau D_B (C_b - C_a)}{\alpha_{bf}}.$$

Practically significant values such as Sherwood number Sh, skin friction C_f and Nusselt number Nu are derived as:

– at $\eta = \pm 1$

$$\mathrm{Nu} = -\theta'(\eta), \quad \mathrm{Sh} = -\phi'(\eta), \quad C_f = c_1 f'(\eta),$$

where the constant c_1 is given by:

$$c_1 = (1-\Phi)^{-2.5}\left((1-\Phi) + \Phi\left(\rho_{sp}/\rho_{bf}\right)\right)^{-1}.$$

In the next section, a derivation and an analysis for the entropy is presented.

3. Entropy analysis

The entropy generation analysis is done in order to understand and minimize the loss of energy and thereby enhancing the efficiency of the model and performance of the device. By the law of increased entropy, the generated entropy is contributed from temperature, viscous dissipation and concentration. Thus, the entropy generation rate, S_G is written as [41]:

$$S_G = \frac{\kappa_{nf}}{T_a^2}\left(\frac{\partial T}{\partial y}\right)^2 + \frac{\mu_{nf}}{T_a}\left(\frac{\partial u}{\partial y}\right)^2 + RD_b\left(\frac{1}{C_a}\left(\frac{\partial C}{\partial y}\right)^2 + \frac{1}{T_a}\left(\frac{\partial T}{\partial y}\right)\left(\frac{\partial C}{\partial y}\right)\right) + \frac{\sigma_{nf} B_0^2}{T_a}u^2. \tag{12}$$

Here, the expressions on the right side are ascribed to the thermodynamic irreversibilities caused by temperature, fluid friction and combined mass and heat transfer. From S_G and characteristic entropy generation rate, $S_{G0} = \kappa_{nf}(T_2\text{-}T_1)^2/(T_1 L)^2$, we write the nondimensional entropy generation number as $N_S = S_G/S_{G0}$.

From Eqs. (7) and (12), we have:

$$\frac{\eta^2}{4}N_s = \frac{1}{\chi}\left(\theta'^2 + c_2\frac{\mathrm{EcPr}}{\Omega_T}f'^2 + c_3 M_m\frac{\Omega_C}{\Omega_T}\left(\frac{\Omega_C}{\Omega_T}\phi' + \theta'\right) + c_4\frac{J}{\Omega_T}f^2\right) = N_{S_h} + N_{S_G} + N_{S_J}\,, \tag{13}$$

where the subscripts S_h, S_G and S_J respectively correspond to the irreversibilities caused by heat transfer and fluid friction, combined heat and mass transfer and Joule heating. The parameters in Eq. (13) are given by constant $\chi = h^2/L^2$, temperature param-

eter $\Omega_T = T_2/T_1$, concentration parameter $\Omega_C = C_2/C_1$, and the parameter of combined mass and heat transfer $M_m = RD_BC_0/\kappa_{bf}$, Eckert number $\mathrm{Ec} = U_0^2/(\kappa_{bf}C_{pbf}(T_2-T_1))$, Prandtl number $\mathrm{Pr} = \mu C_{pbf}/\kappa_{bf}$ and the constants are given by $c_2 = (1-\Phi)^{-2.5}\kappa_{bf}/\kappa_{nf}$ and $c_3 = (1-\Phi)^{2.5}$, $c_4 = (\kappa_{bf}\sigma_{nf})/(\kappa_{nf}\sigma_{bf})$.

Bejan number, $\mathrm{Be} = N_{Sh}/N_S$ determines the principal source for entropy generation [42]. From this ratio, it is dictated that heat transfer mainly influences the entropy if Be > 0.5, while, fluid friction and mass and heat transfer fundamentally contributes to the entropy if Be < 0.5 and all the three irreversibilities contribute equally if Be = 0.5 [43].

4. Numerical solution

The ODEs (8)–(11) are solved by adapting the spectral quasilinearization method (SQLM) [26,44,45] and the solution procedure is as follows:

i. The nonlinear terms about the solution are expanded using the Taylor series, and the higher-order derivatives are neglected.
ii. The spectral collocation method is applied to the linearised equations, and the functions are iterated using Chebyshev polynomials at the collocation points.
iii. A suitable bijection is mapped from the domain to the collocation points.
iv. Approximations and the derivatives are substituted in the linearized equations to obtain a matrix equation, which is solved using MATLAB.

We linearize the nonlinear terms by using the expansion of Taylor series. Let f_r, θ_r and ϕ_r be the solution of the differential equations. Then, assuming f_{r+1}, θ_{r+1} and ϕ_{r+1} to be the improved solutions, the system of ODEs is solved using an iterative method. By expanding the nonlinear terms using the expansion of Taylor series about the solution and discarding the higher derivatives, the following linearized equations and their associated boundary conditions are obtained:

$$f'''_{r+1} + a_{1,r}f''_{r+1} + a_{2,r}f_{r+1} + a_{3,r}\theta_{r+1} + a_{4,r}\phi_{r+1} = a_{5,r}, \quad (14)$$

$$b_{1,r}f_r + \theta''_{r+1} + b_{2,r}\theta'_r + b_{3,r}\phi_r = b_{4,r}, \quad (15)$$

$$c_{1,r}\theta''_{r+1} + \phi''_{r+1} = 0, \quad (16)$$

such that

– at $\eta = -1$: $f_{r+1} - S\,f'_{r+1} = 0, \quad \theta_{r+1} = \phi_{r+1} = 0, \quad (17a)$

– at $\eta = 1$: $f_{r+1} + S\,f'_{r+1} = 0, \quad \theta_{r+1} = \phi_{r+1} = 1. \quad (17b)$

The coefficients in the above equations are given by:

$$a_{1,r} = -A_1R_{sc}, \quad a_{2,r} = -A_4\mathrm{Ha}, \quad a_{3,r} = A_2A_3\frac{\mathrm{Gr}}{\mathrm{Re}}\sin\alpha,$$

$$a_{4,r} = -A_2\frac{\mathrm{Gr}}{\mathrm{Re}}\mathrm{Nr}\sin\alpha, \quad a_{5,r} = A_2P_1, \quad b_{1,r} = 2A_6J\,f_r,$$

$$b_{2,r} = A_5N_b\phi'_r + 2A_5N_t\phi'_r, \; b_{3,r} = A_5N_b\theta'_r,$$

$$b_{4,r} = A_5N_b\theta'_r\phi'_r + A_5N_t\theta'^2_r + A_6J\,f_r^2, \qquad c_{1,r} = \frac{N_t}{N_b}.$$

We apply the collocation method by using Chebyshev polynomials and iterating f, θ and ϕ at the Gauss-Lobatto collocation points $\xi_j = \cos(\pi j/N)$, $j = 0, 1, 2, ..., N$ [45]. Thus, we approximate the unknown functions as:

$$f_{r+1}(\xi) = \sum_{k=0}^{N} f_{r+1}(\xi_k)T_k(\xi_j),$$
$$\theta_{r+1}(\xi) = \sum_{k=0}^{N} \theta_{r+1}(\xi_k)T_k(\xi_j), \quad (18)$$
$$\phi_{r+1}(\xi) = \sum_{k=0}^{N} \phi_{r+1}(\xi_k)T_k(\xi_j),$$

where Chebyshev polynomial $T_k(\xi)$ is given by:

$$T_k(\xi) = \cos(k\cos^{-1}(\xi)).$$

Further, the following equations give the derivatives:

$$\frac{d^r f_{r+1}}{d\,\eta^r} = \sum_{k=0}^{N} D_{kj}^r f_{r+1}(\xi_k), \qquad j = 0, 1, \ldots, N,$$

$$\frac{d^r \theta_{r+1}}{d\,\eta^r} = \sum_{k=0}^{N} D_{kj}^r \theta_{r+1}(\xi_k), \qquad j = 0, 1, \ldots, N, \quad (19)$$

$$\frac{d^r \phi_{r+1}}{d\,\eta^r} = \sum_{k=0}^{N} D_{kj}^r \phi_{r+1}(\xi_k), \qquad j = 0, 1, \ldots, N.$$

Here $\mathcal{D} = D/2$ is called the Chebyshev differentiation matrix.

On substituting Eq. (18) and Eq. (19) in Eqs. (14)–(17), we obtain:

$$AY_{r+1} = R_r, \quad (20)$$

associated with the conditions:

$$(1 + SD_{00})f_{r+1}(\xi_0) + S\sum_{k=1}^{N} D_{0k}f_{r+1}(\xi_k) = 0, \quad (21a)$$

$$\theta_{r+1}(\xi_0) = \phi_{r+1}(\xi_0) = 0, \quad (21b)$$

$$-S\sum_{k=0}^{N-1} D_{Nk}f_{r+1}(\xi_k) + (1 - SD_{NN})f_{r+1}(\xi_N) = 0, \quad (21c)$$

$$\theta_{r+1}(\xi_N) = \phi_{r+1}(\xi_N) = 1. \quad (21d)$$

We choose the initial approximations $f_0 = 0$, $\theta_0 = \phi_0 = (1-\eta)/2$ in order to satisfy Eq. (17) and the Eq. (20) is recursively iterated at ξ_j, $j = 0, 1, ..., N$ by substituting Eq. (21), to the order of approximation. Hence, the obtained solution is graphed and interpreted. These initial conditions are iterated to obtain the numerical solution.

5. Results

The equation (20) is solved to graphically depict the results with interpretations. The parameters are varied in the practical range and the effects of different parameters are studied [46,47]. Since, the Newtonian behavior of water based nanofluid is considered, fixed values of $\Phi = 0.01$ and $\mathrm{Pr} = 6.5$ are taken. The other parameter values are taken to be as $\mathrm{Ec} = 10^{-5}$, $\mathrm{Gr} = 2\times10^5$, $S = 0.5$, $N_b = 4\times10^{-4}$, $\mathrm{Re} = 300$, $N_t = 2\times10^{-4}$, $R_{sc} = 5$, $\alpha = \pi/4$, $J = 3\times10^{-5}$, $\mathrm{Ha} = 2$ and $N_r = 2$, unless mentioned otherwise. The order of SLM approximation is taken to be $N = 100$ and the convergence of results is obtained at a tenth iteration. The results for the case

Table 2. Comparison of $f(\eta)$ calculated by the present method for Ec = R_{SC} = 1, P_1 = -1, Pr = 0.71 and S = J = Ha = 0 and A_i = 1, (i = 1, 2, 3, 4, 5, 6) [48] (an approximation of η values is taken, because of the use of Gauss-Lobatto collocation points).

Present study		Makinde and Eegunjobi [48]	
η	$f(\eta)$	η	$f(\eta)$
0	0	0	0
0.100158	0.038849	0.1	0.038793
0.201048	0.071451	0.2	0.071149
0.299985	0.096387	0.3	0.09639
0.400145	0.113789	0.4	0.113769
0.500000	0.122459	0.5	0.122459
0.601394	0.121461	0.6	0.121546
0.700015	0.110017	0.7	0.11002
0.80021	0.086702	0.8	0.086764
0.900783	0.050207	0.9	0.050545
1	0	1	0

of Ec = R_{sc} = 1, P_1 = −1, Pr = 0.71 and S = J = Ha = 0 agree with the results from Makinde and Eegunjobi [48] (refer to Table 2). Figure 2 depicts the influence of Re on f, N_S and Be. With the rising Reynolds number, viscous forces decrease and the nanofluid moves with a greater velocity. Hence, the flow velocity increases in the proximity of the upper plate and a lesser velocity is observed near the lower plate (Fig. 2a). Similarly, entropy number decreases near the upper plate and increases near the lower plate (Fig. 2b). There is a consequent increase in Bejan number, suggesting the contribution of mass transfer and fluid friction and to the generated entropy (Fig. 2c).

The impacts of α on f, N_S and Be are presented in Fig. 3. As the angle of inclination increases, a drop in velocity is observed (Fig. 3a). Whereas, an increase in angle of inclination values causes an enhancement in N_S values (Fig. 3b). This consequently causes the Bejan number to decrease (Fig. 3c), thus pronouncing the contribution of fluid friction and mass transfer to the generated entropy.

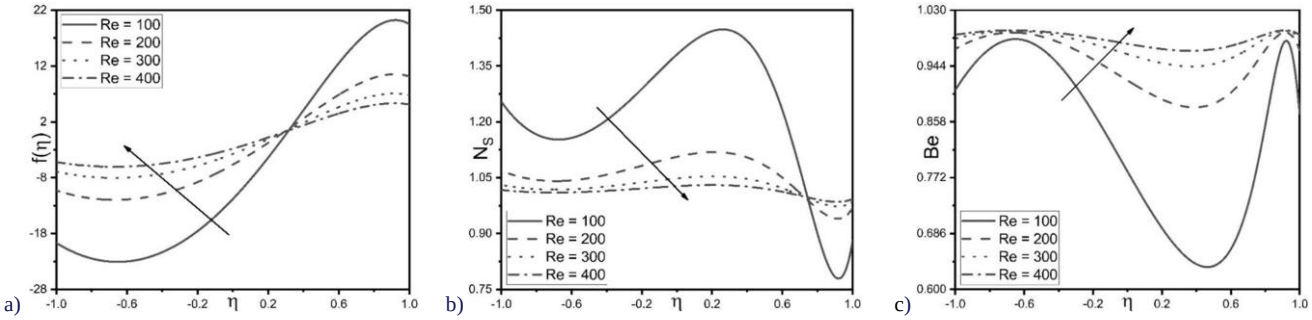

Fig. 2. Impacts of Re on:(a) f, b) N_S and c) Be.

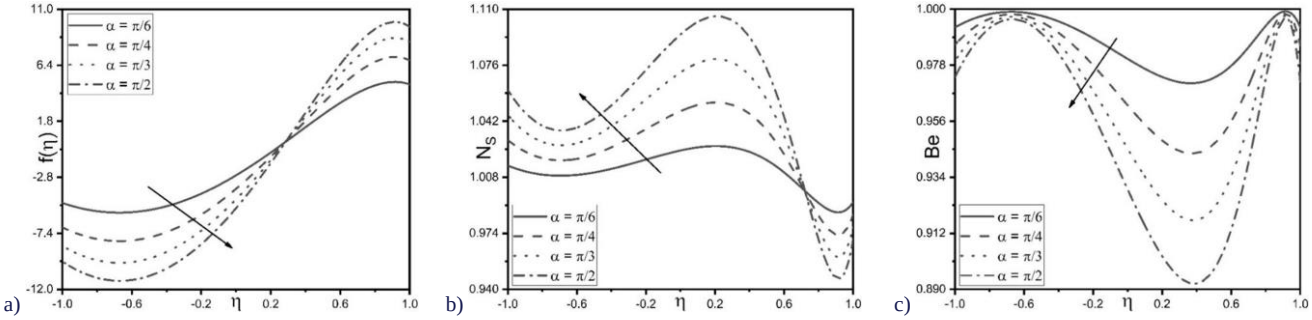

Fig. 3. Impacts of α on: a) f, b) N_S and c) Be.

Figure 4 presents the effects of R_{sc} on f, N_S and Be. As the suction parameter is enhanced, the fluid velocity depletes throughout the channel except near the upper plate. Whereas, the injection parameter increases, the fluid velocity increases throughout the channel except near the upper plate. In the middle of the channel, both suction and injection parameters enhance the velocity (Fig. 4a). Figure 4b represents that the entropy number increases in the middle of the flow channel. This results in the reverse trend of Bejan number (Fig. 4c), indicating the contribution of fluid friction and mass transfer irreversibilities to the generated entropy throughout the channel.

Figure 5 shows the impacts of J on N_S and Be. Increasing the Joule heating parameter increases the entropy generation and hence, N_S increases (Fig. 5a). It impacts on depletion of Bejan number (Fig. 5b). Hence, the Joule heating parameter contributes to entropy generation from combined heat and mass transfer and fluid friction.

It is clear from Fig. 6a that the enhancement in Ha, enhances the fluid velocity, contradicting the anticipated reduction due to the Lorentz force. Similarly, as Ha increases, an increase in entropy number is observed (Fig. 6b). This results in an enhanced Be (Fig. 6c), which signifies the contribution of mass transfer and fluid friction to the generated entropy.

Figure 7 depicts the impacts of S on f, N_S and Be. It is clear from Fig. 7a that the increasing slip velocity values reduce the nanofluid flow velocity near the upper plate. Whereas, it is seen

from Fig. 7b that when *S* increases, the entropy near the surface of the plates decreases and that in the middle of the flow channel increases. This causes an opposite trend in Be (Fig. 7c) thus implying the dominance of fluid friction and mass transfer irreversibilities.

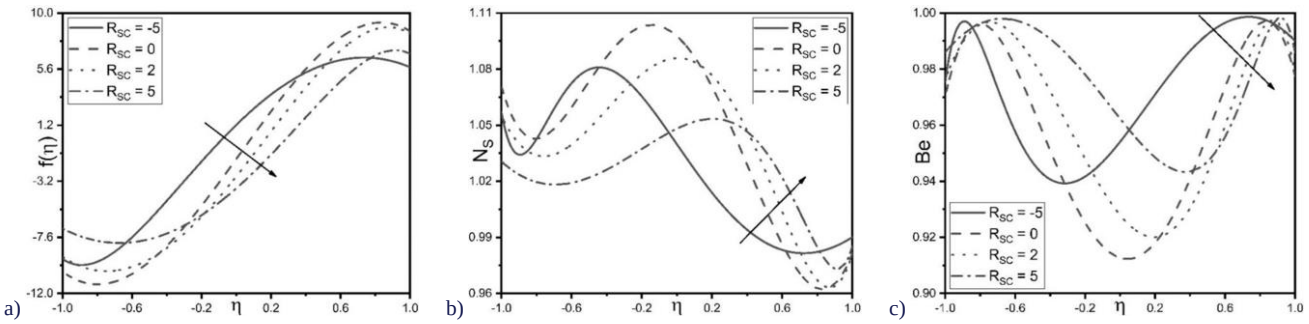

Fig. 4. Impacts of R_{SC} on: a) *f*, b) N_S and c) Be.

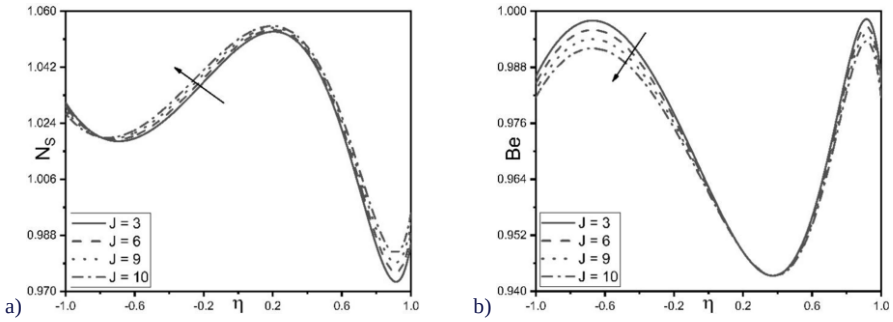

Fig. 5. Impacts of $\boldsymbol{J \times 10^{-5}}$on:(a) N_s and b) Be.

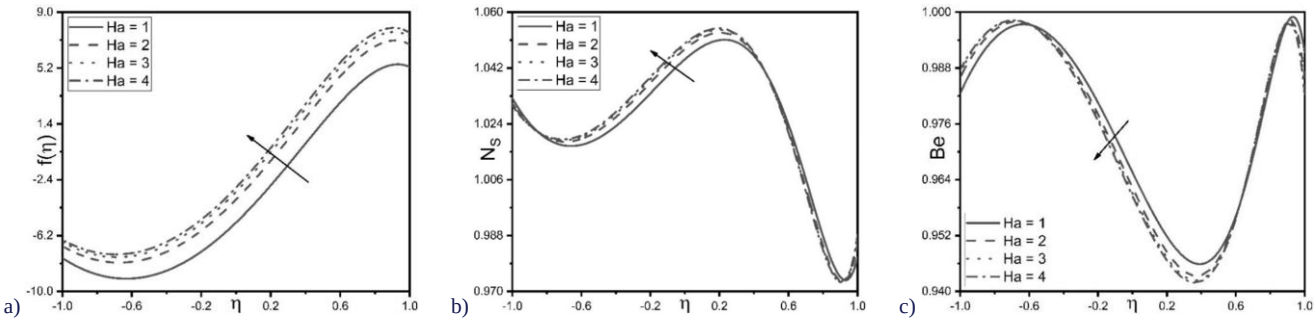

Fig. 6. Impacts of Ha on: a) *f*, b) N_S and (c) Be.

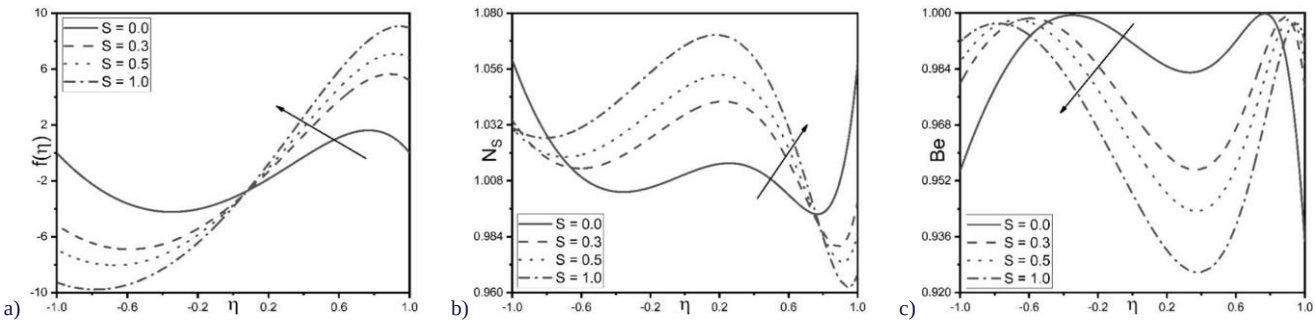

Fig. 7. Impacts of *S* on: a) *f*, b) N_S and c) Be.

Table 3 presents the values for Nu, Sh and C_f at the lower plate for different values of the input parameters. The Nusselt number, by definition, is the ratio of heat transfer due to convection to conduction. Clearly, when the parameters R_{sc}, α, Ha and S are increased, Nu and thereby, convective heat transfer quality enhances. While the values of Ha increase, Nu values are supposed to increase, and an enhancement is observed, thus implying the improvement in convective heat transfer quality. Whereas, the injection parameter, N_b, N_t and J reduce the values of Nu. This means, the Joule heating parameter heats up the surface of the channels by conduction and hence a reduction in Nu is observed. Similarly, when Re, N_b, injection parameter and J values are increased, convective mass transfer increases and hence Sh improves, causing an enhancement in convective mass transfer. Likewise, Ha has an improving effect on mass diffusivity, thus resulting in lesser Sh values. Considering the skin friction drag, the parameter N_b, suction parameter, α and J values have a controlling effect on C_f.

Table 3. Nusselt number, Sherwood number and skin friction values, where $J \times 10^{-5}$.

Re	N_b	N_t	R_{sc}	α	J	Ha	S	$-\theta'(1)$	$-\phi'(1)$	$A_7 f'(1)$
100	0.0004	0.0002	5	π/4	3	2	0.5	1.066592	0.966704	-40.024441
200	0.0004	0.0002	5	π/4	3	2	0.5	1.018198	0.990901	-20.920922
300	0.0004	0.0002	5	π/4	3	2	0.5	1.008085	0.995957	-14.06996
400	0.0004	0.0002	5	π/4	3	2	0.5	1.00445	0.997775	-10.586109
300	0.0002	0.0002	5	π/4	3	2	0.5	1.008119	0.991881	-14.021619
300	0.0004	0.0002	5	π/4	3	2	0.5	1.008085	0.995957	-14.06996
300	0.0006	0.0002	5	π/4	3	2	0.5	1.008008	0.997331	-14.086336
300	0.0008	0.0002	5	π/4	3	2	0.5	1.007919	0.99802	-14.09466
300	0.0004	0.0002	5	π/4	3	2	0.5	1.008085	0.995957	-14.06996
300	0.0004	0.0003	5	π/4	3	2	0.5	1.008003	0.993998	-14.046363
300	0.0004	0.0004	5	π/4	3	2	0.5	1.007921	0.992079	-14.022999
300	0.0004	0.0005	5	π/4	3	2	0.5	1.00784	0.990201	-13.999866
300	0.0004	0.0002	-5	π/4	3	2	0.5	1.015474	0.992263	-18.912752
300	0.0004	0.0002	0	π/4	3	2	0.5	1.019284	0.990358	-20.936399
300	0.0004	0.0002	2	π/4	3	2	0.5	1.014996	0.992502	-18.553952
300	0.0004	0.0002	5	π/4	3	2	0.5	1.008085	0.995957	-14.06996
300	0.0004	0.0002	5	π/6	3	2	0.5	1.003926	0.998037	-9.985362
300	0.0004	0.0002	5	π/4	3	2	0.5	1.008085	0.995957	-14.06996
300	0.0004	0.0002	5	π/3	3	2	0.5	1.012178	0.993911	-17.17123
300	0.0004	0.0002	5	π/2	3	2	0.5	1.016207	0.991896	-19.75859
300	0.0004	0.0002	5	π/4	3	2	0.5	1.008085	0.995957	-14.06996
300	0.0004	0.0002	5	π/4	6	2	0.5	1.006763	0.996619	-14.072372
300	0.0004	0.0002	5	π/4	9	2	0.5	1.00544	0.99728	-14.074783
300	0.0004	0.0002	5	π/4	12	2	0.5	1.004118	0.997941	-14.077193
300	0.0004	0.0002	5	π/4	3	1	0.5	1.007139	0.99643	-15.725448
300	0.0004	0.0002	5	π/4	3	2	0.5	1.008085	0.995957	-14.06996
300	0.0004	0.0002	5	π/4	3	3	0.5	1.008418	0.995791	-13.496468
300	0.0004	0.0002	5	π/4	3	4	0.5	1.008588	0.995706	-13.205481
300	0.0004	0.0002	5	π/4	3	2	0	1.006043	0.996978	-27.092764
300	0.0004	0.0002	5	π/4	3	2	0.3	1.0066	0.9967	-17.493855
300	0.0004	0.0002	5	π/4	3	2	0.5	1.008085	0.995957	-14.06996
300	0.0004	0.0002	5	π/4	3	2	1	1.011167	0.994416	-9.433658

6. Conclusions

On examining the flow of water suspended with GO nanoparticles in between two plates aligned with an angle of inclination and including the impacts of Joule heating, we infer the following:

- Velocity is improved by enhancing the Hartman number, Reynolds number and injection parameter values. Hence, the flow is better in the presence of magnetic field.
- Convective heat transfer is improved by the Hartman number, suction parameter, angle of inclination and slip parameter. Therefore, compared to the flow in a horizontal channel where the slip condition is ignored, better thermal performance is achieved with the inclined channel in the presence of a magnetic field and considering slip conditions.
- Brownian motion of the nanoparticles significantly contributes to mass transfer since convective mass transfer is increased by raising values of the Brownian motion parameter, Reynolds number, injection parameter and Joule heating parameter.
- Since Be > 0.9, heat transfer primarily causes the entropy generation, even though the varying parameter values feebly contribute to entropy due to mass transfer and fluid friction.

The problem considered is useful in automobile radiators, heat exchangers, manufacturing polymers and fertilizers, and food processing. The investigation can be further extended by examining the flow of graphene oxide nanofluid in various other geometries and exploring the nanofluid's non-Newtonian behaviour.

References

[1] Buongiorno, J. (2006). Convective transport in nanofluids. *Journal of Heat Transfer*, 128(3), 240–250. doi: 10.1115/1.2150834

[2] Abro, K.A., & Abdon, A. (2022). A computational technique for thermal analysis in coaxial cylinder of one-dimensional flow of fractional Oldroyd-B nanofluid. *International Journal of Ambient Energy*, 43(1), 5357–5365. doi: 10.1080/01430750.2021.1939157

[3] Akram, M., Jamshed, W., Goud, B.S., Pasha, A.A., Sajid, T., Rahman, M.M., Arshad, M., & Weera, W. (2022). Irregular heat source impact on Carreau nanofluid flowing via exponential expanding cylinder: A thermal case study. *Case Studies in Thermal Engineering*, 36, 102171. doi: 10.1016/j.csite.2021.102171

[4] Shah, R.A., Ullah, H., Khan, M.S., & Khan, A. (2021). Parametric analysis of the heat transfer behavior of the nano-particle ionic-liquid flow between concentric cylinders. *Advances in Mechanical Engineering*, 13(6), 16878140211024009. doi: 10.1177/16878140211024009

[5] Javanmard, M., Salmani, H., Taheri, M.H., Askari, N., & Kazemi, M.A. (2021). Heat transfer of a radial, nanofluid water-graphene oxide hydromagnetic flow between coaxial pipes with a variable radius ratio. *Proceedings of the Institution of Mechanical Engineers, Part E: Journal of Process Mechanical Engineering*, 235(1), 124–133. doi: 10.1177/0954408920948194

[6] Masood, S., & Farooq, M. (2021). Influence of thermal stratification and thermal radiation on graphene oxide-Ag/H_2O hybrid nanofluid. *Journal of Thermal Analysis and Calorimetry*, 143, 1361–1370. doi: 10.1007/s10973-020-10227-7

[7] Ramesh, G.K., Shehzad, S.A., & Izadi, M. (2022). Falkner–Skan flow of aqueous magnetite–graphene oxide nanoliquid driven by a wedge. *Chinese Journal of Physics*, 77, 733–746. doi: 10.1016/j.cjph.2021.07.023

[8] Bhattacharyya, A., Sharma, R., Hussain, S.M., Chamkha, A.J., & Mamatha, E. (2022). A numerical and statistical approach to capture the flow characteristics of Maxwell hybrid nanofluid containing copper and graphene nanoparticles. *Chinese Journal of Physics*, 77, 1278–1290. doi: 10.1016/j.cjph.2021.09.015

[9] Lavine, A.S. (1988). Analysis of fully developed opposing mixed convection between inclined parallel plates. *Wärme-und Stoffübertragung*, 23(4), 249–257. doi: 10.1007/BF01807328

[10] Choi, S.U.S., & Eastman, J.A. (1995). *Enhancing thermal conductivity of fluids with nanoparticles*. Argonne National Lab., Argonne, IL (United States), No. ANL/MSD/CP-84938; CONF-951135-29.

[11] Talabi, S.O., & Nwabuko, U. (1993). Numerical solution of natural convective heat transfer in parabolic enclosures. *International Journal of Heat and Mass Transfer*, 36(17), 4275–4281. doi: 10.1016/0017-9310(93)90090-S

[12] Barai, D.P., Bhanvase, B.A., & Sonawane, S.H. (2020). A review on graphene derivatives-based nanofluids: Investigation on properties and heat transfer characteristics. *Industrial and Engineering Chemistry Research*, 59(22), 10231–10277. doi: 10.1021/acs.iecr.0c00865

[13] Azimi, M., Azimi, A., & Mirzaei, M. (2014). Investigation of the unsteady graphene oxide nanofluid flow between two moving plates. *Journal of Computational and Theoretical Nanoscience*, 11(10), 2104–2108. doi: 10.1166/jctn.2014.3612

[14] Gul, T., Ullah, M.Z., Alzahrani, A.K., & Amiri, I.S. (2019). Thermal performance of the graphene oxide nanofluids flow in an upright channel through a permeable medium. *IEEE Access*, 7, 102345–102355. doi: 10.1109/ACCESS.2019.2927787

[15] Shahzad, F., Jamshed, W., Eid, M.R., El Din, S.M., & Banerjee, R. (2023). Mathematical modelling of graphene-oxide/kerosene oil nanofluid via radiative linear extendable surface. *Alexandria Engineering Journal*, 70, 395–410. doi: 10.1016/j.aej.2023.02.034

[16] Nazari, M.A., Ghasempour, R., Ahmadi, M.H., Heydarian, G., & Shafii, M.B. (2018). Experimental investigation of graphene oxide nanofluid on heat transfer enhancement of pulsating heat pipe. *International Communications in Heat and Mass Transfer*, 91, 90–94. doi: 10.1016/j.icheatmasstransfer.2017.12.006

[17] Dehghan, P., Keramat, F., Mofarahi, M., & Lee, C.H. (2023). Computational fluid dynamic analysis of graphene oxide/water nanofluid heat transfer over a double backward-facing microchannel. *Journal of the Taiwan Institute of Chemical Engineers*, 145, 104821. doi: 10.1016/j.jtice.2023.104821

[18] Pashikanti, J., Thota, S., & Priyadharshini, D.R.S. (2024). Effect of viscous dissipation due to magnetohydrodynamic flow in an inclined channel. *Chinese Journal of Physics*, 87, 82–96. doi: 10.1016/j.cjph.2023.11.015

[19] Javanmard, M., Taheri, M.H., Abbasi, M., & Ebrahimi, S.M. (2018). Heat transfer analysis of hydromagnetic water–graphene oxide nanofluid flow in the channel with asymmetric forced convection on walls. *Chemical Engineering Research and Design*, 136, 816–824. doi: 10.1016/j.cherd.2018.06.041

[20] Hafeez, M., Hashim, & Khan, M. (2020). Jeffrey–Hamel flow of hybrid nanofluids in convergent and divergent channels with heat transfer characteristics. *Applied Nanoscience*, 10, 5459–5468. doi: 10.1007/s13204-020-01427-6

[21] Raza, A., Khan, S.U., Khan, M.I., Farid, S., Muhammad, T., Khan, M.I., & Galal, A.M. (2021). Fractional order simulations for the thermal determination of graphene oxide (GO) and molybdenum disulphide (MoS_2) nanoparticles with slip effects. *Case Studies in Thermal Engineering*, 28, 101453. doi: 10.1016/j.csite.2021.101453

[22] Pavithra, K.M., Hanumagowda, B.N., Varma, S.V.K., Ahammad, N.A., Raju, C.S.K., & Noeiaghdam, S. (2023). The impacts of shape factors in a chemically reacting two-passage vertical channel filled with kerosene-based graphene oxide and MoS2 mixture in a porous medium. *Results in Engineering*, 18, 101050. doi: 10.1016/j.rineng.2021.101050

[23] Akram, S., Athar, M., Saeed, K., Razia, A., Muhammad, T., & Hussain, A. (2023). Hybrid double-diffusivity convection and induced magnetic field effects on peristaltic waves of Oldroyd 4-constant nanofluids in non-uniform channel. *Alexandria Engineering Journal*, 65, 785–796. doi: 10.1016/j.aej.2022.10.039

[24] Nazeer, M. (2023). Multiphase flow development in gravitational and magnetic fields. *Waves in Random and Complex Media*, 1−15. doi: 10.1080/17455030.2023.2193853

[25] Yasin, M., Hina, S., & Naz, R. (2023). Influence of inclined magnetic field on peristaltic flow of Ag–Cu/blood hybrid nanofluid in the presence of homogeneous–heterogeneous reactions with slip condition. *Arabian Journal for Science and Engineering*, 48(1), 31–46. doi: 10.1007/s13369-022-06942-y

[26] Srinivasacharya, D., & Bindu, K.H. (2015). Entropy generation in a micropolar fluid flow through an inclined channel with slip and convective boundary conditions. *Energy*, 91, 72–83. doi: 10.1016/j.energy.2015.08.014

[27] Khan, M.N., Ullah, N., & Nadeem, S. (2021). Transient flow of Maxwell nanofluid over a shrinking surface: Numerical solutions and stability analysis. *Surfaces and Interfaces*, 22, 100829. doi: 10.1016/j.surfin.2020.100829

[28] Khan, M.N., & Nadeem, S. (2020). Theoretical treatment of bio-convective Maxwell nanofluid over an exponentially stretching sheet. *Canadian Journal of Physics*, 98(8), 732–741. doi: 10.1139/cjp-2019-0380

[29] Khan, M.N., & Nadeem, S. (2021). A comparative study between linear and exponential stretching sheet with double stratification of a rotating Maxwell nanofluid flow. *Surfaces and Interfaces*, 22, 100886. doi: 10.1016/j.surfin.2020.100886

[30] Nadeem, S., Khan, M.N., Muhammad, N., & Ahmad, S. (2019). Mathematical analysis of bio-convective micropolar nanofluid. *Journal of Computational Design and Engineering*, 6(3), 233−242. doi: 10.1016/j.jcde.2019.04.001

[31] Khan, M.N., Nadeem, S., & Muhammad, N. (2020). Micropolar fluid flow with temperature-dependent transport properties. *Heat Transfer*, 49(4), 2375–2389. doi: 10.1002/htj.21726

[32] Nadeem, S., Khan, M.N., & Abbas, N. (2020). Transportation of slip effects on nanomaterial micropolar fluid flow over exponentially stretching. *Alexandria Engineering Journal*, 59(5), 3443−3450. doi: 10.1016/j.aej.2020.05.024

[33] Ahmad, S., Nadeem, S., Muhammad, N., & Khan, M.N. (2021). Cattaneo–Christov heat flux model for stagnation point flow of micropolar nanofluid toward a nonlinear stretching surface with slip effects. *Journal of Thermal Analysis and Calorimetry*, 143, 1187–1199. doi: 10.1007/s10973-020-09504-2

[34] Khan, M.N., Nadeem, S., Ullah, N., & Saleem, A. (2020). Theoretical treatment of radiative Oldroyd-B nanofluid with microorganism pass an exponentially stretching sheet. *Surfaces and Interfaces*, 21, 100686. doi: 10.1016/j.surfin.2020.100686

[35] Gul, T., Ullah, M.Z., Alzahrani, A.K., & Amiri, I.S. (2019). Thermal performance of the graphene oxide nanofluids flow in an upright channel through a permeable medium. *IEEE Access*, 7, 102345–102355. doi: 10.1109/access.2019.2927787

[36] Elsaid, K., Abdelkareem, M.A., Maghrabie, H.M., Sayed, E.T., Wilberforce, T., Baroutaji, A., & Olabi, A.G. (2021). Thermophysical properties of graphene-based nanofluids. *International Journal of Thermofluids*, 10, 100073. doi: 10.1016/j.ijft.2021.100073

[37] Al-Sankoor, K., Al-Gayyim, H., Al-Musaedi, S., Asadi, Z., & Ganji, D.D. (2021). Analytically investigating of heat transfer parameters with presence of graphene oxide nanoparticles in Williamson-magnetic fluid by AGM and HPM methods. *Case Studies in Thermal Engineering*, 27, 101236. doi: 10.1016/j.csite.2021.101236

[38] Lide, D.R. (Ed.). (2004). *CRC handbook of chemistry and physics*. (Vol. 85). CRC Press.

[39] Ghadikolaei, S.S., Hosseinzadeh, K.H., Hatami, M., Ganji, D.D., & Armin, M. (2018). Investigation for squeezing flow of ethylene glycol ($C_2H_6O_2$) carbon nanotubes (CNTs) in rotating stretching channel with nonlinear thermal radiation. *Journal of Molecular Liquids*, 263, 10–21. doi: 10.1016/j.molliq.2018.04.141

[40] Chu, Y.M., Nisar, K.S., Khan, U., Kasmaei, H.D., Malaver, M., Zaib, A., & Khan, I. (2020). Mixed convection in MHD water-based molybdenum disulfide-graphene oxide hybrid nanofluid through an upright cylinder with shape factor. *Water*, 12(6), 1723. doi: 10.3390/w12061723

[41] Bejan, A. (1996). Entropy generation minimization: The new thermodynamics of finite-size devices and finite-time processes. *Journal of Applied Physics*, 79(3), 1191–1218. doi: 10.1063/1.362674

[42] Bejan, A., & Kestin, J. (1983). Entropy generation through heat and fluid flow. Journal of Applied Mechanics, 50(2), 475-475. doi: 10.1115/1.3167072

[43] Paoletti, S., Rispoli, F., & Sciubba, E. (1989). Calculation of exergetic losses in compact heat exchanger passages. *ASME, Advanced Energy Systems*, 10(2), 21–29.

[44] Bellman, R.E. (1965). *Quasilinearization and nonlinear boundary-value problems*. (Vol. 3). American Elsevier Publishing Company.

[45] Canuto, C., Hussaini, M.Y., Quarteroni, A., & Zang, T.A. (2007). *Spectral methods: fundamentals in single domains*. Springer Science & Business Media.

[46] Malashetty, M.S., Umavathi, J.C., & Prathap Kumar, J. (2001). Convective magnetohydrodynamic two fluid flow and heat transfer in an inclined channel. *Heat and Mass transfer*, 37(2−3), 259−264. doi: 10.1007/s002310000134

[47] Behseresht, A., Noghrehabadi, A., & Ghalambaz, M. (2014). Natural-convection heat and mass transfer from a vertical cone in porous media filled with nanofluids using the practical ranges of nanofluids thermo-physical properties. *Chemical Engineering Research and Design*, 92(3), 447–452. doi: 10.1016/j.cherd.2013.08.028

[48] Makinde, O.D., & Eegunjobi, A.S. (2013). Effects of convective heating on entropy generation rate in a channel with permeable walls. *Entropy*, 15(1), 220–233. doi: 10.3390/e15010220

Co-published by
Institute of Fluid-Flow Machinery
Polish Academy of Sciences
Committee on Thermodynamics and Combustion
Polish Academy of Sciences

http://www.imp.gda.pl/archives-of-thermodynamics/

Comparative thermo-hydraulic analysis of periodic stepped open micro pin-fin heat sink

Prabhakar Bhandari[a*], Bhavesh Vyas[b], Diwakar Padalia[c], Lalit Ranakoti[d], Yogesh Kumar Prajapati[e], Raghubeer Singh Bangari[f]

[a]Department of Mechanical Engineering, School of Engineering and Technology, K. R. Mangalam University, Gurugram-122103, Haryana, India
[b]Department of Electrical and Electronics Engineering, School of Engineering and Technology, K. R. Mangalam University, Gurugram-122103, Haryana, India
[c]Department of Physics, School of Basic and Applied Sciences, K. R. Mangalam University, Gurugram-122103, Haryana, India
[d]Department of Mechanical Engineering, Graphic Era Deemed to Be University, Dehradun-248002, Uttarakhand, India
[e]Department of Mechanical Engineering, BIT Sindri, Dhanbad-828123, Jharkhand, India
[f]Department of Mechanical Engineering, Graphic Era Hill University, Dehradun-248002, Uttarakhand, India
*Corresponding author email: prabhakar.bhandari40@gmail.com

Received: 29.11.2023; revised: 27.02.2024; accepted: 28.04.2024

Abstract

There is no doubt that the miniaturization of various electronic devices, including processors, servers, micro-electromechanical system devices, etc. has resulted in increased overall performance. However, there is a major problem with thermal management in these devices, as well as in many others. One of the most promising solutions is liquid cooled microchannel heat sink. In the current work, different cases of open micro pin-fin configurations of heat sink were considered. The configurations considered were a uniform height micro pin-fin heat sink, three-stepped unidirectional micro pin-fin heat sink and three-stepped bi-directional micro pin-fin heat sink. These configurations were also oriented in two dissimilar fashions, i.e. inline and staggered, so the total of six heat sink configurations are compared and analysed. Using single phase water as a coolant and copper as a substrate, these configurations were simulated numerically for different Reynolds numbers (10−160) under heat flux of 500 kW/m^2. It can be concluded that at low Reynolds numbers, steepness does not contribute much in both inline and staggered arrangements, while at higher Reynolds numbers, 3 stepped staggered configurations has revealed the best performance due to boosted fluid mixing and more projecting secondary flow. Furthermore, bi-directionality in steepness shows augmented performance only in inline arrangement.

Keywords: Open microchannel heat sink; Periodic stepped; Out of plane fluid mixing; Thermo-hydraulic performance; Numerical analysis

Vol. 45(2024), No. 3, 99–105; doi: 10.24425/ather.2024.151228

Cite this manuscript as: Bhandari, P., Vyas, B., Padalia, D., Ranakoti, L., Prajapati, Y.K., & Bangari, R.S. (2024). Comparative Thermo-hydraulic Analysis of Periodic Stepped Open Micro Pin-fin Heat Sink. *Archives of Thermodynamics*, 45(3), 99−105.

1. Introduction

The trend of miniaturization has led to the increased generation of heat flux in many engineering devices, such as electronic chips and micro electromechanical systems. It is certain that it will reach 10 000 kW/m^2 in the immediate future [1]. It is possible for such devices to fail permanently if heat generation is not properly managed. This quantity of heat cannot be removed

Nomenclature

A – area, mm^2
c_p – specific heat, J/(kg·K)
D_h – hydraulic diameter, mm
H – height, mm
k – thermal conductivity, W/(m·K)
L – length, mm
N – total number of pin fins
$\overline{\mathrm{Nu}}$ – average Nusselt number
Δp – pressure drop, Pa
q – heat flux, kW/m^2
Re – Reynolds number
T – temperature, K
$\overline{T_{bw}}$ – average bottom wall temperature, K
TPF – thermal performance factor
U – velocity, m/s
V – velocity matrix, m/s
W – width, mm

Greek symbols

μ – dynamic viscosity, Pa·s
ρ – density, kg/m^3

Subscripts and Superscripts

avg – average
b – bottom
bulk – bulk fluid
ch – channel
eff – effective
f – fin
in – inlet
l – liquid
o – base configuration
s – substrate
wl – solid liquid interface

Abbreviations and Acronyms

HS – heat sink
MCHS – microchannel heat sink
MEMS – micro-electromechanical system
MPFHS – micro pin fin heat sink
STEP – stepped
UO – uniform

by natural or forced air convection, and a better cooling system is necessary [2].

Micro heat pipes, jet impingement, thermoelectric, carbon nanotubes, spray cooling, and microchannels have proven capable of dissipating an enormous amount of heat [3, 4], and due to its ease of application and smaller coolant volume requirement, microchannel heat sinks (MCHS) have gained extensive popularity in the research fraternity.

Since Tuckerman and Pease [5] implemented microchannels for cooling electronic circuits, various approaches have been used to enhance the cooling performance. A number of external factors, such as vibrations, electric fields, magnetic fields, etc. are used to enhance the performance of MCHS in active techniques [6]. In passive techniques, the innovative geometry of the heat sink and various working fluids have been used to increase performance [7]. Working fluid modification such as nanofluids, phase change material slurries [8,9], and the use of multiphase approach [10] has been more extensively studied, while some innovative designs built into the microchannel are multilayer microchannels, the use of vortex generator in the microchannel, multiple bifurcation, pin-fin arrangement, etc. [6]. The main idea behind using these geometrical altercations is enhanced wetted surface area, i.e. convective area, and better fluid mixing.

Generally, micro pin-fin heat sink (MPFHS) is having pin fin height equivalent to the channel height and termed as closed MPFHS. Next, it was proposed to keep the fins' height lesser than the channel height to achieve the clearance. In order to improve thermal performance, the pin fin tip clearance should be between 20% and 25% of channel height [6]. The same range of tip clearance was also proven through experimental work [11]. It was observed that a larger tip clearance results in lesser convective area while a smaller tip clearance does offers better flow mixing. To further augment the heat transfer capacity, Bhandari and Prajapati [12, 13] opted for a stepped arrangement of MPFHS, replacing the uniform tip clearance arrangement. They found that the pin fin in step size of three rows has yielded better results compared to two and four pin fin rows. They also pointed out that increasing the tip clearance along the flow direction has a better performance than the decreasing pattern. Earlier the stepped arrangement was considered only along the microchannel length direction. To further increase the fluid mixing, Bhandari [14] opted for a stepped arrangement along both the microchannel length and microchannel width directions. The development of stepness in MPFHS is shown in Fig. 1.

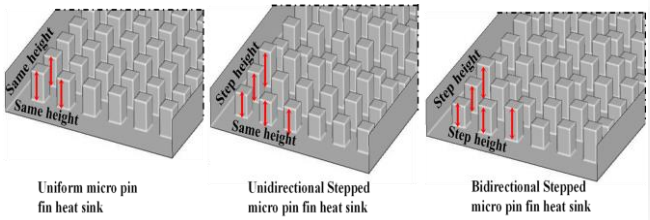

Fig. 1. Various cases of MPFHS.

Two dissimilar pin-fin arrangements, i.e. inline and staggered were often considered in MPFHS designs. An experimental comparison [15] revealed that staggered configurations possess greater heat transfer coefficients and friction factors compared to inline arrangements under similar flow rates and packaging densities. However, prevailing differences in performance diminish with the increasing packaging density. Keshavarz et al. [16] examined the performance of circular and drop shaped MPFHS having inline and staggered arrangements. The authors perceived that the staggered arrangement has a higher outlet temperature for lesser fin density, while the inline arrangement has more outlet temperature for moderate pin-fin density. However, for all pin-fin density configurations, the

staggered arrangement has a higher pressure drop compared to the inline arrangement. In recent work by Bhandari et al. [17], different pin fin shapes were analyzed. They found that four-side arrangements have the best performance among different cases. The fluid flow mixing is one of the important factors that affects the thermo-hydraulic performance [18].

The micro pin fin heat sink represents a crucial innovation with diverse applications across several domains [19−21]. Primarily, it plays a pivotal role in battery thermal management systems, ensuring the efficient dissipation of heat generated during charging and discharging processes. This is particularly relevant in the context of advancing battery technologies, where effective thermal control is imperative for enhancing overall performance and longevity. Moreover, the utilization of micro pin fin heat sinks extends to hydrogen storage systems, contributing to the optimal management of thermal conditions in the storage process. In the realm of solar photovoltaic (PV) technology, these heat sinks find application in cooling systems, addressing the challenge of excess heat accumulation during solar energy conversion [22−26]. Additionally, in electronics cooling, microchannel heat sinks play a vital role in addressing thermal challenges associated with modern, compact electronic devices, enhancing their reliability and longevity [27, 28]. This underscores the versatility of micro pin fin heat sinks in facilitating enhanced thermal regulation across diverse technological domains. Recent advancements in materials and design methodologies further underscore the ongoing development in this field, emphasizing the contemporary relevance of micro pin fin heat sinks in addressing evolving thermal management needs.

In the present work, the directionality of stepped MPFHS configurations has been numerically studied in two different fashions. The total of six different configurations have been compared on the basis of the average Nusselt number ($\overline{\mathrm{Nu}}$), pressure drop (Δp) and thermal performance factor (TPF). It is the primary objective of the existing work to investigate out-of-plane mixing in MPFHS.

2. Mathematical modelling

2.1. Heat sink geometry

A numerical analysis of different MPFHS configurations is carried out in the present work. The total of six MPSHS configurations were chosen, including three in inline arrangement and the others in staggered arrangement. All MPFHS geometrical constructions are as follows:

1) Uniform inline MPFHS (UO inline): In this configuration, pin fins have uniform height throughout the heat sink length and width. Pin fin height of 0.375 mm is kept in channel of height 0.5 mm. Further, fins are arranged in inline style. This configuration is kept as a base configuration to assess the total performance of modified sinks.
2) Uniform staggered MPFHS (UO stagerred): A staggered arrangement of pin-fins in this configuration is characterized by equal height and even spacing.
3) Three-stepped inline unidirectional MPFHS (3 step inline): The pin-fin height differs in three consecutive rows, i.e. along the channel length only.
4) Three-stepped staggered unidirectional MPFHS (3 step staggered): Similar configuration as described in (c) but arranged in staggered fashion.
5) Three-stepped inline bidirectional MPFHS (3 × 3 step inline): Pin-fin height variation takes place along both longitudinal direction and transverse direction in inline fashion.
6) Three-stepped staggered bidirectional MPFHS (3 × 3 step staggered): Similar to 5), but arranged in staggered fashion. The perspective view and top view of 3 × 3 step staggered configuration are depicted in Fig. 2.

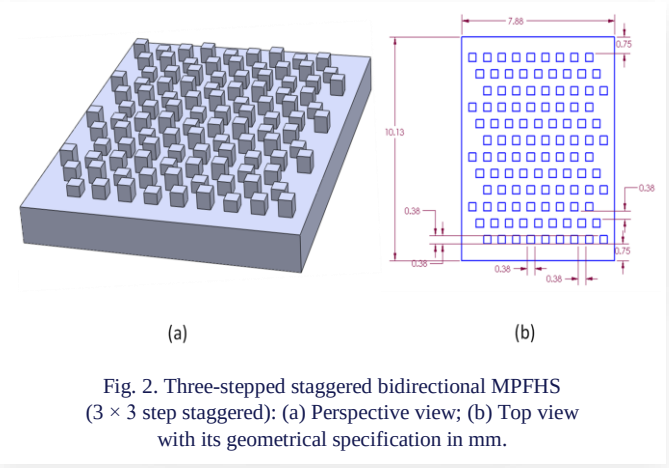

Fig. 2. Three-stepped staggered bidirectional MPFHS (3 × 3 step staggered): (a) Perspective view; (b) Top view with its geometrical specification in mm.

As depicted above, a 3-D model of the heat sinks (HS) has been designed to conduct the current simulation work. The footprint area and overall height of the considered cases are equal, namely 10.13 × 7.875 × 1.5 mm. In all cases, pin fins have a square cross section, which measures 0.375 mm by 0.375 mm. The pin fins are positioned differently across nine columns, each with twelve fins along the channel length. So, the total of 108 pin fins are there in every heat sink. The thorough geometrical specifications of the open MPFHS are tabulated in Table 1.

Table 1. MPFHS geometrical specifications.

Parameter	Value (mm)
MPFHS length (L)	10.125
MPFHS width (W)	7.875
Micro Fin height variation (H_f)	300−375−450
total height of Heat sink ($H = H_{ch}+H_b$)	1.5
Bottom wall thickness (H_b)	1
Footprint dimension of fin (W_f)	0.375×0.375
Pitch between two successive pin-fins along channel length	0.375
Pitch between two successive pin-fins along channel width	0.375
Total fins in each configuration	108

2.2. Solution methodology

Fluid flow and thermal characteristics of projected MPFHS cases under different flow rates were examined using the same operating conditions. Simulations were performed using ANSYS Fluent Version 18.0 commercial code to study the different

heat sink geometries, where geometry and meshing have been carried out in Workbench. Copper is the substrate of the heat sink, while liquid water is the coolant.

The steady-state basic governing equations, i.e. continuity Eq. (1), momentum Eq. (2), and energy Eq. (3) applicable for the fluid flow zone are:

$$\nabla \cdot \left(\rho_l \vec{V}\right) = 0, \tag{1}$$

$$\vec{V} \cdot \nabla\left(\rho_l \vec{V}\right) = -\nabla p + \nabla \cdot \left(\mu_l \nabla \vec{V}\right) + \rho_l \vec{g}, \tag{2}$$

$$\vec{V} \cdot \nabla\left(\rho_l \, c_{p,l} \nabla T_l\right) = \nabla \cdot \left(k_l \, \nabla T_l\right). \tag{3}$$

In the above equations $\vec{V}$ is the velocity matrix. The energy equation for solid substrates is:

$$\nabla \cdot \left(k_s \, \nabla T_s\right) = 0. \tag{4}$$

The thermo-physical properties of single phase liquid water vary with temperature. For more accurate results, the same has also been incorporated into the simulation. The variation of liquid thermophysical properties is a polynomial function of temperature [28, 30], while the substrate material has constant properties. Both properties of substrate and working fluid are listed in Table 2.

Table 2. Thermo-physical property of substrate material and working fluid.

Thermo-physical property	Copper	Working fluid (Water)
Density	8978 kg/m³	$\rho(T) = 765.33 + 1.8142\,T - 0.0035\,T^2$
Specific heat	381 J/(Kg·K)	$c_p(T) = 28070 - 281.7\,T + 1.25\,T^2 - (2.48\times10^{-3})\,T^3 + (1.857\times10^{-6})\,T^4$
Thermal conductivity	387.6 W/(m·K)	$k(T) = -0.5752 + (6.397\times10^{-3})\,T - (8.151\times10^{-6})\,T^2$
Viscosity	------	$\mu(T) = (9.67\times10^{-2}) - (8.207\times10^{-4})\,T + (2.344\times10^{-6})\,T^2 - (2.244\times10^{-9})\,T^3$

The pressure drop was evaluated as a pressure difference between the inlet and outlet. The Reynolds number (Re) was calculated based on the heat sink pin fin hydraulic diameter according to:

$$\mathrm{Re} = \frac{\rho u_{in} D_h}{\mu}. \tag{5}$$

Based on the expression below, the average Nusselt number $\overline{\mathrm{Nu}}$ has been calculated

$$\overline{\mathrm{Nu}} = \frac{hD_h}{k_l} = \frac{q_{eff} D_h}{(T_{avg,wl} - T_{bulk,l}) k_l}, \tag{6}$$

where, the area weighted average temperature of the heat sink's s-l interface is $T_{avg,wl}$. $T_{bulk,\,l}$ is the bulk volumetric working fluid temperature. As the wetted surface area is greater than the foot print area, the effective heat flux (q_{eff}) has been opted in $\overline{\mathrm{Nu}}$.

The effective heat flux is the heat flux applied on the interface and has been evaluated according to Eq. (7):

$$q_{eff} = \frac{A_{bw}}{A_{wl}}, \tag{7}$$

where A_{bw} and A_{wl} refer to the bottom wall surface area or foot-print area and the solid-liquid contact area of the heat sink, respectively. Regardless of the configuration, both areas remain the same.

2.3. Boundary conditions

In current numerical work, a uniform heat flux of 500 kW/m^2 has been applied. Previous studies [6,11] have shown that the heat flux has little influence on microchannel heat sink properties. So, only one heat flux condition has been studied. Except for the bottom wall, all outer walls are adiabatic. Working fluid with a temperature of 298 K was taken with inlet velocity varying from 0.1 to 0.4 m/s. Pressure–velocity coupling was based on the SIMPLE algorithm, and the equations were solved using the Gauss-Seidel iterative technique.

2.4. Grid independence

In order to prevent any errors resulting from coarse mesh, a grid independence test was performed before the broad analysis. The uniform inline (UO) MPFHS case having unit grid size variation was considered. In total, three different cases were simulated with Re = 110 and q = 500 kW/m^2. Table 3 enlists the complete details of the grid independence test. Two parameters – pressure drop (Δp) and average bottom wall temperature ($\bar{T}_{bw}$) were compared for a varying number of elements. It is observed that the differences in results for fine and very fine grid structures are less than 3%, but time taken for the simulation is doubled. So, the fine mesh type is chosen in simulation of all MPFHS cases.

Table 3. Grid independence test performed on uniform inline (UO) configuration for Re = 110.

Mesh Type	Number of elements	Pressure drop	Percentage variation
Coarse	256 849	430.846	--
Fine	1 994 845	458.4352	6.40%
Very Fine	4 674 104	467.694	2.01%
Mesh Type	**Average bottom wall temperature**	**Percentage variation**	
Coarse	335.6415	--	
Fine	333.6879	0.58%	
Very Fine	332.8774	0.24%	

2.5. Model validation

Using the methodologies of the proposed model, the work of Ali and Arshad [29] has been reproduced to validate the present numerical work. Identical boundary conditions and similar micro pin fin geometry have been used to predict the results. Under a heat flux of 37.2 kW/m^2, the bottom wall temperature was compared for different flow rates. Furthermore, it is compared

to the numerical work by Ambreen and Kim [30], as they have also used a similar geometry [29]. Based on the present simulation and the literatures, the predicted average bottom wall temperature is shown in Fig. 3. Observations of the present results show decent agreement with both literatures, with an extreme deviation of 5%.

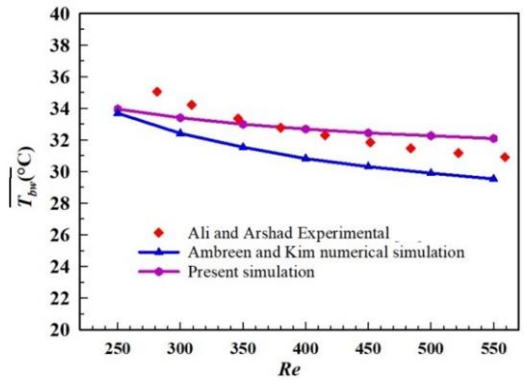

Fig. 3. Present numerical work validation with previous work [29−30].

3. Results and discussion

On simulating different heat sink configurations under heat flux of 500 kW/m^2, the parameters $\overline{\text{Nu}}$ and $\overline{T}_{bw}$ were evaluated for a series of Reynold numbers (Re). The variation of $\overline{\text{Nu}}$ with Re for different MPFHS cases has been shown in Fig. 4(a). As depicted in the figure, with a rise in Re, there is a rise in $\overline{\text{Nu}}$ value but with a decreasing rate. This can be attributed to an increase in entrance length. There is a distinct gap between inline and staggered configurations for all heat sinks, which is quite obvious due to enhanced fluid mixing. It is exciting to note that for inline configurations, 3 × 3 step MPFHS has shown top performance followed by 3 step inline and UO inline configuration. While, for staggered configurations, the differentiation is not clearly visible up to Re < 70, and afterwards, 3 step (staggered) configuration has yielded a better $\overline{\text{Nu}}$ value compared to 3 × 3 step (staggered) and UO (staggered) configuration. The observed conduct is entirely contingent on how the working fluid moves within the heat sink.

The influence of Reynolds number (Re) on the average temperature of the bottom wall ($\overline{T}_{bw}$) was illustrated in Fig. 4(b) for different cases of the heat sink.

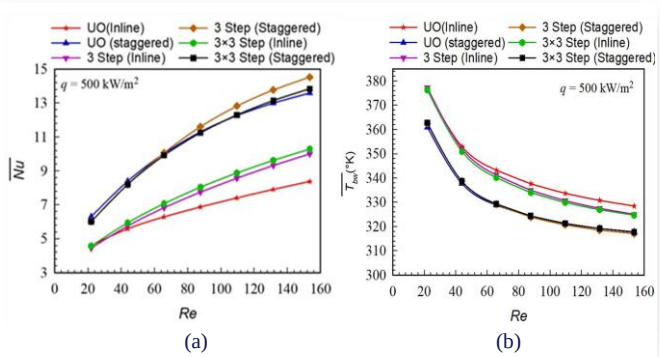

Fig. 4. Deviation of: (a) $\overline{\text{Nu}}$; (b) $\overline{T_{bw}}$ with Re for different MPFHS configuration.

The average bottom wall temperature $\overline{T}_{bw}$ is calculated as the area-weighted normal temperature of the lower wall of the heat sink where the heat flux is applied. Across various configurations of the heat sink, a consistent trend in the bottom wall temperature with respect to Reynolds number was observed. The general understanding is that as the Reynolds number increases, the coolant flow rate also increases, leading to more effective heat transfer from the heat sink and a decreased bottom wall heat sink temperature. A significant difference was observed between inline and staggered arrangements due to better fluid flow through the channel. Among all configurations, 3 step (staggered) configuration has shown the lowest value of $\overline{T}_{bw}$ for Re > 70 and for Re < 70; it is UO staggered configuration. This is due to a higher heat transfer rate in this case. It can be concluded that heat sink usage at low Reynold numbers is not justified as there is less heat transfer than.

The variation of Δp with Re for different MPFHS cases has been plotted in Fig. 5(a). It is recognized that as Re increases, there is a corresponding rise in the pressure drop (Δp) due to elevated flow resistance. Additionally, the gradient of the Δp curve becomes steeper as the Reynolds number value increases. Among different configurations, 3 step staggered configuration has yielded highest value of pressure drop, while UO inline configuration has shown the lowest Δp. This is due to increase in flow obstruction in the heat sink. The gap between inline and staggered arrangements kept on increasing with the rise in Re.

To further evaluate the design efficacy of heat sinks, the thermal performance factor (*TPF)* was plotted in Fig. 5(b). The enhancement of the average Nusselt number through diverse design modifications invariably involves incurring a pressure drop penalty [22]. Consequently, researchers have endeavored to assess the effectiveness of these designs using various parameters such as thermo-hydraulic performance, figure of merit, and coefficient of performance [22,31−33]. In the current study, the overall performance of various heat sink configurations was evaluated based on the parameter *TPF*. The thermal performance factor based on Eq. (8) has been calculated to assess the overall performance of MPFHS configurations.

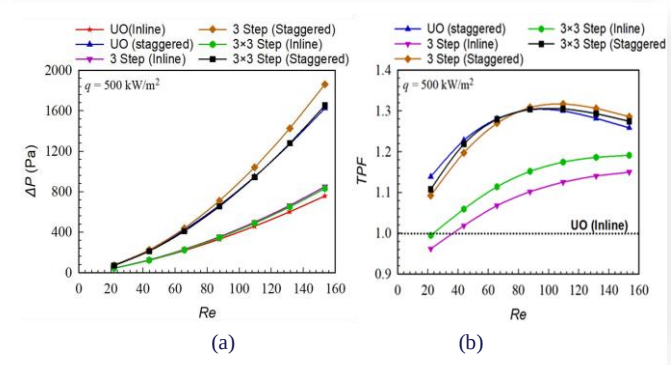

Fig. 5. Deviation of: (a) Δp; (b) *TPF* with Re.

All configurations have shown the *TPF* value > 1 except at lower values of Re. The design modifications have augmented thermal characteristics with the least pressure drop penalty. Among all configurations, UO stepped configuration has the

maximum value of *TPF* up to Re < 80, while for Re > 80, 3 step staggered configuration has depicted the highest *TPF* value.

The TPF value for UO stepped, 3 step staggered and 3 × 3 step staggered configurations of MPFHS has shown an increasing trend up to Re = 80 and afterwards it starts decreasing. This is attributed to exponential enhancement in pumping power at higher Re values. Whereas, the other configurations, i.e. 3 step inline and 3 × 3 step inline have shown an increasing slope with the increase in Reynolds number, and at higher Re values, the curves tend to flatten.

4. Conclusions

In current work, numerical relative analysis has been done for different configurations of open MPFHS. Mainly three design parameters (stepness, arrangement and directionality) are simulated and analysed using six different MPFHS configurations. Using single phase liquid water as a coolant and Cu as a substrate, present cases were compared for a range of Reynolds number and a heat flux of 500 kW/m^2. It can be concluded that stepness in pin fin configurations has yielded more augmentation in the inline arrangement rather than in the staggered arrangement. Furthermore, the stepped arrangement has less impact at low values of Reynolds number, i.e. for Re < 70, its influence kept on increasing with Re. Bi-directional pin fin height variation is beneficial only in the inline arrangement while has a negative impact on the staggered arrangement.

Acknowledgements

This work was supported by the K. R. Mangalam University, Gurugram, Haryana (India) through a Seed Research Grant (KRMU/ADMIN/SEED/2022-23/3493(B). The authors would like to express appreciation to the K. R. Mangalam University's Central Instrumentation Facility for their assistance in facilitating the research work.

References

[1] Lee, J., & Mudawar, I. (2009). Low-temperature two-phase micro-channel cooling for high-heat-flux thermal management of defense electronics. *IEEE Transactions on Components Packaging and Manufacturing Technology*, 32(2), 453–465. doi: 10.1109/ITHERM.2008.4544263

[2] Ahmed, H.E., Salman, B.H., Kherbeet, A.S., & Ahmed, M.I. (2018). Optimization of thermal design of heat sinks: A review. *International Journal of Heat and Mass Transfer*, 118, 129–153. doi: 1016/j.ijheatmasstransfer.2017.10.099

[3] Kandlikar, S.G., & Bapat, A.V. (2007). Evaluation of jet impingement, spray and microchannel chip cooling options for high heat flux removal. *Heat Transfer Engineering*, 28(11), 911–923. doi: 10.1080/01457630701421703

[4] Gururatana, S. (2012). Heat transfer augmentation for electronic cooling. *American Journal of Applied Sciences*, 9(3), 436–439. doi: 10.3844/ajassp.2012.436.439

[5] Tuckerman, D.B., & Pease, R.F.W. (1981). High-performance heat sinking for VLSI. *IEEE Electron Device Letters*, 2(5), 126–129. doi: 10.1109/EDL.1981.25367

[6] Bhandari, P., & Prajapati, Y.K. (2021). Thermal performance of open microchannel heat sink with variable pin fin height. *International Journal of Thermal Sciences*, 159, 106609. doi: 10.1016/j.ijthermalsci.2020.106609

[7] Bhandari, P., Singh, J., Kumar, K., & Ranakoti, L. (2022). A review on active techniques in microchannel heat sink for miniaturization problem in electronic industry. *Acta Innovations*, 45, 45-54. doi: 10.32933/ActaInnovations.45.4

[8] Kumar, N., Singh, P., Redhewal, A.K., & Bhandari, P. (2015). A review on nanofluids applications for heat transfer in microchannels. *Procedia Engineering*, 127, 1197–1202. doi: 10.1016/ j.proeng.2015.11.461

[9] Rajabifar, B. (2015). Enhancement of the performance of a double-layered microchannel heat sink using PCM slurry and nanofluid coolants. *International Journal of Heat and Mass Transfer*, 88, 627–635. doi: 10.1016/j.ijheatmasstransfer.2015.05.007

[10] Bhandari, P., & Prajapati, Y.K. (2017). Flow boiling instabilities in microchannels and their promising solutions – A review. *Experimental Thermal and Fluid Science*, 88, 576-593. doi: 10.1016/j.expthermflusci.2017.04.014

[11] Bhandari, P., & Prajapati, Y.K. (2022). Influences of tip clearance on flow and heat transfer characteristics of open-type micro pin fin heat sink. *International Journal of Thermal Sciences*, 179, 107714. doi: 10.1016/j.ijthermalsci.2021.107714

[12] Bhandari, P., & Prajapati, Y.K. (2021). Fluid flow and heat transfer behavior in distinct array of stepped micro pin fin heat sink. *Journal of Enhanced Heat Transfer*, 28(4), 31–61. doi: 10.1615/JEnhHeatTransf.2021037008

[13] Bhandari, P., & Prajapati, Y.K. (2020). Numerical analysis of different arrangement of square pin-fin microchannel heat sink. In B. Biswal, B. Sarkar, & P. Mahanta (Eds.), *Advances in Mechanical Engineering, Lecture Notes in Mechanical Engineering* (pp. 879–891). Singapore: Springer. doi: 10.1007/978-981-15-0124-1_79

[14] Bhandari, P. (2022). Numerical investigations on the effect of multi-dimensional steepness in open micro pin fin heat sink using single-phase liquid fluid flow. *International Communications in Heat and Mass Transfer*, 138, 106392. doi: 10.1016/j.icheatmasstransfer.2022.106392

[15] Wirtz, R., & Colban, D.M. (1996). Comparison of the cooling performance of staggered and in-line arrays of electronic packages. *Journal of Electronic Packaging, Transactions of the ASME*, 118, 27–30. doi: 10.1115/1.2792123

[16] Keshavarz, A., Lavasani, M., & Bayat, H. (2019). Numerical analysis of effect of nanofluid and fin distribution density on thermal and hydraulic performance of a heat sink with drop-shaped micro pin fins. *Journal of Thermal Analysis and Calorimetry*, 135(2), 1211–1228. doi: 10.1007/s10973-018-7711-z

[17] Bhandari, P., Padalia, D., Ranakoti, L., Khargotra, R., András, K., & Singh, T. (Year). Thermo-hydraulic investigation of open micro prism pin fin heat sink having varying prism sides. *Alexandria Engineering Journal*, 69, 457-468. doi: 10.1016/j.aej.2023.02.016

[18] Bhandari, P., Rawat, K.S., Prajapati, Y.K., Padalia, D., Ranakoti, L., Singh, T., & Joshi, K. (2023). Design modifications in micro pin fin configuration of microchannel heat sink for single-phase liquid flow: A review. *Journal of Energy Storage*, 66, 107548. doi: 10.1016/j.est.2023.107548

[19] Kumari, N., Alam, T., Ali, M.A., Yadav, A.S., Gupta, N.K., Siddiqui, M.I.H., Dobrota, D., & Rotaru, I.M. (2022). Numerical investigation on hydrothermal performance of microchannel heat sink with periodic spatial modification on sidewalls. *Micromachines*, 13, 1986. doi: 10.3390/mi13111986

[20] Saha, S., Alam, T., Siddiqui, M.I.H., Kumar, M., Ali, M.A., Gupta, N.K., & Dobrota, D. (2022). Analysis of microchannel heat sink of silicon material with right triangular groove on sidewall of passage. *Materials*, 15, 7020. doi: 10.3390/ma15197020

[21] Vatsa, A., Alam, T., Siddiqui, M.I.H., Ali, M.A., & Dobrotă, D. (2022). Performance of microchannel heat sink made of silicon material with the two-sided wedge. *Materials*, 15(14), 4740. doi: 10.3390/ma15144740

[22] Bhandari, P., Rawat, K.S., Prajapati, Y.K., Padalia, D., Ranakoti, L., & Singh, T. (2023). A review on design alteration in microchannel heat sink for augmented thermohydraulic performance. *Ain Shams Engineering Journal*, 15(2), 102417. doi: 10.1016/j.asej.2023.102417

[23] Dash, A.P., Prada, T., Alam, T., Siddiqui, M.I.H., Blecich, P., Kumar, M., Gupta, N.K., Ali, M.A., & Yadav, A.S. (2022). Impact on heat transfer rate due to an extended surface on the passage of microchannel using cylindrical ribs with varying sector angle. *Energies*, 15(21), 8191. doi: 10.3390/en15218191

[24] Bhandari, P., Prajapati, Y.K., & Uniyal, A. (2022). Influence of three-dimensionality effects on thermal hydraulic performance for stepped micro pin fin heat sink. *Meccanica*, 58, 2113-2129. doi: 10.1007/s11012-022-01534-4

[25] Bhandari, P., Kumar, K., Ranakoti, L., Bisht, V.S., Lila, M.K., Joshi, K., Raju, N.V.G., Sobti, R., & Jayahari, L. (2023). Thermo-hydraulic investigation of two stepped micro pin fin heat sink having variable step size. *E3S Web of Conferences*, 430, 01177. doi: 10.1051/e3sconf/202343001177

[26] Bhandari, P., Prajapati, Y.K., & Bisht, V.S. (2021). Heat transfer augmentation in micro pin fin heat sink using out of plane fluid mixing. In *Proceedings of the 26th National and 4th International ISHMT-ASTFE Heat and Mass Transfer Conference, IIT Madras* (pp. 1595–1600). Begel House Inc. doi: 10.1615/IHMTC-2021.2400

[27] Bhandari, P., & Prajapati, Y.K. (2021). Experimental investigation of variable tip clearance in square pin fin microchannel heat sink. In *Proceedings of the 26th National and 4th International ISHMT-ASTFE Heat and Mass Transfer Conference, IIT Madras* (pp. 1351–1356). Begel House Inc. doi: 10.1615/IHMTC-2021.2040

[28] Bhandari, P., & Prajapati, Y.K. (2021). Numerical study of fluid flow and heat transfer in stepped micro-pin–fin heat sink. In T. Prabu, P. Viswanathan, A. Agrawal, & J. Banerjee (Eds.), *Fluid Mechanics and Fluid Power, Lecture Notes in Mechanical Engineering* (pp. 373–381). Springer. doi: 10.1007/978-981-16-0698-4_40

[29] Ali, H.M., & Arshad, W. (2015). Thermal performance investigation of staggered and inline pin in heat sinks using water-based rutile and anatase TiO_2 nanofluids. *Energy Conversion and Management*, 106, 793–803. doi: 10.1016/j.enconman.2015.10.015

[30] Ambreen, T., & Kim, M. (2018). Effect of fin shape on the thermal performance of nanofluid-cooled micro pin-fin heat sinks. *International Journal of Heat and Mass Transfer*, 126, 245–256. doi: 10.1016/j.ijheatmasstransfer.2018.05.164

[31] Ghildyal, A., Bisht, V.S., Rawat, K.S., & Bhandari, P. (2023). Effect of D-shaped, reverse D-shaped and U-shaped turbulators in solar air heater on thermohydraulic performance. *Archives of Thermodynamics*, 44(2), 3-20. doi: 10.24425/ather.2023.146556

[32] Thapa, R.K., Bisht, V.S., Rawat, K., & Bhandari, P. (2023). Computational analysis of automobile radiator roughened with rib roughness. *Journal of Heat and Mass Transfer Research*, 9, 209-218. doi: 10.22075/jhmtr.2023.27617.1382

[33] Karmveer, Gupta, N.K., Alam, T., & Singh, H. (2022). An experimental study of thermohydraulic performance of solar air heater having multiple open trapezoidal rib roughnesses. *Heat Transfer*, 1–21. doi: 10.1080/08916152.2022.2139024

Co-published by
Institute of Fluid-Flow Machinery
Polish Academy of Sciences
Committee on Thermodynamics and Combustion
Polish Academy of Sciences

http://www.imp.gda.pl/archives-of-thermodynamics/

Analysis of entropy generation in unsteady flow of nanofluids past a convectively heated moving permeable cylindrical surface

Itumeleng Chokoe[a*], Oluwole Daniel Makinde[a], Ramotjaki Lucky Monaledi[a]

[a] Stellenbosch University, Faculty of Military Science, Private Bag X2, Saldanha, 7395, South Africa
*Corresponding author email: igchokoe21@gmail.com

Received: 12.10.2023; revised: 05.02.2024; accepted: 08.04.2024

Abstract

This paper investigates entropy generation rate in a temperature-dependent variable viscosity unsteady nanofluid flow past a convectively heated impulsively moving permeable cylindrical surface. The governing equations based on the modified Stokes first problem assumption are obtained and transformed using appropriate similarity variables into nonlinear ordinary differential equations. The numerical shooting method together with the Runge-Kutta Fehlberg integration scheme are employed to effectively solve the problem. The effects of related parameters on the nanofluid velocity, temperature, skin friction, Nusselt number, entropy generation rate and Bejan number are displayed graphically and quantitatively explained. It is found that an upsurge in nanoparticles volume fraction enhances the skin friction, Nusselt number, entropy production rate and the Bejan number.

Keywords: Entropy generation; Unsteady nanofluid flow; Permeable cylindrical surface; Numerical shooting method

Vol. 45(2024), No. 3, 107–113; doi: 10.24425/ather.2024.151221

Cite this manuscript as: Chokoe, I., Makinde, O.D., & Monaledi, R.L. (2024). Analysis of entropy generation in unsteady flow of nanofluids past a convectively heated moving permeable cylindrical surface. *Archives of Thermodynamics*, 45(3), 107–113.

1. Introduction

Impulsively moving permeable heated cylindrical surface in an infinite nanofluid medium has a wide range of applications in engineering and industries. Such applications can be found in the production of composite substances, rocket launching, torpedo, missile, fired bullet, the processing of porous materials, submarine, thermal insulation, fuel production, glass processing, and thermal solar panels. Theoretically speaking, this problem is closely related to an extension of Stokes first problem of unsteady boundary layer flow past a moving cylindrical surface, as discussed by Stokes [1]. Meanwhile, Choi [2] coined the term nanofluid to describe the engineered colloidal suspension of nanometer-sized particles in a base fluid. The novelty of nanofluids lies in their heat transfer enhancement capability. Consequently, studies related to the boundary layer flow of nanofluid past a moving surface have attracted global attention due to their useful applications in many industrial and engineering sectors, as highlighted by Kuznetsov and Nield [3] and others [4–7].

In addition, the generation of entropy is also important in ensuring the effective functioning of fluid flow and thermal systems. This concept takes into account the depletion of useful energy within the system, as explained by Bejan [8]. Therefore, reducing the entropy generation rate is important in optimizing

Nomenclature

Be – Bejan number $\left(\mathrm{Be}=\frac{1}{1+\frac{N_2}{N_1}}\right)$

Bi – thermal Biot number $\left(\mathrm{Bi}=\frac{h_f\sqrt{\nu_f t}}{k_f}\right)$

C_f – skin friction

C_p – specific heat at constant pressure, J/(kg s)

Ec – Eckert number

E_g – volumetric entropy generation

h – heat transfer coefficient, W/(m^{2}K)

k – fluid thermal conductivity, W/(m K)

N_1 – irreversibility because of heat transfer

N_2 – entropy generation because of viscous dissipation

N_s – dimensionless entropy production rate

Nu – Nusselt number $\left(\mathrm{Nu}=\frac{a(t)q_w}{k_f(T_f-T_\infty)}\right)$

Pr – Prandtl number $\left(\mathrm{Pr}=\frac{\mu_f C_{pf}}{k_f}\right)$

T – fluid temperature, K

Greek symbols

β – variable viscosity parameter

η – dimensionless gap between two-cylinder

θ – dimensionless temperature

λ – horizontal movement parameter

μ – fluid dynamic viscosity (ambient temperature), kg/(m s)

ρ – density of the fluid, kg/m^3

Abbreviations and Acronyms

ODE – ordinary differential equation

IVP – initial value problem

MHD – magnetohydrodynamic

the thermodynamic performance of many engineering flow processes. Woods [9] states that the first law of thermodynamics is essentially a statement about the conservation of energy, while the second law of thermodynamics highlights how entropy generation makes technological processes irreversible. Theoretical studies on the second law analysis of fluid flow with heat transfer characteristics was pioneered by Bejan [10]. Butt et al. [11] examined the impact of entropy generation on a boundary layer flow and heat transfer of nanofluid over a cylindrical surface. Rana and Shukla [12] analytically investigated the effects of entropy production on hydromagnetic boundary layer flow of nanofluid past a flat plate with aligned magnetic fields, ohmic heating and viscous dissipation. Freidoonimehr and Rahimi [13] reported an exact solution for hydromagnetic nanofluid flow and heat transfer with entropy generation past a permeable stretching/shrinking sheet surface. The problem of inherent irreversibility in nanofluid flow over a convectively heated radially stretching disk was numerically examined by Das et al. [14]. Khan et al [15], explored the theoretical analysis for thermal and mass transport of Maxwell nanofluid along permeable shrinking surface. The results showed that the thermal boundary layer thickness decreases with stronger suction influence, resulting in an increase in heat and mass transfer rate. Zahmatkesh et al. [16] analyzed the effects of entropy generation rate on stagnation point flow of nanofluid towards a permeable cylindrical surface with uniform surface suction and injection. Muhammad and Makinde [17] discussed the thermodynamics irreversibility in an unsteady hydromagnetic mixed convective flow over a porous vertical surface under the combined impact of thermal radiation and velocity slip. Das et al. [18] numerically investigated the unsteady hydromagnetic boundary layer flow and heat transfer of nanofluid past an impulsive convectively heated stretching sheet with heat source/sink. The entropy generation and heat transfer of dissipative mixed convection of nanofluid over a vertical cylindrical surface was explored by Agrawal and Kaswan [19]. Kumar and Mondal [20] studied the flow of heat-radiating hybrid nanofluids through a stretchable rotating disk with entropy generation in the presence of a magnetic field. The effects of entropy generation rate on MHD boundary layer flow of a radiating carbon nano-tubes nanofluid was numerically investigated by Mandal and Pal [21].

The aim of this study is to investigate the rate at which entropy is produced in a flow of nanofluids with temperature-dependent viscosity past a permeable cylindrical surface that is heated and moves impulsively in both vertical and horizontal directions. This research focused on using copper as nanoparticles and water as the base fluid. Previous research has not explored this particular geometry, so this study aims to fill that gap in the literature. Moreover, the inclusion of viscous and porous dissipation terms in the energy equation enables us to examine their effect on fluid flow and heat transfer. The relevant equations governing the system are derived and transformed into ordinary differential equations using appropriate similarity variables. To solve the model problem, a numerical procedure called shooting method is employed, which reformulates the original boundary value problem to a related initial value problem (IVPs) with its appropriate initial conditions, presented by Ha [22]. The resultant IVP is solved numerically using the Runge-Kutta-Fehlberg integration scheme method for solving linear ordinary differential equations. The results obtained show the impact of various parameters on velocity, temperature, skin friction, Nusselt number, entropy generation rate, and Bejan number. These results are presented graphically and discussed in detail.

2. Model problem

Consider an unsteady flow of a variable viscosity Cu-water nanofluid generated by the impulsive motion of a convectively heated permeable cylindrical surface. It is assumed that the cylindrical body is subjected to both horizontal and vertical motion as shown in Fig. 1 below.

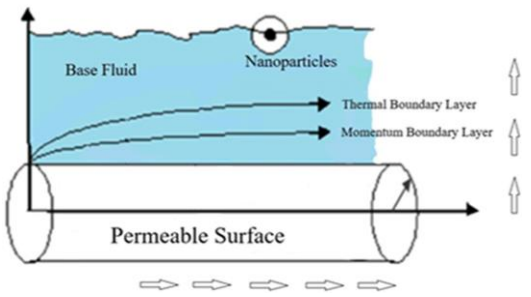

Fig. 1. Geometry of the problem.

The equations that govern the flow field in the boundary layer are based on the above assumptions, the conservation of mass, momentum, energy and entropy generation. Using the boundary layer approximation, as discussed by Munawar et al. [23], the governing equations of continuity, momentum, energy and entropy generation rate in cylindrical coordinates, may be written in the usual notation as [6,16,19,23]:

$$\frac{\partial u}{\partial z} = -\frac{V}{r}, \tag{1}$$

$$\frac{\partial u}{\partial t} + V\left(\frac{\partial u}{\partial r} - \frac{u}{r}\right) = \frac{1}{\rho_{nf} r}\frac{\partial}{\partial r}\left(r\mu_{nf}\frac{\partial u}{\partial r}\right), \tag{2}$$

$$\frac{\partial T}{\partial t} + V\frac{\partial T}{\partial r} = \frac{k_{nf}}{(\rho C_p)_{nf}}\frac{1}{r}\frac{\partial}{\partial r}\left(r\frac{\partial T}{\partial r}\right) + \frac{\mu_{nf}}{(\rho C_p)_{nf}}\left(\frac{\partial u}{\partial r}\right)^2, \tag{3}$$

$$E_g = \frac{k_{nf}}{(T_f - T_\infty)^2}\left(\frac{\partial T}{\partial r}\right)^2 + \frac{\mu_{nf}}{(T_f - T_\infty)}\left(\frac{\partial u}{\partial r}\right)^2, \tag{4}$$

subjected to the boundary conditions

– at $r = a(t)$:

$$u(a,t) = U_0,\ -k_f\frac{\partial T}{\partial r}(a,t) = h_f\left[T_f - T(a,t)\right], \tag{5a}$$

– as $r \to \infty$: $\quad u(\infty,t) \to U_\infty, \quad T(\infty,t) \to T_\infty,$ (5b)

where u is the velocity in the z-direction while V is the velocity in the r-direction of the cylindrical polar coordinates, r is the radius of the cylinder, z is the axial distance, t is the time, U_∞ is the free stream velocity, U_0 is the velocity of cylindrical surface impulsive motion, μ_{nf} – the nanofluid dynamic viscosity, ρ_{nf} – the nanofluid density, T is the temperature, k_{nf} is the conductivity of the nanofluid, $(\rho C_p)_{nf}$ – the specific heat capacitance of nanofluid, T_f is the hot fluid temperature at the surface, T_∞ is the free stream temperature, k_f – thermal conductivity of the base fluid, and h_f is the heat transfer coefficient. The physical properties of water together with copper nanoparticles are listed in Table 1 below.

Table 1. Nanoparticles and base fluid thermophysical properties [25,26].

Materials	ρ [kg/m³]	C_p [J/(kgK)]	k [W/(mK)]
Pure water	997.1	4179	0.613
Copper (Cu)	8933	385	401

2.1. Similarity transformation

The system of differential Equations (1)–(5) consists of coupled nonlinear equations. Specific feasible similarity transformations can be utilized to transform the nonlinear system of partial differential equations into a nonlinear system of ordinary differential equations to achieve such simplifications. The following similarity variables are taken into consideration:

$$\eta = \frac{r}{\sqrt{\nu_f t}} - s, \quad V = -c\sqrt{\frac{\nu_f}{t}}, \quad \theta(\xi) = \frac{T - T_\infty}{(T_f - T_\infty)}, \quad u = U_\infty F(\eta), \tag{6}$$

$$\beta = M\left(T_f - T_\infty\right), \quad \mu_{nf} = \frac{\mu_f e^{-M\left(T_f - T_\infty\right)}}{(1-\phi)^{2.5}}, \quad a(t) = s\sqrt{\nu_f t}\,.$$

By substituting Eq. (6) into Eqs. (1)–(5) we obtain the dimensionless ordinary differential equations:

$$F'' + \left[\frac{1}{\eta+s} - \beta\theta' + A_1A_2e^{\beta\theta}\left(\frac{(\eta+s)}{2} + c\right)\right]F' - \frac{cA_1A_2}{\eta+s}e^{\beta\theta}F = 0, \tag{7}$$

$$\theta'' + \left[\frac{1}{\eta+s} + \mathrm{Pr}A_4A_5\left(\frac{\eta+s}{2} + c\right)\right]\theta' + A_3A_4\mathrm{PrEc}e^{-\beta\theta}(F')^2 = 0, \tag{8}$$

$$N_s = \left(\frac{k_{nf}}{k_f}\right)(\theta')^2 + \frac{\mathrm{PrEc}e^{-\beta\theta}}{(1-\phi)^{2.5}}(F')^2 = 0, \tag{9}$$

subjected to the boundary conditions:

$$F(0) = \lambda, \qquad \theta'(0) = -\mathrm{Bi}\left(1 - \theta(0)\right), \qquad F(\infty) = 1, \qquad \theta(\infty) = 0. \tag{10}$$

The dimensionless parameters are defined as:

$$A_1 = \frac{\rho_{nf}}{\rho_f}, \quad A_2 = (1-\phi)^{2.5}, \quad A_3 = (1-\phi)^{-2.5}, \quad A_4 = \frac{k_f}{k_{nf}}, \quad A_5 = \frac{(\rho C_p)_{nf}}{(\rho C_p)_f}, \quad \lambda = \frac{U_0}{U_\infty}, \tag{11}$$

$$\mathrm{Pr} = \frac{\mu_f C_{pf}}{k_f}, \quad \mathrm{Bi} = \frac{h_f\sqrt{\nu_f t}}{k_f}, \quad \mathrm{Ec} = \frac{U_\infty^2}{(C_p)_f(T_f - T_\infty)}.$$

The physical parameters of interest influencing the flow system are ϕ which represents the nanofluid volume fraction, β representing the variable viscosity parameter of the nanofluid, s representing the vertical movement of the cylindrical surface; Pr is the base fluid Prandtl number (Pr = 6.2), which is a ratio of momentum diffusivity to thermal diffusivity, Ec is the Eckert number that defines a ratio of the advective mass transfer to the heat dissipation, λ is the horizontal movement of the model, $c > 0$ represents nanofluid suction and $c < 0$ is the nanofluid injection, N_s is the dimensionless entropy generation rate and Bi is the Biot number defined as the ratio of thermal resistance between the body and the surface of the body.

Other interesting engineering quantities are the coefficient of skin friction C_f, the Nusselt number Nu and the Bejan number Be, given by the following equations:

$$\mathrm{Re}_t C_f = \frac{e^{-\beta\theta(0)}F'(0)}{(1-\phi)^{2.5}}, \quad \mathrm{Nu} = -s\frac{k_{nf}}{k_f}\theta'(0), \quad \mathrm{Be} = \frac{1}{1+\Phi}, \tag{12}$$

where:

$$C_f = \frac{\tau_w}{\rho_f U_\infty^2}, \quad \mathrm{Nu} = \frac{a(t)q_w}{k_f(T_f - T_\infty)}, \quad \tau_w = \mu_{nf}\frac{\partial u}{\partial r}\Big|_{r=a(t)}, \quad q_w = -k_{nf}\frac{\partial T}{\partial r}\Big|_{r=a(t)}, \quad \mathrm{Re}_t = \frac{U_\infty\sqrt{\nu_f t}}{\nu_f}, \tag{13}$$

$$N_1 = \left(\frac{k_{nf}}{k_f}\right)(\theta')^2, \quad N_2 = \frac{\mathrm{PrEc}e^{-\beta\theta}}{(1-\phi)^{2.5}}(F')^2, \quad \Phi = \frac{N_2}{N_1},$$

and N_1 is the heat transfer irreversibility (HTI), N_2 is the fluid friction irreversibility (FFI), Φ is the irreversibility ratio, τ_w is the cylindrical surface shear stress, q_w is the dimensional heat flux, Re_t is the local Reynolds number.

For a constant viscosity convectional fluid flow past an impermeable stationary cylindrical surface, $\beta = c = \phi = \lambda = 0$ and $s = 1$. The model Eq. (7) is amenable to exact solution based on the boundary conditions in Eq. (10) and we obtain:

$$F(\eta) = \frac{E_i\left(\frac{(y+1)^2}{4}\right) - E_i\left(1,\ \frac{1}{4}\right)}{E_i\left(\frac{(\infty+1)^2}{4}\right) - E_i\left(1,\ \frac{1}{4}\right)}. \quad (14)$$

3. Numerical procedure

The shooting technique with the Runge-Kutta-Fehlberg integral scheme is a numerical method used to solve model equations. The dimensionless boundary value problem in the resulting Eqs. (7)–(8), is converted into an initial value problem (IVP) by letting:

$$x_1 = F(\eta), \quad x_2 = F'(\eta), \quad x_3 = \theta(\eta), \quad x_4 = \theta'(\eta) \quad (15)$$

and obtaining:

$$x_1{}' = x_2 \quad (16)$$

$$x_2{}' = \frac{cA_1A_2}{\eta+s} e^{\beta x_3} x_1 - \left[\frac{1}{\eta+S} - \beta x_4 + A_1A_2 e^{\beta x_3}\left(\frac{(\eta+s)}{2} + c\right)\right] x_2, \quad (17)$$

$$x_3{}' = x_4 \quad (18)$$

$$x_4{}' = -\left[\frac{1}{\eta+s} + P_r A_4 A_5\left(\frac{\eta+s}{2} + c\right)\right] x_4 - A_3A_4P_rE_c e^{-\beta x_3}(x_2)^2, \quad (19)$$

with the initial conditions:

$$x_1(0) = \lambda, \qquad x_2(0) = a_1, \quad (20a)$$

$$x_3(0) = a_2, \ x_4(0) = -Bi(1 - a_2). \quad (20b)$$

The initial values of a_1 and a_2 are guessed initially and successively obtained using the Newton-Raphson method. The numerical value is estimated using the shooting procedure. If these boundary conditions are not satisfied to the required accuracy, the procedure is repeated with a new set of initial conditions until the required accuracy is acquired or a limit to the iteration is reached [23]. The resultant IVP is solved numerically using any appropriate method for solving nonlinear ordinary differential equations (ODE). Then the subsequent system of a set of nonlinear ODEs is solved by using the Runge-Kutta-Fehlberg integration scheme.

4. Results and discussion

To fully understand the heat and mass transfer properties in the overall flow structure, numerical solutions showing the effect of emerging thermophysical parameters on the nanofluids, temperature profile, velocity profiles, skin friction, Nusselt number, entropy generation, and Bejan number are discussed, and graphically displayed in Figs. 2 to 15. To validate the accuracy of our numerical procedure, the numerical results obtained for velocity profiles are compared with their corresponding exact solutions displayed in Eq. (14). A very excellent agreement is achieved as depicted in Table 2. This undoubtedly attests to the accuracy of our numerical procedure and the obtained results. Table 2 presents a comparison between the exact and numerical results when $\beta = c = \phi = \lambda = 0$ and $s = 1$.

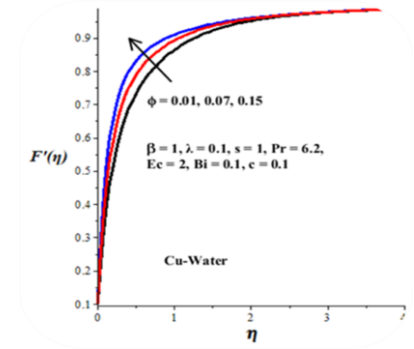

Fig. 2. The impact ϕ of on the velocity profile of Cu-water.

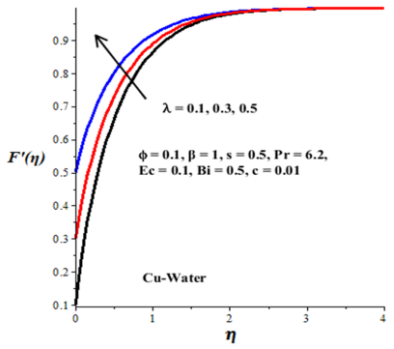

Fig. 3. The impact of λ on the velocity profile of Cu-water.

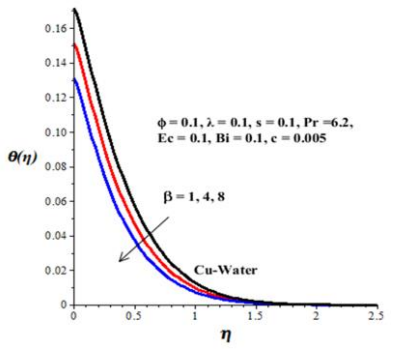

Fig. 4. The impact of β on the temperature profile of Cu-water.

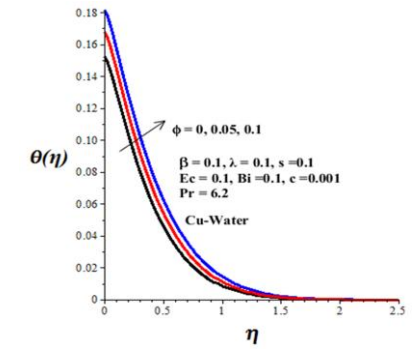

Fig. 5. The impact of ϕ on the temperature profile of Cu-water.

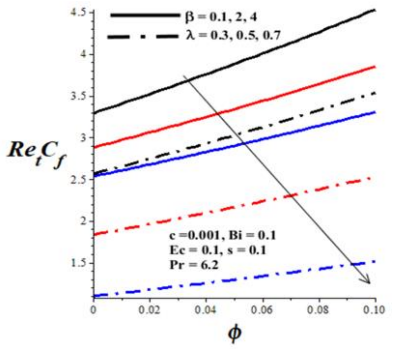

Fig. 6. The impact of ϕ, β and λ on the skin friction of Cu-water.

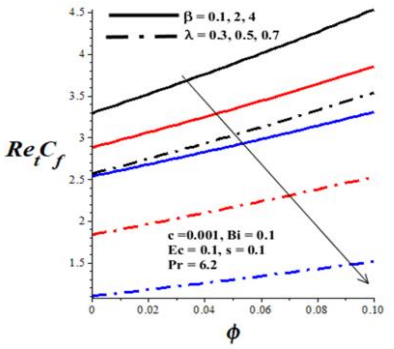

Fig. 7. The impact of s and c on the skin friction of Cu-water.

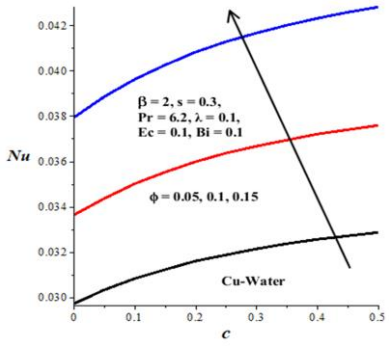

Fig. 8. The impact of ϕ with increase in c on the Nusselt number of Cu-water.

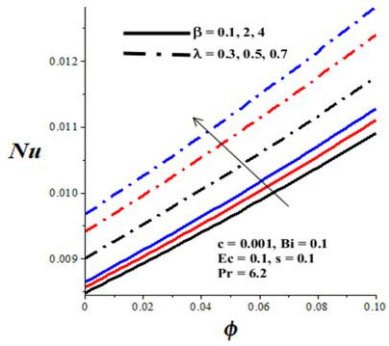

Fig. 9. The impact of β and λ with increase in ϕ on the Nusselt number of Cu-water

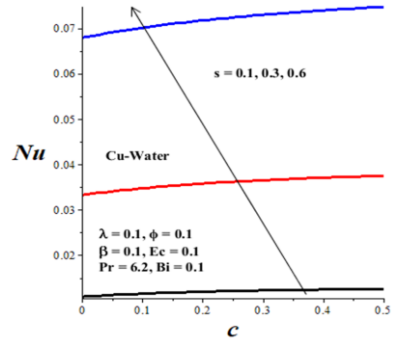

Fig. 10. The impact of s and c on the Nusselt number of Cu-water.

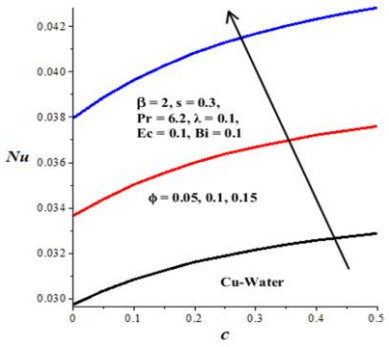

Fig. 11. The impact of ϕ and Ec on the entropy generation of Cu-water.

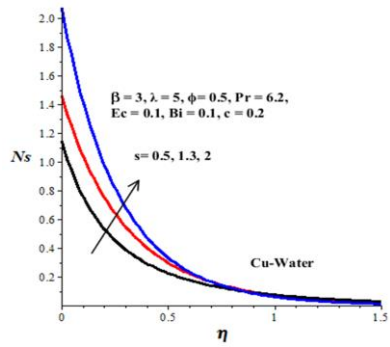

Fig. 12. The impact of s on the entropy generation of Cu-water.

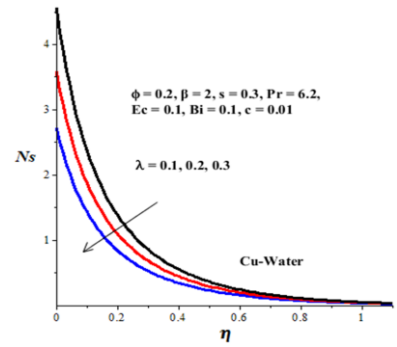

Fig. 13. The impact of λ on the entropy generation of Cu-water.

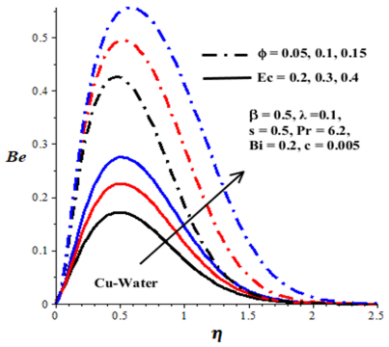

Fig. 14. The impact of ϕ and Ec on the Bejan number of Cu-water.

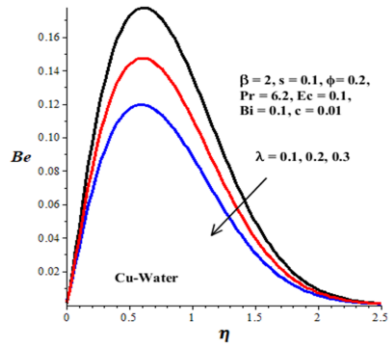

Fig. 15. The impact of λ on the Bejan number of Cu-water.

Table 1. Comparison between the exact and numerical results when $\beta = c = \phi = \lambda = 0$ and $s = 1$.

η	$F(\eta)$, Exact	$F(\eta)$, Numerical
0	0.00000000	0.00000000
0.1	0.13860827	0.13860830
0.3	0.36214317	0.36214315
0.6	0.59814367	0.59814374
1.0	0.78991900	0.78991910
2.0	0.96671207	0.96671210
4.0	0.99974099	0.99974100
∞	1.00000000	1.00000000

For this study, we used Cu-water nanofluid because of its high thermal conductivity. It can be observed from Fig. 2 that there is a decrease in the velocity boundary layer thickness with an increase in ϕ (nanoparticle volume fraction), this may be attributed to a slight increase in the base fluid viscosity due to the presence of nanoparticles. This improves the relationship between Cu-water nanofluid and the heated cylindrical surface resulting in the heat transfer rate enhancement. A similar trend is observed with the rise in the parameter values of λ (surface horizontal motion parameter). As the parameter λ rises, the velocity boundary layer thickness diminished, as a result, the interaction between the nanofluid and the heated cylindrical surface increases as depicted in Fig. 3. Figures 4–5 show the parameter effects on nanofluid thermal boundary layer thickness. A decline in thermal boundary layer thickness and nanofluid temperature are observed with an upsurge in β (variable viscosity parameter). This can be observed by considering Eq. (6), as β increases the viscosity of the nanofluid reduces causing the fluid to be less dense affecting the heat transfer rate of the system (see Fig. 4). In Fig. 5, the temperature profile shows that the temperature of the nanofluid is maximized on the cylindrical surface by heat convection, improving heat transfer and decreasing at a moderate rate towards the free flow temperature far from the surface,

hence an increase in the value of ϕ (nanoparticle volume fraction) escalates the thermal boundary layer thickness.

Figures 6–7 show the parameter effects on skin friction between the nanofluid and the heated surface. It's observed that skin friction lessened with an upsurge in β (variable viscosity parameter) and λ (surface horizontal motion parameter). This is evident that when the value of β amplifies, the nanofluid viscosity is lightened reducing the friction caused by the copper nanoparticle on the cylindrical surface. However, with a rise in the value of ϕ (nanoparticle volume fraction), the skin friction intensifies due to the increasing presence of copper nanoparticles in the base fluid as illustrated in Fig. 6. In Fig. 7, a decline in skin friction is observed with elevated values of s (surface vertical motion parameter) and c (nanofluid suction at the surface). The effects of parameters on the Nusselt number which represents the rate at which heat is transferred from the heated surface to the nanofluid are shown in Figs. 8–10. The heat transfer rate is enhanced with an upsurge in the parameter value of ϕ and c due to elevation in temperature gradient at the surface (see Fig. 8). Similar results are observed in Figs. 9–10 with the rise in β, λ and s. The impact on the entropy generation rate by various parameters is depicted in Figs. 11–13. In general, the entropy generation rate attained its maximum value at the heated cylindrical surface and steadily reduces to the value of zero far away from the heated surface at the free stream region. However, the entropy generation rate is enhanced with an upsurge in parameter values of ϕ, Ec and s (see Figs. 11–12) but lessened with a rise in parameter value of λ (see Fig. 13).

This implies that an intensification in the number of nanoparticles in the base fluid coupled with the vertical motion of the surface may boost the entropy production in the flow process, consequently, lessening the flow efficiency. Figures 14–15 illustrate the parameter effects on the Bejan number which is the ratio of heat transfer irreversibility to the total entropy production in the flow system. Generally, it is observed that the Bejan number is minimum with zero value both at the cylindrical heated surface and the free stream region, however, within the boundary layer region the maximum value of the Bejan number is achieved. This simply implies that only fluid friction irreversibility contributes to the entropy production rate both at the heated surface and free stream region while the effects of both heat transfer and fluid friction irreversibilities are heightened within the boundary layer region. It is fascinating to mention that an increase in ϕ and Ec enhances the impact of heat transfer irreversibility in the flow process (Fig. 14) while an increase in λ lessened the impact of heat transfer irreversibility as depicted in Fig. 15.

5. Conclusions

The inherent irreversibility in unsteady nanofluid flow past a convectively heated impulsively moving permeable cylindrical surface has been investigated. The governing nonlinear differential equations based on modified Stoke's first problem assumption were obtained and numerically examined via the shooting method coupled with the Runge-Kutta-Fehlberg integration scheme. The main results can be summarized as follows:

- The velocity boundary layer thickness is reduced with an upsurge in the nanoparticle's volume fraction and surface horizontal motion.
- The thermal boundary layer thickness diminished with a decrease in nanofluid viscosity but amplified with increasing nanoparticle volume fraction.
- The skin friction reduces with a rise in variable viscosity parameter, surface horizontal motion parameter, surface vertical motion parameter and nanofluid suction at the surface but escalates with a rise in nanoparticle volume fraction.
- The Nusselt number is enhanced with elevated values of nanoparticle volume fraction, variable viscosity parameter, nanofluid suction, horizontal and vertical motion parameters.
- Maximum entropy production occurred at the heated cylindrical surface while the minimum was observed at the free stream region. An increase in nanoparticle volume fraction, Eckert number and surface vertical motion strengthens the entropy generation rate while a rise in horizontal motion lessened it.
- The Bejan number at both the heated surface and free stream is zero, consequently, only fluid friction irreversibility ensued. Within the boundary layer region, both heat transfer irreversibility and fluid friction irreversibility occurred with Be > 0. The Bejan number is enhanced with a rise in nanoparticle volume fraction and Eckert number but lessened with the heated surface horizontal motion.

In conclusion, entropy generation minimization is an essential factor for the efficient performance of a nanofluid thermal boundary layer flow system. This can be achieved by appropriately regulating the values of the emerging thermophysical parameters in the system. This will innovatively boost the coolant effectiveness in various engineering and industrial applications. It is observed that there are strong interdependencies of the flow variables on entropy generation, and the investigation has potential utilizations in the thermal management and energy conversion systems. For future research, concepts such as magneto-hydrodynamic and concentration can be included to better modify the current model.

Acknowledgements

The authors appreciate the constructive improvement suggestions of the anonymous reviewers. This work is based on the research supported wholly/in part by the National Research Foundation of South Africa (Grant Numbers 150670).

References

[1] Stokes, G.G. (1851). On the effect of the internal friction of fluids on the motion of pendulums. *Transactions of the Cambridge Philosophical Society, Part II*, 9, 8–106. doi: 10.4236/ojapps.2014.43010

[2] Choi, S.U.S. (1995). Enhancing thermal conductivity of fluids with nanoparticles. *American Society of Mechanical Engineers. Fluids Engineering Division*, 66, 99–105.

[3] Kuznetsov, A.V., & Nield, D.A. (2010). Natural convection boundary layer flow of a nanofluid past a vertical plate. *International Journal of Thermal Sciences*, 49, 243–247. doi: 10.1016/j.ijthermalsci.2013.10.007

[4] Khan, W.A., & Pop, I. (2010). Boundary-layer flow of a nanofluid past a stretching sheet. *International Journal of Heat and Mass Transfer*, 53(11), 2477–2483. doi: 10.1016/j.ijheatmasstransfer.2010.01.032

[5] Abbas, Z., & Sheikh, M. (2017). Numerical study of homogeneous–heterogeneous reactions on stagnation point flow of ferrofluid with non-linear slip condition. *Chinese Journal of Chemical Engineering*, 25(1), 11–17. doi: 10.1016/j.cjche.2016.05.019

[6] Makinde, O.D., Khan, W., & Khan, Z. (2017). Stagnation point flow of MHD chemically reacting nanofluid over a stretching convective surface with slip and radiative heat. *Part E: Journal of Process Mechanical Engineering*, 231(4), 695–703. doi: 10.1177/0954408916629506

[7] Rashidi, M., Ganesh, N.V., Hakeem, A.A., & Ganga, B. (2014). Buoyancy effect on MHD flow of nanofluid over a stretching sheet in the presence of thermal radiation. *Journal of Molecular Liquids*, 198, 234–238. doi: 10.1016/j.molliq.2014.06.037

[8] Bejan, A. (1996). *Entropy Generation Minimization*. CRC Press: New York, NY, USA.

[9] Woods, L.C. (1975). *The Thermodynamics of Fluid Systems*. Oxford University Press: Oxford, UK.

[10] Bejan, A. (1980). Second law analysis in heat transfer. *Energy*, 5(8–9), 720–732. doi: 10.1016/0360-5442(80)90091-2

[11] Butt, A.S., Tufail, M.N., Ali, A., & Dar, A. (2019). Theoretical investigation of entropy generation effects in nanofluid flow over an inclined stretching cylinder. *International Journal of Exergy*, 28(2), 126–157. doi: 10.1504/IJEX.2019.097976

[12] Rana, P., & Shukla, N. (2018). Entropy generation analysis for non-similar analytical study of nanofluid flow and heat transfer under the influence of aligned magnetic field. *Alexandria Engineering Journal*, 57, 3299–3310. doi: 10.1016/j.aej.2017.12.007

[13] Freidoonimehr, F., & Rahimi, A.B. (2017). Exact solution of entropy generation for MHD nanofluid flow induced by a stretching/shrinking sheet with transpiration: dual solution. *Advances in Powder Technology*, 28(2), 671–685. doi: 10.1016/j.apt.2016.12.005

[14] Das, S., Chakraborty, S., Jana, R.N., & Makinde, O.D. (2016). Entropy analysis of nanofluid flow over a convectively heated radially stretching disk embedded in a porous medium. *Journal of Nanofluids*, 5(1), 48–58. doi: 10.1166/jon.2016.1184

[15] Khan, M.N., Ullah, N., & Nadeem, S. (2021). Transient flow of Maxwell Nanofluid Over a Shrinking Surface: Numerical Solutions and Stability Analysis. *Surfaces and Interfaces*, 22, 100829. doi: 10.1016/j.surfin.2020.100829

[16] Zahmatkesh, R., Mohammadiun, H., Mohammadiun, M., & Dibaei-Bonab, M.H. (2019). Investigation of entropy generation in nanofluid's axisymmetric stagnation flow over a cylinder with constant wall temperature and uniform surface suction-blowing. *Alexandria Engineering Journal*, 58, 1483–1498. doi: 10.1016/j.aej.2019.12.003

[17] Muhammad, A., & Makinde, O.D. (2019). Thermodynamics analysis of unsteady MHD mixed convection with slip and thermal radiation over a permeable surface. *Defect and Diffusion Forum*, 374, 29–46. doi: 10.4028/www.scientific.net/DDF.374.29

[18] Das, S., Chakraborty, S., Jana, R.N., & Makinde, O.D. (2015). Entropy analysis of unsteady magneto-nanofluid flow past accelerating stretching sheet with convective boundary condition. *Applied Mathematics and Mechanics*, 36(12), 1593–1610. doi: 10.1007/s10483-015-2003-6

[19] Agrawal, R., & Kaswan, P. (2022). Minimization of the entropy generation in MHD flow and heat transfer of nanofluid over a vertical cylinder under the influence of thermal radiation and slip condition. *Heat Transfer*, 51, 1790–1808. doi: 10.1002/htj.22375

[20] Kumar, M., & Mondal, P.K. (2022). Irreversibility analysis of hybrid nanofluid flow over a rotating disk: Effect of thermal radiation and magnetic field. *Colloids and Surfaces A: Physicochemical and Engineering Aspects*, 635, 128077. doi: 10.1016/j.colsurfa.2021.128077

[21] Mandal, G., & Pal, D. (2021). Entropy generation analysis of radiated magnetohydrodynamic flow of carbon nanotubes nanofluids with variable conductivity and diffusivity subjected to chemical reaction. *Journal of Nanofluids*, 10, 491–505. doi: 10.1166/jon.2021.1812

[22] Ha, S.N. (2001). A nonlinear shooting method for two-point boundary value problems. *International Journal of Computers and Mathematics with Applications*, 42(10), 1411–1420. doi: 10.1016/S0898-1221(01)00250-4

[23] Munawar, S., Saleem, N., & Mehmood, A. (2016). Entropy production in the flow over a swirling stretchable cylinder. *Thermophysics and Aeromechanics*, 23(3), 435–444. doi: 10.1134/S0869864316030136

[24] Osborne, M.R. (1969). On shooting methods for boundary value problems. *Journal of Mathematical Analysis and Applications*, 27(1). doi: 10.1137/0722018

[25] Das, K. (2013). Mixed convection stagnation point flow and heat transfer of Cu-water nanofluids towards a shrinking sheet. *Heat Transfer*, 42(3). doi: 10.1002/htj.21037

[26] Tie, P., Li, Q., & Xuan, Y. (2014). Heat transfer performance of Cu-water nanofluids in the jet arrays impingement cooling system. *International Journal of Thermal Sciences*, 77, 199–205. doi: 10.1016/j.ijthermalsci.2013.11.007

Co-published by
Institute of Fluid-Flow Machinery
Polish Academy of Sciences
Committee on Thermodynamics and Combustion
Polish Academy of Sciences

http://www.imp.gda.pl/archives-of-thermodynamics/

Unsteady flow of silica nanofluid over a stretching cylinder with effects of different shapes of nanoparticles and Joule heating

Ramzan Ali[a*], Azhar Iqbal[b], Tasawar Abbass[b], Touqeer Arshad[c], Azeem Shahzad[d]

[a]University of Doha for Science and Technology, College of General Education, Department of Mathematics, Doha, Qatar
[b]Department of Mathematics, University of Wah, Wah Cantt, 47040, Pakistan.
[c]Department of Basic Sciences, University of Engineering and Technology, Taxila,47050, Pakistan.
[d]Department of Mathematical Sciences, University of Engineering and Technology, Taxila,47050, Pakistan.
*Corresponding author email: ramzan.ali@udst.edu.qa

Received: 22.04.2024; revised: 09.06.2024; accepted: 01.07.2024

Abstract

Indeed, nanofluids have garnered significant interest in various fields due to their numerous advantages and potential applications. The appeal of SiO_2 nanofluid, in particular, lies in its low preparation cost, simple production process, controlled chemistry, environmental safety and its exceptional ability to be homogeneously suspended in the base fluid, which makes it a promising candidate for a variety of applications. In this study, we investigate the flow analysis of a water based silicon dioxide nanofluid, passing over a stretched cylinder while subjected to a continuous magnetic field, including Joule heating effects. The research involves the development of a mathematical model and the formulation of governing equations represented as partial differential equations. These equations are subsequently transformed into non-linear ordinary differential equations through suitable transformations. To obtain a numerical solution, the MATLAB bvp4c solver technique is employed. The study investigates the implications of dimensionless parameters on velocity and thermal distributions. It is observed that the velocity distribution $f'(\eta)$ exhibits a direct relationship with the volumetric fraction ϕ and an inverse relationship with the unsteadiness parameter S, the magnetic parameter M, and the temperature distribution $\theta(\eta)$ shows an enhancement for the increasing ϕ and M, as well as the Eckert number. However, it declines against S and the Prandtl number. The results for local Nusselt number and skin frictions are depicted in Tables.

Keywords: Joule heating; MHD flow; SiO_2-H_2O nanofluid

Vol. 45(2024), No. 3, 115–126; doi: 10.24425/ather.2024.151222

Cite this manuscript as: Ali, R., Iqbal, A., Abbass, T., Arshad, T., & Shahzad, A. (2024). Unsteady flow of silica nanofluid over a stretching cylinder with effects of different shapes of nanoparticles and Joule heating. *Archives of Thermodynamics*, 45(3), 115–126.

1. Introduction

Nanotechnology is the practice of manipulating matter at the atomic, molecular and supramolecular levels. It encompasses the design and construction of materials, electronics, and structures with dimensions ranging from 1–100 nm. Nanotechnology finds application in diverse fields, such as environmental research, medicine, materials science, energy, and electronics. By working on such a minute scale, nanotechnology opens up new possibilities and potential advancements in various industries and scientific disciplines. Nanofluids refer to colloidal suspensions of nanoparticles within a base fluid. These nanoparticles vary in size from one to one hundred nanometers and can consist of diverse materials, including metals, oxides, carbides, and carbon nanotubes. The base fluid can be water, oil or another type of liquid. The concept of nanofluids was first proposed in the early 1990s [1], and since then, extensive research has been conducted to explore their potential applications in heat transfer. The incorporation of nanoparticles in a nanofluid significantly enhances the thermal conductivity of the base fluid, leading to

Nomenclature

A – proportionality constant
B – magnetic field
b – dimensional constant
Ec – Eckert number
$f'(\eta)$ – dimensionless velocity distribution
K – slip parameter
m – shape factor
Nu – Nusselt number
Pr – Prandtl number
p – pressure
Re – Reynolds number
S – unsteadiness parameter
T – temperature, K
t – time, s
U – surface velocity, m/s

Greek symbols

α, α_1 – dimensional constants
η – similarity variable
$\theta(\eta)$ – dimensionless temperature distribution
ν – kinematic viscosity, m^2/s
μ – dynamic viscosity, Pa·s
ρ – density, kg/m^3
σ – electrical conductivity, S/m
ϕ – volumetric fraction of nanoparticles

Subscripts and Superscripts

f – fluid
nf – nanofluid
s – solid particles

Abbreviations and Acronyms

MHD – magnetohydrodynamics
ODEs – ordinary differential equations
PDEs – partial differential equations

improved heat transfer performance across a wide range of applications such as electronic cooling, using the thermophysical properties of SiO_2 in fuel cell [2], in a lithium ion battery, in the presence of phase change material [3]. Akram et al. [4] studied ethylene glycol based nanofluid for electroosmotic and peristaltic pumping, other authors employed similar nanofluidic models in solar heating systems [5,6], and Ma et al. [7] extended the models for nuclear power plants. Arif et al. [8] studied a fractional model of coupled stress Casson tri-hybrid nano-fluid using dissimilar shape nanoparticles. A mathematical simulations framework is proposed by Akram et al. [9] for peristaltic pumping of nanofluid due to induced magnetic field in a non-uniform channel.

A boundary layer refers to a slender layer of fluid that forms as the fluid flows adjacent to a solid surface. Various engineering disciplines, such as aerodynamics, heat transport and fluid mechanics, extensively depend on the understanding of boundary layer flow. This phenomenon plays a crucial role in generating drag force experienced by objects moving through a fluid, as well as facilitating the exchange of heat and mass between the fluid and the solid item. In 1970, Crane [10] conducted pioneering research on boundary layer flow over a stretching surface. He developed a mathematical model to describe the two-dimensional incompressible flow of a Newtonian fluid within the boundary layer. To solve this model, Crane utilized similarity transformations, a powerful mathematical technique commonly employed in fluid mechanics. Researchers have explored and analyzed the flow behaviour for diverse shapes and arrangements, contributing to a comprehensive understanding of this fundamental fluid mechanics phenomenon.

Ahmed et al. [11] proposed a framework of non-Newtonian fluid model of Jeffrey type over a stretching sheet for a convective heat transfer. Meanwhile, Hayat et al. [12] provided a numerical simulation for heat enhancement using copper nanoparticles dispersed in ethylene glycol, and furthermore studied similar models for diverse geometrical effects [13], and for the axisymmetric stagnation point flow [14] over an unsteady radial surface, the Casson fluid for convective squeeze flow [15]. Jabeen et al. [16] studied numerically Williamson nanofluid in the presence of viscous dissipation for bioconvection and energy activation and the case of inclined stretching cylinder was considered by Othman et al. [17]. In a series of articles, Hayat et al. [18] provided a comparative study of thin film flow for wide range of nanofluidic particles in stretchable surfaces [19] using boundary layer flows [20].

The study of Joule heating in nanofluids is a relatively recent area of research that began in the early 2000s with initial investigations into this phenomenon. Subsequently, there has been a notable increase in research efforts aimed at comprehending the effects of Joule heating on nanofluids. This extensive exploration has demonstrated that Joule heating has a significant impact on the performance of nanofluids, highlighting its importance as a critical factor to be taken into account in various nanofluid-related applications and systems. The effects of Joule heating are determined by the product of the magnetic parameter and the Eckert number. Numerous studies have been conducted to investigate the impact of Joule heating in magnetohydrodynamic (MHD) channels under various conditions. This research aims to understand the influence of Joule heating on fluid flow, heat transfer, and other relevant phenomena in MHD systems. Chen [21] explored the combined heat and mass transfer in buoyancy-induced MHD natural convection flow of an electrically conducting fluid down a vertical plate. Ohmic and viscous heating effects are taken into account. Cao et al. [22] provided an overview of the use of electrohydrodynamics and Joule heating effects of direct current (DC) and alternating current (AC) in microfluidic chips. Hayat et al. [23] analyzed MHD flow of Cu–water nanofluid over a stretched sheet. Joule heating and viscous dissipation effects are also studied in this article. Maraj et al. [24] examined effects of joule heating, partial slip and viscous dissipation on an electrically conducting Casson nanofluid flow, as well as heat and mass transfer, over a nonlinearly stretched horizontal sheet. For Khashi'ie et al. [25] the main objectives of the study are to achieve the duality of solutions and investigate the flow and heat transfer characteristics of the hybrid nanofluid while it passes over a shrinking cylinder with the inf-

luence of Joule heating. Naseem et al. [26] are considering an MHDs boundary layer flow past a flat plate with the inclusion of variable temperature, radiation, Joule heating and viscous dissipation effects. Rehman et al. [27] investigates the characteristics of the melting heat phenomenon in a Powell-Eyring fluid flow deformed by a linearly stretchable sheet near the stagnation point. To disclose the heat transport properties, the study incorporates quadratic thermal stratification, thermal radiation, viscous dissipation and Joule heating. Investigation of the unsteady stagnation-point flow performance of a TiO_2-$C_2H_6O_2$ nanofluid around a shrinking horizontal cylinder is carried out by Makhdoum et al. [28]. The research takes into consideration various influencing factors such as a magnetic field, Joule heating, viscous dissipation, nanoparticles aggregation and mass suction. These elements are studied to understand their effects on the boundary layer flow characteristics of the nanofluid. Raza et al. [29] accomplished analysis of a radiative Sutterby nanofluid flow containing suspended swimming microorganisms over a stretchable cylinder. The article extensively explored the effects of Brownian motion, thermophoresis, Joule heating and viscous dissipation in the presence of stratification parameters. Alsaedi et al. [30] described the bioconvective flow of Reiner-Rivlin liquid susceptible to motile microorganisms.

Wazawa and Nagai [31] analyzed and characterized several parameters in Joule heating due to ion currents through proteins channel, and Manshadi and Beskok [32] extended the idea of Joule heating induced transport in microchannels. In addition, Khan et al. [33] and Narayanaswamy et al. [34] provided a new framework on suppression of heat transfer in vertical tube through suspension of alumina nanoparticles using Joule heating and thermal radiations [35].

The peculiarity of this study lies in its examination of the unsteady flow of nanofluid around a stretchable cylinder. Additionally, the study investigates the influence of different shapes of SiO_2 nanoparticles on the nanofluid's flow behaviour and heat transfer, particularly with consideration of the Joule heating effect. In this study, the impact of relevant factors on the flow and temperature is graphically analyzed. Charts are employed to present the computational results of skin friction coefficient and heat transfer rate. The main findings are systematically organized and summarized in the conclusions section.

2. Physical and mathematical description of the problem

In this particular problem, the stretching of a cylinder with surface velocity along the z-axis

$$U(z,t) = \frac{bz}{1-\alpha_1 t}$$

induces an unsteady three-dimensional (3D) flow of nanofluid, as illustrated in Fig. 1. The temperature field is denoted by

$$T_s(z,t) = T_0 - T_r \frac{bz^2}{2\upsilon_f}(1-\alpha_1 t)^{-3/2},$$

with α_1 and b representing dimensional constants. Here, T_r is the reference temperature, T_0 is the ambient temperature, and υ_f is the kinematic viscosity of the base fluid. Additionally, a uniform magnetic field

$$B(t) = \frac{B_0}{(1-\alpha_1 t)^{1/2}},$$

is considered to act along the radial axis.

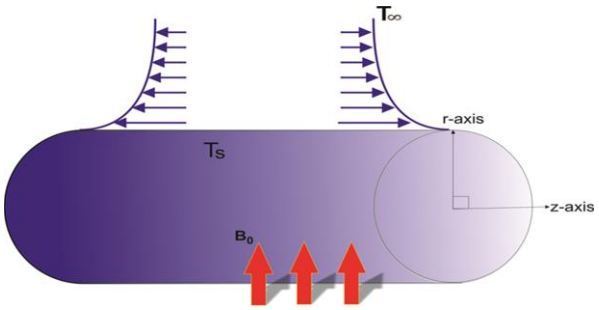

Fig. 1. Physical model of flow, the red-arrow showing the magnetic field along the r-axis.

According to the usual notation, governing equation of continuity, momentum, and thermal energy for the current study are expressed as follows:

$$\frac{\partial}{\partial r(ru)} + \frac{\partial}{\partial z(rw)} = 0, \tag{1}$$

$$\frac{\partial w}{\partial t} + u\frac{\partial w}{\partial r} + w\frac{\partial w}{\partial z} = \frac{\nu_{nf}}{r}\frac{\partial}{\partial r}\left(r\frac{\partial w}{\partial r}\right) - w\frac{\sigma_{nf}}{\rho_{nf}}\cdot\frac{B_0^2}{(1-\alpha_1 t)}, \tag{2}$$

$$\frac{\partial T}{\partial t} + u\frac{\partial T}{\partial r} + w\frac{\partial T}{\partial z} = \frac{\mu_{nf}}{\rho_{nf}C_p}\left(\frac{\partial w}{\partial r}\right)^2 + \alpha_{nf}\left[\frac{\partial^2 T}{\partial r^2} + \frac{1}{r}\left(\frac{\partial T}{\partial r}\right)\right] + \frac{\sigma_{nf}B_0^2}{[\![(\rho C]\!]_p)_{nf}}w^2. \tag{3}$$

Equations (1)–(3) are subjected to the boundary conditions

- at $r = R$: $w = U_w + Av_f\frac{\partial w}{\partial r}, \quad u = 0, \quad T_s = T$
- as $r \to \infty$: $w \to 0, \quad T \to T_0.$ (4)

Thermo-physical properties in Eqs. (1)–(4) are defined in Table 1.

Table 1. Thermophysical properties of nanofluid. [36, 37].

Properties	Mathematical form
Kinematic viscosity	$\nu_{nf} = \frac{\mu_{nf}}{\rho_{nf}}$,
Dynamic viscosity	$\mu_{nf} = \mu_f(1 + A_1\phi + A_2\phi^2)$
Electrical conductivity	$\sigma_{nf} = \sigma_f(1-\phi) + \phi\sigma_s$
Density	$\rho_{nf} = (1-\phi)\rho_f + \phi\rho_s$,
Heat capacity	$(\rho C_p)_{nf} = (1-\phi)(\rho C_p)_f + \phi(\rho C_p)_s$,
Diffusivity	$\alpha_{nf} = \frac{k_{nf}}{(\rho C_p)_{nf}}$,
Thermal conductivity	$\frac{k_{nf}}{k_f} = \left[\frac{k_{s+(m-1)k_f+(m-1)(k_s-k_f)\phi}}{k_{s+(m-1)k_f-(k_s-k_f)\phi}}\right]$.

In addition to the previously mentioned parameters, the equation involves the following coefficients and constants:

- A_1: viscosity enhancement coefficient,
- A_2: heat capacitance coefficient,
- h_f: convective heat transfer constant,
- A: proportionality constant,
- ϕ: volume fraction of SiO_2 in the nanofluid.

These coefficients and constants play crucial roles in determining the behaviour of the nanofluid flow and heat transfer, particularly in relation to the viscosity, heat capacitance, convective heat transfer and the influence of SiO_2 nanoparticles' volume fraction. Table 2 shows the values of the viscosity enhancement coefficient (A_1), heat capacitance coefficient (A_2) and form factors. Table 3 shows the thermo-physical characteristics of the fluid and silica.

Table 2. Impact of incipient factors on skin friction $-f''(0)$.

Ø	S	K	Ec	M	Pr	Sphere	Blade	Cylinder	Platelets
0.02	0.2	0.5	0.5	0.5	6.0	0.80163391	0.9346161	1.1070321	1.2776538
0.04	-	-	-	-	-	0.83543901	1.091834	1.7184747	1.9118712
0.06	-	-	-	-	-	0.87173587	1.2441354	2.5194769	2.64974
0.08		-	-	-	-	0.91043654	1.3928966	3.4801488	3.4868193
0.02	0.0	-	-	-	-	0.77531893	0.90361498	1.0700079	1.2347688
-	0.2	-	-	-	-	0.80163391	0.9346161	1.1070321	1.2776538
-	0.4	-	-	-	-	0.82600329	0.96339731	1.1415057	1.3176906
-	0.6	-	-	-	-	0.84861013	0.99016497	1.1736609	1.3551333
-	0.2	0.5	-	-	-	0.80163391	0.9346161	1.1070321	1.2776538
-	-	1.0	-	-	-	0.5654237	0.66873311	0.80475493	0.94130412
-	-	1.5	-	-	-	0.43972782	0.52414435	0.63632519	0.74994213
-	-	2.0	-	-	-	0.36083911	0.4322793	0.52780859	0.62514519
-	-	0.5	0.0	-	-	0.8016338	0.93461598	1.1070319	1.2776536
-	-	-	0.5	-	-	0.80163391	0.9346161	1.1070321	1.2776538
-	-	-	1.0	-	-	0.80163413	0.93461635	1.1070324	1.2776541
-	-	-	1.5	-	-	0.8016346	0.93461789	1.107034	1.2776558
-	-	-	0.5	0.0	-	0.70500522	0.82146064	0.97286742	1.1232813
-	-	-	-	0.5	-	0.80163391	0.9346161	1.1070321	1.2776538
-	-	-	-	1.0	-	0.87293338	1.0190793	1.2085495	1.3959192
-	-	-	-	1.5	-	0.92945001	1.0865073	1.2902392	1.4917594
-	-	-	-	0.5	4.0	0.8016346	0.93461788	1.107034	1.2776557
-	-	-	-	-	6.0	0.80163391	0.9346161	1.1070321	1.2776538
-	-	-	-	-	8.0	0.80163374	0.93461591	1.1070319	1.2776536
-	-	-	-	-	10.0	0.80163371	0.93461588	1.1070319	1.2776535

Table 3. Impact of emerging parameters on local Nusselt number $-\theta'(0)$.

Ø	S	K	Ec	M	Pr	Sphere	Blade	Cylinder	Platelets
0.02	0.2	0.5	0.5	0.5	6.0	2.9465264	2.9790597	3.0000152	3.0117782
0.04	-	-	-	-	-	2.961509	3.0129846	3.0235016	3.0148118
0.06	-	-	-	-	-	2.9761148	3.0383966	2.9788285	2.9663797
0.08		-	-	-	-	2.9902525	3.0580802	2.8791404	2.8805444
0.02	0.0	-	-	-	-	2.7168342	2.755958	2.78315	2.7987929
-	0.2	-	-	-	-	2.9465264	2.9790597	3.0000152	3.0117782
-	0.4	-	-	-	-	3.162634	3.1899354	3.2055882	3.2138224
-	0.6	-	-	-	-	3.3671808	3.3902631	3.4014138	3.406517
-	0.2	0.5	-	-	-	2.9465264	2.9790597	3.0000152	3.0117782
-	-	1.0	-	-	-	2.7083412	2.7588335	2.8024725	2.8350076
-	-	1.5	-	-	-	2.5314231	2.5880426	2.6408211	2.6826098
-	-	2.0	-	-	-	2.3972012	2.4554346	2.5117424	2.557684
-	-	0.5	0.0	-	-	3.1842384	3.2548878	3.3231226	3.3800661
-	-	-	0.5	-	-	2.9465264	2.9790597	3.0000152	3.0117782
-	-	-	1.0	-	-	2.7088149	2.7032319	2.6769078	2.6434903
-	-	-	1.5	-	-	2.4711049	2.427418	2.3538109	2.2752103
-	-	-	0.5	0.0	-	3.0451521	3.0664606	3.075619	3.0781856
-	-	-	-	0.5	-	2.9465264	2.9790597	3.0000152	3.0117782
-	-	-	-	1.0	-	2.864198	2.9050168	2.9347271	2.9532537
-	-	-	-	1.5	-	2.7932117	2.8406537	2.877529	2.9016253
-	-	-	-	0.5	4.0	2.4022243	2.4339983	2.4567606	2.4710008
-	-	-	-	-	6.0	2.9465264	2.9790597	3.0000152	3.0117782
-	-	-	-	-	8.0	3.4030649	3.4360023	3.4552401	3.4647965
-	-	-	-	-	10.0	3.8038222	3.8370168	3.8546711	3.862244

$$\Psi = (Uvz)^{1/2} R f(\eta), \tag{5a}$$

$$\eta = \frac{r^2 - R^2}{2R}\left(\frac{U}{vz}\right)^{1/2} \tag{5b}$$

$$\theta(\eta) = \frac{T - T_o}{-T_r\left[\frac{bz^2}{2v}\right][1-\alpha_1 t]^{-3/2}}. \tag{5c}$$

In this context, Ψ represents the stream function, while u and w denote the velocity components that satisfy the continuity

equation. The velocity components can be expressed as follows:

$$u = \frac{-1}{r}\frac{\partial \Psi}{\partial z} = \frac{-R}{r}\left(\frac{bv}{1-\alpha_1 t}\right)^{1/2} f(\eta), \tag{6a}$$

$$w = \frac{1}{r}\frac{\partial \Psi}{\partial r} = \frac{bz}{(1-\alpha_1 t)} f'. \tag{6b}$$

Here, u and w are the axial and radial velocity components, respectively, and they are related to the stream function Ψ in such a way that the continuity Eq. (1) remains satisfied.

So by using Eq. (5) and Eq. (6) we have:

$$[1+2C\eta]\epsilon_1 f''' + 2C\epsilon_1 f'' - [\epsilon_3 M + S]f' - \frac{\eta}{2}Sf'' + \\ + ff'' - (f')^2 = 0, \tag{7}$$

$$[1+2C\eta]\theta'' + 2C\theta' + \frac{\Pr}{\epsilon_2}[f\theta' - 2f'\theta - \frac{s}{2}(3\theta + \eta\theta') + \\ + \mathrm{Ec}\,\epsilon_1(1+2C\eta)(f'')^2] + \frac{\epsilon_1 M\,\mathrm{Ec}\,\Pr}{\epsilon_2}(f')^2 = 0, \tag{8}$$

and boundary conditions are:

$$f'(\infty) = 0, \qquad f'(0) = 1 + kf''(0), \\ \theta(0) = 1, \qquad \theta(\infty) = 0, \tag{9}$$

where the Eckert number, curvature parameter, Prandtl number, unsteadiness parameter, magnetic parameter and slip parameter, respectively, are defined as:

$$\mathrm{Ec} = \frac{U^2}{C_p \Delta T}, \qquad C = \sqrt{\frac{(1-\alpha_1 t)\nu_f}{bR^2}}, \qquad \Pr = \frac{\nu_f (\rho C_p)_f}{K_f},$$

$$S = \frac{\alpha_1}{b}, \qquad M = \frac{\sigma_f B_o^2}{\rho_f b}, \qquad K = \mathrm{A}\left[\frac{\nu_f U_w}{z}\right]^{1/2},$$

where

$$\epsilon_1 = \frac{1+\phi A_1 + \phi^2 A_2}{1-\phi+\phi\left(\frac{\rho_s}{\rho_f}\right)}, \qquad \epsilon_2 = \frac{\frac{k_{nf}}{k_f}}{1-\phi+\frac{\phi(\rho C_p)_s}{(\rho C_p)_f}}, \tag{10a}$$

$$\epsilon_3 = \frac{1-\phi+\phi\left(\frac{\sigma_s}{\sigma_f}\right)}{1-\phi+\phi\left(\frac{\rho_s}{\rho_f}\right)}, \qquad \epsilon_4 = \frac{1-\phi+\phi\left(\frac{\sigma_s}{\sigma_f}\right)}{1-\phi+\frac{\phi(\rho C_p)_s}{(\rho C_p)_f}}, \tag{10b}$$

where ϵ_i, $i = 1, 2, 3, 4$, are constants.

The values of Cf and Nu provide valuable insights into the flow and heat transfer characteristics of the nanofluid around the cylinder, and are defined as:

$$Cf = \frac{T_w}{\rho_f {U_w}^2}, \qquad \text{with} \qquad T_w = \mu_{nf}\left[\frac{\partial w}{\partial r}\right]_{r=R},$$

$$\mathrm{Nu} = \frac{r q_w}{K_f(T_s - T_o)}, \qquad \text{with} \qquad q_w = -K_{nf}\left[\frac{\partial T}{\partial r}\right]_{r=R}.$$

They take the dimensionless form as:

$$\mathrm{Re}^{\frac{1}{2}} C_f = (1 + \phi A_1 + \phi^2 A_2) f''(0), \tag{11}$$

and

$$\mathrm{Re}^{\frac{-1}{2}} N_u = -\frac{k_{nf}}{k_f}\theta'(0), \tag{12}$$

where the Reynolds number is defined as $\mathrm{Re} = \frac{Uz}{\nu}$.

3. Numerical procedure

The renowned and efficient BVP4C method in MATLAB is employed to numerically solve the reduced nonlinear system of ordinary differential equations (ODEs) (7) and (8) along with the given boundary conditions (BC) (9). To facilitate the numerical solution, these nonlinear ODEs are converted into a system of first-order ODEs, and the boundary conditions are substituted with appropriate initial conditions by tagging the variables as such:

$$(f,\ f' = \mathrm{y}_1',\ f'' = \mathrm{y}_2',\ \theta,\ \mathrm{y}_4' = \theta') = (\mathrm{y}_1,\ \mathrm{y}_2,\ \mathrm{y}_3,\ \mathrm{y}_4,\ \mathrm{y}_5),$$

so Eqs. (7) and (8) in program's algorithm take the form:

$$f''' = \frac{1}{\epsilon_1(1+2Ct)}\,(-2\epsilon_1 C\mathrm{y}(3) + (\epsilon_3 M + S)\mathrm{y}(2) + \\ + \frac{S\eta\mathrm{y}(3)}{2} - \mathrm{y}(1)\mathrm{y}(3) + \mathrm{y}(2)^2),$$

and

$$\theta'' = \frac{1}{1+2\eta C}(-2C\mathrm{y}(5) - \frac{\Pr}{\epsilon_2}(\mathrm{y}(1)\mathrm{y}(5) - 2\mathrm{y}(2)\mathrm{y}(4) - \\ + \frac{S}{2}(3\mathrm{y}(4) + \eta\mathrm{y}(5)) + Ec\epsilon_1(1+2C\eta)\mathrm{y}(3)^2) + \\ + \frac{\epsilon_1 M\,\mathrm{Ec}\,\Pr}{\epsilon_2}\big(y(2)\big)^2),$$

with corresponding boundary conditions:

$$\mathrm{y}_2(B) = 0, \qquad \mathrm{y}_2(0) = 1 + k\mathrm{y}_3(0), \\ \mathrm{y}_4(0) = 1, \qquad \mathrm{y}_4(B) = 0.$$

4. Results and discussion

This section investigates the impact of emerging physical parameters on numerically calculated velocity and temperature profiles. It looks into the effects of numerous embedding variables on dimensionless velocity and temperature distributions, such as particle concentration, magnetic parameter (M) and Eckert number (Ec). The study intends to obtain insight into how these elements impact the flow and thermal behaviour of the system by analysing them. Furthermore, the study investigates the influence of these values on the skin friction coefficient and Nusselt numbers. The data are given in the form of graphs and charts, which provide a visual representation of the results for easier understanding and interpretation.

4.1. Velocity profile

Figures 2 to 6 show how the $f'(\eta)$ gets affected by variation of the volumetric fraction, slip parameter K, unsteadiness parameter S and magnetic parameter M. Figures 2a–2d demonstrate that as the volume fraction value increases, there is also a corresponding increase in velocity.

This phenomenon is attributed to the rise in dynamic viscosity and momentum diffusion. In Figs. 3a–3d, an inverse relationship is observed between the velocity and increasing values of K. The reason behind this phenomenon is that an increase in K indicates more surface irregularity, which consequently leads to a reduction in velocity at the surface area.

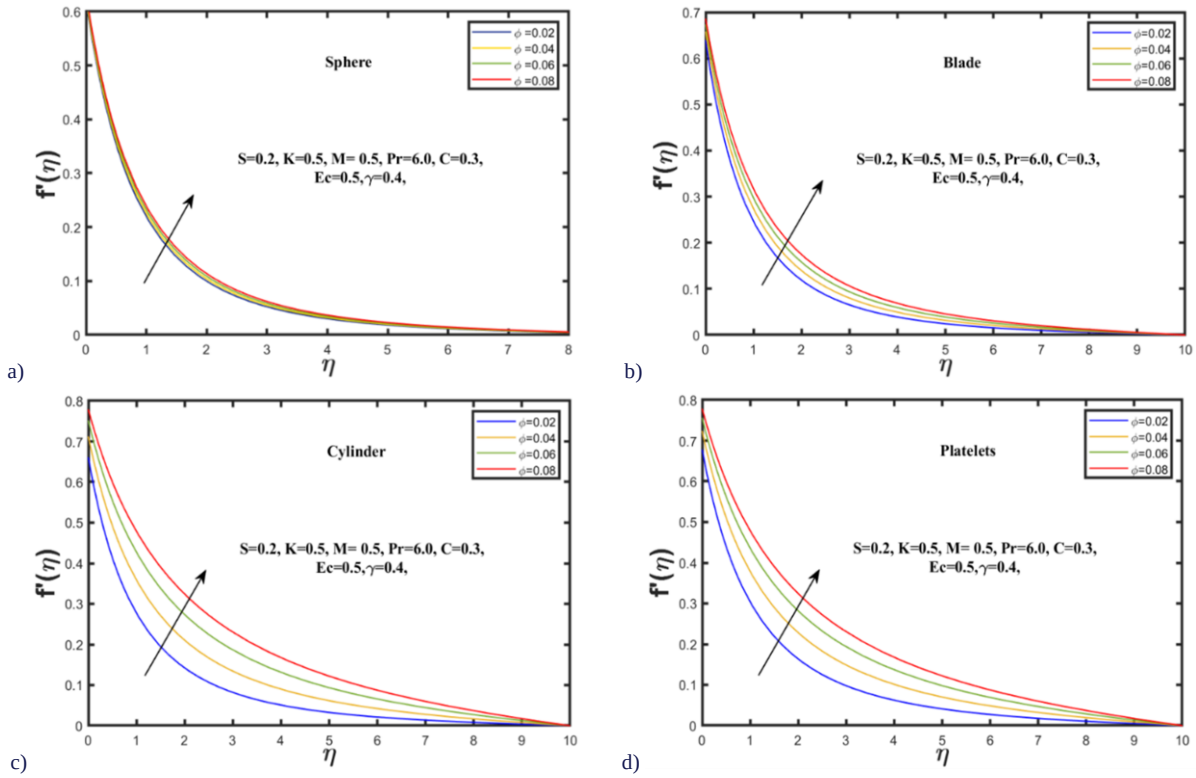

Fig. 2. Impact of ϕ on $f'(\eta)$: a) sphere, b) blade, c) cylinder, d) platelets.

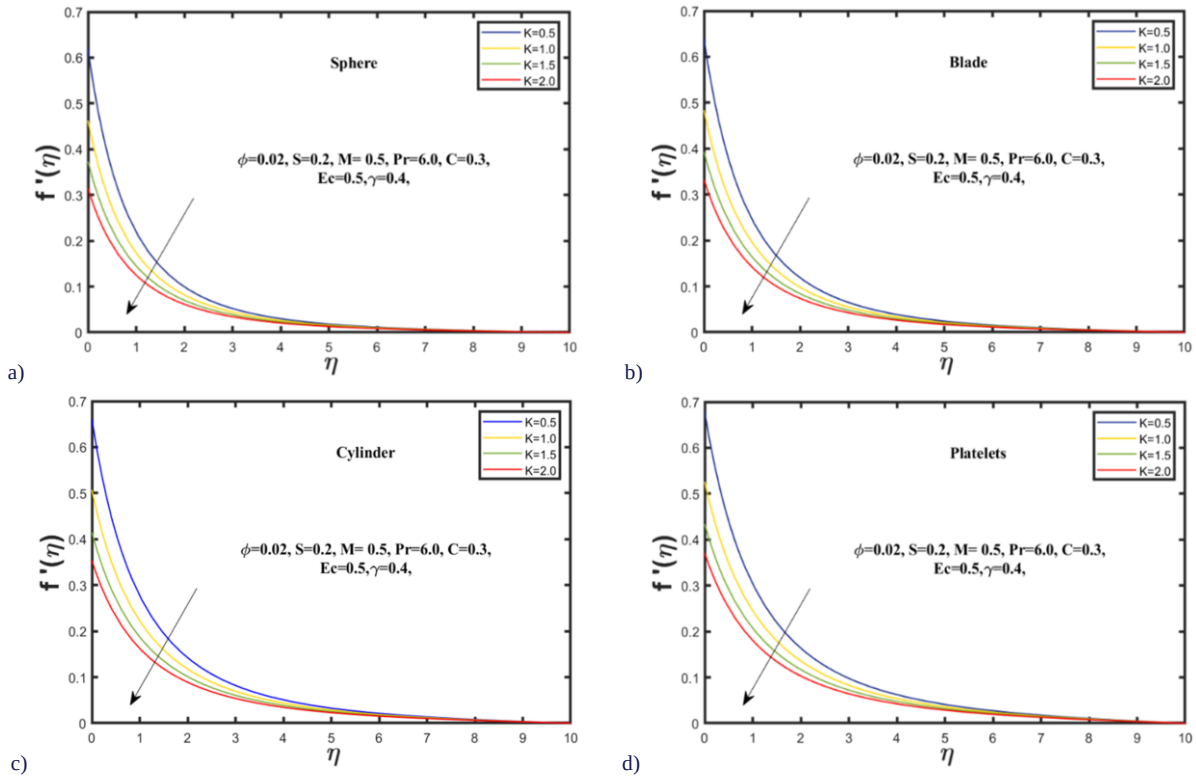

Fig. 3. Impact of K on $f'(\eta)$: a) sphere, b) blade, c) cylinder, d) platelets.

Figures 4a–4d illustrate the relationship between the unsteadiness parameter and velocity. It indicates that the velocity of the nanofluid decreases with an increase in the unsteadiness parameter. This can be attributed to the stretching of the cylinder, which reduces the boundary layer thickness associated with momentum, leading to a decrease in velocity with the unsteady-

ness parameter *S*.

Figures 5a–5d display the impact of the magnetic parameter on the velocity profile. The results reveal that the velocity decreases with increasing values of *M*. This phenomenon can be attributed to the rise in Lorentz force, which creates resistive forces between the layers of nanofluid, leading to a reduction in velocity as the magnetic parameter (*M*) is enhanced.

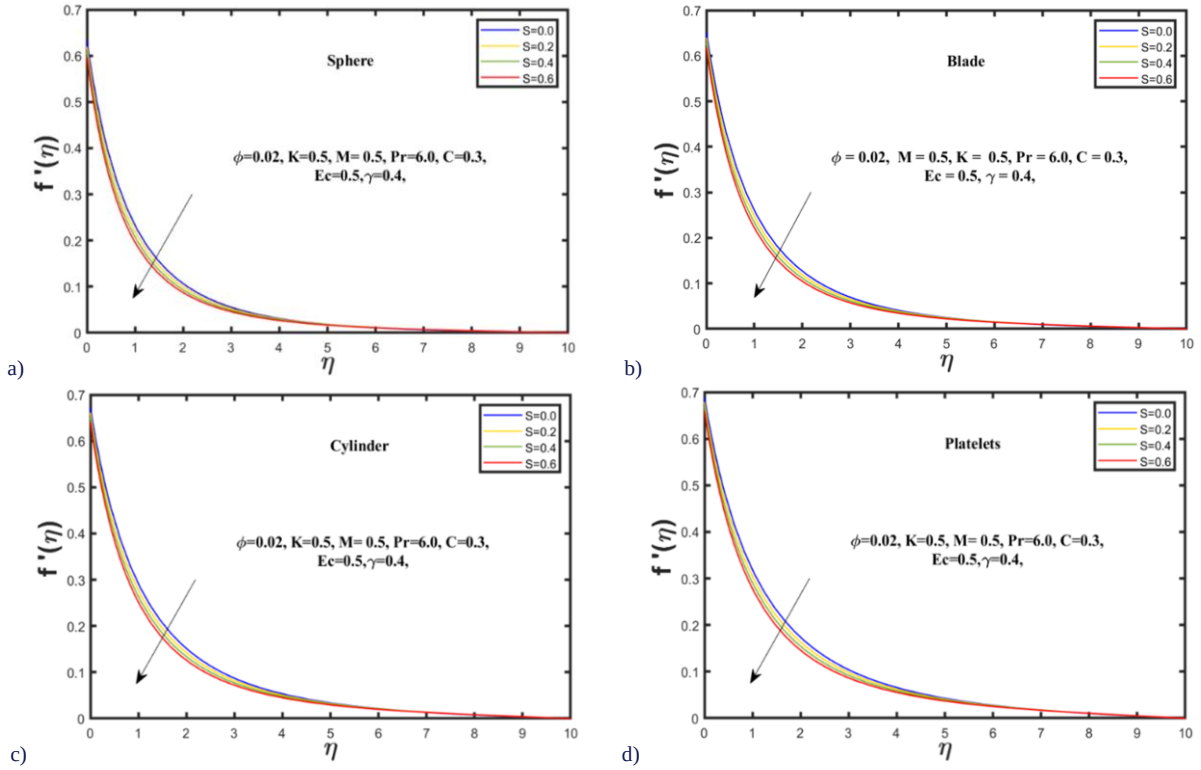

Fig. 4. Impact of *S* on *f* '(*η*): a) sphere, b) blade, c) cylinder, d) platelets.

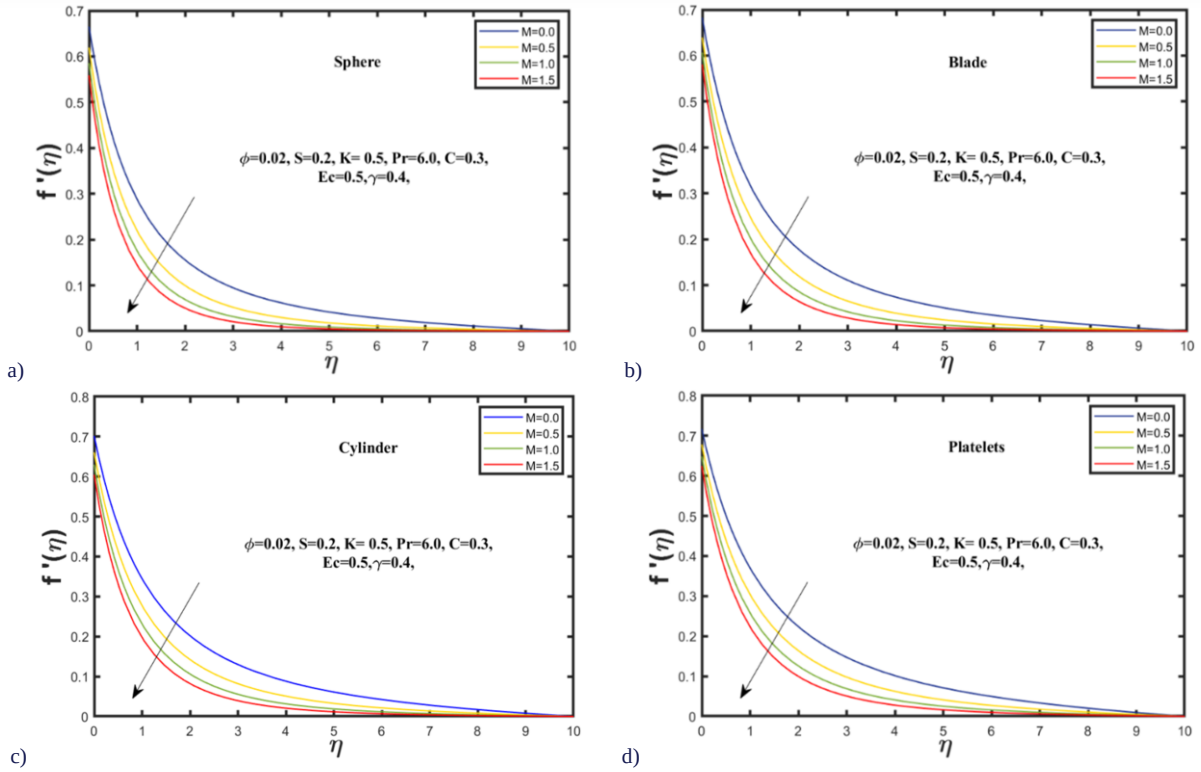

Fig. 5. Impact of *M* on *f* '(*η*): a) sphere, b) blade, c) cylinder, d) platelets.

Figure 6 clarifies the influence of each multi-shape nanoparticle on the velocity profile. The study reveals that the SiO_2-H_2O nanofluid attains its maximum velocity with platelet-shaped particles, outperforming cylinder, blade and sphere-shaped particle nanofluids.

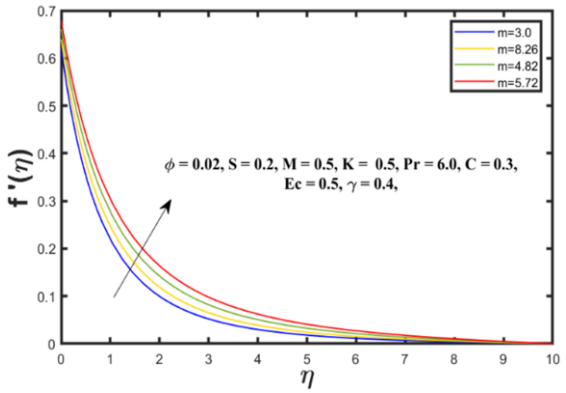

Fig. 6. Depiction of effects of shape factors on velocity.

4.2. Temperature Profile

The effect of volumetric friction on temperature is evident in Figs. 7a–7d. The graph clearly illustrates that an increase in the volumetric fraction value corresponds to a rise in temperature. This phenomenon occurs due to the higher thermal conductivity of the nanoliquid resulting from the increase in volume fraction, leading to higher temperatures.

Figures 8a–8d clearly illustrate that as the value of the unsteadiness parameter *S* increases, there is a noticeable decrease in the temperature profile. This physical phenomenon arises from the fact that the increase in the unsteadiness parameter enhances heat loss due to cylinder stretching. During the stretching scenario of an unstable flow, the distances between the molecules become larger, leading to a proportional decrease in the temperature profile.

Figures 9a–9d highlight the outcomes of the influence of the magnetic parameter *M* on the temperature profile. It is observed that the temperature increases with the rising values of the magnetic parameter. This phenomenon occurs because an increase in the values of the magnetic parameter leads to an upsurge in the magnetic field, which opposes fluid movement and consequently causes an increase in the nanofluid temperature.

In Figs. 10a–10d, it is evident that the Prandtl (Pr) number exhibits an inverse relationship with the temperature profile. This phenomenon occurs because the Pr number reduces the thermal diffusivity of the SiO_2-water nanoliquid and decreases the thickness of the thermal boundary layer. Consequently, heat travels more rapidly through the nanoliquid, leading to the observed inverse relationship between the Prandtl number and the temperature profile.

Figures 11a–11d present the relationship between Eckert's (Ec) number and temperature. The graph shows that the temperature increases as the Ec number is increased. This phenomenon occurs because as the Eckert's number increases, there is a corresponding rise in viscous dissipation and kinetic energy. Consequently, the temperature distribution also increases due to the enhanced energy dissipation in the nanofluid.

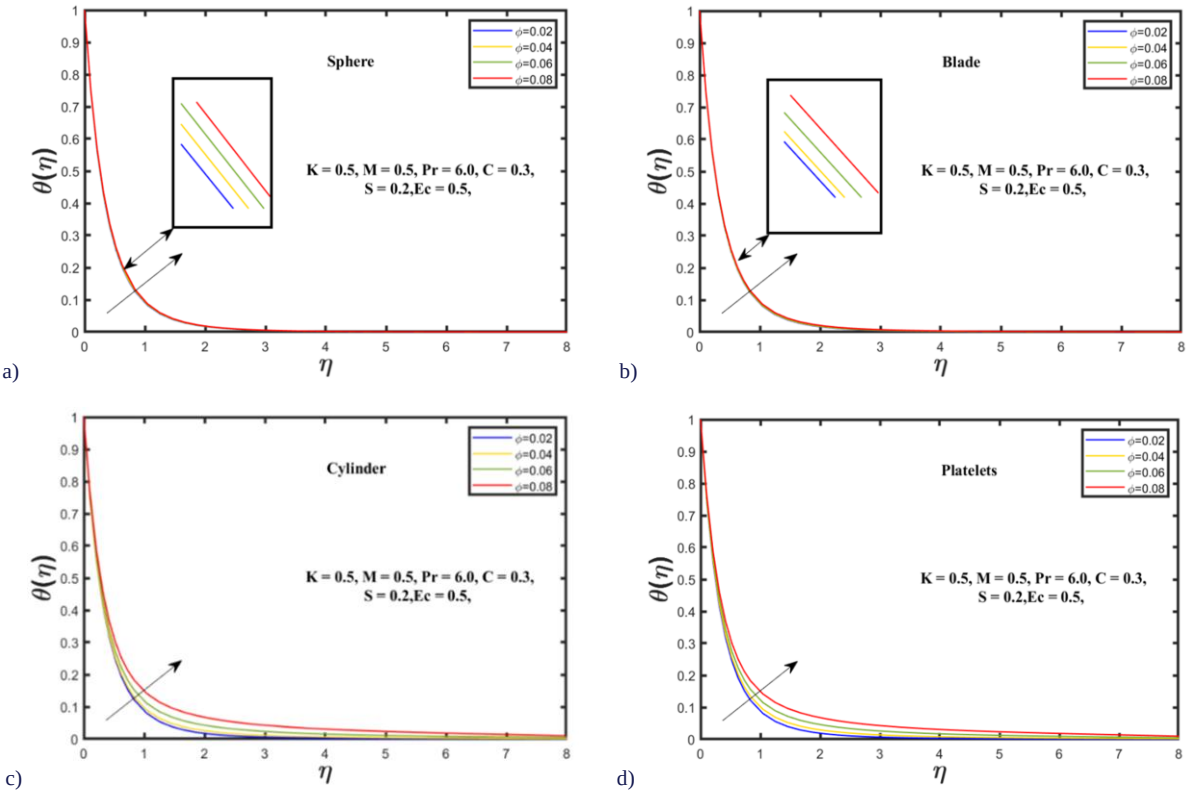

Fig. 7. Impact of volume fraction on $\theta(\eta)$): a) sphere, b) blade, c) cylinder, d) platelets.

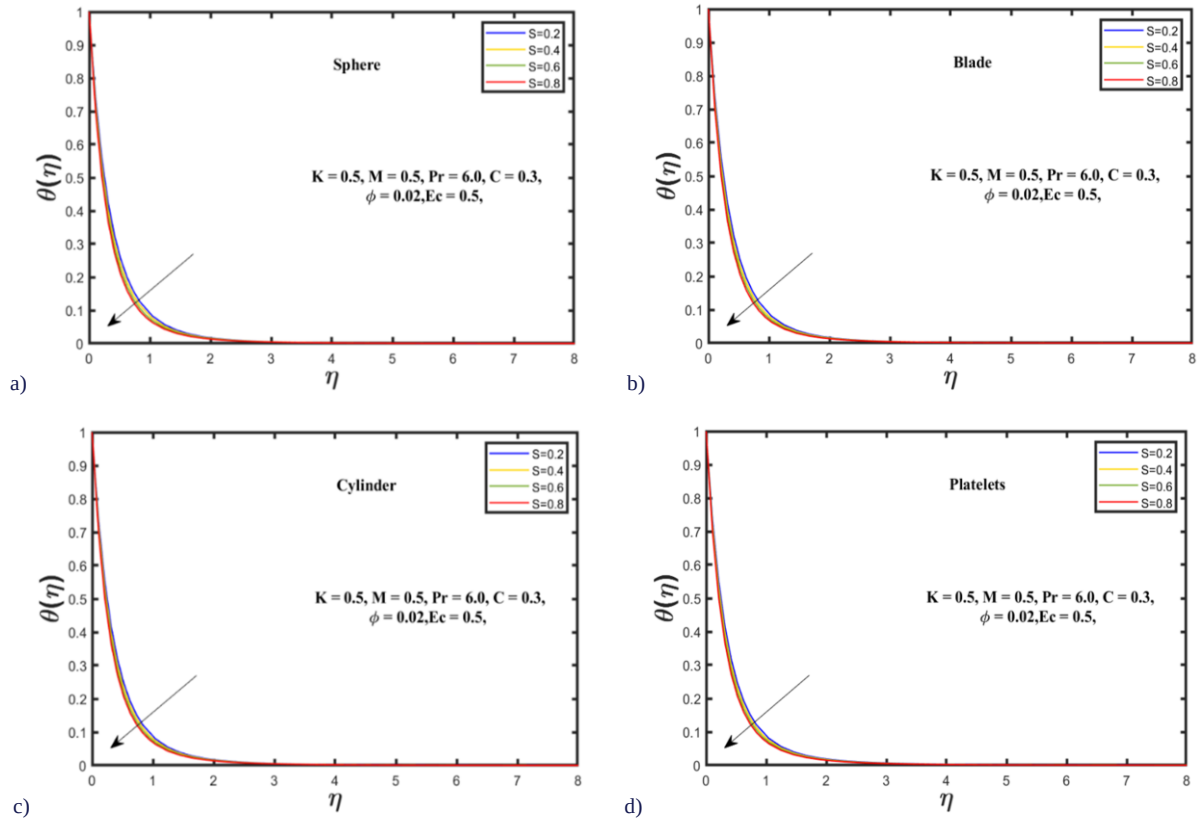

Fig. 8. Effects of S on $\theta(\eta)$): a) sphere, b) blade, c) cylinder, d) platelets.

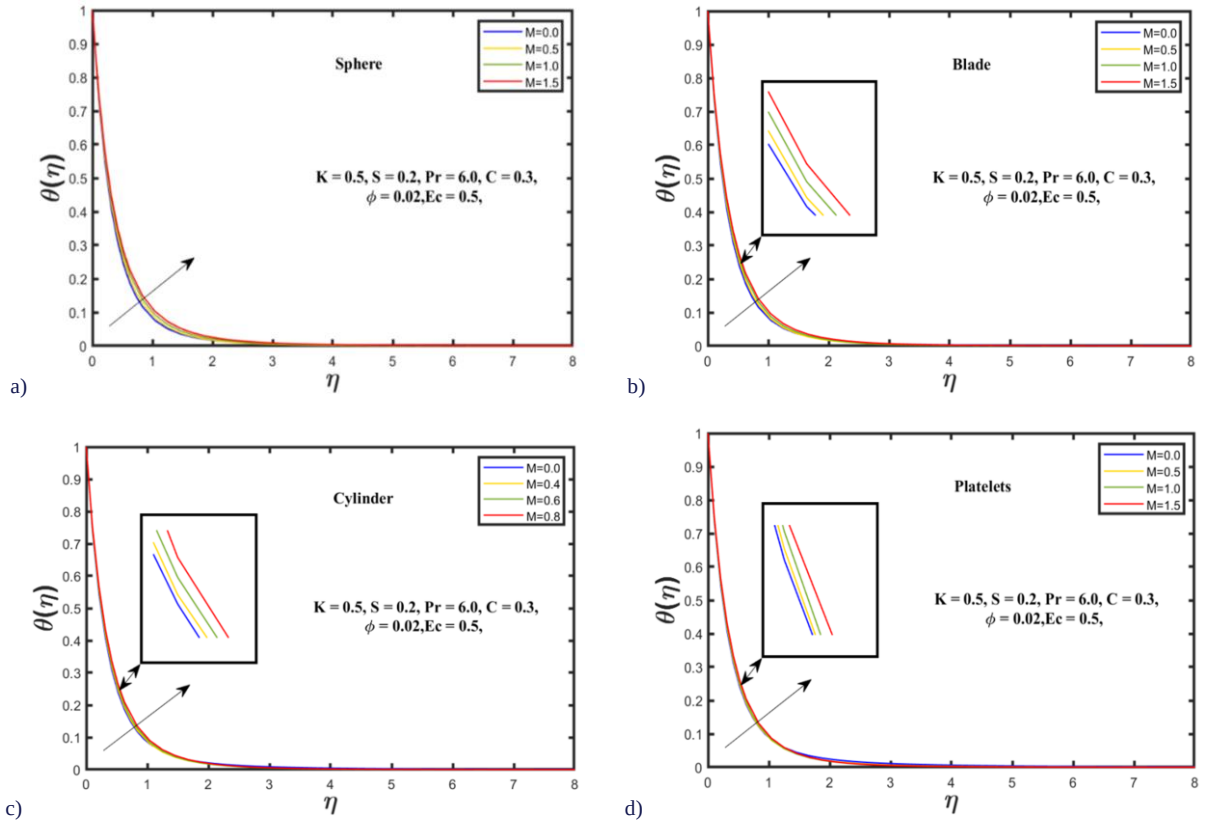

Fig. 9. Effects of M on $\theta(\eta)$): a) sphere, b) blade, c) cylinder, d) platelets.

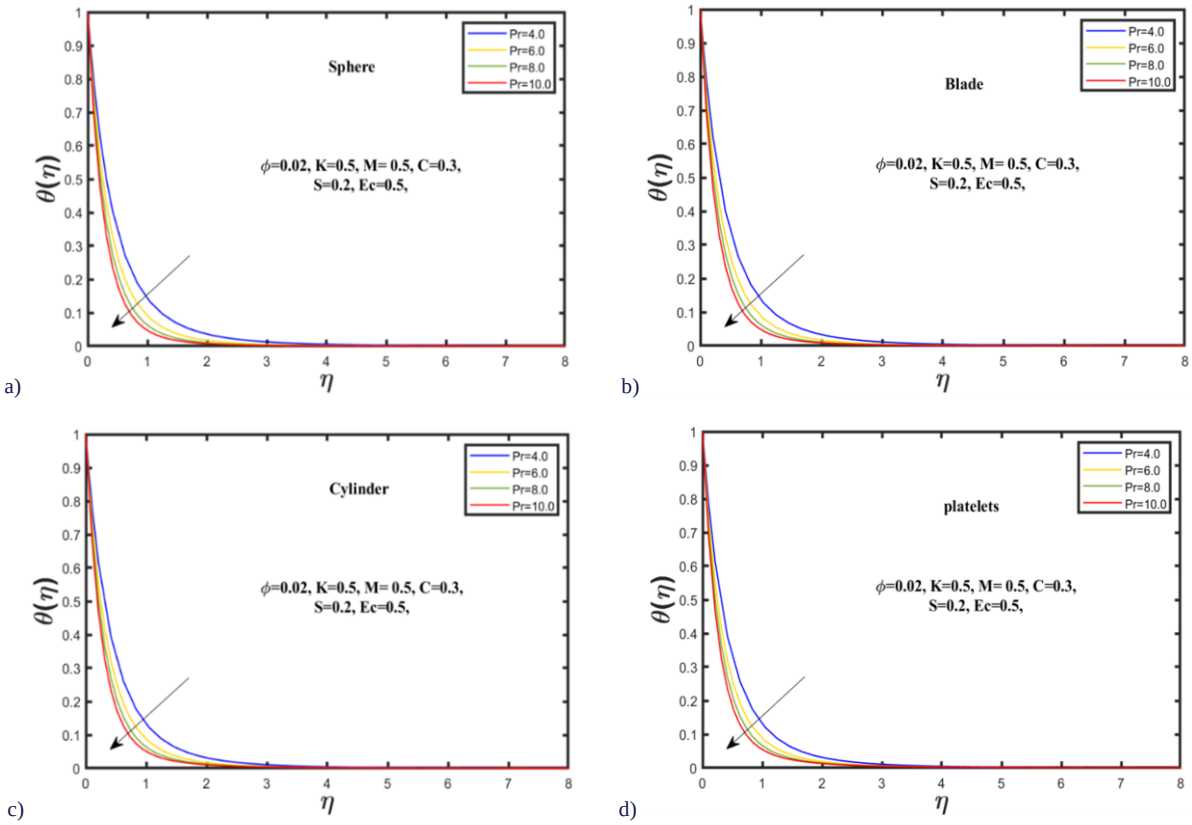

Fig. 10. The effect of Pr on $\theta(\eta)$: a) sphere, b) blade, c) cylinder, d) platelets.

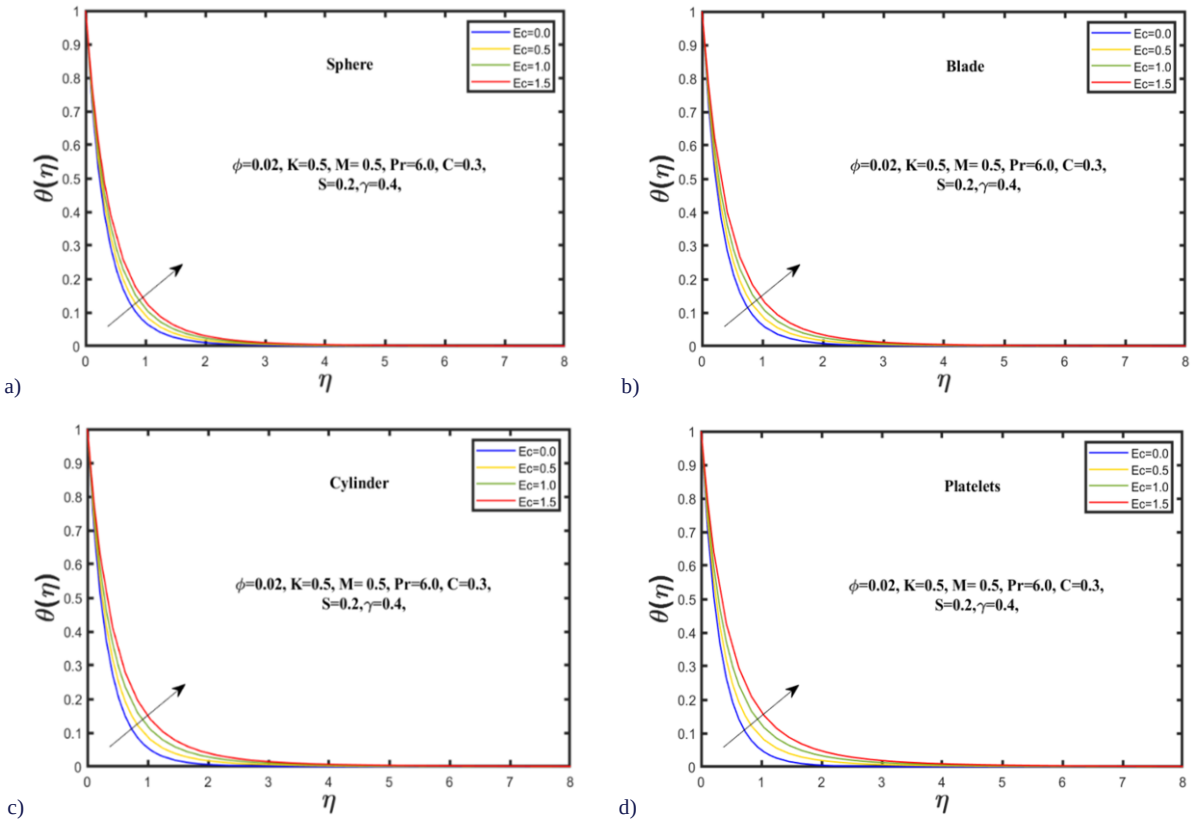

Fig. 11. The effect of Ec on $\theta(\eta)$: a) sphere, b) blade, c) cylinder, d) platelets.

Figure 12 shows the results for the comparison of temperature values for different shape factors m = 3.0, 8.26, 4.82 and 5.72, representing sphere, blade, cylinder and platelet shapes, respectively. It is observed that the maximum temperature is noted for platelet and minimum for sphere-shaped nanoparticles of SiO_2.

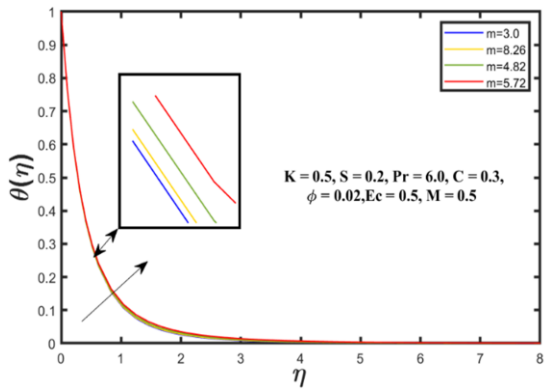

Fig. 12. The effect of different shapes of SiO_2 on $\theta(\eta)$.

4.3. Skin friction and Nusselt number

The study presents numerical values of skin friction in Table 2. It is observed that the skin friction decreases with the slip parameter and increases with the magnetic, volumetric fraction and unsteadiness parameters. Among the different nanoparticle shapes, the platelet shape exhibits both the maximum and minimum values for platelets and sphere-shaped nanoparticles, respectively.

Furthermore, Table 3 illustrates the values of the Nusselt number for variations in the Eckert number, volume percentage, unsteadiness parameter and magnetic parameter. The Nusselt number magnitude decreases with increasing values of M and Ec. Conversely, it increases with higher volumetric percentage and unsteadiness parameter values. Notably, SiO_2 nanoparticles with spherical shapes have the highest Nusselt numbers, while platelet shapes have the lowest values.

5. Conclusions

The study aims to analyze the effects of various parameters on the velocity distribution $f'(\eta)$ and temperature distribution $\theta(\eta)$ in the MHD flow of nanofluids containing different shaped nanoparticles (spherical, platelet, blade and cylinder) in an SiO_2-H_2O nanofluid. The investigations have been focused on understanding how the pertinent parameters impact the velocity and temperature profiles in the system. In conclusion, the velocity profile is positively affected by the volume fraction ϕ, while it is negatively influenced by the slip parameter K, magnetic parameter M and unsteadiness parameter S. The temperature field rises with higher values of volume fraction ϕ, M and Eckert parameter Ec, but decreases with the Prandtl number Pr and unsteadiness parameter S. The skin friction decreases as the slip parameter value increases, but it rises with the magnetic parameter, volume fraction and unsteadiness parameter. The Nusselt number exhibits an increasing trend for increasing values of Pr, ϕ and S, while it decreases with the Eckert number and magnetic parameter.

Acknowledgements

We highly appreciate comments from anonymous reviewers on the initial stage of this manuscript. Indeed, it has improved the quality of the work.

References

[1] Choi, S.U. & Eastman, J.A., (1995). Enhancing thermal conductivity of fluids with nanoparticles. *ASME, 1995 International Mechanical Engineering Congress and Exposition*, 12−17 November, San Francisco, CA, United States.

[2] Talib, S.F.A. Azmi, W.H., Zakaria, I., Mohamed, W., Mamat, A.M.I., Ismail, H., & Daud, W.R.W. (2015). Thermophysical Properties of Silicon Dioxide (SiO2) in Ethylene Glycol/Water Mixture for Proton Exchange Membrane Fuel Cell Cooling Application. *Energy Procedia*, 79, 366–371. doi: 10.1016/j.egypro.2015.11.504

[3] Alsarraf, J., Alnaqi, A.A., & Al-Rashed, A.A.A.A. (2022). Effect of nanoparticles shape on the cooling process of a lithium ion battery in geometry with capillary channels in the presence of phase change material. *Journal of Energy Storage*, 48, 103998. doi: 10.1016/j.est.2022.103998

[4] Akram, J., Akbar, N.S., & Tripathi, D. (2020). Comparative study on ethylene glycol based Ag-Al_2O_3 and Al_2O_3 nanofluids flow driven by electroosmotic and peristaltic pumping: a nano-coolant for radiators. *Physica Scripta*, 95(11), 115208. doi: 10.1088/1402-4896/abbd6b

[5] Camara, S., & Sulin, A.B. (2022). Study of a double-acting solar collector for use in the absorption cooling system in hot regions. *Thermal Science and Engineering Progress*, 31, 101286. doi: 10.1016/j.tsep.2022.101286

[6] Abdullatif Alshuhail, L., Shaik, F., & Syam Sundar, L. (2023). Thermal efficiency enhancement of mono and hybrid nanofluids in solar thermal applications – A review. *Alexandria Engineering Journal*, 68, 365−404. doi:10.1016/j.aej.2023.01.043

[7] Ma, M., Xie, M., & Ai, Q. (2022). Simulation on influences of Al2O3 nanofluids as coolant for nuclear power plant based on modified empirical formula of nanofluids thermal properties at high temperature and high pressure. *Energy Sources, Part A: Recovery, Utilization, and Environmental Effects*, 44(1), 454–468. doi: 10.1080/15567036.2022.2046213

[8] Arif, M., Di Persio, L., Kumam, P., Watthayu, W., & Akgül, A. (2023). Heat transfer analysis of fractional model of couple stress Casson tri-hybrid nanofluid using dissimilar shape nanoparticles in blood with biomedical applications. *Scientific Reports*, 13(1), 4596. doi: 10.1038/s41598-022-25127-z

[9] Akram, S., Athar, M., Saeed, K., Razia, A., Muhammad, T., & Ahmed Alghamdi, H. (2023). Mathematical simulation of double diffusion convection on peristaltic pumping of Ellis nanofluid due to induced magnetic field in a non-uniform channel: Applications of magnetic nanoparticles in biomedical engineering. *Journal of Magnetism and Magnetic Materials*, 569, 170408. doi: 10.1016/j.jmmm.2023.170408

[10] Crane, L.J. (1970). Flow past a stretching plate. *Zeitschrift für angewandte Mathematik und Physik*, 21(4), 645−647. doi: 10.1007/BF01587695

[11] Ahmed, J., Shahzad, A., Khan, M., & Ali, R. (2015). A note on convective heat transfer of an MHD Jeffrey fluid over a stretching sheet. *AIP advances*, 5(11), 117117. doi: 10.1063/1.4935571

[12] Hayat, U., Ali, R., Shaiq, S., & Shahzad, A. (2023). A numerical study on thin film flow and heat transfer enhancement for copper nanoparticles dispersed in ethylene glycol. *Reviews on Advanced Materials Science*, 62(1), doi: 10.1515/rams-2022-0320

[13] Yang, H., Haya, U., Shaiq, S., Shahzad, A., Abbas, T., Naeem, M., Khan, S.U., Labidi, T., Kolsi, L., & Zahid, M.A. (2023). Thermal inspection for viscous dissipation slip flow of hybrid nanofluid (TiO_2–Al_2O_3/$C_2H_6O_2$) using cylinder, platelet and blade shape features. *Scientific Reports*, 13(1), 8316. doi: 10.1038/s41598-023-34640-8

[14] Shaiq, S., Maraj, E.N., & Shahzad, A. (2023). An unsteady instigated induced magnetic field's influence on the axisymmetric stagnation point flow of various shaped copper and silver nanomaterials submerged in ethylene glycol over an unsteady radial stretching sheet. *Numerical Heat Transfer, Part A: Applications*, 85(6), 822−844. doi: 10.1080/10407782.2023.-2193351

[15] Khan, Q., Farooq, M., & Ahmad, S. (2024). Generalized transport analysis on mixed convection squeeze flow of a Casson fluid over an inclined stretching sheet with viscous dissipation and double stratification. *Ain Shams Engineering Journal*, 15(1), 102253. doi: 10.1016/j.asej.2023.102253

[16] Jabeen, K., Mushtaq, M., Mushtaq, T., & Muntazir, R.M.A. (2023). A numerical study of boundary layer flow of Williamson nanofluid in the presence of viscous dissipation, bioconvection, and activation energy. *Numerical Heat Transfer, Part A: Applications*, 85(3), 378−399. doi: 10.1080/10407782.2023.-2187494

[17] Othman, H.A., Ali, B., Jubair, S., Yahya Almusawa, M., & Aldin, S.M. (2023). Numerical simulation of the nanofluid flow consists of gyrotactic microorganism and subject to activation energy across an inclined stretching cylinder. *Scientific Reports*, 13(1), 7719. doi: 10.1038/s41598-023-34886-2

[18] Hayat, U., Shaiq, S., & Shahzad, A. (2023). A Comparative Study of Thin Film Flow of Fe_3O_4 and Al_2O_3 Nanoparticles over Stretching Surface Under the Effect of Viscous Dissipation and Magnetohydrodynamics (MHD). Preprint from *Research Square*. doi: 10.21203/rs.3.rs-2693183/v1

[19] Hayat, T., Razaq, A., Khan, S.A., & Alsaedi, A. (2023). Radiative flow of rheological material considering heat generation by stretchable cylinder. *Case Studies in Thermal Engineering*, 44, 102837. doi: 10.1016/j.csite.2023.102837

[20] Khan, W.A., & Pop, I. (2010). Boundary-layer flow of a nanofluid past a stretching sheet. *International Journal of Heat and Mass Transfer*, 53(11), 2477−2483. doi: 10.1016/j.ijheatmass-transfer.2010.01.032

[21] Chen, C.-H. (2004). Combined heat and mass transfer in MHD free convection from a vertical surface with Ohmic heating and viscous dissipation. *International Journal of Engineering Science*, 42(7), 699−713. doi: 10.1016/j.ijengsci.2003.09.002

[22] Cao, J., Cheng, P., & Hong, F. (2009). Applications of electro-hydrodynamics and Joule heating effects in microfluidic chips: A review. *Science in China Series E: Technological Sciences*, 52(12), 3477−3490. doi: 10.1007/s11431-009-0313-z

[23] Hayat, T., Imtiaz, M., & Alsaedi, A. (2016). Melting heat transfer in the MHD flow of Cu–water nanofluid with viscous dissipation and Joule heating. *Advanced Powder Technology*, 27(4), 1301−1308. doi: 10.1016/j.apt.2016.04.024

[24] Maraj, E.N., Faizan, U., & Shaiq, S. (2019). Influence of Joule heating and Partial Slip on Casson Nanofluid Transport Past a Nonlinear Stretching Planar Sheet. *International Conference on Applied and Engineering Mathematics* (pp. 31−36), 27−29 Aug., Taxila, Pakistan. doi: 10.1109/ICAEM.2019.8853731

[25] Khashi'ie, N.S., Arifin, N.M., Pop, I. & Wahid, N.S. (2020). Flow and heat transfer of hybrid nanofluid over a permeable shrinking cylinder with Joule heating: A comparative analysis. *Alexandria Engineering Journal*, 59(3), 1787−1798. doi: 10.1016/j.aej.2020.04.048

[26] Naseem, T., Fatima, U., Munir, M., Shahzad, A., Kausar, N., Nisar, K.S., Saleel, C.A., & Abbas, M. (2022). Joule heating and viscous dissipation effects in hydromagnetized boundary layer flow with variable temperature. *Case Studies in Thermal Engineering*, 35, 102083. doi: 10.1016/j.csite.2022.102083

[27] Rehman, S., Anjum, A., Farooq, M., Hashim, & Malik, M.Y. (2022). Melting heat phenomenon in thermally stratified fluid reservoirs (Powell-Eyring fluid) with joule heating. *International Communications in Heat and Mass Transfer*, 137, 106196. doi: 10.1016/j.icheatmasstransfer.2022.106196

[28] Makhdoum, B.M., Mahmood, Z., Khan, U., Fadhl, B.M., Khan, I., & Eldin, S.M. (2023). Impact of suction with nanoparticles aggregation and joule heating on unsteady MHD stagnation point flow of nanofluids over horizontal cylinder. *Heliyon*, 9(4), e15012. doi: 10.1016/j.heliyon.2023.e15012.

[29] Raza, R., Naz, R., & Abdelsalam, S.I. (2023). Microorganisms swimming through radiative Sutterby nanofluid over stretchable cylinder: Hydrodynamic effect. *Numerical Methods for Partial Differential Equations*, 39(2), 975−994. doi: 10.1002/num.22913

[30] Alsaedi, A., Razaq, A., Hayat, T., & Khan, S.A. (2023). On bioconvective chemically reactive flow involving applications of magnetohydrodynamic and radiation. *Alexandria Engineering Journal*, 75, 549−563. doi: 10.1016/j.aej.2023.06.015

[31] Wazawa T., & Nagai, T. (2023). Joule heating involving ion currents through channel proteins. *Biophysics and Physicobiology*, 20(3), e200030, doi: 10.2142/biophysico.bppb-v20.0030

[32] Manshadi M.K.D., & Beskok, A. (2023). Competing effects of buoyancy-driven and electrothermal flows for Joule heating-induced transport in microchannels. *Flow*, 3, E23. doi: 10.1017/flo.2023.19

[33] Khan, S.A., Eze, C., Lau, K.T., Ali, B., Ahmad, S., Ni, S., & Zhao, J. (2022). Study on the novel suppression of heat transfer deterioration of supercritical water flowing in vertical tube through the suspension of alumina nanoparticles. I*nternational Communications in Heat and Mass Transfer*, 132, 105893. doi: 10.1016/j.icheatmasstransfer.2022.105893

[34] Narayanaswamy, M., Kandasamy, J., & Sivanandam, S. (2022). Go-MoS_2/Water Flow over a Shrinking Cylinder with Stefan Blowing, Joule Heating, and Thermal Radiation. *Mathematical and Computational Applications*, 27, 110. doi: 10.3390/mca27060110

[35] Ali, A., Khatoon, R., Ashraf, M., & Awais, M. (2022). Cattaneo–Christov heat flux on MHD flow of hybrid nanofluid across stretched cylinder with radiations and Joule heating effects. *Waves in Random and Complex Media* (pp. 1−18). doi: 10.1080/17455030.2022.2145524

[36] Naseem, T., Shahzad, A., Sohail, M., & Askar, S. (20230). Axisymmetric Flow and Heat Transfer in TiO_2/H_2O Nanofluid over a Porous Stretching-Sheet with Slip Boundary Conditions via a Reliable Computational Strategy. *Energies*, 16(2), 681. doi: 10.3390/en16020681

[37] Bibi, S., Elahi, Z., & Shahzad, A. (2020). Impacts of different shapes of nanoparticles on SiO_2 nanofluid flow and heat transfer in a liquid film over a stretching sheet. *Physica Scripta*, 95(11), 115217. doi: 10.1088/1402-4896/abbc9d

Co-published by
Institute of Fluid-Flow Machinery
Polish Academy of Sciences
Committee on Thermodynamics and Combustion
Polish Academy of Sciences

http://www.imp.gda.pl/archives-of-thermodynamics/

Influence of wall temperature on condensation rate in duct flow of humid air: a comprehensive computational study

Jakub Bobrowski[a*], Artur Gutkowski[a]

[a]Lodz University of Technology, Institute of Turbomachinery, 217/221 Wólczanska, 93-005 Łódź, Poland
*Corresponding author email: 248731@edu.p.lodz.pl

Received: 06.02.2024; revised: 27.04.2024; accepted: 05.06.2024

Abstract

In engineering phase-change phenomena are found in a multitude of applications, ranging from refrigeration and air conditioning to steam turbines and petroleum refining. This study investigates the flow of moist air in a circular duct where water vapour condenses in contact with the cold wall of the duct. The investigation delves into the relationship between the condensation mass transfer rate, the heat transfer between the bulk flow and the wall, and the temperature of the wall. The volume of fluid model coupled with the Lee evaporation-condensation model was employed. Five simulations were carried out, involving different wall temperatures while maintaining the same inlet conditions. Condensation was more pronounced at lower wall temperatures, which aligns with the expectations. The heat transfer between the bulk flow and the wall decreased with the decreasing temperature difference. Interestingly, the findings revealed that the surface heat transfer coefficient increased as the wall temperature approached the temperature of the bulk flow. The success of the study suggests potential applications in optimising thermal management systems, with implications for industries where accurate predictions of moisture behaviour and heat transfer are crucial.

Keywords: Computational fluid dynamics; Volume of fluid; Heat transfer; Mass transfer; Condensation

Vol. 45(2024), No. 3, 127–133; doi: 10.24425/ather.2024.151229

Cite this manuscript as Bobrowski, J., & Gutkowski, A. (2024). Influence of wall temperature on condensation rate in duct flow of humid air: a comprehensive computational study. *Archives of Thermodynamics*, 45(3), 127–133.

1. Introduction

Phase changes are ubiquitous in our everyday lives and play a fundamental role in various applications across diverse fields. In engineering, the controlled evaporation and condensation of working fluids are found in a multitude of applications, offering innovative solutions to various challenges. One prominent example can be found in the field of refrigeration and air conditioning. These systems rely on the evaporation and subsequent condensation of a refrigerant to regulate temperatures. The working fluid evaporates within the evaporator coils, absorbing heat from the surrounding environment, thereby cooling the space. The vapourised refrigerant is then compressed, releasing the absorbed heat, and subsequently condensed back into a liquid in the condenser [1,2]. The applicability of phase changes extends beyond refrigeration and air conditioning. Many power plants, both nuclear and fossil fuel-based, use steam turbines to generate electricity. Water is heated to produce high-pressure steam, which drives turbines, and then the steam is condensed back into water, completing a continuous cycle [2]. This phase change mechanism is fundamental to power generation. Another good example of this is distillation, a process which takes advantage of the different characteristics of the substances in a mixture in order to separate them. In the petroleum industry,

Nomenclature

h – surface heat transfer coefficient, W/(m^{2}K)
I – turbulence intensity
M – mass transfer rate, kg/s
n – power-law exponent
P – pressure, Pa
q – heat flux, W/m^2
Q – heat transfer rate, W
r – radial coordinate, m
R – radius of the pipe, m
Re – Reynolds number
RH – relative humidity
T – temperature, K
u – axial velocity, m/s

Subscripts and Superscripts

avg – average
c – condensation
max – maximum value
ref – reference condition
sat – saturation condition
v – vapour
wall – through the wall/on the wall

Abbreviations and Acronyms

RANS– Reynolds averaged Navier-Stokes
VOF – volume of fluid

distillation is used to extract products like liquid petroleum gas and gasoline from crude oil. Similarly, within the alcohol industry, distillation is in the centre of the production of distilled spirits.

Numerous experimental and numerical investigations have been conducted on phase change phenomena. In [3], the volume of fluid method (VOF), coupled with an in-house evaporation-condensation mass transfer model, was employed by the authors to explore phase changes in the internal two-phase flow of R134a refrigerant. The findings showed reasonable agreement with available experimental data. In [4], the condensation of water vapour in the presence of dry air was examined by the authors, who employed two advection equations to monitor the free surface and utilised the Lee model to simulate interfacial mass transfer. The results demonstrated favourable alignment with experimental data, revealing a nearly linear decrease in condensation rate as the dry air mass fraction increased. In the paper [5], the authors delved into the evaporation of a water film in a duct with a humid air flow, where the volume of fluid and Lee model were employed to capture the physics. The evaporation rate was observed to rise with the increasing air temperature and decreasing air flow rate. In [6], a single-phase approach was developed by the authors to model the condensation of vapour in the presence of air, yielding good agreement with experimental data. Interesting conclusions were drawn in [7], where the authors investigated the influence of flow direction on the condensation process in a vertical pipe. The study developed a mathematical model based on conservation equations and validated it through experimental apparatus. Results suggested that co-current gas/liquid flow enhanced heat transfer. Additionally, comparisons between theoretical predictions and experimental findings confirmed the model's accuracy.

In this study, the numerical simulation explores the flow of humid air in a circular duct, where water vapour condenses in contact with the cold wall of the duct. The objective is to evaluate how the wall temperature influences the condensation mass transfer rate of water vapour in the presence of dry air.

2. Materials and methods

The model was prepared and solved within the commercial computational fluid dynamics (CFD) package Ansys Fluent. To simulate this case, the steady-state Reynolds-averaged Navier-Stokes (RANS) approach was adopted, offering a balanced compromise between accuracy and computational cost. RANS modelling stands as the industry standard for heat transfer and mass transfer applications. It has proven to be quite successful at predicting both local and integral quantities in heat and mass transfer applications [4,6,8].

Five simulations were carried out, involving different wall temperatures while maintaining the same inlet conditions, as detailed in Table 1.

Table 1. Simulations.

Simulation number	Inlet conditions	Wall temperature [K]
1	u_{avg} = 3.91 m/s Re = 10^4 T = 303.15 K RH = 95%	278.15
2		283.15
3		288.15
4		293.15
5		298.15

The fluid domain is a cylindrical space bounded by the duct with a standard diameter of 40 mm. In the hypothetical real-life laboratory, the duct extends sufficiently far upstream from the inlet (Fig. 1) for the velocity profile to fully develop and for the

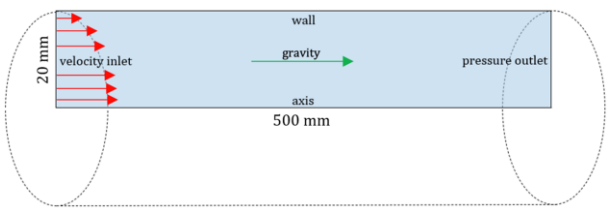

Fig. 1. Boundary conditions.

temperature distribution to plateau, achieving the inlet conditions specified in Table 1. Although the duct is quite lengthy, in this context, focus is put on a segment that is 500 mm in length, whose walls are maintained at a temperature different from that of the upstream part. The copper duct releases heat through forced convection to the surroundings. An external liquid-cooling system is used to maintain a uniform temperature of the segment. Downstream from the outlet, the flow exits into atmospheric conditions. It is important to observe that the shape of the domain, the boundary conditions, and the expected results exhibit axisymmetry (the water condenses as an axisymmetric film because asymmetric dropwise condensation requires vapour additives or surface coatings to maintain, and often transitions to film condensation over time [1]). Hence, the problem can be visualised on the axial-radial plane, where the third circumferential dimension has no impact on the results. With this in mind, the three-dimensional cylinder was simplified into a single rectangular shape measuring 20 mm by 500 mm, as shown in Fig. 1.

Because of limited computational resources, a decision was made to use a coarse discretisation in the bulk flow and utilise mesh adaptation to refine the grid in the near-wall region, thereby increasing both flow-wise and wall-normal resolution. The final mesh is based on a rectangular grid that has 30 cells in the radial direction with a bias factor of 10 000 (creating a decreasing cell height towards the wall) and 50 equally-distributed divisions along the length of the duct. Hanging node mesh adaption [9] was used afterwards. In contrast to mesh refinement achieved by increasing the bias factor or the number of divisions, this approach mitigates the occurrence of excessive aspect ratios in near-wall cells. The refinement region extends approximately 5 mm from the wall (as shown in Fig. 2), reaching well beyond the momentum, thermal and concentration boundary layer. Such discretisation results in approximately 20 cells across the thickness of the water film, which, combined with the carefully chosen numerical schemes, results in an accurate resolution of the near-wall region. The grid has a total of 5400 finite volumes.

The dry air and water vapour mixture was modelled with the use of species transport, treating both species as ideal gases. Although water vapour is close to the saturation line, it can be effectively treated as an ideal gas under such low pressures [2]. Moreover, dry air and water vapour properties exhibit negligible variations within the temperature ranges applied. Since the mass fraction of water vapour is minimal and the properties of water vapour and dry air are rather similar (except for the specific isobaric heat capacity, which is twice as large for water vapour), the properties of humid air were assumed to be identical to those of dry air. Careful consideration was given to the temperature point at which these properties were obtained. While the bulk flow has a temperature of 303.15 K, heat and mass transfer phenomena occur in the colder near-wall region. Hence, the properties of dry air were extracted from tables [10,11] for a temperature of 293.15 K, a value in-between the hot core of the flow and the cold wall. The properties of the mixture are tabulated in Table 2. The molar heat of condensation was set to 4.4×10^7 J/kmol [12].

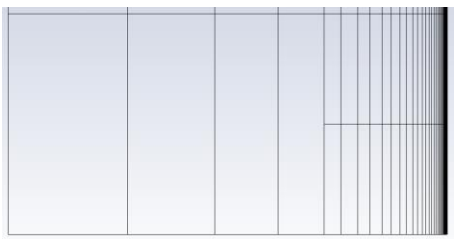

Fig. 2. Grid refinement (radial direction to the right).

Liquid water was modelled as an incompressible fluid. While most of its properties (shown in Table 2) exhibit meagre temperature dependence, the dynamic viscosity of water changes drastically with temperature [13]. In each simulation, the viscosity of water was taken from tables [14] for the temperature of the wall, as tabulated in Table 3.

The closure of the RANS equations was achieved by employing the shear stress transport (SST) turbulence model. Based on the Boussinesq concept of eddy viscosity, this model proves effective for shear flows dominated by one of the turbulent shear stresses, as seen in pipe flows. Moreover, the SST model allows for full boundary layer resolution, a crucial aspect for found widespread use in similar contexts [6, 15,16]. Turbulence damping was implemented to limit unrealistic turbulence production within the interfacial region and help capture the velocity field near the free surface [17–19].

Table 2. Humid air and water properties.

Property	Humid air	Water liquid
Density [kg/m³]	Ideal gas law	1000
Thermal conductivity [W/(K m)]	0.025	0.60
Dynamic viscosity [kg/(m s)]	1.8×10^{-5}	See Table 3
Specific isobaric heat capacity [J/(kg K)]	1000	4200
Mass diffusivity of water vapour in large excess of dry air [m²/s]	2.4×10^{-5}	NA

Table 3. Water liquid dynamic viscosity as a function of temperature.

Wall temperature [K]	Water liquid dynamic viscosity [10^{-3}×kg/(m s)]
278.15	1.5
283.15	1.3
288.15	1.1
293.15	1.0
298.15	0.89

The inlet velocity was defined as a velocity profile, established through the power-law approximation:

$$u(r) = u_{max}\left(1-\frac{r}{R}\right)^{1/n}. \quad (1)$$

For the calculated Reynolds number, the exponent n was estimated to be 5.3 [20].The turbulence properties at the inlet were

provided implicitly in terms of the hydraulic diameter and turbulence intensity, in accordance with the Fluent guidelines [19]. From the equation [19,21]

$$I = 0.16\,\mathrm{Re}^{-1/8}, \tag{2}$$

the inlet turbulent intensity was estimated to be 5%.

A gauge pressure of 0 Pa was specified at the outlet, and the reference pressure was set to 101 325 Pa.

The temperature on the outer side of the wall specified as a parameter T_{wall}, and the thermal resistance of the wall was defined based on a thickness of 2 mm and the thermal conductivity of copper, which is 390 W/(m K).

In the examined scenario, water vapour experiences local cooling in proximity to the walls, leading to its condensation as a liquid film [1]. This represents a case of stratified flow, where phases are separated into distinct layers with a well-defined interface. The VOF model, designed for such applications [9], was employed in this study. The model has found widespread use in modelling multiphase flows [3–5,8].

The implicit scheme was used, wherein the phase continuity equation is solved iteratively together with momentum and pressure [18]. The interface modelling type was set to 'Sharp', the preferred option for distinct and well-defined interfaces between phases [19]. Although interfacial anti-diffusion is typically suggested for sharp interfaces resolved on meshes with high aspect ratios [18,19], it was deliberately left inactive. This decision was made due to the recommendation for allowing some numerical diffusion when the evaporation-condensation mass transfer mechanism is enabled [19]. Since gravitational forces acting on the water film are significant, the 'Implicit Body Force' formulation was enabled, in accordance with [17,19].

The evaporation-condensation approach utilised the Lee model, with the evaporation and condensation coefficients set to 10 and 20 000, respectively, in accordance with [22]. This model is widely used in modelling interfacial mass transfer [3–6,8].

The saturation temperature was defined as a function of water vapour pressure through a 'User Defined Function'. It utilises the Antoine equation to compute and return the saturation temperature [23,24]:

$$T_{sat} = \frac{B}{A - \log_{10}\frac{P_v}{10^5\ \mathrm{Pa}}} - C + 273.15\ \mathrm{K}. \tag{3}$$

For water, the equation parameters are approximately as follows: A = 5.1156, B = 1687.5 and C = 230.17. These parameters have been fine-tuned for use within the temperature range of 273 K to 473 K and under pressures ranging from 1 kPa bar to 1600 kPa [24]. Although the current set of coefficients is applicable for vapour pressures greater than 1 kPa, its range of applicability in this study can be expanded. At 1 kPa, the calculated saturation temperature is 280 K, a value that approaches the lower limit of the thermal range observed within the pipe. Under lower pressures, the calculated saturation temperature decreases below the minimum temperature within the domain (regardless of whether the formula overestimates or underestimates the result), thereby maintaining a gaseous state in the respective cells.

The solver was run in the double-precision mode, the recommended approach for high-aspect-ratio meshes [19]. The simulation employed a pressure-based, steady-state solver with enabled pressure-velocity coupling, following the guidelines outlined in [9]. Moreover, the 'Coupled with Volume Fractions' option was enabled. The pressure interpolation scheme was set to 'Modified Body Force Averaged', which provides better stability for multiphase flows with body forces compared to its alternatives [9]. Additionally, the gradient reconstruction scheme was selected as 'Least Squares Cell Based', following the recommendation outlined in [9]. The spatial discretisation of momentum, turbulence, density, energy and species transport equations was set to 'Second Order Upwind'.

The volume fraction interface scheme was set to 'Modified HRIC'. While offering inferior interface resolution compared to the compressive scheme [18], a more diffusive discretisation is recommended when the evaporation-condensation mass transfer mechanism is enabled [19].

'Pseudo-Transient' under-relaxation was activated. This approach not only accelerates the convergence of steady-state problems but can also assist in the convergence of mildly unsteady flows [17].

To assess iterative and spatial convergence, the approach involved monitoring equation residuals and five integral output quantities: the water mass flow rate through the outlet, the total water film mass, the condensation mass transfer rate, the average total specific enthalpy at the outlet, and the total heat transfer rate through the wall. Both the residuals and the monitors flatlined, indicating iterative convergence. Moreover, the global balance of air/water mass and energy was verified. The grid was refined near the wall to guarantee maximum accuracy within the constraints of available computational resources.

3. Results and discussion

The results presented below are from the first simulation with a wall temperature of 278.15 K. The results from the subsequent simulations exhibit the same tendencies, differing only in values due to the progressively higher wall temperature.

The radial distribution of the mass fraction of water vapour is shown in Fig. 3 (plotted on the inlet, outlet as well as 100 mm, 200 mm, 300 mm and 400 mm from the inlet). It is evident that the vapour content consistently decreases along the stream. The most significant decline occurs just downstream from the inlet, coinciding with the steepest slope of the water film thickness (Fig. 8).

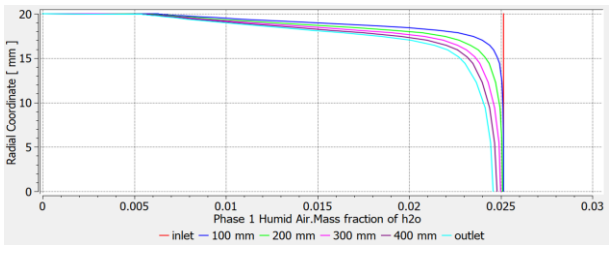

Fig. 3. Water vapour mass fraction profiles (for T_{wall} = 278.15 K).

The reduction in water vapour content results in the buildup of dry air near the wall. The presence of a non-condensable gas, such as dry air, has an adverse effect on condensation heat transfer [1]. This can be explained as follows: upon condensation of vapour mixed with a non-condensable gas, only the non-condensable gas is present near the wall. This gas layer serves as a barrier between the vapour and the surface. The vapour now has to diffuse through the non-condensable gas before reaching the surface, leading to a decreased mass and heat transfer rate.

The effectiveness of heat transfer between a fluid and a solid surface can be quantified by the surface heat transfer coefficient [19]:

$$h = \frac{q_{wall}}{T_{ref} - T_{wall}}. \quad (4)$$

It represents the rate of heat transfer per unit area per unit temperature difference between the surface and the fluid. The higher the heat transfer coefficient, the more effectively heat is transferred between the surface and the fluid.

Here, the reference temperature T_{ref} is set equal to the inlet temperature of 303.15 K. Using the average temperature on the axis, which would appear more representative of the bulk temperature, yields nearly identical results.

The presence of air, coupled with the increasing water film thickness (which can be treated as a conductive resistance due to its laminar nature [25]) and an increasing thermal boundary layer thickness, impedes heat transfer between the hot stream and the surroundings of the duct. This tendency is visible in Fig. 4. The surface heat transfer coefficient decreases in the downstream direction as both the thermal boundary layer and the water film grow.

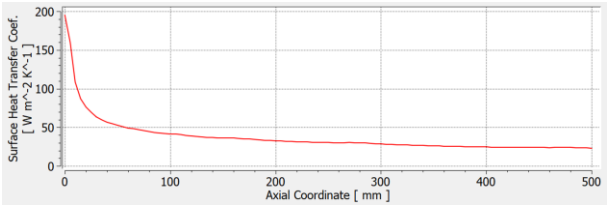

Fig. 4. Surface heat transfer coefficient along the pipe (for T_{wall} = 278.15 K).

The tendencies described above are evident in all five simulations. Some interesting patterns emerge when comparing the results for different wall temperatures. An approximately linear increase in the surface heat transfer coefficient is observed as the wall temperature approaches the freestream temperature, as shown in Fig. 5.

In free convection (single-phase flow with constant fluid properties), the heat transfer coefficient tends to increase with a growing temperature difference between the wall and the bulk flow. However, this correlation is not prominent in forced convection [25]. It can be concluded that the variability in the surface heat transfer coefficient is, to a great extent, caused by condensate formation. This trend can be explained as follows: at a higher wall temperature, the water film becomes thinner due to both reduced water viscosity and a lower condensation rate.

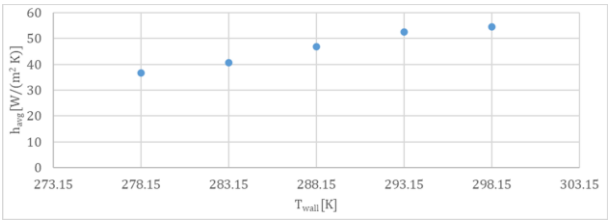

Fig. 5. Average surface heat transfer coefficient as a function of wall temperature.

A thinner water film poses less resistance to heat flow, resulting in the observed increase in the surface heat transfer coefficient.

To validate this hypothesis, simulations or experiments need to be conducted, as no correlations between the heat transfer coefficient and the temperature difference were identified in the literature.

Despite the variation in the surface heat transfer coefficient, the negative relationship between the total heat transfer rate and the temperature difference remains observable, as depicted in Fig. 6. Heat transfer becomes null when the wall temperature equals the temperature of the flow, as indicated on the graph with point T_{wall} = 303.15 K, manually added for clarity.

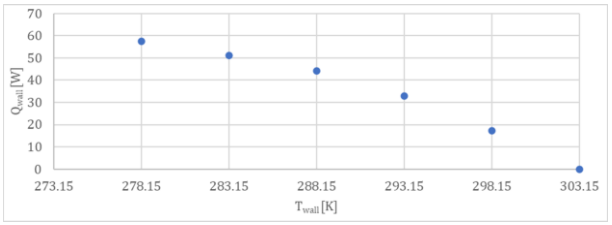

Fig. 6. Total heat transfer rate through the wall as a function of wall temperature.

While the surface heat transfer coefficient follows an intriguing trend, the variation in the condensation mass transfer rate aligns with expectations. The condensation mass transfer rate steadily decreases as the temperature of the wall increases, as can be observed in Fig. 7. No condensation would occur if the temperature of the wall and the flow were equal, as marked by the manually added point T_{wall} = 303.15 K.

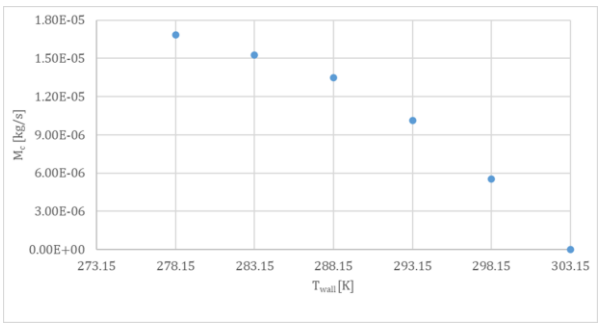

Fig. 7. Condensation mass transfer rate as a function of wall temperature.

With increasing temperature, the air's moisture-holding capacity increases. Eventually, mass transfer between the phases ceases when the temperature near the free surface reaches the dew-point temperature of the bulk flow.

As the rate of mass transfer through condensation diminishes, the water film contracts, as illustrated in Fig. 8. The reduction in thickness with each simulation is further intensified by a decrease in the viscosity of the liquid water.

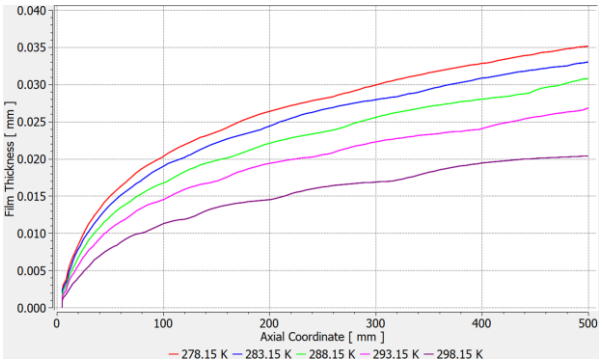

Fig. 8. Water film thickness as a function of wall temperature.

The undulating shape of the profiles is a result of how the software interpolates the value of liquid volume fraction within each computational cell. As an illustration, an interfacial cell may have a value of 0.6, while the radially adjacent cells have values of 0 and 1. An interpolation is required to determine the theoretical position of a point with a value of 0.5 (used as an iso-value to plot the film thickness). The accuracy of this interpolation largely depends on the spatial resolution of the interfacial region.

4. Summary

Throughout this study, a computational fluid dynamics model was developed to simulate the flow of moist air in a circular duct, where moisture condenses upon contact with the cold wall of the duct.

The volume of fluid surface-tracking model, ideal for stratified flows, was applied to model the free surface. The Lee model was used to compute the interfacial mass transfer through condensation, with model coefficients drawn from the literature. Additionally, a 'User-Defined Function' was developed in the C programming language to set the saturation temperature as a function of vapour pressure using the Antoine equation.

The dry air and water vapour mixture was modelled using species transport, treating both species as ideal gases with constant fluid properties. Liquid water was modelled as an incompressible fluid, with constant properties and a viscosity that was constant but different for each simulation.

The closure of the Reynolds-averaged Navier-Stokes equations was achieved by employing the shear stress transport turbulence model recommended for most industrial applications. Based on the Boussinesq concept of eddy viscosity, the shear stress transport formulation leverages the strengths of two widely adopted turbulence models: k-ω and k-ε.

Five simulations were carried out, involving different wall temperatures while maintaining the same inlet conditions. Condensation was more pronounced at lower wall temperatures, which aligns with expectations. The heat transfer between the bulk flow and the wall decreased with the increasing wall temperature. Interestingly, the findings revealed that the surface heat transfer coefficient increased as the wall temperature approached the temperature of the bulk flow.

The findings, particularly the observation that surface heat transfer coefficient increases with the decreasing temperature difference between the wall and the bulk flow, contribute to a deeper understanding of heat exchange processes. The success of the study suggests potential applications in optimising thermal management systems, with implications for industries where accurate predictions of moisture behaviour and heat transfer are crucial.

References

[1] Cengel, Y.A. (2002). *Heat Transfer: A practical approach*. McGraw-Hill.

[2] Cengel, Y.A., Boles, M A., & Kanoğlu, M. (2011). *Thermodynamics: An engineering approach*. McGraw-Hill.

[3] Ganapathy, H., Shooshtari, A., Choo, K., Dessiatoun, S., Alshehhi, M.M.M.O., & Ohadi, M. (2013). Volume of fluid-based numerical modeling of condensation heat transfer and fluid flow characteristics in microchannels. *International Journal of Heat and Mass Transfer*, 65, 62–72. doi: 10.1016/j.ijheatmasstransfer.2013.05.044

[4] Phan, T.H., Won, S.S., & Park, W.G. (2018). Numerical simulation of air-steam mixture condensation flows in a vertical tube. *International Journal of Heat and Mass Transfer*, 127, 568–578. doi: 10.1016/j.ijheatmasstransfer.2018.08.043

[5] El Baamrani, H., Bammou, L., Aharoune, A., & Boukhris, A. (2021). Volume of fluid (VOF) modeling of liquid film evaporation in mixed convection flow through a vertical channel. *Mathematical Problems in Engineering*, 2021, 9934593. doi:10.1155/2021/9934593

[6] Kumar, G.V., Cammiade, L.M., Kelm, S., Prakash, K.A., Groß, E.M., Allelein, H.J., & Rohlfs, W. (2021). Implementation of a CFD model for wall condensation in the presence of non-condensable gas mixtures. *Applied Thermal Engineering*, 187, 116546. doi: 10.1016/j.applthermaleng.2021.116546

[7] Pele, C., Baudoin, B., & Barrand, J.P. (1994). Effect of humid air flow rate on the filmwise condensation inside a vertical cooled pipe: numerical and experimental study. *International Journal of Heat and Mass Transfer*, 37(13), 1829–1837. doi: 10.1016/0017-9310(94)90323-9

[8] Szijártó, R., Badillo, A., Ničeno, B., & Prasser, H.M. (2017). Condensation models for the water–steam interface and the volume of fluid method. *International Journal of Multiphase Flow*, 93, 63–70. doi: 10.1016/j.ijmultiphaseflow.2017.04.002

[9] Ansys Inc. (2022). *Ansys Fluent theory guide*.

[10] https://www.engineersedge.com/physics/viscosity_of_air_dynamic_and_kinematic_14483.htm [accessed 25 Dec. 2023].

[11] https://www.engineeringtoolbox.com/air-diffusion-coefficient-gas-mixture-temperature-d_2010.html [accessed 25 Dec. 2023].

[12] https://www.engineeringtoolbox.com/water-properties-d_1573.html [accessed 20 Nov. 2023].

[13] https://www.engineersedge.com/physics/water__density_viscosity_specific_weight_13146.htm [accessed 25 Dec. 2023].

[14] https://wiki.anton-paar.com/en/water/ [accessed 25 Dec. 2023].
[15] Widiawaty, C.D., Siswantara, A.I., Gunadi, G.G.R., Pujowidodo, H., & Syafei, M.H G. (2020). A CFD simulation and experimental study: predicting heat transfer performance using SST k-ω turbulence model. *IOP Conference Series: Materials Science and Engineering*, 909(1), 012004. IOP Publishing.
[16] Močnik, U., Blagojevič, B., & Muhič, S. (2020). Numerical analysis with experimental validation of single-phase fluid flow in a dimple pattern heat exchanger channel. *Journal of Mechanical Engineering/Strojniški Vestnik*, 66(9), 544–553. doi: 10.5545/sv-jme.2020.6776
[17] Pawłucki, M., & Kryś, M. (2020). *CFD for engineers*, Gliwice: Helion (in Polish).
[18] Ansys Inc. (2015). *Multiphase modeling using ANSYS Fluent*.
[19] Ansys Inc. (2022). *Ansys Fluent user's guide*.
[20] https://www.nuclear-power.com/nuclear-engineering/fluid-dynamics/turbulent-flow/power-law-velocity-profile-turbulent-flow/ [accessed 21 Nov. 2023].
[21] https://www.cfd-online.com/Wiki/Turbulence_intensity [accessed 21 Nov. 2023].
[22] Lee, W.H. (1980). A pressure iteration scheme for two-phase flow modeling. In *Multiphase Transport Fundamentals, Reactor Safety, Applications* (T.N. Veziroglu, ed.), (pp. 407–431). Hemisphere.
[23] Antoine, M.C. (1888). Nouvelle relation entre les tensions et les temperatures. *C. r. held Seanc. Acad. Sci. Paris*, 107, 681–684.
[24] Poling, B.E., Prausnitz, J.M., & O'connell, J.P. (2001). *The properties of gases and liquids*: Vol. 5. Mcgraw-Hill.
[25] Welty, J., Rorrer, G.L., & Foster, D.G. (2020). *Fundamentals of momentum, heat, and mass transfer*. John Wiley & Sons.

Co-published by
Institute of Fluid-Flow Machinery
Polish Academy of Sciences
Committee on Thermodynamics and Combustion
Polish Academy of Sciences

http://www.imp.gda.pl/archives-of-thermodynamics/

Asymmetrical melting and solidification processes of phase change material and the challenges for thermal energy storage systems

Inge Magdalena Sutjahja[a*], Akhmad Yusuf[a], Yunita Anggraini[a], Shofi Dhiya Ulhaq[a], Daniel Kurnia[a], Surjamanto Wonorahardjo[b]

[a] Physics Department, FMIPA, Institut Teknologi Bandung, Jl. Ganesha No. 10, Bandung 40132, Indonesia
[b]Building Technology Research Group, SAPPK, Institut Teknologi Bandung, Jl. Ganesha No. 10, Bandung 40132, Indonesia
*Corresponding author email: im_sutjahja@itb.ac.id

Received: 23.12.2023; revised: 10.05.2024; accepted: 28.05.2024

Abstract

The melting and solidification processes of the organic phase change material – lauric acid exposed to air were experimentally studied to investigate the heat exchange and its effect on the heat transfer behaviour inside a shell as well as its phase-change characteristics. Lauric acid was placed in spherical shells made of polyvinyl chloride with diameters of 44, 63, and 74 mm. This study was based on analyses of the surface temperature and vertical temperature distribution data inside the shells. We found that the phase change characteristics were strongly related to the dominant heat transfer mechanism. In this case, melting was dominated by convection, whereas solidification was dominated by conduction. The convection intensity increased as the shell diameter increased. Further analysis revealed the melting and solidification periods. In contrast to latent heat release accompanying solidification, latent heat absorption accompanied by melting does not occur at a constant temperature, although it has a smaller temperature gradient than does sensible heat absorption. Based on the asymmetry between the melting and solidification processes, we discuss various possible strategies by which to control the charging and discharging of the phase change material by restraining the heat transfer rate to optimise its performance as a latent thermal energy storage material.

Keywords: Phase change material; Lauric acid; Heat transfer rate; Asymmetry melting and solidification; Heat transfer control

Vol. 45(2024), No. 1, 135–147; doi: 10.24425/ather.2024.151224

Cite this manuscript as: Sutjahja, I.M., Yusuf, A., Anggraini, Y., Ulhaq, S.D., Kurnia, D., & Wonorahardjo, S. (2024). Asymmetrical melting and solidification processes of phase change material and the challenges for thermal energy storage systems. *Archives of Thermodynamics*, 45(3), 135−147.

1. Introduction

Organic phase-change materials (PCMs) for latent thermal energy storage (TES) have emerged as suitable materials for storing and releasing large amounts of energy at relatively constant temperatures during the solid-to-liquid phase transition, or vice versa [1,2]. Organic PCMs have several attractive features such as congruent melting, high latent heat of fusion, nontoxicity, nonflammability, little or no volume change, extremely small or even negligible supercooling, low cost, high thermal stability, good chemical stability over many thermal cycles, compatibility with several types of container materials, and environmental and human friendliness [3–7]. Among the organic PCMs, saturated

Nomenclature

A – heat transfer area, m^2
h – convective heat transfer coefficient, W/(m^{2}K)
L – length, m
P – power density, W/m^2
$\dot{Q}$ – rate of heat, W
t_f – beginning of freezing time, min
t_{if} – end of the solidification, min
t_m – beginning of melting time, min
t_{pm} – end of melting time, min
T_b – temperature at half-bottom, inside the sample, °C
T_c – temperature at centre, inside the sample, °C
T_f – freezing temperature, °C
T_m – melting temperature, °C
$T_{s,b}$ – temperature at bottom surface, °C
$T_{s,u}$ – temperature at upper surface, °C
T_u – temperature at half-upper, inside the sample, °C

Greek symbols

Δt_c – solidification period, min
Δt_m – melting period, min
κ – thermal conductivity, W/(m K)

Subscripts

a – ambient
c – container
w – boundary

Abbreviations and Acronyms

LA – lauric acid
HTF – heat transfer fluid
PCM – phase change material
TES – thermal energy storage

fatty acids with the general formula $CH_3(CH_2)_nCOOH$ are of particular interest because the melting temperature of a material is proportional to the number of carbon atoms, that is the chemical bond between carbon and hydrogen. Therefore, this material can be easily selected for certain applications. Fatty acids have been used in several fields including building components [8–10], solar energy storage applications [6], temperature-regulated drug-delivery systems [11], and biological applications [12].

For energy storage applications in buildings, the macroencapsulation of organic PCMs is beneficial because of their simplicity and relatively low cost [13–15]. It is implemented as either an internal thermal mass [16,17] or a building envelope [13,15] to reduce building energy consumption, reduce the cooling load, achieve room cooling, and improve indoor thermal comfort. Focusing on the spherical geometry, which exhibits the highest thermal performance [18], the heat transfer rate of PCMs in spherical cells can be easily adjusted from the surface-area-to-volume ratio [19]. In practical applications, the common phase change of PCM is solid-to-liquid (melting) or vice versa (solidification). The melting and solidification processes of PCM involve conduction and convection heat transfers, each with different characteristics and heat transfer rates [20]. In addition, depending on the effects of gravitation on the solid phase of the PCM, the melting process can follow one of two possible mechanisms: constrained or unconstrained. In constrained melting, the solid PCM is prevented from sinking to the bottom of the sphere using a glass-enclosed thermocouple, whereas in unconstrained melting, the solid PCM sinks to the bottom of the sphere owing to gravity [21]. The melting rate is slower in constrained fusion than in unconstrained fusion [21,22].

Numerous theoretical, simulation and experimental studies have been performed to study the melting and solidification of PCMs in a spherical geometry, as summarised in Table 1, which outlines the surrounding fluid as the heat transfer fluid (HTF) as well as the output parameters from the study. In addition to the temperature difference and surface area, the properties of the fluid, nature of the fluid motion, and bulk fluid velocity are variables that determine the convection heat transfer coefficient for the heat exchange rate between the PCM and the environment as well as the heat transfer rate inside the PCM. The higher the density of the fluid and faster the fluid motion, the greater the convective heat transfer [20]. As shown in Table 1, water is commonly used as the fluid; however, for various applications, PCM can be used with different types of HTF, including air [23,24]. Because of the relatively high density, viscosity and thermal conductivity of water compared with air, a steady state can be achieved in a relatively short time, after which the surface temperature of the PCM can be assumed constant. This condition allows for a comparison between the results of the experimental and simulation studies, with the time evolution of the liquid or solid fraction as a common comparative output parameter. The results of the experimental and simulation studies show that during a solid-to-liquid phase change using water at a constant temperature or water with variable electrical power [25], the temperature inside the PCM increases sharply around the melting point [21,26–28]. This contrasts with the liquid-to-solid phase change that occurs at relatively constant temperature [29]. For melting and solidification with forced air convection [30], a high transfer rate obliterates the phase change characteristics at a constant temperature. The drastic change in the PCM temperature during the phase transition raises the question of its capability as a latent TES that can absorb and release a relatively large amount of thermal energy at a constant temperature.

In this study, the melting and solidification processes of an organic PCM of lauric acid (LA) encapsulated in a spherical shell exposed to a natural air environment were experimentally studied to investigate the relationship between the dominant heat transfer and heat transfer rate, and its implication on the phase change characteristics for its application as latent thermal energy storage. The use of air instead of water as the medium for the phase change of LA allowed us to study the heat exchange process in detail owing to the slower heat transfer rate. Based on the asymmetry between the melting and solidification processes, we discuss several possible methods for controlling the heat transfer rate to optimise the performance of a PCM as a latent TES.

Table 1. Phase change studies of PCMs contained in a spherical enclosure with environmental conditions and output parameters.

Author/Ref.	Process		Method		HTF/Environment condition	Output parameter
	Melting	Solidification	Theory/simulation	Experiment		
Tan, 2008 [21]	√			√	Water bath with constant temperatures	Melting phase front, liquid fraction, time dependent temperature
Kothari et al., 2020 [22]	√		√		A constant wall temperature	Melt fraction
Rizan et al., 2012 [25]	√			√	Water bath with constant heat rates at surface	Phase front and isotherm, melt-fraction, Stefan number
Galione et al., 2015 [26]	√	√	√		Water bath at a constant temperature	Time dependent temperature, liquid fraction, temperature map
Hosseinizadeh et al., 2013 [27]	√		√	√	Constant wall temperatures	Melt fraction, melting phase front, temperature contour and streamline, heat flux, time dependent temperature, Nusselt number
Tan et al., 2009 [28]	√		√	√	Constant surface wall temperature	Melt fraction, streamline, temperature contour, time dependent temperature
Ismail and Moraes, 2009 [29]		√	√	√	Constant surface temperatures	Time dependent temperature, solidified mass fraction
Ettouney et al., (2005) [30]	√	√		√	Air at constant temperatures and different velocities.	Time dependent temperature, Nusselt number, Fourier number
Toledo et al., 2022 [31]	√	√	√		Water bath at constant temperatures	Liquid fraction, heat flow, Nusselt number
Assis et al., 2007 [32]	√		√	√	Constant wall temperatures	Melt fraction, heat flux
Li et al., 2017 [33]	√		√		Water bath at constant temperatures	Melt fraction
Ghosh et al., 2019 [34]		√	√		Constant surface temperature	Melt fraction, heat flux
Nazzi Ehms et al., 2018 [35]		√	√		Constant surface temperatures	Solid/liquid fraction, heat flux, streamline, temperature line, heat flux
Assis et al., 2009 [36]		√	√	√	Uniform wall temperatures	Melt fraction
Li et al., 2015 [37]	√	√		√	Water bath with a constant temperature	Time dependent temperature
Prabakaran et al., 2020 [38]	√			√	Constant temperature bath of water	Time dependent temperature

2. Materials and methods

We use technical LA with a purity of ≥ 98%. The thermophysical parameters of LA are listed in Table 2.

Table 2. Thermophysical parameters of LA from the previous experimental studies (*s*: solid, *l*: liquid).

Thermophysical parameters	Value	Ref.
Melting temperature, °C	45	[39]
Freezing temperature, °C	41	[39]
Latent heat, kJ/kg	187	[39]
Density, kg/m^3	940 (*s*), 885 (*l*)	[40]
Specific heat, kJ/kg °C	2.18 (*s*), 2.39 (*l*)	[40]
Thermal conductivity, W/m °C	0.169 (*s*), 0.144 (*l*)	[39]
Viscosity, kg/m s	3.74 (55 °C) 4.565 (70 °C) 6.325 (80 °C)	[39]

Figure 1 shows the experimental setup used to study the melting and solidification of LA in air. Three spherical shells with outer diameters of 44 mm, 63 mm, and 74 mm were filled with LA. We used commercial spherical shells, which were made of polyvinyl chloride with a thickness of approximately 0.5 mm. The mass of the sample inserted into the sphere was reduced by approximately 1% of its maximum value, allowing volume expansion during phase transition. The melting process was performed in a cubical adiabatic bath that could be set to a maximum temperature of 87°C, provided by four heating elements connected to a voltage controller and a step-down transformer for temperature setting. For homogeneous temperature distribution, the heating elements were covered with ceramic and glass wool and placed at the bottom of the room. The ceramic acts as a thermal mass that stabilises the temperature when the PCM shell is inserted. The maximum difference in the temperature along the vertical configuration is approximately 1°C.

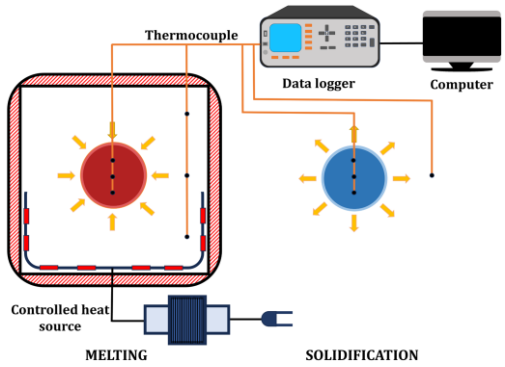

Fig. 1. Experimental setup for melting and solidification LA in air environment.

The temperature sensor consists of a T-type thermocouple with an accuracy of 0.2% + 1°C and is part of a multichannel data logger. Temperature data were recorded at time intervals of 5 s. For each spherical LA, three temperature sensors tied to a stick were placed vertically inside the shell, and two temperature sensors were placed at the upper and lower parts of the outer surface of the shell, as shown in Fig. 2. The positions of the temperature sensors and their symbols are listed in Table 3.

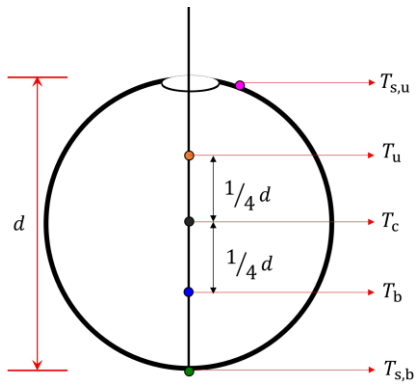

Fig. 2. Sensor position and symbol.

Table 3. Position of temperature sensors and its symbols.

Position	Symbol
Upper surface	$T_{s,u}$
Half-upper, inside the sample	T_u
Centre, inside the sample	T_c
Half-bottom, inside the sample	T_b
Bottom surface	$T_{s,b}$

For the melting process, the solid LA at room temperature (25°C) was exposed to an 80°C environment in an adiabatic room. However, for the solidification process, the melted LA at 80°C was cooled to room temperature in a natural air environment at 25°C. For each process, the experiment was repeated thrice to ensure data repeatability.

3. Results and discussion

3.1. The heat absorption associated with the melting process of lauric acid

Figure 3(i) illustrates the temperature versus time for the melting process of LA in a spherical shell with a diameter of 44 mm for the sensors on the upper (T_u), centre (T_c), and bottom (T_b) of the shell, along with the surface temperature data for $T_{s,u}$ and $T_{s,b}$. In addition to the LA temperature, the temperature data of T_u were influenced by the opening at the top of the shell. Hence, the small opening acts as a medium for convection in air. Furthermore, both surface temperatures were affected by the outside air temperature and the LA temperature inside the shell.

Starting from a room temperature of approximately 25°C, the melting process of LA involves the absorption of sensible heat in the solid phase with a significant temperature change up to the melting temperature (T_m), followed by latent heat absorption from the solid-to-liquid phase change process at T_m and subsequent sensible heat absorption in the liquid phase. Heat absorption in the sensible and latent phases is indicated by temperature changes, although the solid-to-liquid phase transition occurs with a smaller temperature gradient than that in the sensible phase. Latent heat absorption at a relatively constant temperature occurred only for the sensor at the bottom (T_b). This result is in agreement with those of previous experimental studies on the melting of PCM using a water bath with a relatively small temperature gradient [37,38].

The dominance of the convection heat transfer mode during the melting process was indicated by the different temperature profiles inside and on the surface of the shell. Because of air convection outside the shell, T_{su} was always higher than T_{sb}, except at the beginning and end of the process, when equilibrium occurred. The skin of the shell provided thermal resistance between the outside air and the PCM inside the shell such that T_u was lower than T_{su} and T_b was lower than T_{sb}. The temperature differences ($T_{s,u}$–T_c) and ($T_{s,b}$–T_c) (Fig. 3(ii)) are proportional to the heat exchanged between the PCM and the environment. Anisotropic heat exchange characteristics were observed for the upper and lower surfaces of the shell; however, they decreased as they approached thermal equilibrium. A large heat exchange occurred during the solid-to-liquid phase transition (see Section 3.3 for the analysis, as indicated by the dotted and dashed lines in Figs. 3(i) and 3(ii)). Concerning the melting mechanism, constrained melting occurs from the beginning up to a certain time, depending on the shell diameter, as indicated by $T_b < T_{sb}$. As time increases, the solid part of the LA collapses; therefore, $T_b > T_{sb}$, and constrained melting was replaced by unconstrained melting. For various shell diameters, a transition from constrained to unconstrained melting occurred at approximately 70 min for 44 mm, 108 min for 63 mm, and 130 min for 74 mm, as indicated by the valley in (T_{sb}–T_c) in Fig. 3(ii).

To study the heat transfer inside the shell during melting, Fig. 4 shows the temperature distribution along the vertical direction at certain times. From this heat absorption profile, we observed that inside the PCM shell, the melting process started from the upper part to the bottom, such that $T_u > T_c > T_b$ for all measurements. This result suggests that the phase transition process at the upper part is the fastest, followed by that at the centre and bottom parts of the shell, because of the sinking of the solid phase to the bottom owing to its higher density. From the heat conduction mode in the solid phase, heat transfer was converted into heat convection, as signified by the asymmetric temperature profiles inside the shell and the large temperature difference or gap in the temperature distribution. The convection at the upper part of the shell was stronger than that at the centre and bottom.

From the beginning (left panel of Fig. 4) to the end of the melting process (right panel of Fig. 4), the temperature distribution shown in Fig. 4 clearly indicated a larger convection with increasing shell diameter. This was also clarified by the difference between T_u and T_b with respect to dimensionless time, which was defined as the absolute time divided by the shell radii, as shown in Fig. 5. As the shell diameter increases, the (T_u–T_b) values increase, implying a higher convection intensity [30]. In

addition, for each shell, the temperature difference of (T_u–T_b) showed double peaks, with a smaller peak after the beginning of the melting time and a larger peak before the end of the melting time (see Section 3.3 for the analysis of the melting period).

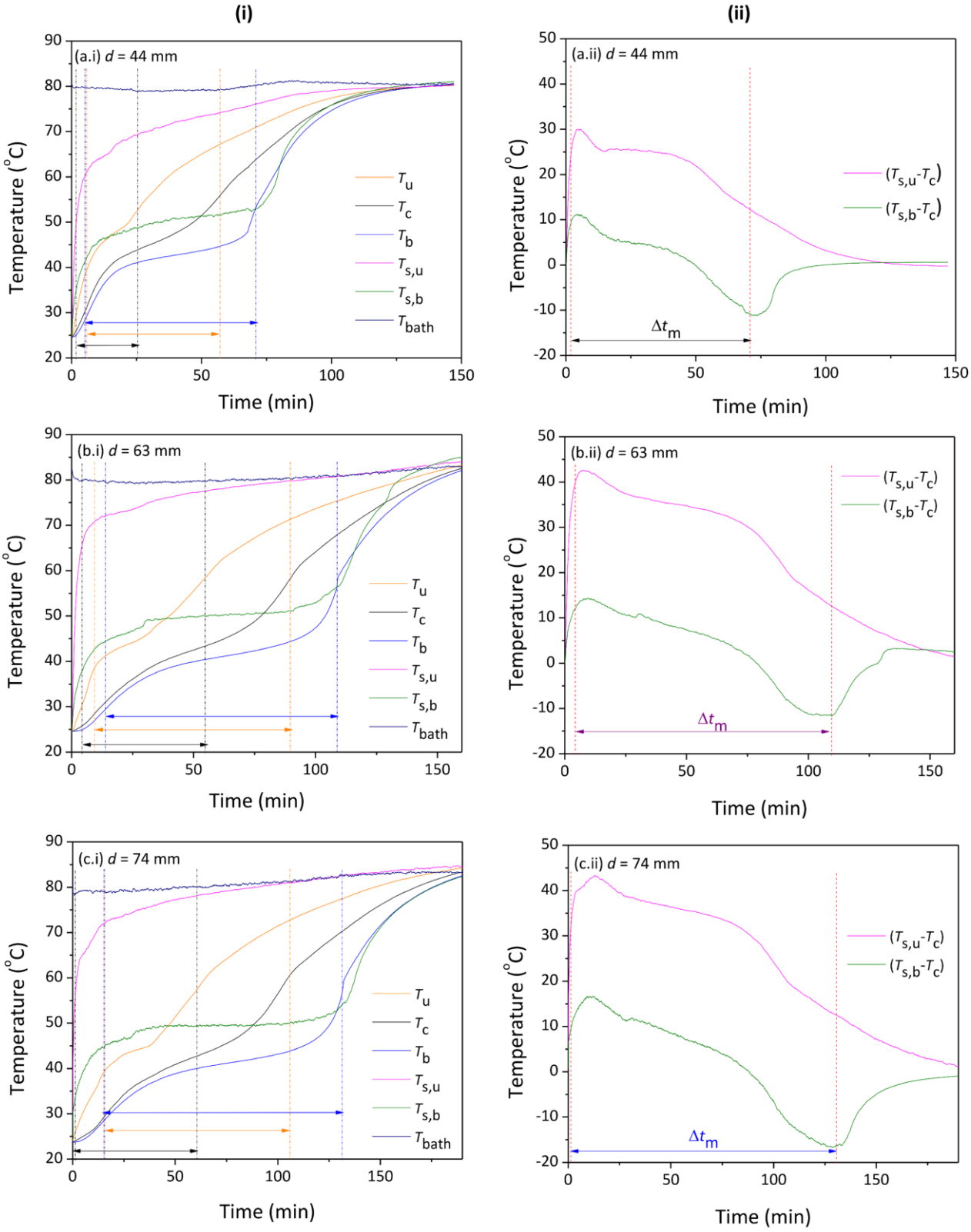

Fig. 3. Experimental data of the melting of LA in a spherical shell with outer diameters of (a) 44 mm, (b) 63 mm, and (c) 74 mm. Left (i): temperature data inside the sample (T_u, T_c, and T_b), surface temperature data ($T_{s,u}$ and $T_{s,b}$), and bath temperature (T_{bath}). Vertical dotted lines denote the phase transition region for each sensor inside the shell. Right (ii): the temperature differences of ($T_{s,u}$–T_c) and ($T_{s,b}$–T_c) with vertical dashed lines denote the melting period.

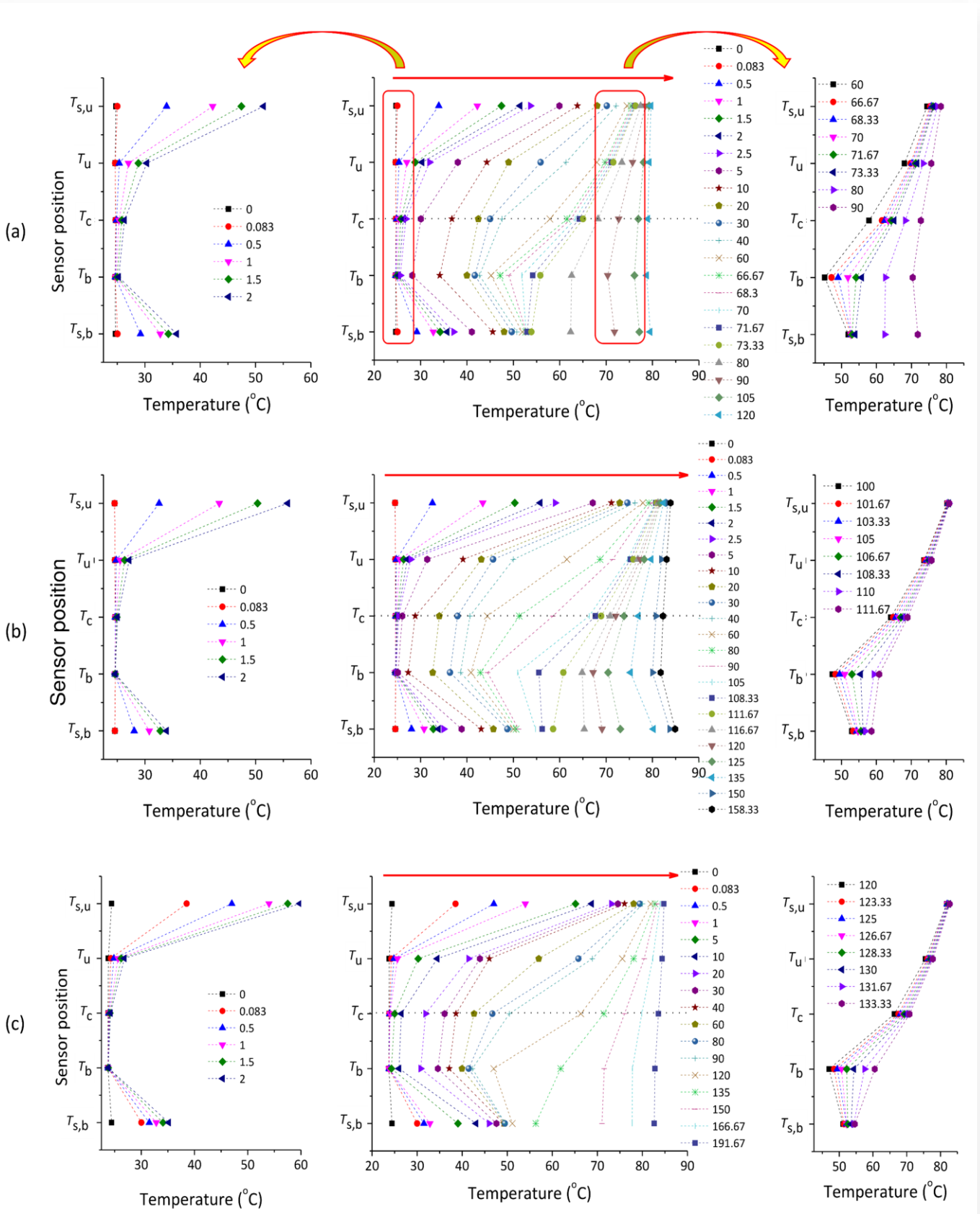

Fig. 4. Temperature distribution along the vertical direction at certain times (in minute) during melting of LA in a spherical shell with diameters of (a) 44 mm, (b) 63 mm, and (c) 74 mm (the arrow indicates the process direction). Middle column: overall time range, left column: beginning of process, right column: near end process.

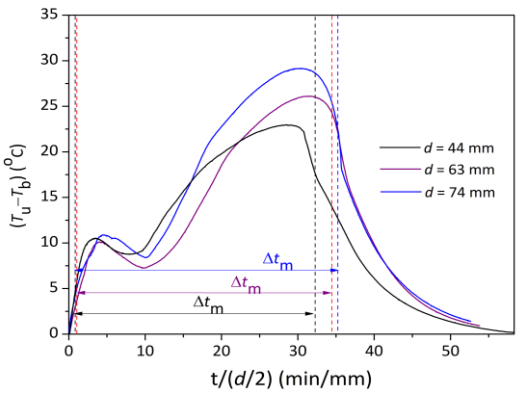

Fig. 5. Effect of shell size on convection. Vertical and horizontal lines indicate the phase transition region for each shell size.

3.2. The heat release associated with the solidification process of lauric acid

From the time-dependent temperature during the solidification process (Fig. 6(i)), we observed that starting from a high temperature of approximately 80°C, the solidification process of LA involved the release of sensible heat in the liquid phase with a significant temperature change up to the freezing temperature (T_f), followed by latent heat release from the liquid-to-solid phase change process at T_f and the subsequent sensible heat release in the solid phase. No significant differences were observed in the temperature data at the centre and bottom of the sample. Furthermore, the liquid-to-solid phase transition occurred at a relatively constant temperature of 43°C, and no supercooling was observed in the freezing curve.

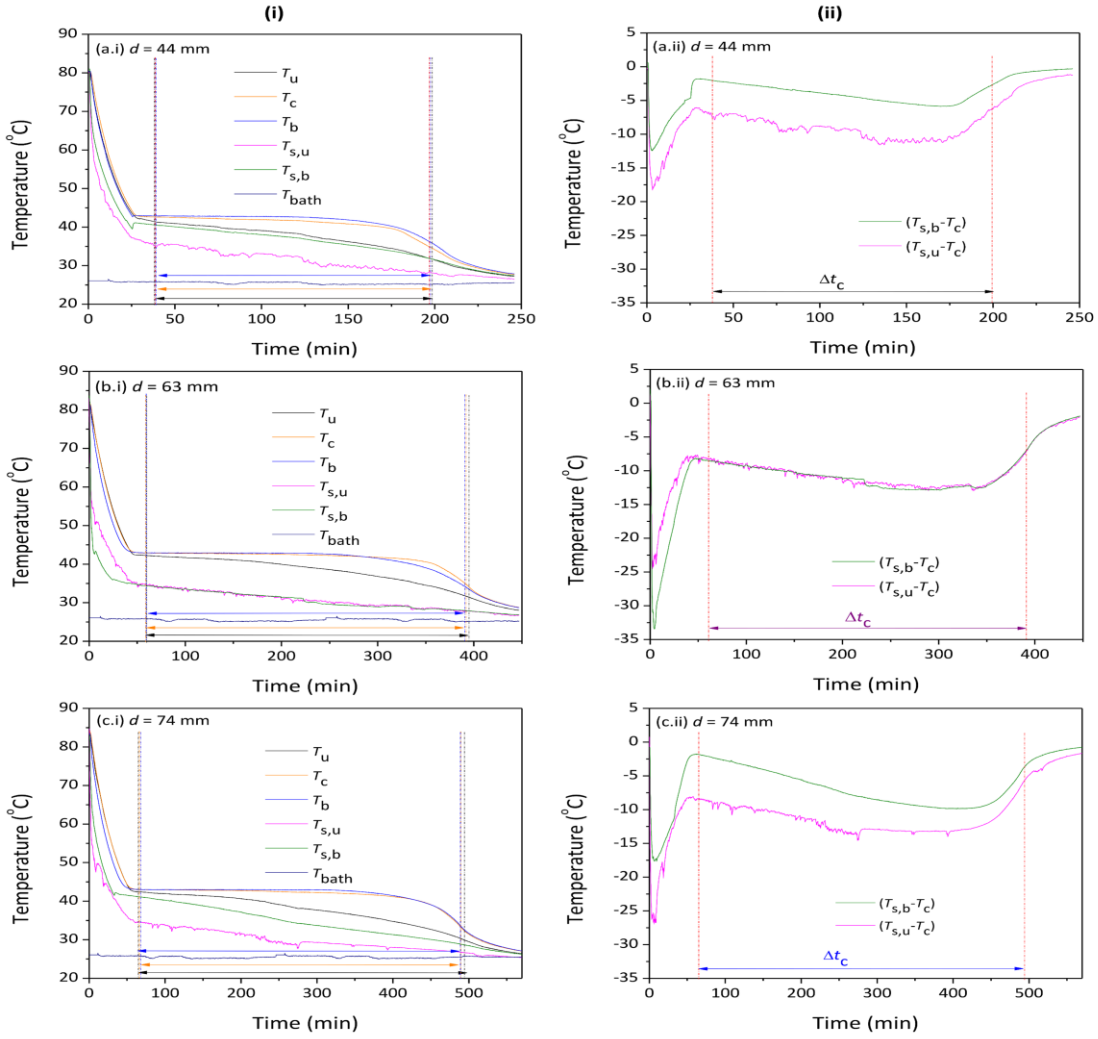

Fig. 6. Time-dependent temperature data during the solidification of LA in a spherical shell with outer diameters of (a) 44 mm, (b) 63 mm, and (c) 74 mm. Left (i): temperature data inside the sample (T_u, T_c, and T_b), surface temperature data ($T_{s,u}$ and $T_{s,b}$), and bath temperature (T_{bath}). Vertical dotted lines denote the phase transition region for each sensor inside the shell. Right (ii): the temperature differences of ($T_{s,u}$–T_c) and ($T_{s,b}$–T_c) with vertical dashed lines denote the solidification period.

Compared with melting, the isotropic heat exchange over the surface of the shell is shown in Fig. 6 (ii) which shows a similarity in the temperature differences of ($T_{s,u}$–T_c) and ($T_{s,b}$–T_c).

The temperature distributions at certain times during solidification are shown in Fig. 7. Initially, the temperature distribution inside the shell was relatively homogenous, and the surface

temperature was lower than that inside the shell owing to the influence of the environment. With increasing time, the temperature distribution inside the shell became inhomogeneous, and a gap in the temperature distribution was observed. Because of convection, T_c was always higher than T_u and T_u was higher than T_b. The gap in the temperature distribution diminished after a certain time, that is approximately 30, 40 and 60 minutes for shell diameters of 44, 63 and 74 mm, respectively. Hence, the heat transfer mechanism may change from convection to conduction following the phase change process.

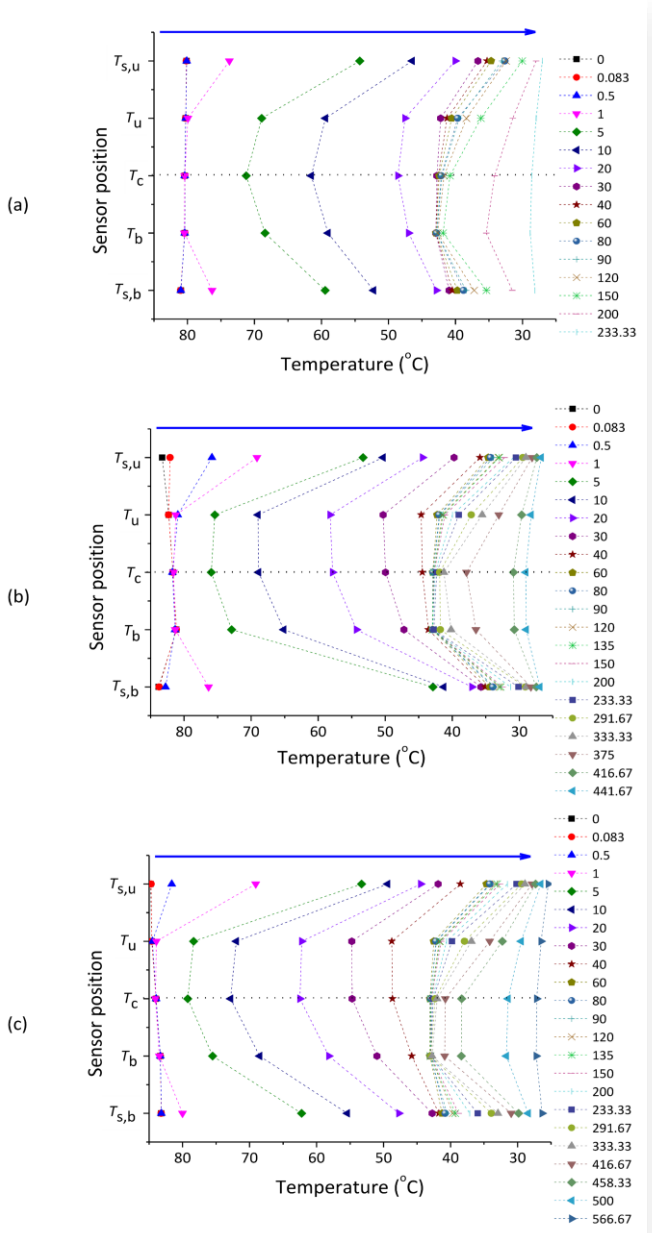

Fig. 7. Temperature distribution along the vertical direction at certain times (in minute) during the solidification of LA in a spherical shell with diameters of (a) 44 mm, (b) 63 mm, and (c) 74 mm.

3.3. Controlling the heat transfer rate of PCM

During the charging and discharging processes of PCM, heat exchange between PCM and its environment occurs at the surface layer of the shell, and is dominated by conduction and convection. The rate of heat conduction through a wall is expressed using Fourier's equation [20] and is proportional to the temperature difference across the wall (ΔT) and the heat transfer area (A) but is inversely proportional to the wall thickness (L)

$$\dot{Q}_{\text{conduction}} = -\kappa_c A \frac{\Delta T}{L}, \quad (1)$$

where κ_c is the thermal conductivity of the container material and is a measure of its ability to conduct heat. Despite the complexity of convection, the rate of convection heat transfer is proportional to the temperature difference, and is conveniently expressed by Newton's law of cooling as follows [20]:

$$\dot{Q}_{\text{convection}} = hA(T_w - T_{\text{PCM}}), \quad (2)$$

where h is the convective heat transfer coefficient, A is the surface area through which the convective heat transfer occurs, T_w is the boundary temperature, and T_{PCM} is the temperature of the PCM. We note that h is not a property of the material, as the thermal conductivity is, because it is dependent on several external factors, such as the properties of the fluid, pressure, and fluid velocity.

The melting and solidification processes of PCM-based TES systems are highly complex and involve conduction and natural convection heat transfer mechanisms with different dominant mechanisms. The power density of the PCM as a TES system can be calculated as:

$$P = \kappa_{\text{PCM}} \frac{dT}{dx} + h(T_{\text{PCM}} - T_a), \quad (3)$$

where κ_{PCM} is the thermal conductivity of PCM and T_a is the ambient temperature.

Focusing on constrained melting, the description of the melting mechanism begins with PCM initially in the solid phase with conductive heat transfer. As time increased at the beginning of the melting process, the liquid phase started to form when the solid–liquid interface was parallel to the heating boundary. In this case, the heat transfer process was still dominated by heat conduction [38,41], and the liquid formation of PCM was relatively constant because of the direct contact between the inner wall and solid PCM [27,41]. As melting progressed, the layer of liquid PCM increased, particularly at the upper part of the shell [27,37–38,41]; thus, the heat conduction was significantly reduced. Hence, a transition stage from dominant heat conduction to heat convection occurred [38], and the shape of the solid–liquid interface was no longer parallel to the heating boundary. Instead, it had an irregular curve shape with a position slightly lower than the centre of the shell owing to the higher density of the solid phase [21,41]. This irregularly shaped phase front was caused by natural convection when the liquid layer thickness increased. In this case, natural convection occurred because the warm liquid PCM rose along the hot wall, whereas the cooler liquid in the centre flowed down to replace the warmer fluid. This phenomenon creates unstable fluid circulation inside the shell, known as 'buoyancy-driven convection' [21,42]. With an increase in the amount of liquid phase, the size of the solid phase decreased before finally reaching a fully melted state.

In the solidification process, the initial condition was a melted PCM with dominant convective heat transfer. As time increased, the temperature of the liquid layer adjacent to the inner wall decreased, and solidification propagated slowly towards the centre of the sphere concentrically, with the solid–liquid interface being relatively parallel to the cool boundary [37,43]. As cooling progressed, the temperature and liquid fraction decreased rapidly, and the buoyancy-driven convection moved the cooler liquid downward owing to its higher density. Under these conditions, the solid–liquid interface was relatively spherically symmetric, with the solid phase being thicker at the bottom of the shell, and a transition from the dominant heat convection stage to the heat conduction transition stage occurred [30,35]. As time increased, the amount of cold-liquid PCM decreased before the PCM reached its full solid state. However, at the end of solidification, the front phase is relatively irregular owing to the formation of voids caused by the shrinkage of the solid PCM [43]. The number, size and distribution of voids are influenced by the initial temperature and liquid viscosity of the PCM, in addition to the ratio of the surface area relative to the volume of the sphere (A/V), because a larger surface area provides a faster cooling rate and makes it easier to trap voids [44].

Following the T-history method [45,46], we considered the time derivative of the PCM temperature to determine the melting and solidification periods. The resulting dT/dt–t graph plotted along the T–t graph is shown in the upper part of Fig. 8. For melting (left), each of the three temperature sensors exhibits two peaks (t_m and t_{pm}) on the derivative curve corresponding to the beginning and end of melting. The melting period Δt_m was determined as the difference between t_m from T_u data and t_{pm} from T_b data. In contrast, for solidification (right), the three temperature sensors showed a constant value of zero in the temperature derivative curve at almost the same time (t_f) owing to the latent heat release, and an inflection point (t_{if}) in the $dT/dt - t$ curve marked the end of the solidification process [47,48]. The solidification period Δt_c is defined as the difference between t_{if} and t_f, with t_{if} obtained from T_u data. The results (bottom part of Fig. 8) show that the melting and solidification periods increased with increasing shell size because of the larger amount of stored heat, which agrees with the results of previous studies [33,49–51].

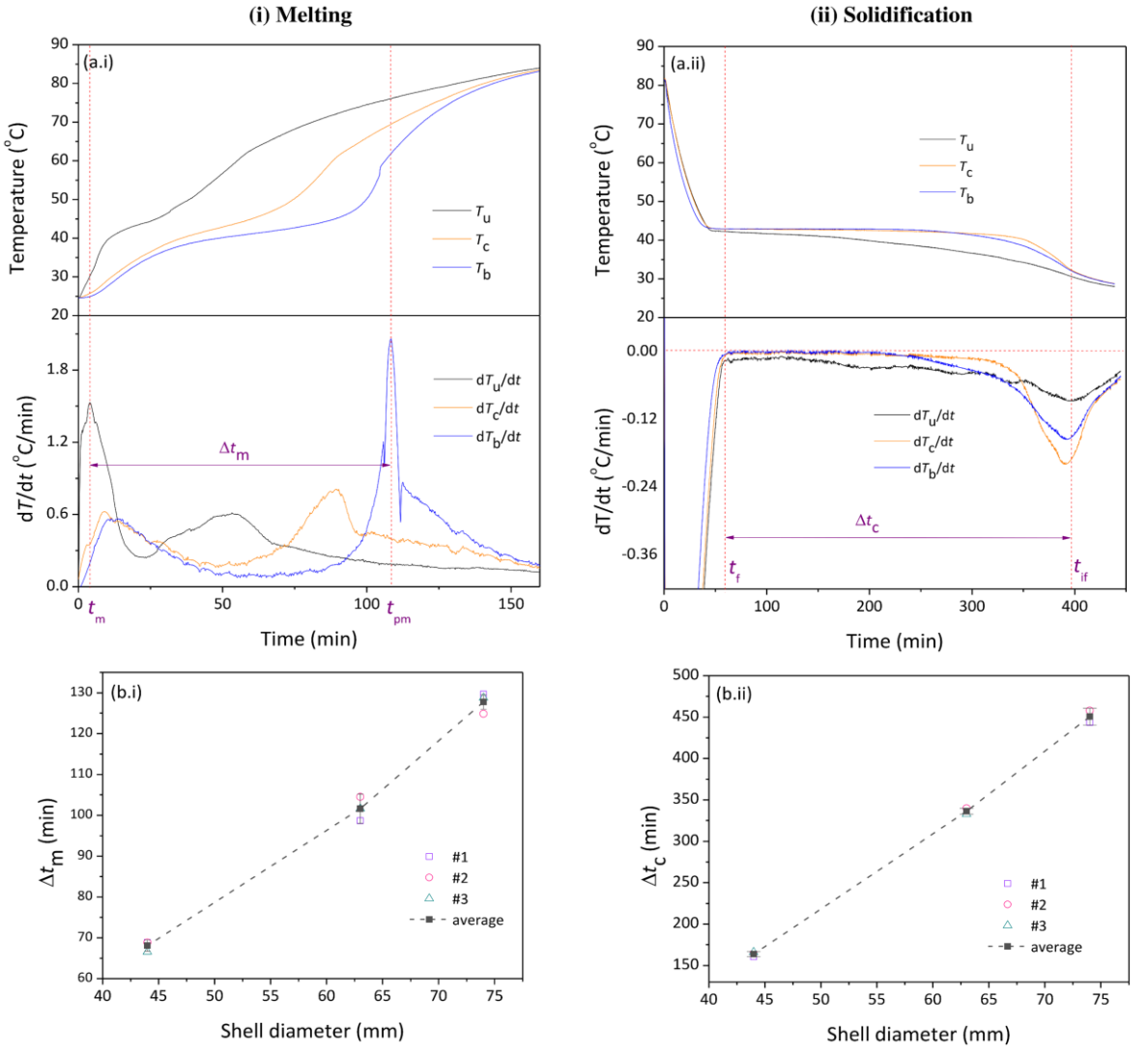

Fig. 8. Time-dependent temperature data of T_u, T_c, and T_b and their time derivatives to determine the melting (left) and solidification (right) periods; and bottom: the melting/solidification periods of LA in a spherical shell with various diameters. For each shell size, we show the data from three repetitive measurements with means and standard deviations.

An asymmetry exists between the behaviours of the melting and solidification processes. In other words, melting and solidification do not simply reverse the process direction. The melting process was dominated by natural convection [27,37,38], whereas the solidification process was dominated by heat conduction [30,37,50]. As shown in bottom of Fig. 8, shorter melting period associated with heat absorption than the solidification period associated with the heat release agrees with the prediction that convection is considerably more efficient than conduction for heat transfer [20]. With convective dominance, the heat transfer rate of the melting process is highly sensitive to the properties of the surrounding fluid, nature of the fluid motion, and bulk fluid velocity.

The optimal performance of PCM for diurnal applications requires a balance between the charging and discharging periods. This can be achieved, for example, by using different heat transfer fluids as media during melting and solidification. From a geometric perspective, for the spherical geometry of the PCM, by decreasing the diameter of the sphere, the *A*/*V* ratio can be increased to enhance the heat transfer [27]. Additionally, various active and passive methods can be used to control the heat transfer rate of PCM [52,53]. Passive methods involve using additives or surface modification techniques to increase the thermal conductivity of PCM or composite PCM. This method is typically performed by adding dopant particles with high thermal conductivity to the PCM [54,55], inserting a metal matrix into the PCM [56], extending the surface using finned tubes with various geometries [57], using porous materials [58], or microencapsulating the PCM [59]. The active method relies on an external field, such as mechanical disturbances, vibrations, ultrasound, electric fields, or magnetic fields [60]. The effectiveness of ultrasound in enhancing heat transfer is closely related to the ultrasonic power and action time [61]. In the case of an electric field, electric body forces, including the Coulomb forces produced by an external electric field, induce flow [62], bubble generation [63,64], or complex compounds [63,65–67] that enhance heat transfer. In contrast, the effect of a magnetic field or its combination with magnetic dopant particles [68–70] controls the convective heat transfer from the PCM and modifies the shape of the solid-liquid interface [71]. The effectiveness of electric and magnetic fields is closely related to the polarisability and magnetisation of the material and its effect on the change in the Gibbs free energy [72,73]. We note that apart from different heat transfer mechanisms, from a thermodynamic point of view, melting is related to an increase in the entropy of the system, whereas solidification is related to a decrease in entropy. These two processes are irreversible to each other [74]. Finally, the asymmetry between melting and solidification may be intricately related to the asymmetry between heating and cooling, as has been recently studied in the thermal kinematics of microscopic systems [75].

4. Conclusions

In this paper, we present the results of an experimental study on the heat exchange of the organic phase change material (PCM) of lauric acid in a spherical shell in an air environment as well as its implications for the heat transfer mode inside the shell and phase change characteristics. From the time-dependent temperature data inside and on the surface of the shell, we found that melting was dominated by convection, whereas solidification was dominated by conduction. The convection intensity increases with increasing shell size. Hence, the melting process depends on the properties of the surrounding fluid, nature of the fluid motion, and bulk fluid velocity. Owing to the relatively high convection transfer rate, latent heat absorption following a solid-to-liquid phase change does not occur at a constant temperature. The sensor at the bottom half of the shell showed a smaller temperature gradient in the latent phase than in the solid and liquid sensible phases. This differs from the solidification process, in which a latent heat release accompanied by a liquid-to-solid phase transition occurs at a relatively constant temperature. In addition, for a given shell size, the melting period was shorter than the solidification period.

Because of the asymmetry between the melting and solidification processes, controlling the heat transfer rate is important for achieving a balance between charging and discharging to optimise the performance of PCM for diurnal applications. From a geometric point of view, this can be achieved by choosing a certain shell diameter, considering that the *A*/*V* ratio increases with a decreasing shell diameter, which enhances the heat transfer. From the heat transfer medium, a fluid with a higher density, such as water, is suitable for solidification while melting in an air environment because of its longer solidification time. In addition, we discuss active and passive methods for controlling heat transfer in PCM. Passive methods rely on the use of dopant particles, metal matrices, and surface modifications, whereas active methods require additional external energy, such as mechanical energy, electrical or magnetic field energy. However, because of the different dominant heat transfer mechanisms for melting and solidification, different strategies may be applied to the two processes. Controlling heat transfer in the charging and discharging processes of PCM is highly beneficial for future PCM technologies, although it is challenging for practical applications.

Acknowledgements

This study presents the output of the P2MI ITB 2024 research scheme. We thank Editage (www.Editage.com) for English language editing.

References

[1] Magendran, S.S., Saleem, F., Khan, A., Mubarak, N.M., & Vaka, M. (2019). Synthesis of organic phase change materials (PCM) for energy storage applications : A review. *Nano-Structures & Nano-Objects*, 20, 100399. doi: 10.1016/j.nanoso.2019.100399

[2] Fleischer, A.S. (2015). *Thermal energy storage using phase change materials: Fundamentals and applications*. Springer Briefs in Applied Sciences and Technology. Springer Cham. doi: 10.1007/978-3-319-20922-7

[3] Sari, A. (2003). Thermal reliability test of some fatty acids as PCMs used for solar thermal latent heat storage applications, *Energy Conversion and Management*, 44(14), 2277–2287. doi: 10.1016/S0196-8904(02)00251-0

[4] Sarı, A., & Kaygusuz, K. (2003). Some fatty acids used for latent heat storage : thermal stability and corrosion of metals with

respect to thermal cycling. *Renewable Energy*, 28, 939–948. doi: 10.1016/S0960-1481(02)00110-6

[5] Majó, M., Sánchez, R., Barcelona, P., García, J., Fernández, A.I., & Barreneche, C. (2021). Degradation of fatty acid phase-change materials (PCM): New approach for its characterization. *Molecules*, 26(4), 1–11. doi: 10.3390/molecules26040982

[6] Kahwaji, S., Johnson, M.B., Kheirabadi, A.C., Groulx, D., & White, M.A. (2017). Fatty acids and related phase change materials for reliable thermal energy storage at moderate temperatures. *Solar Energy Materials and Solar Cells*, 167, 109–120. doi: 10.1016/j.solmat.2017.03.038

[7] Rozanna, D., Chuah, T.G., Salmiah, A., Choong, T.S.Y., & Sa'ari, M. (2005). Fatty Acids as Phase Change Materials (PCMs) for Thermal Energy Storage: A Review. *International Journal of Green Energy*, 1**(**4), 495–513. doi: 10.1081/ge-200038722

[8] Nazari, M., Jebrane, M., & Terziev, N. (2021). Multicomponent bio-based fatty acids system as phase change material for low temperature energy storage. *Journal of Energy Storage*, 39, 10264. doi: 10.1016/j.est.2021.102645

[9] Duquesne, M., Mailhé, C., Doppiu, S., Dauvergne, J.L., Moreno, S.S., Godin, A., Fleury, G., Rouault, F., & del Barrio, E.P. (2021). Characterization of Fatty Acids as Biobased Organic Materials for Latent Heat Storage. *Materials*, 14(16), 4707. doi: 10.3390/ma14164707

[10] Kurdi, A., Almoatham, N., Mirza, M., Ballweg, T., & Alkahlan, B. (2021). Potential phase change materials in building wall construction − a review. *Materials*, 14, 18. doi: 10.3390/ma14185328

[11] Hyun, D.C., Levinson, N.S., Jeong, U., & Xia, Y. (2014). Emerging applications of phase-change materials (PCMs): Teaching an old dog new tricks. *Angewandte Chemie International Edition*, 53(15), 3780–3795. doi: 10.1002/anie.201305201

[12] Zare, M., & Mikkonen, K.S. (2023). Phase Change Materials for Life Science Applications. *Advanced Functional Materials*, 33, 2213455. doi: 10.1002/adfm.202213455

[13] Rathore, P.K.S., & Shukla, S.K. (2019). Potential of macroencapsulated PCM for thermal energy storage in buildings: A comprehensive review. *Construction and Building Materials*, 225, 723–744. doi: 10.1016/j.conbuildmat.2019.07.221

[14] Liu, Z., Teng, R., & Sun, H. (2022). Application of Phase Change Energy Storage in Buildings: Classification of Phase Change Materials and Packaging Methods. *Thermal Science*, 26(5), 4315–4332. doi: 10.2298/TSCI211122045L

[15] Liu, Z., Yu, Z.(J.), Yang, T., Qin, D., Li, S., Zhang, G., Haghighat, F., & Joybari, M.M. (2018). A review on macro-encapsulated phase change material for building envelope applications. *Building and Environment*, 144, 281–294. doi: 10.1016/j.buildenv.2018.08.030

[16] Wonorahardjo, S., Sutjahja, I.M., & Kurnia, D. (2019). Potential of Coconut Oil for Temperature Regulation in Tropical Houses. *Journal of Engineering Physics and Thermophysics*, 92**(**1), 80−88. doi: 10.1007/s10891-019-01909-7

[17] Wonorahardjo, S., Sutjahja, I.M., Damiati, S.A., & Kurnia, D. (2020). Adjustment of indoor temperature using internal thermal mass under different tropical weather conditions. *Science and Technology for the Built Environment*, 26(2), 115–127. doi: 10.1080/23744731.2019.1608126

[18] Wei, J., Kawaguchi, Y., Hirano, S., & Takeuchi, H. (2005). Study on a PCM heat storage system for rapid heat supply. *Applied Thermal Engineering*, 25(17–18), 2903–2920. doi: 10.1016/j.applthermaleng.2005.02.014

[19] Archibold, A.R., Gonzalez-Aguilar, J., Rahman, M.M., Yogi Goswami, D., Romero, M., & Stefanakos, E.K. (2014). The melting process of storage materials with relatively high phase change temperatures in partially filled spherical shells. *Applied Energy*, 116, 243–252. doi: 10.1016/j.apenergy.2013.11.048

[20] Cengel, Y.A. (2002). *Heat Transfer, A Practical Approach*, (2nd ed.). McGraw Hill.

[21] Tan, F.L. (2008). Constrained and unconstrained melting inside a sphere. *International Communications in Heat Mass Transfer*, 35(4), 466–475. doi: 10.1016/j.icheatmasstransfer.2007.09.008

[22] Kothari, R., Revankar, S.T., Sahu, S.K., & Kundalwal, S.I. (2020). A comparative study of constrained and unconstrained melting inside a sphere. *International Conference on Nuclear Engineering Collacated with the ASME 2020 Power Conference*, ICONE 3, V003T12A002. 4-5 August, Virtual conference. doi: 10.1115/ICONE2020-16056.

[23] Goel, V., Dwivedi, A., Kumar, R., Kumar, R., Pandey, A.K., Chopra, K., & Tyagi, V.V. (2023). PCM-assisted energy storage systems for solar-thermal applications: Review of the associated problems and their mitigation strategies. *Journal of Energy Storage*, 69, 107912. doi: 10.1016/j.est.2023.107912

[24] Du, K., Calautit, J., Wang, Z., Wu, Y., & Liu, H. (2018). A review of the applications of phase change materials in cooling, heating and power generation in different temperature ranges. *Applied Energy*, 220, 242–273. doi: 10.1016/j.apenergy.2018.03.005

[25] Rizan, M.Z.M., Tan, F.L., & Tso, C.P. (2012). An experimental study of n-octadecane melting inside a sphere subjected to constant heat rate at surface. *International Communications in Heat Mass Transfer*, 39(10), 1624–1630. doi: 10.1016/j.icheatmasstransfer.2012.08.003

[26] Galione, P.A., Lehmkuhl, O., Rigola, J., & Oliva, A. (2015). Fixed-grid numerical modeling of melting and solidification using variable thermo-physical properties - Application to the melting of n-Octadecane inside a spherical capsule. *International Communications in Heat Mass Transfer*, 86, 721–743. doi: 10.1016/j.ijheatmasstransfer.2015.03.033

[27] Hosseinizadeh, S.F., Rabienataj Darzi, A.A., Tan, F.L., & Khodadadi, J.M. (2013). Unconstrained melting inside a sphere. *International Journal of Thermal Sciences*, 63, 55–64. doi: 10.1016/j.ijthermalsci.2012.07.012

[28] Tan, F.L., Hosseinizadeh, S.F., Khodadadi, J.M., & Fan, L. (2009). Experimental and computational study of constrained melting of phase change materials (PCM) inside a spherical capsule. *International Journal of Heat and Mass Transfer*, 52(15–16), 3464–3472. doi: 10.1016/j.ijheatmasstransfer.2009.02.043

[29] Ismail, K.A.R., & Moraes, R.I.R. (2009). A numerical and experimental investigation of different containers and PCM options for cold storage modular units for domestic applications. *International Journal of Heat and Mass Transfer*, 52, 4195–4202. doi: 10.1016/j.ijheatmasstransfer.2009.04.031

[30] Ettouney, H., El-Dessouky, H., & Al-Ali, A. (2005). Heat transfer during phase change of paraffin wax stored in spherical shells, *Journal of Solar Energy Engineering*, 127**(**3), 357–365. doi: 10.1115/1.1850487

[31] Cofré-Toledo, J., Roa-Cossio, D., Vasco, D.A., Cabeza, L.F., & Rouault, F. (2022). Numerical simulation of the melting and solidification processes of two organic phase change materials in spherical enclosures for cold thermal energy storage applications. *Journal of Energy Storage*, 51, 104337. doi: 10.1016/j.est.2022.104337

[32] Assis, E., Katsman, L., Ziskind, G., & Letan, R. (2007). Numerical and experimental study of melting in a spherical shell. *International Journal of Heat and Mass Transfer*, 50(9–10), 1790–1804. doi: 10.1016/j.ijheatmasstransfer.2006.10.007

[33] Li, W., Li, S.G., Guan, S., Wang, Y., Zhang, X., & Liu, X. (2017). Numerical study on melt fraction during melting of phase change material inside a sphere. *International Journal of Hydrogen Energy*, 42(29), 18232–18239. doi: 10.1016/j.ijhydene.2017.04.136

[34] Ghosh, D., Guha, C., & Ghose, J. (2019). Numerical investigation of paraffin wax solidification in spherical and rectangular cavity. *Heat Mass Transfer*, 55, 3547–3559. doi: 10.1007/s00231-019-02680-4

[35] Nazzi Ehms, J.H., De Césaro Oliveski, R., Oliveira Rocha, L.A., & Biserni, C. (2018). Theoretical and numerical analysis on phase change materials (PCM): A case study of the solidification process of erythritol in spheres. *International Journal of Heat and Mass Transfer*, 119, 523–532. doi: 10.1016/j.ijheatmasstransfer.2017.11.124

[36] Assis, E., Ziskind, G., & Letan, R. (2009). Numerical and experimental study of solidification in a spherical shell. *Journal of Heat and mass Transfer*, 131(2), 024502. doi: 10.1115/1.2993543

[37] Li, W., Wang, Y.H., & Kong, C.C. (2015). Experimental study on melting/solidification and thermal conductivity enhancement of phase change material inside a sphere. *International Communications in Heat Mass Transfer*, 68, 276–282. doi: 10.1016/j.icheatmasstransfer.2015.09.004

[38] Prabakaran, R., Kumar, J.P.N., Mohan Lal, D., Selvam, C., & Harish, S. (2020). Constrained melting of graphene-based phase change nanocomposites inside a sphere. *Journal of Thermal Analysis and Calorimetry*, 139(2), 941–952. doi: 10.1007/s10973-019-08458-4

[39] Sutjahja, I.M., Anggraini, Y., & Yusuf, A. (2024). Acceleration of Heat Discharge of Composite Lauric Acid Using Magnetic Dopant. *Journal of Energy Storage*, 86, 111219. doi: 10.1016/j.est.2024.111219

[40] Shokouhmand, H., & Kamkari, B. (2013). Experimental investigation on melting heat transfer characteristics of lauric acid in a rectangular thermal storage unit. *Experimental Thermal and Fluid Science*, 50, 201–212. doi: 10.1016/j.expthermflusci.2013.06.010

[41] Sattari, H., Mohebbi, A., Afsahi, M.M., & Yancheshme, A.A. (2017). CFD simulation of melting process of phase change materials (PCMs) in a spherical capsule. *International Journal of Refrigeration*, 73, 209–218. doi: 10.1016/j.ijrefrig.2016.09.007

[42] Khodadadi, J.M., & Zhang, Y. (2001). Effects of buoyancy-driven convection on melting within spherical containers. *International Journal of Heat and Mass Transfer*, 44(8), 1605–1618. doi: 10.1016/S0017-9310(00)00192-7

[43] Chan, C.W., & Tan, F.L. (2006). Solidification inside a sphere - An experimental study. *International Communications in Heat Mass Transfer*, 33(3), 335–341. doi: 10.1016/j.icheatmasstransfer.2005.10.010

[44] Revankar, S.T., & Croy, T. (2007). Visualization study of the shrinkage void distribution in thermal energy storage capsules of different geometry. *Experimental Thermal and Fluid Science*, 31(3), 181–189. doi: 10.1016/j.expthermflusci.2006.03.026

[45] Peck, J.H., Kim, J.J., Kang, C., & Hong, H. (2006). A study of accurate latent heat measurement for a PCM with a low melting temperature using T-history method. *International Journal of Refrigeration*, 29(7), 1225–1232. doi: 10.1016/j.ijrefrig.2005.12.014

[46] Yinping, Z., & Yi, J. (1999). A simple method, the T-history method, of determining the heat of fusion, specific heat and thermal conductivity of phase-change materials. *Measurement Science and Technology*, 10(3), 201–205. doi: 10.1088/0957-0233/10/3/015

[47] Hong, H., Kim, S.K., & Kim, Y.S. (2004). Accuracy improvement of T-history method for measuring heat of fusion of various materials. *International Journal of Refrigeration*, 27, 360–366. doi: 10.1016/j.ijrefrig.2003.12.006

[48] Sutjahja, I.M., Silalahi, A., Kurnia, D., & Wonorahardjo, S. (2018). Thermophysical parameters and enthalpy-temperature curve of phase change material with supercooling from T-history data. *UPB Scientific Bulletin, Series B: Chemistry and Materials Science*, 80(2), 57–70.

[49] Lago, T.G.S., Ismail, K.A.R., Lino, F.A.M., & Arabkoohsar, A. (2020). Experimental correlations for the solidification and fusion times of PCM encapsulated in spherical shells. *Experimental Heat Transfer*, 33(5), 440–454. doi: 10.1080/08916152.2019.1656301

[50] Ismail, K.A.R., & Moraes, R.I.R. (2009). A numerical and experimental investigation of different containers and PCM options for cold storage modular units for domestic applications. *International Journal of Heat and Mass Transfer*, 52, 19–20, 4195–4202. doi: 10.1016/j.ijheatmasstransfer.2009.04.031

[51] Chandrasekaran, P., Cheralathan, M., & Velraj, R. (2015). Influence of the size of spherical capsule on solidification characteristics of DI (deionized water) water for a cool thermal energy storage system – An experimental study. *Energy*, 90, 807–813. doi: 10.1016/j.energy.2015.07.113

[52] Diaconu, B.M., Cruceru, M., & Anghelescu, L. (2023). A critical review on heat transfer enhancement techniques in latent heat storage systems based on phase change materials. Passive and active techniques, system designs and optimization, *Journal of Energy Storage*, 61, 106830. doi: 10.1016/j.est.2023.106830

[53] Jegadheeswaran, S., Sundaramahalingam, A.,, &, Pohekar, S.D. (2021). Alternative Heat Transfer Enhancement Techniques for Latent Heat Thermal Energy Storage System: A Review. *International Journal of Thermophysics*, 42, 171. doi: 10.1007/s10765-021-02921-x

[54] Sutjahja, I.M., Silalahi, A.O., Wonorahardjo, S., & Kurnia, D. (2019). Thermal conductivity of phase-change material $CACL_2{\cdot}6H_2O$ with ZnO nanoparticle dopant based on temperature-history method. *Revista Romana de Materiale / Romanian Journal of Materials*, 49(2), 185–192.

[55] Sutjahja, I.M., Silalahi, A.O., Kurnia, D., & Wonorahardjo S. (2019). The role of particle dopant to the thermal conductivities of PCM coconut oil by means of the T-history method. *Journal of Physics: Conference Series*, 1204, 012056. *The 7th Asian Physics Symposium*, 29-31 August 2017, Bandung, Indonesian. doi:10.1088/1742-6596/1204/1/012056

[56] Jourabian, M., Farhadi, M., & Rabienataj Darzi, A.A. (2016). Heat transfer enhancement of PCM melting in 2D horizontal elliptical tube using metallic porous matrix. *Theoretical and Computational Fluid Dynamics*, 30, 579–603. doi: 10.1007/s00162-016-0402-0

[57] Sayehvand, H.-O., Abolfathi, S., & Keshavarzian, B. (2023). Investigating heat transfer enhancement for PCM melting in a novel multi-tube heat exchanger with external fins. *Journal of Energy Storage*, 72, 108702. doi: 10.1016/j.est.2023.108702

[58] Zhao, C.Y., Zhou, D., & Wu, Z.G. (2011). Heat transfer of phase change materials (PCMs) in porous materials. *Frontiers in Energy*, 5, 174–180. doi: 10.1007/s11708-011-0140-3

[59] Rostami, J. (2021). Convective heat transfer by micro-encapsulated PCM in a mini-duct. *International Journal of Thermal Sciences*, 161, 106737. doi: 10.1016/j.ijthermalsci.2020.106737

[60] Wu, Y., Zhang, X., Xu, X., Lin, X., & Liu, L. (2020). A review on the effect of external fields on solidification, melting and heat transfer enhancement of phase change materials, *Journal of Energy Storage*, 31, 101567. doi: 10.1016/j.est.2020.101567

[61] Zhang, N., & Du, Y. (2018). Ultrasonic enhancement on heat transfer of palmitic-stearic acid as PCM in unit by experimental study. *Sustainable Cities and Society*, 43, 532–537. doi: 10.1016/j.scs.2018.08.040

[62] Sun, Z., Zhang, Y., Luo, K., Pérez, A.T., Yi, H., & Wu, J. (2022). Experimental investigation on melting heat transfer of an organic material under electric field. *Experimental Thermal and Fluid Science*, 131, 110530. doi: 10.1016/j.expthermflusci.2021.110530

[63] Shahriari, A., Acharya, P.V., Carpenter, K., & Bahadur, V. (2017). Metal-Foam-Based Ultrafast Electronucleation of Hydrates at Low Voltages. *Langmuir*, 33(23), 5652–5656. doi: 10.1021/acs.langmuir.7b00913

[64] Carpenter, K., & Bahadur, V. (2016). Electronucleation for Rapid and Controlled Formation of Hydrates. *Journal of Physical Chemistry Letters*, 7(13), 2465–2469. doi: 10.1021/acs.jpclett.6b01166

[65] Sutjahja, I.M., Rahman, A., Putri, R.A., Swandi, A., Anggraini, R., Wonorahardjo, S., Kurnia, D., & Wonorahardjo, S. (2019). Electrofreezing of the phase-change material $CaCl_2 \cdot 6H_2O$ and its impact on supercooling and the nucleation time. *Hemijska Industrija*, 73, 363–374. doi: 10.2298/ HEMIND190803034S

[66] Putri, R.A., Yusuf, A., Rahman, A., Anggraini, Y., Kurnia, D., Wonorahardjo, S., Wonorahardjo, S., & Sutjahja, I.M. (2021). Reduction of the supercooling of $Ca(NO_3)_2 \bullet 4H_2O$ using electric field and nucleating agent effects. *Journal of Energy Storage*, 42, 103020. doi: 10.1016/j.est.2021.103020

[67] Swandi, A., Rahman, A., Putri, R.A., Anggraini, R., Kurnia, D., Wonorahardjo, S., & Sutjahja, I.M. (2021). Effect of copper electrode geometry on electrofreezing of the phase-change material CaCl2·6H2O. *Journal of Non-Equilibrium Thermodynamics*, 46(2), 163-174. doi: 10.1515/jnet-2020-0066

[68] Anggraini, Y., Yusuf, A., Viridi, S., Kurnia, D., Wonorahardjo, S., & Sutjahja, I.M. (2024). Magnetic Dopant and Field Effects on the Heat Discharge of Organic PCM based Lauric Acid. *Experimental Thermal and Fluid Science*, 152, 111105. doi: 10.1016/j.expthermflusci.2023.111105

[69] Sheikholeslami, M., & Mahian, O. (2019). Enhancement of PCM solidification using inorganic nanoparticles and an external magnetic field with application in energy storage systems. *Journal of Cleaner Production*, 215, 963–977. doi: 10.1016/j.jclepro.2019.01.122

[70] Zandie, M., Moghaddas, A., Kazemi, A., Ahmadi, M., Feshkache, H.N., Ahmadie, M.H., & Shafripur, M. (2022). The impact of employing a magnetic field as well as Fe_3O_4 nanoparticles on the performance of phase change materials. *Engineering Applications of Computational Fluid Mechanics*, 16(1), 196–214. doi: 10.1080/19942060.2021.2006092

[71] Haddad, Z., Iachachene, F., Zidouni, F., & Oztop, H.F. (2022). Magnetic field effects on melting and solidification of PCMs in an isosceles triangular cavity. *Journal of Thermal Analysis and Calorimetry*, 147, 4697–4709. doi: 10.1007/s10973-021-10857-5

[72] Yusuf, A., Putri, R.A., Rahman, A., Anggraini, Y., Kurnia, D., Wonorahardjo, S., & Sutjahja, I.M. (2021). Time-Controlling the Latent Heat Release of Fatty Acids using Static Electric Field. *Journal of Energy Storage*, 33, 102045. doi: 10.1016/j.est.2020.102045

[73] Rahman, A., Yusuf, A., Putri, R.A., Anggraini, Y., Pujaningsih, F.B., Kurnia, D., Wonorahardjo, S., & Sutjahja, I.M. (2021). Effect of static magnetic field on nucleation of cobalt nitrate hexahydrate. *Materials Research*, 24(6), e20210088. doi: 10.1590/1980-5373-MR-2021-0088

[74] Zemansky, M.W., & Dittman, R.H. (1997). *Heat and Thermodynamics*. McGraw-Hill.

[75] Ibáñez, M., Dieball, C., Lasanta, A., Godec, A., & Rica, R.A. (2024). Heating and cooling are fundamentally asymmetric and evolve along distinct pathways. *Nature Physics*, 20(1), 135–141. doi: 10.1038/s41567-023-02269-z

Co-published by
Institute of Fluid-Flow Machinery
Polish Academy of Sciences
Committee on Thermodynamics and Combustion
Polish Academy of Sciences

http://www.imp.gda.pl/archives-of-thermodynamics/

Convection and heat transfer analysis of Cu-water rotatory flow with non-uniform heat source

Alfunsa Prathiba[a*], P. Johnson Babu[b], Manthri Sathyanarayana[c], B. Tulasi Lakshmi Devi[d], Shanker Bandari[e]

[a]Department of Mathematics, CVR College of Engineering, Hyderabad, India
[b]Department of Physics and Electronics, St. Joseph's Degree & PG College, 5-9-1106 King Koti, Main Road, Hyderabad - 500029, Telangana, India
[c]Department of Mathematics & Statistics, St.Joseph's Degree & PG College, 5-9-1106 King Koti, Main Road, Hyderabad - 500029, Telangana, India
[d]Department of Mathematics, Koneru Lakshmaiah Education Foundation, Telangana, India
[e]Department of Humanities and Sciences, CVR College of Engineering, Telangana, India
*Corresponding author email: alphonsaperli@gmail.com

Received: 29.11.2023; revised: 23.02.2024; accepted: 10.06.2024

Abstract

This article explores the phenomenon of natural convection in the rotatory flow of Cu-water nanofluid under the influence of non-uniform heat source. In order to design more effective and efficient cooling systems, this work attempts to increase our understanding of how nanofluids behave in the presence of non-uniform heat sources, convection, and rotatory force. The higher order partial differential equations governing the flow are remodelled into ordinary differential equations using similarity transformations. The remodelled equations were solved using shooting methodology and the Lobatto-III A algorithm. The impacts of various parameters such as the Richardson number ($1 < Ri < 4$), the Schmidt number ($0.5 < Sc < 2$), nanoparticle's volume fraction ($0.02 < \phi < 0.08$), etc. on velocity, concentration and temperature was analysed. One of the main findings of this analysis was study of the impact of the space dependent heat source ($0.2 \leq A \leq 1$) and the temperature dependent internal heat source ($0 \leq B \leq 0.5$) on the heat regulation. Furthermore, increasing the quantity of the nano-additives and improving the fluid's thermophysical properties intensified the acceleration of the fluid elements in the flow region. The presence of spatial and temperature-sensitive parameters facilitated quantification of the effects of a standard and variable heat source in combination of Coriolis force in the case of a Cu-water flow. The findings of the investigation will be helpful in the process of medical, architectural planning systems, oil recovery systems and so on.

Keywords: Coriolis force; Lobatto IIIA technique; Richardson number; Volume fraction of Cu nanoparticle; Non-uniform heat source

Vol. 45(2024), No. 3, 149–157; doi: 10.24425/ather.2024.151225

Cite this manuscript as: Prathiba, A., Babu, P.J., Sathyanarayana, M., Devi, B.T.L., & Bandari, S. (2024), Convection and heat transfer analysis of Cu-water rotatory flow with non-uniform heat source. *Archives of Thermodynamics*, 45(3), 149–157.

1. Introduction

The heat transmission process in nanofluids is important for many industrial and manufacturing applications. Initially, a sizable number of engineering applications relied solely on traditional heat transfer agents. However, currently they are used in intense cooling processes [1]. Further, the unique characteristic of matter at the nanoscale in nanotechnology has become a pop-

Nomenclature

A – coefficient of space dependent source/sink
a – constant ($a > 0$)
B – coefficient of temperature dependent heat source/sink
C – concentration of the species
C_p – specific heat at constant pressure constant pressure, J kg^{-1}K^{-1}
C_w – free stream concentration
C_∞ – uniform constant concentration
D – mass diffusivity coefficient
$\bar{g}$ – gravitational acceleration, m s^{-2}
k – thermal conductivity, W m^{-1}K^{-1}
Pr – Prandtl number
q''' – rate of internal heat generation/absorption
R_0 – rotational parameter
Re – Reynolds number
Ri – Richardson number
Sc – Schmidt number
T – fluid temperature, K
T_w – surface temperature, K
T_∞ – ambient temperature, K
U_w – free flow velocity
u, v, w– x, y, z components of velocity, m s^{-1}
x, y, z– Cartesian coordinates, m

Greek symbols

β – thermal expansion coefficient, K^{-1}
ν – kinematic viscosity, m^{2}s^{-1}
ϕ – nanoparticle's volume fraction
ρ – fluid density, kg m^{-3}
Ω – angular velocity, rad s^{-1}
μ – dynamic viscosity, kg m^{-1}s^{-1}
η – similarity variable
Θ – dimensionless temperature
Φ – dimensionless concentration

Subscripts and Superscripts

f – fluid
nf – nano fluid
s – solid particle
w – condition at wall
∞ – ambient condition
' – differentiation with respect to η

Abbreviations and Acronyms

MHD– magnetohydrodynamic

ular research topic in the twenty-first century. This resulted due to the limitations of thermal conduction of the aforementioned agents. Heat transfer efficiency can be considerably enriched by including metallic and non-metallic particles in ordinary fluids. The rise in the thermal conductivity of nanofluid has spurred a flurry of activity in the field of flow analysis. The thermal conductivity of several common fluids, such as water, toluene, ethylene glycol and mineral oils, is negligible. To overcome the issue of lower thermal conductivity of the above mentioned fluids Choi introduced the suspension of nanometre-sized particles (10–100 nm) or fibres into the conventional fluids [2]. To put it another way: nanoparticle-encapsulated fluids offer superior gripping, dispersion and scattering capabilities when applied to a solid substrate. Nanofluids have been the subject of much study for applications in engineering and manufacturing, especially as heat transfer fluids. These nanoparticle-containing fluids have many uses in a wide range of industries [2]. Scholars have examined several facets of nanofluids, such as enhancing thermal conductivity, integrating nanoparticles, and other associated domains [2–5].

Convective heat transfer in nanofluid has multiple uses and is essential in research and engineering [6]. Nanofluids are practically used in every technology that requires heat transfer agents for temperature control, such as renewable radiation, nuclear reactors, etc. As a result, fluid dynamics experts have paid particular attention to the field of nanofluids in recent years, owing to potential applications in various sectors [7].The influence of an exogenous directed magnetic force on heat exchange and entropy formation of nanofluid flow of Cu-water in a heated open cavity from beneath was investigated numerically by Mehrez et al. [8]. Punith Gowda et al. [9] explored the steady Marangoni driven boundary layer flow, mass and heat transfer properties of a nanofluid. Their findings indicate that strengthening the Marangoni number upgrades the flow velocity and lowers heat transfer. Yacob et al. [7] examined the steady 3D flow across a rotating extending/diminishing sheet fluid containing SCNT (single-walled carbon nanotubes) and MCNTs (multi-walled carbon nanotubes) in kerosene and water as base fluids. Faisal Shahzad et al. [10] studied the Fe_2O_4-H_2O flow sandwiched between two gyrating plates, presuming porosity in the top side, in order to create forced convection, the bottom surface was assumed to move at a variable speed. Through their meticulous analysis, Ashraf et.al. forecasted how heat and fluid would move around a non-conducting horizontal circular cylinder implanted in a porous material at various angles [11].

The magneto-thermoanalysis of electrically conducting flow over the vertically symmetric heated plate using the Keller box method was done by Ullah et al. [12]. Further, the importance of the convective heat transfer with various fluids in different conditions and flow regimes can be learned from the papers [13–17].

The exploration of heat production or absorption impacts the moving fluids. It is crucial due to various physical issues. With the rapid advancement of digital means, adequate refrigeration of electrical devices have become necessary. This equipment includes everything from single transistors to mainframe computers, energy suppliers, and telephone switchboards [18]. Hasarika et al. [4] in their theoretical investigation using the perturbation technique examined the impact of the nanoparctical volume fraction along with thermo-diffusion on a chemically retorting MHD (magnetohydrodynamic) Cu-water fluid flow. They discovered that "cupper particles had a better conductivity than

water based particles". And a noteworthy finding in their study is that the flow velocities are increased due to the influence of internal heat, diffusion and core heat generation.

One of the most important factors in changing the direction of fluid flow is the Coriolis force [19]. It is equivalent to other inertial forces such as magnetohydrodynamic forces and viscous forces in the fundamental equations of fluid dynamics. Liquid flow on the surface of the Earth is influenced by a number of forces, including friction, centrifugal, gravitational and pressure gradient forces. On the other hand, the Coriolis force usually has little effect on transport phenomena in the situations of atmosphere and water. This is most noticeable when the liquid motion speed is much slower than the rotating speed, which makes the Coriolis effect insignificant and the reason it is not commonly noticed on Earth. However, studies on the Coriolis force's effects on various liquid streams have been conducted in recent decades and each of these analyses have identified that this force has a significant impact of the flow velocities [20–22].

The analysis of the current research has been done based on the above literature assessment. As per the gap identified by the authors, the impact of non-uniform heat on rotatory nanofluid flow has not been investigated in any methodical paper. Thus, the prime objective of this paper is to analyse the predominance of a non-uniform heat source and convective rotatory flow of Cu-water nanofluid across a stretched sheet. Typical applications for rotating flows include centrifugal filtering, cooling high-speed aircraft skins, anticyclone flow circulation, and the geological stretching of tectonic plates under rotating oceans [2].

2. Problem formulation

A steady, incompressible nanofluid rotating flow over an elongating sheet under the stimulus of convection in the presence of a non-uniform source or sink has been considered for this study [23]. Its basic prototype of the flow is demonstrated in Fig. 1. The rotatory nanofluid flow is considered in the region $z \geq 0$. The *xy*-plane is anticipated to be linearly stretching in the direction of the flow with the free flow velocity $U_w = ax$, where $a > 0$ is a constant. The fluid is a copper-comprising water-based nanofluid. This two-component mixture flow is assumed under the following conditions [24]:

a) no chemical reaction,

b) minimal amount of viscous dissipation,

c) insignificant radiative heat transportation,

d) ensuring that there is no slip between the base fluid H_2O, and the nanoparticles (Cu) and that they are in thermal equipoise [24].

Centred on the above hypotheses, the governing equations of the flow are [25,26]:

$$\frac{\partial u}{\partial x}+\frac{\partial v}{\partial y}+\frac{\partial w}{\partial z}=0, \tag{1}$$

$$u\frac{\partial u}{\partial x}+v\frac{\partial u}{\partial y}+w\frac{\partial u}{\partial z}=\frac{\mu_{nf}}{\rho_{nf}}\frac{\partial^2 u}{\partial z^2}+2\Omega v+\bar{g}\beta_{nf}(T-T_\infty), \tag{2}$$

$$u\frac{\partial v}{\partial x}+v\frac{\partial v}{\partial y}+w\frac{\partial v}{\partial z}=\frac{\mu_{nf}}{\rho_{nf}}\frac{\partial^2 v}{\partial z^2}-2\Omega u, \tag{3}$$

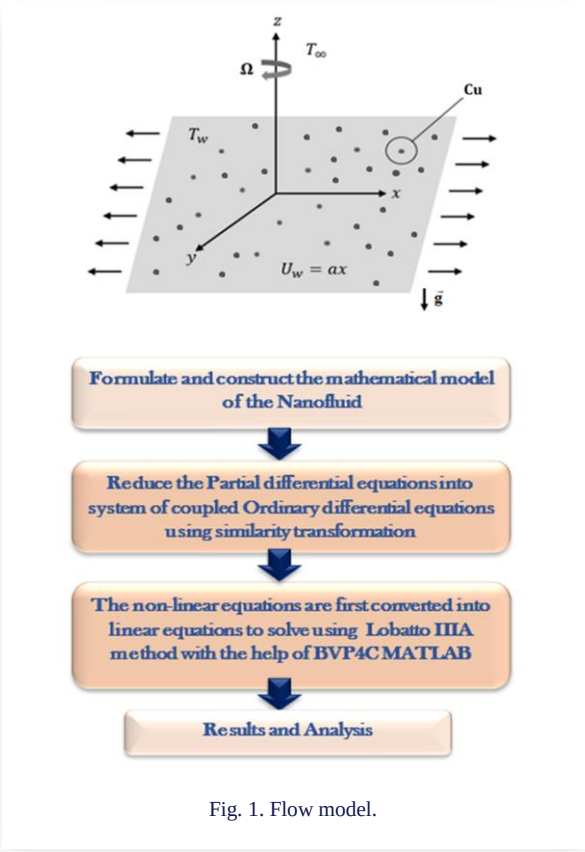

Fig. 1. Flow model.

$$u\frac{\partial T}{\partial x}+v\frac{\partial T}{\partial y}+v\frac{\partial T}{\partial z}=\frac{k_{nf}}{(\rho C_p)_{nf}}+\frac{q'''}{(\rho C_p)_{nf}}\tau, \tag{4}$$

$$u\frac{\partial C}{\partial x}+v\frac{\partial C}{\partial y}+w\frac{\partial C}{\partial z}=D_{nf}\frac{\partial^2 C}{\partial z^2}. \tag{5}$$

The boundary conditions are:

$$u=U_w,\ v=0,\ w=0,\ T=T_w,\ C=C_w\ \text{ as }\ z\to 0,$$
$$u\to 0, v\to 0, w\to 0,\ T\to T_\infty; C\to C_\infty\ \text{ as }\ z\to\infty, \tag{6}$$

where (u,v,w) are velocity components along the *x*-, *y*-, and *z*-directions, respectively, T and C are the temperature and concentration, $\bar{g}$ is the gravitational acceleration, and μ_{nf} is the dynamic viscosity [2]; ρ_{nf} is the density, k_{nf} is the thermal conductivity, $(\rho\beta)_{nf}$ is the thermal expansion coefficient of nanofluid [2], q''' is the rate of internal heat generation/absorption [27], $(\rho Cp)_{nf}$ is the heat capacitance, D_{nf} is the mass diffusivity [28] of the nanofluid, which are given by:

$$q''' = \frac{\alpha_f U_w}{x\nu_f}[A(T_w-T_\infty)f'(\eta)+B(T-T_\infty)],$$

$$\mu_{nf}=\frac{\mu_f}{(1-\phi)^{5/2}},$$

$$\rho_{nf}=(1-\phi)\rho_f+\phi\rho_s,$$

$$k_{nf}=k_f\left[\frac{k_s+2k_f-2\phi(k_f-k_s)}{k_s+2k_f+\phi(k_f-k_s)}\right],$$

$$(\rho C_p)_{nf}=(1-\phi)(\rho C_p)_f+\phi(\rho C_p)_s,$$

$$(\rho\beta)_{nf} = (1-\phi)(\rho\beta)_f + \phi(\rho\beta)_s,$$

$$D_{nf} = \frac{D_f}{1-\phi}. \quad (7)$$

The subscripts *nf*, *f* and *s* indicate the properties of nanofluid, base fluid ($\phi = 0$),and the solid nanoparticle. ϕ is the 'significant volume fraction of the nanoparticle' of (Cu), *A* and *B* are the coefficients of 'space and temperature-dependent heat source/sink', respectively [27]. The condition $A, B > 0$ relates to 'internal heat generation' and $A, B < 0$ corresponds to 'internal heat absorption' [27].

Let us consider the following similarity transformations [7]:

$$\eta = \sqrt{\frac{a}{v}}z,\ u = axF'(\eta),\ v = axG(\eta),\ w = -\sqrt{av}F(\eta),$$

$$\Theta(\eta) = \frac{T-T_\infty}{T_w-T_\infty},\ \Phi(\eta) = \frac{C-C_\infty}{C_w-C_\infty}. \quad (8)$$

The above transformation completely satisfies Eq. (1) and Eqs. (2)–(5), along with the boundary conditions, Eqs. (6), transformed into highly non-linear ordinary differential equations (ODEs), which can be given as:

$$\frac{\mu_{nf}}{\mu_f}\frac{\rho_f}{\rho_{nf}}F''' + \frac{\beta_{nf}}{\beta_f}\mathrm{Ri}\Theta = (F')^2 - FF'' - 2R_0G, \quad (9)$$

$$\frac{\mu_{nf}}{\mu_f}\frac{\rho_f}{\rho_{nf}}G'' = F'G - G'F + 2R_0F, \quad (10)$$

$$\frac{k_{nf}}{k_f}\frac{(\rho C_p)_f}{(\rho C_p)_{nf}}[\Theta'' + AF' + B\Theta] + \mathrm{Pr}F\Theta' = 0, \quad (11)$$

$$\Phi'' + \frac{\mathrm{Sc}}{(1-\phi)}F\Phi' = 0, \quad (12)$$

with the boundary conditions:

$$F'(\eta) = 1,\ G(\eta) = 0,\ F(\eta) = 0,\ \Theta(\eta) = 1,\ \Phi(\eta) = 1 \text{ at } \eta = 0,$$

$$F'(\eta) \to 0,\ G(\eta) \to 0,\ \Theta(\eta) \to 0,\ \Phi(\eta) \to 0 \text{ as } \eta \to \infty. \quad (13)$$

The parameters involved in the above equations are:

- rotational parameter: $R_0 = \frac{\Omega}{a}$,
- Prandtl number: $\mathrm{Pr} = \frac{v_f}{a_f}$,
- Schmidt number: $\mathrm{Sc} = \frac{v_f}{D_f}$.

The expression for the local drag force coefficients C_{fx} and C_{fy}, heat transfer coefficient Nu_x and the mass transfer coefficient Sh_x can be defined as:

$$C_{fx} = \frac{\tau_{xz}}{\frac{1}{2}\rho U_w^2},\quad C_{fy} = \frac{\tau_{yz}}{\frac{1}{2}\rho U_w^2},$$

$$\mathrm{Nu}_x = \frac{xq_w}{k(T_w-T_\infty)},\ \mathrm{Sh}_x = \frac{xq_m}{D_M(C_w-C_\infty)},$$

in which τ_{xz}, τ_{yz} indicate the shear stress and q_w, q_m represent the heat and mass flux at the walls of the sheet. Applying the transformations, Eqs. (8), the above expressions are transformed into:

$$\mathrm{Re}_x^{1/2}C_{fx} = \frac{\mu_{nf}}{\mu_f}F''(0),\quad \mathrm{Re}_x^{1/2}C_{fy} = \frac{\mu_{nf}}{\mu_f}G'(0),$$

$$\mathrm{Re}_x^{-1/2}\mathrm{Nu}_x = -\frac{k_{nf}}{k_f}\Theta'(0),\ \mathrm{Re}_x^{-1/2}\mathrm{Sh}_x = -\frac{D_{nf}}{D_f}\Phi'(0). \quad (14)$$

3. Methodology of the solution

Equations (9) to (12) combined with the boundary conditions are solved by implementing the Lobatto IIIA method using BVP4C numerical code in the MATLAB software [30]. To implement this method, the non-linear equations are first converted into linear equations by opting the following procedure and then converting the equations compatible to be solved by the MATLAB code:

$$f_1 = F,\quad f_2 = F',\quad f_3 = F'',$$

$$F''' = f_3' = -A_1A_2[f_1f_3 + 2R_0g_1 - (f_2)^2 + A_4\mathrm{Ri}\Theta_1],$$

$$g_1 = G,\ g_2 = G',\ G'' = g_2' = A_1A_2[-f_1g_2 + 2R_0f_1 + f_2g_1],$$

$$\theta_1 = \Theta(\eta),\ \theta_2 = \Theta'(\eta),$$

$$\theta_3 = \theta_2' = -\frac{\mathrm{Pr}k_f}{k_{nf}}[A_3f_1\theta_2] - Af_2 - B\theta_1, \quad (15)$$

$$\Phi_1 = \Phi,\ \Phi_2 = \Phi',\ \Phi_3 = -\frac{\mathrm{Sc}f\Phi'}{(1-\phi)},$$

$$A_1 = \frac{\mu_f}{\mu_{nf}},\ A_2 = \frac{\rho_{nf}}{\rho_f},\ A_3 = \frac{(\rho C_p)_{nf}}{(\rho C_p)_f},\ A_4 = \frac{(\beta)_{nf}}{(\beta)_f}. \quad (16)$$

The modified boundary conditions are:

$$f_1 = 0,\ f_2 = 1,\ g_1 = 0,\ \theta_1 = 1,\ \Phi_1 = 1 \text{ as } \eta \to 0,$$

$$f_2 \to 0,\ g_1 \to 0,\ \theta_1 \to 0,\ \Phi_1 \to 0 \text{ as } \eta \to \infty. \quad (17)$$

The thermophysical properties of nanoparticles and base fluid are placed in Table 1, these values have been utilised to calculate the values mentioned in Eqs. (16).

Table 1. Physical property parameters used for the analysis [4].

Properties	Base fluid (water)	Nano-particles (Cu)
Thermal conductivity, k ($\mathrm{Wm^{-1}K^{-1}}$)	0.613	400
Density, ρ ($\mathrm{kgm^{-3}}$)	997.1	8933
Specific heat, C_p ($\mathrm{Jkg^{-1}K^{-1}}$)	4179	385
Thermal expansion coeff., β ($\mathrm{K^{-1}}$)	36.2×10^{-5}	1.67×10^{-5}

The MATLAB BVP4C programme implements the Lobatto IIIA collocation Runge-Kutta (RK) method [31]. The code was validated by calculating the values of C_{fx}, C_{fy} and Nu_x for the base fluid when $R_0 = 0, 0.5, 1, 2$. These obtained values were then compared with the previously published findings in Tables 2 and 3. The results demonstrate a strong agreement between the obtained results and the exiting literature.

Table 2. Comparison of the values of $\mathrm{Re}_x^{1/2}C_{fx}$ and $\mathrm{Re}_x^{1/2}C_{fy}$ for base fluid when ϕ = Ri = A = B = Sc = 0.

	Salleh et al. [7]		Present findings	
R_0	$\frac{\mu_{nf}}{\mu_f}F''(0)$	$\frac{\mu_{nf}}{\mu_f}G'(0)$	$\frac{\mu_{nf}}{\mu_f}F''(0)$	$\frac{\mu_{nf}}{\mu_f}G'(0)$
0.00	-1.00000	0.00000	-1.000000	0.000000
0.50	-1.13838	-0.51276	-1.138411	-0.512802
1.00	-1.32503	-0.83809	-1.325031	-0.837121
2.00	-1.65240	-1.28726	-1.652392	-1.287301

Table 3. Comparison of calculated values of $\mathrm{Re}_x^{-1/2}\mathrm{Nu}_x$ for base fluid.

	Nadeem et al. [32]	Salleh et al. [7]	Current findings
R_0	$\frac{-k_{nf}}{k_f}\Theta'(0)$	$\frac{-k_{nf}}{k_f}\Theta'(0)$	$\frac{-k_{nf}}{k_f}\Theta'(0)$
0.00	1.770948	1.770948	1.77094791
0.50	1.725631	1.725631	1.72563892
1.00	1.660286	1.660286	1.66028591
2.00	1.533487	1.533487	1.53348701

4. Results and discussion

Equations (9) and (12) subject to the boundary conditions, Eq. (13), are solved numerically using the Lobatto III A (Runge-Kutta) method in MATLAB. The impact of relevant factors, to be precise Ri, A, B, Sc, ϕ, etc. on the velocity, mass and heat transfer of the rotatory flow over an elongated sheet are discussed. The non-dimensional parameter values such as Ri = 0.2, $R_0 = 0.02$, $\phi = 0.05$, Sc = 0.5, $A = 0.2$ and $B = 0.3$ are kept as common in the entire analysis unless stated otherwise.

The effect of the Richardson number (Ri) and the rotation parameter R_0 on the profiles of primary and secondary velocities as well as on the temperature and concentration of the Cu-water nanofluid is observed in Figs. 2 to 5. It is evident from the figures that the amplified values of Ri improve the primary velocity gradient $F'(\eta)$, whereas the secondary velocity gradient $G(\eta)$, thermal and concentration boundary layers exhibit the opposite behaviour. These oscillations in secondary velocity gradient, resulting from the angular momentum's excess convection, occurred in the boundary layer's physical space.

The primary velocity layer diminishes with magnification in rotational parameter R_0 as displayed in Fig 2. With rising in R_0, the profile of the secondary velocity gradient takes an S-shape as illustrated in Fig 3. This occurs as a result of the Coriolis force, which when the moving plate is suddenly set in motion, acts as a constraint in the primary fluid flow. It is possible to state that the Coriolis force stopped fluid flow in the primary flow direction to create a secondary and cross flows in the flow field [33]. Figures 4 and 5 depict that growth in R_0 leads to the increase in $\Theta(\eta)$ and $\Phi(\eta)$ profiles.

For the positive values of A and B, as demonstrated in Fig. 6, the magnification of the space and time-dependent non-uniform heat source/sink leads to the enhancement of the primary velocity gradient and fall in profiles of the secondary velocity.

The temperature rises as A and B increase, as shown in Fig. 7. The height of the concentration boundary layer decreases when A and B increase, as seen in Fig. 8. Physically these effects

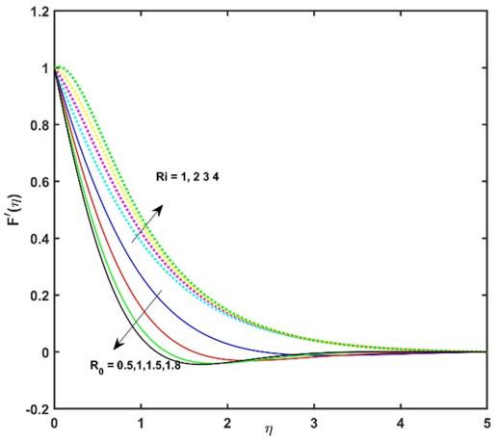

Fig. 2. Impact of rotation parameter (R_0) and Richardson parameter (Ri) on $F'(\eta)$.

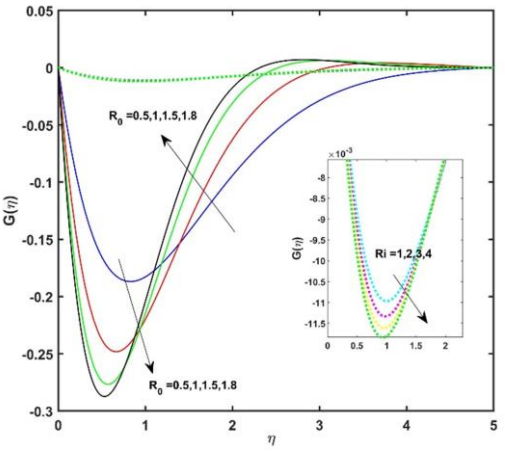

Fig. 3. Impact of R_0 and Ri on $G(\eta)$.

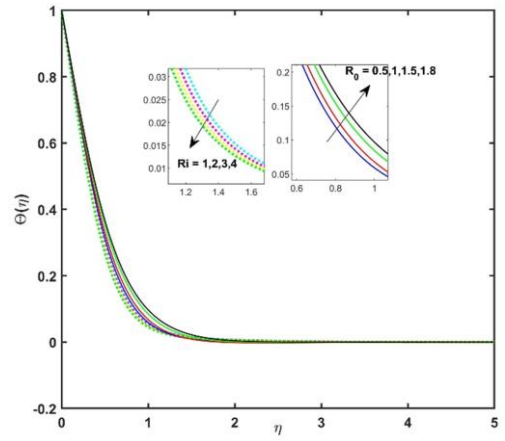

Fig. 4. Impact of R_0 and Ri on $\Theta(\eta)$.

can be related to the fact that the growth in the values of A and B prominently rises the temperature of the nanofluid, and the nanoparticles diffuse from higher to lower thermal areas, lowering the concentration boundary layer.

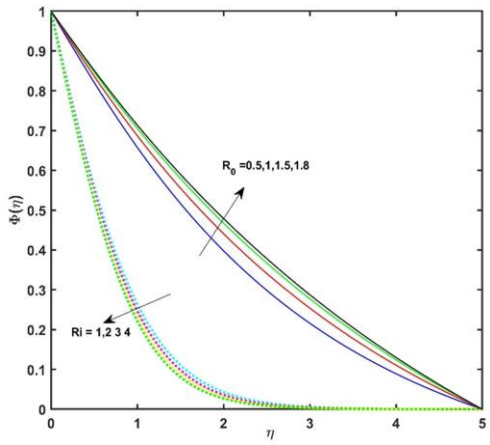

Fig. 5. Impact of R_0 and Ri on $\Phi(\eta)$.

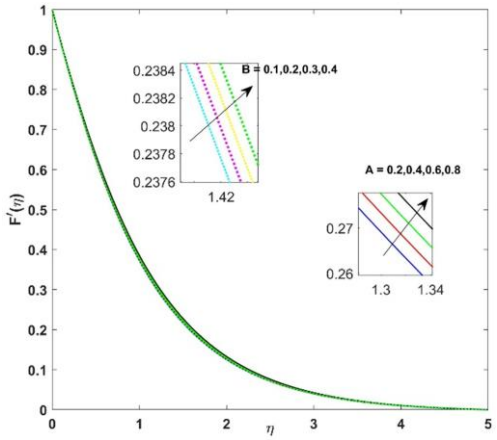

Fig. 6. Impact of A and B on $F'(\eta)$.

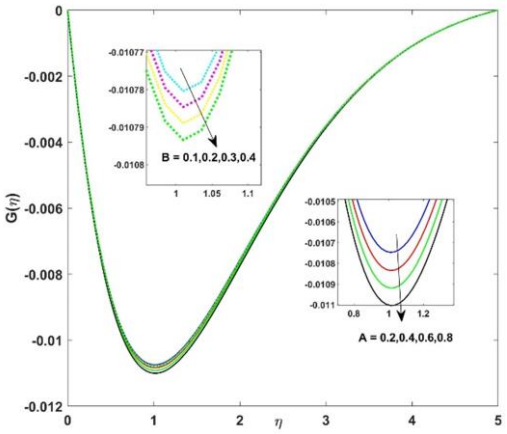

Fig. 7. Impact of A and B on $G(\eta)$.

Figure 9 displays the impact of time and spatial reliable heat sources on the concentration profile. We observe that the concentration boundary layer of the nanoparticles decreases with an increase in values of A and B. Figure 10 displays the effect of Cu-nanoparticle volume fraction (ϕ) change on the physical parameters of the rotating flow. As the values of ϕ escalate, the primary velocity and concentration of species fall. Moreover, increasing the volume percent of nanoparticles increases the thermal conductivity, the secondary velocity gradient, and thermal boundary layer. This is because the volume density of nanofluids increases with the volume fraction of nanoparticles, slowing the flux of nanofluids, thickening the thermal boundary layer, increasing the thermal conductivity and accelerating the surface heat transfer coefficient [34].

The 'molecular diffusivity' deteriorates as the Schmidt number develops and the concentration boundary layer shrinks, as exhibited in Fig. 11.

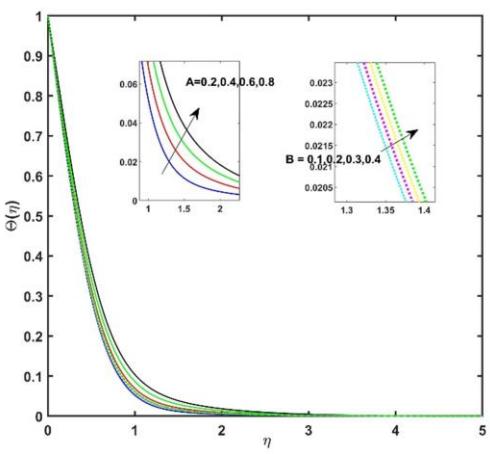

Fig. 8. Impact of A and B on $\Theta(\eta)$.

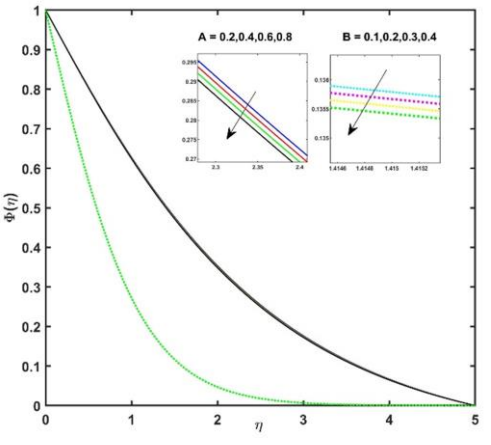

Fig. 9. Impact of A and B on $\Phi(\eta)$.

From Table 4 we observe that the production of thermal energy increases as A and B increase. As a result, the nanofluid temperature rises, causing the Nusselt number to decrease and drop, while the Sherwood number tends to rise. With the increase in Sc, the Nusselt number decreases, and the Sherwood

Table 4. The calculated values of C_{fx}, C_{fy}, $-\frac{k_{nf}}{k_f}\theta'(0)$ and $-\frac{1}{1-\phi}\phi'(0)$ for different values of the physical parameters.

Parameter	$\frac{\mu_{nf}}{\mu_f}f''(0)$	$\frac{\mu_{nf}}{\mu_f}g'(0)$	$Re_x^{-1/2}Nu_x$	$Re_x^{-1/2}Sh_x$	Parameter	$\frac{\mu_{nf}}{\mu_f}f''(0)$	$\frac{\mu_{nf}}{\mu_f}g'(0)$	$Re_x^{-1/2}Nu_x$	$Re_x^{-1/2}Sh_x$
R_0 = 0.0	-1.0114290	0.0000000	1.8681770	0.4433540	B = 0.1	-1.0165690	-0.0412950	1.9697570	0.3898610
R_0 = 1.0	-1.5410230	-1.4232460	1.7145830	0.3827830	B = 0.2	-1.0118770	-0.0413400	1.9175650	0.3903580
R_0 = 1.5	-1.8342400	-1.8399630	1.5827540	0.3620820	B = 0.3	-1.0070340	-0.0413870	1.8643150	0.3908740
R_0 = 1.8	-1.9978780	-2.0498870	1.4998280	0.3528740	B = 0.4	-1.0020290	-0.0414360	1.8099550	0.3914080
Ri = 0.5	-1.0070340	-0.0413870	1.8643150	0.3908740	φ = 0.0	-0.7324850	-0.0249520	1.7003820	0.4301090
Ri = 1.0	-0.5236630	-0.0434250	1.9352600	0.4133410	φ = 0.1	-0.7898190	-0.0279390	1.7360860	0.4309590
Ri = 2.0	-0.0665240	-0.0450680	1.9952570	0.4318640	φ = 0.3	-0.8458140	-0.0309340	1.7710520	0.4327930
Ri = 2.5	0.3710150	-0.0464600	2.0477770	0.4477820	φ = 0.5	-0.9011610	-0.0339670	1.8049780	0.4355000
A = 0.2	-1.0237050	-0.0400830	1.9513770	0.4421270	Sc = 0.0	-1.0070340	-0.0413870	1.8643150	0.3908740
A = 0.4	-0.9999550	-0.0404290	1.7839950	0.4444610	Sc = 0.3	-1.0070340	-0.0413870	1.8643150	0.6329460
A = 0.6	-0.9757630	-0.0407730	1.6134640	0.4468200	Sc = 0.5	-1.0070340	-0.0413870	1.8643150	0.8261700
A = 0.8	-0.9511620	-0.0411140	1.4398230	0.4491990	Sc = 0.6	-1.0070340	-0.0413870	1.8643150	0.9892370

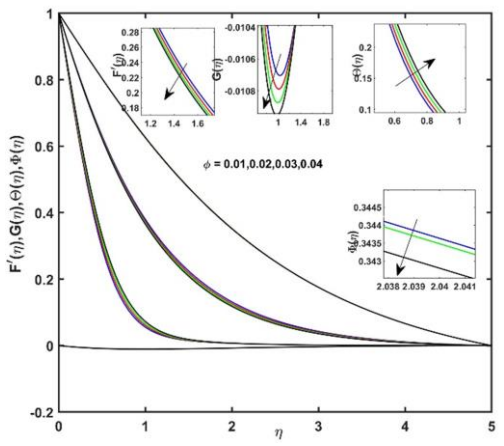

Fig. 10. Impact of Φ on $F'(\eta)$, $G(\eta)$, $\Theta(\eta)$ and $\Phi(\eta)$.

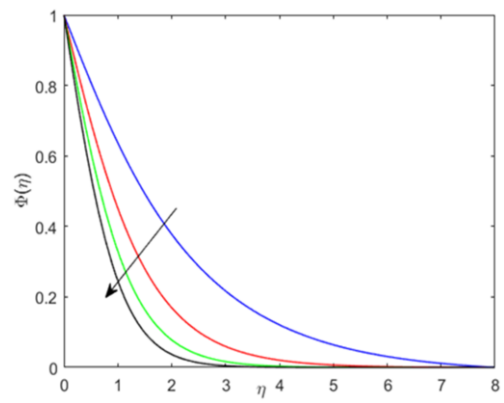

Fig. 11. Impact of Sc on $\Phi(\eta)$.

number increases. The higher the Sc, the lower the molecule diffusivity and the smaller the concentration boundary layer.

The improvement in the values of Ri and ϕ leads to the enrichment of the Nusselt number and the mass diffusivity coefficient. On the other hand, their enlargement results in the drop of primary and secondary drag friction values as shown in Table 4.

5. Conclusions

This study concentrated on the impacts of convection, uneven heat production and uneven heat absorption on the rotating flow of Cu-water nanofluid. In order to assess several properties, such as velocity, mass and heat transfer, we performed mathematical evaluations of the governing equations. The results we obtained are beneficial. These estimations, which were derived over a broad range of parameter values, provide a thorough grasp of the system under study.

The key observations after an intensive and integrated mathematical study are:

- The velocity, temperature and concentration boundary layers are significantly impacted by the Coriolis force. Secondary flow patterns are created as a result of the velocity boundary layer's deflection and deviation. The Coriolis force affects temperature gradients and can lead to the creation of thermal anomalies in thermal boundary layers. Similar to this, the Coriolis force influences solute transport in the concentration boundary layer, causing mixing and changing concentration distributions. The precise effect of the Coriolis force on these boundary layers relies on a number of variables, including the strength of force, the strength of flow and interactions with other forces in the system.
- Richardson's number governs the balance between buoyancy and other forces (inertia, thermal diffusion or diffusion) in the velocity, heat and concentration boundary layers. It determines the thickness, turbulence and heat or mass transfer properties of these boundary layers. The specific effect of Richardson's number on each boundary layer depends on the specific flow conditions and the relative importance of different forces in the system.
- Nu and Sh values both increase when copper nanoparticles are added to base fluids. It increases Nu to increase the efficiency of heat transmission and Sh to increase the efficiency of mass transfer. These outcomes are advantageous for many technical applications that need for effective mass and heat transport.

- Skin friction increases with rising Schmidt number, volume fraction parameter and heat source values.
- Under the impact of the forces at play, the nanoparticles in the range of parameters examined neither settle nor separate from the primary nanofluid. They may be mixed and displaced, yet they stay suspended.

References

[1] Ragupathi, P., Hakeem, A.K.A., Al-Mdallal, Q.M., Ganga, B., & Saranya, S. (2019). Non-uniform heat source/sink effects on the three-dimensional flow of Fe_3O_4/Al_2O_3 nanoparticles with different base fluids past a Riga plate. *Case Studies in Thermal Engineering*, 15, 100521. doi: 10.1016/j.csite.2019.100521

[2] Hyder, A., Lim, Y. J., Khan, I., & Shafie, S. (2023). Unveiling the performance of Cu-water nanofluid flow with melting heat transfer, MHD, and thermal radiation over a stretching/shrinking sheet. *ACS Omega*, 32(8), 29424–29436.

[3] Iftikhar, N., Rehman, A., & Sadaf, H. (2021). Theoretical investigation for convective heat transfer on Cu/water nanofluid and (SiO_2-copper)/water hybrid nanofluid with MHD and nanoparticle shape effects comprising relaxation and contraction phenomenon. *International Communications in Heat and Mass Transfer*, 120, 105012. doi: 10.1016/j.icheatmasstransfer.2020.105012

[4] Hazarika, S., Ahmed, S., & Yao, S.-W. (2023). Investigation of Cu-water nano-fluid of natural convection hydro-magnetic heat transport in a Darcian porous regime with diffusion-thermo. *Applied Nanoscience*, 13(1), 283–293. doi: 10.1007/s13204-020-01655-w

[5] Uddin, M.J., & Rasel, S.K. (2019). Numerical analysis of natural convective heat transport of copper oxide-water nanofluid flow inside a quadrilateral vessel. *Heliyon*, 5(5), e01757. doi: 10.1016/j.heliyon.2019.e01757

[6] Babu, R.S., Kumar, B.R., & Makinde, O.D. (2018). Chemical reaction and thermal radiation effects on MHD mixed convection over a vertical plate with variable fluid properties. *Defect and Diffusion Forum*, 387, 332–342. doi: 10.4028/www.scientific.net/DDF.387.332

[7] Yacob, N.A., Dzulkifli, N.F., Salleh, S.N.A., Ishak, A., & Pop, I. (2022). Rotating flow in a nanofluid with CNT nanoparticles over a stretching/shrinking surface. *Mathematics*, 10(1), 7. doi: 10.3390/math10010007

[8] Mehrez, Z., El Cafsi, A., Belghith, A., & Le Quéré, P. (2015). MHD effects on heat transfer and entropy generation of nanofluid flow in an open cavity. *Journal of Magnetism and Magnetic Materials*, 374, 214–224. doi: 10.1016/j.jmmm.2014.08.010

[9] Punith Gowda, R.J., Naveen Kumar, R., Jyothi, A.M., Prasannakumara, B.C., & Sarris, I.E. (2021). Impact of binary chemical reaction and activation energy on heat and mass transfer of Marangoni driven boundary layer flow of a non-Newtonian nanofluid. *Processes*, 9(4), 702. doi: 10.3390/pr9040702

[10] Shahzad, F., Jamshed, W., Sajid, T., Nisar, K.S., & Eid, M.R. (2021). Heat transfer analysis of MHD rotating flow of Fe_3O_4 nanoparticles through a stretchable surface. *Communications in Theoretical Physics*, 73(7), 75004. doi: 10.1088/1572-9494/abf8a1

[11] Ashraf, M., Ullah, Z., Zia, S., Alharbi, S.O., Baleanu, D., & Khan, I. (2021). Analysis of the physical behavior of the periodic mixed-convection flow around a nonconducting horizontal circular cylinder embedded in a porous medium. *Journal of Mathematics*, 2021(1), 8839146. doi: 10.1155/2021/8839146

[12] Ullah, Z., Akkurt, N., Alrihieli, H.F., Eldin, S.M., Alqahtani, A.M., Hussanan, A., et al. (2022). Temperature-dependent density and magnetohydrodynamic effects on mixed convective heat transfer along magnetized heated plate in thermally stratified medium using Keller box simulation. *Applied Sciences*, 12(22), 11461. doi: 10.3390/app122211461

[13] Khan, M.N., & Nadeem, S. (2020). Theoretical treatment of bioconvective Maxwell nanofluid over an exponentially stretching sheet. *Canadian Journal of Physics*, 98(8), 732–741. doi: 10.1139/cjp-2019-0380

[14] Khan, M.N., Hussien, M.A., Allehiany, F.M., Ahammad, N.A., Wang, Z., & Algehyne, E.A. (2023). Variable fluid properties and concentration species analysis of a chemically reactive flow of micropolar fluid between two plates in a rotating frame with cross diffusion theory. *Tribology International*, 189, 108943. doi: 10.1016/j.triboint.2023.108943

[15] Khan, M.N., Ahmad, S., Alrihieli, H.F., Wang, Z., Hussien, M. A., & Afikuzzaman, M. (2023). Theoretical study on thermal efficiencies of Sutterby ternary-hybrid nanofluids with surface catalyzed reactions over a bidirectional expanding surface. *Journal of Molecular Liquids*, 391 B, 123412. doi: 10.1016/j.molliq.2023.123412

[16] Sathyanarayana, M., & Goud, T.R. (2023). Numerical study of MHD Williamson-nano fluid flow past a vertical cone in the presence of suction/injection and convective boundary conditions. *Archives of Thermodynamics*, 44(2), 115–138. doi: 10.24425/ather.2023.146561

[17] Madhusudhana Rao, B., Gopal D., Kishan N., Ahmed Saad, & Durga Prasad P. (2020). Heat and mass transfer mechanism on three-dimensional flow of inclined magneto Carreau nanofluid with chemical reaction. *Archives of Thermodynamics*, 41(2), 223–238. doi: 10.24425/ather.2020.133630

[18] Das, S., Jana, N.R., & Makinde, O.D. (2014). MHD boundary layer slip flow and heat transfer of nanofluid past a vertical stretching sheet with non-uniform heat generation/absorption. *International Journal of Nanoscience*, 13(3), 1–12. doi: 10.1142/S0219581X14500197

[19] Oke, A.S., Prasannakumara, B.C., Mutuku, W.N., Gowda, R.J. P., Juma, B.A., Kumar, R.N., & Bada, O.I. (2022). Exploration of the effects of Coriolis force and thermal radiation on water-based hybrid nanofluid flow over an exponentially stretching plate. *Scientific Reports*, 12, 21733. doi: 10.1038/s41598-022-21799-9

[20] Owhaib, W., Basavarajappa, M., & Al-Kouz, W. (2021). Radiation effects on 3D rotating flow of Cu-water nanoliquid with viscous heating and prescribed heat flux using modified Buongiorno model. *Scientific Reports*, 11, 20669. doi: 10.1038/s41598-021-00107-x

[21] Ragulkumar, E., Palani, G., Sambath, P., & Chamkha, A.J. (2023). Dissipative MHD free convective nanofluid flow past a vertical cone under radiative chemical reaction with mass flux. *Scientific Reports*, 13, 2878. doi: 10.1038/s41598-023-28702-0

[22] Jalili, P., Sadeghi Ghahare, A., Jalili, B., & Domiri Ganji, D. (2023). Analytical and numerical investigation of thermal distribution for hybrid nanofluid through an oblique artery with mild stenosis. *SN Applied Sciences*, 5(95). doi: 10.1007/s42452-023-05312-z

[23] Farrukh, B.M., Chen, G.M., & Tso, C.P. (2021). Viscous dissipation effect on CuO-water nanofluid-cooled microchannel heat sinks. *Case Studies in Thermal Engineering*, 26, 101159. doi: 10.1016/j.csite.2021.101159

[24] Sheikholeslami, M., Ashorynejad, H.R., Domairry, G., & Hashim, I. (2012). Flow and heat transfer of Cu-water nanofluid between a stretching sheet and a porous surface in a rotating system. *Journal of Applied Mathematics*, 2012(1), 421320. doi: 10.1155/2012/421320

[25] Hayat, T., Imtiaz, M., & Alsaedi, A. (2016). Melting heat transfer in the MHD flow of Cu–water nanofluid with viscous dissipation and Joule heating. *Advanced Powder Technology*, 27(4), 1301–1308. doi: 10.1016/j.apt.2016.04.024

[26] Owhaib, W., Basavarajappa, M., & Al-Kouz, W. (2021). Radiation effects on 3D rotating flow of Cu-water nanoliquid with viscous heating and prescribed heat flux using modified Buongiorno model. *Scientific Reports*, 11(1), 20669. doi: 10.1038/s41598-021-00107-x

[27] Triveni, B., Rao, M. V.S., Gangadhar, K., & Chamkha, A.J. (2023). Heat transfer analysis of MHD Casson nanofluid flow over a nonlinear stretching sheet in the presence of nonuniform heat source. *Numerical Heat Transfer, Part A: Applications*, 85(13), 2145–2164. doi:10.1080/10407782.2023.2219831

[28] Khan, U., Zaib, A., Khan, I., & Nisar, K. S. (2020). Activation energy on MHD flow of titanium alloy (Ti6Al4V) nanoparticle along with a cross flow and streamwise direction with binary chemical reaction and non-linear radiation: Dual solutions. *Journal of Materials Research and Technology*, 9(1), 188–199. doi: 10.1016/j.jmrt.2019.10.044

[29] Aybar, H., Sharifpur, M., Azizian, M.R., Mehrabi, M., & Meyer, J.P. (2015). A review of thermal conductivity models for nanofluids. *Heat Transfer Engineering*, 36(13), 1085–1110. doi: 10.1080/01457632.2015.987586

[30] Gamaoun, F., Ullah, Z., Ameer Ahammad, N., Fadhl, B.M., Makhdoum, B.M., & Abbas Khan, A. (2023). Effects of thermal radiation and variable density of nanofluid heat transfer along a stretching sheet by using Keller box approach under magnetic field. *Thermal Science and Engineering Progress*, 41, 101815. doi: 10.1016/j.tsep.2023.101815

[31] Prathiba, A., & Akavaram, V.L. (2022). Numerical investigation of a convective hybrid nanofluids around a rotating sheet. *Heat Transfer*, 51(4), 3353–3372. doi: 10.1002/htj.22454

[32] Hayat, T., Nadeem, S., & Khan, A.U. (2020). Aspects of 3D rotating hybrid CNT flow for a convective exponentially stretched surface. *Applied Nanoscience*, 10(8), 2897–2906. doi: 10.1007/s13204-019-01036-y

[33] Mohd Zin, N.A., Khan, I., Shafie, S., & Alshomrani, A.S. (2017). Analysis of heat transfer for unsteady MHD free convection flow of rotating Jeffrey nanofluid saturated in a porous medium. *Results in Physics*, 7, 288–309. doi: 10.1016/j.rinp.2016.12.032

[34] Abbas, W., & Magdy, M.M. (2020). Heat and mass transfer analysis of nanofluid flow based on Cu, Al2O3, and TiO2 over a moving rotating plate and impact of various nanoparticle shapes. *Mathematical Problems in Engineering*, 2020. doi: 10.1155/2020/9606382

Co-published by
Institute of Fluid-Flow Machinery
Polish Academy of Sciences
Committee on Thermodynamics and Combustion
Polish Academy of Sciences

http://www.imp.gda.pl/archives-of-thermodynamics/

Effect of variable thermal conductivity in semiconducting medium underlying an elastic half-space

Praveen Ailawalia[a*], Priyanka[b]

[a]Department of Mathematics, University Institute of Sciences, Chandigarh University, Gharuan, Mohali, Punjab, India
[b]I.G.N College, Ladwa, Haryana, India
**Corresponding author email:* praveen_2117@rediffmail.com

Received: 16.07.2023; revised: 06.03.2024; accepted: 9.05.2024

Abstract

The aim of the present work is to discuss the effect of varying thermal conductivity in a semiconducting medium under photothermal theory. An infinite elastic half-space is overlying the infinite semiconducting medium, and a constant mechanical force is applied along the interface. The normal mode analysis method is applied to find the analytic components of displacement, stress, carrier density and temperature distribution. It was found that all physical quantities are affected by variable thermal conductivity. The novelty of the paper lies in the fact that no such a problem of variable thermal conductivity has been discussed by any researcher so far.

Keywords: Semiconducting medium; Thermal conductivity; Temperature distribution; Normal mode analysis; Carrier density

Vol. 45(2024), No. 3, 159–166; doi: 10.24425/ather.2024.151226

Cite this manuscript as: Ailawalia.P., & Priyanka (2024). Effect of variable thermal conductivity in semiconducting medium underlying an elastic half-space. *Archives of Thermodynamics*, 45(3), 159–166.

1. Introduction

Semiconductor materials are being considered important in current years due to their wide utilization in various fields of science and engineering. The plasma waves get generated due to the excitation of electrons under exposure to a beam of laser or sunlight. As a result, the interaction between the thermal wave, elastic wave and plasma wave occurs. Gordon et al. [1] and Kreuzer [2] made remarkable contributions in developing the photothermal theory. Mandelis et al. [3] studied the coupling of thermoelastic and electronic waves under photothermal theory. Todorovic [4] investigated plasmaelastic and thermoelastic waves in the semiconducting medium. Song et al. [5] worked on a reflection problem in a semiconducting medium for finding reflection coefficient ratios. Othman et al. [6] explained the wave propagation problem in a semiconducting medium in the context of Lord-Shulman (LS) theory. Ailawalia et al. [7] analysed the influence of mechanical force at the interface of semiconducting half-space and thermoelastic micropolar cubic crystal. Alzahrani and Abbas [8] studied a two-dimensional semiconducting medium under thermoelastic theory with one relaxation time. Hobiny [9] explored wave propagation in a semiconducting medium under a hyperbolic two-temperature model without energy dissipation. Saeed et al. [10] introduced a novel model for studying photothermal interaction in a rotating microstretch semiconductor medium subjected to initial stress.

Nomenclature

a – wave number in the x-direction
C_d – coefficient related to diffusion of carriers
C_s – specific heat, J/(kg K)
E_s – gap in energy of valence and conduction band of the semiconductor, J
e_{ij} – strain tensor
F – mechanical force
K_0^s – arbitrary constant
K_1 – physical parameter
K^s – thermal conductivity, W/(m K)
N – carrier density, kg/m^3
N_0 – carrier concentration at temperature T in equilibrium
$\vec{r}$ – position vector
T – temperature, K
T_0 – reference temperature, K
t – time, s
$\vec{u}$ – displacement vector
u, w– x, z components of velocity, m/s
u_i – components of velocity (i = 1, 2, 3), m/s
x, y, z– Cartesian coordinates, m
x_i, – Cartesian coordinates (i = 1, 2, 3), m

Greek symbols

α – thermal expansion coefficient, 1/K
β – coefficient of electronic deformation
γ – $\gamma = (3\lambda^s + 2\mu^s)\alpha$
δ – $\delta = (3\lambda^s + 2\mu^s)\beta$
δ_{ij} – Kronecker delta
κ – coupling parameter for the thermal activation, = $\left(\frac{\partial N_0}{\partial t}\right)\left(\frac{1}{\tau}\right)$
λ, μ – Lame's constants
ρ – density, kg/m^3
τ – photogenerated carrier lifetime
ω – complex time constant

Subscripts and Superscripts

e – elastic medium
s – semiconducting medium
$u_{i,j}$ – differentiation of u_i with respect to x_i
$(\cdot)^*$ – amplitude of the variables

Hilal [11] demonstrated photothermal interaction in a micro-elongated semiconducting medium under the influence of gravity. Kaur et al. [12] explained photo-thermo-elastic interactions in an infinite semiconducting rotating solid cylinder subjected to the magnetic field and hall current. Lotfy et al. [13] put forward a novel model for investigating non-local semiconductor medium. Azhar et al. [14] studied the reflection problem in a non-local semiconducting medium under the effect of hall current and magnetic field.

Under exposure to high temperature, the thermal conductivity of an elastic material is found experimentally to be varied with temperature. Therefore, the thermal conductivity cannot be treated as constant. El-Bary [15] introduced a mathematical model for studying layered thin plate subjected to variable thermal conductivity. Ezzat and Youssef [16] studied thermoelastic medium subjected to variable electrical and thermal conductivity under the theory of one relaxation time. Sherief and Abd El-Latief [17] explored the impact of variable thermal conductivity in an elastic half-space with respect to the theory of fractional thermoelasticity. Zenkour and Abbas [18] applied finite element method for obtaining thermal stress for a hollow cylinder in a temperature dependent thermoelastic medium. Yasein et al. [19] demonstrated the effect of varying thermal conductivity in a semiconducting medium subjected to thermal ramp type in the context of dual-phase-lag (DPL) and L-S model of thermoelasticity. Abbas et al. [20] analysed the behaviour of semiconducting medium with cylindrical cavities subjected to variable thermal conductivity. Alzahrani et al. [21] discussed eigen value problem for variable thermal conductivity in a porous medium. Marin et al. [22] explored porothermoelastic materials subjected to fractional time derivatives by applying the finite element method. Lotfy and El-Bary [23] proposed an elastic-thermodiffusion model for studying photothermal interactions in a semiconductor subjected to mechanical ramp type and variable thermal conductivity. Hobiny and Abbas [24] utilised the finite element method for describing thermoelastic interaction in an orthotropic material with spherical cavities under variable thermal conductivity. Kumar et al. [25] explained thermodynamical interactions for a thermodiffusive medium subjected to rotation and gravitational effect. El-Sapa et al. [26] demonstrated the influence of variable thermal conductivity on wave propagation in a non-local semiconducting medium.

The present research work deals with investigating the effect of varying thermal conductivity in a semiconducting medium. The problem has been modelled as an elastic half-space overlying the semiconducting half-space. The analytic components of displacement, stress, carrier density and temperature distribution are obtained by applying the normal mode technique. It was observed that all considered physical quantities depend on variable thermal conductivity.

2. Governing equations of the problem

Let us take a semiconducting half-space with an overlying elastic half-space. A mechanical load of magnitude F is acting on the boundary separating the two half-spaces. Further, we consider coordinate system (x, y, z) in which z-axis is taken in vertically downward direction. The region $z \geq 0$ is occupied by the semiconducting half-space (medium I) and the region $z < 0$ by elastic-half space (medium II) as represented in Fig. 1.

The fundamental equations for a semiconducting medium after neglecting body forces are given by Lotfy [27]:

$$\mu^s \nabla^2 \vec{u}(\vec{r}, t) + (\lambda^s + \mu^s)\nabla\left(\nabla \cdot \vec{u}(\vec{r}, t)\right) +$$

$$-\gamma \nabla T - \delta \nabla N = \rho \frac{\partial^2 \vec{u}(\vec{r}, t)}{\partial t^2}. \quad (1)$$

The coupled equations for the semiconducting medium are given by Song et al. [28]:

$$K^s \nabla^2 T - \frac{E_s}{\tau} N + \gamma T_0 \nabla \cdot \frac{\partial \vec{u}}{\partial t} - \rho C_s \frac{\partial T}{\partial t} = 0. \quad (2)$$

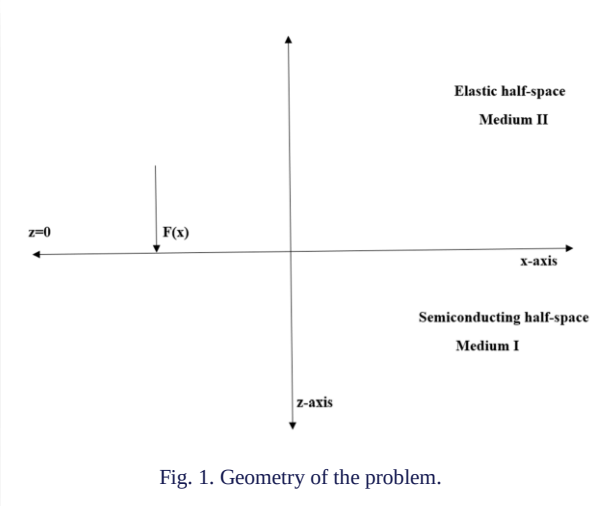

Fig. 1. Geometry of the problem.

$$C_d\nabla^2 N - \frac{1}{\tau}N + \kappa T - \frac{\partial N}{\partial t} = 0. \quad (3)$$

Further the stress-strain relations for the considered medium are given by Lotfy [27]:

$$\sigma_{ij} = 2\mu^s e_{ij} + \left(\lambda^s u_{k,k} - \delta N - \gamma T\right)\delta_{ij}, \quad (4)$$

where

$$e_{ij} = \frac{1}{2}\left(u_{j,i} + u_{i,j}\right).$$

The fundamental relations for elastic half-space are given by Ewing et al. [29]:

$$\mu^e\nabla^2\vec{u}^e(\vec{r},t) + (\lambda^e + \mu^e)\nabla\left(\nabla\cdot\vec{u}^e(\vec{r},t)\right) = \rho^e\frac{\partial^2\vec{u}^e(\vec{r},t)}{\partial t^2}, \quad (5)$$

$$\sigma^e_{lk} = \lambda^e u^e_{r,r}\delta_{lk} + \mu^e\left(u_{l,k} + u_{k,l}\right), \quad r,l,k = 1,2,3. \quad (6)$$

3. Formulation of the problem

We assume that the waves are propagating in *x*-*z* plane. Hence the displacement vector in the semiconducting medium is considered as $\vec{u} = (u, 0, w)$, where $u = u(x,z,t)$, $w = w(x,z,t)$. Equations (1)–(4) in two dimensions can be expressed as:

$$(\lambda^s + 2\mu^s)\frac{\partial^2 u}{\partial x^2} + (\lambda^s + \mu^s)\frac{\partial^2 w}{\partial x\partial z} + \\ + \mu^s\frac{\partial^2 u}{\partial z^2} - \gamma\frac{\partial T}{\partial x} - \delta\frac{\partial N}{\partial x} = \rho\frac{\partial^2 u}{\partial t^2}, \quad (7)$$

$$\mu^s\frac{\partial^2 w}{\partial x^2} + (\lambda^s + \mu^s)\frac{\partial^2 u}{\partial x\partial z} + (\lambda^s + 2\mu^s)\frac{\partial^2 w}{\partial z^2} + \\ -\gamma\frac{\partial T}{\partial z} - \delta\frac{\partial N}{\partial z} = \rho\frac{\partial^2 w}{\partial t^2}, \quad (8)$$

$$K^s\Delta T - \frac{E_s}{\tau}N + \gamma T_0\frac{\partial}{\partial t}\left(\frac{\partial u}{\partial x} + \frac{\partial w}{\partial z}\right) - \rho C_s\frac{\partial T}{\partial t} = 0, \quad (9)$$

$$C_d\Delta N - \frac{1}{\tau}N + \kappa T - \frac{\partial N}{\partial t} = 0, \quad (10)$$

$$\sigma_{xx} = (\lambda^s + 2\mu^s)\frac{\partial u}{\partial x} + \lambda^s\frac{\partial w}{\partial z} - (\gamma T + \delta N), \quad (11)$$

$$\sigma_{zz} = (\lambda^s + 2\mu^s)\frac{\partial w}{\partial z} + \lambda^s\frac{\partial u}{\partial x} - (\gamma T + \delta N), \quad (12)$$

$$\sigma_{zx} = \mu^s\left(\frac{\partial u}{\partial z} + \frac{\partial w}{\partial x}\right), \quad (13)$$

where: $\Delta = \frac{\partial^2}{\partial x^2} + \frac{\partial^2}{\partial z^2}$.

Further for the elastic half space, Eqs. (5) and (6) in two-dimensions can be reduced as:

$$(\lambda^e + 2\mu^e)\frac{\partial^2 u^e}{\partial x^2} + (\lambda^e + \mu^e)\frac{\partial^2 w^e}{\partial x\partial z} + \mu^e\frac{\partial^2 u^e}{\partial z^2} = \rho^e\frac{\partial^2 u^e}{\partial t^2}, \quad (14)$$

$$\mu^e\frac{\partial^2 w^e}{\partial x^2} + (\lambda^e + 2\mu^e)\frac{\partial^2 w^e}{\partial z^2} + (\lambda^e + \mu^e)\frac{\partial^2 u^e}{\partial x\partial z} = \rho^e\frac{\partial^2 w^e}{\partial t^2}, \quad (15)$$

$$\sigma^e_{xx} = (\lambda^e + 2\mu^e)\frac{\partial u^e}{\partial x} + \lambda^e\frac{\partial w^e}{\partial z}, \quad (16)$$

$$\sigma^e_{zz} = (\lambda^e + 2\mu^e)\frac{\partial w^e}{\partial z} + \lambda^e\frac{\partial u^{\mathrm{e}}}{\partial x}, \quad (17)$$

$$\sigma^e_{zx} = \mu^e\left(\frac{\partial u^e}{\partial z} + \frac{\partial w^e}{\partial x}\right). \quad (18)$$

Under exposure to high temperature, heat conductivity K^s depends on the temperature of the medium, therefore it must be taken as variable as given by Lotfy [30]:

$$K^s(T) = K^s_0(1 + K_1 T). \quad (19)$$

We can use the Kirchhoff transformation for conversion of thermal conduction equation into linear form by the following relation given by Lotfy [30]:

$$\hat{T} = \frac{1}{K^s_0}\int_0^T K^s(\xi)d\xi. \quad (20)$$

Differentiating (20) with respect to x_i we get

$$K^s_0\hat{T}_{,i} = K^s(T)T_{,i}. \quad (21)$$

Differentiating the above equation again with respect to x_i we get

$$K^s_0\widehat{T_{,ii}} = \left(K^s(T)T_{,i}\right)_{,i}. \quad (22)$$

Above equation has the following linear form after removing non-linear terms:

$$K^s_0\widehat{T_{,ii}} = K^s(T)T_{,ii}. \quad (23)$$

In $\widehat{T_{,ii}}$ the subscript should be treated as *ii* in Eqs. (22) and (23), though it appears as *ll* under $\hat{T}$ due to some software issue.

Differentiating (20) with respect to t we get

$$K^s_0\widehat{T_{,t}} = K^s(T)T_{,t}. \quad (24)$$

Equations (7) to (13) can be rewritten using (19)–(24) as:

$$(\lambda^s + 2\mu^s)\frac{\partial^2 u}{\partial x^2} + (\lambda^s + \mu^s)\frac{\partial^2 w}{\partial x\partial z} + \\ +\mu^s\frac{\partial^2 u}{\partial z^2} - \gamma\frac{\partial\hat{T}}{\partial x} - \delta\frac{\partial N}{\partial x} = \rho\frac{\partial^2 u}{\partial t^2}, \quad (25)$$

$$\mu^s\frac{\partial^2 w}{\partial x^2} + (\lambda^s + \mu^s)\frac{\partial^2 u}{\partial x\partial z} + (\lambda^s + 2\mu^s)\frac{\partial^2 w}{\partial z^2} + \\ -\gamma\frac{\partial\hat{T}}{\partial z} - \delta\frac{\partial N}{\partial z} = \rho\frac{\partial^2 w}{\partial t^2}, \quad (26)$$

$$K_0^s \Delta\hat{T} - \frac{E_s}{\tau} N + \gamma T_0 \frac{\partial}{\partial t}\left(\frac{\partial u}{\partial x} + \frac{\partial w}{\partial z}\right) - \rho C_s \frac{\partial \hat{T}}{\partial t} = 0, \quad (27)$$

$$C_d \Delta N - \frac{1}{\tau} N + \kappa \hat{T} - \frac{\partial N}{\partial t} = 0, \quad (28)$$

$$\sigma_{xx} = (\lambda^s + 2\mu^s)\frac{\partial u}{\partial x} + \lambda^s \frac{\partial w}{\partial z} - \left(\gamma \hat{T} + \delta N\right), \quad (29)$$

$$\sigma_{zz} = (\lambda^s + 2\mu^s)\frac{\partial w}{\partial z} + \lambda^s \frac{\partial u}{\partial x} - \left(\gamma \hat{T} + \delta N\right), \quad (30)$$

$$\sigma_{zx} = \mu^s \left(\frac{\partial u}{\partial z} + \frac{\partial w}{\partial x}\right). \quad (31)$$

Further, for simplicity we use dimensionless quantities written below:

$$x' = \frac{1}{c_l t^*} x,\ z' = \frac{1}{c_l t^*} z,\ u' = \frac{1}{c_l t^*} u,\ w' = \frac{1}{c_l t^*} w,$$

$$t' = \frac{t}{t^*},\ \sigma'_{ij} = \frac{\sigma_{ij}}{\mu^s}, \hat{T}' = \frac{\gamma \hat{T}}{(\lambda^s + 2\mu^s)},\ N' = \frac{\delta N}{(\lambda^s + 2\mu^s)},$$

$$u^{e\prime} = \frac{1}{c_l t^*} u^e,\ w^{e\prime} = \frac{1}{c_l t^*} w^e,\ \sigma_{ij}^{e\prime} = \frac{\sigma_{ij}{}^e}{\mu^e}. \quad (32)$$

where:

$$c_l^2 = \frac{(\lambda^s + 2\mu^s)}{\rho}, \quad t^* = \frac{K_0^s}{C_s c_l^2}.$$

Using dimensionless variables (32) in Eqs. (25) to (31) we get equations as:

$$\frac{\partial^2 u}{\partial x^2} + b_{11}\frac{\partial^2 u}{\partial z^2} + b_{11}\frac{\partial^2 w}{\partial x \partial z} - \frac{\partial \hat{T}}{\partial x} - \frac{\partial N}{\partial x} = \frac{\partial^2 u}{\partial t^2}, \quad (33)$$

$$b_{12}\frac{\partial^2 u}{\partial x \partial z} + \frac{\partial^2 w}{\partial z^2} + b_{11}\frac{\partial^2 w}{\partial x^2} - \frac{\partial \hat{T}}{\partial z} - \frac{\partial N}{\partial z} = \frac{\partial^2 w}{\partial t^2}, \quad (34)$$

$$a_{15}\Delta\hat{T} + a_{16}\frac{\partial \hat{T}}{\partial t} + a_{17} N + a_{18}\left(\frac{\partial^2 u}{\partial x \partial t} + \frac{\partial^2 w}{\partial z \partial t}\right) = 0, \quad (35)$$

$$a_{11}\Delta N + a_{12} N + a_{13}\frac{\partial N}{\partial t} + a_{14}\hat{T} = 0, \quad (36)$$

$$\sigma_{xx} = b_{13}\frac{\partial u}{\partial x} + b_{14}\frac{\partial w}{\partial z} - b_{13}\hat{T} - b_{13} N, \quad (37)$$

$$\sigma_{zz} = b_{14}\frac{\partial u}{\partial x} + b_{13}\frac{\partial w}{\partial z} - b_{13}\hat{T} - b_{13} N, \quad (38)$$

$$\sigma_{zx} = \left(\frac{\partial u}{\partial z} + \frac{\partial w}{\partial x}\right). \quad (39)$$

Further for the elastic half space, Eqs. (14)–(18) in dimensionless form can be reduced as:

$$c_{11}\frac{\partial^2 u^e}{\partial x^2} + c_{12}\frac{\partial^2 w^e}{\partial x \partial z} + c_{13}\frac{\partial^2 u^e}{\partial z^2} = \frac{\partial^2 u^e}{\partial t^2}, \quad (40)$$

$$c_{13}\frac{\partial^2 w^e}{\partial x^2} + c_{11}\frac{\partial^2 w^e}{\partial z^2} + c_{12}\frac{\partial^2 u^e}{\partial x \partial z} = \frac{\partial^2 w^e}{\partial t^2}, \quad (41)$$

$$\sigma_{xx}^e = c_{14}\frac{\partial u^e}{\partial x} + c_{15}\frac{\partial w^e}{\partial z}, \quad (42)$$

$$\sigma_{zz}^e = c_{14}\frac{\partial w^e}{\partial z} + c_{15}\frac{\partial u^e}{\partial x}, \quad (43)$$

$$\sigma_{zx}^e = \left(\frac{\partial u^e}{\partial z} + \frac{\partial w^e}{\partial x}\right). \quad (44)$$

Here:

$$a_{11} = \frac{C_d}{\delta c_l^2 t^{*2}},\ a_{12} = -\frac{1}{\tau\delta},\ a_{13} = -\frac{1}{t^*\delta},\ a_{14} = \frac{\kappa}{\gamma},$$

$$a_{15} = \frac{K_0^s}{\gamma t^* C_s},\ a_{16} = -\frac{(\lambda^s + 2\mu^s)}{\gamma},\ a_{17} = \frac{E_s(\lambda^s + 2\mu^s)t^*}{\tau\delta\rho C_s},\ a_{18} = \frac{\gamma T_0}{\rho C_s},$$

$$b_{11} = \frac{\mu^s}{(\lambda^s + 2\mu^s)},\ b_{12} = \frac{\lambda^s + \mu^s}{\lambda^s + 2\mu^s},\ b_{13} = \frac{\lambda^s + 2\mu^s}{\mu^s},\ b_{14} = \frac{\lambda^s}{\mu^s},$$

$$b_{14} = \frac{\lambda^s}{\mu^s},\ c_{11} = \frac{\lambda^e + 2\mu^e}{\rho^e C_l^2},\ c_{12} = \frac{\lambda^e + \mu^e}{\rho^e C_l^2},\ c_{13} = \frac{\mu^e}{\rho^e C_l^2},$$

$$c_{14} = \frac{\lambda^e + 2\mu^e}{\mu^e},\ c_{15} = \frac{\lambda^e}{\mu^e}.$$

4. Normal mode analysis

We use the following normal mode analysis for obtaining the solution for above considered physical variables:

$$\left[u, w, \hat{T}, N, \mathrm{u}^e, \mathrm{w}^e\right] = \left[u^*, w^*, \widehat{T^*}, N^*, \mathrm{u}^{e*}, \mathrm{w}^{e*}\right](z) e^{\omega t + iax}. \quad (45)$$

Using the solutions given by (45) in (33)–(36), we obtain the following equations in coupled form as:

$$(b_{11}D^2 + e_{15})u^* + iab_{12}Dw^* - ia\widehat{T^*} - iaN^* = 0, \quad (46)$$

$$iab_{12}Du^* + (D^2 + e_{16})w^* - D\widehat{T^*} - DN^* = 0, \quad (47)$$

$$e_{13}u^* + e_{14}Dw^* + (a_{15}D^2 + e_{12})\widehat{T^*} + a_{17}N^* = 0, \quad (48)$$

$$a_{14}\hat{T}^* + (a_{11}D^2 + e_{11})N^* = 0. \quad (49)$$

On solving these coupled equations (46) to (49), we get the following eighth-order differential equation:

$$[g_8 D^8 + g_9 D^6 + g_{10} D^4 + g_{11} D^2 + g_{12}]\left(u^*, w^*, \widehat{T^*}, N^*\right) = 0. \quad (50)$$

Similarly, using the solutions given by (45) in (40)–(41), we obtain the following equations in coupled form:

$$(c_{13}D^2 + e_{17})u^{e*} + iac_{12}Dw^{e*} = 0, \quad (51)$$

$$(c_{11}D^2 + e_{18})w^{e*} + iac_{12}Du^{e*} = 0. \quad (52)$$

On solving these coupled Eqs. (51) and (52), we get the following fourth-order differential equation:

$$[g_{13}D^4 + g_{14}D^2 + g_{15}](u^{e*}, w^{e*}) = 0. \quad (53)$$

Here:

$$e_{11} = -a_{11}a^2 + a_{12} + a_{13}\omega,\ e_{12} = -a_{15}a^2 + a_{16}\omega,$$

$$e_{13} = ia\omega a_{18},\ e_{14} = \omega a_{18},\ e_{15} = -(a^2 + \omega^2),$$

$$e_{16} = -(b_{11}a^2 + \omega^2),\ e_{17} = -(c_{11}a^2 + \omega^2),$$

$$e_{18} = -(c_{13}a^2 + \omega^2),$$

$$f_1 = iaa_{15}b_{12},\ f_2 = ia(e_{12}b_{12} + e_{14}),\ f_3 = -e_{14}b_{11},$$

$$f_4 = iae_{13}b_{12} - e_{14}e_{15},\ f_5 = ia(a_{17}b_{12} + e_{14}),$$

$$f_6 = b_{11},\ f_7 = e_{15} + e_{16}b_{11} + a^2 b_{12}{}^2,\ f_8 = e_{15}e_{16},$$

$$f_9 = ia(b_{12} - 1),\ f_{10} = -iae_{16},$$

$$g_1 = f_1 f_6,\ g_2 = f_2 f_6 + f_1 f_7 - f_3 f_9,$$

$$g_3 = f_2 f_7 + f_1 f_8 - f_3 f_{10} - f_4 f_9,\ g_4 = f_2 f_8 - f_4 f_{10},$$

$$g_5 = f_5 f_6 - f_3 f_9,\ g_6 = f_5 f_7 - f_4 f_9 - f_3 f_{10},$$

$$g_7 = f_5 f_8 - f_4 f_{10},\ g_8 = a_{11} g_1,\ g_9 = e_{11} g_1 + a_{11} g_2,$$

$$g_{10} = e_{11} g_2 + a_{11} g_3 - a_{14} g_5,$$

$$g_{11} = e_{11} g_3 + a_{11} g_4 - a_{14} g_6,$$

$$g_{12} = e_{11} g_4 - a_{14} g_7,\ g_{13} = c_{11} c_{13},$$

$$g_{14} = c_{11} e_{17} + c_{13} e_{18} + a^2 {c_{12}}^2,\ g_{15} = -e_{18} e_{17}.$$

Using radiation conditions $u^*,\ w^*, \widehat{T^*},\ N^* \to 0$ as $z \to \infty$, the solution of Eq.(50) can be written as:

$$\widehat{T^*} = \sum_{j=1}^{4} C_j\, e^{-k_j z}, \tag{54}$$

$$u^* = \sum_{j=1}^{4} A_j\, e^{-k_j z}, \tag{55}$$

$$w^* = \sum_{j=1}^{4} B_j\, e^{-k_j z}, \tag{56}$$

$$N^* = \sum_{j=1}^{4} \mathrm{E}_j\, e^{-k_j z}, \tag{57}$$

where k_j^2 $(j = 1,\ 2,\ 3,\ 4)$ are roots of Eq. (50). Also using Eqs. (46)–(49), the coupling constants A_j, B_j, E_j are given by $A_j = L_j C_j$, $B_j = M_j C_j$, and $E_j = N_j C_j$, where:

$$L_j = \frac{h_1 k_j^4 + h_2 k_j^2 + h_3}{h_4 k_j^4 + h_5 k_j^2 + h_6},$$

$$M_j = \frac{h_7 k_j^6 + h_8 k_j^4 + h_9 k_j^2 + h_{10}}{h_{11} k_j^5 + h_{12} k_j^3 + h_{13} k_j},$$

$$N_j = -\frac{a_{14}}{a_{11} k_j^2 + e_{11}}$$

and

$$h_1 = -f_1 a_{11},\ h_2 = -f_2 a_{11} - f_1 e_{11},\ h_3 = f_5 a_{14} - f_2 e_{11},$$

$$h_4 = f_3 a_{11},\ h_5 = f_4 a_{11} + f_3 e_{11},\ h_6 = f_4 e_{11},$$

$$h_7 = -a_{15} f_3 a_{11},$$

$$h_8 = e_{13} f_1 a_{11} - a_{15} f_3 e_{11} - a_{11} f_3 e_{12} - a_{15} f_4 a_{11},$$

$$h_9 = a_{17} f_3 a_{14} + e_{13} f_2 a_{11} + e_{13} f_1 e_{11} - e_{12} f_3 e_{11} +$$

$$-e_{12} f_4 a_{11} - a_{15} f_4 e_{11},$$

$$h_{10} = a_{17} f_4 a_{14} - e_{13} f_5 a_{14} + e_{13} f_2 e_{11} - e_{12} f_4 e_{11},$$

$$h_{11} = a_{11} f_3 e_{14},$$

$$h_{12} = a_{11} f_4 e_{14} + e_{14} f_3 e_{11}, h_{13} = e_{11} f_4 e_{14}.$$

Using Eqs. (54)–(57), we obtain the expressions for all physical quantities as:

$$\hat{T} = \sum_{j=1}^{4} C_j\, e^{-k_j z} e^{\omega t + iax}, \tag{58}$$

$$u = \sum_{j=1}^{4} C_j\, L_j e^{-k_j z} e^{\omega t + iax}, \tag{59}$$

$$w = \sum_{j=1}^{4} C_j\, M_j e^{-k_j z} e^{\omega t + iax}, \tag{60}$$

$$N = \sum_{j=1}^{4} C_j\, N_j e^{-k_j z} e^{\omega t + iax}, \tag{61}$$

$$\sigma_{xx} = \sum_{j=1}^{4} \left[iab_{13} L_j - b_{14} k_j M_j - b_{13} N_j - b_{13} \right] \times$$
$$\times\, C_j e^{-k_j z} e^{\omega t + iax}, \tag{62}$$

$$\sigma_{zz} = \sum_{j=1}^{4} \left[-b_{13} k_j M_j + iab_{14} L_j - b_{13} N_j - b_{13} \right] \times$$
$$\times\, C_j e^{-k_j z} e^{\omega t + iax}, \tag{63}$$

$$\sigma_{zx} = \sum_{j=1}^{4} \left[-k_j L_j + iaM_j \right] C_j\, e^{-k_j z} e^{\omega t + iax}. \tag{64}$$

Using radiation conditions $u^{e*},\ w^{e*} \to 0$ as $z \to \infty$, the solution of Eq. (53) can be written as:

$$u^{e*} = \sum_{p=5}^{6} F_p\, e^{k_p z}, \tag{65}$$

$$w^{e*} = \sum_{p=5}^{6} G_p\, e^{k_p z}, \tag{66}$$

where k_p^2 $(j = 5, 6)$ are roots of Eq. (53). Also using Eqs. (51)–(52), the coupling constant G_p is given by $G_p = O_p F_p$, where:

$$O_p = -\frac{c_{13} k_p^2 + e_{17}}{iac_{12} k_p}.$$

Using Eqs. (65)–(66), we obtain the expressions for all physical quantities in elastic half-space as:

$$u^e = \sum_{p=5}^{6} F_p\, e^{k_p z} e^{\omega t + iax}, \tag{67}$$

$$w^e = \sum_{p=5}^{6} O_p F_p\, e^{k_p z} e^{\omega t + iax}, \tag{68}$$

$$\sigma_{xx}^e = \sum_{p=5}^{6} \left[iac_{14} + c_{15} k_p O_p \right] F_p\, e^{k_p z} e^{\omega t + iax}, \tag{69}$$

$$\sigma_{zz}^e = \sum_{p=5}^{6} \left[iac_{15} + c_{14} k_p O_p \right] F_p\, e^{k_p z} e^{\omega t + iax}, \tag{70}$$

$$\sigma_{zx}^e = \sum_{p=5}^{6} \left[iaO_p + k_p \right] F_p\, e^{k_p z} e^{\omega t + iax}. \tag{71}$$

5. Boundary conditions

For evaluating the constants C_j $(j = 1, 2, 3, 4)$ and F_p $(p = 5, 6)$, the following boundary conditions are applied:

1) A mechanical force $Fe^{\omega t + iax}$ is applied at $z = 0$ along the normal direction:

$$\sigma_{zz} = \sigma_{zz}^e - Fe^{\omega t + iax}. \tag{72}$$

2) The tangential stress vanishes at $z = 0$:

$$\sigma_{zx} = \sigma_{zx}^e. \tag{73}$$

3) The surface $z = 0$ is thermally insulated:

$$\frac{\partial T}{\partial z} = 0. \tag{74}$$

4) The carrier density at $z = 0$ is

$$C_d \frac{\partial N}{\partial z} = \kappa N. \tag{75}$$

5) The tangential displacement is continuous at $z = 0$:

$$u = u^e. \tag{76}$$

6) The normal displacement is continuous at $z = 0$:

$$w = w^e. \tag{77}$$

Using Eqs. (58)–(64) and (67)–(71) in Eqs. (72)–(77), we get the following non-homogenous system of four equations:

$$a_1^{**}C_1 + a_2^{**}C_2 + a_3^{**}C_3 + a_4^{**}C_4 + a_5^{**}F_5 + a_6^{**}F_6 = -F, \tag{78}$$

$$b_1^{**}C_1 + b_2^{**}C_2 + b_3^{**}C_3 + b_4^{**}C_4 + b_5^{**}F_5 + b_6^{**}F_6 = 0, \tag{79}$$

$$k_1C_1 + k_2C_2 + k_3C_3 + k_4C_4 = 0, \tag{80}$$

$$e_1^{**}C_1 + e_2^{**}C_2 + e_3^{**}C_3 + e_4^{**}C_4 = 0, \tag{81}$$

$$L_1C_1 + L_2C_2 + L_3C_3 + L_4C_4 - F_5 - F_6 = 0, \tag{82}$$

$$M_1C_1 + M_2C_2 + M_3C_3 + M_4C_4 - O_5F_5 - O_6F_6 = 0. \tag{83}$$

where:

$$a_j^{**} = -b_{13}k_jM_j + iab_{14}L_j - b_{13}N_j - b_{13},$$

$$a_p^{**} = -[c_{14}k_pO_p + iac_{15}],$$

$$b_j^{**} = iaM_j - k_jL_j, b_p^{**} = -\left[k_p - iaO_p\right],$$

$$e_j^{**} = \left(\frac{\kappa}{C_d} + k_j\right)N_j, \ \ j = 1,2,3,4, \ \ p = 5,6.$$

For evaluating the values of constants C_j $(j = 1, 2, 3, 4)$ and F_p $(p = 5, 6)$, the system of Eqs. (78)–(83) are solved using MATLAB. After evaluating the values of these constants, the expressions for temperature distribution, components of displacement, carrier density and components of stress can be obtained by the expressions (58)–(64).

Using Eqs. (19) and (20), the relation between the temperature T and the operator $\hat{T}$ can be written as

$$T = \frac{1}{K_1}\left[\sqrt{1 + 2K_1\hat{T}} - 1\right] = \frac{1}{K_1}\left[\sqrt{1 + 2K_1\widehat{T^*}e^{\omega t + iax}} - 1\right]. \tag{84}$$

The temperature, components of displacement, stresses and carrier density may also be expressed in terms of K_1 as:

$$T = \frac{1}{K_1}\left[\sqrt{1 + 2K_1\sum_{j=1}^{4} C_j\, e^{-k_jz}e^{\omega t + iax}} - 1\right], \tag{85}$$

$$u = \frac{L^{**}}{2}\left[K_1\left(T + \frac{1}{K_1}\right)^2 - \frac{1}{K_1}\right]e^{\omega t + iax}, \tag{86}$$

$$w = \frac{M^{**}}{2}\left[K_1\left(T + \frac{1}{K_1}\right)^2 - \frac{1}{K_1}\right]e^{\omega t + iax}, \tag{87}$$

$$\sigma_{xx} = \frac{1}{2}\left[K_1\left(T + \frac{1}{K_1}\right)^2 - \frac{1}{K_1}\right][iab_{13}L^{**} - b_{13} - b_{13}N^{**}]e^{\omega t + iax} +$$

$$- b_{14}M^{**}\sum_{j=1}^{4} k_j\, C_j e^{-k_jz}e^{\omega t + iax}, \tag{88}$$

$$\sigma_{zz} = \frac{1}{2}\left[K_1\left(T + \frac{1}{K_1}\right)^2 - \frac{1}{K_1}\right][iab_{14}L^{**} - b_{13} - b_{13}N^{**}]e^{\omega t + iax} +$$

$$- b_{13}M^{**}\sum_{j=1}^{4} k_j\, C_j e^{-k_jz}e^{\omega t + iax}, \tag{89}$$

$$\sigma_{zx} = \left\{\begin{matrix} -L^{**}\sum_{j=1}^{4} k_j\, C_j e^{-k_jz} + \\ + \frac{iaM^{**}}{2}\left[K_1\left(T + \frac{1}{K_1}\right)^2 - \frac{1}{K_1}\right] \end{matrix}\right\}e^{\omega t + iax}, \tag{90}$$

$$N = \frac{N^{**}}{2}\left[K_1\left(T + \frac{1}{K_1}\right)^2 - \frac{1}{K_1}\right]e^{\omega t + iax}, \tag{91}$$

where:

$$L^{**} = \frac{h_1r^4 + h_2r^2 + h_3}{h_4r^4 + h_5r^2 + h_6},$$

$$M^{**} = \frac{h_7r^6 + h_8r^4 + h_9r^2 + h_{10}}{h_{11}r^5 + h_{12}r^3 + h_{13}r},$$

$$N^{**} = -\frac{a_{14}}{a_{11}r^2 + e_{11}}.$$

6. Numerical results

For the numerical justification of the analytical results obtained, we take example of silicon (Si) as semiconducting medium for which related values of constants are given by Song et al. [28] as:

$\lambda^s = 3.64\times10^{10}$ N/m^2, $\mu^s = 5.46\times10^{10}$ N/m^2, $\rho = 2330$ kg/m^3,

$T_0 = 800$ K, $\tau = 5\times10^{-5}$ s, $C_d = 2.5\times10^{-3}$ m^2/s, $C_s = 695$ J/(kg K),

$E_s = 1.11$eV, $\alpha = 4.14\times10^{-6}$/K, $K_0^s = 150$W/(m K),

$\beta = -9\times10^{-31}$m^3, $F = 1.0$, $\kappa = 2.0$.

Further the physical constants for elastic medium – granite – are given by Bullen [31]:

$\rho^e = 2.65\times10^3$kg/m^3, $\lambda^e = 2.238\times10^3$N/m^2, $\mu^e = 2.238\times10^3$ N/m^2.

All calculations have been done at the surface $x = 1$, $t = 1$. Further $\omega = \omega_0 + i\xi$, where $\omega_0 = -0.03$, $\xi = 0.01$. The graphs are obtained for constant and variable thermal conductivity by taking three values of K_1, namely 0, –2 and –5, respectively.

6.1. Results and discussion

Figure 2 shows the variation of normal displacement against horizontal distance. Parameter K_1 represents thermal conductivity of the medium. $K_1 = 0$, when the variables are independent of thermal conductivity, and when K_1 is not equal to zero $(K_1 = -2, -5)$, then the variables are dependent on thermal conductivity. The value of normal displacement decreases with an increase in horizontal distance for both the cases. In the case of variable thermal conductivity, the magnitude of normal displacement decreases with increase in value of K_1.

Figure 3 shows variation of normal stress with horizontal distance. The value of normal stress increases as the horizontal distance increases in the case of constant thermal conductivity. The similar behaviour is observed for $K_1 = -5$. But for

$K_1 = -2$, the magnitude of normal stress first increases to attain the maximum value, then follows a sharp decrease.

Figure 4 shows variation of carrier density against horizontal distance. The value of carrier density increases sharply for constant thermal conductivity following a sharp decrease. But for variable thermal conductivity, the magnitude of carrier density varies inversely with value of K_1.

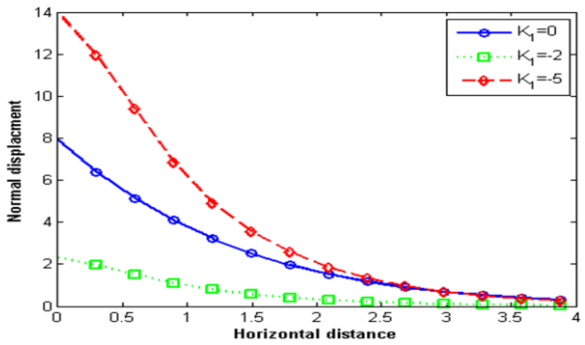

Fig. 2. Variation of normal displacement against horizontal distance.

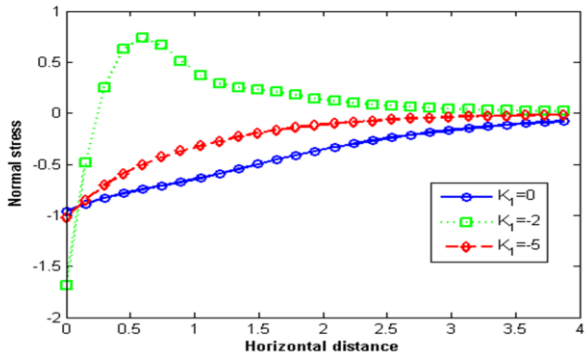

Fig. 3. Variation of normal stress against horizontal distance.

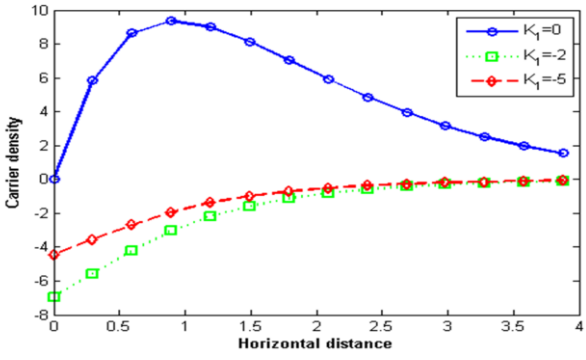

Fig. 4. Variation of carrier density against horizontal distance.

Figure 5 shows variation of temperature against horizontal distance. The magnitude of temperature increases exponentially, then becomes constant for all values of K_1. Further for variable thermal conductivity, the temperature varies inversely with parameter K_1.

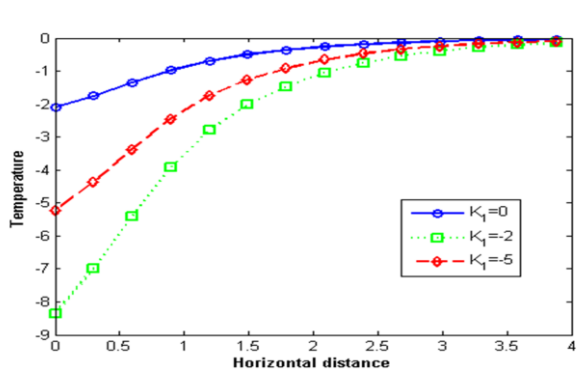

Fig. 5. Variation of temperature against horizontal distance.

7. Conclusions

The following conclusions can be drawn from the performed study on the effect of variable thermal conductivity in semiconducting medium underlying an elastic half-space:

1) The variable thermal conductivity has a considerable effect on all the physical quantities.
2) The maximum variation is obtained for carrier density in context of constant and variable thermal conductivity.
3) All the physical quantities are inversely proportional to the value of parameter K_1 , except normal stress.
4) This research work finds its application in different fields of engineering to calculate displacement, stress and carrier density in semiconductors subjected to variable thermal conductivity.
5) This problem has its importance due to the fact that physical properties of a material change drastically when there is a change in temperature.

References

[1] Gordon, J.P., Leite, R.C.C., Moore, R.S., Porto, S.P.S., & Whinnery, J.R. (1965). Long-transient effects in lasers with inserted liquid samples. *Journal of Applied Physics*, 36(1), 3–8. doi: 10.1063/1.1713919

[2] Kreuzer, L.B. (1971). Ultralow gas concentration infrared absorption spectroscopy. *Journal of Applied Physics*, 42(7), 2934–2943. doi: 10.1063/1.1660651

[3] Mandelis, A. (1997). Thermoelectronic-wave coupling in laser photothermal theory of semiconductors at elevated temperatures. *Optical Engineering (Redondo Beach, Calif.)*, 36(2), 459–468. doi: 10.1117/1.601217

[4] Todorović, D.M. (2005). Plasmaelastic and thermoelastic waves in semiconductors. *Journal de Physique IV (Proceedings)*, 125, 551–555. doi: 10.1051/jp4:2005125127

[5] Song, Y.Q., Bai, J.T., & Ren, Z.Y. (2012). Study on the reflection of photothermal waves in a semiconducting medium under generalized thermoelastic theory. *Acta Mechanica*, 223, 1545–1557. doi: 10.1007/s00707-012-0677-1

[6] Othman, M.I., Tantawi, R.S., & Eraki, E.E. (2016). Propagation of the photothermal waves in a semiconducting medium under L-S theory. *Journal of Thermal Stresses*, 39(11), 1419–1427. doi: 10.1080/01495739.2016.1216063

[7] Ailawalia, P., Sachdeva, S. K., Singh Pathania, D.S., & Hong Wu, Y. (2017). Effect of mechanical force along the interface of

semi-infinite semiconducting medium and thermoelastic micropolar cubic crystal. *Cogent Mathematics*, 4(1), 1347991. doi: 10.1080/23311835.2017.1347991

[8] Alzahrani, F.S., & Abbas, I.A. (2018). Photo-thermoelastic interactions in a 2D semiconducting medium. *European Physical Journal Plus*, 133, 505. doi: 10.1140/epjp/i2018-12285-5

[9] Hobiny, A. (2020). Effect of the hyperbolic two-temperature model without energy dissipation on photo-thermal interaction in a semi-conducting medium. *Results in Physics*, 18, 103167. doi: 10.1016/j.rinp.2020.103167

[10] Saeed, A.M., Lotfy, K., El-Bary, A., & Ahmed, M.H. (2021). Thermoelastic with photogenerated model of rotating microstretch semiconductor medium under the influence of initial stress. *Results in Physics*, 31, 104967. doi: 10.1016/j.rinp.2021.104967

[11] Hilal, M.I.M. (2022). Photothermal excitation and Thomson impact in a semiconductor microelongated thermoelastic medium with microtemperatures in the gravity. *Zeitschrift Fur Angewandte Mathematik Und Mechanik*, 102(12), e202200175. doi: 10.1002/zamm.202200175

[12] Kaur, I., Singh, K., & Craciun, E.M. (2022). A mathematical study of a semiconducting thermoelastic rotating solid cylinder with modified Moore–Gibson–Thompson heat transfer under the Hall effect. *Mathematics*, 10(14), 2386. doi: 10.3390/math10142386

[13] Lotfy, K., Ahmed, A., El-Bary, A., & Tantawi, R.S. (2023). A novel stochastic model of the photo-thermoelasticity theory of the non-local excited semiconductor medium. *Silicon*, 15, 437–450. doi: 10.1007/s12633-022-02021-x

[14] Azhar, E., Ali, H., Jahangir, A., & Anya, A.I. (2023). Effect of Hall current on reflection phenomenon of magneto-thermoelastic waves in a non-local semiconducting solid. *Waves in Random and Complex Media*, 1–18. doi: 10.1080/17455030.2023.2182146

[15] Youssef, H.M., & El-Bary, A.A. (2006). Thermal shock problem of a generalized thermoelastic layered composite material with variable thermal conductivity. *Mathematical Problems in Engineering*, 2006, 87940, 1–14. doi: 10.1155/mpe/2006/87940

[16] Ezzat, M.A., & Youssef, H.M. (2009). State space approach for conducting magneto-thermoelastic medium with variable electrical and thermal conductivity subjected to ramp-type heating. *Journal of Thermal Stresses*, 32(4), 414–427. doi: 10.1080/01495730802637233

[17] Sherief, H., & Abd El-Latief, A.M. (2013). Effect of variable thermal conductivity on a half-space under the fractional order theory of thermoelasticity. *International Journal of Mechanical Sciences*, 74, 185–189. doi: 10.1016/j.ijmecsci.2013.05.016

[18] Zenkour, A.M., & Abbas, I.A. (2014). Nonlinear transient thermal stress analysis of temperature-dependent hollow cylinders using a finite element model. *International Journal of Structural Stability and Dynamics*, 14(7), 1450025. doi: 10.1142/S0219455414500254

[19] Yasein, M., Mabrouk, N., Lotfy, K., & EL-Bary, A.A. (2019). The influence of variable thermal conductivity of semiconductor elastic medium during photothermal excitation subjected to thermal ramp type. *Results in Physics*, 15, 102766. doi: 10.1016/j.rinp.2019.102766

[20] Abbas, I., Hobiny, A., & Marin, M. (2020). Photo-thermal interactions in a semi-conductor material with cylindrical cavities and variable thermal conductivity. *Journal of Taibah University for Science*, 14(1), 1369–1376. doi: 10.1080/16583655.2020.1824465

[21] Alzahrani, F., Hobiny, A., Abbas, I., & Marin, M. (2020). An eigenvalues approach for a two-dimensional porous medium based upon weak, normal and strong thermal conductivities. *Symmetry*, 12(5), 848. doi: 10.3390/sym12050848

[22] Marin, M., Hobiny, A., & Abbas, I. (2021). The effects of fractional time derivatives in porothermoelastic materials using finite element method. *Mathematics*, 9(14), 1606. doi: 10.3390/math9141606

[23] Lotfy, K., & El-Bary, A. (2022). Elastic-thermal-diffusion model with a mechanical ramp type and variable thermal conductivity of electrons–holes semiconductor interaction. *Waves in Random and Complex Media*, 1–20. doi: 10.1080/17455030.2022.2078521

[24] Hobiny, A., & Abbas, I. (2023). Generalized thermoelastic interaction in orthotropic media under variable thermal conductivity using the finite element method. *Mathematics*, 11(4), 955. doi: 10.3390/math11040955

[25] Kumar, S., Kadian, A., & Kalkal, K.K. (2023). Thermoelastic interactions in a rotational medium having variable thermal conductivity and diffusivity with gravitational effect. *Waves in Random and Complex Media*, 1–22. doi: 10.1080/17455030.2023.2205964

[26] El-Sapa, S., El-Bary, A.A., & Lotfy, K. (2023). Effect of an excited non-local microelongated semiconductor with variable thermal conductivity on the propagation of photo-thermoelastic waves. *Optical and Quantum Electronics*, 55(6), 569. doi: 10.1007/s11082-023-04836-3

[27] Lotfy, K. (2017). Photothermal waves for two temperature with a semiconducting medium under using a dual-phase-lag model and hydrostatic initial stress. *Waves in Random and Complex Media*, 27(3), 482–501. doi: 10.1080/17455030.2016.1267416

[28] Song, Y., Bai, J., & Ren, Z. (2012). Reflection of plane waves in a semiconducting medium under photothermal theory. *International Journal of Thermophysics*, 33, 1270–1287. doi: 10.1007/s10765-012-1239-4

[29] Ewing, W.M., Jardetzky, W.S., Press, F., & Beiser, A. (1957). *Elastic Waves in Layered Media*. McGraw-Hill.

[30] Lotfy, K. (2019). Effect of variable thermal conductivity during the photothermal diffusion process of semiconductor medium. *Silicon*, 11, 1863–1873. doi: 10.1007/s12633-018-0005-z

[31] Bullen, K.E. (1963). *An Introduction of the Theory of Seismology*. Cambridge University Press.

Co-published by
Institute of Fluid-Flow Machinery
Polish Academy of Sciences
Committee on Thermodynamics and Combustion
Polish Academy of Sciences

http://www.imp.gda.pl/archives-of-thermodynamics/

ARCHIVES OF THERMODYNAMICS

Flame stabilization and combustion enhancement in a scramjet combustor by varying strut injection angles

Venkateshwaran Vanamamalai[a], Padmanathan Panneerselvam[a*]

[a]School of Mechanical Engineering, Vellore Institute of Technology, Vellore, Tamilnadu- 632014, India
*Corresponding author email: padmanathan.p@vit.ac.in

Received: 03.02.2024; revised: 11.06.2024; accepted: 12.06.2024

Abstract

The present study explores the characteristics of reacting flow in a scramjet combustor with struts, focusing particularly on implementing different injection strategies. A three-dimensional DLR scramjet combustor is utilised to assess the impact on the system, incorporating multiple injections and varying injection angles on the triangular wedge. The analysis considers three injectors with parallel, upward and downward injections at angles of 15° and 30°. The numerical investigation is conducted under a constant total pressure of 7.82 bar, a temperature of 340 K, and an airspeed of Mach 2 at the inlet. The results highlight the significance of injector location and shape in promoting flame stabilization. Furthermore, injection angles play a crucial role in mitigating shockwave intensity. The numerical analysis involves a steady-state Reynolds-averaged Navier-Stokes equation with the shear stress transport k–ω turbulence model. The obtained results were analyzed by examining the critical variables such as Mach number, static pressure and combustion efficiency across the combustor. Based on the computational results, injecting fuel upward not only increases the overall pressure loss but also enhances the subsonic regime downstream of the strut, which leads to better mixing and combustion efficiencies. This is primarily due to shockwave generation from the edges of the strut and the interactions with the fuel stream shear layers.

Keywords: Hydrogen fuel; Combustion efficiency; Scramjet combustor; Flame stabilization; Strut injector

Vol. 45(2024), No. 3, 167–178; doi: 10.24425/ather.2024.151227

Cite this manuscript as: Vanamamalai, V., & Panneerselvam, P. (2024). Flame stabilization and combustion enhancement in a scramjet combustor by varying strut injection angles. *Archives of Thermodynamics*, 45(3), 167–178.

1. Introduction

Scramjet engines operate as air-breathing propulsion systems, enabling them to attain hypersonic speeds while maintaining regular functionality. These engines produce thrust by compressing incoming air and combusting it with pre-existing onboard fuel, making them well-suited for efficiently propelling high-speed vehicles like missiles or aircraft. The application of scramjet engines becomes imperative for hypersonic and supersonic flight, characterized by vehicle speeds exceeding Mach 5 [1–4]. The ineffectiveness of conventional jet engines at hypersonic speeds is attributed to the challenges posed by shockwaves and increased drag. In contrast, scramjet engines outperform in high-velocity environments, given their specific design for such conditions. However, it is crucial to acknowledge that scramjet engines encounter various technological hurdles that require resolution. [5–7]. Attaining steady combustion during hypersonic speeds is a challenge due to the rapid air velocity. To address this, various geometric shapes, including cavities [8–12], struts [13–18], pylons [19–22], and shockwave generators [23,24], have been employed within the combustor. These design modifications aim to enhance mixing and combustion processes, mit-

Nomenclature

A – area of the cross-section, m^2
$\dot{m}$ – overall mass flux, kg/s
P – static pressure, Pa
P_0 – total or stagnation pressure, Pa
T – static temperature, K
u – axial velocity, m/s
X – axial distance from the inlet, m
Y – distance, m
Y – mass fraction

Greek symbols

η_C – combustion efficiency, %
η_t – total pressure loss, %
ρ – density, kg/m^3

Subscripts and Superscripts

H_2 – hydrogen
H_2O – water
N_2 – nitrogen
O_2 – oxygen

Abbreviations and Acronyms

AUSM– advection upwind splitting method
CFD – computational fluid dynamics
CFL – Courant-Friedrichs-Lewy
GIT – grid independence test
RANS– Reynolds-averaged Navier-Stokes (equations)
SST – shear stress transport

igating the difficulties associated with high-speed airflow and contributing to more effective combustion at hypersonic speeds. This phenomenon induces turbulent flow, effectively promoting the mixing of fuel and air. Consequently, it leads to an improved efficiency in the combustion process.

Effectively controlling shockwaves is a crucial consideration in the design and operation of a scramjet engine. The rapid flow of air and fuel through the combustor creates conditions that can give rise to shockwaves. These shockwaves stem from the compression and heating of incoming air, causing abrupt changes in both pressure and temperature within the engine. Shockwaves play a significant role in governing and maintaining the combustion process [25–27]. Their function involves ensuring that the air and fuel mixture remains confined within the combustor for a sufficient duration. Engineers employ diverse design strategies to mitigate the adverse effects of these factors. Intricate geometries within the combustor are often utilized to control the flow and minimize the impact of shockwaves [28,29].

Cavities are commonly integrated into scramjet combustors to enhance mixing and combustion processes. These structures induce turbulence, promoting better fuel-air mixing and, consequently, improving combustion efficiency. The incorporation of cavities contributes to an expanded surface area, thereby enhancing the combustion process. This leads to improved efficiency and accelerated fuel burning within the scramjet engine. Furthermore, cavities contribute to flame stabilization and help prevent flame blowout [30]. Li et al. [31] investigated the impact of different depths and diameters of multi-cavities on a Mach 2.52 flow. They have focused on the flow structure and mixing effectiveness at various pressure ratios across different cavity depths. The study revealed that increasing cavity depth and utilizing multiple cavities with a maximum number of injections could lead to improved mixing compared to a single injection. This improvement is attributed to the generation of shock waves and the separation of the shear layer. Jeyakumar et al. [32] experimentally examined cavity-based reacting and non-reacting flow in circular cross sectional combustor. They tested various cavity configurations such as fore wall modifications [33], aft wall angles with single and dual step angles [34], various cavity depths [35], and transverse upstream injection [36] within the scramjet combustor. Their findings demonstrate that employing transverse upstream injection with aft wall angle cavities results in lower stagnation pressure loss compared to rectangular cavities. Additionally, they observed uniform mixing with increasing injection pressures.

Kannaiyan [37] examines the supersonic combustion of ethylene was investigated in various combustor configurations, including the baseline design without a cavity, a configuration featuring a square cavity, and another with an angled cavity. The findings unequivocally show that the model combustor, distinguished by a shallow and sloped aft-wall cavity, exhibits the longest residence period and the highest level of heat release. Moreover, it is noted that the influence of a cavity with a reduced length-to-depth ratio on the estimation of residence time and heat release is negligible. The research conducted by Liu et al. [38] investigated the application of cavity-based scramjet engines in both counter-jet and co-jet configurations. The study's results indicate that the counter-jet configuration has a more pronounced impact on fuel mixing compared to the co-jet configuration. This effect is attributed to the proximity of the main eddy to the counter jet, facilitating an efficient distribution of fuel through the primary circulation. The findings suggest that the penetration of hydrogen in counter jets is approximately 25% higher compared to co-jets. Feng et al. [39] conducted research on the combustion behaviors of powder fuels within a cavity-based supersonic combustion chamber. The findings suggest that steady burning of the powder fuel is achievable in the presence of supersonic wind. The main areas of flame dispersion occur within the cavity's interior and the shear layer, near the boundary layer of the expansion region. As the air-to-fuel ratio increases, the total pressure loss beside the combustion chamber decreases. However, the efficiency of powder particle combustion exhibits the opposite trend. In the cavity-based supersonic combustor, reducing the amount of air to fuel mixture proves advantageous.

An experimental investigation was conducted on a combined fuel injection method involving a strut/wall configuration by Qiu et al. [40]. The primary goal of this investigation was to improve the combustion performance in a flush-wall scramjet combustor fueled with liquid kerosene. The results suggest that the combustion intensity of the core flame increases with a higher fuel equivalency ratio. The combustion process includes the

propagation of the core flame toward the combustor sidewall, igniting the fuel present on the wall, and leading to the formation of a wall flame. The presence of the wall flame induces thermal choking downstream of the strut, thereby enhancing the flame within the core. The performance of the combustor and the characteristics of the flame are influenced by the different fuel distribution strategies employed. Additionally, the positioning of wall fuel injectors is optimized to enhance combustion efficiency. Steady and unsteady flow characteristics of strut-based scramjet combustors with implications of the dual cavity and various cavity locations were analyzed numerically by Rajesh et al. [41,42], Athithan et al. [43] and Jeyakumar et al. [44]. The results reveal that the dual cavity is shifted away from the strut injector, and a lateral expansion of the combustion zone is observed. This phenomenon improves combustion propensity and facilitates a decrease in combustor length.

Flame propagation characteristics and combustion performance with multiple struts and fueled by liquid kerosene were examined by Qiu et al. [45]. The study concentrated on examining fuel distribution patterns, particularly investigating different single-strut injection methods and expanding the analysis to include up to five injection struts. The findings demonstrated an enhancement in fuel mixing efficiency, reaching a value of 53.8%, with an increase in the number of injection struts. The discussion revolved around the interaction that occurs between the flame of the ignition and injection struts. A technique for augmenting the width of flame spread, without the need for additional energy input, was suggested, drawing upon the inherent properties of flame propagation. Kummitha et al. [46] concentrated on analyzing wedge-shaped and revolved wedge-shaped injectors to explore the possibility of improving mixing by increasing interactions between the shear mixing layer and shock wave. The results indicate that the newly designed struts achieved complete mixing at a distance of 0.180 m from the combustor inlet. This accomplishment was accompanied by an average gain in mixing efficiency of 9%, with a corresponding increase in pressure losses of 12%.

Much of the research on strut combustor scramjets has primarily focused on a single injector located at the central strut. While numerous studies have reported numerical results using a two-dimensional scramjet combustor with a strut, the development of three-dimensional scramjet combustors has lagged. This current work addresses supersonic flows at high speeds, highlighting the significant impact of a wedge on flow characteristics. The presence of a wedge contributes to the development of gradients in flow properties, including pressure, velocity, and density. This study also emphasized investigating various injection angles within the strut, to create more disruptions in the flow field and enhance diverse interactions between shear layers, shock waves, and flow streams. Understanding the flow physics associated with injection angles in strut-based supersonic flow is vital for optimizing mixing mechanisms, controlling flow characteristics, and improving the efficiency of scramjet combustion. Given that higher injection angles can significantly disrupt the boundary layer formed along surfaces, leading to increased flow separation, boundary layer instabilities, and potential impacts on combustion performance, lower injection angles were chosen for this study. The research has systematically explored the impact and importance of the injection position on mixing enrichment specifically in the context of the strut base.

2. Numerical methodology

2.1. Geometric modelling

A numerical analysis was performed on a scramjet combustor utilizing angular injection within a strut-based configuration. In this study, two distinct injection angles with three-hole injections were selected and compared against a parallel injection method. Specifically, injection angles of 15° and 30° were employed using upward and downward injection techniques. The hydraulic diameter of the injection holes for the three injection ports was consistently maintained at 1 mm. The gaseous state of hydrogen is utilized as the reactive fluid, being injected from the strut base under sonic conditions. The incoming free stream air reaches the entrance of the combustor with Mach 2. The dimensions of the scramjet model are 300 mm in length, 45 mm in breadth, and 50 mm in height. The leading edge of the strut is positioned at a distance of 68 mm from the air intake while maintaining a vertical distance of 25 mm above the bottom wall. The half angle of the strut remains constant at 6°. The length of the strut is measured at 32 mm. The upper wall features a divergence angle of 3°, starting 100 mm from the inlet of the combustor, as illustrated in Fig.1, and terminating at its outlet. The separation between the base of the strut and the entrance of the combustor measures 100 mm.

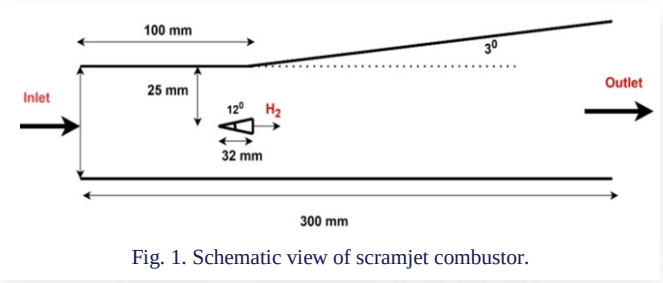

Fig. 1. Schematic view of scramjet combustor.

2.2. Numerical modelling

The study of the scramjet combustor entails solving three-dimensional conservative equations governing the conservation of mass, momentum, and energy. The primary challenge in studying supersonic flows lies in developing reliable turbulence models that allow for the examination of the underlying flow structure [47]. The current approach utilizes the Shear Stress Transport (SST) k–ω turbulence model to solve the compressible Reynolds-averaged Navier-Stokes (RANS) equations. The k–ω SST model is considered the most accurate turbulence model for scramjets [48]. It enables predictions of mixing layers, negative pressure gradients, and separated flows, making it suitable for a comprehensive analysis of scramjet flows [49]. In the ANSYS Fluent framework [50], the finite volume approach is employed to discretize the governing equations of the flow. The modelling of the working fluid as an ideal gas, along with the use of a mix-

ing-law equation, allows for the capture of both density and viscosity fluctuations. The combination of the Advection Upwind Splitting Method (AUSM) with a higher-order upwind approach enhances convergence and yields more accurate results [51]. Ensuring stability involves preventing divergence and maintaining the Courant-Friedrichs-Lewy (CFL) value at 0.5 [52], providing a reliable approach to guarantee a stable solution.

2.3. Discretization and grid independence test

The three-dimensional grid generation for the strut-based scramjet combustor was completed using Ansys ICEM R22, employing hexahedral elements. The O-Grid method was utilized to discretize the injectors, enabling the creation of structured grids closely aligned with the geometry to ensure an accurate representation of the flow domain. To capture shockwaves and boundary layer interactions effectively, the y+ value is kept below 1 near the wall boundaries. Additionally, the grid elements are maintained with a minimum angle of approximately 45° and a skewness of around 0.9 to ensure optimal grid quality. A grid independence test is essential to ensure computational consistency. To enhance the accuracy of numerical results while minimizing computational cost and time, three different element sizes were employed to optimize grid resolution. Grid independence test (GIT) was conducted on a three-dimensional supersonic combustor, employing three different mesh element sizes: 3.5 million, 6.6 million, and 9.9 million elements. The discretized 3D scramjet combustor and zoomed view of the O-Grid mesh is depicted in Fig. 2.

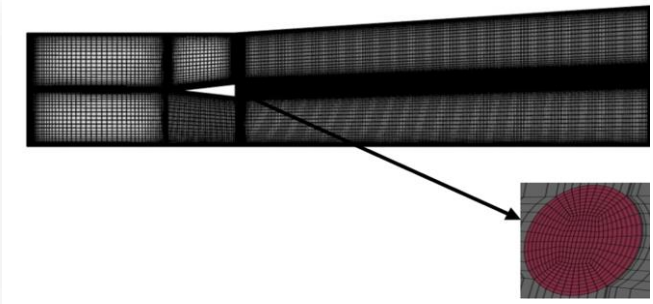

Fig. 2. Three-dimensional mesh of the scramjet combustor.

The investigation involved measuring total pressure and Mach number along the centerline of the combustor. Figures 3a and 3b illustrate minimal variation among the three mesh element sizes concerning both the bottom wall pressure and axial pressure plots. To minimize convergence time, medium size mesh elements were selected for this investigation.

2.4. Boundary conditions

The steady-state three-dimensional modeling of the strut-based scramjet combustor employs specific boundary conditions were shown in Table 1.

Table 1. Inlet boundary conditions for air and fuel.

Condition	Air	Hydrogen
Mach number	2.0	1.0
Velocity	730 m/s	1200 m/s
Density (ρ)	1.002 kg/m^3	0.097 kg/m^3
Static pressure (P)	100 000 Pa	100 000 Pa
Total or stagnation pressure (P_0)	782 444 Pa	189 292 Pa
Static temperature (T)	340 K	250 K
Mass fraction of hydrogen (Y_{H2})	0	1
Mass fraction of water (Y_{H2O})	0.032	0
Mass fraction of oxygen (Y_{O2})	0.232	0
Mass fraction of nitrogen (Y_{N2})	0.736	0

The static pressure and Mach number of the entering airflow have been provided, making the far-field the definition for air and fuel inlet. Due to the density-based solver, the operating conditions were stated to be zero. For the walls of the combustor and the strut, a no-slip wall condition has been defined. The outlet from the combustor is characterized by a pressure outlet.

2.5. Combustion modelling

In the context of investigating the combustion characteristics of supersonic flow, the computational analysis incorporates the utilization of species transport [53] and eddy dissipation models. The utilization of the eddy dissipation concept is employed as a means to streamline the complex connections between turbulence and chemistry, while also aligning with empirical observations [54]. The selection of a single-step reaction process over multistep hydrogen reaction models is based on the superior outcomes it offers in terms of overall combustor performance. The utilization of a single-step reaction mechanism has the added benefit of reducing the computational period required for solving the reaction equation [55]:

$$2H_2 + O_2 \rightarrow 2H_2O. \quad (1)$$

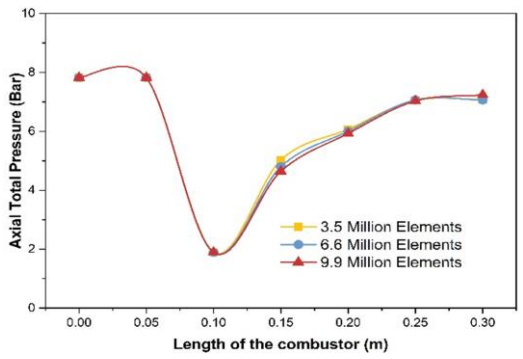

a)

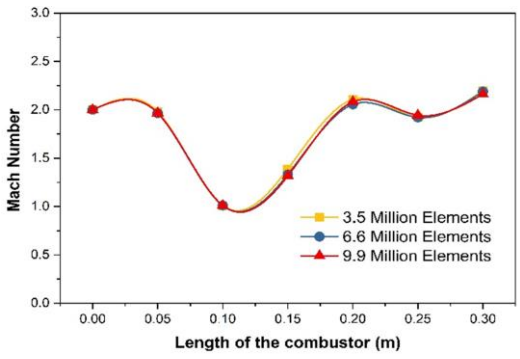

b)

Fig. 3. Grid independence study: a) static pressure along the bottom wall of the combustor, b) axial pressure along the centerline of the combustor

2.6. Validation

The assessment of the steady-state simulation results involved a comparative analysis carried out by Oevermann [47] at the DLR (German Aerospace Center) scramjet combustor. The present study has been validated for both reacting and non-reacting conditions. In the non-reacting conditions, the analysis includes the consideration of static pressure at the bottom wall and centerline. In contrast, for reactive cases, the study demonstrates the distribution of velocity magnitude and temperature. From Figs. 4 a and b, the observed agreement between the simulation outcomes and empirical data includes consistent findings related to strut-generated shock, wall-reflected shock waves, and the distribution of wall static pressure. The observed slight fluctuations in static pressure near the boundary may be attributed to unexpected turbulence vortices close to the wall. The numerical results exhibit a similar pattern and only marginal variation when compared with experimental observations.

The validation process for reacting flows encompasses considerations of combustion chemistry, incorporating the eddy dissipation model, and solving species transport equations. The velocity distributions at X = 78 mm, X = 125 mm, and X = 207 mm along the axial plane are depicted in Figs. 5a to 5c.

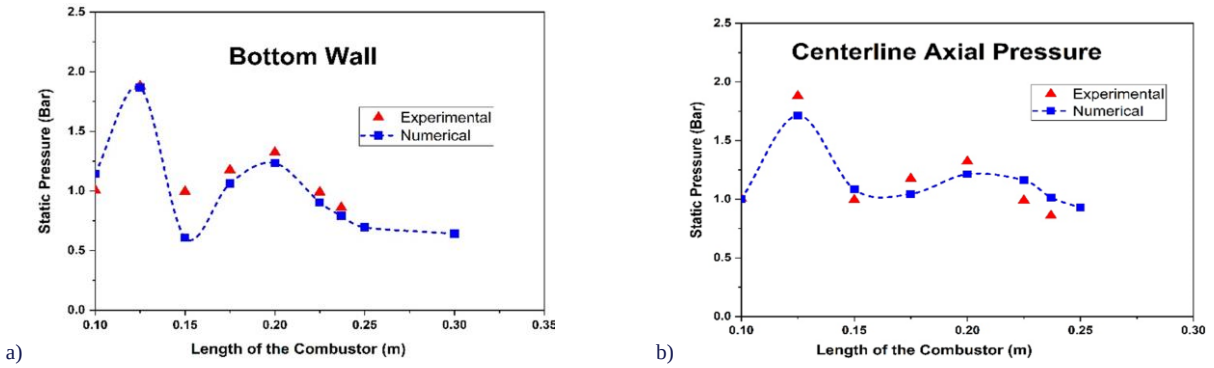

Fig. 4. Validation for 3-dimensional scramjet combustor using pressure plots (non-reacting): a) static pressure at bottom wall, b) static pressure at a distance of Y = 25 mm.

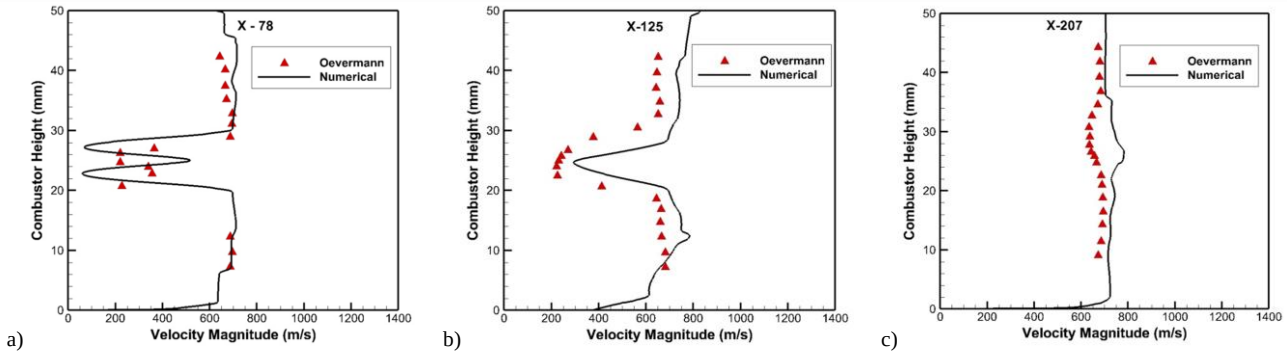

Fig. 5. Validation of axial velocity plots for reacting flow with Oevermann [47] at: a) X = 78 mm, b) X = 125 mm, c) X = 207 mm.

The comparison reveals a high level of concordance between experimental findings and numerical simulations, with minimal discernible deviation. Figures 6a to 6c illustrates the temperature distribution along the strut-based scramjet combustor at axial positions of X = 78 mm, X = 125 mm and X = 233 mm from the inlet. The numerical predictions closely align with experimental observations. Discrepancies between the high-temperature values obtained in experiments and those predicted numerically can be attributed to heat transfer effects and three-dimensional vortices. Nevertheless, the study demonstrates the competence of the numerical approach employed here in analyzing diverse configurations of strut-based scramjet combustors.

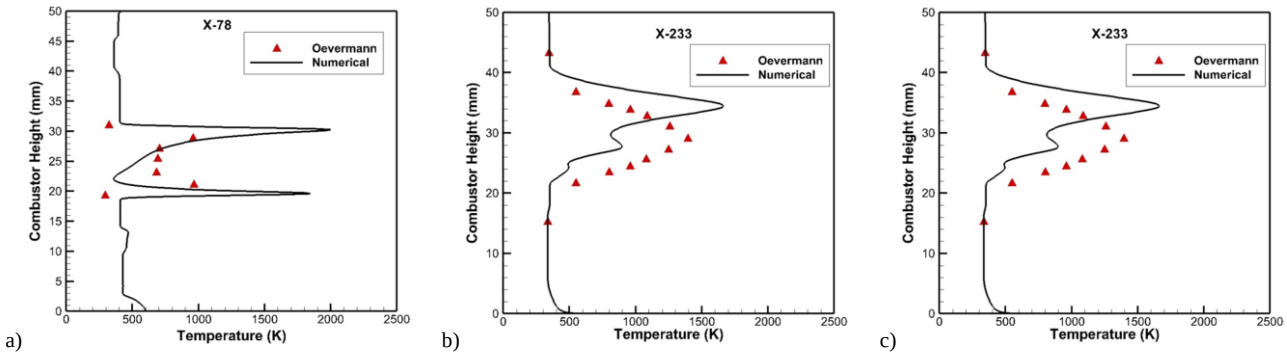

Fig. 6. Validation of static temperature with Oevermann [47] at: a) X = 78 mm, b) X = 125 mm, c) X = 233 mm.

3. Results and discussion

In this study, computational fluid dynamics (CFD) is employed for numerical analysis to investigate the mixing performance associated with different strut injection techniques in the DLR scramjet combustor. The primary objective is to assess the performance characteristics of a strut-based scramjet combustor under varying injection angles and directions. A recently updated three-dimensional numerical investigation further explores the impact of angled injectors, pointing both above and downward, on the overall performance of a strut-based scramjet engine. The numerical solution for steady-state flow under identical operational variables and boundary conditions is obtained by solving the RANS equations.

The density contours for different injection angles, both upward and downward configurations, are illustrated in Figs.7a to 7e, respectively.

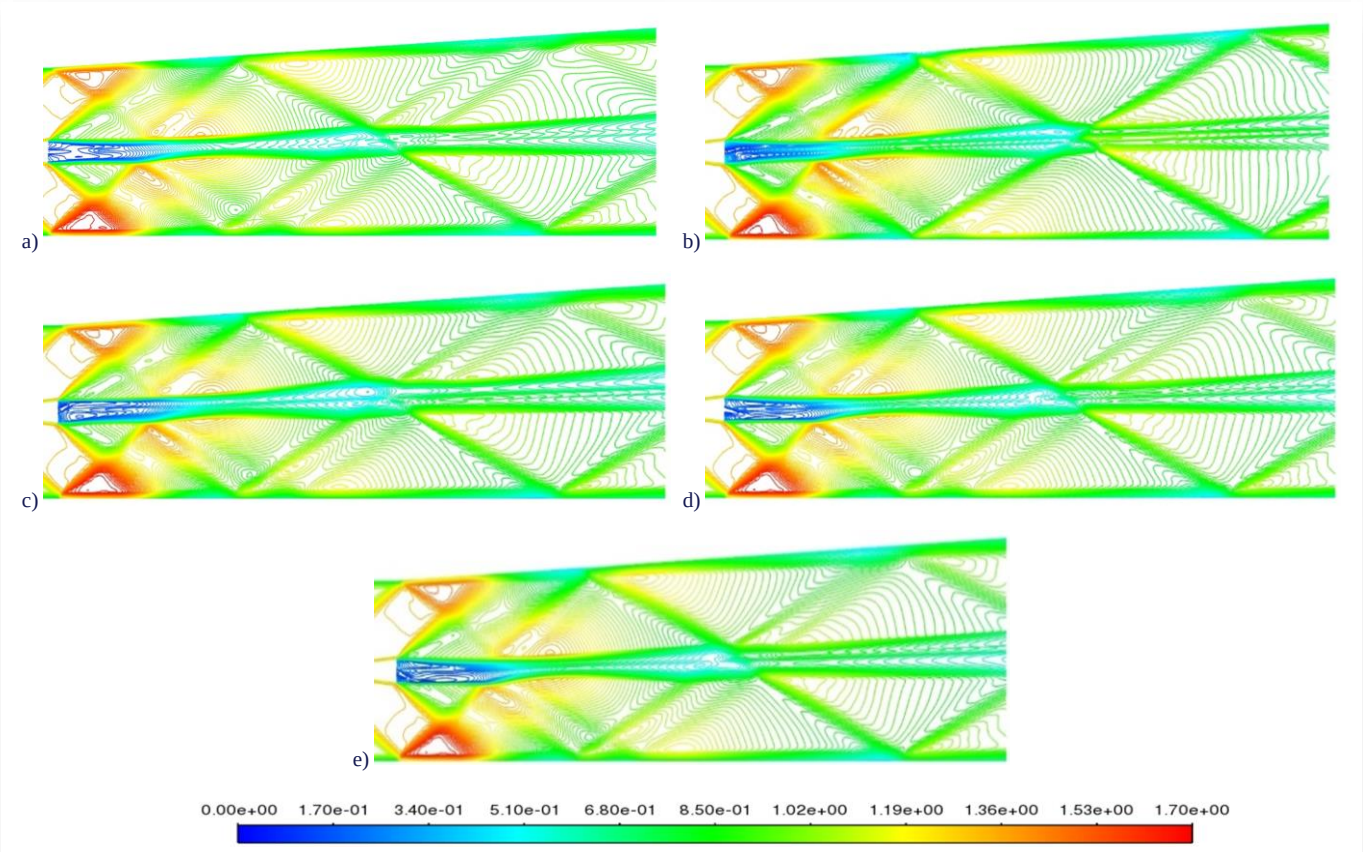

Fig. 7. Contours of density in kg/m³: a) parallel injection, b) 15° upward injection, c) 30° upward injection, d) 15° downward injection, e) 30° downward injection.

An *XY* plane has been established at the center of the combustor to visualize density and Mach number contours for four distinct injection methods: 15° upward, 15° downward, 30° upward, and 30° downward. These injections induce shockwave interactions and recirculation zones, significantly impacting the supersonic flow field. Notably, robust shocks originate from the leading edge of the strut and undergo reflection upon encountering the Combustor wall. Subsequently, these reflected shocks experience distortion at various points downstream of the strut. The shockwaves generated at the trailing edges of the strut interact with the shockwave reflected on the combustor wall, leading to a subsequent reduction in strength as they approach the bottom wall of the combustor. Interestingly, it has been noted that the strength of the reflected shock wave is contingent on the injection angle, as depicted in Fig. 7. This variability is visually represented in the density contour for both injection angles and directions.

Figure 8 represents a graphical depiction of the Mach number distribution throughout the flow field, enabling the identification of regions characterized by supersonic or subsonic flow, as well as the presence of shock waves. The development of the subsonic region occurs downstream of injection struts due to the shock and shear layer interactions. This region enables the mixing of hydrogen and air, facilitating the combustion process. The width of the subsonic area was observed to expand as the injection angle was raised, as shown in Figs. 8b–8e when compared to parallel injection. A discernible L-shaped pattern was found in Figs. 8c and 8e when employing downward injection angles. Additionally, it was discovered that boundary layer separation occurred when the flow encountered the inclination of the top wall. The magnitude of the oblique shock intensifies and causes a reduction in the velocity of the fluid downstream of the strut. The presence of these recirculation zones results in the deceleration of the high velocity flow within the combustor, hence causing a decrease in the Mach number of the combustor as measured along its length.

3.1. The effect of wall-static pressure

The graphical representation in Fig. 9a and 9b depicts the static pressure distribution along the bottom wall and axis of the combustor. Notably, the pressure levels observed at the inlet of the combustor consistently exhibited a high degree of uniformity.

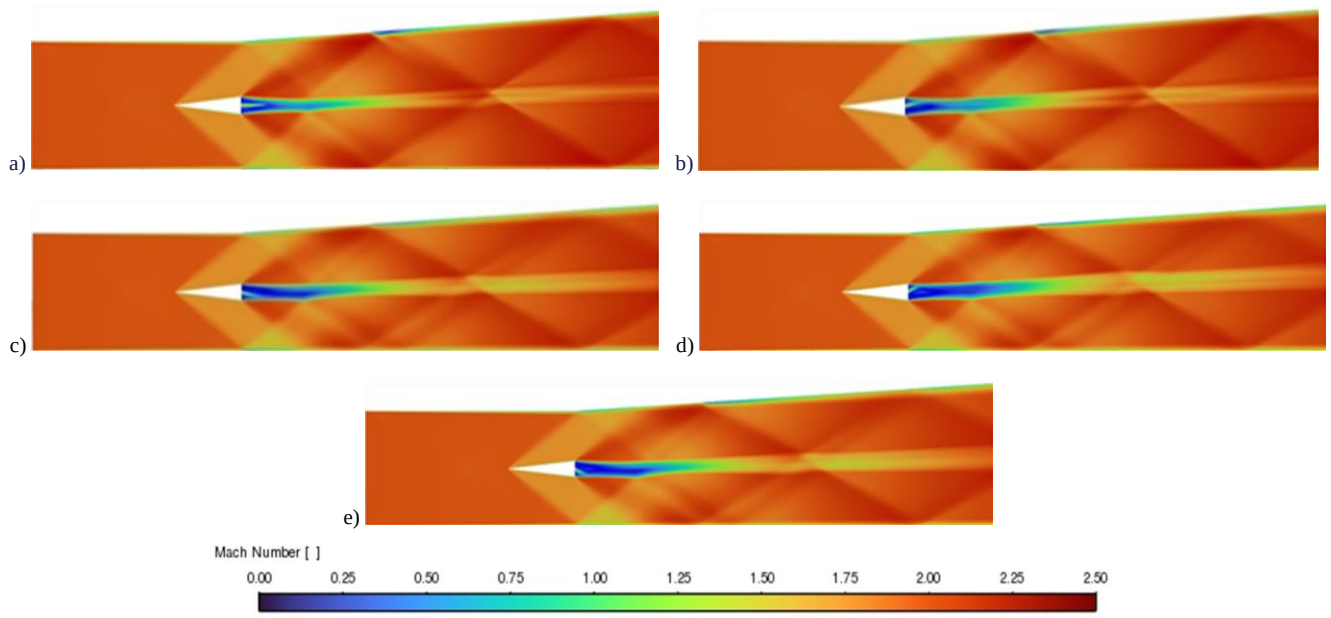

Fig. 8. Mach contours (a) Parallel injection (b) 15^0 Upward injection (c) 15^0 Downward injection (d) 30^0 Upward injection (e) 30^0 Downward injection.

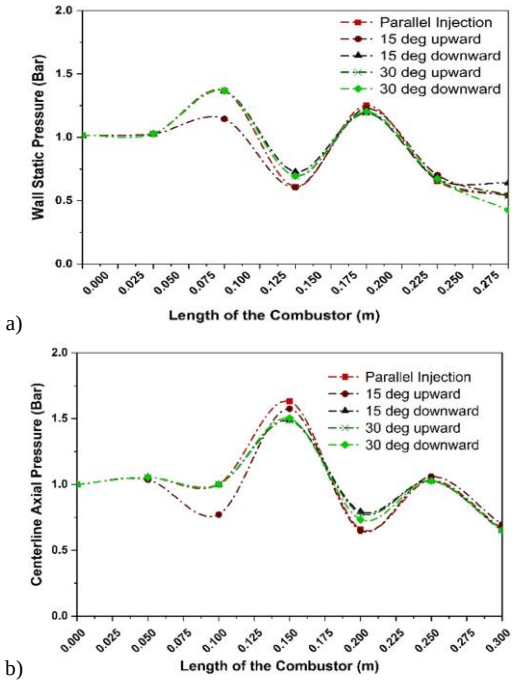

Fig. 9. Static pressure distribution for different injection angles: a) wall static pressure, b) axial pressure.

In Fig. 9a, the representation shows the static pressure exerted by the bottom wall of the combustor. Notably, as the waves developed, the pressure at a distance of 0.15 m from the leading edge of the strut decreased. An interesting observation is the significant recirculation generated at the trailing edge of the strut, stemming from upstream injection at a distance of 0.2 m, indicating the presence of elevated pressure levels. Remarkably, the range of pressures at the exit of the combustor remained consistent for both injections with varying angles.

Figures 9a and 9b highlight a significant difference in the static pressure applied to the wall by distinct configurations of struts. Axial pressure measurements were taken using the centerline of the combustor as a reference point. Notably, a higher pressure was observed at a distance of 0.15 m, attributable to the injection pressure at the midpoint of the strut. Comparing angled injection to parallel injection, it is evident that angled injection leads to a higher pressure exerted at the center of the combustor compared to the center of the strut. The presence of the recirculation area located in the central region of the strut base, as depicted in Fig. 9b for the 15° upward injection, leads to a higher injection pressure compared to the other two scenarios.

3.2. Static temperature

Temperature graphs in a scramjet combustor commonly depict the spatial distribution of temperature along the longitudinal or vertical axis of the combustor. The presented charts offer valuable insights into the combustion process and the spatial distribution of temperature for different injection angles within the combustor. From Fig. 10, it is observed that in each case at X = 128 mm, the static temperature profile exhibits a high degree of similarity, indicating a reduced level of combustion and mixing of air and fuel near the injection area when compared to the outer regions of the streams. In all instances, it can be observed that at X = 128 mm, the temperature profile exhibits a high degree of similarity, indicating a reduced level of mixing and combustion of the fuel and air near the injection site in comparison to the boundary of the streams. Additionally, it can be noted that as the flow progresses towards the exit of the combustor, there is a reduction in temperature along the axial distance from the inlet at X = 175 mm, X = 207 mm, and X = 283 mm. The DLR scramjet model exhibits a concentration of maximum temperature within

the central region of the combustor. The subsonic zone is where intense combustion occurs as a result of the intense interactions between shock waves and the fuel shear layer. Additionally, the flow downstream is decelerated due to shock-shock interactions. Furthermore, the interaction between the fuel-air stream and the strut injector occurs at a location further downstream. The highest recorded temperature was obtained at a distance of X = 128 mm from the combustor inlet. This finding is further substantiated by the presented data in Figs. 10a to 10d, where the peak temperature was observed within the range of Y = 0.20 mm to Y = 0.35 mm.

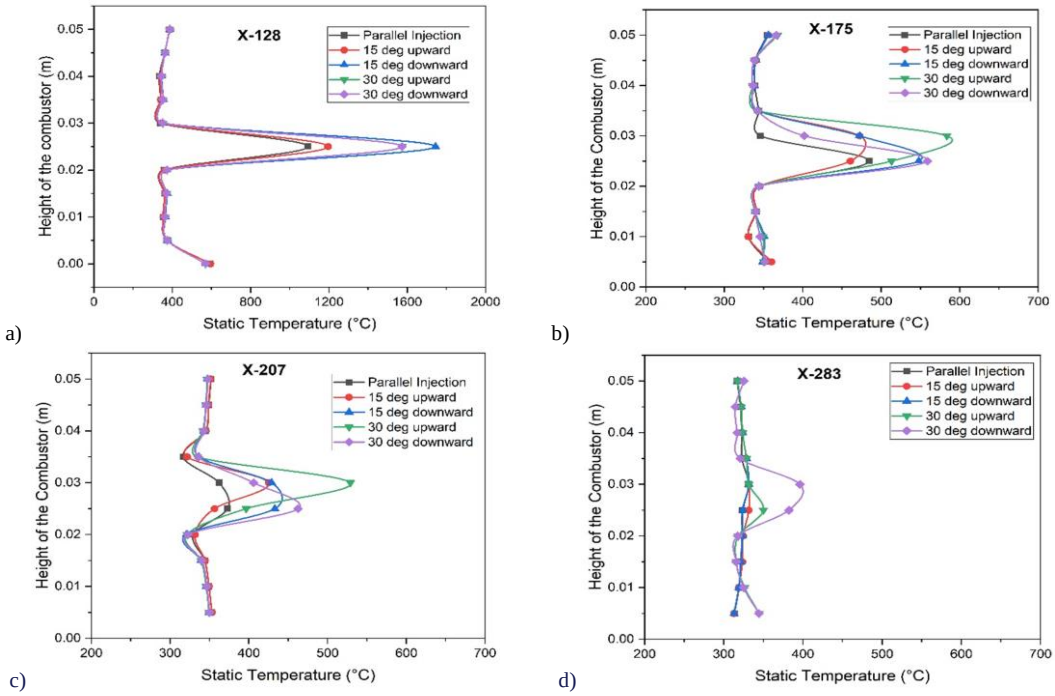

Fig. 10. Temperature profile along the combustor at a distance of: a) X = 128 mm, b) X = 157 mm, c) X = 207 mm, d) X = 283 mm.

3.3. Performance analysis

3.3.1. Combustion efficiency

The most crucial variables for achieving optimal performance in scramjet combustors are the efficiency of mixing and combustion. The air-fuel mixing efficiency of any position across the stream can be determined by calculating the average values and expressing it as the ratio of the stoichiometric hydrogen mass flux to the overall hydrogen mass flux. This representation is as follows[56]:

$$\eta_C = 1 - \frac{\int A(X)\rho_{gas} u Y_{H_2} dA}{\dot{m}_{H2(inj)}} = 1 - \frac{\dot{m}_{H2(X)}}{\dot{m}_{H2(inj)}}, \qquad (2)$$

where Y_{H2} stands for the hydrogen mass percentage and gas density, while A represents the area of the cross-section. Additionally, u indicates the axial velocity. Assuming that $\dot{m}_{H2(inj)}$ signifies the overall hydrogen mass flux and $\dot{m}_{H2(X)}$ the hydrogen mass flux about X.

Figure 11a illustrates the fluctuation in the combustion efficiency of the DLR scramjet model as a function of various injection angles. The phenomenon of shockwave and fuel stream shear layer interaction is observed to occur predominantly in the downstream region of the strut.

The existence of a subsonic region near the strut area enhances the mixing process, contributing to an overall improvement in combustion efficiency. One more observation is noted, comparing all cases with parallel injection, 15° upward injection having complete combustion attained with minimum combustor length nearly x = 0.11 m.

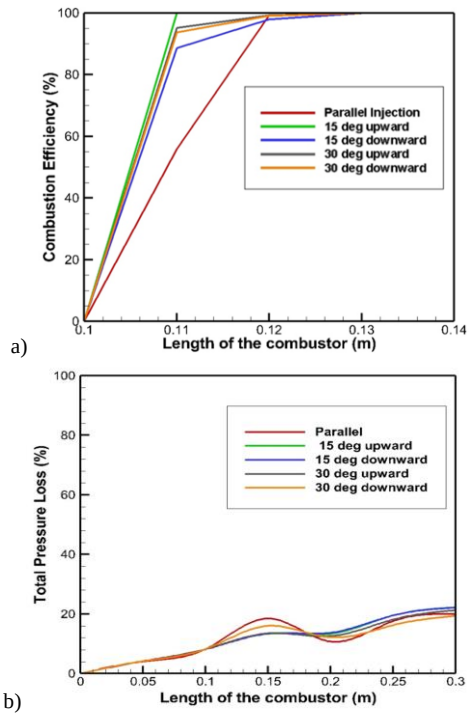

Fig. 11. (a) Combustion efficiency, and (b) total pressure loss of strut-based scramjet combustor with various injection angles.

3.3.2. Total pressure loss

Another important analysis to access the scramjet combustor performance is the total pressure loss. Illustrated in Fig. 11b is the total pressure loss corresponding to different angles of injection utilized within a strut-based scramjet combustor along its axial length. The fluctuations in pressure loss are attributed to the generation of shockwaves originating from the strut. The total pressure loss is calculated using the formula outlined below [47]:

$$\eta_t = 1 - \frac{\int_A P_0 \rho u dA}{\int_A P_{0(\text{inlet})} \rho u dA}. \quad (3)$$

Comparatively, angled injections in the scramjet combustor result in higher total pressure losses than parallel injections due to the increased strength of shockwaves. Notably, higher pressure loss is evident downstream of the strut during angled injection, primarily attributed to multiple shockwaves and their interactions with the fuel stream shear layer that decelerate the flow in the combustor. Specifically, a significant increase in pressure loss of approximately 20% is observed for upward injection angle, stemming from augmented shear layer formation and the emergence of recirculation zones in the downstream region. Additionally, an intriguing trend emerges from the Fig. 11b total pressure loss exhibits a notable decrease with increasing injection angle when compared to parallel injection configurations.

3.4. H_2 and H_2O mass fraction

The estimation of mixing and combustion characteristics for the strut-based scramjet combustor is based on the mass fractions of H_2 and H_2O in its distribution. If the combustion conditions are optimized to achieve complete combustion, the mass fraction of hydrogen can drop. Figs. 12a and 12b illustrate the mass percent of hydrogen and H_2O over the length of the combustor. A range of mass fraction variation was recorded within the distance range of 0.1 m to 0.15 m from the entrance of the combustor. Based on the findings depicted in Fig. 10a, it can be observed that optimizing the combustion conditions for achieving complete combustion may result in a drop in the hydrogen mass fraction. Figure 13 illustrates the concentration of H_2 and H_2O, expressed as mass fractions, at different axial locations within the combustor.

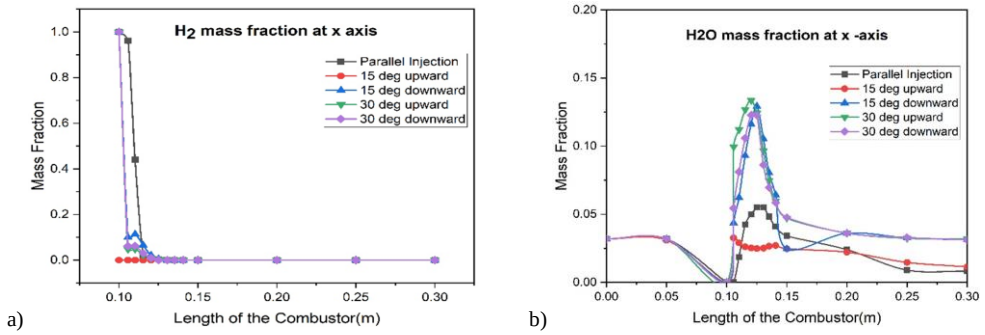

Fig. 12. Mass fraction along the length of the combustor: a) H_2 mass fraction, b) H_2O mass fraction.

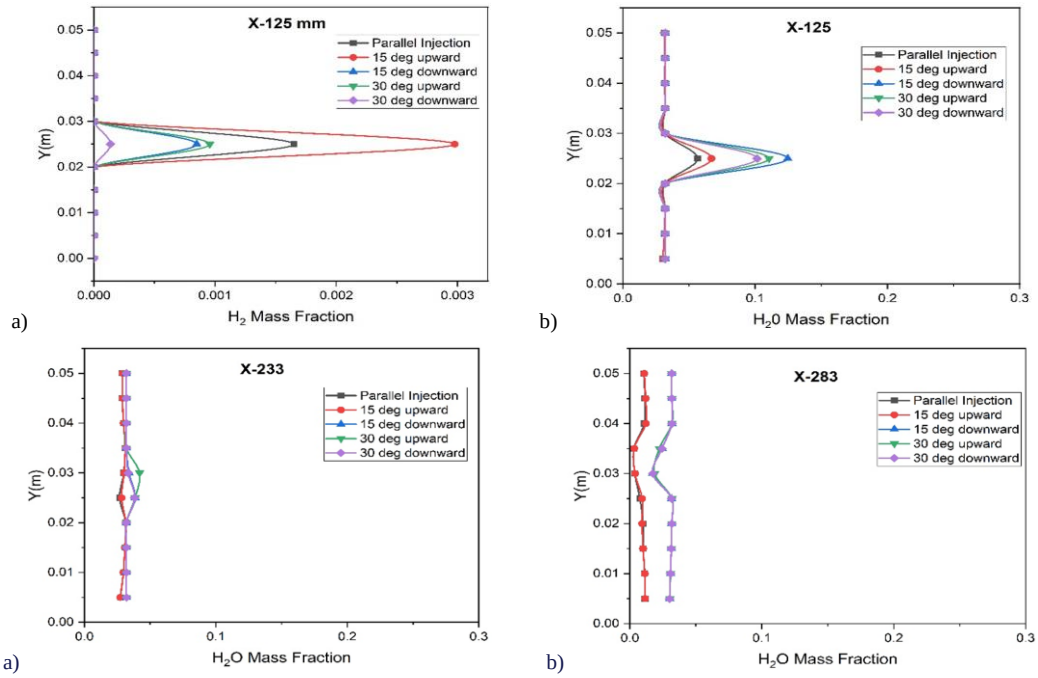

Fig. 13. H_2 and H_2O distribution at the crosswise locations of the combustor: a) H_2 mass fraction at X = 125 mm, b) H_2O mass fraction at X = 125 mm, c) H_2O mass fraction at X = 207 mm, d) H_2O mass fraction at X = 283 mm.

Figure 13 displays a discernible disparity in the H_2 mass fraction, which is found to be at a low concentration, and the H_2O mass fraction, which exhibits a substantially greater profile, specifically at the position X = 125 mm. Therefore, the implementation of angled injection in the scramjet combustor enhances combustion efficiency. The hydrogen is nearly depleted at X = 207 mm and X = 283 mm. The results of the investigation indicate that the mass fraction of H_2O is significantly higher when employing a downward injection angle at the position X =125 mm. The H_2O mass fraction graphs reveal that a similar large variation was seen in the strut wake zone. As indicated by the mass fraction graphs, it is evident that the implementation of angled injection results in the nearly complete consumption of fuel.

4. Conclusion

The numerical investigation of the three-dimensional DLR combustor is conducted and subsequently compared with experimental data. The injection of hydrogen fuel is accomplished by the utilization of a strut-type injector, which employs a range of injection angles in the direction of flow. The computational simulations employed in this study are based on the three-dimensional RANS equations. The simulations utilize the SST $k–\omega$ model to accurately predict the effects of turbulence. Additionally, the eddy-dissipation approach is employed to represent the single-step hydrogen reaction in the reacting flow. The analysis of the combustor includes an assessment of flow characteristics such as shock waves, static pressure and temperature distributions, mass fraction of hydrogen and steam, and performance parameters at different locations. The present study yields the following findings:

- From density contours, the shock interaction within the combustor led to the creation of strong recirculation zones along both the upper and lower walls. These recirculation zones play a vital role in aiding the mixing process and fostering the stabilization of the flame. The rise in pressure is ascribed to the interaction between shock waves and the separation of the boundary layer. Consequently, the downstream flow undergoes a deceleration, accompanied by a decrease in the intensity of the shocks.
- The hydrogen mass fraction profile exhibited a peak at X = 0.125 m, indicating improved mixing and combustion efficiency. This suggests that angled injection enhances the effectiveness of the scramjet combustor. The H_2 mass fraction exhibits near-complete consumption at X = 0.207 m and X = 0.283 m, indicating efficient fuel utilization. H_2O mass fraction is maximum while using of downward injection angle at X = 0.125 m. From mass fraction graphs, it can be observed that the fuel is completely burnt before it leaves the scramjet combustor.
- It is evident that upward injection angles yield superior mixing characteristics in comparison to downward injections. Notably, the subsonic region near the strut which enhances the mixing and combustion efficiencies, and angled injections, particularly upward ones, demonstrate enhanced combustion characteristics within the region of X = 0.12 m.
- The total pressure loss is higher for upward injection angles than parallel and downward injection, primarily due to shockwave generation from the leading edge of the struts. In this study, it's observed that the total pressure loss for upward injection angles is 20% and downward injection angles exhibit a 15%. It is also noted that both upward and downward injection angles have higher total pressure loss compared to parallel injection due to the emergence of additional shockwaves downstream of the strut. Despite this increased pressure loss, upward injection angles are preferred because they achieve high combustion efficiency within the shortest combustion length.

Acknowledgements

The authors are thankful to the utilization of computational facility in VIT University co-funded by the Erasmus+ Programme of the European Union, for giving the necessary permission and facilities to perform the present study.

References

[1] Curran, E.T. (2001). Scramjet engines: The first forty years. *Journal of Propulsion and Power*, 17(6), 1138–1148. doi: 10.2514/2.5875

[2] Das, N., Pandey, K.M., & Sharma, K.K. (2020). A brief review on the recent advancement in the field of jet engine - scramjet engine. In *Materials Today: Proceedings*, pp. 6857–6863. Elsevier Ltd. doi: 10.1016/j.matpr.2020.12.1035

[3] Choubey, G., Pandey, K.M., Maji, A., & Deshamukhya, T. (2017). A brief review on the recent advances in scramjet engine. In *AIP Conference Proceedings*, American Institute of Physics Inc. doi: 10.1063/1.4990189

[4] Fry, R.S. (2004). A Century of Ramjet Propulsion Technology Evolution. *Journal of Propulsion and Power*, 20(1), 27–58. doi: 10.2514/1.9178

[5] Barzegar Gerdroodbary, M., Ganji, D.D., & Amini, Y. (2015). Numerical study of shock wave interaction on transverse jets through multiport injector arrays in supersonic crossflow. *Acta Astronautica*, 115, 422–433. doi: 10.1016/j.actaastro.2015.06.002

[6] Yan, L., Wu, H., Huang, W., bin Li, S., & Liu, J. (2020). Shock wave/turbulence boundary layer interaction control with the secondary recirculation jet in a supersonic flow. *Acta Astronautica*, 173, 131–138. doi: 10.1016/j.actaastro.2020.04.003

[7] Huang, W., Tan, J.G., Liu, J., & Yan, L. (2015). Mixing augmentation induced by the interaction between the oblique shock wave and a sonic hydrogen jet in supersonic flows. *Acta Astronautica*, 117, 142–152. doi: 10.1016/j.actaastro.2015.08.004

[8] Ben-Yakar, A., & Hanson, R.K. (2001). Cavity Flame-Holders for Ignition and Flame Stabilization in Scramjets: An Overview. *Journal of Propulsion and Power*, 17 (4), 869–877. doi: 10.2514/2.5818

[9] Qiuru, Z., Huanli, Y., & Jian, D. (2021). Effects of cavity-induced mixing enhancement under oblique shock wave interference: numerical study. *International Journal of Hydrogen Energy*, 46(72), 35706–35717.

[10] Dhankarghare, A.A., Jayachandran, T., & Muruganandam, T.M. (2022). Comparative investigation of strut cavity and wall cavity in supersonic flows. *Aerospace Science and Technology*, 124, 107520. doi: https://doi.org/10.1016/j.ast.2022.107520

[11] Edalatpour, A., Hassanvand, A., Gerdroodbary, M.B., Moradi, R., & Amini, Y. (2019). Injection of multi hydrogen jets within cavity flameholder at supersonic flow. *International Journal of Hydrogen Energy*, 44(26), 13923–13931. doi: 10.1016/j.ijhydene.2019.03.117

[12] Cai, Z., Wang, T., & Sun, M. (2019). Review of cavity ignition in supersonic flows. *Acta Astronautica.*, 165, 268–286. doi: 10.1016/j.actaastro.2019.09.016

[13] He, Q., Li, J., Wen, W., Ding, Y., Li, J., & Peng, C. (2023). Experimental determination and modeling of density, viscosity, and

surface tension for sulfolane + ethyl acetate and + *n*-propyl acetate. *Journal of Chemical and Engineering Data*, 68(4), 793–804. doi: 10.1021/acs.jced.2c00706

[14] Liu, C., Zhang, J., Jia, D., & Li, P. (2022). Experimental and numerical investigation of the transition progress of strut-induced wakes in the supersonic flows. *Aerospace Science and Technology*. 120, 107256. doi: 10.1016/j.ast.2021.107256

[15] An, B., Sun, M., Wang, Z., & Chen, J. (2020). Flame stabilization enhancement in a strut-based supersonic combustor by shock wave generators. *Aerospace Science and Technology*. 104, 105942. doi: 10.1016/j.ast.2020.105942

[16] Wu, K., Zhang, P., Yao, W., & Fan, X. (2019). Computational realization of multiple flame stabilization modes in DLR strut-injection hydrogen supersonic combustor. *Proceedings of the Combustion Institute. International Symposium on Combustion*, 37(3), 3685–3692. doi: 10.1016/j.proci.2018.07.097

[17] Lakka, S., Randive, P., & Pandey, K.M. (2021). Implication of geometrical configuration of cavity on combustion performance in a strut-based scramjet combustor. *Acta Astronautica*, 178, 793–804. doi: 10.1016/j.actaastro.2020.08.040.

[18] Dinde, P., Rajasekaran, A., & Babu, V. (2006). 3D numerical simulation of the supersonic combustion of H_2. *The Aeronautical Journal*, 110(1114), 773–782. doi: 10.1017/S0001924000001640

[19] Liu, Y., Sun, M., Liang, C., Yu, J., & Li, G. (2019). Flowfield structures of pylon-aided fuel injection into a supersonic crossflow. *Acta Astronautica*, 162, 306–313. doi: 10.1016/j.actaastro.2019.06.022

[20] Oamjee, A., & Sadanandan, R. (2019). Fuel injection location studies on pylon-cavity aided jet in supersonic crossflow. *Aerospace Science and Technology*, 92, 869–880. doi: 10.1016/j.ast.2019.07.021

[21] Li, Z., Barzegar Gerdroodbary, M., Sheikholeslami, M., Shafee, A., Babazadeh, H., & Moradi, R. (2020). Mixing enhancement of multi hydrogen jets through the cavity flameholder with extended pylon. *Acta Astronautica*, 175, 300–307. doi: 10.1016/j.actaastro.2020.06.002

[22] Sekar, A., Chakraborty, M., & Vaidyanathan, A. (2022). Mixing characteristics of liquid jet injected behind a curved pylon in supersonic flow. *Experimental Thermal and Fluid Science*, 134, 110570. doi: 10.1016/j.expthermflusci.2021.110570

[23] Zhang, L., Sheng, Z., & Dan, Y. (2023). Effects of sawtooth grooves on supersonic combustion. *Aerospace Science and Technology*, 136, 108223. doi: 10.1016/j.ast.2023.108223

[24] Du, Z., Huang, W., Yan, L., Chen, Z., & Moradi, R. (2019). Mixing augmentation mechanism induced by the dual injection concept in shcramjet engines. *Acta Astronautica*, 156, 1–13. doi: 10.1016/j.actaastro.2018.11.019

[25] Barzegar Gerdroodbary, M., Jahanian, O., & Mokhtari, M. (2015). Influence of the angle of incident shock wave on mixing of transverse hydrogen micro-jets in supersonic crossflow. *International Journal of Hydrogen Energy*, 40(30), 9590–9601. doi: 10.1016/j.ijhydene.2015.04.107

[26] Zuo, Q., Yu, H., Dai, J., Yan, Y., & Chen, L. (2022). Numerical study of injection strategy based on cavity combustor under oblique shock wave interference. *International Journal of Hydrogen Energy*, 47(86), 36693–36702. doi: 10.1016/j.ijhydene.2022.08.225

[27] Zhang, Y., Wang, B., Zhang, H., & Xue, S. (2015). Mixing Enhancement of Compressible Planar Mixing Layer Impinged by Oblique Shock Waves. *Journal of Propulsion and Power*, 31(1), 156–169. doi: 10.2514/1.B35423

[28] Peng, Y., Barzegar Gerdroodbary, M., Sheikholeslami, M., Shafee, A., Babazadeh, H., & Moradi, R. (2020). Mixing enhancement of the multi hydrogen fuel jets by the backward step. *Energy*, 203, 117859. doi: 10.1016/j.energy.2020.117859

[29] Li, Z., Manh, T.D., Barzegar Gerdroodbary, M., Nam, N.D., Moradi, R., & Babazadeh, H. (2020). The influence of the wedge shock generator on the vortex structure within the trapezoidal cavity at supersonic flow. *Aerospace Science and Technology*, 98(5), 105695. doi: 10.1016/j.ast.2020.105695

[30] Gruber, M.R., Baurle, R., Mathur, T., & Hsu, K.-Y. (2001). Fundamental Studies of Cavity-Based Flameholder Concepts for Supersonic Combustors. *Journal of Propulsion and Power*, 17(1), 146–153. doi: 10.2514/2.5720

[31] Li, Z., Manh, T.D., Barzegar Gerdroodbary, M., Nam, N.D., Moradi, R., & Babazadeh, H. (2020). Computational investigation of multi-cavity fuel injection on hydrogen mixing at supersonic combustion chamber. *International Journal of Hydrogen Energy*, 45(15), 9077–9087. doi: 10.1016/j.ijhydene.2020.01.096

[32] Jeyakumar, S., Balachandran, P., Indira, S., & Thillai Arasu, P. (2006). Studies on combustion in supersonic flows. *Asian Journal of Chemistry*, 18(4), 2557–2561.

[33] Jeyakumar, S., Venkateshwaran, V., Surjith, N., Karkuvel Raja, A., & Samy, G.S. (2017). Experimental Investigations on Aft Ramp Cavities with Fore Wall Modifications in Scramjet Combustors BT. *Fluid Mechanics and Fluid Power – Contemporary Research*. (pp. 1203–1212), New Delhi, Springer India.

[34] Jeyakumar, S., Balachandran, P., & Indira, S. (2006). Experimental Investigations on Supersonic Stream Past Axisymmetric Cavities. *Journal of Propulsion and Power*, 22(5), 1141–1144. doi: 10.2514/1.21024

[35] Jeyakumar S., & Jayaraman, K. (2018). Effect of finite width cavity in axisymmetric supersonic flow field. *Proceedings of the Institution of Mechanical Engineers, Part G: Journal of Aerospace Engineering*, 232(1), 180–184. doi: 10.1177/0954410016674036

[36] Assis, S.M., Jeyakumar S., & Jayaraman, K. (2019). The Effect of Transverse Injection Upstream of an Axisymmetric Aft Wall Angled Cavity in a Supersonic Flow Field. *Journal of Physics: Conference Series*, 1276. I*nternational Conference on Recent Advances in Fluid and Thermal Sciences*, 5–7 December 2018, Dubai, U.A.E. doi: 10.1088/1742-6596/1276/1/012019

[37] Kannaiyan, K. (2020). Computational study of the effect of cavity geometry on the supersonic mixing and combustion of ethylene. *Journal of Computational Science*, 47. doi: 10.1016/j.jocs.2020.101243

[38] Liu, X., Barzegar Gerdroodbary, M., Sheikholeslami, M., Moradi, R., Shafee, A., & Li, Z. (2020). Effect of strut angle on performance of hydrogen multi-jets inside the cavity at combustion chamber. *International Journal of Hydrogen Energy*, 45(55), 31179–31187. doi: 10.1016/j.ijhydene.2020.08.124

[39] Feng, Y., Luo, S., Song, J., Xia, K., & Xu, D. (2023). Numerical investigation on the combustion characteristics of aluminum powder fuel in a supersonic cavity-based combustor. *Applied Thermal Engineering*, 221, 119842. doi: 10.1016/j.applthermaleng.2022.119842

[40] Qiu, H., Zhang, J., Gao, J., Chang, J., &. Bao, W. (2021). Research on combustion performance optimization in scramjet combustor with strut/wall combined fuel injection scheme. *Aerospace Science and Technology*, 109, 106376. doi: 10.1016/j.ast.2020.106376

[41] Rajesh, A.C., Jeyakumar, S., Jayaraman, K., & Karaca, M. (2023). Steady and unsteady flow characteristics of dual cavity in strut injection scramjet combustor. *International Journal of Hydrogen Energy*, 48(72), 28174–28186. doi: 10.1016/j.ijhydene.2023.04.017

[42] Rajesh, A.C., Jeyakumar, S., Jayaraman, K., Karaca, M., & Athithan, A.A. (2023). The implications of dual cavity location in a strut-mounted scramjet combustor. *International Communications in Heat and Mass Transfer*, 145, part B, 106855. doi: 10.1016/j.icheatmasstransfer.2023.106855.A

[43] Athithan, A., Jeyakumar, S., & Poddar, S. (2021). Influence of wall mounted ramps on DLR strut scramjet combustor under non-reacting flow field. *Materials Today: Proceedings*, 56(5), 3002−doi: 10.1016/j.matpr.2021.11.347

[44] Jeyakumar, S., Kandasamy, J., Karaca, M., Karthik, K., & Sivakumar, R. (2021). Effect of hydrogen jets in supersonic mixing using strut injection schemes. *International Journal of Hydrogen Energy*, 46(44), 23013–23025. doi: 10.1016/j.ijhydene.2021.04.123

[45] Qiu, H., Lin, L., Zhang, J., Zhang, S., & Bao, W. (2023). Influence of multi-strut interaction on flame propagation and combustion performance in a large aspect ratio combustor. *Aerospace Science and Technology*, 137. doi: 10.1016/j.ast.2023.108193

[46] Kummitha, O.R., Pandey, K.M., & Padidam, A.K.R. (2021). Effect of a revolved wedge strut induced mixing enhancement for a hydrogen fueled scramjet combustor. *International Journal of Hydrogen Energy*, 46(24), 13340–13352. doi: 10.1016/j.ijhydene.2021.01.089

[47] Oevermann, M. (2000). Numerical investigation of turbulent hydrogen combustion in a SCRAMJET using flamelet modeling. *Aerospace Science and Technology*, 4(7), 463–480. doi: 10.1016/S1270-9638(00)01070-1

[48] Menter, F.R. (1994). Two-equation eddy-viscosity turbulence models for engineering applications. *AIAA Journal*, 32(8), 1598–1605. doi: 10.2514/3.12149

[49] Li, C., Chen, X., Li, Y., Musa, O., Zhu, L., & Li, W. (2019). Role of the backward-facing steps at two struts on mixing and combustion characteristics in a typical strut-based scramjet with hydrogen fuel. *International Journal of Hydrogen Energy*, 44(52). 28371–28387. doi: 10.1016/j.ijhydene.2019.09.023

[50] Aravind S., & Kumar, R. (2019). Supersonic combustion of hydrogen using an improved strut injection scheme. *International Journal of Hydrogen Energy*, 44(12), 6257–6270. doi: 10.1016/j.ijhydene.2019.01.064

[51] Choubey G., & Pandey, K.M. (2018). Effect of variation of inlet boundary conditions on the combustion flow-field of a typical double cavity scramjet combustor. *International Journal of Hydrogen Energy*, 43(16), 8139–8151. doi: 10.1016/j.ijhydene.2018.03.062

[52] Yarasai, S.S., Ravi, D., & Yoganand, S. (2022). ScienceDirect Numerical investigation on the performance and combustion characteristics of a cavity based scramjet combustor with novel strut injectors. *International Journal of Hydrogen Energy*, 48(14), 5681–5695. doi: 10.1016/j.ijhydene.2022.11.150

[53] Tu, J., Yeoh, G.H., Liu, C., & Tao, Y. (2023). *Computational fluid dynamics: a practical approach*. Elsevier.

[54] Kassem, H.I., Saqr, K.M., Aly, H.S., Sies, M.M., & Wahid, M.A. (2011). Implementation of the eddy dissipation model of turbulent non-premixed combustion in OpenFOAM. *International Communications in Heat and Mass Transfer*, 38(3), 363–367. doi: 10.1016/j.icheatmasstransfer.2010.12.012

[55] Kumaran K., & Babu, V. (2009). Investigation of the effect of chemistry models on the numerical predictions of the supersonic combustion of hydrogen. *Combustion and Flame*, 156(4), 826–841. doi: 10.1016/j.combustflame.2009.01.008

[56] Gerlinger, P., Stoll, P., Kindler, M., Schneider, F., & Aigner, M. (2008). Numerical investigation of mixing and combustion enhancement in supersonic combustors by strut induced streamwise vorticity. *Aerospace Science and Technology*, 12(2), 159–168. doi: 10.1016/j.ast.2007.04.003

Co-published by
Institute of Fluid-Flow Machinery
Polish Academy of Sciences
Committee on Thermodynamics and Combustion
Polish Academy of Sciences

http://www.imp.gda.pl/archives-of-thermodynamics/

Unsteady flow of a couple stress fluid due to sudden withdrawal of pressure gradient in a parallel plate channel

Donga Anjali[a], Naresh Reddimalla[a], Josyula Venkata Ramana Murthy[a*]

[a]Department of Mathematics, National Institute of Technology Warangal, Telangana 506004, India
*Corresponding author email: jvr@nitw.ac.in

Received: 30.11.2023; revised: 06.03.2024; accepted: 20.05.2024

Abstract

The investigation of the couple stress fluid flow behaviour between two parallel plates under sudden stoppage of the pressure gradient is considered. Initially, a flow of couple stress fluid is developed between the two parallel plates under a constant pressure gradient. Suddenly, the applied pressure gradient is stopped, and the resulting unsteady flow is studied. This type of flow is known as run-up flow in the literature. Now the flow is expected to come to rest in a long time. Usually, these types of problems are solved by using the Laplace transform technique. There are difficulties in obtaining the inverse Laplace transform; hence, many researchers adopt numerical inversions of Laplace transforms. In this paper, the problem is solved by using the separation of variables method. This method is easier than the transform method. The velocity field is analytically obtained by applying the usual no-slip condition and hyper-stick conditions on the plates, and hence the volumetric flow rate is derived at subsequent times. The steady state solution before the withdrawal of the pressure gradient is matched with the initial condition on time. The rest time, i.e. the time taken by the fluid to come to rest after the pressure gradient is withdrawn is calculated. The graphs for the velocity field at different times and different couple stress parameters are drawn. In the special case when a couple stress parameter approaches infinity, couple stress fluid becomes a viscous fluid. Our results are in good agreement with this special case.

Keywords: Couple stress fluids; Hyper-stick condition; Velocity field; Variable separable method; Volumetric flow rate; Pressure gradient

Vol. 45(2024), No. 3, 179–184; doi: 10.24425/ather.2024.151220

Cite this manuscript as: Anjali, D., Reddimalla, N., & Ramana Murthy, J.V. (2024). Unsteady flow of a couple stress fluid due to sudden withdrawal of pressure gradient in a parallel plate channel. *Archives of Thermodynamics*, 45(3), 179–184.

1. Introduction

A couple stress fluid displays distinctive behaviour, shaped by internal rotational effects resulting from the interaction of forces and moments within the material. In fluid mechanics, these properties influence how the fluid responds to external forces, impacting factors like flow characteristics, stress distribution, and deformation. In unsteady flow, the dynamic behaviour of a couple stress fluid is characterized by the interaction of rotational forces within the material, impacting fluid flow patterns and responses, particularly in the presence of changes in external forces. The couple stress fluid based on pure kinematic behaviour was proposed mathematically by Stokes in 1966 [1]. The couple stress fluid shows the rotational effects and sustention of couple stresses which were not observed for Newtonian fluids. The properties of the couple stress fluids when they flow past a sphere and spheroid have been studied [2]. A method was developed for free convection in magnetohydrodynamics (MHD)

Nomenclature

G – nondimensional pressure gradient
h – half of the distance between the plates, m
P – pressure, Pa
p – nondimensional pressure
Q – volumetric flow rate, m^3/s
S – couple stress parameter
t – nondimensional time
T – time, s
U – velocity in Y- direction, m/s
u – nondimensional velocity
u_s – steady state velocity, m/s
u_t – transient state velocity, m/s

Greek symbols

η – coefficient of couple stress viscosity, N s
λ – separation constant
μ – coefficient of viscosity, Pa s
ρ – density of the fluid, kg/m^3

Abbreviations and Acronyms

HAM – homotopy analysis method
LHS – left hand side
MHD – magnetohydrodynamic
RHS – right hand side

flows using Laplace transforms, which was applied to a thermal shock problem [3]. The authors compared the results between the analytic and numerical solutions by applying the HAM technique and shooting method on the axisymmetric flow of an electrically conducting viscous fluid in the presence of a magnetic field over a non-linear stretching sheet [4]. The authors focused on the exact solution for an MHD boundary layer problem for momentum and heat transfer in Jeffrey fluid flow over a non-isothermal stretching sheet in the presence of dissipative energy, thermal radiation, and internal heat source [5]. The effects of Soret and Dufour on velocity, temperature, and concentration were discussed in the three-dimensional MHD flow of Oldroyd-B fluid [6]. Heat transfer and effects of various embedding parameters on the flow were discussed on three-dimensional flow couple stress fluid with convective boundary conditions by employing the HAM technique [7]. The authors investigated non-Newtonian fluid flows due to the sudden application of pressure gradient. In their study, the velocity field is obtained by Laplace transforms and by separation of variables [8,9]. The effects of directional permeability on the Couette flow of immiscible Newtonian fluids are explored in an anisotropic medium [10]. The authors examined the flow of electrically conducting immiscible Newtonian fluids with variable viscosity through an inclined channel under the influence of a magnetic field [11]. The fourth-order accuracy boundary value problem is applied to get the numerical solution by considering slip conditions on the magnetic effect on radiative inclined magneto-hydrodynamic mixed convection hybrid nanofluid flow through an inclined shrinking permeable plate [12]. The author used the HAM technique to examine the couple stress fluid flow between two curved plates with the porous medium [13]. The entropy production in a couple stress fluid flow regions is observed to be smaller than that of the micro-polar fluid flow region [14]. They examined the flow of electrically conducting immiscible Newtonian fluids with variable viscosity through an inclined channel in the presence of a magnetic field [15]. The authors investigated the characteristics of entropy production, temperature-dependent thermal conductivity, variable viscosity, and a couple stress parameters on non-immiscible fluids in an inclined porous channel [16].

A special type of flow named “run-up flows” for the case of viscoelastic fluids was introduced by Kazakia and Rivlin [17]. Later Rivlin used Laplace transforms theoretically and extensively to investigate the flows formed in run-up flows [18–20]. Almost in the same period, a similar problem of step jump velocities in shear flows was studied by Narain and Joseph [21]. Researchers explored the run-up flows of couple stress fluids and micro-polar fluids through the application of Laplace transforms [22,23]. Additionally, the study delved into the run-up flows of Maxwell fluids, employing Laplace transforms as well [24]. Subsequent investigations were extended to explore run-up flows, considering Hall effects on the flow of Rivlin-Ericksson fluids [25]. Another aspect of interest involved the examination of run-up flows of conducting liquid within an annulus [26]. Notably, recent research focused on magneto-hydrodynamic (MHD) fluid run-up flows, employing Laplace transforms for analysis [27]. Many authors solved the problems with run-up and similar flows using numerical inversion of Laplace transform techniques [28,29]. As an extension of [22], the present work investigates the unsteady flow of a couple stress fluid between two parallel plates using the separation of variables technique. The advantage of this method is that it is easy to obtain solutions and can avoid the difficulty in inverting Laplace transforms.

2. Statement of the problem and mathematical formulation

Examining the fully developed steady flow of incompressible couple stress fluid between two parallel plates under a constant pressure gradient, we investigate the scenario where the pressure gradient is suddenly stopped. This leads to the study of the subsequent transient flow, focusing on the extended period required for the fluid to rest. We derive the duration for the fluid to reach a state of rest and estimate the volumetric flow rate during this process.

The linear momentum equation for a couple stress fluid [1] is given by:

$$\rho \frac{\partial U}{\partial T} = -\frac{\partial P}{\partial X} + \mu \frac{\partial^2 U}{\partial Y^2} - \eta \frac{\partial^4 U}{\partial Y^4}, \tag{1}$$

where p is the pressure, ρ is the density, T is time, μ and η are coefficients of viscosity and couple stress viscosity, respectively.

We introduce the following non-dimensional scheme:

$$X = hx, \quad Y = hy, \quad T = \frac{\rho h^2 t}{\mu}, \quad U = \frac{\mu u}{\rho h},$$

$$P = \frac{\mu^2}{\rho h^2} p, \quad S^2 = \frac{h^2 \mu}{\eta}. \tag{2}$$

The quantities on LHS are physical quantities and non-dimensional quantities are on RHS.

Substituting Eq. (2) in Eq. (1), we get the following non-dimensional equation for velocity u:

$$\rho \frac{\partial u}{\partial t} = -\frac{\partial p}{\partial x} + \frac{\partial^2 u}{\partial y^2} - \frac{1}{S^2}\frac{\partial^4 u}{\partial y^4}. \tag{3}$$

Equation (3) can be solved under the following conditions (Fig. 1):

1. No slip condition $u = 0$ at $y = \pm 1$.
2. Hyper stick condition (angular velocity is zero $\nabla \times \bar{q} = 0$, where $\bar{q}$ is fluid velocity) gives: $\frac{\partial u}{\partial y} = 0$ at $y = \pm 1$. In general, when the surface is under rotation, we take type A condition, or no couple stresses condition on the surface. When the surface is not under rotation, we take type B condition or no angular velocity or hyper-stick condition on the surface.
3. $\frac{\partial p}{\partial x} = \begin{cases} -G & \text{for} \quad t < 0, \\ 0 & \text{for} \quad t \geq 0. \end{cases}$

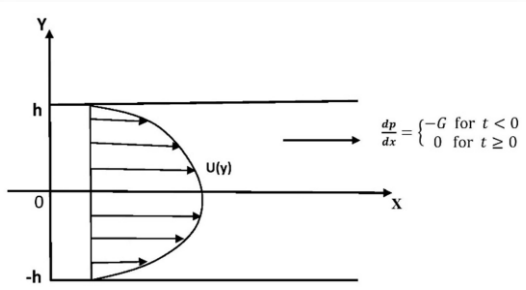

Fig. 1. Graphical representation of the problem.

3. Solution procedure

We assume the solution for Eq. (3) as

$$u = \begin{cases} u_s(y) & \text{for} \quad t < 0, \\ u_t(y,t) & \text{for} \quad t \geq 0, \end{cases} \tag{4}$$

where u_s is steady state fully developed flow under constant pressure gradient G and u_t is transient or unsteady state solution such that:

$$0 = G + \frac{\partial^2 u_s}{\partial y^2} - \frac{1}{S^2}\frac{\partial^4 u_s}{\partial y^4}, \tag{5}$$

and

$$\frac{\partial u_t}{\partial t} = \frac{\partial^2 u_t}{\partial y^2} - \frac{1}{S^2}\frac{\partial^4 u_t}{\partial y^4}. \tag{6}$$

Equations (5) and (6) are subjected to the following conditions:

$$u_s(\pm 1) = 0, \; u_t(\pm 1, t) = 0, \; \frac{\partial u_s}{\partial y}(\pm 1) = 0, \; \frac{\partial u_t}{\partial y}(\pm 1, t) = 0, \tag{7}$$

and $u_t(y,0) = u_s$ and $u_t(y,t) = 0$ as $t \to \infty$.

Equation (5) is an ordinary differential equation and is re-written as:

$$u_s'^v - S^2 u_s'' = S^2 G. \tag{8}$$

The solution of Eq. (8) under conditions for u_s in Eq. (7) is:

$$u_s(y) = \frac{G}{2}(1 - y^2) + \frac{G}{S \sinh S}(\cosh Sy - \cosh S). \tag{9}$$

We assume the solution of Eq. (6) in the form

$$u_t(y,t) = E(y)F(t). \tag{10}$$

Substituting Eq. (10) in Eq. (6) and rearranging we get

$$\frac{F'}{F} = \frac{E'' - \frac{1}{S^2}E'^v}{E} = -\lambda^2, \tag{11}$$

where F' is derivative with respect to t and E' is derivative with respect to y, the separation constant is taken as negative to satisfy the condition at $t = \infty$.

This gives $F' + \lambda^2 F = 0$ and $E'^v - S^2 E'' - \lambda^2 S^2 E = 0$ with the auxiliary equation $m^4 - S^2 m^2 - \lambda^2 S^2 = 0$, i.e.

$$m^2 = \frac{S^2 \pm \sqrt{S^2 + 4S^2\lambda^2}}{2} = \frac{S^2}{2}\left(1 \pm \sqrt{1 + \frac{4\lambda^2}{S^2}}\right),$$

$$m_{1,2} = \pm \frac{S}{\sqrt{2}} \sqrt{1 + \sqrt{1 + \frac{4\lambda^2}{S^2}}},$$

and

$$m_{3,4} = \pm \frac{S}{\sqrt{2}} \sqrt{1 - \sqrt{1 + \frac{4\lambda^2}{S^2}}},$$

are the roots of the auxiliary equation.

The solution for u_t is given by:

$$u_t(y,t) = \sum_{\lambda} e^{-\lambda^2 t} (A_\lambda \cosh m_1 y + B_\lambda \sinh m_1 y + C_\lambda \cos m_3 y + D_\lambda \sin m_3 y). \tag{12}$$

Constants in Eq. (12) are found from the conditions in Eq. (7):

$u_t(1,t) = 0 \Rightarrow A\cosh m_1 + B\sinh m_1 + C\cos m_3 + D\sin m_3 = 0$

$u_t(-1,t) = 0 \Rightarrow A\cosh m_1 - B\sinh m_1 + C\cos m_3 - D\sin m_3 = 0$

which implies:

$$B\sinh m_1 + D\sin m_3 = 0,$$

and

$$A\cosh m_1 + C\cos m_3 = 0.$$

Again $\frac{\partial u_t}{\partial y}(1,t) = 0$ gives:

$$m_1 A\sinh m_1 + m_1 B\cosh m_1 + m_3 C\sin m_3 + m_3 D\cos m_3 = 0$$

and $\frac{\partial u_t}{\partial y}(-1,t) = 0$ gives:

$$-m_1 A\sinh m_1 + m_1 B\cosh m_1 + m_3 C\sin m_3 + m_3 D\cos m_3 = 0$$

which implies that $m_1 A\sinh m_1 - m_3 C\sin m_3 = 0$

and $m_1 B\cosh m_1 + m_3 D\cos m_3 = 0.$

Then, from equations of B and D, we get:

$$B = -D\frac{\sin m_3}{\sinh m_1} = -D\frac{m_3\cos m_3}{m_1\cosh m_1}, \quad (13)$$

and from equations of A and C, we get:

$$A = -C\frac{\cos m_3}{\cosh m_1} = C\frac{m_3\sin m_3}{m_1\sinh m_1}. \quad (14)$$

Substituting (13) and (14) in Eq. (12), we get:

$$u_t(y,t) = \sum e^{-\lambda^2 t} A\left\{\cosh m_1 y - \frac{\cosh m_1}{\cos m_3}\cos m_3 y\right\} + \\ + \sum e^{-\lambda^2 t} B\left\{\sinh m_1 y - \frac{\sinh m_1}{\sin m_3}\sin m_3 y\right\}. \quad (15)$$

Rearranging Eq. (14) we get:

$$z = m_1\tanh m_1 + m_3\tan m_3 = 0. \quad (16)$$

The zeroes of Eq. (16) will give the values of the separation constant λ.

The initial condition at $t = 0$, $u_t(y,t) = u_s(y)$, yields $B = 0$ (since u_t is an even function, the odd function terms will vanish). Hence at $t = 0$, we have:

$$\frac{G}{2}(1-y^2) + \frac{G\coth S}{S}\left(\frac{\cosh Sy}{\cosh S} - 1\right) = \sum A_n\left(\frac{\cosh m_1 y}{\cosh m_1} - \frac{\cos m_3 y}{\cos m_3}\right). \quad (17)$$

From Eq. (11) at a fixed value of S, for a range of λ from 0 to 100, we find m_1 and m_3 values. With these values of m_1 and m_3, we obtain z from Eq. (16). Thus, we can plot for z for the values of λ as shown in Fig. 2.

From this graph, the roots for λ are obtained, and then m_1 and m_3 corresponding to these roots λ are found from Eq. (11).

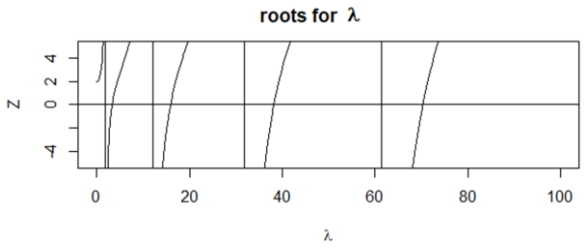

Fig. 2. Graph for finding roots of z (λ) = 0.

The first five roots for λ and the corresponding values for m_1 and m_3 are shown in Table 1.

Table 1. The first five values of separation constant λ.

n	λ_n	$z(\lambda_n)$	m_1	m_3
1	3.297	0.000399	2.981	2.2115
2	15.909	– 0.00088	5.8207	5.4663
3	38.193	– 0.00074	8.8551	8.6262
4	70.305	0.00042	11.9425	11.7739
5	112.271	0.0008	15.0516	14.9181

To obtain A_n, we solve n equations from Eq. (17) by evaluating Eq. (17) at n equally spaced points y_i, or alternately multiply Eq. (17) by $\left(\frac{\cosh m_1 y}{\cosh m_1} - \frac{\cos m_3 y}{\cos m_3}\right)$ and integrate w.r.t. y between the limits –1 to 1. We get n equations in A_n, and A_n is obtained by solving this system. The values of A_n by collocation method are given in Table 2.

Table 2. The values of A_n.

Coefficients	A_1	A_2	A_3	A_4	A_5
Values	0.6821	0.0137	0.00156	0.00035	0.000013

We observe that the collocation method gives a very accurate solution. Then finally, we get:

$$u_t = u_t(y, t \geq 0) = \sum_{n=1}^{5} e^{-\lambda_n^2 t} A_n\left(\frac{\cosh m_1 y}{\cosh m_1} - \frac{\cos m_3 y}{\cos m_3}\right), \quad (18)$$

and the volumetric flow rate Q at any time t is given by:

$$Q = 2\sum_{n=1}^{\infty} e^{-\lambda_n^2 t} A_n\left(\frac{\tanh m_1}{m_1} - \frac{\tan m_3}{m_3}\right). \quad (19)$$

4. Results and discussion

The unsteady flow of a couple stress fluid between two parallel plates due to the sudden withdrawal of an applied constant pressure gradient is studied. The expressions for the velocity for the transient state and volumetric flow rate are derived and shown in Eqs. (18) and (19), respectively. The velocity profiles for u_t versus distance y at different times t at fixed couple stress parameters (S = 2) are shown in Fig. 3a for G = 5 and Fig. 3b for G = 10, respectively. From Fig. 3, we notice that for 0.5 units of time, u_t becomes almost zero, i.e. the flow comes to rest by 0.5 units of non-dimensional time. And we observe that as G increases, the velocity increases. Initially, velocity starts from higher values and becomes zero by about 0.5 units of times at S = 2. This is because when the pressure gradient increases, the applied force on the flow increases, increasing velocity.

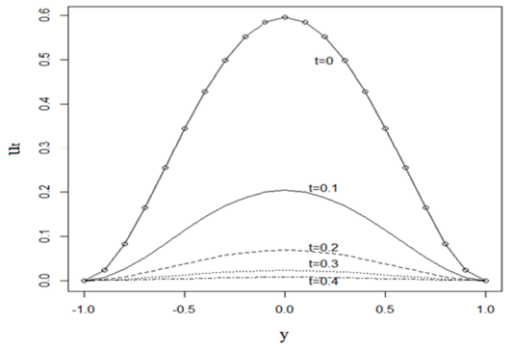

a)

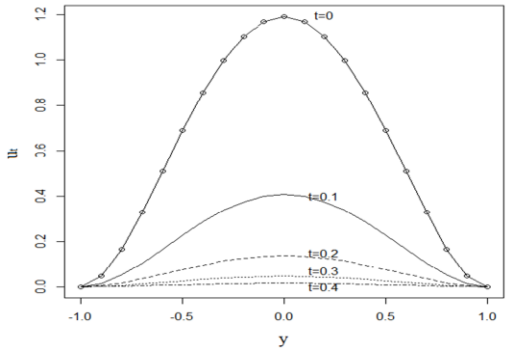

b)

Fig. 3. Velocity profiles (u_t) for S = 2 at pressure gradient G = 5 (a) and pressure gradient G = 10 (b), for various time values.

The velocity profiles u_t at fixed pressure gradient (G = 10) for various values of couple stress parameter (S) are depicted in Fig. 4a for t = 0.1 and Fig. 4b for t = 0.6, respectively. From Fig. 4, one can observe that, as the couple stress parameter increases, the velocity values also increase, which is in good agreement with [22]. As S increases, couple stresses decrease, leading to a reduction in the energy required for particle rotation and subsequently causing an increase in velocity. As S increases, the fluid approaches viscous fluid as a limiting case. Consequently, we can infer that viscous fluids consistently exhibit higher velocities compared to fluids with couple stresses at any given time.

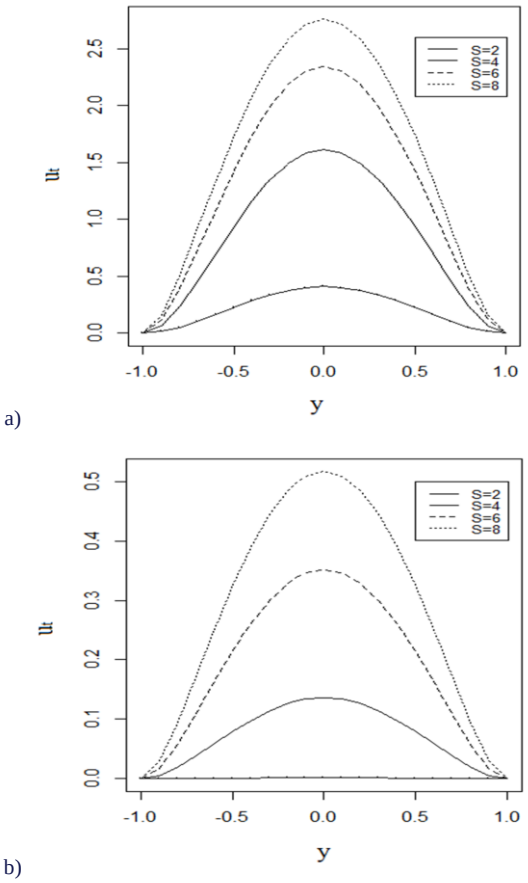

Fig. 4. Velocity profiles (u_t) at G = 10, t = 0.1 (a) and G = 10, t = 0.6 (b), for various values of couple stress parameter (S).

Figure 5 depicts the relationship between the pressure gradient and rest time for different values of the couple stress parameter (S). It is observed that with an increase in the couple stress parameter, the rest time also increases. Moreover, as the pressure gradient rises, the rest time experiences a gradual increase. This is because, as observed in Fig. 4, as S increases, couple stresses decrease and hence the energy spent for generating couples and rotation decreases; hence, fluid takes more time to rest.

Figure 6 illustrates the time versus volumetric flow rate for various couple stress parameter values. Notably, the flow rate rapidly decreases to zero as time progresses. Additionally, an increase in the couple stress parameter (S) corresponds to an increase in the volumetric flow rate. Consequently, we deduce that in the limiting case of a couple stress fluid, viscous fluids exhibit higher volumetric flow rates and velocities compared to corresponding couple stress fluids. This result correlates with the observations in Fig. 3 and Fig. 4. As S increases, velocity increases and hence, the volumetric flow rate also increases.

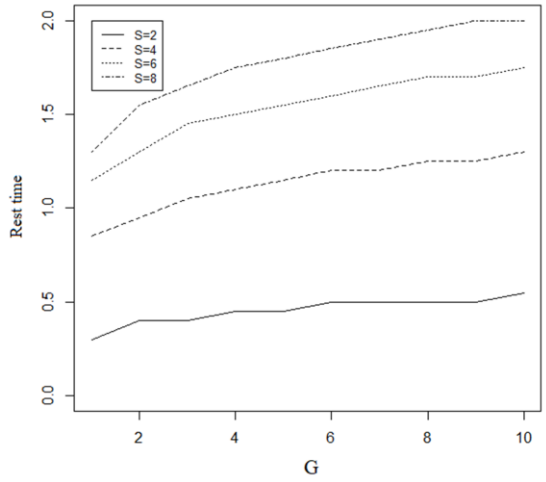

Fig. 5. Pressure gradient vs. rest time at different values of S.

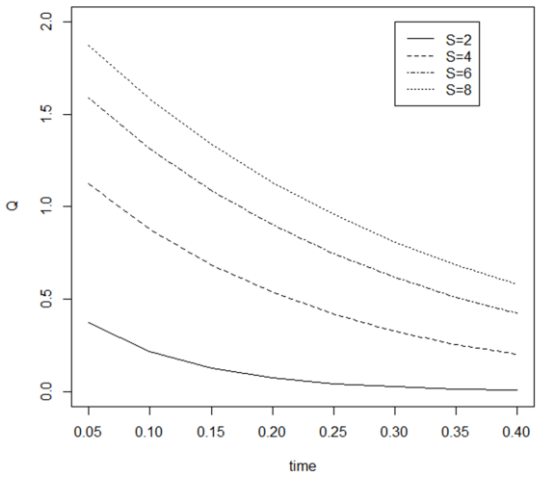

Fig. 6. Time vs. volumetric flow rate (Q) for varying values of S.

5. Conclusions

This paper examines the unsteady flow of a couple stress fluid between two parallel plates following the sudden removal of a pressure gradient. The initial state involves both upper and lower plates being stationary, and flow initiation occurs through a constant pressure gradient. The study focuses on the flow patterns resulting from the sudden withdrawal of the pressure gradient, observing that the flow eventually stops after a certain duration. It is observed that:

- The velocity for viscous fluids is more than for the couple stress fluids at any given time.
- Viscous fluids take longer to rest than couple stress fluids.
- A rise in pressure gradient slowly increases the rest time of the fluid.

- The volumetric flow rate at any given time for viscous fluids is more than for the couple stress fluids.

References

[1] Stokes, V.K. (1984). Couple stresses in fluids. In *Theories of Fluids with Microstructure: An Introduction* (pp. 34−80). Springer, Berlin, Heidelberg.

[2] Rao, S.L., & Iyengar, T.K.V. (1985). *Analytical and computational studies in couple stress fluid flows:* UGC Research project C-8-4/82 SR III.

[3] Ezzat, M.A. (2001). Free convection effects on perfectly conducting fluid. *International Journal of Engineering Science*, 39(7), 799−819. doi: 10.1016/S0020-7225(00)00059-8

[4] Ali, R., Nazar, M., Bilal, M., & Salem, A. (2016). Analytic and numerical solutions for axisymmetric flow with partial slip. *Engineering with Computers*, 32, 149−154. doi: 10.1007/s00366-015-0405-2

[5] Ahmed, J., Khan, Z.H., Malik, M.Y., Hussain, A., & Gayathri, D. (2015). A note on convective heat transfer of an MHD Jeffrey fluid over a stretching sheet. *AIP Advances*, 5(11), 117117. doi: 10.1063/1.4935571

[6] Farooq, A., Ali, R., & Benim, A.C. (2018). Soret and Dufour effects on three-dimensional Oldroyd-B fluid. *Physica A: Statistical Mechanics and Its Applications*, 503, 345−354. doi: 10.1016/j.physa.2018.02.204

[7] Ali, R., Hussain, M.Y., Jamil, M., & Suleman, M. (2020). Computational approach on three-dimensional flow of couple-stress fluid with convective boundary conditions. *Physica A: Statistical Mechanics and Its Applications*, 553, 124056. doi: 10.1016/j.physa.2019.124056

[8] Erdogan, M.E., & Imrak, C.E. (2005). On unsteady unidirectional flows of a second grade fluid. *International Journal of Non-Linear Mechanics*, 40(10), 1238−1251. doi: 10.1016/j.ijnonlinmec.2005.05.004

[9] Erdoğan, M.E., & Imrak, C.E. (2007). On some unsteady flows of a non-Newtonian fluid. *Applied Mathematical Modelling*, 31(2), 170−180. doi: 10.1016/j.apm.2005.08.019

[10] Jaiswal, S., & Yadav, P.K. (2023). Physics of generalized Couette flow of immiscible fluids in anisotropic porous medium. *International Journal of Modern Physics B*, 2450377. doi: 10.1142/S0217979224503776

[11] Yadav, P.K., & Verma, A.K. (2023). Analysis of the MHD flow of immiscible fluids with variable viscosity in an inclined channel. *Journal of Applied Mechanics and Technical Physics*, 64(4), 618−627. doi: 10.1134/S0021894423040077

[12] Yadav, S., Yadav, S., & Yadav, P.K. (2024). The mixed convection thermally radiated hybrid nanofluid flow through an inclined permeable shrinking plate with slip condition and inclined magnetic effect. *Chinese Journal of Physics*, 89, 1041-1050. doi: 10.1016/j.cjph.2023.12.039

[13] Yadav, P.K., & Yadav, N. (2023). A study on the flow of couple stress fluid in a porous curved channel. *Computers & Mathematics with Applications*, 152, 1−15. doi: 10.1016/j.camwa.2023.10.004

[14] Yadav, P.K., & Yadav, N. (2023). Entropy generation analysis in micropolar-couple stress fluid's flow in an inclined porous channel using Homotopy Analysis Method. *Chinese Journal of Physics*, 86, 469−496. doi: 10.1016/j.cjph.2023.10.024

[15] Yadav, P.K., & Verma, A.K. (2023). Analysis of the MHD flow of immiscible fluids with variable viscosity in an inclined channel. *Journal of Applied Mechanics and Technical Physics*, 64(4), 618−627. doi: 10.1134/s0021894423040077

[16] Kumar, A., & Yadav, P.K. (2023). Entropy generation analysis of non-miscible couple stress and Newtonian fluid in an inclined porous channel with variable flow properties: HAM Analysis. *International Journal of Modern Physics B*, 2450390. doi: 10.1142/s0217979224503909

[17] Kazakia, J.Y., & Rivlin, R.S. (1981). Run-up and spin-up in a viscoelastic fluid I. *Rheologica Acta*, 20, 111−127. doi: 10.1007/BF01513054

[18] Rivlin, R.S. (1982). Run-up and spin-up in a viscoelastic fluid. II. *Rheologica Acta*, 21, 107−111. doi: 10.1007/BF01736411

[19] Rivlin, R.S. (1982). Run-up and spin-up in a viscoelastic fluid. III. *Rheologica Acta*, 21, 213−222. doi: 10.1007/978-1-4612-2416-7_151

[20] Rivlin, R.S. (1983). Run-up and spin-up in a viscoelastic fluid. IV. *Rheologica Acta*, 22, 275−283. doi: 10.1007/BF01359127

[21] Narain, A., & Joseph, D.D. (1982). Linearized dynamics for step jumps of velocity and displacement of shearing flows of a simple fluid. *Rheologica Acta*, 21(3), 228−250. doi: 10.1007/BF01515712

[22] Devakar, M., & Iyengar, T.K.V. (2010). Run up flow of a couple stress fluid between parallel plates. *Nonlinear Analysis: Modelling and Control*, 15(1), 29−37. doi: 10.15388/na.2010.15.1.14362

[23] Devakar, M., & Iyengar, T.K.V. (2011). Run up flow of an incompressible micropolar fluid between parallel plates–A state space approach. *Applied Mathematical Modelling*, 35(4), 1751−1764. doi: 10.1016/j.apm.2010.10.007

[24] Qadri, S.Y., & Krishna, M.V. (2013). Run-Up Flow of a Maxwell Fluid through a Parallel Plate Channel. *American Journal of Computational Mathematics*, 3(2013), 109−120. doi: 10.4236/ajcm.2013.34039

[25] Krishna, M.V., & Qadri, S.Y. (2016). Run-up Flow of Oldroyd-B Fluid through a Parallel plate channel. *IOSR Journal of Mathematics*, 12(5), 1−8. doi: 10.9790/5728-1205030108

[26] Jibril, H.M., Jha, B.K., & Yusuf, K.L. (2019). Run-up Flow of an electrically Conducting Fluid In The Presence Of Transverse Magnetic Field in Annulus. *Mathematical Association of Nigeria*, 44, 98−107.

[27] Jha, B.K., Jibril, H.M., & Yusuf, K.L. (2023). Run-up flow of MHD fluid between parallel porous plates in the presence of transverse magnetic field. *Heat Transfer*, 52(3), 2651−2670. doi: 10.1002/htj.22799

[28] Honig, G., & Hirdes, U. (1984). A method for the numerical inversion of Laplace transforms. *Journal of Computational and Applied Mathematics*, 10(1), 113−132. doi: 10.1016/0377-0427(84)90075-X

[29] Rani, D., Mishra, V., & Cattani, C. (2018). Numerical inversion of Laplace transform based on Bernstein operational matrix. *Mathematical Methods in the Applied Sciences*, 41(18), 9231−9243. doi: 10.1002/mma.5188

Co-published by
Institute of Fluid-Flow Machinery
Polish Academy of Sciences
Committee on Thermodynamics and Combustion
Polish Academy of Sciences

http://www.imp.gda.pl/archives-of-thermodynamics/

Exergetic performance coefficient analysis of direct methanol fuel cell

Xinjia Guo[a], Zhanghao Lu[b], Zheshu Ma[a*], Hanling Song[a], Yuting Wang[a]

[a]College of Automobile and Traffic Engineering, Nanjing Forestry University, Nanjing, 210037, China
[b]School of Mechanical and Automobile Engineering, Jinken College of Technology, Nanjing, 211156, China
*Corresponding author email: mazheshu@njfu.edu.cn

Received: 27.10.2023; revised: 17.02.2024; accepted: 10.03.2024

Abstract

In order to improve the output performance of direct methanol fuel cell, the finite-time thermodynamic model of direct methanol fuel cell is developed in this paper. Then, mathematical expressions for energy efficiency, power density, exergy efficiency and exergy coefficient of performance are derived. In addition, the effects of operating temperature, inlet pressure and membrane thickness on the performance of direct methanol fuel cells are considered. The results show that the exergetic performance coefficient not only considers the exergy loss rate to minimize the loss, but also the power density of the direct methanol fuel cell to maximize its power density and improve its efficiency. Therefore, the exergetic performance coefficient is a better performance criterion than conventional power and efficiency. In addition, increasing the inlet pressure and decreasing the membrane thickness can significantly improve the exergetic performance coefficient and energy efficiency.

Keywords: Direct methanol fuel cell; Exergy analysis; Exergetic performance coefficient

Vol. 45(2024), No. 3, 185–195; doi: 10.24425/ather.2024.151230

Cite this manuscript as: Guo, X., Lu, Z., Ma, Z., Song, H., & Wang, Y. (2024). Exergetic performance coefficient analysis of direct methanol fuel cell. *Archives of Thermodynamics*, 45(3), 185–195.

1. Introduction

Liquid methanol is considered to be a suitable fuel for fuel cell vehicles due to its high energy density, easier storage, and the fact that it can continue to be used in conventional fuel tanks when applied to vehicles. Methanol is very stable as a fuel, has low volatility and remains liquid over a range of temperatures. As a result, direct methanol fuel cells (DMFCs) are widely used in small portable devices (e.g. laptops and portable power supplies) [1,2] and large installations (e.g. vehicles and stationary power generation equipment) [3,4].

Currently, DMFC research consists mainly of performance testing of internal components such as membranes and catalysts. Yildirim et al. [5] prepared sulfonated poly(phthalazinone ether ketone) impregnated microporous membrane – into a polyethylene support (SPPEK-PE) and pure SPPEK membrane, set different methanol concentrations and conducted experiments in order to analyze the effect of different polymer membrane impregnation on the performance of DMFC fuel cell. The experimental results showed that SPPEK-PE enhanced the performance of DMFC. Li et al. [6] synthesized a novel bifunctional polyhedral oligomeric silsesquioxane (POSS) with vinyl and su-

Nomenclature

A – effective area of the electrode, m^2
A_L – corresponding thermal leakage area,m^2
C_p – constant specific heat of the gas, constant
E_{nernst} – reversible potential, V
e_n^{ch} – chemical exergetic energy of each component, kJ/kg
ex – exergy, kJ/kg
ex_{rw} – recoverable residual exergy, kJ/kg
ex_{uw} – non-recoverable residual exergy, kJ/kg
F – Faraday
f_{exd} – exergy destruction factor
$G_{f,liq}$ – liquid Gibbs function, J
ΔH – total energy absorbed from methanol and oxygen, J
Δh – change in standard molar enthalpy, kJ/kg
K_L – thermal leakage coefficient
k – specific heat rate, J/(kg·K)
j – current density, A/m^2
j_0 – exchange current density, A/m^2
j_1 – limiting current density, A/m^2
n – number of electron transfers
P – power density of DMFC, W/m^2
$\overline{P}$ – maximum output power density of DMFC, W/m^2
P_{max} – maximum output power density of DMFC at operating temperatures, W/m^2
$P_{1,max}$ – maximum power density of DMFC at operating pressure p = 1 atm, W/m^2
p_0 – standard pressure, atm
Q_H – remaining component of the thermal rate of DMFC, J
Q_L – thermal leakage rate from DMFC to the environment, J
R – equivalent resistance caused by the three overpotentials, Ω
R_{ohm} – operating temperature of DMFC, K
r_{rw} – recoverable residual exergy ratio
r_{uw} – non-recoverable residual exergy ratio
T – temperature of the DMFC, K
T_0 – temperature of the environment, K
t_{mem} – thickness of the membrane, cm
V – voltage, V
x_n – molar fraction of the components

Greek symbols

α – transfer coefficient
β – magnification constant
η – output efficiency

Subscripts and Superscripts

act – activation overpotential
CO_2 – carbon dioxide
cell – fuel cell
ch – chemical
conc – concentration overpotential
H – hydrogen
H_2O – water
in – inlet
meoh – methanol
n – number
O_2 – oxygen
ohm – ohmic overpotential
out – outlet
ph – physical
rw – recoverable residual exergy
uw – non-recoverable residual exergy

Abbreviations and Acronyms

DMFC – direct methanol fuel cell
ECOP – ecological coefficient of performance
EDI – environmental destruction index
EPC – exergetic performance coefficient
POSS – polyhedral oligomeric silsesquioxane
SPPEK – sulfonated poly(phthalazinone ether ketone)

lfonic groups (Vi-POSS-SO_3Na) and crosslinked it by a simple in situ heat treatment, which significantly improved the properties of this proton exchange membrane. Huang et al. [7] used sulfonated spunlace carbon as a filler for SPEEK membranes, and the synthesized membranes showed improved performance as DMFC. The results showed that the MOF-C-SO3H@SPEEK membrane has good ionic conductivity compared to Nafion 115, and its special structure helps to reduce methanol penetration from the anode to the cathode, and promotes the speed of protons across the membrane. Yogarathinam et al. [8] embedded proton membrane (SPEEK) of DMFC with (PANI-A-BN). The results showed that the water absorption (58.42 %) and ionic conductivity of the PANI-A-BN/SPEEK membrane could be significantly enhanced. The methanol permeability of BN and functionalized BN embedded in SPEEK nanocomposite membranes was significantly reduced.

Currently, the methanol single cell is studied in a large number of theoretical and experimental studies. Yuan et al. [9] achieved a reduction in methanol volatility and methanol permeation using capillary distillation. Experiments were then designed to demonstrate the reduction of the relative volatility of methanol/water by the selected carbon aerogel. The results show that by providing a suitable methanol/water ratio in the vapor supply to DMFC, methanol permeation and water deficiency can be significantly mitigated, resulting in DMFC that exhibits excellent performance and stability. Mathew et al. [10] designed, fabricated and tested DMFC stacks with an effective area of 16 cm^2 and experimentally investigated the effect of various operating parameters on the performance of DMFC stacks. The results show that increasing battery temperature, cathode flow rate and methanol concentration can improve the performance of DMFC. Li et al. [11] developed an energy analysis model for direct methanol fuel cells and derived expressions for electrical, thermal and total energy efficiencies. Hotz et al. [12] performed a numerical analysis of the energy efficiency of direct methanol fuel cells, showing the importance of exergy analysis of the fuel cell as part of the overall thermal system for power generation. Yang et al. [13] developed a semi-empirical model of a direct methanol fuel cell and experimentally investigated the performance of four operating parameters, such as temperature and methanol concentration, under different operating conditions. Liu et al. [14] developed a finite-time thermodynamic model of PEMFC, including exergy efficiency and ECOP. The findings show that the heat loss of components such as functioning fuel cells is the most serious. At low current densities, the ecological performance and economy of the fuel cell system is

better, while at high current densities, the exergy loss and net power of the system increases. Li et al. [15] proposed an ecological performance factor and an ecological objective function, which are defined as the ratio of power to power loss and the difference between power and power loss. In the above study, the aspect of exergy analysis to get the performance metrics of DMFC under various operating conditions and using the performance metrics to define the output performance of DMFC is still not enough.

In recent years, finite-time thermodynamics (FTT) has been used to criticize various kinds of thermodynamic processes and cycles. Chen et al. [16] applied finite-time thermodynamics for exergy analysis in a solar thermal power system and found that the system had a positive impact on both energy and exergy performance. Qi et al. [17] developed a finite-time thermodynamic model of a two-stage multivariable temperature difference generator, considered losses such as external heat transfer and collector radiation losses, and studied the basic performance of the system. The results showed that the system performance is optimal when the external heat transfer form and internal structure parameters are optimized. Qi et al. [18] developed a thermo-Brownian heat engine model based on finite-time thermodynamics, and numerically investigated the heat transfer process and the influence of important parameters on the output performance of the system. The results showed that enhanced heat transfer can improve the performance of the system.

The electrochemical model of DMFC can be modeled as finite-time thermodynamic model through exergy analysis, which can be used for thermodynamic performance study [19,20] and optimization to get the best performance [21]. Currently, typical optimal finite-time thermodynamic objective functions include exergy loss, exergy efficiency, ecological coefficient of performance [22], ecological function [23], and entropy yield. Akkaya et al. [24] defined the coefficient of exergy performance (EPC) for analyzing the performance of solid oxide fuel cell. EPC is a thermal-ecological indicator that combines energy and hydronium parameter functions. Therefore, EPC allows for a better evaluation of thermodynamic processes and cycles that include DMFC than traditional performance metrics such as power and efficiency.

In this paper, finite-time thermodynamics is introduced to analyze the irreversibility of DMFC, and a mathematical model of DMFC considering irreversible loss is established, which not only explored the thermodynamic performance of DMFC under different parameters, better defined the source of polarization loss of the fuel cell and provided a direction for the improvement of the performance of the fuel cell, but the result obtained can also provide some kinds of theoretical instructions for the optimized design and practical usage of fuel cell.

2. Theory and methodology

2.1. Working principle of DMFC

DMFC consists of an electrode plate, catalyst layer, diffusion layer, proton exchange membrane, diffusion layer and electrolyte, and its working principle is as follow [25,26] (Fig. 1): during its operation, CH_3OH is continuously transported to the anode chamber, where it reacts with H_2O to form CO_2, H^+ and e^- with the assistance of the anode catalyst, and the generated CO_2 is discharged from the outlet of the anode chamber. H^+ reaches the cathode chamber through the proton exchange membrane and converges with e^- and O_2 transferred from the external circuit to produce H_2O, which is discharged from the outlet of the cathode chamber.

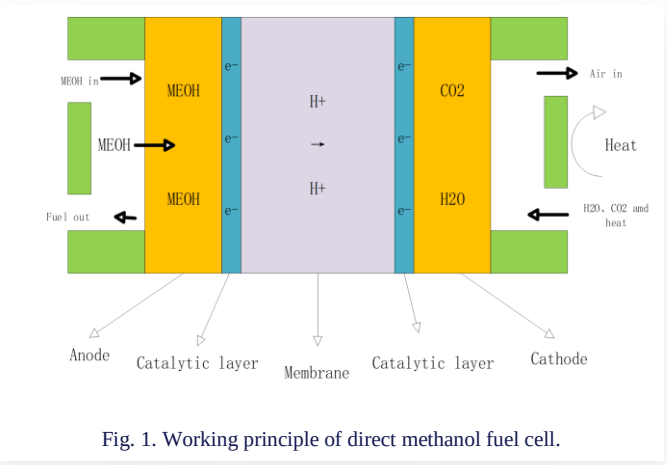

Fig. 1. Working principle of direct methanol fuel cell.

The electrochemical reaction equations of DMFC are:

- Anode:

$$CH_3OH + H_2O \rightarrow CO_2 + 6H^+ + 6e^-, \quad (1)$$

- Cathode:

$$\frac{3}{2}O_2 + 6H^+ + 6e^- \rightarrow 3H_2O, \quad (2)$$

- Over reaction:

$$CH_3OH + \frac{3}{2}O_2 \rightarrow CO_2 + 2H_2O. \quad (3)$$

The main assumptions cited in the DMFC system model are as follows:

1. DMFC system is working in steady state.
2. All types of gases in DMFC are ideally compressible, with air consisting of 21% oxygen and 79% nitrogen.
3. Only physical and chemical exergy is considered, no potential exergy and kinetic exergy are considered.
4. The distribution characteristics of the temperature of the electric stack are not considered.
5. The operating temperature of the stack is uniform.

For DMFC, the reversible potential can be given by the equation [27]:

$$E_{nernst} = -\frac{G_{f,liq}}{nF} + \frac{RT}{nF} + \ln\left[\frac{P_{meoh}\left(P_{O_2}^{\frac{3}{2}}\right)}{P_{CO_2}\left(P_{H_2O}\right)^2}\right]. \quad (4)$$

In Eq. (4), $G_{f,liq}$ is the liquid Gibbs function; n is the number of electron transfers; F is the Faraday constant; T is the operating temperature of DMFC; R is the gas constant.

2.2. Overpotential of DMFC

Polarization can have a significant impact on the performance of DMFC. The causes of polarization phenomena include polar-

ization caused by the electrochemical reaction rate of the active substances at the positive and negative electrodes being less than the rate of electron movement, and polarization caused by the depletion of reactants that cannot be replenished in time at the electrode surface. This means that some energy will be consumed to overcome this resistance during DMFC operation. In general, the polarization phenomenon produces three types of overpotentials: activation overpotential, ohmic overpotential, and concentration overpotential.

The electrochemical reaction rate of DMFC affects the activation overpotential. When the electrochemical reaction rate of positive and negative active substances is less than the rate of electron movement, the polarization loss is more serious, the loss generated by activated polarization increases, and the activation overpotential increases. In addition, the higher the activity of the catalyst used for the cathode and anode, the lower the activation loss generated, and the activation overpotential will be reduced accordingly. The activation overpotential V_{act} can be expressed as follows [27]:

$$V_{act} = \frac{RT}{\alpha nF} \log \frac{j}{j_0}, \tag{5}$$

where α is the transfer coefficient and j_0 is the exchange current density.

Ohmic polarization is polarization due to the contact resistance that exists between the electrolyte, the electrode material, the diaphragm resistance and the various component parts. For DMFCs, the ohmic resistance consists of two main components: the resistance of the ions as they cross the proton exchange membrane and the resistance of the electrons as they reach the end of the electrode. The ohmic overpotential V_{ohm} can be expressed as follows [27]:

$$V_{ohm} = jR_{ohm}, \tag{6}$$

$$R_{ohm} = \int_0^{t_{mem}} \frac{dt_{mem}}{0.04107 + 0.01878e^{100t_{mem}}}, \tag{7}$$

where R_{ohm} is the equivalent resistance caused by the three overpotentials, l_{mem} is the thickness of the membrane.

In the working process of DMFC, concentration polarization occurs when the electrode surface is not replenished in time because the reactants are consumed too quickly, and the electrode reaction surface is unable to maintain the concentration of the reaction gas as it should be. The expression for the concentration overpotential V_{conc} is as follows [27]:

$$V_{conc} = \left(1 + \frac{1}{\beta}\right) \frac{RT}{nF} \ln\left(1 - \frac{j}{j_1}\right), \tag{8}$$

where β is the magnification constant and j_1 is the limiting current density.

The irreversible output voltage V_{cell} of the DMFC can be expressed as:

$$V_{cell} = E_{nernst} - V_{act} - V_{conc} - V_{ohm} = -\frac{G_{f,liq}}{nF} + \frac{RT}{nF} + \ln\left[\frac{P_{meoh}\left(P_{O_2}^{\frac{3}{2}}\right)}{P_{CO_2}\left(P_{H_2O}\right)^2}\right] - \frac{RT}{\alpha nF} \lg \frac{j}{j_0} - jR_{ohm} - \left(1 + \frac{1}{\beta}\right) \frac{RT}{nF} \ln\left(1 - \frac{j}{j_1}\right). \tag{9}$$

The power density of DMFC can be expressed as:

$$P = V_{cell}\, jA, \tag{10}$$

where j is the current density and A is the effective area of the electrode.

As an energy conversion device, the output efficiency of DMFC can be shown in Eq. (7) [23]:

$$\eta = -\frac{P}{\Delta H}, \tag{11}$$

where ΔH is the total energy absorbed from methanol and oxygen, which can be expressed as [22]:

$$\Delta H = -\frac{jA\Delta h}{nF}, \tag{12}$$

where Δh is the change in standard molar enthalpy.

The thermal leakage rate from DMFC to the environment can be expressed as [28]:

$$Q_L = K_L A_L (T - T_0), \tag{13}$$

where K_L and A_L represent the thermal leakage coefficient and the corresponding thermal leakage area, respectively. T_0 is the temperature of the environment.

Following the first law of thermodynamics, the remaining component of the thermal rate of DMFC can be expressed as:

$$Q_H = -\Delta H - P - Q_L = \frac{A}{nF}[-(1-\eta)j\Delta h - b_1(T - T_0)], \tag{14}$$

where, $b_1 = \frac{nFK_LA_L}{A}$ [28].

2.3. Exergetic performance analysis of DMFC

The output performance of DMFC is reduced due to different irreversible loss, including heat loss, gas-flow channel friction loss, leakage current and polarization loss. Exergy analysis evaluates the actual useful fraction of energy and can therefore be used as a measure of the quality of the energy released by the DMFC. The exergy balance of DMFC is show in Fig. 2.

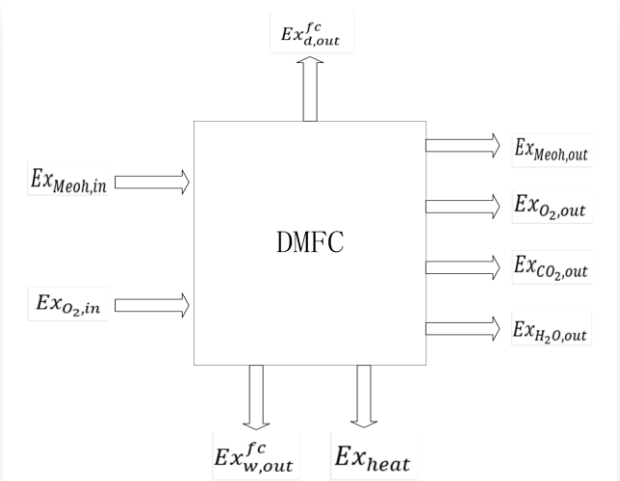

Fig. 2. Exergy balance of DMFC.

In the reaction process of DMFC, only physical and chemical exergy are considered [29,30]. The expressions of physical and chemical exergy are as follows [31,32]:

$$(ex)^{ph}=C_pT_0\left[\frac{T}{T_0}-1-\ln\left(\frac{T}{T_0}\right)+\ln\left(\frac{p}{p_0}\right)^{\frac{k-1}{k}}\right], \quad (15)$$

$$(ex)^{ph}=\sum x_n e_n^{ch}+RT_0\sum x_n \ln x_n, \quad (16)$$

where C_p is the constant specific heat of the gas, p_0 is the standard pressure, K is the specific heat rate, x_n is the molar fraction of the components and e_n^{ch} is the chemical exergetic energy of each component.

In DMFC, the total input exergy and output exergy are shown as follows:

$$ex_{in}=-\frac{jA}{nF}\left(ex_{meoh}+\frac{3}{2}ex_{O_2}\right), \quad (17)$$

$$ex_{out}=-\frac{jA}{nF}\left(2ex_{H_2O}+ex_{CO_2}\right). \quad (18)$$

In practice, the quality of energy decreases during transfer processes, including friction, drag, radiation and heat transfer. Exergy loss can be used to express the degree of irreversibility of the energy transfer process. For DMFC, the lower the exergy loss in the thermodynamic process, the higher the effective utilization of energy [32]:

$$ExD=ex_{in}-ex_{out}-P-Q_H\left(1-\frac{T}{T_0}\right). \quad (19)$$

The recoverable residual exergy ratio can be assumed to be the ratio of the recoverable residual exergy of the DMFC to the total exergy input. The recoverable residual exergy ratio can be expressed as:

$$r_{rw}=\frac{ex_{rw}}{ex_{in}}. \quad (20)$$

The non-recoverable residual exergy ratio includes the physical consumption of unused methanol and unused oxygen and heat, as well as the logistical exergy to generate water. The ratio of non-recoverable residual energy can be expressed as:

$$r_{uw}=\frac{ex_{uw}}{ex_{in}}. \quad (21)$$

In the above equation, ex_{rw} and ex_{uw} can be calculated by the following equations, respectively:

$$ex_{uw}=\dot{m}_{Meoh,out}\times ex^{ch}_{Meoh,out}+\dot{m}_{O_2,out}\times ex^{ch}_{O_2,out}, \quad (22)$$

$$ex_{rw}=\dot{m}_{Meoh,out}\times ex^{ph}_{Meoh,out}+\dot{m}_{O_2,out}\times ex^{ph}_{O_2,out}+$$
$$+\dot{m}_{HO_2,out}\times ex_{HO_2}+Ex_Q. \quad (23)$$

The exergy destruction factor is an important parameter of DMFC that indicates the impact of DMFC on exergy sustainability.exergy destruction factor can be expressed as:

$$f_{exd}=\frac{ExD}{ex_{in}}. \quad (24)$$

The environmental destruction index is used to indicate the residual exergy output that cannot be recovered from DMFC operation and the environmental impact caused by exergy destruction. This coefficient rises with the decrease of exergy efficiency. Therefore, for the practical application of DMFC, EDI should be fully considered, and appropriate operating and design conditions should be selected. The optimal reference value of "1" for EDI indicates the reversibility of exergy efficiency, where the residual exergy that cannot be recycled is close to zero. EDI is a function of *ExD*, the non-recyclable residual exergy ratio and the environmental damage factor and can be expressed as:

$$\mathrm{EDI}=(r_{uw}+f_{exd})\frac{ex_{in}}{P}=\frac{ex_{uw}-ExD}{ExD}. \quad (25)$$

In DMFC systems, energy analysis can analyze and study the processes of energy flow, conversion and storage in the system, while exergy performance analysis can visually grasp the impact of irreversible loss in the system on DMFC. Based on ecological and DMFC performance considerations, the performance of DMFC is evaluated by combining both energy and energy performance aspects, and the evaluation indicator is defined as an alternative criterion, which is more accurate and practical, and can be expressed as:

$$\mathrm{EPC}=\frac{P}{ExD}=\frac{E_{cell}jA}{ex_{in}-ex_{out}-P-Q_H\left(1-\frac{T}{T_0}\right)}. \quad (26)$$

2.4. Comparison of different objective functions

There are dimensional and order-of-magnitude differences between the indicators, therefore, in order to visualize the relationship between EPC, *P*, η and *ExD* more conveniently and intuitively, this paper uses a dimensionless method for numerical study and analysis. The dimensionless functions of EPC, *P*, η and *ExD* are expressed as EPC = EPC/EPC$_{max}$, $P = P/P_{max}$, $ExD = ExD/ExD_{max}$, $\eta = \eta_{ex}/\eta_{ex_{max}}$, $\eta = \eta/\eta_{max}$.

The dimensionless maximum output power density of DMFC can be expressed as follows:

$$\bar{P}=\frac{P_{max}}{P_{1,max}}, \quad (27)$$

where P_{max} is the maximum output power density of DMFC at different operating temperatures, and $P_{1,max}$ is the maximum power density of DMFC at operating pressure p = 1 atm. The dimensionless methods of output efficiency, exergy efficiency and exergy performance coefficient corresponding to the maximum power density are similar to the dimensionless maximum power density.

3. Results and discussion

In existing systems for evaluating DMFC performance, power and efficiency are commonly used. However, power and efficiency are only evaluated from the perspective of mechanical, friction loss to the performance of DMFC. Heat loss is also a very important phenomenon in practical applications. DMFC generates a large amount of heat loss during operation, so heat dissipation needs to be taken into account when evaluating its performance. EPC is defined as the ratio of power to heat dissi-

pation, taking into account both mechanical and heat loss. The conclusions obtained when evaluating the performance of DMFC using EPC will be more realistic and accurate.

The relevant parameters in the DMFC model are shown in Table 1. According to the input parameters, the thermodynamic irreversibility and exergy performance coefficients of DMFC with different operating parameters were investigated.

Table 1. Relevant data of DMFC.

Parameter	Value
Current Density, I (Am^{-2})	0-20000
Faraday Constant, F ($Cmol^{-1}$)	96485
Gas Constant, R ($Jmol^{-1}K^{-1}$)	8.314
Number of electrons, n	6
Ambient Temperature, T (K)	298.15
Anode Pressure (atm)	1 [33]
Cathode Pressure (atm)	1 [33]
Anode Gas Compositions	100 % MEOH [33]
Cathode Gas Compositions	21 % O_2; 79 % N_2 [33]
Transfer coefficient, α	0.3 [33]
Active area, A (cm^{-2})	25 [33]

Figure 3 compares the predicted model potential and experimental data of DMFC at 333–353 K (p = 1 atm; l_{mem} = 0.02 mm). From the experimental results in Fig. 3, it can be seen that the error between the predicted data and the experimental data is about 11%. This experimental result shows that the model has good accuracy. The relationship between polarization loss potential, output voltage and current density is shown in Fig. 3.

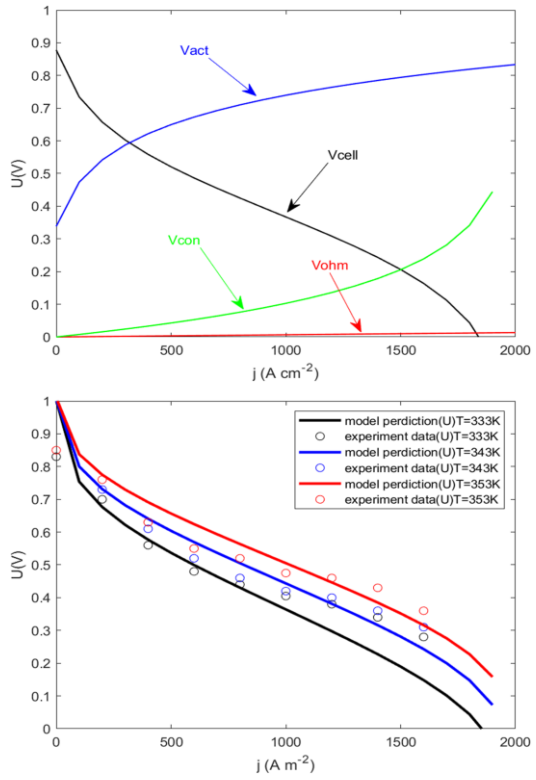

Fig. 3. Comparison of predicted model voltage and power density with experimental data[30].

As shown in Fig. 3, all three overpotentials increase with increasing current density, where the concentration overpotential increases exponentially, the activation overpotential increases logarithmically, and the ohmic overpotential increases by a small amount. When in the lower current density region, the activation overpotential rises sharply in this region, and activation loss dominates in this phase. In the medium to high current density part, the increase in concentration overpotential is larger, and in this stage, the concentration overpotential has a greater effect on the voltage variation.

3.1. Comparsion of relationship between EPC, *P*, *ExD* and *η*

As can be seen in Fig. 4, when the EPC reaches its maximum value, the efficiency is 0.41, $\eta_{ex}/\eta_{ex_{max}}$ is 1, and P/P_{max} is 0.55. This means that the power density under the EPC is very close to the maximum value. When P is at its maximum value, the efficiency is 0.24, $\eta_{ex}/\eta_{ex_{max}}$ is 0.34, and EPC/EPC_{max} is 0.57. Obviously, compared with P_{max}, if EPC_{max} is used as the standard, the efficiency of the breakdown is improved by 66%, the breakdown loss is reduced by 70%, the efficiency is improved by 41%, and the power density is reduced by 45%. Therefore, this paper derives EPC , which takes into account not only the exergy loss to minimize the loss but also the power density of DMFC to maximize the power and improve its output performance.

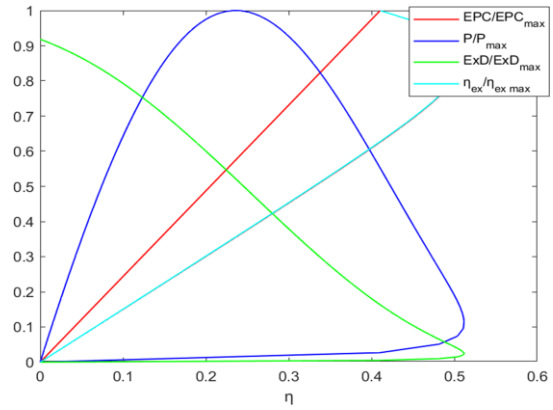

Fig. 4. The relationship between η and dimensionless EPC, P, η_{ex}.

It can be seen from Fig. 5 that the working temperature has a very obvious effect on the output performance of DMFC, which is mainly due to the fact that when the working temperature increases, the activity of the cathode and anode catalysts is enhanced, which improves the electrochemical reaction rate of the positive and negative active substances; the diffusion coefficient of the reacting gases is increased, and the internal mass transfer conditions are improved. Both $\overline{P}$ and $\overline{EPC}$ of DMFC increase with the increase of operating temperature, and in the low current density region, the performance improvement brought by increasing temperature is much smaller than that in the high current density region. This is mainly due to the reason that in the low current density region, the electrochemical reaction has just started, the electrochemical reaction rate is low, and the op-

erating temperature has little effect on the electron and proton activity, so increasing the operating temperature has little effect on the electrochemical reaction rate, and only increasing the current density can accelerate the electrochemical reaction rate. Then, the irreversible loss of DMFC is dominated by activation loss in the low current density region, while the increase of activation loss in the high current density region gradually tends to smooth out.

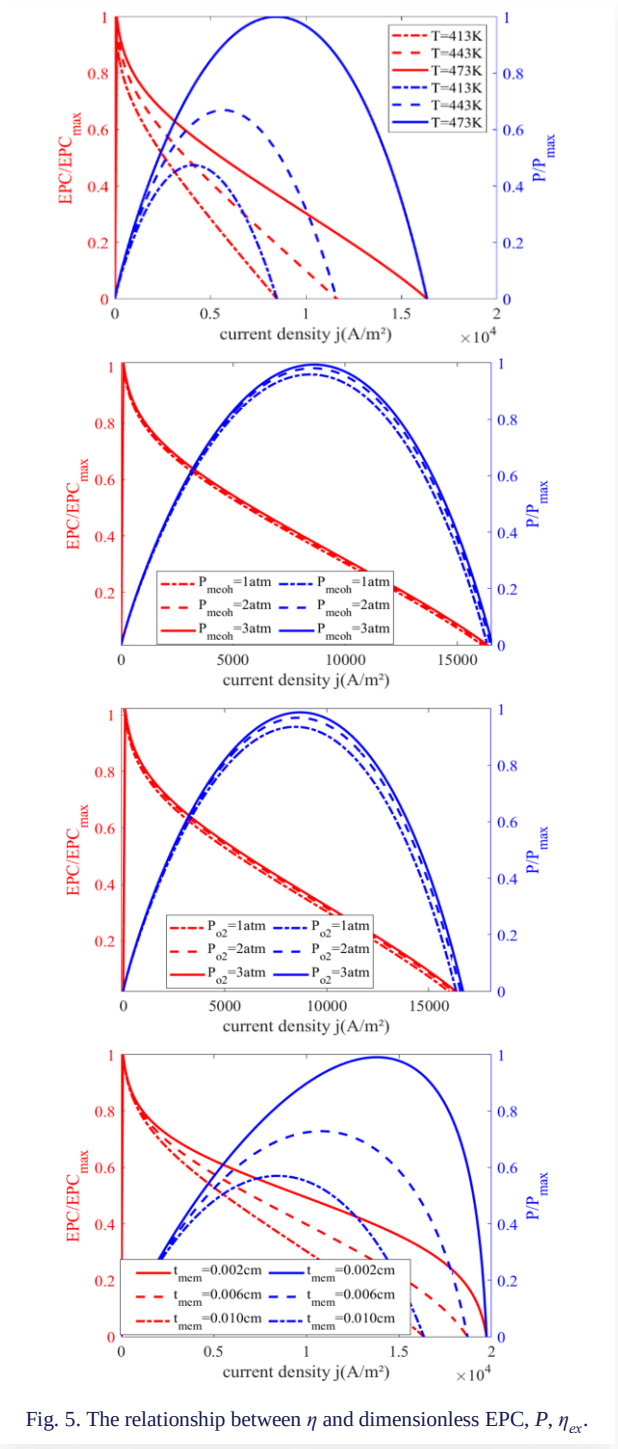

Fig. 5. The relationship between η and dimensionless EPC, P, η_{ex}.

It can also be seen from Fig. 5 that increasing the inlet pressure can improve $\overline{P}$ and $\overline{\mathrm{EPC}}$ of DMFC, but the improvement from the inlet pressure is not obvious. Increasing the inlet pressure can increase the supply rate of reactants, and the concentration gradient of the reactants involved in the reaction and supply is reduced, so that the concentration loss is reduced, and the power dissipation becomes smaller and $\overline{P}$ increases. Increasing the inlet pressure also improves the mass transfer of the reactants at both poles, expelling the water vapor generated at the cathode more easily, taking away more heat, reducing irreversible exergy loss, and improving the $\overline{\mathrm{EPC}}$.

Figure 6 reflects the power density of DMFC and the variation of EPC with the inlet pressure at different operating temperatures. It is obvious that the maximum power density of DMFC constantly increases with the increase of inlet gas. Since the exchange current density increases with the increase of operating pressure, the activation polarization loss will decrease and the reversible potential will increase. Therefore, as the operating pressure increases, the irreversible loss of DMFC decreases and the maximum power density of DMFC increases accordingly. Numerically, when the operating temperature is 453 K and the operating temperature of DMFC increases from 1 atm to 3 atm, the maximum power density of DMFC increases from 1563 W/m^2 to 1689 W/m^2, an improvement of only 8%, and EPC increases from 0.3344 to 0.3528, an improvement of 5.5%. Numerical analysis shows that the increase in operating pressure does not improve the DMFC performance as significantly as the increase in operating temperature. In addition, increasing the operating pressure requires additional power consumption to compress the inlet reactants.

Figure 7 reflects the power density of DMFC and the variation of EPC with operating temperature at different inlet air. It can be seen from the figure that the maximum power density of DMFC becomes larger as the operating temperature increases. This is due to the fact that the increase in the operating temperature leads to an increase in the exchange current density and hence the activation overpotential decreases with the increase in the exchange current density. At the same time, the increase in the operating temperature increases the proton conductivity and thus decreases the ohmic overpotential of DMFC. As a result, the power loss from ohmic overpotential and activation overpotential will be reduced. When the inlet pressure is 1 atm and the operating temperature is 413 K, the corresponding maximum power density is 371 W/m^2, and when the operating temperature increases to 473 K, the corresponding maximum power density reaches 1833 W/m^2, which indicates that when the operating temperature of DMFC increases from 413 K to 473 K, the maximum power density of the DMFC increases by 4.94 times. The results show that DMFC can significantly increase its maximum power density by choosing the right operating temperature range.

The DMFC operating parameter variation range is show in Table 2.

Table 2. DMFC operating parameter variation range.

Parameter	Value
Operating temperature, T_0 (K)	413-473
Electrolyte thickness, l_{mem} (cm)	0.0005-0.0015
Intake pressure P_{O_2}, P_{meoh} (atm)	1-5

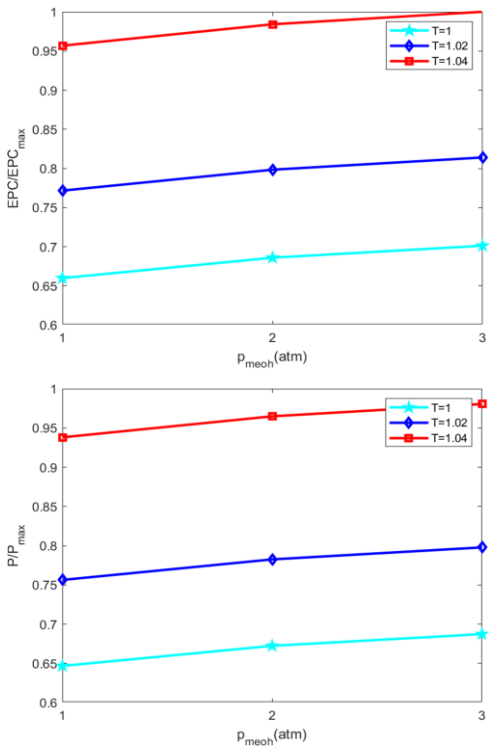

Fig. 6. $\overline{EPC}$ and $\overline{P}$ variation with the operating pressure.

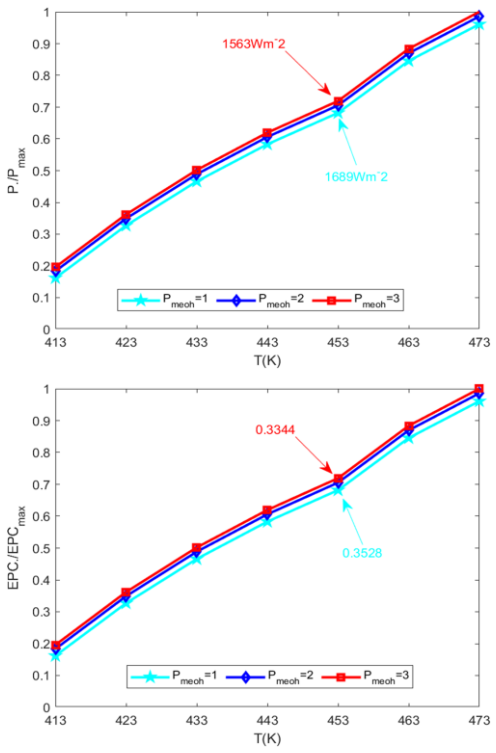

Fig. 7. $\overline{EPC}$ and $\overline{P}$ variation with the operating pressure.

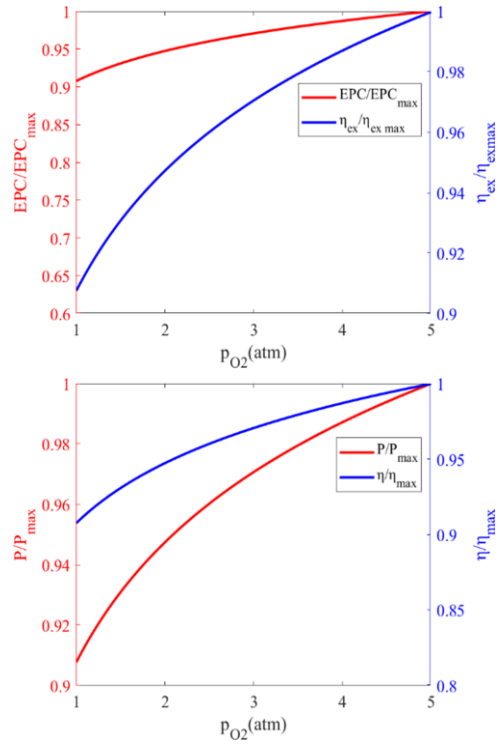

Fig. 8. The effect of inlet pressure P_{O_2} on the performance of DMFC.

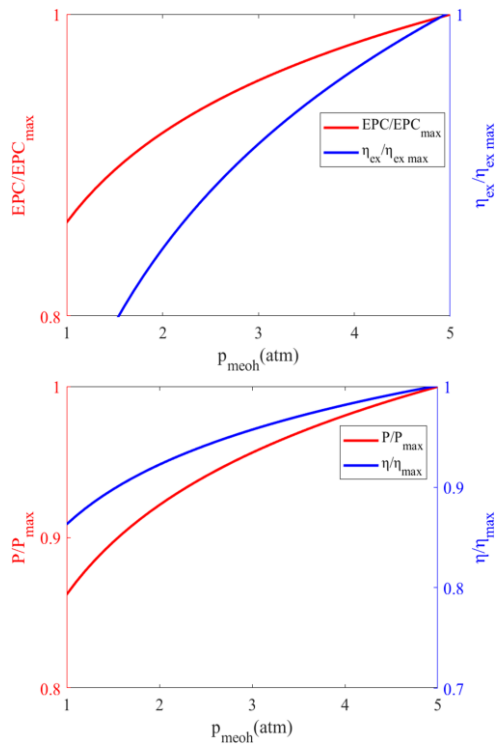

Fig. 9. The effect of inlet pressure P_{meoh} on the performance of DMFC.

Another factor that affects the performance of DMFC is the inlet pressure. On the one hand, increasing the inlet pressure accelerates the diffusion of reactant gases and improves the conditions for the mass transfer process between methanol and oxygen. In addition, it increases the concentration of reactants and reduces the effect of concentration polarization on the reversible potential. Figures 8 and 9 represent the effect of oxygen and methanol inlet pressures on DMFC performance, respectively.

From the figures, it can be seen that the power density and efficiency of DMFC increases with the increase of methanol and oxygen inlet pressures. The increase in power density and effi-

ciency in numerical value is not significant when the oxygen inlet pressure increases from 1 atm to 5 atm, but the value of power density increases significantly when the methanol inlet pressure increases from 1 atm to 5 atm, and the efficiency also increases at the same time. The power density and efficiency curves gradually decrease with the increase of methanol pressure because when the methanol concentration is too high, the rate of increase of reversible potential loss due to the concentration polarization is higher than the rate of decrease of reversible potential loss due to the increase of methanol pressure, so the power density and efficiency performance curves gradually smooth out.

Figure 10 reflects the effect of membrane thickness on DMFC power density, efficiency, exergy efficiency and EPC. It can be seen from the figure that the power density, efficiency and exergy efficiency and EPC all increase with decreasing membrane thickness, which is mainly due to the fact that decreasing proton membrane thickness will make the path length between the ions crossing from the anode to the cathode shorter, resulting in a lower ohmic potential of DMFC. However, if the proton membrane is too thin, it will lead to the penetration of methanol fuel from the anode to the cathode through the concentration difference, and cause problems such as short circuit and proton membrane rupture. Therefore, choosing the right proton membrane is crucial to enhance the performance of DMFC.

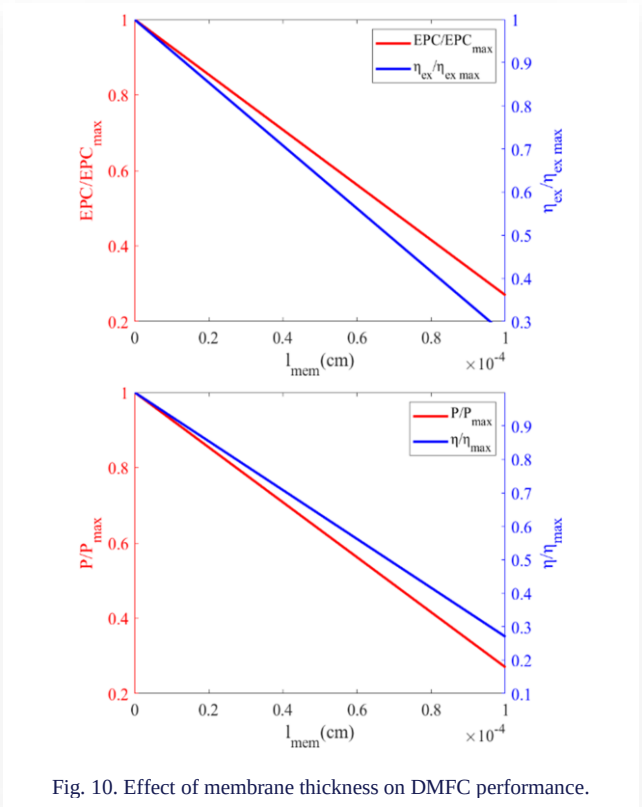

Fig. 10. Effect of membrane thickness on DMFC performance.

Figure 11 shows the relationship between EPC and efficiency before and after optimization of DMFC parameters. It can be seen that the EPC increases with increasing inlet pressure when the set membrane thickness l_{mem} and efficiency η are the same, increasing the inlet pressure can significantly improve the EPC of DMFC, indicating that the operating pressure has an effect on the power density and exergy destruction rate. When the operating pressure is the same, the efficiency of DMFC can be improved by improving the membrane thickness. By increasing the operating pressure and reducing the membrane thickness, the efficiency and EPC of DMFC will be significantly improved, which not only reduces the fuel consumption but also the heat loss in energy. However, if the thickness of the membrane is too low, methanol will come to the cathode side through the proton membrane more easily, which aggravates the methanol crossover phenomenon, thus accelerating the corrosion of DMFC and reducing the service life of DMFC.

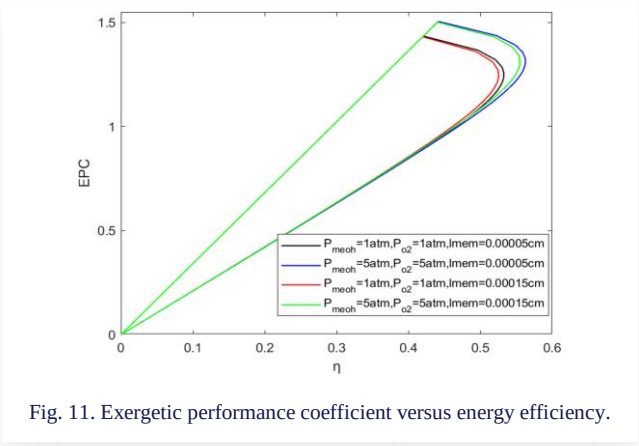

Fig. 11. Exergetic performance coefficient versus energy efficiency.

In addition, when higher pressure is provided to the inlet, extra power is consumed to compress the inlet reactant. In practice, when DMFC is applied to vehicles, the EPC and efficiency of DMFC can be improved by increasing the inlet pressure and reducing the membrane thickness.

4. Conclusions

In order to evaluate the thermodynamic performance of DMFC, the finite-time thermodynamic method is used to model DMFC considering three overpotentials and a new criterion, and exergy performance factor, the ratio of power to exergy loss rate are proposed to analyze the performance of DMFC. Relationships between EPC, power density, exergy efficiency and energy efficiency are obtained, and the results show that EPC can replace power density as a new performance metric. In the analysis of DMFC model, the effect of different parameters on power density, efficiency, exergy efficiency and EPC is analyzed. Analysis of the data reveals that EPC has the same trend as energy efficiency but represents different specific meanings. EPC_{max} stands for the fact that DMFC has the highest external output while minimizing the dissipation in the environment. Therefore, the higher the EPC_{max} of DMFC, the better the performance in terms of energy and ecology. In addition, increasing the inlet pressure and decreasing the film thickness can significantly improve the energy efficiency. This new criterion can be used in the future engineering field to analyze fuel cell vehicles.

Acknowledgement

We gratefully acknowledge the financial support of the Scientific Research Foundation of Nanjing Forestry University (No. GXL2018004).

References

[1] Mallick, R.K., Thombre, S.B., & Shrivastava, N.K. (2015). A critical review of the current collector for passive direct methanol fuel cells. *Journal of Power Sources*, 285, 510–529. doi: 10.1016/j.jpowsour.2015.03.089

[2] Kamarudin, S.K., Achmad, F., & Daud, W.R.W. (2009). Overview on the application of direct methanol fuel cell (DMFC) for portable electronic devices. *International Journal of Hydrogen Energy*, 34(16), 6902–6916. doi: 10.1016/j.ijhydene.2009.06.013

[3] Kimiaie, N., Wedlich, K., Hehemann, M., Lambertz, R., Mueller, M., Korte, C., & Stolten, D. (2014). Results of a 20 000 h lifetime test of a 7 kW direct methanol fuel cell (DMFC) hybrid system - Degradation of the DMFC stack and the energy storage. *Energy & Environmental Science*, *7*(9), 3013–3025. doi: 10.1039/C4EE00749B

[4] Karaoglan, M.U., Ince, A.C., Colpan, C.O., & Selman, J.R. (2019). Simulation of a hybrid vehicle powertrain having direct methanol fuel cell system through a semi-theoretical approach. *International Journal of Hydrogen Energy*, 44(34), 18981−18992. doi: 10.1016/j.ijhydene.2018.11.039]

[5] Yildirim, M.H., Schwarz, A., Stamatialis, D.F., & Wessling, M. (2009). Impregnated membranes for direct methanol fuel cells at high methanol concentrations. *Journal of Membrane Science*, 328, 127–133. doi: 10.1016/j.memsci.2008.11.051

[6] Li, Z., Hao, X., Cheng, G., Huang, S., Han, D., Xiao, M., Wang, S., & Meng, Y. (2021). In situ implantation of cross-linked functional POSS blocks in Nafion® for high performance direct methanol fuel cells. *Journal of Membrane Science*, 640(119798), 119798. doi: 10.1016/j.memsci.2021.119798.

[7] Huang, H.H., Ma, Y.F., Jiang, Z.Q., & Jiang, Z.J. (2021). Spindle-like MOFs-derived porous carbon filled sulfonated poly (ether ether ketone): A high performance proton exchange membrane for direct methanol fuel cells. *Journal of Membrane Science*, 636(119585). doi: 10.1016/j.memsci.2021.119585

[8] Yogarathinam, L.T., Jaafar, J., Ismail, A.F., Goh, P.S., Gangasalam, A., Hanifah, M.F.R., Wong, K.C., Subramaniam, M.N., & Peter, J. (2021). Functionalized boron nitride embedded sulfonated poly (ether ether ketone) proton exchange membrane for direct methanol fuel cell applications. *Journal of Environmental Chemical Engineering*, 9(5), 105876. doi: 10.1016/j.jece.2021.105876

[9] Yuan, W., Hou, C., Wu, J., Zhang, Y., & Zhang, X. (2023). A direct methanol fuel cell with outstanding performance via capillary distillation. *Chemical Engineering Journal (Lausanne, Switzerland: 1996)*, 470(143663), 143663. doi: 10.1016/j.cej.2023.143663.

[10] Mathew, A.S., Naigil, B., George, E., Benny, E., & Baby, R. (2022). Design, fabrication and testing of a direct methanol fuel cell stack. *Journal: Materials Today: Proceedings*, 58(1), 400–406. *International Conference on Artificial Intelligence and Energy Systems*, 12–13 June, 2021, Jaipur, India. doi: 10.1016/j.matpr.2022.02.338

[11] Li, X., He, Y., Yin, B., Miao, Z., & Li, X. (2008). Exergy flow and energy utilization of direct methanol fuel cells based on a mathematic model. *Journal of Power Sources*, 178(1), 344–352. doi: 10.1016/j.jpowsour.2007.08.019

[12] Hotz, N., Lee, M.T., Grigoropoulos, C.P., Senn, S.M. & Poulikakos, D. (2006). Exergetic analysis of fuel cell micropowerplants fed by methanol. *International Journal of Heat and Mass Transfer*, 49(15–16), 2397–2411. doi: 10.1016/j.ijheatmasstransfer.2006.03.007

[13] Yang, Q.-W., Hu, X.-Q., Lei, X.-C., Zhu, Y., Wang, X.-Y., & Ji, S.-C. (2018). Adaptive operation strategy for voltage stability enhancement in active DMFCs. *Energy Conversion and Management*, 168, 11–20. doi: 10.1016/j.enconman.2018.04.110

[14] Liu, G., Qin, Y., Yin, Y., Bian, X., & Kuang, C. (2020). Thermodynamic modeling and exergy analysis of proton exchange membrane fuel cell power system. *International Journal of Hydrogen Energy*, 45(54), 29799–29811. doi: 10.1016/j.ijhydene.2019.08.203

[15] Li, C., Liu, Y., Xu, B., & Ma., Z. (2019). Finite time thermodynamic optimization of an irreversible proton exchange membrane fuel cell for vehicle use. *Processes*, 7(7), 419. doi: 10.3390/pr7070419

[16] Chen, Y.Z., Zhao, D.D., Xu, J.Z., Wang, J., & Lund, P.D. (2021). Performance analysis and exergo-economic optimization of a solar-driven adjustable tri-generation system. *Energy Conversion and Management*, 233, 113873. doi: 10.1016/j.enconman.2021.113873

[17] Qi, C.Z., Du, Y.X., Chen, L.E., Yin, Y., & Ge, Y.L. (2023). Modeling and thermodynamic optimization of a solar-driven two-stage multi-element thermoelectric generator. *Journal of Cleaner Production*, 418, 138147. doi: 10.1016/j.jclepro.2023.138147

[18] Qi, C.Z., Chen, L.E., Ge, Y.L., Feng, H., & He, Z.(2022). Heat transfer effect on the performance of thermal Brownian heat engine. *Energy Reports*, 8, 3002−3010. doi: 10.1016/j.egyr.2022.02.063

[19] Bahrami, H., & Faghri, A. (2011). Exergy analysis of a passive direct methanol fuel cell. *Journal of Power Sources*, 196(3), 1191−1204. doi: 10.1016/j.jpowsour.2010.08.087

[20] Ishihara, A., Mitsushima, S., Kamiya, N., & Ota, K. (2004). Exergy analysis of polymer electrolyte fuel cell systems using methanol. *Journal of Power Sources*, 126(1−2), 34−40. doi: 10.1016/j.jpowsour.2003.08.029

[21] Mert, S.O., & Özçelik, Z. (2013). Multi-objective optimization of a direct methanol fuel cell system using a genetic-based algorithm. *International Journal of Energy Research*, 37(10), 1256−1264. doi: 10.1002/er.2963

[22] Li, D., Li, S., Ma, Z., Xu, B., Lu, Z., Li, Y., & Zheng, M. (2021). Ecological performance optimization of a high temperature proton exchange membrane fuel cell. *Mathematics*, 9(12), 1378. doi: 10.3390/math9121332

[23] Li, C., Xu, B., & Ma, Z. (2020). Ecological performance of an irreversible proton exchange membrane fuel cell. *Science of Advanced Materials*, 12(8), 1225–1235. doi: 10.1166/sam.2020.3846

[24] Akkaya, A.V., Sahin, B., & Erdem, H.H. (2007). Exergetic performance coefficient analysis of a simple fuel cell system. *International Journal of Hydrogen Energy*, 32(17), 4600–4609. doi: 10.1016/j.ijhydene.2007.03.038

[25] Rosenthal, N.S., Vilekar, S.A., & Datta, R. (2012). A comprehensive yet comprehensible analytical model for the direct methanol fuel cell. *Journal of Power Sources*, 206, 129–143. doi: 10.1016/j.jpowsour.2012.01.080

[26] Bahrami, H., & Faghri, A. (2013). Review and advances of direct methanol fuel cells: Part II: Modeling and numerical simulation. *Journal of Power Sources*, 230, 303–320. doi: 10.1016/j.jpowsour.2012.12.009

[27] Lee, W.-Y., Kim, M., Sohn, Y.-J., & Kim, S.-G. (2016). Power optimization of a combined power system consisting of a high-temperature polymer electrolyte fuel cell and an organic Rankine cycle system. *Energy*, 113, 1062–1070. doi: 10.1016/j.energy.2016.07.093

[28] Guo, X., Zhang, H., Yuan, J., Wang, J., Zhao, J., Wang, F., Miao, H., & Hou, S. (2019). Energetic and exergetic analyses of a combined system consisting of a high-temperature polymer electrolyte membrane fuel cell and a thermoelectric generator with Thomson effect. *International Journal of Hydrogen Energy*, 44(31), 16918–16932. doi: 10.1016/j.ijhydene.2019.04.215

[29] Taner, T. (2018). Energy and exergy analyze of PEM fuel cell: A case study of modeling and simulations. *Energy*, 143, 284–294. doi: 10.1016/j.energy.2017.10.102

[30] Cohce, M.K., Dincer, I., & Rosen, M.A. (2011). Energy and exergy analyses of a biomass-based hydrogen production system. *Bioresource Technology*, 102(18), 8466–8474. doi: 10.1016/j.biortech.2011.06.020

[31] Obara, S., Tanno, I., Kito, S., Araki, M., & Sazaki, S. (2008). Exergy analysis of the woody biomass Stirling engine and PEM-FC combined system with exhaust heat reforming. *International Journal of Hydrogen Energy*, 33(9), 2289–2299. doi: 10.1016/j.ijhydene.2008.02.035

[32] Dincer, I., Hussain, M.M., & Al-Zaharnah, I. (2005). Energy and exergy utilization in the agricultural sector of Saudi Arabia. *Energy Policy*, 33(11), 1461–1467. doi: 10.1016/j.enpol.2004.01.004

[33] Sharifi, S., Rahimi, R., Mohebbi-Kalhori, D., & Çolpan, C. Ö. (2020). Coupled computational fluid dynamics-response surface methodology to optimize direct methanol fuel cell performance for greener energy generation. *Energy*, 198, 117293. doi: 10.1016/j.energy.2020.117293

Co-published by
Institute of Fluid-Flow Machinery
Polish Academy of Sciences
Committee on Thermodynamics and Combustion
Polish Academy of Sciences

http://www.imp.gda.pl/archives-of-thermodynamics/

Multi-optimization of thermodynamic performance of an HT-PEM fuel cell based on MOPSO algorithm

Yuting Wang[a], Zheshu Ma[a*], Yongming Gu[a], Qilin Guo[a]

[a] Nanjing Forestry University, College of Automobile & Traffic Engineering, 210037, China
* Corresponding author email: mazheshu@njfu.edu.cn

Received: 27.03.2024; revised: 09.05.2024; accepted: 12.06.2024

Abstract

In this study, an irreversible thermodynamic model for the high temperature proton exchange membrane fuel cell taking electrochemical and heat losses into account is developed. The power density, exergy destruction index, exergy sustainability index and ecological coefficient of performance is derived. The model was validated against experimental data. The influence of parameters on the irreversible thermodynamic performance of high temperature proton exchange membrane fuel cell are considered. The multi-objective particle swarm optimization algorithm is utilized to optimize the power, ecological coefficient of performance and efficiency. The population distribution of the optimization variables was analyzed using a three-dimensional Pareto frontier analysis, and results show that the maximum power density, maximum efficiency and maximum ecological coefficient of performance being 6340 W/m^2, 64.5% and 1.723 respectively, which are 43.28%, 3.7% and 17.8% higher than the preoptimized high temperature proton exchange membrane fuel cell. Moreover, the nondominated sorting genetic algorithm II and simulated annealing algorithm have been chosen versus multi-objective particle swarm optimization algorithm for making the optimization comparative analysis.

Keywords: HT-PEMFC; Irreversible thermodynamic; Exergy; Parameter optimization; MOPSO algorithm

Vol. 45(2024), No. 3, 197–208; doi: 10.24425/ather.2024.151231

Cite this manuscript as: Wang, Y., Ma, Z., Gu, Y., & Guo Q. (2024). Multi-optimization of thermodynamic performance of an HT-PEM fuel cell based on MOPSO algorithm. *Archives of Thermodynamics*, 45(3), 197–208.

1. Introduction

The high temperature proton exchange membrane fuel cell (HT-PEMFC) is regarded as an alternative device to make up for the shortcomings of PEMFC with the advantages of simpler water and thermal management, faster electrochemical reaction rates and higher utilization of waste heat [1]. However, it is accompanied by significant irreversible thermal losses which lead to limit the broader application of HT-PEMFC [2–4].

Irreversible thermodynamic loss refers to the energy loss that occurs in the process of energy conversion or transfer that is not completely recoverable [5]. In thermodynamic systems, irreversible processes lead to an increase in the entropy of the system, which results in thermodynamically irreversible losses. Regarding fuel cells, irreversible thermodynamic losses are inevitably caused by heat transfer and chemical reactions in the system, such as polarization losses caused by the electrochemical reaction process of the fuel cell, heat losses that cannot be converted into electrical energy during the working process, and resistance losses caused by the current passing through the resistive elements in the cell. These irreversible thermodynamic losses have a significant impact on the performance and efficiency of fuel cells, which can be minimized by optimizing the

Nomenclature

A – activation area, cm^2
C_p – constant specific heat of the gas, J/(kg K)
DL – phosphate doping level
E – potential, V
Ex – exergy, W/m^2
e_n^{ch} – chemical exergy, J/mol
F – Faraday's constant, C/mol
f_{exd}^{fc} – exergy dissipation rate
ΔG – Gibbs free energy change, J/mol
$\Delta \dot{H}$ – enthalpy transition, W/m^2
j – current density, A/m^2
K – specific heat rate, J/(kg K)
n – number of electrons transferred
P – power density, W/m^2
p – pressure, atm
R – gas constant, J/(mol K)
RH – relative humidity, %
r – waste exergy ratio
ΔS – variation of standard molar entropy, J/mol
T – operating temperature, K
T_0 – ambient temperature, K
t – thickness, cm
U – voltage, V
x_n – mole fraction

Greek symbols

α – transfer coefficient
$\dot{\delta}$ – entropy production
η_{ex}^{fc} – exergy efficiency
σ – proton conductivity, S/m

Subscripts and superscripts

act – activation
ch – chemical
con – concentration
d – dissipation
fc – fuel cell
mem – membrane
ohm – ohmic
ph – physical
rev – reversible
rw – recyclable exergy waste
uw – unrecyclable exergy waste
w – waste exergy

Abbreviations and Acronyms

HT-PEMFC– high temperature proton exchange membrane fuel cell
ECOP – ecological coefficient of performance
EDI – exergy destruction index
ESI – exergy sustainability index
MOPSO– multi-objective particle swarm optimization
NSGA – nondominated sorting genetic algorithm
ORC – organic Rankine cycle
PBI – polybenzimidazole
SA – simulated annealing

design and improving the materials to achieve higher efficiency and performance of fuel cells [6]. A large number of researchers have made efforts to find more efficient materials and design methods in order to minimize these losses and improve the sustainability of fuel cells [7–9].

Numerous studies have been conducted to analyze and optimize the irreversible performance of fuel cells according to the first and second laws of thermodynamics. Atak et al. [10] investigated the thermodynamic performance of PEMFC using energy analysis and exergy analysis under a certain range of temperature and pressure, and the results showed that increasing the temperature improves the power density and exergy efficiency, and increasing the current density leads to an improvement in the entropy production, however, the effect of the pressure change on the irreversibility of PEMFC is not as visible as that of the temperature. Chen et al. [11] established a degradation model for predicting the lifetime of PEMFC and analyzed the thermodynamic performance during the whole lifetime based on the model, as well as discussing the influence of various currents on power, degradation rate and thermal efficiency. Lu et al. [12] proposed a PEMFC and organic Rankine cycle (ORC) cogeneration system to generate electricity by recovering the waste heat from the fuel cell stack through the ORC subsystem, and analyzed the thermodynamic performance under steady state and dynamic conditions based on this system. The results show that the exergy efficiency of this PEMFC system can reach 51% and the energy efficiency can reach 75%, and the rate of electric efficiency decrease with increasing current is reduced. Tayfun Özgür end Yakaryilmaz [13] investigated the energy and exergy performance of a PEMFC with output power of 1 kW, and the experimental results showed that the energy efficiency of the PEMFC was 45.58%, and that increasing the temperature and pressure allowed an increase in the physical exergy of all the reactants and products.

The performance can be significantly improved by numerically analyzing and optimizing the operating and design parameters of the PEMFC, which is a well-designed approach to save experimental expenses and time, and is more conducive to overall energy efficiency than time-consuming and laborious experimental studies. A large number of researchers have studied fuel cells using advanced optimization algorithms and parametric analysis methods [14,15]. Chen et al. [16] analyzed the electrochemical and thermodynamic properties of PEMFC using parametric studies, and achieved efficiency and power improvement by optimizing the operating parameters of PEMFC using a novel evolutionary algorithm, and the final optimization results showed that the energy efficiency of PEMFC could reach 79% and the power could reach 8.04 kW. Xu et al. [17] investigated the effects of operating parameters on the irreversibility and exergy performance of HT-PEMFC under different operating conditions and optimized the performance of HT-PEMFC using Manta Ray Foraging Optimization Algorithm. Lin et al. [18] analyzed the exergy efficiency of HT-PEMFC using the meta-heuristics method as well as evaluated and optimized the thermodynamic irreversibility of HT-PEMFC using an improved collective animal behavior algorithm. The results show that the algorithm has stronger convergence speed and optimization efficiency compared to the genetic algorithm. It is evident from pre-

vious studies that optimization of parameters to match the best operating conditions of the HT-PEMFC can reduce irreversible losses and improve efficiency.

The multi-objective particle swarm optimization (MOPSO) is to use the external population archive to store all the current non-dominated solutions, and regard the individuals in the external archive as the elite individuals, control the direction of population evolution through the elite individuals, and guide the population to approximate the real Pareto frontier, and take the particles in the external archive as the obtained approximation of the Pareto optimal solution at the end of the algorithm operation. The MOPSO algorithm has been widely used in the energy field to solve multi-objective optimization problems. Ehyaei et al. [19] used MOPSO algorithm to optimize the thermodynamic performance of parabolic through collector based on energy, exergy and economic analysis, and the optimal results were calculated with maximum exergy efficiency and minimum heat generation. Yuan et al. [20] designed an optimization algorithm based on the MOPSO algorithm and grey correlation analysis, as well as employed this algorithm to optimize a multi-objective energy scheduling problem for a hybrid solid oxide fuel cell and solar hybrid cogeneration system.

Few literatures about ecological performance analysis in HT-PEMFC have been published by far and even fewer papers focus on the ecological coefficient of performance (ECOP) as an optimization function for the thermodynamic performance of HT-PEMFC. The ECOP is an important evaluation index for irreversible thermodynamic and ecological performance, and optimizing ECOP can reduce power loss to benefit the environment. Therefore, in this paper, the ECOP, P and efficiency as the multi-objective optimization function for analyzing and optimizing the thermodynamic performance while maintaining the power of HT-PEMFC is still required. The population distribution of the optimization variables was analyzed using a 3D Pareto frontier analysis, and the popular nondominated sorting genetic algorithm II (NSGA-II) and simulated annealing algorithm (SA) have been chosen versus MOPSO algorithm for making the optimization comparative analysis.

2. Model development

The principles of redox reactions can be simplified and stated as follows [16]:

$$\mathrm{H_2} \rightarrow 2\mathrm{H^+} + 2e^-, \tag{1}$$

$$2\mathrm{H^+} + \frac{1}{2}\mathrm{O_2} + 2e^- \rightarrow \mathrm{H_2O} + \text{heat}, \tag{2}$$

$$\mathrm{H_2} + \frac{1}{2}\mathrm{O_2} \rightarrow \mathrm{H_2O} + \text{heat} + \text{electricity}. \tag{3}$$

In addition, some assumptions about modeling are provided below:

- The HT-PEMFC is operated in steady state [4].
- The fuel is a mixture of hydrogen and water [21].
- The movement of reactants exhibits laminar flow [10].
- The consideration of kinetic and potential energy of hydrogen is omitted [16].
- The corrosion reactions at the electrodes are neglected [22].

The values of basic designing and operating parameters used in this paper are obtained from Ref. [22], which can be shown in Table 1.

Table 1. Operating and design parameters [22].

Parameter	Value	Unit	Parameter	Value	Unit
T	413~473	K	R	8.314	J/(mol·K)
p	1~3	atm	j	0~20000	A/m²
RH	0~7.6	%	T_0	298.15	K
DL	2~10	-	α	0.25	-
t_{mem}	0.005	cm	n	2	-
F	96485	C/mol	A_{mem}	600	cm²

2.1. Electrochemical description

The reversible voltage E_{rev} can be calculated by [1]:

$$E_{rev} = E_r^0 + \frac{\Delta S}{nF}(T - 298.15) + \frac{RT}{n_e F}\ln\left(\frac{p_{\mathrm{H_2}} p_{\mathrm{O_2}}^{0.5}}{p_{\mathrm{H_2O}}}\right), \tag{4}$$

where E_r^0 is the ideal standard potential, R is the gas constant, ΔS is the variation of standard molar entropy, T is the temperature. The correlation between ΔS and T reads:

$$\frac{\Delta S}{n_e} = -18.449 - 0.01283T. \tag{5}$$

(1) Activation overpotential

The E_{act} taking the effect of leakage current into account can be calculated by:

$$E_{act} = \frac{RT}{\alpha nF}\ln\left(\frac{j + j_{leak}}{j_0}\right), \tag{6}$$

where α is the transfer coefficient, j is the current density, j_{leak} is the leakage current density, j_0 is the exchange current density. The correlation between j_{leak} and T is calculated by [2]:

$$\ln j_{leak} = -2342.9\left(\frac{1}{T}\right) + 9.0877. \tag{7}$$

(2) Ohmic overpotential

The E_{ohm} is given by:

$$E_{ohm} = j(R_{ion} + R_{ele}) = jR_{ion} = j\frac{t_{mem}}{\sigma_{mem}}, \tag{8}$$

where t_{mem} is the thickness of the membrane, σ_{mem} is the proton conductivity.

(3) Concentration overpotential

The E_{con} is expressed as [3]:

$$E_{con} = \left(1 + \frac{1}{\alpha}\right)\frac{RT}{nF}\ln\left(\frac{j_L}{j_L - j}\right), \tag{9}$$

where j_L is the limiting current density.

The total internal resistance due to these three overpotentials can be calculated by:

$$R_{int} = \frac{E_{act} + E_{ohm} + E_{con}}{A_{mem} j}, \tag{10}$$

where A_{mem} is the activated area.

Combining Eqs. (6)–(10), the voltage U can be calculated as:

$$U = E_{rev} - \left(1 + \frac{1}{\alpha}\right)\frac{RT}{nF}\ln\left(\frac{j_L}{j_L - j}\right) - \frac{RT}{\alpha nF}\ln\left(\frac{j + j_{leak}}{j_0}\right) - j\frac{t_{mem}}{\sigma_{mem}}. \quad (11)$$

The power density can be calculated as:

$$P = jU = j(E_{rev} - E_{con} - E_{act} - E_{ohm}). \quad (12)$$

2.2. Thermodynamic description

When fuel cell operates, oxygen and hydrogen interact in a redox reaction [11], and the total energy released by the electrochemical reaction is equivalent to enthalpy variation, i.e. $-\Delta\dot{H}$, which can be calculated by:

$$-\Delta\dot{H} = -\frac{jA\Delta h}{nF}. \quad (13)$$

The $-\Delta\dot{H}$ can be described by:

$$-\Delta\dot{H} = -\Delta G - T\Delta S. \quad (14)$$

Total energy can be categorized into electrical energy and thermal energy, which is due to the enthalpy variation being lower than the Gibbs free energy, and a portion that cannot be converted to electricity is released to thermal energy [4]. This fraction is denoted by $-\Delta G + \Delta\dot{H}$, which is equal to $T\Delta S$, and ΔS is called the entropy [2].

Based on the laws of thermodynamics, thermal efficiency can be calculated by [2]:

$$\eta = \frac{P}{-\Delta\dot{H}}. \quad (15)$$

Based on the representation of *ECOP* in Ref. [5], it can be calculated by:

$$ECOP = \frac{PT}{T_0(-\Delta\dot{H} - P)}. \quad (16)$$

ECOP is a crucial irreversible thermodynamic indicator due to the advantage of compromising the weights of power and efficiency.

Moreover, the exergy analysis of irreversible thermodynamics is used to study and optimize the recoverable energy and unrecoverable losses during fuel cell operation [6]. The exergy balance can be represented as:

$$Ex_{in}^{fc} = P + Ex_{w,out}^{fc} + Ex_d^{fc}, \quad (17)$$

where Ex_{in}^{fc} is the total input exergy, $Ex_{w,out}^{fc}$ is the waste exergy, and Ex_d^{fc} is the exergy dissipation.

Therefore, the exergy dissipation can be obtained as:

$$Ex_d^{fc} = Ex_{in}^{fc} - P - Ex_{w,out}^{fc}. \quad (18)$$

Recoverable exergy wastes are losses that can be recycled, e.g. remaining hydrogen can be recycled and used to generate energy [6], the unrecoverable exergy waste is a loss that cannot be reused, such as waste heat:

$$Ex_{w,out}^{fc} = Ex_{rw}^{fc} + Ex_{uw}^{fc}, \quad (19)$$

where Ex_{rw}^{fc} is the recoverable exergy, and Ex_{uw}^{fc} is the unrecoverable exergy.

The recoverable exergy is mainly the chemical exergy of the remaining hydrogen and oxygen and can be expressed as:

$$Ex_{rw}^{fc} = n_{\mathrm{H}_2,out} \cdot ex_{\mathrm{H}_2,out}^{ch} + n_{\mathrm{O}_2,out} \cdot ex_{\mathrm{O}_2,out}^{ch}, \quad (20)$$

where $n_{\mathrm{H}_2,out}$ is the mole fraction of hydrogen, $ex_{\mathrm{H}_2,out}^{ch}$ is the standard chemical exergy of hydrogen, $n_{\mathrm{O}_2,out}$ is the mole fraction of oxygen, and $ex_{\mathrm{O}_2,out}^{ch}$ is the standard chemical exergy of oxygen.

The unrecoverable exergy is mainly the physical exergy of the discharged hydrogen, oxygen and water as well as the waste heat, and can be expressed as [1]:

$$Ex_{uw}^{fc} = (n_{\mathrm{H}_2,out} \cdot ex_{\mathrm{H}_2,out}^{ph} + n_{\mathrm{O}_2,out} \cdot ex_{\mathrm{O}_2,out}^{ph} + \\ + n_{\mathrm{H_2O},out} \cdot ex_{\mathrm{H_2O},out}^{ph}) + Q_{w,out}^{fc}\left(1 - \frac{T_0}{T}\right), \quad (21)$$

where $n_{\mathrm{H_2O},out}$ is the mole fraction of water, $ex_{\mathrm{H_2O},out}^{ph}$ is the standard chemical exergy of water, and $Q_{w,out}^{fc}$ is the waste heat of the fuel cell.

The exergy destruction index *EDI* is used to numerically describe the environmental impact of unrecoverable exergy losses in this paper, and larger values of *EDI* indicating that the irreversible thermodynamic process is more damaging to environment; it can be calculated by [7]:

$$EDI = \frac{Ex_{uw}^{fc} + Ex_d^{fc}}{P}. \quad (22)$$

The exergy sustainability index *ESI* can be calculated by [2]:

$$ESI = \frac{P}{EDI \cdot (P + Ex_{w,out}^{H_2} + Ex_{w,out}^{O_2} + Ex_d^{fc})}. \quad (23)$$

2.3. MOPSO optimization

2.3.1. Description of MOPSO algorithm

The MOPSO is a bionic algorithm derived from imitating the hunting behaviour of birds, which is based on the principle of randomly distributing a certain number of particles in the feasible domain, and each particle flies at a certain speed and direction and adjusts the direction and speed of the next moment by combining with its own current optimal position and the optimal position of the group, and ultimately achieves the purpose of searching for the optimal solution domain [8].

Suppose the search space is D dimensional and the entire particle population is N_S, the velocity and position of the particle i at the t iteration are $v_i^t = (v_{i,1}^t, v_{i,2}^t, \ldots, v_{i,D}^t)$, and $x_i^t = (x_{i,1}^t, x_{i,2}^t, \ldots, x_{i,D}^t)$, respectively; the optimal position searched so far by the particle i at the t iteration is $p_i^t = (p_{i,1}^t, p_{i,2}^t, \ldots, p_{i,D}^t)$, i.e. the personal best position; the optimal position searched so far by the population at the t iteration is $g^t = g_1^t, g_2^t, \ldots, g_D^t, ,$ i.e. the global best position. At the $t+1$ iteration, the particles adjust their forthcoming velocity and location in the search space, incorporating insights gained from their personal history as well as the sharing experiences of the

entire population [8,9]. The velocity and position updates of the particle swarm optimization algorithm with inertia weights can be represented by Eq. (24) and (25), respectively:

$$v_{i,j}^{t+1} = \omega^* v_{i,j}^t + c_1 r_1 (p_{i,j}^t - x_{i,j}^t) + c_2 r_2 (g_j^t - x_{i,j}^t), \quad (24)$$

$$x_{i,j}^{t+1} = x_{i,j}^t + v_{i,j}^{t+1}, \quad (25)$$

where t is the number of iterations, c_1, c_2 are constants, r_1, r_2 are random numbers, ω^* is the inertia weight, $p_{i,j}^t$ is the individual position, g_j^t is the global optimum position, and $j = 1,2,\ldots,D$ is the dimension.

The position of the particle is updated schematically as shown in Fig. 1.

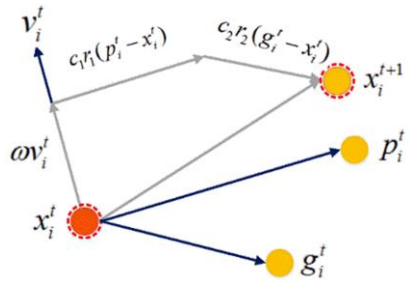

Fig. 1. Schematic diagram for updating the position of a particle.

2.3.2. Determination of optimization variables and objective function

Considering that the thermodynamic performance of HT-PEMFC is affected by multiple parameters and there are various indexes to evaluate the irreversible loss in the working process from different perspectives, and that each performance evaluation index has its advantages and imperfections. Based on the established model and previous studies, it is seen that the operating and design parameters such as the temperature T, pressure p, relative humidity RH, and phosphate doping level DL have a large impact on the performance of the HT-PEMFC, and different configurations of the operating parameters determine the output performance of the HT-PEMFC. Therefore, in this paper, not only the effects of the above parameters on the thermodynamic performance of HT-PEMFC are analyzed, but also these parameters are used as optimization variables to improve the thermodynamic performance of HT-PEMFC. Moreover, the power P and efficiency η are the most widely used basic metrics for evaluating fuel cells, while $ECOP$ is an important indicator in thermodynamics to quantify the irreversible thermodynamic loss of fuel cells; therefore, the P, efficiency η, and $ECOP$ are selected as the objective functions in order to improve the output performance of the HT-PEMFC in a more comprehensive way and to reduce the irreversible thermodynamic loss in this paper. The range of the determined optimization variables and the objective function are shown in Table 2.

Table 2. The optimization variables and the objective function.

Optimization variables and ranges		Objective function
T	413~473 K	P
p	1~3 atm	η
RH	0~7.6 %	$ECOP$
DL	2~10	-
j	0~20000 A/m^2	-

The flowchart of the MOPSO algorithm is shown in Fig. 2. The optimization procedure is as follows:

1) Initialize the random parameters, and create the external archive.
2) Calculate the objective function of the particle swarm. Evaluate the particles and conduct Pareto sorting.

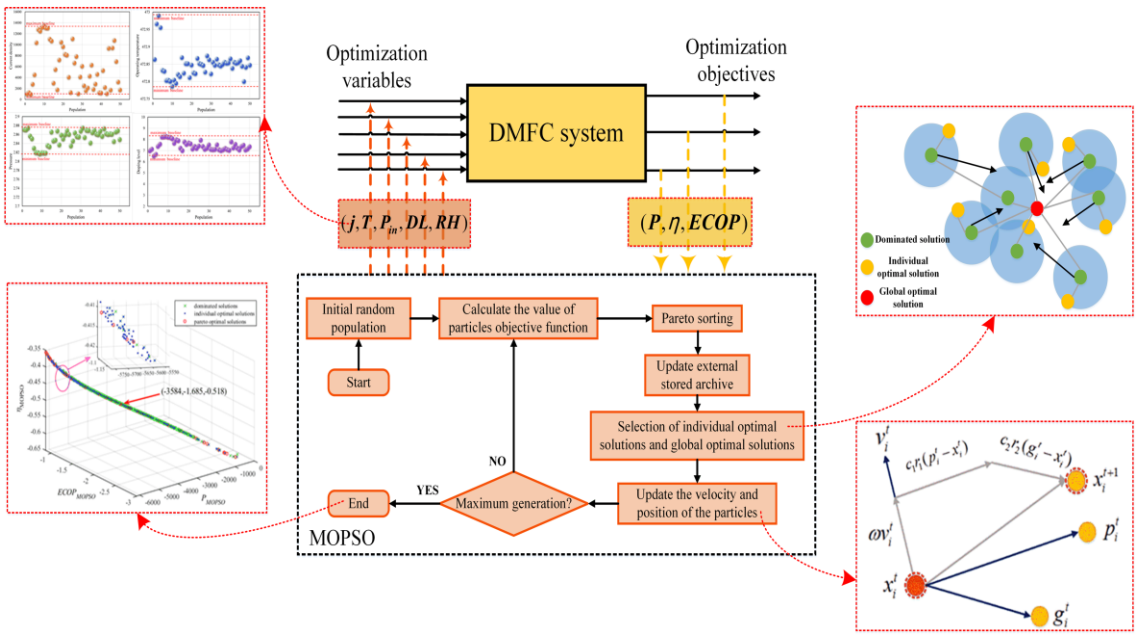

Fig. 2. The flowchart of the MOPSO algorithm.

3) Store the non-dominated solutions into the external archive and update it.
4) Select the individual optimal solution and the global optimal solution.
5) Update the velocity and position of the particles.
6) Return to 2) if the maximum iteration is not reached, and exit the loop if the maximum iteration is reached.

3. Results and discussion

3.1. Validation of the HT-PEMFC model

The output voltage of HT-PEMFC versus j found based on the above equations for the E_{rev}, E_{con}, E_{ohm}, E_{act} is illustrated in Fig. 3a To verify the *U-I* curve, Fig. 3b shows the comparison between model predictions and experimental data of Scott et al. [10]. It can be seen that the theoretical predictions are basically consistent with the experimental data.

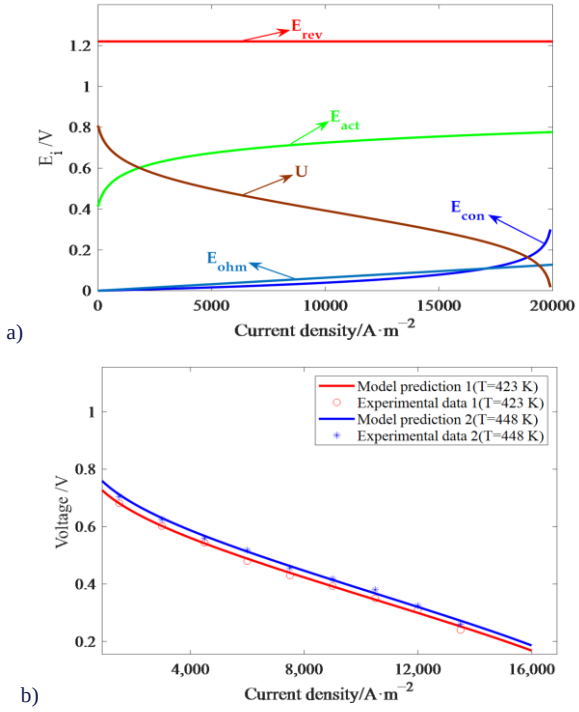

Fig. 3. The model validation: a) curves of potential, activation overpotential, concentration overpotential, ohmic overpotential and voltage versus current density, b) comparison of curves between model results and experimental data.

3.2. Effect of operating and design parameters

It can be seen from Fig. 4a and Fig. 4b that increasing the temperature of HT-PEMFC has an obvious effect on *P*, *ECOP* and *EDI*, mainly due to the fact that the increase in temperature enhances the catalytic activity of the electrodes, which accelerates the redox reaction rate of hydroxide. The maximum power density can reach 5300 W/m^2 when the temperature is 473 K, which is an increase of 58.3% compared to when the temperature is 413 K. As the electrochemical reaction proceeds, *P*, *ESI* and *ECOP* are significantly enhanced by increasing temperature, but *EDI* is decreased, this is due to the fact that the elevation of *T* greatly enhances the electrochemical reaction rate, which reduces the fuel emissions and facilitates the reduction of the loss of exergy and the impact on the environment.

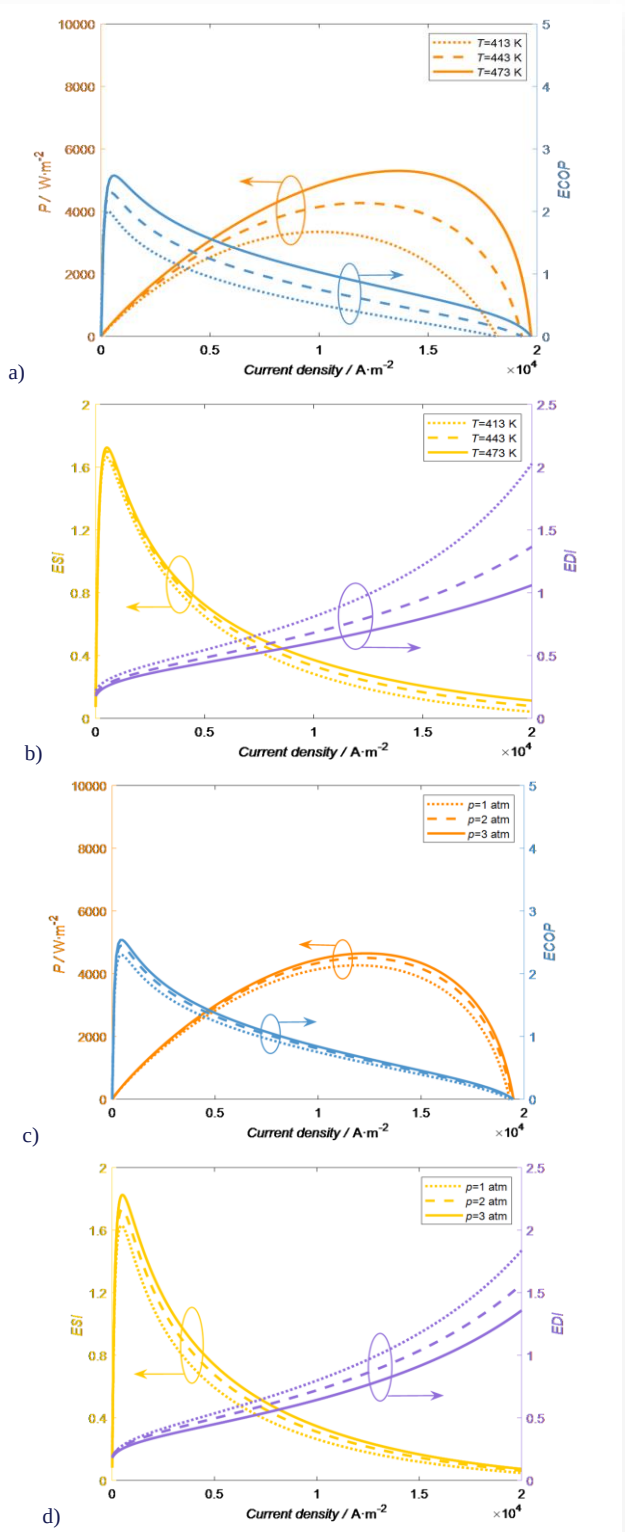

Fig. 4. Curves of *P* and *ECOP* versus current density under: a) different operating temperature, c) different operating pressure. Curves of *ESI* and *EDI* versus current density under: b) different temperature, d) different pressure.

From Figs. 4c and 4d, the maximum power density can reach 4648 W/m^2 when the pressure is 3 atm, which is an increase of 8.9% compared to when the operating pressure is 1 atm. It is

clear that *P*, *ECOP*, *ESI* and *EDI* are less affected by pressure in the range of low current densities, which is due to the low rate of electrochemical reaction. The rate of electrochemical reaction is rising very quickly in the range of high current densities, the irreversible losses are reduced by increasing pressure.

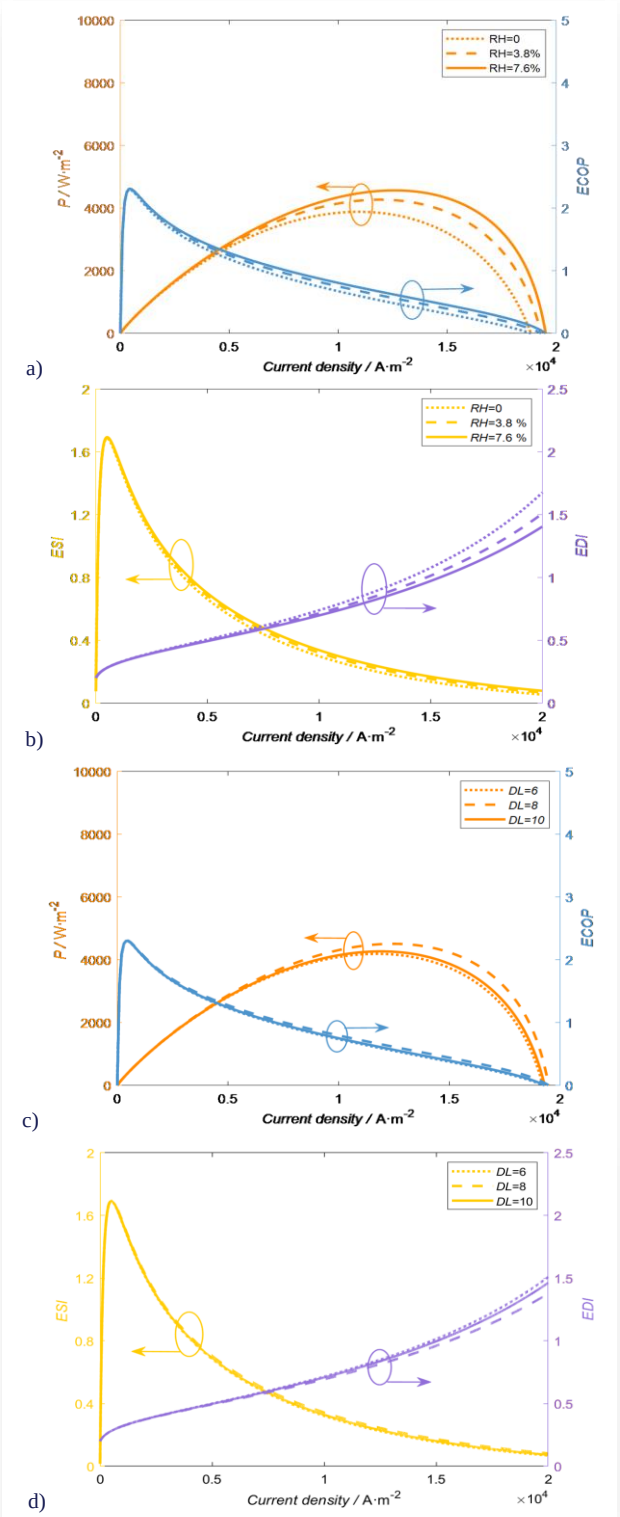

Fig. 5. Curves of *P* and *ECOP* versus current density under: a) different relative humidity, c) different *DL*. Curves of *ESI* and *EDI* versus current density under: b) different relative humidity, d) different *DL*.

The proton conductivity is increased by improving relative humidity, as shown in Fig. 5a and Fig. 5b, where *P* and *ECOP* are enhanced by increasing relative humidity.

When the relative humidity is 7.6%, the maximum power density of HT-PEMFC can reach 4565 W/m^2, which is an increase of 17.7% compared to when the relative humidity is zero. As illustrated in Fig. 5c and Fig. 5d, *P*, *ECOP* and *ESI* first grow and then fall with the rise of *DL*, reaching a maximum at *DL* of 8. A proper increase in *DL* can help to improve proton conductivity while reducing irreversible losses. However, excessive *DL* can damage the structure of PBI, such as affecting the attachment rate of phosphoric acid on the catalytic layer, and resulting in a decrease in proton conductivity [7].

3.3. Optimization results

The optimized Pareto frontier curve of the MOPSO algorithm is shown in Fig. 6. The green fork represents the dominated solutions of the MOPSO algorithm, the blue dots are the individual optimal solutions, and the red hexagrams are the non-dominated group optimal solutions, i.e. the Pareto frontier. Because the MOPSO algorithm procedure used in this paper is a minimum value seeking method, the function set in this procedure is the opposite of the objective function, i.e. $P_{MOPSO}(x_k) = -P(x_k)$, $ECOP_{MOPSO}(x_k) = -ECOP(x_k)$, $\eta_{MOPSO}(x_k) = -\eta(x_k)$, thus seeking the maximum value of the original function, therefore the axis in Fig. 6 is minus. Since the three optimization objective functions of *P*, efficiency and *ECOP* are taken into account, the final optimization result should not only be picked in the Pareto frontier, but also satisfy that each objective function should not be worse. Therefore, after carrying out several optimizations, we chose the Pareto point with the coordinates of –3584, 1.685, −0.518, and its corresponding values of the optimal parameter variables are shown in Table 3.

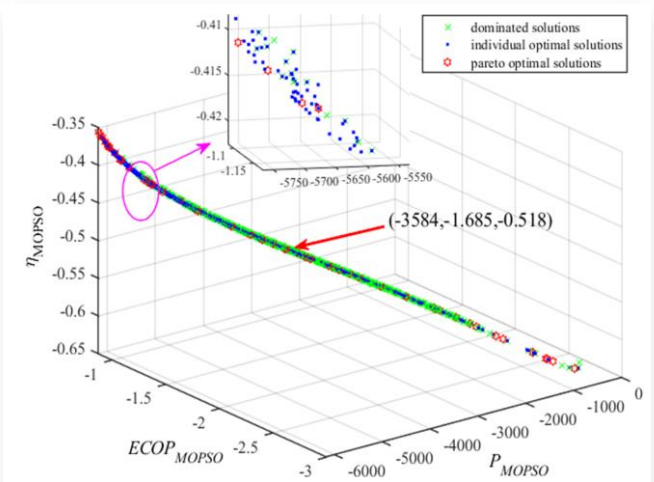

Fig. 6. The optimized Pareto frontier curve of the MOPSO algorithm.

The population distribution of the optimization variables corresponding to the Pareto optimal solutions is shown in Fig. 7. The distribution of current densities is shown in Fig. 7a, and it can be seen that the current densities corresponding to the optimal solutions obtained from the MOPSO optimization are uniformly distributed between 0 and 14000 A/m^2, which is due to

the optimal solutions of the multi-objective optimization selecting different values of weights for each objective. The distribution of operating temperatures is shown in Fig. 7b, and it can be seen that most of the temperatures corresponding to the optimal solutions are between 472.8 K and 472.9 K, which indicates that higher temperatures are useful for the power, efficiency and *ECOP*. The distribution of pressures is shown in Fig. 7c, and it can be seen that most of the pressures corresponding to the optimal solutions are in the range of 2.82 atm to 2.88 atm, which indicates that higher pressures are beneficial for improving performance. The distribution of *DL* is shown in Fig. 7d, and most of the pressures corresponding to the optimal solutions are between 7 and 8, which shows that the *DL* should not be either excessive or insufficiently low for improving irreversible thermodynamic performance.

Table 3. Optimal parameter selection for HT-PEMFC.

	Preoptimized	MOPSO	NSGA-II	SA1	SA2	SA3
Objectives	-	*P, ECOP, η*	*P, ECOP, η*	*P*	*ECOP*	*η*
***j* (A/m²)**	0~20000	7825	6629	13974	5994	6069
***T* (K)**	443	472.88	471.98	469.08	462.00	464.20
***p* (atm)**	2	2.98	2.92	3.00	2.66	3.00
***RH* (%)**	3.8	7.15	7.20	7.48	7.52	7.11
DL	6	8.23	7.90	8.37	9.00	7.60

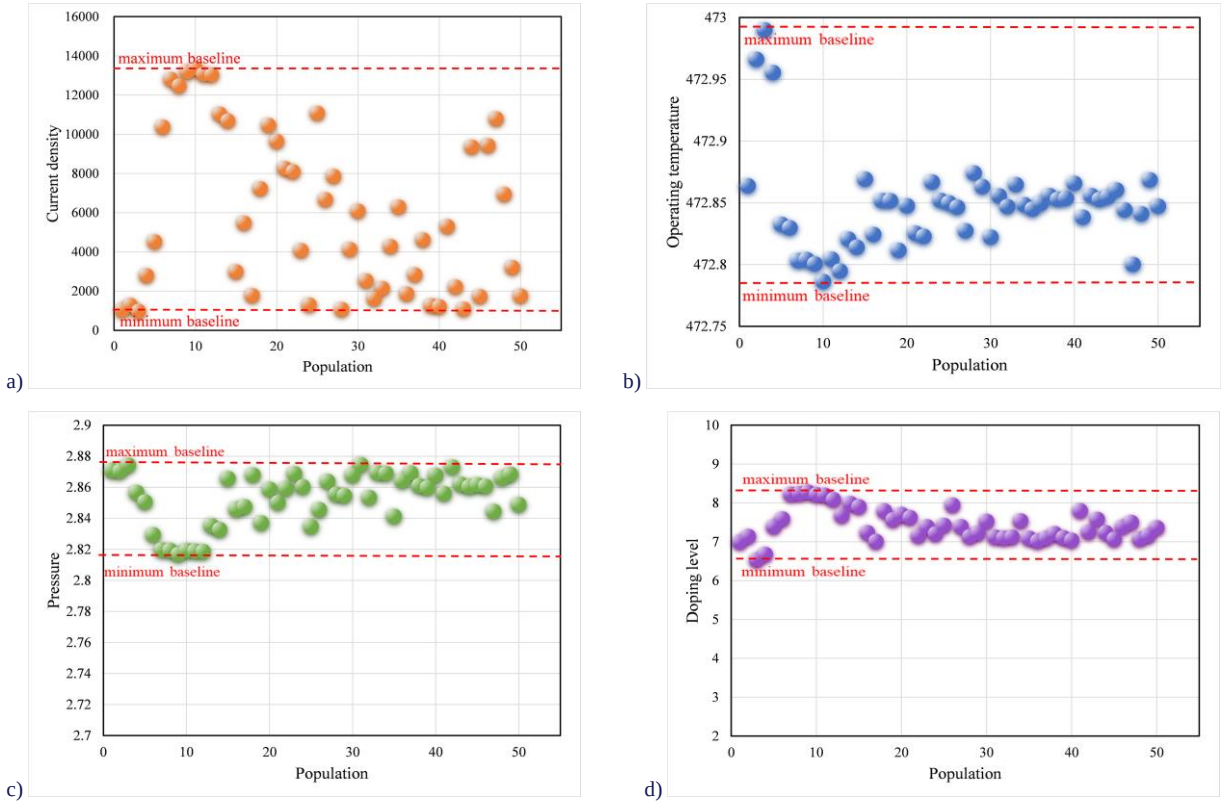

Fig. 7. Population distributions of current density (a), operating temperature (b), pressure (c) and doping level (d).

The optimized Pareto frontier curve of NSGA-II algorithm is shown in Fig. 8a, the red pentagrams are the Pareto frontier of multi-objective optimization, after performing several optimizations, we chose the Pareto point with the coordinates 3088, 1.87, 0.5413, and the values of the optimal parameter variables corresponding to it are shown in Table 3.

The optimization results of the SA algorithm are shown in Figs. 8b, 8c and 8d. In this study, the SA algorithm is a single objective optimization algorithm. Therefore, the optimization objective functions are power density, *ECOP* and efficiency, and the optimized solutions tend to be stable after several optimizations. The three optimal solutions with power density, *ECOP* and efficiency as the optimization objective functions are 6281.67 W/m^2, 1.617 and 51.1%, respectively, and the corresponding values of the optimal parameter variables are shown in Table 3.

In order to compare the convergence speed and optimization accuracy of two multi-objective algorithms more precisely, the Ackley test function is introduced in this paper for comparative analysis, which can detect the global convergence speed of an algorithm. The directional gradients of the Ackley function are various when the dimension increases. As shown in Fig. 9 for

the graph of Ackley, it can be seen that its minimal value is 0. The optimization algorithm can easily fall into the trap of local minimal value. In order to fairly evaluate the advantages and disadvantages of the algorithms, the number of iterations set are all 500, and the population size are all 100. In the NSGA-II algorithm involving crossover probability and mutation probability, are set to 0.7 and 0.01, respectively. whereas in the MOPSO algorithm involving the initial inertia factor weights are set to 0.9, and the inertia factor at the time of iterating to the maximum number of evolutionary generations is 0.4.

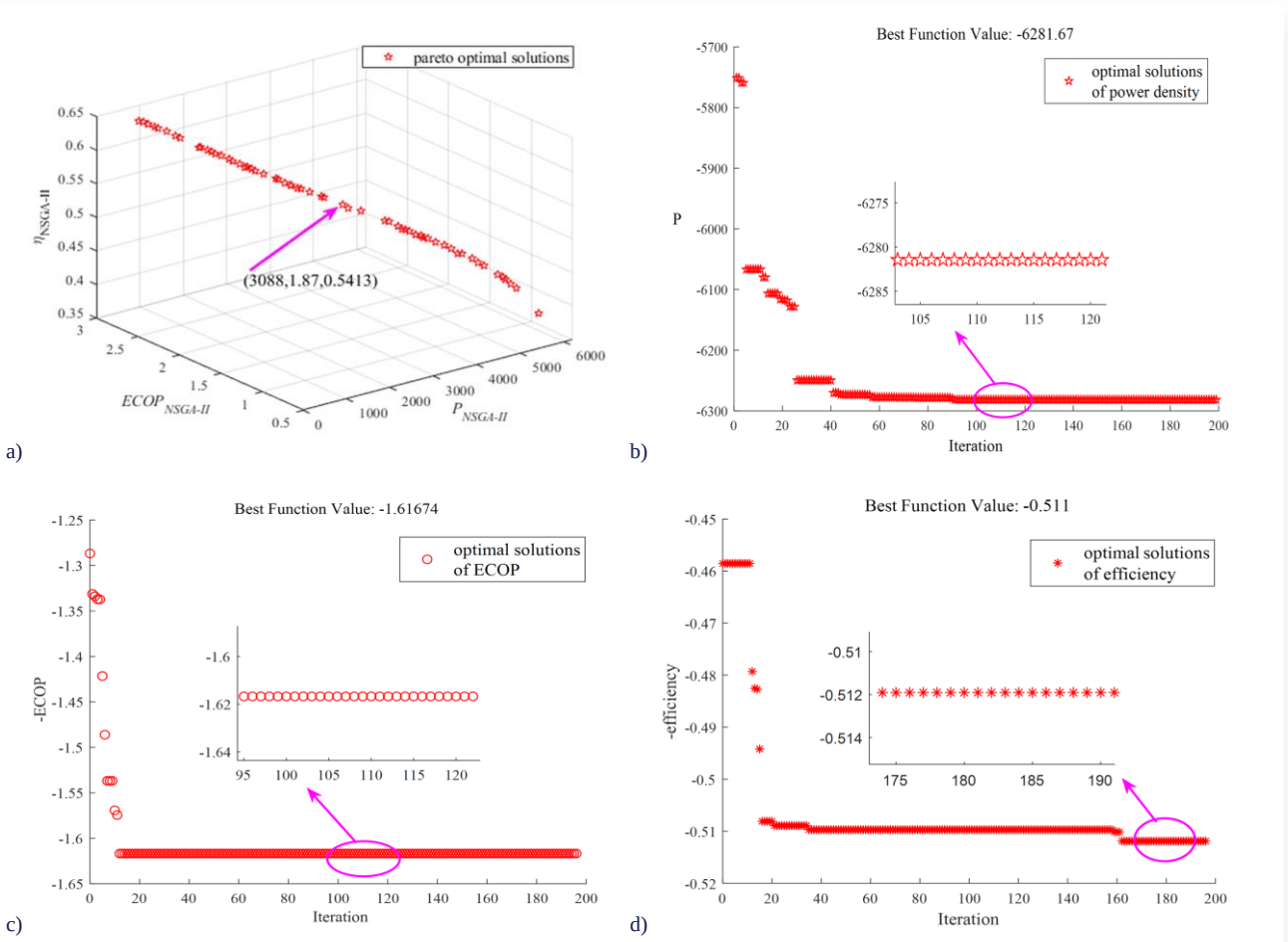

Fig. 8. The optimized Pareto frontier curve of NSGA-II algorithm (a) and the optimization results of the SA algorithm (b-d).

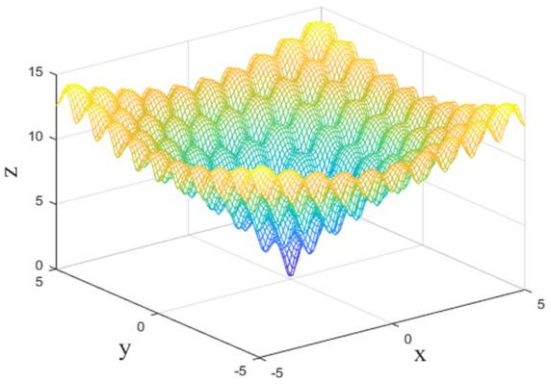

Fig. 9. A graph of the Ackley test function.

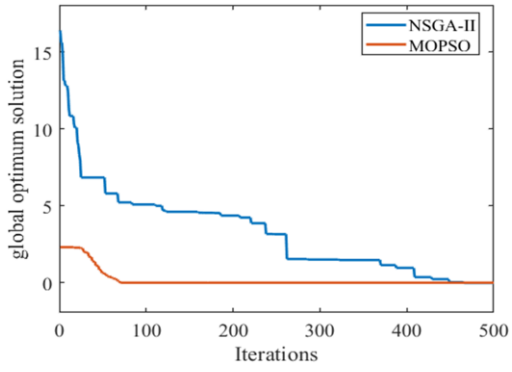

Fig. 10. Comparison of global optimal solutions.

The variation of the global optimal solution with the number of iterations for the MOPSO algorithm and the NSGA-II algorithm for optimization of the Ackley test function is shown in Fig. 10. It can be seen that the MOPSO algorithm finds the global minima within less than 100 iterations, while the NSGA-II algorithm finds the minima only after a number of iterations greater than 400.

Figure 11 shows the variation of the individual (historical) optimal solutions of the MOPSO algorithm and the NSGA-II algorithm with the number of iterations in finding the optimal so-

lution to the Ackley test function when the spatial dimensions of the Ackley test function are taken from the first to the tenth dimension. It can be seen that the MOPSO algorithm is the first to find the extrema in most cases. However, the NSGA-II algorithm always has problems finding local minima, such as in the 1st, 3rd and 10th dimension cases. Moreover, the NSGA-II algorithm shows oscillatory changes in the historical optimal solution when the number of iterations is small.

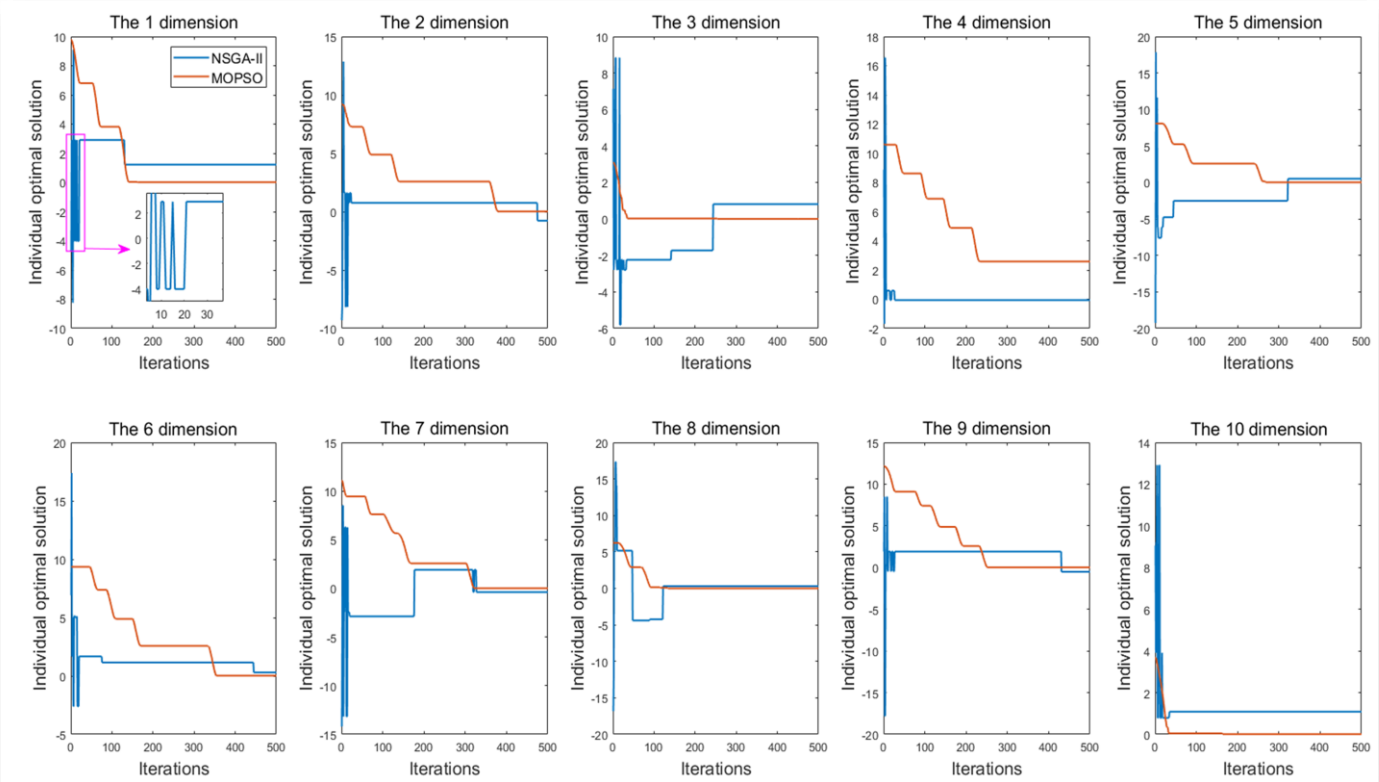

Fig. 11. The variation of the individual (historical) optimal solutions of the MOPSO algorithm and the NSGA-II algorithm.

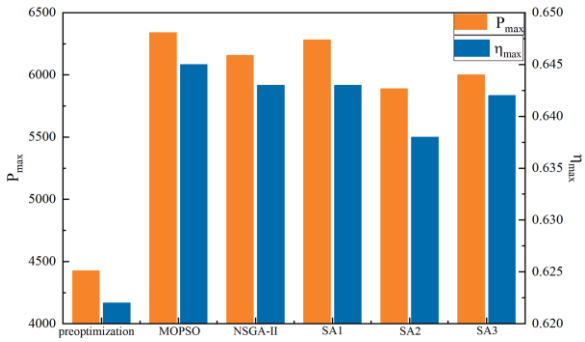

Fig. 12. The optimal result comparison for maximum power density and maximum efficiency.

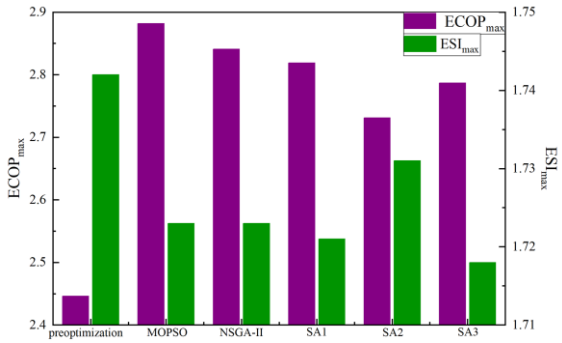

Fig. 13. The optimal result comparison for maximum ECOP and maximum ESI.

From the above results, it can be seen that the MOPSO algorithm is faster in finding the optimum compared to the NSGA-II algorithm and is more accurate and less likely to fall into local extremes.

By using the optimal parameters of the MOPSO algorithm as inputs to the HT-PEMFC model, the obtained maximum power density, maximum efficiency, maximum *ECOP* and maximum *ESI* are compared with the preoptimized results and the results optimized by other algorithms as shown in Figs. 12 and 13. The MOPSO algorithm yields the best performance, with the maximum power density, maximum efficiency, and maximum *ECOP* being 6340 W/m^2, 64.5% and 1.723, respectively, which are 43.28%, 3.7% and 17.8% higher than the preoptimized HT-PEMFC, but the maximum *ESI* is slightly reduced.

4. Conclusions

An irreversible thermodynamic model of HT-PEMFC is established to study the effects of different operating parameters and design parameters on the thermodynamic performance, four parameters including *T*, *DL*, *p*, and *RH* are considered in this work, while *P*, *ECOP* and efficiency are used as the optimization objective functions. The primary findings are summarized as follows:

1) The validation of the irreversible thermodynamic model for HT-PEMFC was conducted through comparison with experimental data.
2) Temperature and pressure have a significant effect on the increase of *P*, *ECOP*, *ESI* and decrease of *EDI*, while *DL* and *RH* have a lesser effect.
3) The population distribution of the optimization variables of the optimal solutions is analyzed based on the 3D Pareto frontier of the MOPSO algorithm, which results in a uniform distribution of the current density in the operating range due to the different weight accounting for each optimization objectives. Temperature and pressure are maintained in the high value region of the operating range, while *DL* is stably distributed between 7 and 8.
4) Parameter optimization of HT-PEMFC using MOPSO algorithm and comparison with the optimization results of NSGA-II algorithm and SA algorithm show that MOPSO algorithm performs well for multi-objective optimization as a function of *P*, *ECOP* and efficiency, with the maximum power density, maximum efficiency, and maximum *ECOP* being 6340 W/m^2, 64.5% and 1.723, respectively, which are 43.28%, 3.7% and 17.8% higher than those of the preoptimized HT-PEMFC.

The conclusions obtained in this paper regarding the future development of HT-PEMFC design and integration into existing systems are: firstly, by considering the effects of temperature and pressure on performance, new membrane electrode materials can be investigated and developed to adapt to operating environments at higher temperatures and pressures, which can help to improve the stability and durability of HT-PEMFC. Secondly, when integrating into an existing system, the effects of operating and design parameters need to be considered, and the system architecture and operating conditions need to be adjusted accordingly, and the MOPSO algorithm can provide guidance for the design of HT-PEMFC systems to achieve optimal performance. In addition, in terms of optimization algorithm selection, future HT-PEMFC developments could consider using the MOPSO algorithm as the preferred parameter optimization algorithm to achieve multi-objective optimization of power, ecological performance and efficiency. By comparing the optimization results of different parameter combinations, the optimal system configuration can be determined to guide future HT-PEMFC development.

Acknowledgements

The research was supported by the financial support of the National Natural Science Foundation of China (No. 51306079 and 51176069), the Postgraduate Research & Practice Innovation Program of Jiangsu Province and Scientific Research Foundation of Nanjing Forestry University (No. GXL2018004).

References

[1] Abdul Rasheed, R.K., Liao, Q., Caizhi, Z., & Chan, S.H. (2017). A review on modelling of high temperature proton exchange membrane fuel cells (HT-PEMFCs). *International Journal of Hydrogen Energy*, 42(5), 3142–3165. doi: 10.1016/j.ijhydene.2016.10.078

[2] Li, Y., Yang, M., Ma, Z., Zheng, M., Song, H., & Guo, X. (2022). Thermodynamic modeling and exergy analysis of a combined High-temperature proton exchange membrane fuel cell and ORC system for automotive applications. *International Journal of Molecular Sciences*, 23(24). doi: 10.3390/ijms232415813

[3] Rosli, R.E., Sulong, A.B., Daud, W R. W., Zulkifley, M.A., Husaini, T., Rosli, M.I., Majlan, E.H., & Haque, M.A. (2017). A review of high-temperature proton exchange membrane fuel cell (HT-PEMFC) system. *International Journal of Hydrogen Energy*, 42(14), 9293–9314. doi: 10.1016/j.ijhydene.2016.06.211

[4] Rosli, R.E., Sulong, A.B., Daud, W.R.W., Zulkifley, M.A., Husaini, T., Rosli, M.I., Majlan, E.H., & Haque, M.A. (2017). Modeling and analysis of a 5 kW HT-PEMFC system for residential heat and power generation. *International Journal of Hydrogen Energy*, 42(3), 1698–1714. doi: 10.1016/j.ijhydene.2016.10.152

[5] Yang, M., & Tian, J. (2023). Longitudinal and Lateral Stability Control Strategies for ACC Systems of Differential Steering Electric Vehicles. *Electronics*, 12(19). doi: 10.3390/electronics12194178

[6] Chen, Z., Zuo, W., Zhou, K., Li, Q., Huang, Y., & E, J. (2023). Multi-factor impact mechanism on the performance of high temperature proton exchange membrane fuel cell. *Energy*, 278, 127−982. doi: 10.1016/j.energy.2023.127982

[7] Lei, G., Zheng, H., Zhang, J., Siong Chin, C., Xu, X., Zhou, W., & Zhang, C. (2023). Analyzing characteristic and modeling of high-temperature proton exchange membrane fuel cells with CO poisoning effect. *Energy*, 282, 128−305. doi: 10.1016/j.energy.2023.128305

[8] Jannat, S., Rashtchi, H., Atapour, M., Golozar, M.A., Elmkhah, H., & Zhiani, M. (2019). Preparation and performance of nanometric Ti/TiN multi-layer physical vapor deposited coating on 316L stainless steel as bipolar plate for proton exchange membrane fuel cells. *Journal of Power Sources*, 435, 226−818. doi: 10.1016/j.jpowsour.2019.226818

[9] Salimi Nanadegani, F., Nemati Lay, E., & Sunden, B. (2020). Computational analysis of the impact of a micro porous layer (MPL) on the characteristics of a high temperature PEMFC. *Electrochimica Acta*, 333, 135−552. doi: 10.1016/j.electacta.2019.135552

[10] Atak, N.N., Dogan, B., & Yesilyurt, M.K. (2023). Investigation of the performance parameters for a PEMFC by thermodynamic analyses: Effects of operating temperature and pressure. *Energy*, 282, 128907. doi: 10.1016/j.energy.2023.128907

[11] Chen, X., Xu, J., Yang, C., Fang, Y., Li, W., Zhang, Y., Wan, Z., & Wang, X. (2021). Thermodynamic and economic study of PEMFC stack considering degradation characteristic. *Energy Conversion and Management*, 235. doi: 10.1016/j.enconman.2021.114016

[12] Lu, X., Du, B., Zhu, W., Yang, Y., Xie, C., Tu, Z., Zhao, B., Zhang, L., Song, J., & Deng, Z. (2023). Thermodynamic and dynamic analysis of a hybrid PEMFC-ORC combined heat and power (CHP) system. *Energy Conversion and Management*, 292, 117408. doi: 10.1016/j.enconman.2023.117408

[13] Özgür, T., & Yakaryilmaz, A. C. (2018). Thermodynamic analysis of a Proton Exchange Membrane fuel cell. *International Journal of Hydrogen Energy*, 43(38), 18007−18013. doi: 10.1016/j.ijhydene.2018.06.152

[14] Wang, B., Wu, K., Xi, F., Xuan, J., Xie, X., Wang, X., & Jiao, K. (2019). Numerical analysis of operating conditions effects on PEMFC with anode recirculation. *Energy*, 173, 844−856. doi: 10.1016/j.energy.2019.02.115

[15] Xia, S., Lin, R., Cui, X., & Shan, J. (2016). The application of orthogonal test method in the parameters optimization of PEMFC

under steady working condition. *International Journal of Hydrogen Energy*, 41(26), 11380−11390. doi: 10.1016/j.ijhydene.2016.04.140

[16] Chen, X., Li, W., Gong, G., Wan, Z., & Tu, Z. (2017). Parametric analysis and optimization of PEMFC system for maximum power and efficiency using MOEA/D. *Applied Thermal Engineering*, 121, 400−409. doi: 10.1016/j.applthermaleng.2017.03.144

[17] Xu, H., Song, H., Xu, C., Wu, X., & Yousefi, N. (2020). Exergy analysis and optimization of a HT-PEMFC using developed Manta Ray Foraging Optimization Algorithm. *International Journal of Hydrogen Energy*, 45(55), 30932−30941. doi: 10.1016/j.ijhydene.2020.08.053

[18] Lin, D., Yehong, H., & Khodaei, H. (2020). Application of the meta-heuristics for optimizing exergy of a HT-PEMFC. *International Journal of Energy Research*, 44(5), 3749−3761. doi: 10.1002/er.5163

[19] Ehyaei, M.A., Ahmadi, A., El Haj Assad, M., & Salameh, T. (2019). Optimization of parabolic through collector (PTC) with multi objective swarm optimization (MOPSO) and energy, exergy and economic analyses. *Journal of Cleaner Production*, 234, 285−296. doi: 10.1016/j.jclepro.2019.06.210

[20] Yuan, X., Liu, Y., & Bucknall, R. (2021). Optimised MOPSO with the grey relationship analysis for the multi-criteria objective energy dispatch of a novel SOFC-solar hybrid CCHP residential system in the UK. *Energy Conversion and Management*, 243. doi: 10.1016/j.enconman.2021.114406

[21] Thosar, A.U., Agarwal, H., Govarthan, S., & Lele, A.K. (2019). Comprehensive analytical model for polarization curve of a PEM fuel cell and experimental validation. *Chemical Engineering Science*, 206, 96−117. doi: 10.1016/j.ces.2019.05.022

[22] Guo, Y., Guo, X., Zhang, H., & Hou, S. (2020). Energetic, exergetic and ecological analyses of a high-temperature proton exchange membrane fuel cell based on a phosphoric-acid-doped polybenzimidazole membrane. *Sustainable Energy Technologies and Assessments*, doi: 10.1016/j.seta.2020.100671

[23] Li, D., Li, S., Ma, Z., Xu, B., Lu, Z., Li, Y., & Zheng, M. (2021). Ecological Performance Optimization of a High Temperature Proton Exchange Membrane Fuel Cell. *Mathematics*, 9(12). doi: 10.3390/math9121332

[24] Scott, K., Pilditch, S., & Mamlouk, M. (2007). Modelling and experimental validation of a high temperature polymer electrolyte fuel cell. *Journal of Applied Electrochemistry*, 37(11), 1245−1259. doi: 10.1007/s10800-007-9414-1

Co-published by
Institute of Fluid-Flow Machinery
Polish Academy of Sciences
Committee on Thermodynamics and Combustion
Polish Academy of Sciences

http://www.imp.gda.pl/archives-of-thermodynamics/

Integrating PEM fuel cell control with building heating systems: A comprehensive thermal and control model analysis

Robert Matysko[a*]

[a]Institute of Fluid-Flow Machinery, Polish Academy of Sciences, Fiszera 14 st., Gdańsk 80-231, Poland
*Corresponding author email: matyskor@imp.gda.pl

Received: 24.08.2023; revised: 17.02.2024; accepted: 10.05.2024

Abstract

In the paper, a model of a heated building using a PEM (proton exchange membrane) fuel cell is presented. This work introduces a novel and more comprehensive depiction of the thermal processes occurring within a fuel cell under transient conditions. The developed PEM fuel cell model was synergistically incorporated with a thermodynamic model of a building. The resulting mathematical framework provides insights into the building's performance concerning fluctuating ambient temperatures and the heating system powered by the PEM cell. The developed mathematical model delineates the interplay between the building's thermodynamics and the fuel cell in the context of the devised heating control system featuring an indirect heat distribution mechanism.

Keywords: PEM fuel cell; Thermal dynamics; Building heating system; Transient model; Waste heat recovery

Vol. 45(2024), No. 3, 209–219; doi: 10.24425/ather.2024.151232

Cite this manuscript as: Matysko, R. Integrating PEM fuel cell control with building heating systems: A comprehensive thermal and control model analysis. *Archives of Thermodynamics*, 45(3), 209–219.

1. Introduction

This paper explains the control process of a PEM cell concerning the utilisation of waste heat within buildings. The supply of fuel and oxidant to the fuel cell is facilitated through a valve system actuated by stepper motors. Given the proportional demand for reaction substrates, it becomes feasible to employ a single regulator with suitably chosen stepper motor-driven valves to energize the PEM cell. The second regulator finds application in the PEM cell's cooling system – this configuration could also function as a means to distribute heat to the building's rooms. Based on existing literature, this paper introduces a new continuous control system employing a singular SIMO (Single Input, Multiple Output) type regulator for the PEM cell. Furthermore, the article presents an innovative fuel cell temperature control system, that exploits the potential for waste heat recovery and subsequent utilization for heating purposes. A novel mathematical model, encompassing the fuel cell's temperature control process to meet heat demands within buildings is proposed.

Nomenclature

A – heat transfer surface, channel cross-section normal to flow, m^2
c – specific heat, J/(kg K)
c_i – molar specific heat (i = H_2, O_2, H_2O), J/(mol K)
$e(t)$ – control deviation
G – Laplace transform transfer function
h – specific enthalpy, J/kg
H – enthalpy of formation, J/mol
I – electric current, A
k – overall heat transfer coefficient, W/(m^2K)
m – mass, kg
$\dot{n}$ – molar flow, mol/s
P – electrical power, W
$\dot{Q}$ – heat flux, W
s – Laplace operator
S – channel cross-section normal to flow, m^2
t – time, s
T – temperature, K
U – voltage, V
w – flow velocity, m/s
x – flow path between inlet and outlet of the heat exchanger, m

Greek symbols

ρ – density, kg/m^3

Subscripts and Superscripts

b – room under study
bw – solid wall (without glazing) between the room under study and the external environment
d – differentiating (in reference to gain)
gd – ground
h – heater
i – integrating (in reference to gain)
in – inlet
k_1 – corridor
k_2 – corridor
l – saturated liquid water
net – total heat balance
o – external environment
out – outlet
p – proportional (in reference to gain)
p_n – adjacent rooms (n = 1,…,5)
s – ceiling, saturated water vapour
set – controller setting
str – acquired stream
uj – latent and sensible heat
w – glazed wall between the room under study and the external environment
win – inlet water
$chem$ – chemical reaction
$wout$ – outlet water

Abbreviations and Acronyms

PEM – proton exchange membrane
PID – proportional-integral-derivative

Over the past century, a variety of power systems dedicated to energy conversion has emerged – extending beyond the confines of the Rankine vapour cycle. Among these systems, fuel cells stand out as prominent examples. Fuel cells are predominantly associated with energy conversion mechanisms rooted in hydrogen oxidation without combustion. The fuel cell landscape encompasses a variety of types, including Solid Oxide Fuel Cells (SOFC), Proton Exchange Membrane Fuel Cells (PEMFCs), Alkaline Fuel Cells (AFC), and Phosphoric Acid Fuel Cells (PAFC), among others. Fuel cells readily lend themselves to mathematical modelling concerning the thermodynamic processes involved. The control process of PEM fuel cells was described by Nehrir and Wang [1]. Their study offers a relatively comprehensive model of the PEM fuel cell, and while the heat exchange with the surroundings is somewhat simplified, the mathematical description precludes the estimation of temperature elevation in the fuel cell's coolant.

The current body of literature not only encompasses transient models for PEM cells [1] but also includes more intricate elucidations of the processes occurring in these cells. Notably, certain papers offer more detailed insights into phenomena like two-phase flow [2]. However, these models are predominantly tailored to PEM cells operating under steady-state conditions. Consequently, they are inadequate for simulating the behaviour of PEM cells during start-up, shutdown, or when subjected to varying heat loads over time – scenarios that include heat recovery, a factor that directly affects the energy efficiency of fuel cells.

In the Abdin et al. study [3], a transient model was meticulously developed to delineate the chemical and electrochemical processes in a fuel cell. Although somewhat lacking precision in explaining thermal processes, it proved useful in understanding PEM fuel cell dynamics from an electro-technical perspective. Taner [4] characterised electrical parameters related to substrate pressure in the fuel cell, employing a steady-state PEM cell model to determine cell exergy He evaluated a PEM fuel cell's performance based on operating pressure and voltage parameters, finding energy and exergy efficiencies of 47.6% and 50.4%, respectively, and highlighting wastewater management's importance in fuel cell lifespan. In another study [5], Taner compared traditional PEM fuel cell systems with nano-designed versions, demonstrating significantly higher energy (72.4%) and exergy (85.22%) efficiencies in the latter, and suggesting that pressure and flow rate optimizations can greatly enhance thermodynamic efficiency. Naqvi et al. [6] conducted a techno-economic and enviro-economic analysis of hydrogen production using an optimised alkaline electrolyser. The authors developed a prototype that efficiently produced oxyhydrogen gas, evidencing economic feasibility with a favourable payback period. Lastly, paper [7] introduces an innovative PEM electrolyser prototype for hydrogen generation, featuring Cr-C coated SS304 bipolar plates and a specialized chemical mixture, achieving a production rate of 6 m³/h and an economically advantageous payback period, showcasing efficiency and cost-effectiveness.

In the context of the study of Sudarshan and Dhananjay [8], PEM cell dynamics is characterised by assuming equal partial

pressures for hydrogen and oxygen. Notably, the model's implementation in SIMULINK software falls short of accommodating temperature variations in the PEM fuel cell's cooling medium. A detailed description of physical models situating the PEM cell in a three-dimensional space under steady-state conditions is presented in the study of Mingruo et al. [9]. Herein, the authors presented the PEM cell voltage/current characteristic observed under steady conditions.

Moving forward, Ziogou et al. [10] not only modelled the PEM cell but also confirmed the model predictions through experimental validation, focusing on the cell's electrodynamic attributes. The work [11] details PEM cell test outcomes while incorporating PI and Fuzzy Logic regulators for control. Describing an alternative configuration, Waseem and Ghait [12] outlined a PEM cell model wherein substrate production was driven by PV cells. A distinct model, as presented in [13], explicates the dynamics of proton diffusive transport through the PEM cell's membrane.

Given that the primary application of PEM fuel cells revolves around electricity generation, the prevailing literature predominantly emphasizes models aimed at calculating electricity and voltage parameters. Notably, software tools like Matlab/Simulink, particularly within the Simscape™ Electrical™ toolbox [14], have integrated models of diverse fuel cell types (e.g., PEM, SOFC, AFC), primarily focused on configuring electricity and voltage attributes. Regrettably, the models integrated within this software fail to account for the thermal characteristics of the cell arising from heat dissipation into the surroundings and the cell's interaction with heating systems.

Within the realm of literature, the examination of building dynamics finds expression through the utilisation of the thermoelectric analogy, a concept comprehensively expounded upon in studies [15,16]. In [17], fundamental principles related to heat management and the quantification of energy balances within buildings are elucidated, alongside the presentation of guidelines for constructing such energy balances. Mathematically detailing heat flow between heated and unheated spaces is a relatively straightforward task. Nevertheless, due to the reliance on factors such as wall materials, inter-room thermal processes, and ambient thermal conditions, the actual process of formulating equations governing heat transfer becomes protracted and intricate.

Windows significantly influence building energy use and thermal comfort. While many models exist for assessing indoor thermal comfort, the effect of solar radiation is often neglected. Song et al. [18] applied the SMRT (simplified mean radiant temperature)-air temperature deviation method to evaluate solar radiation's impact on indoor comfort during the initial design phase. Focusing on office buildings in various orientations and climates, the findings indicate a more pronounced impact of solar radiation in colder climates, especially through east and west-facing windows. Adjusting the Solar Heat Gain Coefficient (SHGC) of windows could reduce discomfort by over 86% across all climates, aiding designers in enhancing indoor thermal comfort. Wonorahardjo et al. [19] explored how various façade systems impact thermal comfort and Urban Heat Island (UHI) effects. Their study involved outdoor field measurements on materials like brick, concrete, low-E (low-emissivity) glass, and Aluminium Composite Panel (ACP), focusing on solar exposure effects on façade surface temperatures. Additional lab experiments under simulated solar exposure assessed the thermal behaviour of these materials. Findings showed that brick walls stored and emitted heat, affecting both indoor and outdoor temperatures. Adding ACP to brick walls significantly lowered indoor temperatures but may contribute to UHI. Insulation materials like newspaper and corn husk mats were effective in reducing indoor temperatures during the heating period but slightly increased outdoor temperatures. The study underscored the importance of considering both indoor and outdoor temperatures in building design for thermal comfort and UHI mitigation.

In HVAC system design, balancing user comfort and energy consumption often leads to a conflict, requiring Pareto-optimal controls. While indoor air temperature is a common control parameter, it does not always accurately capture perceived thermal comfort due to sensor placement. Computational fluid dynamics (CFD) can help develop more effective control strategies [20]. A comparative study between PMV (predicted mean vote)-based thermal comfort control and traditional temperature-based control in a sunlit office room showed that an iterative approach for adjusting air supply flow can better meet ISO 7730 comfort standards. CFD simulations compared air temperature distribution and ventilation effectiveness for both strategies, analysing thermal indices and energy savings. The PMV-based control not only enhanced thermal comfort in the glazed office but also reduced energy use by 1.6% daily.

A numerical study in research [21] examines the energy consumption of bedroom task/ambient air conditioning (TAC) across different climate zones, focusing on a PMV-based control strategy for night-time energy use. Two traditional operating modes were analysed: variable supply air temperature (VAT) and variable supply air flow rate (VAF). Results showed that VAT mode reduces energy consumption significantly more than VAF, with savings of at least 10% in Beijing, 19% in Shanghai, and 18% in Guangzhou. An optimized mode, VFT-LowE, which combines variable flow rate and temperature, was found to save up to 6.5% more energy than VAT mode in Guangzhou. The study also highlighted that the highest energy-saving potential is observed in warmer climates, reaching up to 403 kJ per night in Beijing and around 1100 kJ in Shanghai and Guangzhou. The findings suggested the effectiveness of optimized TAC operation modes in reducing energy consumption, particularly in hotter climates.

Buyak et al., in the previous work [23], based on experimental analysis demonstrated that enhancing thermal insulation to Swedish standards and adopting intermittent heating can significantly reduce energy consumption. However, they also highlighted the need for additional electric heating during transition periods to maintain comfort, potentially increasing energy consumption. The results of the research might be useful for identifying the thermal characteristics of a building, even though they did not include a mathematical description of the building that could be used to simulate its thermal dynamics. A mathematical model of such a building is presented in the present work.

2. Mathematical modelling of a building heated by a PEM cell

This section provides an in-depth analysis of a mathematical model that comprehensively covers various facets of the PEM cell control system. Specifically, the focus lies on both electricity generation and the recovery process of waste heat. The model incorporates the utilization of logarithmic temperature differences as output parameters, serving as a metric for assessing the stability of the PEM cell. Furthermore, the chapter introduces a mathematical model adapted to a building with a PEM cell, utilized primarily for heating purposes.

The thermal dynamics of room, subject to temperature fluctuations, is influenced by a myriad of factors. These factors encompass solar radiation exposure within the room, the operation of electrical and heating appliances, occupancy levels, the effectiveness of the ventilation system, as well as heat exchange with the external environment and the ground.

The ambient temperature within a designated room is an outcome of achieving a balance between heat influx and dissipation. When heat dissipation surpasses influx, a gradual temperature decrease is observed. Conversely, heat influx higher than dissipation leads to temperature elevation. The equilibrium between these heat factors holds pivotal importance in maintaining the desired room temperature. Notably, such equilibrium is predominantly attainable under stable operating conditions, a criterion upon which heat-providing systems are designed. Real-world scenarios, however, entail dynamic heat influx and dissipation, resulting in fluctuating and occasionally uneven heat distribution across various rooms.

Accurately quantifying heat flow through the walls delineating the volume of a heated room proves to be a complex task. This section presents a mathematical model that determines the diurnal oscillations of the temperature (T_b) in the analysed room. These fluctuations are driven by the introduction of warm water sourced from the PEM fuel cell. The spatial proximity of the room to heated chambers (T_{p1}, T_{p2}, T_{p3}, T_{p4}, T_{p5}) and unheated halls (T_{k1} and T_{k2}) establishes boundaries with the external environment, potentially extending to the ground surface based on geographical nuances (Fig. 1).

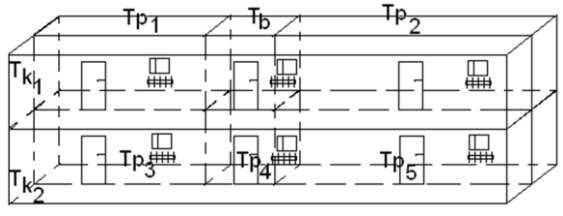

Fig. 1. Diagram depicting the configuration of the simulated rooms.

The computations were performed to determine the temperature changes that occur due to the difference between the heat demand (losses) and the heat supplied (gains) from the PEM fuel cell.

Figure 2 depicts a negative feedback loop where the controlled variables of molar hydrogen expenditure (nH_2) and molar oxygen expenditure (nO_2) depend on the temperature T3 of the water (H_2O) exiting the fuel cell and PID (proportional-integral-derivative) controller settings.

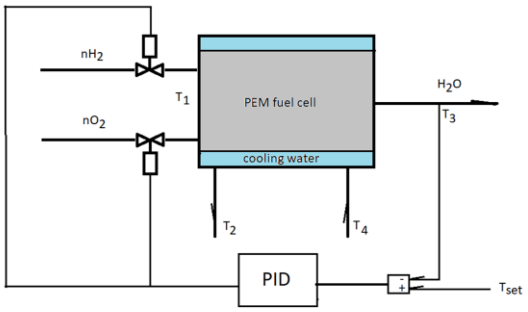

Fig. 2. PID control system for the PEM fuel cell.

The mathematical model of the room operates under the following assumptions and simplifications [23]:

1) It depicts daily temperature fluctuations during winter.
2) Heat gains from solar radiation and electrical appliances have been excluded.
3) Changes in humidity, as well as gains and losses through the ventilation system, have not been considered.
4) The anticipated sinusoidal temperature changes within the room are linked to the controller.
5) The ambient temperature is represented by a signal that linearly increases and decreases.
6) Heat transfer coefficients are assumed to be the same for walls adjacent to external surroundings and unheated rooms.

While in operation, the PEM fuel cell (Fig. 2) generates electricity and concurrently produces thermal energy. The model applied to the fuel cell is based on the following assumptions [1]:

1) It operates transiently.
2) The fuel cell's characterisation employs spatial parameters.
3) Control of the modelled fuel cell is based on the logarithmic temperature difference between the cell and the cooling water. The temperature of cooling water is set at a level that optimizes its applicability for heating purposes.
4) The entire heat generated during the reaction is effectively transferred to the heating system.
5) Fluid flow within the fuel cell is turbulent, characterised by a Reynolds number (Re) exceeding 10000.
6) The discrepancy in enthalpy during the phase transition between steam and water is determined by a value dependent on the saturation pressure of the two-phase mixture.

The mathematical model for the building includes the equations describing the temperature changes over the time within: (i) the analysed room, (ii) room $p1$, (ii) room $p2$, (iii) room $p3$, (iv) room $p4$, and (v) hall $k1$, and (vi) hall $k2$, respectively:

$$\frac{dT_b}{dt}m_b c_b = A_{b-p1}k_{b-p1}(T_{p1}-T_b) + A_{b-p2}k_{b-p2}(T_{p2}-T_b) + A_{b-p3}k_{b-p3}(T_{p3}-T_b) + A_{b-p4}k_{b-p4}(T_{p4}-T_b) + \\ +A_{b-p5}k_{b-p5}(T_{p5}-T_b) + A_{b-s}k_{b-s}(T_o-T_b) + A_{b-w}k_{b-w}(T_o-T_b) + A_{b-k1}k_{b-k1}(T_{k1}-T_b) + \\ +A_{b-k2}k_{b-k2}(T_{k2}-T_b) + A_{h-pb}k_{h-pb}(T_h-T_{pb}), \quad (1)$$

$$\frac{dT_{p1}}{dt}m_{p1}c_{p1} = A_{b-p1}k_{b-p1}(T_b-T_{p1}) + A_{k1-p1}k_{k1-p1}(T_{k1}-T_{p1}) + A_{k2-p1}k_{k2-p1}(T_{k2}-T_{p1}) + \\ +A_{p1-p3}k_{p1-p3}(T_{p3}-T_{p1}) + A_{p1-p4}k_{p1-p4}(T_{p4}-T_{p1}) + A_{p1-w}k_{p1-w}(T_o-T_{p1}) + \\ +A_{p1-bw}k_{p1-bw}(T_o-T_{p1}) + A_{p1-s}k_{p1-s}(T_o-T_{p1}) + A_{h-p1}k_{h-p1}(T_h-T_{p1}), \quad (2)$$

$$\frac{dT_{p2}}{dt}m_{p2}c_{p2} = A_{b-p2}k_{b-p2}(T_b-T_{p2}) + A_{k1-p2}k_{k1-p2}(T_{k1}-T_{p2}) + A_{k2-p2}k_{k2-p2}(T_{k2}-T_{p2}) + \\ +A_{p4-p2}k_{p4-p2}(T_{p4}-T_{p2}) + A_{p5-p2}k_{p5-p2}(T_{p5}-T_{p2}) + A_{p2-w}k_{p2-w}(T_o-T_{p2}) + \\ +A_{p2-bw}k_{p2-bw}(T_o-T_{p2}) + A_{p2-s}k_{p2-s}(T_o-T_{p2}) + A_{h-p2}k_{h-p2}(T_h-T_{p2}) \quad (3)$$

$$\frac{dT_{p3}}{dt}m_{p3}c_{p3} = A_{b-p3}k_{b-p3}(T_b-T_{p3}) + A_{k1-p3}k_{k1-p3}(T_{k1}-T_{p3}) + A_{k2-p3}k_{k2-p3}(T_{k2}-T_{p3}) + \\ +A_{p4-p3}k_{p4-p3}(T_{p4}-T_{p3}) + A_{p3-w}k_{p3-w}(T_o-T_{p3}) + A_{p3-bw}k_{p3-bw}(T_o-T_{p3}) + \\ +A_{p3-gd}k_{p2-gd}(T_{gd}-T_{p3}) + A_{h-p3}k_{h-p3}(T_h-T_{p3}), \quad (4)$$

$$\frac{dT_{p4}}{dt}m_{p4}c_{p4} = A_{b-p4}k_{b-p4}(T_b-T_{p4}) + A_{k1-p4}k_{k1-p4}(T_{k1}-T_{p4}) + A_{k2-p4}k_{k2-p4}(T_{k2}-T_{p4}) + \\ +A_{p4-w}k_{p4-w}(T_o-T_{p4}) + A_{p4-gd}k_{p4-gd}(T_{gd}-T_{p4}) + A_{h-p4}k_{h-p4}(T_h-T_{p4}) + \\ +A_{p1-p4}k_{p1-p4}(T_{p1}-T_{p4}) + A_{p2-p4}k_{p2p4}(T_{p2}-T_{p4}) + A_{p3-p4}k_{p3-p4}(T_{p3}-T_{p4}) + A_{p5-p4}k_{p5-p4}(T_{p5}-T_{p4}), \quad (5)$$

$$\frac{dT_{p5}}{dt}m_{p5}c_{p5} = A_{b-p5}k_{b-p5}(T_b-T_{p5}) + A_{k1-p5}k_{k1-p5}(T_{k1}-T_{p5}) + A_{k2-p5}k_{k2-p5}(T_{k2}-T_{p5}) + \\ +A_{p5-w}k_{p5-w}(T_o-T_{p5}) + A_{p5-bw}k_{p5-bw}(T_o-T_{p5}) + A_{p5-gd}k_{p5-gd}(T_{gr}-T_{p5}) + A_{h-p5}k_{h-p5}(T_h-T_{p5}) + \\ +A_{p1-p4}k_{p1-p4}(T_{p1}-T_{p4}) + A_{p2-p5}k_{p2-p5}(T_{p2}-T_{p5}) + A_{p5-p4}k_{p5-p4}(T_{p4}-T_{p5}), \quad (6)$$

$$\frac{dT_{k1}}{dt}m_{k1}c_{k1} = A_{b-k1}k_{b-k1}(T_b-T_{k1}) + A_{k1-p1}k_{k1-p1}(T_{p1}-T_{k1}) + A_{k1-p2}k_{k1-p2}(T_{p2}-T_{k1}) + \\ +A_{k1-p3}k_{k1-p3}(T_{p3}-T_{k1}) + A_{k1-p4}k_{k1-p4}(T_{p4}-T_{k1}) + A_{k1-p5}k_{k1-p5}(T_{p5}-T_{k1}) + \\ +A_{k1-k2}k_{k1-k2}(T_{k2}-T_{k1}) + 2\cdot A_{k1-w}k_{k1-w}(T_o-T_{k1}) + A_{k1-s}k_{k1-s}(T_s-T_{k1}), \quad (7)$$

$$\frac{dT_{k2}}{dt}m_{k2}c_{k2} = A_{b-k2}k_{b-k2}(T_b-T_{k2}) + A_{k2-p1}k_{k2-p1}(T_{p1}-T_{k2}) + A_{k2-p2}k_{k2-p2}(T_{p2}-T_{k2}) + \\ +A_{k2-p3}k_{k2-p3}(T_{p3}-T_{k2}) + A_{k2-p4}k_{k2-p4}(T_{p4}-T_{k2}) + A_{k2-p5}k_{k2-p5}(T_{p5}-T_{k2}) + \\ +A_{k1-k2}k_{k1-k2}(T_{k1}-T_{k2}) + 2\cdot A_{k2-w}k_{k2-w}(T_o-T_{k2}) + A_{k2-gd}k_{k2-gd}(T_{gd}-T_{k2}), \quad (8)$$

where: m – mass, T – temperature, c – specific heat, A – heat transfer surface area, channel cross-section normal to flow, k – overall heat transfer coefficient, t – time. In Eqs. (1)–(8), the subscripts refer to the following, respectively: $k1$, $k2$ – corridor, gd – ground, h – heater; b – room under study, bw – solid wall (without glazing) between the room under study and the external environment, o – external environment; $p1,\ldots,p5$ – adjacent rooms, w – glazed wall between the room under study and the external environment.

Heating for the building is obtained by utilising water from the fuel cell's cooling system, which is controlled by a PID controller. The mathematical representation of both the control system for the hot water supply and the controller is presented below.

The heating process is described by the equation:

$$\rho c S\frac{dT_h}{dt} = \rho w c S\frac{T_{win,h}-T_h}{\Delta x/2} - \rho w c S\frac{T_h-T_{wout,h}}{\Delta x/2} - \\ -A_h k_h \frac{(T_{win,h}-T_h)-(T_{wout,h}-T_h)}{\ln\left(\frac{(T_{win,h}-T_h)}{(T_{wout,h}-T_h)}\right)}, \quad (9)$$

where: S – pipeline cross-section, ρ – density, x – flow path between inlet and outlet of the heat exchanger, w – flow velocity, *win* – inlet water; *wout* – outlet water.

The process of regulation of flow through the heat exchanger is determined by the correlation:

$$G_{PID}(s) = \left(K_p + \frac{K_i}{s} + K_d s\right) = \\ = k_p\left(e(t) + \frac{1}{T_i}\int_0^t e(t)dt + T_d\frac{de(t)}{dt}\right), \quad (10)$$

$$e(t) = (w_{set} - w), \quad (11)$$

$$K_p = k_p,\ K_i = \frac{k_p}{T_i},\ K_d = k_d T_d, \quad (12)$$

where: $e(t)$ – control deviation; s – Laplace operator, k – gain of the PID controller; T – time constant. The respective subscripts are: p – proportional; d – differentiation; i – integration; *set* – controller setting.

The PEM cell model addresses transient conditions; nonetheless, this model takes into account heat exchange with the

surroundings, phase transitions, and chemical reactions occurring within the PEM fuel cell. The electrical impedance of the materials used to construct the PEM cell was not considered.

The energy balance of the PEM cell can be formulated by the following equation:

$$\dot{Q}_{net} = \dot{Q}_{chem} - P - \dot{Q}_{uj} - \dot{Q}_{str}, \quad (13)$$

where $\dot{Q}$ is the heat flux, P is the electrical power. Subscript *net* refers to the total heat balance, *chem* to the chemical reaction, *uj* to the latent and sensible heat, and *str* to the acquired stream.

The heat generated by hydrogen consumption in the PEM cell can be described by the equation:

$$\dot{Q}_{chem} = \dot{n}_{\mathrm{H_2}} \Delta H, \quad (14)$$

where $\dot{n}_{H_2}$ is the molar concentration of the reacted hydrogen and ΔH represents the overall enthalpy change during the chemical reaction.

The electrical power generated in the PEM cell is dependent on voltage and current, according to:

$$P = UI, \quad (15)$$

where I is an electric current and U stands for voltage.

The latent and sensible heat depends on the molar energy fluxes of the individual components (hydrogen (H_2), oxygen (O_2), and water (H_2O)) involved in reactions within the PEM cell, as well as the gas-liquid phase transitions that occur, and is expressed by:

$$\begin{aligned}\dot{Q}_{uj} = &\dot{n}_{\mathrm{H_2},out} c_{\mathrm{H_2}} (T - T_o) + \dot{n}_{\mathrm{O_2},out} c_{\mathrm{O_2}} (T - T_o) + \\ &+ \dot{n}_{\mathrm{H_2O}} c_{\mathrm{H_2O}} (T - T_o) + \dot{n}_{\mathrm{H_2O}} (h_S - h_l)\end{aligned}, \quad (16)$$

where: $\dot{n}$ – molar flow rate of a substance, h_s – molar enthalpy of water steam, J/mol; h_l – molar enthalpy of liquid water, J/mol; c_i (i = H_2, O_2, H_2O) – molar specific heat.

The heat transferred from the fuel cell to the heating system is connected to the rate of heat transfer (k), the surface area for heat exchange, and the logarithmic temperature difference (ΔT_{log}), according to equations:

$$\dot{Q}_{str} = A_{PEM} k_{PEM} \frac{(T_{PEM} - T_{wout,PEM}) - (T_{PEM} - T_{win,PEM})}{\ln\left(\frac{(T_{PEM} - T_{wout,PEM})}{(T_{PEM} - T_{win,PEM})}\right)}, \quad (17)$$

$$\dot{Q}_{str} = A_h k_h \frac{(T_{win,h} - T_h) - (T_{wout,h} - T_h)}{\ln\left(\frac{(T_{win,h} - T_h)}{(T_{wout,h} - T_h)}\right)}, \quad (18)$$

Additionally, the transferred heat is defined by the energy balance:

$$\begin{aligned}\dot{Q}_{str} &= \rho w c S\left(T_{win,h} - T_{wout,h}\right) = \\ &= \rho w c S\left(T_{wout,PEM} - T_{win,PEM}\right).\end{aligned} \quad (19)$$

During transient conditions, the term $\dot{Q}_{net}$ representing the change in dynamic heat flux is variable. Under steady conditions $\dot{Q}_{net}$=0. Since the computations were carried out considering transient conditions, the dynamic heat flux is related to the mass of the PEM cell, its overall specific heat, and the temporal temperature change, following the equation:

$$\dot{Q}_{net} = mc \frac{dT}{dt}. \quad (20)$$

The model equations were formulated within the SIMULINK software environment. In the context of the PEM cell, the input parameters were selected to match the parameters reported in [1].

3. Determination of dynamic parameters for building and the PEM fuel cell

3.1. Calculation results for the PEM cell

While examining the fuel cell, its operation was simulated in scenarios both with and without negative feedback. The PID controller (Fig. 1) was incorporated within the negative feedback loop (Fig. 2). Given that the water temperature leaving the fuel cell must remain above 320 K for the underfloor heating system, the logarithmic temperature difference was identified as the analysed state parameter within the negative feedback loop. The flowchart outlining the equations describing the PEM cell model is presented in Fig. 3, and Fig. 4 displays the chart of the PID continuous control system within the negative feedback loop.

The regulatory system of the PEM cell model encompasses an output variable, *Tout*, along with two input variables. These inputs are managed utilising the output signal from the PID system – the molar stream $\dot{n}_{\mathrm{H_2}}$ and the molar stream $\dot{n}_{\mathrm{O_2}}$.

The process of linearizing the open feedback loop system was conducted for a MISO (multi-input, single-output) configuration. This was carried out with the purpose of evaluating the stability of the cell model's response to variations in hydrogen and oxygen supply caused by logarithmic temperature fluctuations. The outcomes of the linearization procedure for the input variable $\dot{n}_{\mathrm{H_2}}$, and the output variable ΔT_{log} of the control object defined as:

$$\Delta T_{log} = \frac{(T_{PEM} - T_{wout,PEM}) - (T_{PEM} - T_{win,PEM})}{\ln\left(\frac{(T_{PEM} - T_{wout,PEM})}{(T_{PEM} - T_{win,PEM})}\right)}, \quad (21)$$

is exhibited in the form of a transfer function:

$$G_{\dot{n}_{H_2}}(s) = \frac{-0.0001512}{s + 0.002122}, \quad (22)$$

where s stands for the Laplace operator.

Similarly, the outcomes of linearizing the control system with respect to the input molar oxygen flow rate ($\dot{n}_{\mathrm{O_2}}$) and the same ΔT_{log} (Eq. (21)) as an output variable, is expressed in the form of a transfer function:

$$G_{\dot{n}_{O_2}}(s) = \frac{-0.00007748}{s + 0.002122}. \quad (23)$$

Linearization of the closed-loop feedback system was carried out, employing the fuel cell's setpoint temperature as the input variable and the fuel cell's logarithmic temperature differ-

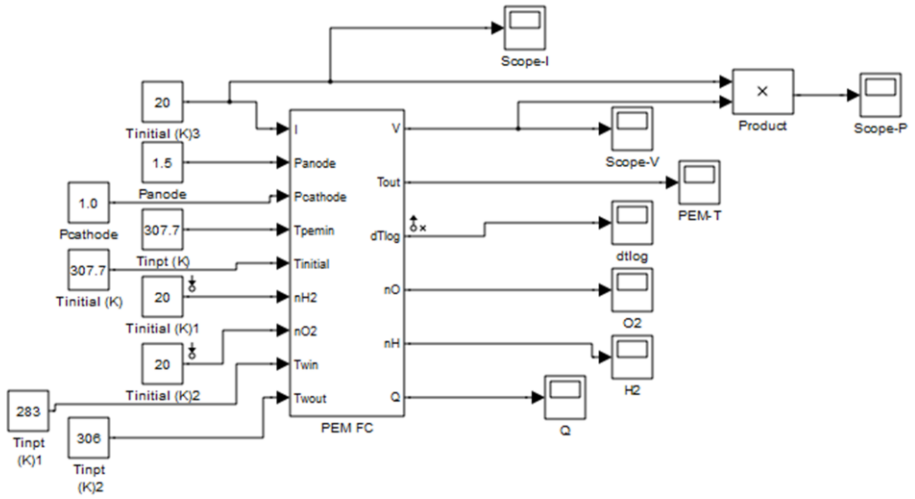

Fig. 3. The flowchart depicting input and output parameters concerning a PEM fuel cell operating in an open feedback loop configuration, excluding any regulatory mechanisms.

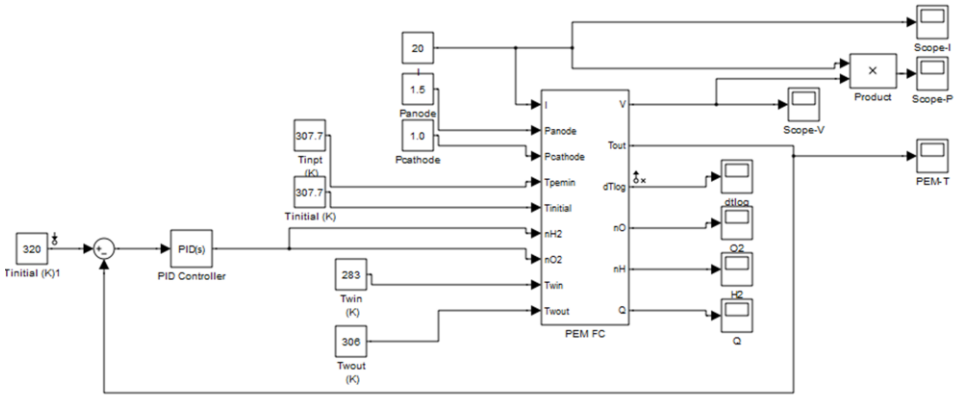

Fig. 4. The flowchart illustrating input and output parameters pertaining to PEM fuel cell with a feedback loop that integrates the PID regulation system.

ence as the output variable. This linearization was specifically applied to a single-input single-output (SISO) object featuring an internal feedback loop responsible for regulating the fuel cell's operating temperature:

$$G_{T_{in}}(s) = \frac{0{,}00005913s + 0{,}0000001578}{s^3 + 0{,}01241s^2 + 0{,}00006092s^2 + 0{,}0000001042}. \quad (24)$$

The behaviour of the closed-loop control system, in conjunction with the designated regulator's setpoint parameters, concerning the stability of the logarithmic temperature difference, is of utmost importance due to its impact on the ability to uphold the thermal characteristics of the simulated building's heating system.

The calculation results for the fuel cell's operation with and without a feedback loop are presented in Figs. 5–7. Figure 5 illustrates the power produced by the fuel cell, while Fig. 6 displays the voltage generated within the fuel cell.

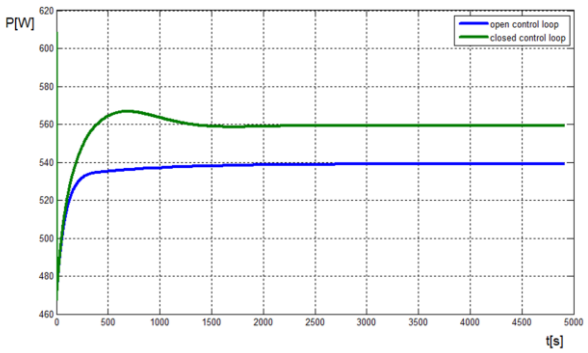

Fig. 5. The power output of the PEM fuel cell under open and closed-loop feedback conditions.

In Figs. 5 and 6, two responses can be observed, where both power and voltage exhibit a more flattened characteristic in the case of an open feedback loop. For the feedback loop, overshooting occurs due to the regulation process involving the mass flow rate of individual streams feeding the PEM cell.

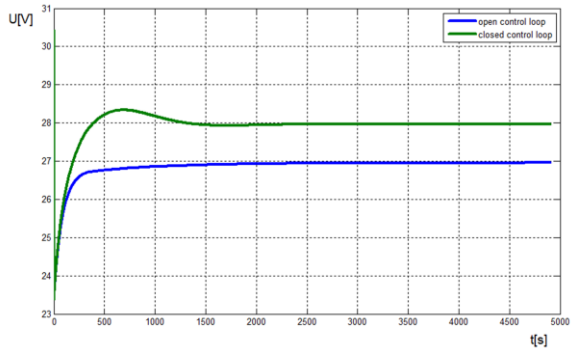

Fig. 6. Voltage on the PEM fuel cell during open and closed-loop feedback operation.

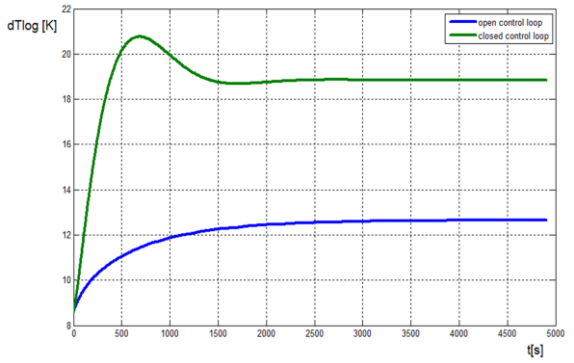

Fig. 7. The logarithmic temperature difference of the PEM fuel cell during operation within an open and closed feedback loop.

Figure 7 depicts the logarithmic temperature difference, which is significant for the heating system of a building.

Furthermore, Fig. 8 provides a graphical representation of the heat generated by the fuel cell, and Fig. 9 exhibits the temperature of the liquid leaving the fuel cell. As it can be seen, the

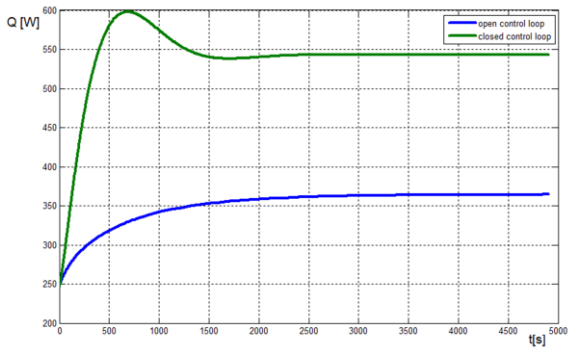

Fig. 8. The heat flow directed to the cooling water during operation within an open and closed feedback loop.

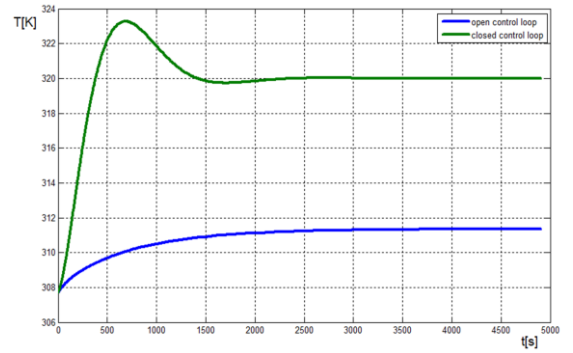

Fig. 9. The operational temperature of the PEM fuel cell during operation within an open and closed feedback loop.

fuel cell temperature increases abruptly in response to the chemical processes occurring in the fuel cell. The results of calculations for the molar oxygen and hydrogen flow rates are shown in Figs. 10 and 11, respectively. They indicate that the molar flow rates of reactants supplied over time cause an overshoot of the fuel cell temperature above the setpoint. Once the temperature exceeds the setpoint (320 K), the molar flowrates are stabilized, resulting in maintaining both thermal and electrical power at a higher level.

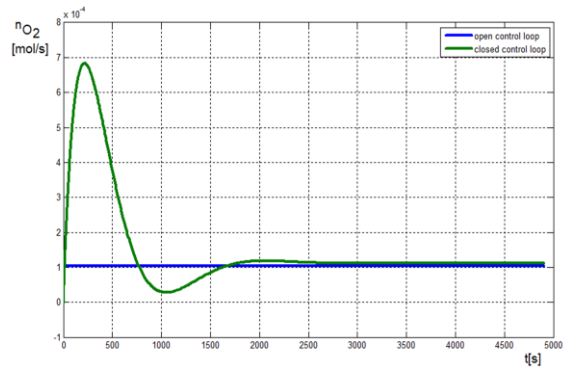

Fig. 10. The molar oxygen flow rate during operation within an open and closed feedback loop.

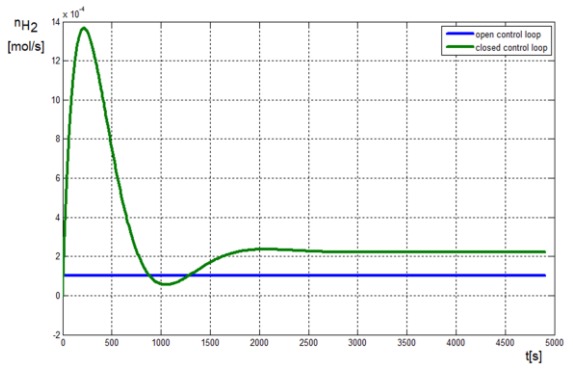

Fig. 11. The molar hydrogen flow rate during operation within an open and closed feedback loop.

In the case of implementing a feedback loop associated with maintaining the outlet temperature of the PEM cell at a specified useful level in the space heating process, an increase in the logarithmic temperature difference is observed (Fig. 7) as well as an increase in the thermal power of the fuel cell (Fig. 8).

Figures from 4 to 9 depict a slight over-regulation of the fuel cell's parameters associated with the regulator's operation, from which the control signals are transmitted to the actuator systems (supply valves). As a result, it becomes essential that the actuator systems (valves) facilitate a wide range of molar flow rates, as illustrated in Fig. 10 and Fig. 11. The molar flow rate experiences a sevenfold increase during transient conditions compared to steady conditions, which corresponds to the initial phases of the fuel cell's chemical reactions. During the initial period, the actuator systems should enable achieving significantly high molar flow rates for both the fuel and the oxidant. Failure of the actuator systems to provide adequately high molar flow rates of reaction substrates could potentially extend the startup time and the duration required to attain the conditions required by the heating systems. For this PEM cell, the elongation of this time could range from 2500 to 4000 seconds.

Figure 12 presents the control error values before processing the signal in the PID controller and the output signal from this controller, whereas Fig. 13 displays the Bode plots, showing both the amplitude and phase characteristics of the controlled system within the closed feedback loop. Upon scrutinizing the Bode plots constructed for the PEM cell control system (Fig. 13), it can be inferred that the system remains stable across the entire amplitude spectrum and exhibits a notably substantial phase margin (approximately 90 degrees).

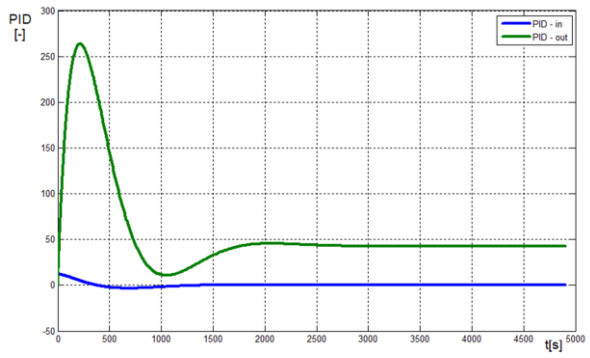

Fig. 12. The control signals at the input and output of the PID regulator.

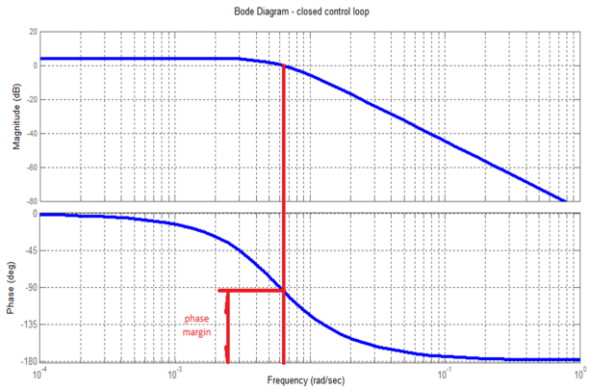

Fig. 13. The Bode plots of the PEM cell system with a closed feedback loop.

2.2. Transient analysis of a building heated by the PEM cell

The investigation involved calculations for determining the thermodynamics of a building heated by a PEM cell. Figure 14 illustrates the signal connections among the PEM cell model, the heating system, and the building, all designed within the SIMULINK software.

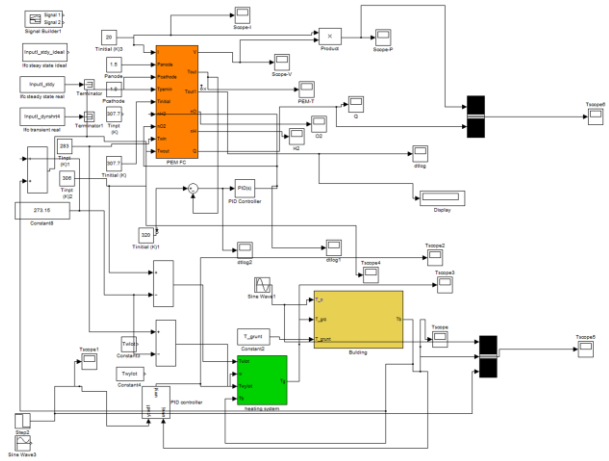

Fig. 14. Implementation of the simulated building heated by the PEM cell, developed in SIMULINK software.

Figure 15 demonstrates variations in the logarithmic temperature difference between the PEM cell and the heating system within heated rooms. The predicted variations of ambient temperature, heated room temperature, and the setpoint temperature of the regulatory system are displayed in Fig. 16. Figure 17 exhibits fluctuations in the operating temperature of the PEM cell. Figure 18 portrays the heat supplied to the heated room (Q) and the electric power produced by the PEM cell (P).

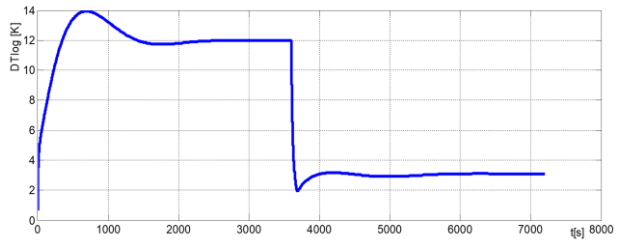

Fig. 15. The logarithmic temperature difference between the PEM cell and the heated water.

Based on the conducted calculations, it is evident that unheated rooms, such as adjacent halls without heating, exert a notable influence on heat losses from the heated rooms. This effect is primarily due to the lack of insulation in the separating walls

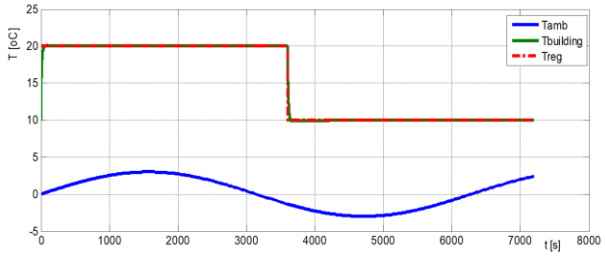

Fig. 16. Ambient temperature, the heated building's temperature and the regulator's setpoint.

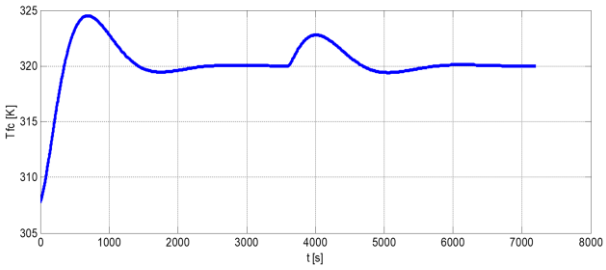

Fig. 17. The operating temperature of the fuel cell.

and the inherent lack of airtightness in front doors and windows in stairwells. Heating of these halls, coupled with ventilation-related losses, can significantly perturb a building's energy balance, subsequently leading to escalated operating costs for the heating system. Addressing this concern, enhancing insulation within the halls becomes imperative.

This situation is especially evident in Fig. 5, where the temperature rise in the halls contiguous to the heated rooms occurs at a relatively gradual pace. This behaviour is attributed to the interplay of ambient temperature and the heat transfer coefficient of the non-insulated walls. The oscillation in ambient temperature T_o (variation between approximately –3°C and +3°C as in Fig. 16) is attenuated due to heat penetration through the walls, having minimal effect on room temperatures. The minor temperature fluctuations (Fig. 17), arising from the operation of the thermostatic valve within the building's heating system, are mitigated by the mass flow rate of heating water obtained from the PEM fuel cell via the PID regulator, as described by Eq. (10). Consequently, the fuel cell maintains stable thermal parameters for the cooling system. As a result, the heat derived from the PEM fuel cell also remains stable.

Discussing the potential use of waste heat from fuel cells for heating purposes is intriguing, yet it requires in-depth analysis. Understanding the heat transfer processes from cells to the building's heating system and the technical aspects of integrating these two systems are pivotal. Optimal utilisation of waste heat can significantly amplify the overall energy efficiency of the system.

One crucial aspect worth highlighting is the efficiency of proton exchange membranes (PEM) in fuel cells. This membrane plays a pivotal role by enabling the flow of protons between the anode and cathode, thereby generating electric current. However, in practice, the effectiveness of PEMs can be hindered by factors such as humidity, temperature, and the presence of impurities. Hence, continuous research into refining membrane technology is essential to ensure reliability and efficiency.

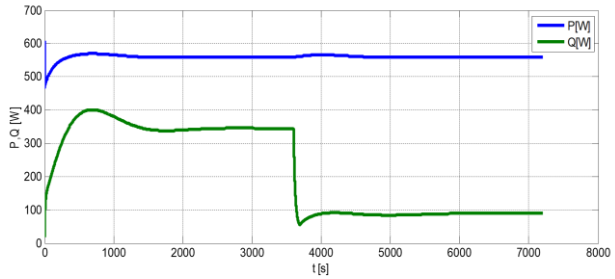

Fig. 18. The thermal power (Q) employed for heating purposes and the electrical power (P) produced by the PEM cell.

3. Conclusions

In the realm of cutting-edge building technology, this work presents a pioneering exploration in the field of sustainable thermal management by integrating Proton Exchange Membrane (PEM) fuel cells into the heating systems of modern structures. At its core, this investigation pivots on the innovative utilisation of waste heat emanating from PEM fuel cells, repurposing it as a strategic asset to foster a more energy-efficient and sustainable approach to building heating.

The cornerstone of this research lies in the development and presentation of a robust mathematical model. This model serves as a sophisticated analytical tool, meticulously mapping out the intricate interactions between the thermal dynamics inherent to PEM fuel cells and the variable heating demands typical of contemporary buildings. This is particularly emphasized under transient operational conditions, a crucial factor in optimizing the system's overall performance.

A focal point of the study is the operational parameters of the PEM cells. When situated within a closed feedback loop, these cells exhibit an operating temperature orbiting around 320 K. This is contrasted with their performance in an open feedback loop, where the temperature is capped at a slightly lower threshold of 312 K. The research underscores the efficacy of a regulatory system capable of modulating the molar flow rates of hydrogen and oxygen, adjusting them to the stoichiometric amounts required for the cell's chemical reactions. The ingenuity of this system lies in its dual-regulation capability, allowing for controlling both oxygen and hydrogen molar flow rates with precision.

When the PEM cell is configured to function as a cogeneration unit, the study reveals its capacity to achieve optimal cooling water thermal parameters. This facilitates the concurrent generation of both heat and electrical power, a testament to the cell's versatility and efficiency. Theoretical analyses deduce that the thermal inertia of adjoining unheated rooms plays a significant role in the overall thermal balance, mainly governed by the

heat transfer coefficients, and the physical characteristics of the walls.

The research highlights the stabilizing role of the proportional-integral-derivative (PID) regulator in maintaining the cooling water supply to the fuel cell. This regulator effectively mitigates minor fluctuations induced by the building's heating system thermostat, ensuring consistent operational conditions.

The paper further delves into the thermal implications of unheated rooms on the overall heat loss in heated spaces, advocating for the strategic insulation of these areas. This insight holds particular relevance for older buildings that may lack modern insulation standards, suggesting potential retrofitting solutions to enhance their energy efficiency.

In conclusion, this work not only charts new territory in the field of building heating systems but also sets forth a comprehensive roadmap for future research. It calls for an in-depth exploration into areas such as membrane efficiency, advanced control strategies, and the integration of renewable energy sources. This forward-thinking perspective holds the promise of harnessing the full potential of PEM fuel cell technology, potentially leadinga transformative shift in the landscape of heating technology.

References

[1] Nehrir, M., & Wang, C. (2009). *Modeling and control of fuel cells*. IEEE Press, John Wiley & Sons, Inc.

[2] Spiegel, C. (2008). *PEM fuel cell modeling and simulation using MATLAB*. Academic Press.

[3] Abdin, Z., Webb, M. C., & Gray, A. (2016). PEM fuel cell model and simulation in MATLAB/Simulink based on physical parameters. *Energy*, 116, 1131–1144. doi: 10.1016/j.energy.2016.05.096

[4] Taner, T. (2018). Energy and exergy analyze of PEM fuel cell: A case study of modeling and simulations. *Energy*, 143, 284–294. doi: 10.1016/j.energy.2017.10.102

[5] Taner, T. (2021). The novel and innovative design with using H2 fuel of PEM fuel cell: Efficiency of thermodynamic analyze. *Fuel*, 302, 121109. doi: 10.1016/j.fuel.2021.121109

[6] Naqvi, S.A.H., Taner, T., Ozkaymak, M., & Hafiz, M.A. (2022). Hydrogen production through alkaline electrolyzers: A techno-economic and enviro-economic analysis. *Chemical Engineering and Technology*, 46(3), 474–481. doi: 10.1002/ceat.202200234

[7] Taner, T., Naqvi, S.A.H., & Ozkaymak, M. (2019). Techno-economic analysis of a more efficient hydrogen generation system prototype: A case study of PEM electrolyzer with Cr-C coated SS304 bipolar plates. *Fuel Cells*. doi: 10.1002/fuce.201700225

[8] Sudarshan, L.C., & Dhananjay, T.B. (2017). Modeling and performance evaluation of PEM fuel cell by controlling its input parameters. *Energy*, 138, 437–445. doi: 10.1016/j.energy.2017.07.063

[9] Mingruo, H., Anzhong, G., Minghua, W., Xinjian, Z., & Lijun, Y. (2004). Three dimensional, two phase flow mathematical model for PEM fuel cell: Part I. Model development. *Energy Conversion and Management*, 45, 1861–1882. doi: 10.1016/j.enconman.2003.09.009

[10] Ziogou, C., Voutetakis, S., Papadopoulou, S., & Georgiadis, M.C. (2011). Modeling, simulation and experimental validation of a PEM fuel cell system. *Computers and Chemical Engineering*, 35, 1886–1900. doi: 10.1016/j.compchemeng.2010.11.018

[11] Vida, M., & Gholamreza, K. (2012). Dynamic modeling, optimization and control of power density in a PEM fuel cell. *Applied Energy*, 93, 98–105. doi: 10.1016/j.apenergy.2011.12.067

[12] Waseem, S., & Ghait, W. (2015). Modeling and analysis of renewable PEM fuel cell system. In *International Conference on Technologies and Materials for Renewable Energy, Environment and Sustainability, TMREES15*. *Energy Procedia*, 74, 87–101. doi: 10.1016/j.egypro.2015.07.506

[13] Horng-We, W. (2016). A review of recent development: Transport and performance modeling of PEM fuel cells. *Applied Energy*, 165, 81–1062. doi: 10.1016/j.apenergy.2015.12.011

[14] MathWorks. (n.d.). *Simscape Electrical*. https://uk.mathworks.com/products/simscape-electrical.html [accessed 1 Sept. 2023]

[15] Capizzi, G., Sciuto, G.L., Cammarata, G., & Cammarata, M. (2017). Thermal transients simulations of a building by a dynamic model based on thermal-electrical analogy: Evaluation and implementation issue. *Applied Energy*, 199, 323–334. doi: 10.1016/j.apenergy.2017.05.099

[16] Mikielewicz, J. (1995). *Modeling of thermal and flow processes*. Maszyny Przepływowe, vol. 17, Ossolineum, Wrocław (in Polish).

[17] Charun, H. (2005). *Fundamentals of energy management. Part 2, Examples of application*. Wydawnictwo Politechniki Koszalińskiej, Koszalin (in Polish).

[18] Song, B., Bai, L., & Yang, L. (2022). Analysis of the long-term effects of solar radiation on the indoor thermal comfort in office buildings. *Energy*, 247, 123–499. doi: 10.1016/j.energy.2022.123499

[19] Wonorahardjo, S., Sutjahja, I., Mardiyati, Y., Andoni, H., Achsani, A.R., Steven, S., Dixon, T., Ekrem, T., Müslüm, A., & Rahmah, N. (2022). Effect of different building façade systems on thermal comfort and urban heat island phenomenon: An experimental analysis. *Building and Environment*, 217(12b), 109063. doi: 10.1016/j.buildenv.2022.109063

[20] Wu, J., Li, X., Yang, L., Yan, Y., & Tu, J. (2020). A PMV-based HVAC control strategy for office rooms subjected to solar radiation. *Building and Environment*, 177, 106–863. doi: 10.1016/j.buildenv.2020.106863

[21] Mao, N., Hao, J., He, T., Song, M., Xu, Y., & Deng, S. (2019). PMV-based dynamic optimization of energy consumption for a residential task/ambient air conditioning system in different climate zones. *Renewable Energy*, 142, 41–54. doi: 10.1016/j.renene.2019.04.118

[22] Buyak, N., Bilous, I., Pavlenko, A., Sapunov, A., Biriukov, D., & Dashenko, V. (2023). Dynamic interdependence of comfortable thermal conditions and energy efficiency increase in a nursery school building for heating and cooling period. *Energy*, 283, 129076. doi: 10.1016/j.energy.2023.122195

[23] Matysko, R., & Dyczkowska, M. (2018). Thermal dynamics of a building. *Transactions of the Institute of Fluid-Flow Machinery*, 141, 31–40.

Co-published by
Institute of Fluid-Flow Machinery
Polish Academy of Sciences
Committee on Thermodynamics and Combustion
Polish Academy of Sciences

http://www.imp.gda.pl/archives-of-thermodynamics/

Evaluation of degradation factor effect on solar panels performance after eight years of life operation

Ali Hussein Obaid[a], Emad Jaleel Mahdi[a], Isam Azeez Hassoon[a], Hussein Fawzi Hussein[b*], Adil Abd Al-Sahib Jasime[a], Ammar Noori Jafarf[a], Ali Sabih Abdulghanig[a]

[a]Ministry of Science and Technology, Directorate of Environment and Renewable Energy, Energy Management Center, 55509 Al-Jadriya, Iraq
[b]Ministry of Science and Technology, Directorate of Materials Researches, Advanced Materials Research Center, 55509 Al-Jadriya, Iraq
*Corresponding author email: husseinalaubi@live.co.uk

Received: 25.03.2024; revised: 07.05.2024; accepted: 12.06.2024

Abstract

Most high-quality solar panel products suffer from performance degradation at an annual rate of 0.4–0.5% per year during their specified normal operational life of 25–30 years. This percentage increases in areas with hot climates and roof photovoltaic systems and varies according to the quality, guarantee and reliability of the solar panel manufacturers. The aim of this research is to assess the degradation rates of solar panels in the city of Baghdad and to determine their impact on the investment feasibility of residential systems under hot climatic conditions. In this research, an evaluation of performance of photovoltaic solar panels working in a 2 kWp system connected to the electrical grid was done under the operational climatic conditions in the evaluation area (Baghdad, Iraq). The degradation rate of all photovoltaic system modules during the operation time from 2015–2023 is equal to 4.74% (0.593% / year). For comparison, a new monocrystalline solar panel of power 185.94 Wp with an old solar panel of monocrystalline type of power 183.33 Wp (which previously was installed in 2015) were installed at the same tilt angle of 30°, and evaluated during the operation months starting in March and ending in November of the year 2023. The degradation rates per year of an aged solar panel were determined to range from 0.441% to 0.850%, with an average value of 0.788% per year. After undergoing a correction process to align the maximum power values of the old and new solar panels, the corrected degradation rates per year values ranged from 0.391% to 0.684% per year, with an average value of 0.621% per year, which closely matches the degradation rate of all photovoltaic system modules at 0.593% per year.

Keywords: Solar panel performance; Evaluation of PV; PV operational life; Panel degradation rate

Vol. 45(2024), No. 3, 221–226; doi: 10.24425/ather.2024.151223

Cite this manuscript as: Obaid, A.H., Mahdi, E.J., Hassoon, I.A., Hussein, F.H., Jasime, A.A.A-S., Jafarf, A.N., & Abdulghanig, A.S. Evaluation of degradation factor effect on solar panels performance after eight years of life operation. *Archives of Thermodynamics*, 45(3), 221–226.

1. Introduction

The topic of evaluating the performance of photovoltaic systems (PV), specifically the performance of solar panels during their operational life has become extremely important to focus an increased attention of photovoltaic solar energy researches. When investing in the solar photovoltaic energy field, many criteria must be taken into account to ensure the system's performance reliability. The most important criterion that specialists in the solar photovoltaic energy field care about is the solar panel's degradation, which reduces their production power and is included in the panel's nameplate [1,2]. Solar panel manufac-

Nomenclature

$\% D.R$ – degradation rate in the performance of the solar panels, %
$I_{max.}$ – maximum current, A
$I_{s.c.\ .}$ – current of short circuit, A
$P_{max\ (2015)}$ – max. output power of solar panels measured in 2015, W
$P_{max\ (2023)}$ – max. output power of solar panels measured in 2023, W
$P_{max\ (new)}$ – measured max. output power of new solar panel, W
$P_{max\ (old)}$ – measured max. output power of old solar panel, W
V_{max} – maximum voltage, V
$V_{o.c.}$ – voltage of open circuit, V

Abbreviations and Acronyms

CdTe – cadmium telluride
CIGS – copper indium gallium selenide
EVA – ethylene-vinyl acetate
PID – potential-induced degradation
PV – photovoltaic
UV – ultraviolet (radiation)

turers offer to their customers a warranty ranging from 25–30 years with about a 20% decrease in power. Recent studies have proven degradation rates of 0.6–0.7% annually [3].

Solar panel technology continues to develop until the degradation rate has commonly reached below 1% a year. Currently, despite the development of technology, rates of deterioration are inevitable. However, work can be done to reduce and slow down the degradation rate by choosing the solar panel's technical quality and providing appropriate environmental conditions for the solar system operation [4]. The typical degradation rate of silicon cell technology (Mono-Si, Poly-Si) is 0.4–0.5% / year, for thin film cell technologies (CdTe, CIGS) it is 0.5% / year. The appropriate degradation rate power for mono-crystalline silicon cells with back contact technology can be considered about 0.35% / year [5].

For example, the degradation rate in the solar panel's capacity is 0.8% in year two, which means that the solar panel's productivity will be at a rate of 99.2% of their total output; by the end of the 25-year operating life, the productivity rate will be 82.5%. The most durable solar panel with a degradation rate of 0.5% will have a productivity of about 87.5% of its production power upon its first installation [6]. To estimate the solar panel productivity of any system, one can simply multiply the degradation rate by the number of years required and subtract the result from the total value of 100% [7]. When the topic relates to the solar panel's degradation rate concept, it is necessary to look at the solar panel's performance warranty. Typically, a performance warranty is a 25-year warranty and will guarantee that your solar panels maintain a certain percentage of their original output each year. The panel's performance warranty period varies depending on the quality of the product, and this gives an idea of the solar panel's operational life [8,9].

Since solar panels installed in outdoor locations will be exposed to various and changing weather conditions such as solar radiation, high temperature, humidity, rain, etc., which have a significant effect on their performance over time [10,11]. Aging degradation is one of the main reasons for the decrease in solar panel power [12]. The first type of deterioration that affects the solar panel is the potential-induced degradation (PID). This deterioration occurs between the conductive solar panel parts and the grounding system as a result of the high voltage between conductive parts [13,14]. The second degradation that occurs in the solar panel is due to exposure to light that contains ultraviolet rays, which causes solar cell discoloration. This is known as light degradation [15,16].

Environmental factors contribute to increasing the solar panel's degradation, including high temperature, humidity, wind, and mechanical stress, which work to change the solar panel's physical specifications [17,18]. Common physical effects caused by environmental conditions, as previous studies have shown, are discoloration, corrosion, delamination, and cracking. Corrosion between solar cells and connections is caused by atmospheric humidity and leakage current. The delamination observed between the solar cells and the encapsulation material of solar panels is attributed to metal corrosion induced by high humidity levels. [19]. Optical transmission losses have an impact on the solar panel's productivity due to the discoloration caused by ultraviolet rays. Other effects that affect solar panel's productivity are dust storms and lightning strikes that strike the solar panel's metal parts [20].

There are several ways to diagnose defects in solar panels, such as visual inspection, conductivity testing, electrical insulation, and electrical luminescence, in addition to electrical specifications [21]. The solar panel's electrical specifications are tested individually to diagnose the current-voltage curve under normal solar radiation by using a curve tracer device. Appearance defects in the solar panel, such as cracks and discoloration for solar panel parts, can be diagnosed by visual inspection. The electroluminescence test is an important preliminary test to prevent the development of cell defects by applying a forward bias to the solar panel [22]. Defects in the packaging between the solar cells and the front glass cover with the filling glue material and defects in the back packaging with ethylene-vinyl acetate (EVA) cause discoloration in the solar panel. The EVA changes colour from light yellow to dark brown as the discoloration progresses [23].

The solar panel emits a low-intensity emission due to the electron-hole pair recombination. This emission is within the spectral region near the infrared 1000–1300 nm, which can be detected by a thermal camera [24]. The test environment varies according to the type of test. Electroluminescence test requires a dark environment within indoor tests, but it can be conducted in outdoor field conditions [25]. Thermal camera is used to inspect solar panel defects in large-scale solar power plants, by diagnosing temperature changes in the solar panels at the plant. Visual inspection is an effective method for identifying defects in a solar panel and has been supported by numerous research studies [26]. The US National Renewable Energy Laboratory announced in its 2017 report that degradation defects common in solar panels for the last 10 years were hotspots (33%) followed by ribbon discoloration (20%), glass breakage (12%), en-

capsulate discoloration (10%), cell breakage (9%) and potential-induced degradation PID (8%) [27].

The reason for these cases are the stresses to which the solar panel is exposed, in addition to humidity, ultraviolet (UV) radiation, temperature, wind, hail, and high system voltages as well as other factors such as broken interconnects, hot spots, corrosion, encapsulate discoloration and delamination [28]. The cause of solar panel failure is mainly related to the construction, packaging, design and operating environment [29]. Hot spots in the solar panel damage the solar panel as a result of the high solar cell temperatures due to the external shadow and the shadow that is formed as a result of interference between the solar cells within the solar panel or intermittent contacts between the cells and mismatch between them [30,31]. In this research, the degradation of the solar panel was measured after eight years of exposure of the solar panel to different conditions within a site of the city of Baghdad.

2. Materials and methods

In this research, an evaluation of the performance of solar panels for a photovoltaic system with a maximum power of about 2kWp connected to the electrical grid was conducted using the performance analyzer device (PV Analyzer model Solmetric PVA-600) during the year 2023 to evaluate the degradation occurring in the power produced by the solar panels of the system over eight years after their installation in the field.

Note that, this system was installed on the roof of the building at a Baghdad site, at a constant tilt angle throughout the year of 30˚. The practical part included the following steps:

- The performance of the solar panels of the system as a whole was evaluated on 8/14/2023 and compared with the performance of the system's solar panels previously measured on 8/12/2015 according to the results documented in our previous research [17]. The solar panels of the system are shown in Fig. 1.

Fig. 1. The solar panels of the system 2 kWp.

- The evaluation results which were recorded previously in August 2015 and currently in August 2023 (after eight years of life operation of the system) by PV Analyzer model Solmetric PVA-600, were documented as shown in Fig. 2.
- To reinforce the obtained result in the second step, as shown in Fig. 3, a new solar panel with maximum power of 185.94 Wp (of monocrystalline type) with a fixed tilt angle of 30° was installed next to an old solar panel, also a product by the same factory, with maximum power of 183.33 Wp (of monocrystalline type), previously installed in 2015 at the same tilt angle.

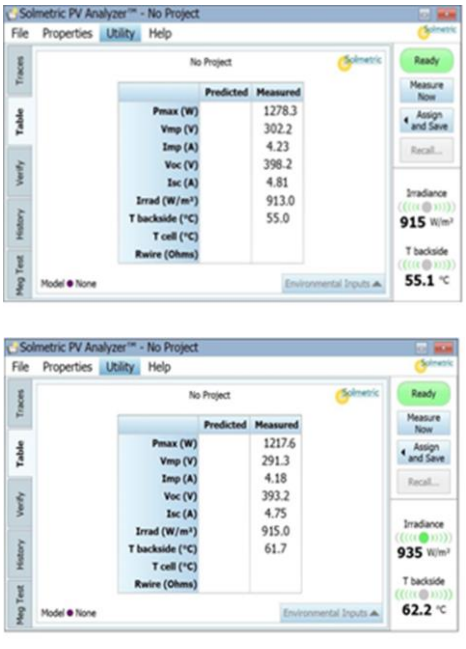

Fig. 2. System test results in August 2015 (a) and August 2023 (b) by PV Analyzer.

Fig. 3. New module and old module.

- After completing the installation of the new solar panel on the metal structure, performance evaluation readings were taken for the old and new solar panels at the same time by the performance analyzer device once every month, starting in March and ending in November of the year 2023.

The percentage of decrease in the total maximum output power of the solar panels of the system, which is called the degradation rate in the performance of the solar panels (% *D.R*) was calculated according to the following Eq. (1):

$$\%\, D.R \;= \frac{P_{\max\,(2015)} - P_{\max\,(2023)}}{P_{\max\,(2015)}} \times 100\ \%, \qquad (1)$$

where $P_{\max\,(2015)}$ and $P_{\max\,(2023)}$ denote the maximum output power of solar panels measured in 2015 and 2023, respectively.

Note that this slight difference in the maximum power values of the two solar panels and their dissimilarity is due to the tolerance imposed in the production of solar panels by the manufacturer. Table 1 explains technical specifications of the two solar panels at standard conditions, which were used in this research.

Table 1. Standard conditions test of the two solar panels.

Module specifications	PV Module (2015)	PV Module (2023)
P_{max}	183.33 W	185.94 W
$V_{o.c.}$	45.19 V	45.37 V
$I_{s.c.}$	5.41 A	5.51 A
V_{max}	36.43 V	36.62 V
I_{max}	5.03 A	5.8 A
Max. system voltage	1000 $V_{d.c.}$	1000 $V_{d.c.}$

3. Results and discussion

The obtained results from the evaluating process of the performance of all the system's solar panels via the performance analyzer device were documented for the years 2023 and 2015 in the same month in August, as shown in Fig. 2. As found from Fig. 2 using Eq. (1), the performance degradation rate of the solar panels (% *D.R*) for the total PV system during eight years of the system's operational life was calculated at 4.74%, and therefore the annual performance degradation rate of the system solar panels was equal to 0.593% / year (see Table 2), due to the system's panels being exposed to fluctuating environmental factors and continuous exposure to influential ultraviolet rays during this period.

Table 2. % *D.R* for the total PV system during eight years.

Time	P_{max} (total modules)	Total % *D.R* (8 years)	% *D.R*/year
12/08/2015	1278.3 W	4.74%	0.593%
14/08/2023	1217.6 W		

Figure 4 shows the incident solar radiation rates every month, starting in March and ending in November, whereas Fig. 5 exhibits the maximum output power from the two solar panels (new and old) recorded via the performance analyzer device for these months.

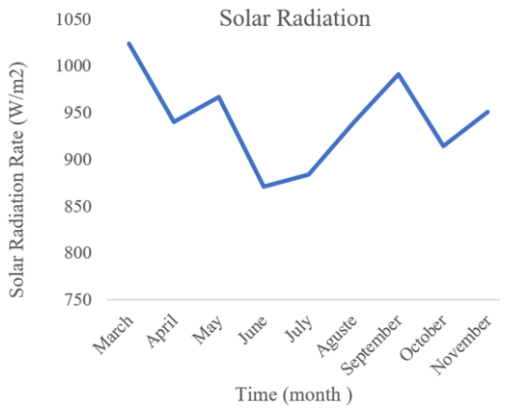

Fig. 4. The change of solar radiation rate with months.

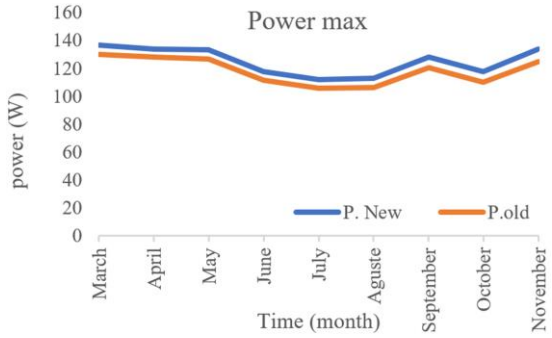

Fig. 5. Maximum output power of two solar panels.

The degradation rate % *D.R* and % *D.R* / year for the old solar panel which is selected from the PV system (of 2 kWp), was calculated monthly using Eq. (2):

$$\%\, D.R \;= \frac{P_{\max(new)} - P_{\max(old)}}{P_{\max(new)}} \times 100\ \%, \qquad (2)$$

where $P_{max\ (new)}$ and $P_{max\ (old)}$ represent the measured maximum output power of the new and old solar panel, respectively.

Due to the production tolerance, and the discrepancy between the maximum power value of the new and old solar panels – 185.94 Wp for the new panel and 183.33 Wp for the old one (based on the available solar panels) – we observe a lack of equality in the maximum power output

The calculation was done to correct the values of practical % *D.R* accurately by multiplying the maximum power results of the old solar panel by a factor equal: 185.94 / 183.33 = 1.014. A correction was made for the results of the performance degradation values of the old solar panel, which should be accurate to a very high degree. The process of correcting values of % *D.R* is shown in Fig. 6.

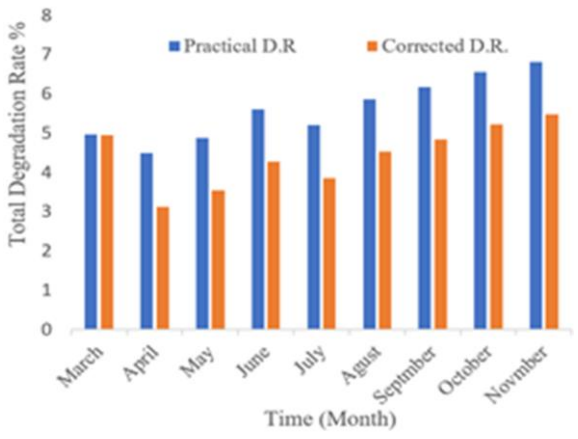

Fig. 6. The total degradation rate.

Figure 6 illustrates the annual performance degradation rate of the old solar panel (2015) over eight years of its operational life in the PV system compared to the performance of the new solar panel (2023). The obtained value of % *D.R* / year during the operation months ranged from 0.441–0.850% / year and the average of these values equal to 0.788%. The % *D.R* per year

values, after undergoing a correction process to align with the maximum power values of the selected solar panels for real evaluation, ranged from 0.391% to 0.684% per year, with an average value of 0.621% per year.

The average value of the % *D.R* per year, after correction (*0.621% per year), for the aged solar panel used under the operational climatic conditions in the evaluation area (Baghdad, Iraq) closely aligns with the performance degradation rate of all PV system solar panels, which was 0.593% per year. These values were deemed logical and consistent with the natural rates of performance degradation for panels of this type, specifically manufactured using monocrystalline technology, as indicated by previous research mentioned in the theoretical framework of this study.

In general, the annual performance degradation rate % *D.R* / year of PV solar panels varies depending on the classification of the solar cell preparation technology, the guarantee, the brand of solar panel you purchase, environmental factors and climatic conditions that are exposed to it. These factors pose a major challenge to the generated electrical energy by PV solar panels. Finally, solar panel with low degradation rates will produce more energy and will be considered as the better one before purchasing and using it in PV solar systems. Proper maintenance of your solar panel system can result in a decrease in the annual rate of solar panel degradation and prolong their life (25–30 years), which includes regularly inspecting your solar panels, and exposed wires checking, and keeping your solar panels clean, free of dirt and debris, and away from the shade of trees.

4. Conclusions

In this research, the evaluation of PV solar panels performance 2 kWp connected to the electrical grid. The performance degradation rate (% *D.R*) of all PV system modules (2 kWp) over eight years of operation, from 2015 to 2023, was calculated for a previous performance evaluation conducted in August 2015. It is equal to % *D.R* = 4.74%, or 0.593% per year. The calculated values of % *D.R* per year for the old solar panel during the operational months ranged from 0.441% to 0.850% per year for each month, with an average of 0.788% per year, While the obtained values of % *D.R*/year – corrected after a correction process ranged from 0.391–0.684%/year with the average value equal to *0.621%/ year. The corrected average value of % *D.R*/year for the used old solar panel is very close to the value of %*D.R*/year of all PV system modules (0.593% / year) under the operational climatic conditions in the evaluation area (Baghdad, Iraq).

References

[1] Aboagye, B., Gyamfi, S., Ofosu, E. A., & Djordjevic, S. (2021). Degradation analysis of installed solar photovoltaic (PV) modules under outdoor conditions in Ghana. *Energy Reports*, 7, 6921–6931. doi: 10.1016/j.egyr.2021.10.097

[2] Aboagye, B., Gyamfi, S., Ofosu, E. A., & Djordjevic, S. (2022). Characterisation of degradation of photovoltaic (PV) module technologies in different climatic zones in Ghana. *Sustainable Energy Technologies and Assessments*, 52, 102034. doi: 10.1016/j.seta.2022.102034

[3] Aghaei, M., Fairbrother, A., Gok, A., Ahmad, S., Kazim, S., Lobato, K., & Kettle, J. (2022). Review of degradation and failure phenomena in photovoltaic modules. *Renewable and Sustainable Energy Reviews*, 159, 112160. doi: 10.1016/j.rser.2022.112160

[4] Campbell, J., Zemen, Y., Richardson, B., & Striner, B. (2012). Photovoltaic module performance and degradation as compared in distinct climatic regions. *2012 38th IEEE Photovoltaic Specialists Conference* (pp. 001250–001255). 03-08 June, Austin, USA. doi: 10.1109/PVSC.2012.6317829

[5] Carr, A.J., & Pryor, T.L. (2004). A comparison of the performance of different PV module types in temperate climates. *Solar energy*, 76(1–3), 285–294. doi: 10.1016/j.solener.2003.07.028

[6] Da Fonseca, J.E.F., de Oliveira, F.S., Prieb, C.W.M., & Krenzinger, A. (2020). Degradation analysis of a photovoltaic generator after operating for 15 years in southern Brazil. *Solar Energy*, 196, 196–206. doi: 10.1016/j.solener.2019.12.002

[7] Dos Santos, S.A.A., Torres, J.P.N., Fernandes, C.A., & Lameirinhas, R.A.M. (2021). The impact of aging of solar cells on the performance of photovoltaic panels. *Energy Conversion and Management: X*, 10, 100082. doi: 10.1016/j.ecmx.2021.100082

[8] Dunlop, E.D., & Halton, D. (2006). The performance of crystalline silicon photovoltaic solar modules after 22 years of continuous outdoor exposure. *Progress in photovoltaics: Research and Applications*, 14(1), 53–64. doi: 10.1002/pip.658

[9] Gyamfi, S., Aboagye, B., Peprah, F., & Obeng, M. (2023). Degradation analysis of polycrystalline silicon modules from different manufacturers under the same climatic conditions. *Energy Conversion and Management: X*, 20, 100403. doi: 10.1016/j.ecmx.2023.100403

[10] Herrmann, W., Bogdanski, N., Reil, F., Köhl, M., Weiss, K.A., Assmus, M., & Heck, M. (2010). PV module degradation caused by thermomechanical stress: real impacts of outdoor weathering versus accelerated testing in the laboratory. In *Reliability of Photovoltaic Cells, Modules, Components, and Systems III*, Vol. 7773 (pp. 145–153). SPIE. doi: 10.1117/12.862616

[11] Huang, C., & Wang, L. (2018). Simulation study on the degradation process of photovoltaic modules. *Energy conversion and management*, 165, 236-243. DOI: 10.1016/j.enconman.2018.03.087

[12] Ibne Mahmood, F., & TamizhMani, G. (2023). Impact of different backsheets and encapsulant types on potential induced degradation (PID) of silicon PV modules. *Solar Energy*, 252, 20-28. doi: 10.1016/j.solener.2023.01.048

[13] Ishii, T., & Masuda, A. (2017). Annual degradation rates of recent crystalline silicon photovoltaic modules. *Progress in Photovoltaics: Research and Applications*, 25(12), 953–967. doi: 10.1002/pip.2914

[14] Jordan, D.C., & Kurtz, S.R. (2013). Photovoltaic degradation rates—an analytical review. *Progress in photovoltaics: Research and Applications*, 21(1), 12–29. doi: 10.1002/pip.1182

[15] Karahüseyin, T., & Abbasoğlu, S. (2022). Performance Loss Rates of a 1 MWp PV Plant with Various Tilt Angle, Orientation and Installed Environment in the Capital of Cyprus. *Sustainability*, 14(15), 9084. doi: 10.3390/su14159084

[16] Kim, J., Rabelo, M., Padi, S.P., Yousuf, H., Cho, E.C., & Yi, J. (2021). A review of the degradation of photovoltaic modules for life expectancy. *Energies*, 14(14), 4278. doi: 10.3390/en14144278

[17] Hussain, M.T., & Mahdi, E.J. (2018). Assessment of Solar Photovoltaic Potential in Iraq. *Journal of Physics: Conference Series*, 1032, 012007. The Sixth Scientific Conference "Renewable Energy and its Applications" 21–22 February, Karbala, Iraq. doi: 10.1088/1742-6596/1032/1/012007

[18] Koch, S., Weber, T., Sobottka, C., Fladung, A., Clemens, P., & Berghold, J. (2016). Outdoor electroluminescence imaging of crystalline photovoltaic modules: Comparative study between manual ground-level inspections and drone-based aerial surveys. In *32nd European Photovoltaic Solar Energy Conference and Exhibition* (pp. 1736–1740), 20-24 June, Munich, Germany. doi: 10.4229/EUPVSEC20162016-5BV.4.33

[19] Koester, L., Lindig, S., Louwen, A., Astigarraga, A., Manzolini, G., & Moser, D. (2022). Review of photovoltaic module degradation, field inspection techniques and techno-economic assessment. *Renewable and Sustainable Energy Reviews*,165, 112616. doi: 10.1016/j.rser.2022.112616

[20] Lillo-Sánchez, L., López-Lara, G., Vera-Medina, J., Pérez-Aparicio, E., & Lillo-Bravo, I. (2021). Degradation analysis of photovoltaic modules after operating for 22 years. A case study with comparisons. *Solar Energy*, 222, 84-94. doi: 10.1016/j.solener.2021.04.024

[21] Luceño-Sánchez, J.A., Díez-Pascual, A.M., & Peña Capilla, R. (2019). Materials for photovoltaics: State of art and recent developments. *International Journal of Molecular Sciences*, 20(4), 976. doi: 10.3390/ijms20040976

[22] Luo, W., Clement, C.E., Khoo, Y.S., Wang, Y., Khaing, A.M., Reindl, T., & Pravettoni, M. (2021). Photovoltaic module failures after 10 years of operation in the tropics. *Renewable Energy*, 177, 327–335. doi: 10.1016/j.renene.2021.05.097

[23] Luo, W., Khoo, Y.S., Hacke, P., Naumann, V., Lausch, D., Harvey, S.P., & Ramakrishna, S. (2017). Potential-induced degradation in photovoltaic modules: a critical review. *Energy and Environmental Science*, 10(1), 43–68. doi: 10.1039/C6EE03375C

[24] Ndiaye, A., Charki, A., Kobi, A., Kébé, C.M., Ndiaye, P.A., & Sambou, V. (2013). Degradations of silicon photovoltaic modules: A literature review. *Solar Energy*, 96, 140–151. doi: 10.1016/j.solener.2013.07.005

[25] Piliougine, M., Oukaja, A., Sánchez-Friera, P., Petrone, G., Sánchez-Pacheco, F. J., Spagnuolo, G., & Sidrach-de-Cardona, M. (2021). Analysis of the degradation of single-crystalline silicon modules after 21 years of operation. *Progress in Photovoltaics: Research and Applications*, 29(8), 907–919. doi: 10.1002/pip.3392

[26] Raghuraman, B., Lakshman, V., Kuitche, J., Shisler, W., Tamizh-Mani, G., & Kapoor, H. (2006). An overview of SMUD's outdoor photovoltaic test program at Arizona State University. *Conference Record of the 2006 IEEE 4th World Conference on Photovoltaic Energy Conference*, Vol. 2 (pp. 2214–2216). 7–12 May, Waikoloa, USA. doi: 10.1109/WCPEC.2006.279497

[27] Reis, A.M., Coleman, N.T., Marshall, M.W., Lehman, P.A., & Chamberlin, C.E. (2002). Comparison of PV module performance before and after 11-years of field exposure. *Conference Record of the Twenty-Ninth IEEE Photovoltaic Specialists Conference* (pp. 1432–1435). 20-24 May, New Orleans, USA. doi: 10.1109/PVSC.2002.1190878

[28] Sander, M., Dietrich, S., Pander, M., Ebert, M., & Bagdahn, J. (2013). Systematic investigation of cracks in encapsulated solar cells after mechanical loading. *Solar Energy Materials and Solar Cells*, 111, 82–89. doi: 10.1016/j.solmat.2012.12.033

[29] Santhakumari, M., & Sagar, N. (2019). A review of the environmental factors degrading the performance of silicon wafer-based photovoltaic modules: Failure detection methods and essential mitigation techniques. *Renewable and Sustainable Energy Reviews*, 110, 83–100. doi: 10.1016/j.rser.2019.04.064

[30] Tsanakas, J.A., Ha, L., & Buerhop, C. (2016). Faults and infrared thermographic diagnosis in operating c-Si photovoltaic modules: A review of research and future challenges, *Renewable and Sustainable Energy Reviews*, 62, 695–709. doi: 10.1016/j.rser.2016.05.002

[31] Virtuani, A., Caccivio, M., Annigoni, E., Friesen, G., Chianese, D., Ballif, C., & Sample, T. (2019). 35 years of photovoltaics: Analysis of the TISO-10-kW solar plant, lessons learnt in safety and performance—Part 1. *Progress in Photovoltaics: Research and Applications*, 27(4), 328–339. doi: 10.1002/pip.3098

Contents

Selected papers from the 25th Jubilee Congress of Thermodynamicists, 11–14 September, Gdańsk, Poland

Other papers

Contents (*cont'd*)